IAEA nuclear fusion

REVIEW • OPEN ACCESS

Scrape-off layer and divertor physics: Chapter 5 of the special issue: on the path to tokamak burning plasma operation

To cite this article: K. Krieger *et al* 2025 *Nucl. Fusion* **65** 043001

OPEN ACCESS
IOP Publishing | International Atomic Energy Agency Nuclear Fusion

Nucl. Fusion **65** (2025) 043001 (151pp) https://doi.org/10.1088/1741-4326/adaf42

Scrape-off layer and divertor physics

Chapter 5 of the special issue: on the path to tokamak burning plasma operation

K. Krieger[1,*], **S. Brezinsek**[2,3], **J.W. Coenen**[2,4], **H. Frerichs**[4], **A. Kallenbach**[1], **A.W. Leonard**[5], **T. Loarer**[6], **S. Ratynskaia**[7], **N. Vianello**[8,9], **N. Asakura**[10], **M. Bernert**[1], **D. Carralero**[11], **R. Ding**[12], **D. Douai**[6], **T. Eich**[1,13], **Y. Gasparyan**[14], **A. Hakola**[15], **Y. Hatano**[16], **M. Jakubowski**[17], **M. Kobayashi**[18], **S. Krasheninnikov**[19], **S. Masuzaki**[18], **T. Nakano**[10], **R. Neu**[1], **R.A. Pitts**[20], **J. Rapp**[21], **K. Schmid**[1], **O. Schmitz**[4], **D. Tskhakaya**[22], **L. Wang**[12], **T. Wauters**[20] and **S. Wiesen**[2,23]

[1] Max-Planck-Institut für Plasmaphysik, 85748 Garching, Germany
[2] Forschungszentrum Jülich, Institut für Energie & Klimaforschung—Plasmaphysik, 52425 Jülich, Germany
[3] Faculty of Mathematics and Natural Sciences, Heinrich Heine University Düsseldorf, 40225 Düsseldorf, Germany
[4] University of Wisconsin Madison, Madison, WI 53706, United States of America
[5] General Atomics, San Diego, CA 92186, United States of America
[6] CEA, IRFM, 13108 Saint Paul Lez Durance, France
[7] KTH Royal Institute for Technology, Space & Plasma Physics, 10044 Stockholm, Sweden
[8] Consorzio RFX (CNR, ENEA, INFN, Università di Padova, Acciaierie Venete SpA), C.so Stati Uniti 4, 35127 Padova, Italy
[9] Istituto per la Scienza e la Tecnologia dei Plasmi, CNR, Padova, Italy
[10] National Institutes for Quantum Science and Technology (QST), Naka, Ibaraki 311-0193, Japan
[11] Laboratorio Nacional de Fusión, CIEMAT, Madrid 28040, Spain
[12] Institute of Plasma Physics, Chinese Academy of Sciences, Hefei 230031, China
[13] Commonwealth Fusion Systems, Devens, MA 01434, United States of America
[14] National Research Nuclear University MEPhI, 115409 Moscow, Russian Federation
[15] VTT, Espoo 02044, Finland
[16] Tohoku University, Sendai 980-8579, Japan
[17] Max-Planck-Institut für Plasmaphysik, 17491 Greifswald, Germany
[18] National Institute for Fusion Science, Toki, Gifu 5095292, Japan
[19] University of California San Diego, Dept Mechanical & Aeronautics Engineering, La Jolla, CA 92093, United States of America
[20] ITER Organization, Route de Vinon-sur-Verdon, 13067 St Paul Les Durance, France
[21] Oak Ridge National Laboratory, Oak Ridge, TN 37831, United States of America
[22] Institute of Plasma Physics of the Czech Academy of Sciences, 18200 Prague 8, Czech Republic
[23] DIFFER—Dutch Institute for Fundamental Energy Research, De Zaale 20, 5612 AJ Eindhoven, Netherlands

---

[*] Author to whom any correspondence should be addressed.

1741-4326/25/043001+151$33.00 Printed in the UK

E-mail: karl.krieger@ipp.mpg.de

Received 19 June 2024, revised 15 December 2024
Accepted for publication 28 January 2025
Published 10 March 2025

Abstract

Since the publication of the review *Progress in the ITER Physics Basis* (PIPB) in 2007, significant progress has been made in understanding the processes at the plasma-material interface. This review, part of the ITPA Nuclear Fusion Special Issue *On the Path to Burning Plasma Operation*, presents these developments, focusing on key areas such as the physics of plasma exhaust, plasma-material interactions, and the properties of plasma-facing materials and their evolution under plasma exposure. The coordinated efforts of the *ITPA Topical Group on Scrape-Off Layer and Divertor Physics* (DivSOL) have been instrumental in identifying and addressing critical research and development issues in numerous collaborative experimental and modelling projects.

This paper is part of the Special Issue: *On the Path to Tokamak Burning Plasma Operation: A collection of papers prepared by the ITPA Topical Physics Groups reviewing progress in the development of the physics basis for burning plasma operation*.

Keywords: plasma boundary, plasma exhaust, plasma-wall interaction, plasma-facing materials

(Some figures may appear in colour only in the online journal)

Contents

Glossary

0D	0-Dimensional.
1D	1-Dimensional.
2D	2-Dimensional.
3D	3-Dimensional.
2V	2-dimensional in Velocity space.
3V	3-dimensional in Velocity space.
ADAS	Atomic data and analysis structure (atomic database).
AGHS	Advanced gas handling system.
AUG	ASDEX upgrade.
AXUV	Absolute extreme ultra violet spectral range.
BG	BackGround (plasma).
BIXS	β-ray induced x-ray spectrometry.
CAD	Computer aided design.
CAPS	Chemically assisted physical sputtering.
CB	Cassette body.
CD$_4$	Deuterated methane.
CFC	Carbon fibre composite.
CMOD	Alcator C-Mod.
CPS	Capillary porous system.
CQ	Current quench (during a disruption).
CX	Charge exchange.
CXN	Charge exchange neutral atoms.
DAE	Differential-algebraic equation.
DBTT	Ductile to brittle transformation temperature.
DFT	Density functional theory.
DIVSOL	ITPA scrape-off-layer and divertor topical group.
DMS	Disruption mitigation system.
DSMC	Direct simulation Monte Carlo method.
DSOL	Joint research tasks of ITPA TG DivSOL.
DT	Deuterium tritium mix.
EBSD	Electron backscatter diffraction.
EC	Electron cyclotron.
ECH	Electron cyclotron heating.
ECR	Electron cyclotron resonance.
ECWC	Electron cyclotron wall cleaning.
ECRH	Electron cyclotron resonance heating.
EDA	Enhanced D-alpha (H-mode).
ELM	Edge localised mode.
EM	Electro–magnetic.
ETB	Edge transport barrier.
FIB	Focused ion beam.
FPO	Full power operation phase in ITER.
FSM	Free-streaming model (of ELM propagation).
FW	First wall.
FWP	First wall panel.
GDB	Glow discharge boronisation.
GDC	Glow discharge cleaning.
GPI	Gas puff imaging diagnostic.
H-mode	Plasma high-confinement operation mode.
HFS	High field side.
HFSHD	High field side high density.
HHF	High heat flux.
HI	Hydrogen isotopes.
IBA	Ion beam analysis.
ICH	Ion cyclotron heating.
ICRF	Ion cyclotron resonance frequency.
ICRH	Ion cyclotron resonance heating.
ICWC	Ion cyclotron wall cleaning.
ILW	JET ITER Like wall configuration.
IPB	ITER physics base [1].
IR	Infrared spectral range.
ISP	Inner strike point.
IT	Inner target.
ITB	Internal transport barrier.
ITER	International Thermonuclear Experimental Reactor.
ITG	Ion-temperature-gradient.
ITPA	International Tokamak Physics Activity.
IWL	Inner-wall limited (discharge).
L-mode	Plasma high-confinement operation mode.
LCFS	Last closed flux surface.
LE	Leading edge (of a plasma facing component).
LFN	Large-scale fibre-form nanostructure.
LFS	Low-field side.
LH	Lower hybrid.
LIBS	Laser induced breakdown spectroscopy.
LID-QMS	Laser induced desorption QMS.
LIM	Limiter.
MARFE	Multifaceted asymmetric radiation from the edge.
MB	Monoblock.
MD	Molecular dynamics.
MHD	Magneto hydro dynamics.
NBI	Neutral beam injection.
NMR	Nuclear magnetic resonance.
NRA	Nuclear reaction analysis.
NTB	Nano tendril bundle.
OES	Optical emission spectroscopy.
OHS	Optical hot spots.
OMP	Outer mid-plane.
OSM	Onbion-skin model.
OSP	Outer strike point.
OT	Outer target.
PFC	Plasma facing component.
PFM	Plasma facing material.
PFPO	Pre fusion power operation (in ITER).
PFR	Private flux region.
PFS	Plasma facing surface.
PFU	Plasma facing unit.
PIC	Particle in cell modelling.
PIPB	Progress in the ITER physics basis [2].
PIXE	Proton induced x-ray emission spectroscopy.
PM	Post mortem.
PSI	Plasma-surface interactions.
PWI	Plasma-wall interactions.
QCE	Quasi continuous exhaust regime.
QCM	Quasi-coherent mode.
QH	Quiescent H-mode.
QMS	Quadrupole mass spectroscopy.
R&D	Research and development.
RBS	Rutherford backscattering spectroscopy.
RDW	Resistive drift waves.
RE	Runaway electron.
RF	Radio frequency.
RFA	Retarding field analyser.
RMP	Resonant magnetic perturbation.
SCL	Space charge limited.
SEM	Scanning electron microscopy.
SIMS	Secondary ion mass spectroscopy.
SMBI	Supersonic molecular beam injection.

SOL	Scrape-off layer.
SP	Strike point.
STEM	Scanning transmission electron microscope.
TDS	Thermal desorption spectroscopy.
TEM	Transmission electron microscopy.
TF	Toroidal field.
TG	Topical group.
TQ	Thermal quench during a disruption.
TS	Thomson scattering.
TZM	Titanium–zirconium–molybdenum alloy.
UDP	Upper dump plate.
UFO	Unknown flying object.
VDE	Vertical displacement event.
VIS	Visual spectral range.
VPS	Vacuum plasma spray.
W-CPS	Tungsten capillary system.
W-MB	Tungsten mono block.
W-PFC	Tungsten plasma facing component.
XPR	X-point radiator.
XPS	X-ray photo electron spectroscopy.
XRD	X-ray diffraction.
ZF	Zonal flow.

1. Introduction

Since the publication of the first *ITER Physics Basis* (IPB) in 1999 [1] and its update *Progress in the ITER Physics Basis* (PIPB) in 2007 [2], significant progress has been made in understanding the processes that determine the properties of the plasma edge region and the divertor, their influence on the power and particle exhaust, and the interaction of the plasma with the FW components[24].

This chapter of the ITPA Nuclear Fusion Special Issue presents the progress made since the publication of the PIPB in the main topical areas related to plasma edge properties, plasma exhaust and plasma wall interactions. Much of this progress has been achieved through the coordinated research activities of the ITPA Topical Group on SOL and Divertor Physics (DivSOL). The main objective of the Topical Group was to identify, in collaboration with the ITER Organisation, urgent research and development issues and to formulate joint tasks (DSOL) with dedicated experiment proposals to address and resolve these issues. Many of the publications cited in this chapter originate from presentations and discussions within these DSOL tasks.

It should be noted that, for the sake of brevity, many abbreviations and acronyms are used throughout this document. Due to the length of the text, it is not practical to rely solely on definitions at their first use. To avoid the reader having to search the entire manuscript for a definition, a Glossary of all abbreviations has been included at the beginning of the chapter. In addition, for reference, the main regions of a divertor tokamak plasma and the main plasma-facing wall components are indicated in figure 1 based on a CAD view of the ITER vessel. For an introduction to the field, the reader is referred to [6].

The extrapolation from today's medium-sized machines to ITER-sized thermonuclear devices relies on increasingly sophisticated simulation codes validated on the current devices. However, many principal parameters can be described by simple scaling laws. These include the scaling of the width of the plasma SOL and the resulting width of the plasma footprint at the divertor targets, the scaling of the energy density of the H-mode ELM transients at both the divertor targets and the FW, and the scaling of the energy densities at the FW components during disruptions and VDEs. For a detailed discussion of the latter, the reader is referred to section 3 in the chapter on *MHD, Disruptions and Control* [7].

For the plasma physical aspects of power and particle exhaust, the extrapolation to ITER-sized devices showed that in order to meet the thermo-mechanical boundary conditions imposed by the PFCs and materials, measures are required to control and mitigate both steady state and transient power loads, such as by plasma detachment in the divertor, the use of seeded impurities to distribute power loads over larger wall areas by volumetric radiation, the use of RMP coils to control plasma pedestal and ELM properties. This also includes the disruption avoidance and mitigation systems discussed in sections 3.2 and 3.4 of the chapter on *MHD, Disruptions and Control* [7].

With regard to the FW and the PFMs used, the main issues include the processes that determine the lifetime of the PFCs under both steady state and transient thermal and particle loads, in particular the erosion of wall material by incident plasma ions and atoms, the resulting contamination of the plasma by impurities, and the migration and deposition of the eroded material. Another related issue is the conditioning of the FW to control both the source of wall impurities and the associated source of recycling plasma fuel, which can have a major impact on plasma operation. PWI processes are also critical to the nuclear safety of machines operating with thermonuclear plasmas. These include first and foremost the tritium inventory bound in the vessel by co-deposition of tritium fuel with migrating wall material and the implantation and subsequent permeation of tritium in the FW, but also the formation of dust inventories in the vessel by various erosion and damage processes. In a fusion reactor with steady-state plasma operation, the injected deuterium and tritium fuel species and the added extrinsic impurity gases must be continuously circulated by pumping in order to remove the helium produced in the $\mathrm{D}+\mathrm{T} \rightarrow (\alpha + 3.5\,\mathrm{MeV}) + (n + 14.1\,\mathrm{MeV})$ fusion reactions to prevent the accumulation of helium ash in the confined plasma. While most of the ions impinging on FW surfaces are reflected or desorbed as neutral atoms to return to the plasma as recycling source, a fraction of the neutral gas in the divertor volume is continuously pumped out at a rate determined by the capacity of the pumping system for a given gas species and the

---

[24] The progress on R&D described in this chapter includes topics of relevance to ITER, as well as to burning plasmas more generally. In some cases, the underlying physics R&D activities were motivated by specific features of the ITER 2016 staged approach baseline (see ITER Research Plan for 2016 staged approach baseline ITR-2018-3 (provisional version) [3] and ITR-2024-5 (final version) [4] for details). The new ITER baseline 2024 currently under elaboration proposes modifications to several of these features (e.g. FW material, heating and current drive mix, etc), as introduced in P. Barabaschi *et al* (29th IAEA Fusion Energy Conference, London, UK, 2023 [5]), which will require additional R&D beyond that described in this chapter.

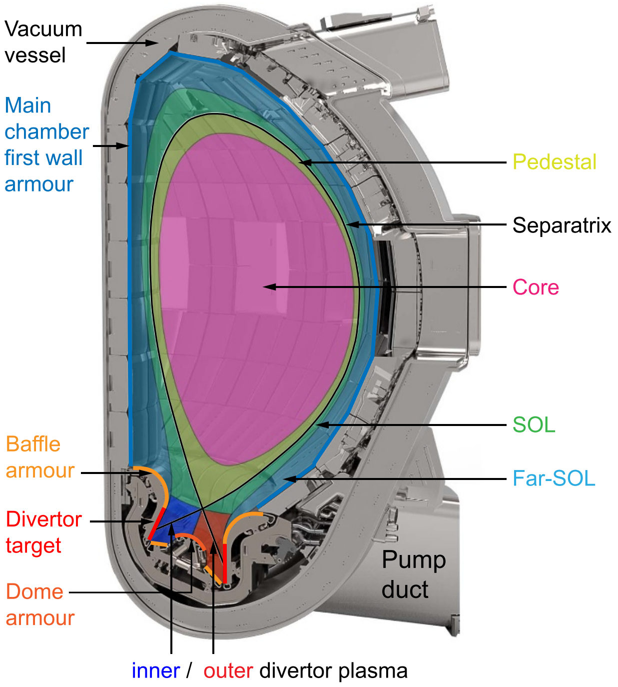

Figure 1. CAD view of an ITER vessel sector with a poloidal cross-section illustrating the main PFCs (main chamber first wall, baffle, divertor targets, divertor dome) and principal plasma regions (core, pedestal, SOL, far-SOL, inner- and outer divertor).

achievable neutral compression in the divertor volume and the pump ducts. This particularly affects the pump out efficiency for helium, which is discussed in section 3.2 of the chapter on *Transport and Confinement* of this Special Issue [8].

For the steady-state power exhaust in an ITER-sized thermonuclear device, a key parameter is the width of the parallel power transport channel in the plasma boundary region, defined by the characteristic exponential fall-off length λ_q. This results from the interplay of radial and parallel boundary transport processes and ultimately determines both the power flux reaching the divertor target plate and the power load on the main chamber wall. While a comprehensive theory of the dominant transport mechanisms in the plasma boundary and divertor is still not established, significant progress in plasma diagnostics and modelling has led to a much improved understanding of the underlying physical processes since the publication of the respective chapter in the 2007 PIPB. Apart from local phenomena, this development extends in particular to the global system from the bottom of the pedestal outwards to the near and far SOL, the main wall and on to the divertor, where strong, partly non-linear, interdependencies between the different regions have been uncovered that strongly affect the overall plasma behaviour. The related results are presented and discussed in detail in section 2.

The machine size scaling of the unmitigated stationary power flux density at the divertor target showed that it would be impossible to satisfy the thermo-mechanical boundary conditions on the material side without additional means to dissipate a fraction of the power crossing the separatrix before it reaches the divertor surface. In medium-sized tokamaks with carbon-based divertor PFCs, the radiation from eroded carbon established an intrinsic self-regulating feedback mechanism capable of producing the required volumetric power loss fraction while being compatible with detached plasma conditions in the divertor [9]. With the transition from carbon-dominated FW configurations to all-metal PFC devices, the radiative loss fraction due to metallic impurity species in the plasma boundary and divertor region was much too small. Therefore, carbon as a radiator had to be replaced by externally seeded impurities. In addition, suitable feedback signals and actuators had to be developed to control and maintain both the radiation level and the plasma detachment at levels compatible with a burning fusion plasma [10]. These developments took place mostly after the publication of the PIPB and are presented and discussed in section 3.

The energy confinement required for a burning plasma requires plasma operation in the high-confinement (H-mode) regime. This introduces an additional problem to power exhaust in the form of the repeated power transients associated with ELMs, which result in the sudden ejection of a significant fraction of the pedestal energy and particle inventory into the boundary plasma. The expelled plasma is mainly transported to the divertor target, but also partly to the FW, where it leads to transient power and particle loads, which can cause both structural damage in the plasma-facing components and increased erosion and corresponding impurity sources compared to the steady state case. These implications have motivated strong efforts to improve the understanding of the underlying processes and to develop both empirical and theoretical scalings of the ELM energy density in the boundary plasma and of the ELM frequency as a function of plasma pedestal parameters. In addition, due to the unfavourable dependency of the ELM energy density on the machine size, considerable effort was devoted to the development of H-mode scenarios with reduced ELM size and increased ELM frequency. The results obtained after the publication of the PIPB are presented and discussed in section 4.

Apart from the reduction of steady state divertor power loads by impurity radiation, the repeated power load transients due to ELMs required development of mitigation measures based on active control of ELM frequency and power density. This has been achieved by active control schemes using e.g. pellet injection and fuel gas feed or vertical kicks of the plasma induced by the vertical field coils as actuators. The main new method developed and investigated after the publication of the PIPB was based on additional magnetic coil systems to create suitable 3D perturbation fields, which in turn allowed the ELM behaviour to be controlled over a wide operational range by modifying the plasma pedestal structure and edge transport properties. While the effects of RMP application on pedestal properties and plasma confinement are discussed in the *Pedestal and Edge Physics* chapter of this special issue [11], the section 5 in this chapter focuses on the effects and consequences on plasma exhaust and the resulting power and particle loads on plasma-facing components.

The intense stationary plasma flux and the even higher repeated transient flux due to ELMs impacting the HHF target areas of the divertor lead to erosion of the PFMs, thereby creating a source of plasma impurities and reducing component lifetime through material removal. An additional source of plasma impurities results from the comparatively lower particle flux to the FW, which, however, extends over a much larger area than the divertor. Although material erosion by sputtering is well understood, significant progress has been made since the publication of the PIBP in understanding the prompt redeposition and long-range migration of eroded material, which can greatly reduce gross erosion but also leads to the formation of deposited layers with implications for in-vessel fuel inventory and dust formation. Both experimental results and progress in predictive modelling of these processes are discussed and presented in section 6.

Both the formation of deposited material layers with co-deposition of fuel ions and the implantation of fuel ions in the plasma-facing material surface lead to the gradual accumulation of a bound tritium inventory in the vessel of a nuclear fusion device. This inventory is of great significance for the nuclear safety of the device, as some of it may be released to the outside and ultimately to the environment in the event of an accident involving a breach of the vessel or building containment. As a consequence, the nuclear operating licence specifies an upper limit for the tritium inventory in the vessel. Since the publication of the 2007 PIPB, this has motivated a major research effort to characterise and accurately predict the T inventory growth rate, the results of which are presented and discussed in section 7. These new results, and the resulting increased confidence in predictive models, led to the most consequential design change of ITER, involving the complete elimination of carbon as a divertor material. In addition, it was found that even with reduced T inventory growth rates in an all-metal FW configuration, periodic recovery of retained T was still required to remain below the licence limit. As such procedures had previously focused on the removal of carbon-based co-deposited layers, in the absence of carbon the T-inventory was expected to be mainly determined by co-deposits with beryllium, requiring the development of alternative removal methods, also discussed in section 7. In addition, the T inventory, and in particular the removal and reprocessing of tritium, was found to be significantly affected by the introduction of extrinsic seeding gases, in particular with the initially favoured chemically reactive nitrogen, which added the complication of ammonia formation in the plasma with a corresponding presence of ammonia in the exhaust gas. As a consequence, considerable efforts were made to replace nitrogen with noble gas species such as neon, as discussed in section 3.

The lifetime of plasma-facing components is affected not only by material loss due to erosion, discussed in section 6, but also by progressive degradation of their thermo-mechanical properties caused by their sustained exposure to high particle flux and a large number of repetitive power and particle flux transients. For devices beyond ITER, the effect of long-term irradiation by the 14 MeV fusion neutrons also becomes highly significant. At moderate power loads, the main ageing effects identified in the research are changes in surface morphology such as roughening, bubble and blister formation and, in the case of He exposure of tungsten, the formation of tendril-like surface *fuzz*. Ongoing implantation of plasma impurities also leads to a gradual change in surface composition. The main consequences of these effects are degradation of erosion properties and HI uptake. At high power loads and high transient cycle numbers, the ageing effects extend deeper into the bulk material. Repeated strain and stress, and in the case of tungsten, recrystallisation due to frequent heating above the DBTT, cause progressive degradation of the thermo-mechanical properties, ultimately leading to the formation of cracks at the surface which can grow and propagate into the bulk of the material, creating a potential hazard if the cracks reach the cooling tube structure. Many of these effects are amplified by the synergistic effects of the combined particle, power and neutron exposure. Corresponding results since the publication of the 2007 PIPB are discussed in section 8.

In devices with metallic PFCs, exposure to excessive transient heat flux excursions above the thermal design limits of the components can ultimately lead to melting and potentially severe damage to the component. A better understanding of the mechanical and thermal loads during plasma disruptions has motivated the introduction of improved mitigation systems. Even with mitigation systems, disruptions, as well as slower power transients from VDEs, are still expected to locally reach or even exceed the thermo-mechanical limits of the FW elements. The mitigation of disruptions also increases the risk of formation of REs, which can deposit excessive local power loads deep inside the PFCs, potentially leading to the breakage of cooling pipes. In addition, the impact of accidental unmitigated ELMs can lead to a sequence of many melting events in the high heat load area of the divertor targets. The potential consequences for the integrity and lifetime of both the FW and the divertor motivated a strong research and development effort to improve the understanding and prediction of melt events on metallic FW components. Experiments have provided the necessary data base for the validation of dedicated predictive codes developed specifically for the simulation of melt events and their consequences on surface morphology and PFC integrity in ITER. These new developments and the results obtained are discussed in section 9.

For the engineering design of ITER, further refinement of the design of the main chamber FW panels and protection LIMs has been motivated by new estimates of FW loads during phases of direct plasma-wall contact, such as plasma ramp-up and ramp-down [12], and by experimental results indicating significant particle and power flux values expected for the far SOL plasma during plasma flat-top phases in the diverted configuration [13]. In order to avoid excessive local power loads with the consequences described in sections 8 and 9, the design of the divertor target plates also had to be refined by introducing appropriate shaping of both the individual tungsten MBs and the entire PFUs. These developments are discussed in a number of detailed reviews [14–16] and will therefore only be briefly summarised in this review.

2. Scrape-off-layer and divertor transport

2.1. Introduction

Despite the general improvement in diagnostic capabilities and theoretical understanding, a comprehensive description of the dominant transport mechanism in the peripheral region from the separatrix to the SOL and divertor is currently lacking. To understand the implications, it is worth recalling that the SOL width is determined by the competition between parallel, diamagnetic (tangential to the magnetic surfaces and normal to the field lines) and perpendicular transport. While the parallel transport is well described by classical conduction and convection with possible kinetic corrections at very low collisionality (parallel heat and viscosity flux limiting correction factors), both the poloidal and the radial transport are strongly influenced by the turbulence generally observed in the SOL.

The precise region where this turbulence develops, as well as its underlying mechanism, still remain an important open issue for SOL transport. Nonetheless, a number of observations have been made in recent years which helped in narrowing down this problem. First, whenever imaging diagnostics have been able to observe with the appropriate resolution at the boundary between confined and unconfined region, fluctuations are observed to originate in the region across the separatrix and then propagating into the SOL (see e.g. [17] and reference therein for an overview of the experimental evidences). Uncertainty on the exact separatrix location does not allow a precise determination of turbulence origin in the confined or unconfined region, but all the information so far confirm the region across the separatrix as the origin of fluctuations later observed in the SOL. Similarly, it is generally reported that suppression of turbulence in the pedestal region (such as the one observed whenever H-mode is established) leads to a clear reduction of turbulence in the SOL, especially in the region near the separatrix. Therefore, the current leading assumption is that SOL turbulence develops in some region close to the pedestal bottom and separatrix, where different modes could be driven unstable by the strong radial variations of the main plasma parameters (density, electron and ion temperature, ion viscosity). These modes, which may be also partially damped by shear flows present in the same location, would then spread across the separatrix into the SOL. It must be pointed out that local SOL conditions are still very relevant in this picture: as will be discussed later, they determine the characteristics of fluctuations and turbulent structures such as filaments—particularly so in the far SOL and thus define transport, even if they do not directly give rise to the modes seeding the turbulence. Further complications for the theoretical understanding and numerical simulation of anomalous plasma transport arise, for example, from: (i) the large number of processes affecting the averaged kinetic plasma profiles (e.g. plasma recycling at material surfaces and neutral ionisation, heat flux from the core, impurity radiation loss, etc) thus affecting the stability of different modes; (ii) orders-of-magnitude differences in both the time and spatial scales of plasma turbulence and transport, which ultimately settles the averaged plasma parameter; (iii) the geometric complexity of properly describing the transition between closed and open field lines, and accounting for the vanishing of the poloidal magnetic field around the X-point. In this sense, substantial advances have also been made in recent years, including the development of the flux-coordinate independent approach and the extension of first-principles, gyro-kinetic codes to the trans-separatrix region and divertor geometries (see e.g. the discussion in [18]).

All this introduces large uncertainties in extrapolation to future devices, including ITER, since the current ITER design is based on a number of assumptions about the expected transport level [16]. In this respect, enormous efforts have been made in the last years to determine the correct scaling law for the density and heat flux decay lengths, λ_n and λ_q respectively, which are essential to provide the physics constraints for the proper design of the plasma-facing components. As a final comment, the bottom of the pedestal, the separatrix, the divertor region, the main SOL and the FW should be considered as a global system in which different feedback systems are at play. This has clear implications, for example, in setting different decay lengths for fluxes of both heat and particles in different radial regions of the SOL, in identifying the so-called *near SOL* which extends a few mm beyond the magnetic separatrix and is clearly closely linked to the outer confined region, and the *far SOL* which, as will be reported later, exhibit a different, clearly non-diffusive nature of transport.

In the following we summarise the current understanding of the physical mechanisms that ultimately determine the expected level of transport in terms of the expected characteristic scale lengths λ_q and λ_n. The near SOL, the far SOL and the divertor are all elements with feedback interactions and are typically non-linearly cross-correlated. Integrated modelling approaches (e.g. JINTRAC [19–22] and TOPIC-IB [23]) attempt to provide an interface between the distinct but interlinked regions of interest. However, for physical understanding it is usually best to first assess the most relevant processes that determine critical parameters such as the peak heat flux on the target or the degradation of the pedestal by the presence of impurities and hence the core performance. With this in mind, and to keep things as simple as possible, the regions are discussed separately in the following sections.

2.2. The near SOL width

As already stated among the big uncertainties for proper extrapolation and to provide reliable engineering constraints to future devices, is the determination of the heat and particle transport foreseen towards the divertor and FW components. In particular a large improvement in the empirical projections has been obtained, under the auspices of the ITPA, by assembling a six machines (AUG, JET, DIII-D, Alcator C-Mod, NSTX and MAST) international database of H-mode heat flux decays in inter-ELM attached conditions [24]. The database has been assembled by assuming a purely exponential radial decay of the parallel heat flux as a function of the

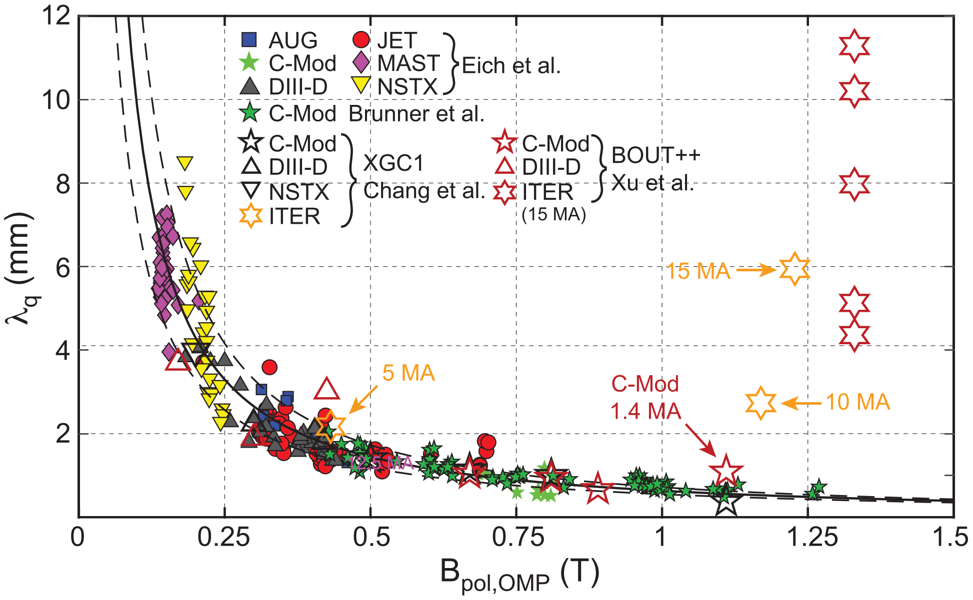

Figure 2. Compilation of published measurements and simulations of the H-mode, inter-ELM near SOL heat flux channel width, λ_q. Experimental points marked Eich *et al* include the original database [24] from which the regression ($\lambda_q(\mathrm{mm}) = (0.63 \pm 0.08) \times B_{\mathrm{pol,OMP}}^{-1.19\pm0.08}(\mathrm{T})$) given by the solid line was derived (dashed lines indicate the error bars on the regression). The Alcator C-Mod data marked Brunner *et al* are those from a more recent, much larger measurement set on Alcator C-Mod extending to $B_{\mathrm{pol,OMP}} \approx 1.25\,\mathrm{T}$ [25]. The code simulation points marked XGC1 and BOUT++ are the data published respectively in [26, 27] and [28]. The points at $I_{\mathrm{p}} = 15\,\mathrm{MA}$ for ITER correspond to baseline burning plasma conditions (note that the values of $B_{\mathrm{pol,OMP}}$ differ slightly among the two codes owing to differences in the source of the magnetic equilibria and initial plasma scenarios obtained by the two simulation teams). The XGC1 case at $I_{\mathrm{p}} = 10\,\mathrm{MA}$ has a much higher value of $B_{\mathrm{pol,OMP}}$ than would be expected from a simple linear reduction from the points at 15 MA; it is derived from an advanced (steady state) scenario simulation and magnetic equilibrium at $Q = 5$ and is thus not directly comparable to the baseline H-mode cases at 15 MA and at 5 MA. It does, however, have the merit of demonstrating that there is at least an intermediate point lying between the predicted very narrow λ_q which follows the empirical regression at low I_{p} and the much broader values at high current. This behaviour is identified in [28] as due to a progressive transition from neoclassical orbit driven ion losses to weakly collisional trapped electron mode turbulence.

distance for the magnetic separatrix $q(r) = q_{\|}\,\mathrm{e}^{-(R-R_{\mathrm{sep}})/\lambda_q}$, with a characteristic heat flux decay length λ_q depending only on upstream OMP SOL parameters and magnetic connection length. To account for the heat transport into the PFR, generally observed through a process of diffusion/dissipation along the divertor leg between the X-point and the target, the previous formula is convoluted with a Gaussian spreading with a width S, generally referred as *power spreading parameter* resulting in the following expression for the power flux profile at the OT [24]:

$$q(\bar{s}) = \frac{q_0}{2} \times \exp\left(\left(\frac{S}{2\lambda_q}\right)^2 - \frac{\bar{s}}{\lambda_q f_{\mathrm{x}}}\right) \times \operatorname{erfc}\left(\frac{S}{2\lambda_q} - \frac{\bar{s}}{S f_{\mathrm{x}}}\right) + q_{\mathrm{BG}} \tag{1}$$

where $\bar{s} = f_{\mathrm{x}}(R_{\mathrm{sep}} - R)$ with f_{x} the effective flux expansion and q_{BG} the background heat flux.

A remarkable result has been the observation that the heat flux decay length λ_q, in the H-mode attached divertor regime, scales with the inverse of the poloidal magnetic field B_{p} (the so called Eich scaling) and turned out to be independent from the machine size, reconciling the scaling from Alcator C-Mod ($R = 0.67\,\mathrm{m}$) to JET ($R = 2.96\,\mathrm{m}$). The same trend, being verified up to poloidal field at the OMP in the ITER range [25], would provide an extremely low value for ITER full current operation of the order of $\lambda_q \lesssim 1\,\mathrm{mm}$. The multi-machine database, including the aforementioned extension, is shown in figure 2. Such a scaling has found a theoretical interpretation in the framework of the so-called heuristic drift model based on the neoclassical orbit-driven ion losses for weakly collisional edge plasma [29]. 3D numerical simulations of inter-ELM H-mode relevant experimental data from existing tokamaks HL-2A, Alcator C-Mod, DIII-D, NSTX and EAST were performed as well using fluid BOUT++ [27, 30, 31] and particle-in-cell XGC1 code [26, 28, 32] including the most recent Alcator C-Mod high current scenarios with poloidal magnetic field of the order of the ITER expected value [28]. Even though the BOUT++ and XGC codes have a very different physics they claim a good agreement with the inter-machine scaling [24] for current tokamaks. Among the main conclusions drawn by these simulations is the large existing plasma blobby transport, propagating from the pedestal into the SOL which nevertheless do not affect the divertor heat flux width, the latter being dominated by ion neoclassical drift motion in accordance with the heuristic drift model [29].

However, when extrapolated to ITER 15 MA scenarios, both codes predict a strong deviation from the Eich scaling, with a 6-fold increase in the heat e-folding length to values of ≈6 mm or even higher. The explanations offered by the two approaches are different: the BOUT++ simulations suggest a regime transition from drift-dominated transport in current devices to turbulence-dominated one, caused by increased turbulence in the pedestal steep gradient propagating into the SOL and thus contributing to the spreading of the heat flux. It should be noted, however, that the phenomena described are inherently non-stationary and thus cannot be directly mapped into the steady-state inter-ELM SOL width scaling. The predictions of the gyro-kinetic code XGC1 are attributed to additional physical processes implemented: the authors claim that the increase of λ_q is primarily caused by the longer radial correlation length of the edge turbulence, which is mainly due to the neoclassical $\mathbf{E}\times\mathbf{B}$ flow shear rate being weaker with increasing $\rho_{\mathrm{i,pol}}/a$ as in the ITER full-scale simulations. Here, $\rho_{\mathrm{i,pol}}$ is the poloidal gyro radius. Indeed, a new formula (equation (6) in [28]) has been proposed, where on top of the already established dependence of the ion orbit width parameter, $1/B_{\mathrm{pol}}$, a second dependence on the parameter $a/\rho_{\mathrm{i,pol}}$ has been added:

$$\lambda_q = \lambda_q^{\mathrm{Eich}}\left(1 + 1.08\times{}^{-10}\left(B_{\mathrm{pol,MP}}\frac{a}{\rho_{\mathrm{i,pol}}}\right)^4\right) \tag{2}$$

where the $\lambda_q^{\mathrm{Eich}}$ represents the result of regression #14 in [24]. This inclusion of the parameter $a/\rho_{\mathrm{i,pol}}$, roughly proportional to the ion banana width in the edge region, determines the strength of the neoclassical effects including the background $\mathbf{E}\times\mathbf{B}$ shearing rate: as the ratio becomes bigger (as in the case of ITER with respect to present tokamaks even with similar edge poloidal field) the shearing rate becomes smaller thus allowing turbulent modes to grow and spread into the SOL enhancing the heat flux power deposition length. Figure 2 summarises the present experimental observations as well as the simulation validation and extrapolation: a clear increase is expected to happen at a poloidal magnetic field comparable to the one expected for ITER at higher current. In this context it should be mentioned that ITER simulations at reduced current (5 MA) predict a heat flux decay length in agreement with the Eich scaling [28], thus supporting the idea of a transition from a neoclassically dominated to a turbulence dominated regime with increasing plasma current, as suggested by ITER simulations at higher current (10 MA and 15 MA). For completeness, the 10 MA scenario is derived from advanced (steady state) simulations of a $Q = 5$ plasma, and the corresponding magnetic equilibrium exhibits a much higher value of $B_{\mathrm{pol,OMP}}$ than what we would expect from a linear reduction from the 15 MA case. Nevertheless, despite not being directly comparable, these simulations still have the merit of proving the progressing increase of λ_q as current is raised from the 5 MA ITER case (in line with the empirical regression) to the full current at 15 MA. It should also be emphasised that the extrapolation to ITER size and the corresponding predicted increase in heat flux decay length for high current operation is far from being a consolidated result. The two codes used for these simulations predict a comparable increase, but for different physical mechanisms, and there is a clear need to address the problem further, both from a numerical and an interpretative point of view.

It should also be emphasised that the above numerical studies for ITER plasmas have been carried out for fully attached divertor conditions, but as clarified in [16], ITER will operate with a partially detached divertor, achieved by a combination of extrinsic impurity injection and high neutral pressure in the divertor chamber. Under these conditions, current tokamaks exhibit high separatrix density and collisionality ν^*_{sep} where several experimental observations [33–36] provide evidence for an increase in the heat decay length. The important role of separatrix collisionality is also highlighted in comprehensive 3D turbulence simulations [37–41]: here the results of 3D turbulence simulations showing only marginal agreement with experimental results [42–44]. However, a clear reduction of anomalous transport with decreasing collisionality appears to be a well-established numerical observation in support of recent experimental observations [45, 46]. In this respect extension of the original formulation of heuristic drift model has been proposed, in the so called generalised heuristic drift model [47], to account for enhanced electron parallel confinement time in the SOL due to increase resistivity which qualitatively account for the experimental observed increase of λ_q at high density/collisionality.

The heat flux width λ_q is naturally connected to the scaling of temperature and density $\lambda_{T_{\mathrm{e}}}, \lambda_n$: thus any consideration about the scaling of the heat flux will have consequences as well on the expected amount of near and far SOL particle fluxes. If parallel heat transport in the SOL is dominated by Spitzer (collisional) parallel heat conduction of electrons, then temperature and power fall-off length are related by $\lambda_{T_{\mathrm{e}}} \approx \frac{7}{2}\lambda_q$. Such a relation has been confirmed to hold for ASDEX-Upgrade [33] and reasonably well for JET [48, 49]. In AUG [33], temperature and density are also found to be strongly related being $\lambda_{T_{\mathrm{e}}} \approx \frac{2}{3}\lambda_n$. For intermediate and low collisionality, the parallel heat flux is flux-limited, the sheath determines the heat flux decay length and the relation is modified in the following way [50]:

$$\lambda_q^{\mathrm{flux-limited}} = \left(\frac{3/2}{\lambda_{T_{\mathrm{e}}}} + \frac{1}{\lambda_n}\right)^{-1} \tag{3}$$

which is found to hold for the TCV tokamak where the multi-machine ITPA scaling is not fulfilled [51]. Also to note that, the aforementioned effects of broadening of heat flux with local separatrix density/collisionality, might act differently on the heat and particle channels, as clarified in [34].

The heat flux decay length investigation was extended as well to LIM plasmas scenarios: these effort was deemed particularly interesting, given that inner or outer wall LIM are generally used for plasma startup before X-point formation. The original design of inner wall first panel for ITER was reconsidered, after the initial observation of a double exponential decay on the parallel heat flux SOL profiles of inward limited plasmas on JET [52] with a much steeper λ_q in the near SOL. This motivated investigations on multiple devices [53–55] where the heat flux profiles in IWL L-mode plasmas has been derived either from IR or from spanning a wide range

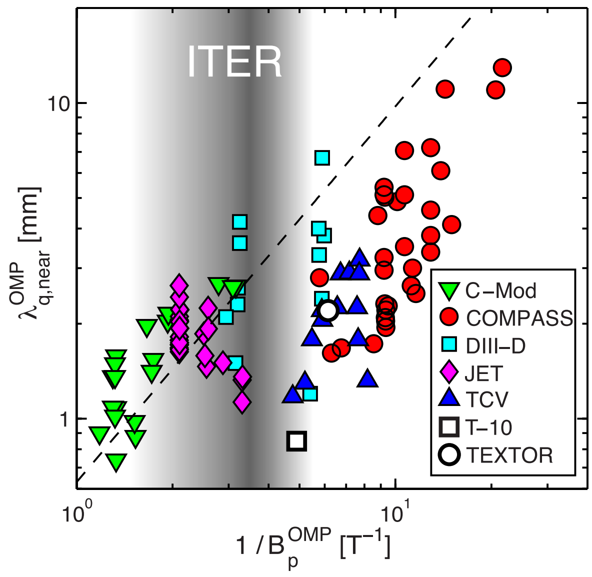

Figure 3. $\lambda_{q,\mathrm{near}}^{\mathrm{OMP}}$ measured in different inboard-limited plasma experiments, plotted as a function of $1/B_{\mathrm{p}}^{\mathrm{OMP}}$. Dashed: H-mode divertor plasma scaling from [29]. Shaded: approximate range of $1/B_{\mathrm{p}}^{\mathrm{OMP}}$ during inboard-limiter start-up in ITER. © 2015, The ITER Organization [53]. This image is hereby used courtesy of the ITER Organization.

in machine size from COMPASS to JET. The *narrow feature*, i.e. the existence of a steep near SOL e-folding length has been observed in all the tokamaks and as shown in figure 3, the narrow λ_q is found to scale with poloidal gyro radius, consistently with the already mentioned H-mode scaling and heuristic drift model. Worth mentioning, that based on these observation, ITER Inner Wall LIM panels shapes have been modify for being able to handle reduced heat flux width λ_q with respect to the original design [53].

2.3. Classical drift and transport in the SOL

An ordering parameter of classical drifts that characterises the drift strength in a fusion reactor is given by the normalised ion gyro radius $\rho^* = \rho/R = \rho/(aA)$ with aspect ratio $A = R/a$. Current devices demonstrate that low- to medium-Z impurities seem to be generally shifted from the LFS towards the HFS with $\mathbf{E} \times \mathbf{B}$ drift with the ion magnetic drift directed into an active lower divertor. This drift-induced change of flow can be balanced by thermal and friction forces in the SOL, especially at low densities, partly maintaining the LFS impurity concentration. From the simple ρ^*-scaling, one would expect then that at reactor scale (e.g. ITER with $R = 6\,\mathrm{m}$) the impact of drift on the recirculation of flows of plasma species would be less efficient. At high divertor densities like in ITER, impurity transport is expected to be less affected by drift-flows themselves as such, since enhanced turbulent transport and interaction with recycling neutrals provokes redistribution of impurities between HFS and LFS. In this subsection, the community effort to understand better the relevance of classical drifts also at reactor scale (high-power and high-density plasmas) is presented and the model validation activities are summarised.

As a first order approximation, classical cross-field transport is determined by motion of charged particles in stationary magnetic and electric fields, which could exhibit as well spatial inhomogeneities, and Coulomb collisions. Despite the fact that particle and energy losses due to classical transport are determined by local plasma parameters and gradients, the processes governing these fluxes may occur on a larger scale up to the order of the tokamak minor radius. In addition, the presence of *open magnetic flux surfaces* and in particular of the boundary layer between confined and unconfined regions, induces, for semi-collisional charged particles, an additional loss channel know as *prompt-losses* [56–61]. This effect may be interpreted as an extension of neoclassical transport into the open magnetic field with a characteristic radial extent of the order of banana width $\Delta_{\mathrm{b,e/i}} \sim q\,\rho_{\mathrm{e,i}}$ where q is the safety factor and $\rho_{\mathrm{e,i}}$ is the electron/ion Larmor radius. Prompt-losses may be relevant, affecting the magnitude of radial electric field and consequently turbulence suppression in H-mode pedestal. Nevertheless, despite the large amount of work dedicated to the physics of prompt losses, the results of analysis of experimental data from different tokamaks remain rather controversial. Indeed while on AUG it is claimed to provide a modest contribution (10%–20%) to the edge radial electric field [59], the data from DIII-D tokamak seems to indicate a stronger impact [60, 61]: such a controversy clearly calls for additional research in order to assess the possible role on future devices. From the numerical point of view, comprehensive simulations of the edge and SOL plasmas with 2D SOLPS transport codes based on fluid Braginskii equations and accounting for drifts and currents show a good agreement of simulated and experimental profiles of electrostatic potential at the mid-plane [62] (and references therein). The role of drifts, and in particular of $\mathbf{E} \times \mathbf{B}$ has been proven to contribute substantially to charged particle recirculation in the divertor region and furthermore to change according to recycling conditions. 2D numerical models have been able to reproduce these effects which can be quite relevant around the X-point as observed both numerically and experimentally [63–66].

Simulating classical drifts with fluid-plasma/kinetic-neutral 2D edge codes such as SOLPS-ITER [67, 68] or EDGE2D-EIRENE [69, 70] adds increased complexity to achieve numerical convergence that exists already without inclusion of the drifts. Hence many authors preferred to reduce the numerical model, for example employing a fluid-model for neutral transport or relaxing convergence criteria w.r.t. the chosen time-step in the code. Over the past decade however, 2D edge plasma codes have demonstrated to be more reliable when including classical drifts, capturing experimentally observed trends, including a cross-machine comparison (e.g. for L-mode using UEDGE [71]). Although not always quantitatively exact, significant progress has been made especially for the full metallic wall configurations like JET [72, 73]. The absence of carbon in metallic devices does allow a disentanglement of relevant processes (e.g. classical drifts) in the understanding of the power and particle exhaust problem.

With the absence of carbon as the primary plasma impurity and radiator it is also possible to eliminate some of the free parameters for impurity transport from the models, i.e. chemical sputtering and consequences from hydro-carbon transport physics and retention in amorphous carbon layers. But even in such a less complex case, the disentanglement of physics processes relevant for example for the redistribution of particle flows by drifts and the impact on divertor dissipation is a difficult task. Most notably in this respect is the work on Alcator C-Mod [74], and more recently on TCV L-mode plasmas [75] for a carbon wall and [76] for a full-W wall in AUG. A comparative assessment for JET and AUG for nitrogen seeded L-mode plasmas attempting to derive model-based scalings for radiation including drifts was presented in [77, 78].

For H-modes, a numerical assessment with SOLPS5.0 has shown that most experimental measurements can be reproduced in the fluctuating [79] and completely detached plasma scenarios in nitrogen-seeded AUG H-modes [80, 81]. However, the neutral density and compression in the (sub-) divertor could not be reproduced using the experimental upstream profiles [81]. This persistent discrepancy with the experiment manifests in the simulations by an underprediction of the neutral flux densities, the line-integrated Balmer line intensities (D_δ and D_ϵ) and the deuterium fuelling rates. With the addition of drifts, it has been demonstrated that an accurate matching of experimental measurements in both divertors is possible—as opposed to matching the outer divertor only [82]. This pivotal study was the first to demonstrate that the high-field side (HFS) region, influenced by the drift effects, plays a critical role for the overall plasma solution because of its impact on the fuelling of the confined plasma, the distribution of neutral particle sources, and the degree of neutral compression achievable in the divertor. Moreover, the self-consistent build-up of the high density high field region, as a consequence of $\mathbf{E} \times \mathbf{B}$ eddy flows, has been found in recent results from JOREK simulations [83]. The observed inverted radial density profiles on the HFS together with the drift flows lead to plasma flow into the confined plasma, accountable for the fuelling of the confined plasma and therefore eliminating a long-standing discrepancy in the neutral compression ratio of modelling and experiment. Consequently, the model of the perpendicular diffusive transport coefficients and/or the application of a convective transport component could be reconciled, allowing to increase the divertor neutral density similar to experimental levels—along with neutral radiation levels, the deuterium fuelling rates and the measured electron densities in the inner divertor volume. The activation of drifts and currents in very recent simulations of XPR regimes induced by strong nitrogen radiation improved the agreement with the AUG measurements by the divertor TS diagnostic, especially on the high-field side [84].

Neon is currently favoured for ITER to avoid issues of plasma chemistry (production of tritiated ammonia) and another long-lasting question is whether neon would perform as good as nitrogen as a divertor radiator in H-mode ITER regimes. Whereas for AUG it was problematic to sustain a neon seeded discharge in H-mode, JET demonstrated stable conditions in case of power $P_{\mathrm{NBI}} > 24\,\mathrm{MW}$. Recent simulations with SOLPS-ITER for such JET high-power discharges showed [85], that neon performs as efficiently as nitrogen at moderate separatrix $Z_{\mathrm{eff}} < 1.5$ for partially detached conditions (corresponding, respectively, to N and Ne concentrations higher than 0.7% and 0.4% at the main chamber separatrix). This modelling clearly reveals the importance of drift flows also for the ITER case, redistributing plasma between the divertor plates through the PFR, and thus potentially limiting the ITER divertor operational space (see figure 14 in [16]). At deeper detachment the retention of nitrogen was better than for neon in the model, partly related to a system size effect but at higher power however this effect might be again moderated. A more detailed multi-machine simulation exercise for AUG-JET-ITER was also undertaken to further quantify this scale size effect for seeded H-mode conditions with drifts turned on [86]. The main results were that, (a) the outboard and inboard divertors are more symmetric for larger machines, with the symmetry increasing with higher seeding, i.e. for more detached divertors; (b) in smaller machines drift effects are more significant and divertor asymmetries more pronounced, as expected from a simple scaling with $\rho^*_{\mathrm{SOL}} = \rho/L_{\mathrm{c}} \propto (q_{95}R)^{-1}$; (c) in larger devices the ionisation of neutral particles takes place closer to the targets and neutral impurities are better confined in the divertor (first ionisation potential effect); and (d) in larger devices with larger power, neon radiation is as efficiently localised in the divertor region as for nitrogen, and thus heat load control in ITER with neon seeding is expected to be as nearly equally effective as in JET. However, the work in [86] did not consider a change of near-SOL transport to reflect the $\lambda_q \propto 1/I_{\mathrm{p}}$ dependence of the Eich-scaling [24], and the drift strength may rather obey a scaling $\rho^*_{\lambda_q} = \rho/\lambda_q \propto I_{\mathrm{p}}$ that is independent of the major radius R.

The structures of plasma flow, electrostatic potential and electric current in classic SOL are rather complex and determined not only by drifts, but also by a contact with conducting surfaces (divertor targets) as well as by the ionisation sources and energy sinks [87]. Such complexity could be illustrated by the fact that for the radial scale of the SOL $\sim q\rho_{\mathrm{i}}$ and electrostatic potential $\sim T_{\mathrm{e}}/e$, the $\mathbf{E} \times \mathbf{B}$ drift velocity becomes comparable with poloidal projection of plasma flow along the magnetic field lines with Mach number order unity, which causes plasma pressure variation along the magnetic field [88]. On the other hand, as already said, upstream plasma potential profile and consequently radial electric field are strongly influenced by the conditions met at the boundary and in particular from the target recycling conditions. Numerical investigations revealed indeed different radial electric field strength and radial profiles depending on the divertor geometry [89], PFCs materials [90] and recycling states modified by the presence of extrinsic impurities [91]. Whenever experimentally investigated, the clear dependence of upstream radial electric field on divertor temperature and profiles has been confirmed [92].

2.4. Turbulent transport in the near and far scrape off layer

As already mentioned, not all the physical processes observed in the SOL region can be ascribed to classical or neoclassical effects. On the contrary, anomalous transport represents the main source of losses in particular for the electron channel both for heat and particles. The proper description of anomalous transport in the SOL can still be reasonably well described in a fluid collisional regime, being collisionality $\nu^* = qR/\lambda_C \gtrsim 1$ (with q the safety factor, R the major radius and λ_C the Coulomb mean free path) although, it does not guarantee that more collisionless regions, adjacent to the SOL, do not alter anomalous transport in the SOL due to the turbulence spreading. It is widely accepted indeed that in the H-mode pedestal the turbulence is significantly suppressed by velocity shear effects [93]. In particular, analysis of the ion and electron heat fluxes in the AUG H-mode pedestal [94] shows that whereas ion heat flux is rather well described by the neoclassical heat diffusivity, the electron one is well above the corresponding neo-classical values and is comparable with the ion one (although with a large error-bar). The fact that velocity shear layers only suppress ion-scale turbulence is well documented [93], and the reduction of inter-ELM fluctuations observed in the SOL during H-mode would indicate that the surviving electron-scale turbulence are most likely not sufficient to seed large turbulent structures in the SOL, although differences may arise according to the explored plasma condition as later described.

The disparate scales involved, as well as the different collisionality of pedestal and SOL, which as aforementioned are tightly connected, implies that the numerical investigation of the physics of anomalous transport and comparison with experimental data is only possible through complex numerical simulations which are presently at the limit of current numerical capabilities and extrapolation to full size devices for ITER class experiments are demanding exa-scale class simulations.

Overarching issues of anomalous SOL plasma transport are the role and interplay of different players, namely *broad band electromagnetic turbulence* and *blobs* [95, 96] high-density plasma filaments extended along the magnetic field lines which intermittently peel off from the vicinity of the separatrix and ballistically propagate in the radial direction. Broadband turbulence not only contributes to anomalous transport as already documented in several devices such as TCV, JET, AUG, Alcator C-Mod, DIII-D [97–105] but also due to non-linear effects may represent the source of both blobs and to some extent ZFs in the edge of the confined region.

Concerning blobs, improvement in diagnostic capabilities provided the possibility to image these filaments and properly track their motion (see [17] and reference therein for a review) underlying their capabilities to travel with a radial speed of the order of 100–500 m s^{-1} as seen for example in figure 4. Their general features are presently well understood and documented in particular in L-mode with a local pressure perturbation in the perpendicular plane and extended along the parallel direction with $k_\perp/k_\parallel \gg 1$. The self-consistent electric field, generated by a charge polarisation force as for example the curvature drive, determines the aforementioned $\mathbf{E} \times \mathbf{B}$ radial motion of the blob. The magnitude of the electric field, which ultimately determines the convective radial velocity, depends on the balancing of the current source term (the charge polarisation force) with the parallel and perpendicular loss current in the so called *blob electrical circuits*. Several different current closure schemes have been proposed (see for example [95]), each of them determine different blob-size/velocity scaling: at very low collisionality the blobs are in the so-called *sheath limited regime* extending up to the OT with the dominant return current flowing to the sheath and limited by the sheath-resistivity. Another possible mechanism, dubbed as *ideal ballooning regime*, occurs whenever the curvature drive (assumed here as the main charge-polarisation drive) is balanced by the polarisation current. Sufficiently close to the X-point, as is the case in some regions of a diverted tokamak geometry, the dominant return current path is the cross-field resistivity, which is magnified by the strong squeezing of the magnetic flux tubes near the X-point due to magnetic shear and poloidal flux expansion. Such a regime is generally called as *resistive X-point regime*: in this case the current-return path perpendicular to the flux tube is reduced by the strong compression due to the large magnetic shear close to the X-point. Finally in the case of very high collisionality the filament is in the so-called *resistive ballooning regime*, no more electrically connected to the target and the ion polarisation drift is the dominant return current. What matters most in the determination of the different blob-regimes is the different scaling properties of the convective velocity with respect to their size which ultimately influence the amount of transport radially convicted outwards. From the experimental point of view, several clear indications confirm the large electron density perturbation associated to these blobs [97–105, 107–110], as well as a clear indication of associated electron [105, 111] and ion temperature [53, 103, 112–115] fluctuations. It is worth remembering that the equipartition time between ions and electrons is much larger than the transit time of the parallel ion heat flux, resulting in $T_\mathrm{i}/T_\mathrm{e} > 1$ at the separatrix and throughout the SOL. The experimental observation nevertheless, with ion temperature values about 2–3 times larger than the electron one are unlikely to be ascribed to this simple parallel transport mechanism and have a strong implication as well on the dynamics of turbulence resulting in different ion and electron e-folding length in the SOL [103, 114]. The high T_i values measured at filaments may be relevant as separatrix temperatures are increased in ITER, since the radial propagation of these structures may transport such energetic particles close to the FW. This potential problem was partially assuaged by recent experiments [116, 117], which provided observation of strongly skewed ion temperature distribution functions with the tendency towards a reduction of the $T_\mathrm{i}/T_\mathrm{e}$ ratio as line average density is increased. Several investigations on the parallel extension of the filaments reveal how these are elongated from OMP to the X-point [118] and even up to the target [119, 120], with a clear associated pattern of parallel current [121, 122]. It is worth mentioning that most of blob characterisations have been obtained in L-mode, due to

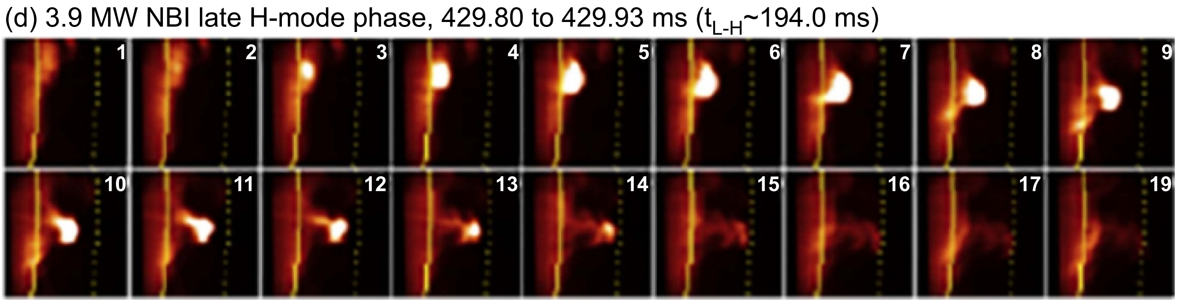

Figure 4. Different levels of activity are observed during H-mode with the GPI (gas puff imaging) diagnostic on NSTX. Each box in these image sequences shows a 24 × 24 cm portion of the edge just above the outer mid-plane. The inter-frame time is 7 μs. Reprinted from [106], Copyright (2011), with permission from Elsevier.

the easiness of the measurements as well as the availability of local information from insertable probes, but whenever diagnostics are capable of investigating H-mode [46, 102, 116, 123–127], no significant differences were observed on blob properties between L-mode and inter-ELM filaments at least in low density Type-I scenarios. It is commonly accepted that the plasma anomalous transport and corresponding non-linearly generated structures such as the blobs in the vicinity of the separatrix, SOL, and divertor regions are related to the turbulence driven by the curvature effects, resulting, for example, in resistive ballooning (RB) instability (which resembles the Rayleigh-Taylor instability in a stratified fluid situated in a gravity field), RDWs, and the ∇T_e instability, associated with the electron temperature gradient and sheath effects, in the SOL. Actually several experimental observations [128–133] revealed that intermittent filamentary structures emerge as well in the divertor regions below the X-point without being necessarily correlated with mid-plane ones. They are observed to propagate in the PFR as well, with a still undetermined role on transport spreading into the PFR. For these structures, the main drive remains mostly drift-interchange due to the combination of curvature effect and RDWs [133]. However, additional underlying mechanisms have been proposed such as Kelvin–Helmholtz instability, which could arise because of the sheared $\mathbf{E} \times \mathbf{B}$ flow that forms around the separatrix developing along the divertor leg [134], and have an overall effect of reducing turbulent transport into the PFR. Nevertheless, in practice all these modes could be unstable and undergo complex non-linear interactions with each other.

Finally, strong toroidally symmetric $\mathbf{E} \times \mathbf{B}$ flows are expected to arise at the edge of the confined region. They are driven by neoclassical as well as turbulent effects. The former include diamagnetic flows, poloidal and toroidal rotation, as well as the ion *prompt losses* through the LCFS to PFCs. Turbulence can modify all of these, and additionally it can sustain so called ZF through the nonlinear Reynolds stress [135–137]. Whereas the neoclassical effects produce $\mathbf{E} \times \mathbf{B}$ flows with a characteristic *radial* scale-length of the order of the scale length of plasma parameters and supra-thermal ion banana width, respectively, the latter mechanism could generate ZF in the so-called *meso-scale* radial wavelength (larger than the ion gyro-radius, but smaller than the machine size). This mechanism can arise from different kinds of micro-turbulence: for example, 2D simulations of RDW turbulence [138, 139] have shown the development of jet-like narrow zonal flows with a width of a few ion sound gyroradii, ρ_s [139], with the capability of trapping turbulent eddies and reduce the corresponding anomalous transport. Similarly, ZF generation from ITG turbulence has been shown in gyro-kinetic simulations [140]. The eddy trapping effect becomes stronger at lower collisionality [141], thus suggesting a lowering of the zonal flow beneficial effects at higher collisionality like the one foreseen for ITER separatrix operation. It is worth mentioning that zonal flows do not directly contribute to the convective transport but can modify it due to their effects in the dynamics of both broadband turbulence and blobs.

In order to tackle the described complex behaviour several different approaches have been pursued from the theoretical/numerical point of view. Analytical and semi-analytical considerations focused primarily on some conceptual issues of edge plasma turbulence and comparison of major findings and trends with experimental data (including an interplay of nonlinear zonal flow generation and turbulence induced transport as well as the blob velocity scaling corresponding to different regimes of blobs, see reviews of [95, 96, 135, 136] and reference therein). Numerically, simplified turbulent models, often performed in 2D or 3D flux-tube spatial domains, have been developed primarily for the determination of key physical ingredients of anomalous transport in highly non-linear regimes [138, 142–146] or in reduced form by simple collisionality dependent diffusion in EDGE2D-EIRENE [147]. Finally a complete treatment of the edge plasma transport in fully 3D geometry is possible, although extremely demanding at ITER scale in term of numerical costs: on this respect different approaches and codes have been developed as GDB [38], XGC [26], BOUT++ [148], GRILLIX [149], Gkeyll [150], GBS [39, 151], Tokam3X and SOLEDGE3X [152], GENE [153], PICLS [154], COGENT [155] and GENE-X [18] with different implementation from fluid to gyro-fluid and gyro-kinetic, both with continuum and PIC discretisation, solvers which have been extended in recent years in order to account for proper treatment of X-point topology and complex wall geometry as well as including additional elements such as the interaction with the neutrals. It is worth mentioning that the present ITER divertor design is based on 2D SOLPS and

SOLPS-ITER codes [16] which assumes radially varying diffusive transport coefficients which are not coming from first-principle evaluation as the ones obtained from previously mentioned turbulent codes. An approach recently considered the possibility to include non-diffusive transport into standard 2D suite of codes using different techniques [152, 156–164]. This can be considered as a reduced method to account for anomalous transport without the need for full-scale 3D turbulence codes.

2.5. Far SOL transport and link to divertor and separatrix condition

Among the rationale for investigating the near and far SOL transport is the determination of the particle transport and corresponding scale length which ultimately provide information for extrapolation of sputtering rates of FW and divertor targets. Such consideration needs to account for the foreseen operational space of future devices, with high separatrix density, and in order to ensure maximum tolerable loads and avoid W recrystallisation, high divertor neutral pressure and at least partial [16] if not full [165] detachment mostly ensured by extrinsic impurity seeding. When present devices are operated at high density with intense gas fuelling, a progressive flattening and broadening of the SOL density profile is observed, a process known as *shoulder formation*. Such a process has been extensively documented in L-mode [97, 166–173] with some common clear observations related to the increase of the filament activity primarily due to variation of the blob size [171, 174, 175], blob radial velocity [103, 127] and the corresponding convective components of radial transport [103, 176]. It is worth noting as well that with increased fuelling also the plasma flow in the SOL is modified, with even an inversion of the poloidal flow direction of the fluctuations as reported in [177–179] and variation of parallel Mach number at the mid-plane [103, 179].

In experiments performed in L-mode without extrinsic impurities, it has been commonly observed that the SOL density profile broadening starts forming when the divertor moves into a high-recycling condition [127, 172, 174, 180]. These observations suggested that divertor collisionality, described by the parameter $\Lambda \propto L_{\|} \nu_{\mathrm{ei}}/c_{\mathrm{s}}$, would properly describe the appearance of a density shoulder primarily causing the filament to detach from the OT and increase, according to the two-region theory proposed in [181], their radial velocity and correspondingly their convective transport contribution [103, 169]. Actually further experiments where collisionality has been varied using either geometrical shape variation [171, 172], or increasing collisionality via extrinsic impurities only [172, 173, 180], revealed that the proposed framework was not universal, with no upstream profile modification observed whenever high recycling or detachment was achieved by pure impurity seeding. On the other side, numerical simulations pointed towards a strong role played by the mid-plane neutral density [116, 182, 183] with a major role played by neutrals coming from target recycling highlighted on AUG: nevertheless all these numerical verifications required an additional power flowing into the far SOL which can only be accounted for by an increased convective filamentary contribution. The numerical evidences of the role of neutrals are experimentally supported by evidence collected in several devices: both on AUG [184] and on JET [172], upstream modification have been correlated with experimental observation of an increase of neutral density in the divertor region, further spreading into the main chamber. Similarly EAST experimental data highlight the dominant role played by neutral pressure with respect to the one induced by nitrogen-induced detachment [175] in the process of upstream shoulder formation. Recent results from TCV [176], with comparison between baffled and unbaffled discharges points as well towards an important role played by mid-plane neutral pressure in order to observe SOL density profile flattening and broadening. The picture arising from L-mode plasmas is thus that shoulder formation requires several ingredients: a certain mechanism of increased intermittent transport ensuring enough power reaching the far SOL, a reduced parallel flow, as confirmed as well by 3D turbulence simulation including neutral species [185, 186], and an increase of local neutral sources either via target or FW recycling. The reduction of far SOL ion temperature observed along density shoulder formation [103] represents a further experimental evidence supporting the role of local ionisation process.

Shoulder formation is observed as well in H-mode [35, 46, 116, 127, 172, 175, 187, 188] with the plasma at most in high recycling state without the need to be detached, and with a stronger dependence on the level of fuelling [46, 116, 127]: example of the observed evolution of upstream profiles for three different devices are provided in figure 5. No shoulder formation has been observed in cases where strong divertor dissipation is reached using nitrogen seeding only [172, 189] consistent with the model proposed in [183]. In cases where upstream density profile broadening is observed, the λ_q at the target increases as well [35, 46, 190]. It is worth noting that, experimentally, the operation at very high level of fuelling (even without seeding) is generally associated to a modification of the ELM regimes, often with a transition to small-ELM regimes/quasi-continuous exhaust (QCE) regime [35], in particular whenever strong plasma shaping with high top triangularity and elongation is exploited. H-mode high density shoulder formation is also associated to an increased filamentary activity [46, 127, 188]: inter-ELM blobs exhibit larger size and higher radial velocity [46, 126, 189]. Together with shoulder formation experiments confirm a higher filament detection frequency [126] and observations support clear indication of enhanced activity close to the separatrix in the confined region. Leveraging on pioneering work of [142–144], a framework for the interpretation of increasing activity at such high density has been recently proposed [34, 45] where the plasma condition is described by a *turbulence parameter* $\alpha_{\mathrm{t}} \propto q_{\mathrm{cyl}}\, \nu_{\mathrm{ei}}^{*}$ evaluated with density and temperature just inside the separatrix. Such a parameter has been shown to regulate the strength of resistive interchange transport relative to drift-wave turbulence by setting the parallel adiabatic response and thus the phase shift between density and potential perturbation [144]. Experimentally it has been shown that the parameter α_{t} increases with the divertor fuelling and divertor

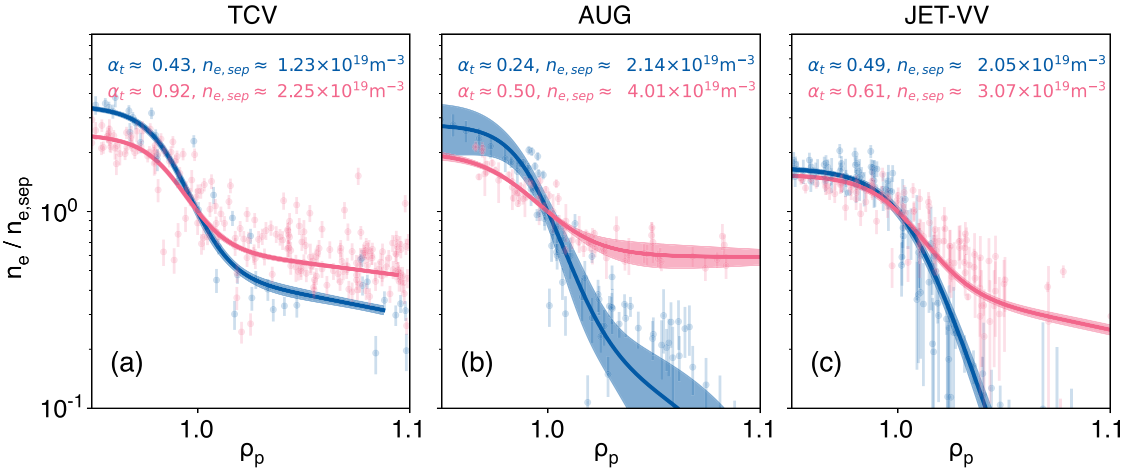

Figure 5. Upstream profiles normalised to the density at the separatrix for three different tokamaks (TCV, ASDEX Upgrade, JET) at two different levels of fuelling. Profiles are ELM filtered at low density (with 70%–90% of ELM cycle considered), whereas at high density whenever small-ELM regimes are reached the entire profiles are considered. Corresponding values of the turbulence parameter α_t as described in [34] are provided. Data elaborated from [191].

neutral pressure [46, 191] primarily due to an increase of the separatrix density with relatively small variation of the separatrix temperature with increased neutral pressure [192]. This corresponding modification of α_t, according to the theory is associated with an increase of the interchange type turbulence finally responsible for an increase of the number of filaments expelled from the confined region into the SOL as shown for example in [126]. These filaments exhibit a larger radial velocity [46, 126, 191] and an increase of their frequency as well, thus contributing to the increase of the convective radial transport, which may still represent a substantial fraction of P_{SOL} tens of mm away from the separatrix [103]. In this sense, recent calorimetry measurements on AUG provide evidence of an increase of the energy deposited onto the FW whenever shoulder formation is achieved at large values of α_t [193].

The extrapolation of the present observations to next step devices is not straightforward. Indeed, the almost linear relation observed in small machines between fuelling level and increasing separatrix density and separatrix collisionality or α_t [46, 191] will not be fulfilled with a highly compressive divertor as the one designed for ITER [194]. Instead, the separatrix density at ITER will most likely saturate with increasing neutral pressure at the target [194], due to the highly compressive divertor design reducing the neutral leakage from divertor chamber to main SOL and thus limiting the neutral density at the mid-plane. This effect will be reinforced by another key difference, ascribed to the fuelling method: for ITER, core fuelling is mostly ensured by pellets rather than gas puffing. The investigation of shoulder formation whenever the plasma is mainly fuelled through pellets is less extensive in present experiments: preliminary indications suggest that steeper near SOL e-folding lengths are observed with pellets [195] with respect to gas fuelling cases but clearly further investigations are needed as the ones proposed in [36]. It is unclear whether this is due to a lower recycling neutral flux, either at the target or at the mid-plane, in the pellet scenarios investigated, or to alterations in the necessary radial transport that ensures sufficient power for the re-ionisation of the recycling neutrals. In any case, further well-designed experiments are required to understand the mechanisms at play qualitatively.

One possible way in which this effect may be offset is through the main wall recycling, which might combine with a broadened SOL density profile to reach a high-recycling regime as the one reported in Alcator C-Mod [196]. In this condition the turbulence-increased perpendicular heat fluxes would provide the energy to keep the ionisation front away from the separatrix. In this sense, studies in present-day machines offer different interpretations which still require further investigation to incorporate them into a single picture. SOLPS-ITER simulations reproducing the shoulder formation in AUG indicate that main wall recycling plays a minor role as a source of neutrals [183], the latter being dominated by target recycling. However, previous simulations carried out with EMC3-EIRENE in AUG [182] pointed towards a stronger effect of main flux recycling although a proper comparison of the ionisation source caused by either main chamber or divertor recycling was missing. Similarly, recent simulations carried out in JET with SOLPS-ITER and EDGE2D conclude that main wall recycling represents a significant contribution to neutral density at the mid-plane and strongly influences $n_{\mathrm{e,sep}}$ [197]. Clearly the relative contribution of main chamber vs divertor target recycling may further depend on divertor neutral leakage or overall machine size and, as aforementioned, further experiment and modelling are needed. The role of the main wall recycling is also linked to the PFM: high-Z metals like tungsten have a substantially higher reflection coefficient for impinging hydrogenic ions than carbon or low-Z metals like beryllium. Since reflected ions have much higher energies (in the range of tens of eV) than thermally desorbed ones, they have a significantly larger mean free path, thus penetrating closer to the separatrix and leading to steeper density gradients inside the separatrix [198]. Regarding potential isotope effects, it is worth mentioning that density profile broadening are observed as well in tritium plasmas [199] confirming the near SOL e-folding length increase with separatrix collisionality. A subset of these T experiments exhibit complete flat density profiles: these cases cannot be identified by an anomalously higher separatrix collisionality, confirming that high ν^*_{sep} or α_{t} is mandatory but not sufficient to ensure a density shoulder formation. Also in these cases, similarly to [193], the wall temperature increases with a significant time rate and this has been attributed to increased SOL NBI ionisation due to the denser far SOL. In this sense, the enhanced thermal transport observed in presence of shoulder formation could have two main consequences: first, if a substantial fraction of P_{SOL} is convicted by filaments, separate e-folding lengths could appear for the ion and electron species. Since $\lambda_{q,\mathrm{i}} \gg \lambda_{q,\mathrm{e}}$, the near-SOL could still be dominated by an Eich-like narrow λ_q. However, the fraction of the power not being transported by electron parallel conduction in the near SOL would result in lower maxima in the heat flux distribution on the target. This kind of double-λ_q SOL has been reported in the upper divertor of AUG, where the wider field of view allowed for the observation of the longer $\lambda_{q,\mathrm{i}}$ tail [190]. Second, the enhanced flows onto the main wall may have a direct impact on the erosion rates of the PFCs depending on the material they are made of. The previously discussed cooling of ions after shoulder formation should be confirmed as soon as possible, since the sputtering yield of Be is dramatically changed when the energy of the impinging hydrogenic ions—or more typically, a sufficiently populated high energy tail of its distribution—approaches the 100 eV range. On the other hand, the expected SOL hydrogenic ion energy levels would pose no erosion issue for a W-coated wall, unless a substantial concentration of impurities is transported along with the blobs [200].

All these factors imply that, although ITER separatrix density may achieve the level of collisionality (or α_{t}) needed to stimulate the ballooning turbulence in the separatrix region to ensure higher transport into the SOL, the level of ionisation source at the mid-plane might prevent the formation of a density shoulder, unless main wall recycling, for which the selected material will play a critical role, may be sufficient to sustain the enhanced densities. Finally, the main effects of a shoulder formation might be a partial reduction of the maximum heat fluxes onto the targets and a potential enhancement of the erosion rates at the main wall. This last effect would be severely mitigated either if the cooling of ions after shoulder formation is confirmed or if W is selected as the FW material. In this respect the effort done by 3D turbulence codes to self consistently include neutral atoms and molecules [44, 185, 201] may provide the answer, once the numerical schemes will be optimised up to the point of being able to simulate ITER scale scenarios.

2.6. Divertor transport and its influence on upstream plasma parameters

Important for the understanding of divertor detachment is detailed knowledge about the competing effects in a dense divertor. Various overview papers exists with references therein that discuss different aspects of the physics of detached divertors, including basic experimental observations (for an early assessment see [202]), basic detachment physics [203–206] and edge modelling and validation activities [72, 73, 207, 208]. Significant progress on the physics understanding could be achieved with the absence of C in metallic devices such as the JET-ILW that allowed a better disentanglement of relevant processes in the understanding of the power and particle exhaust problem. For a 2D divertor plasma model allowing an adequate prediction of the ITER divertor operational space the following features should be included to reproduce all the stages of the transition into detachment [79] on the basis of operational constraints as input parameter (system size and geometry, neutral pressure, particle throughput and SOL power flow) [72]:

- the cross-field drifts (i.e. $\mathbf{E}\times\mathbf{B}$ and grad-B drifts, section 2.3),
- a SOL transport model which does reflect also the advective nature of transverse turbulent transport (sections 2.4 and 2.5),
- and as complete as possible kinetic neutral physics model including volume recombination and, concomitantly,
- a representative geometric model for the vessel structure and internal divertor components at least in 2D, including an adequate model for neutral conductances up to the pumping region.

Consequently, it is almost impossible to derive a simple scaling law for power and particle exhaust in the divertor to predict edge plasma and neutral conditions at a reactor scale. Some features of the ramified physics can be maintained in the parametric sense. In unseeded H-mode and L-mode gas scans on JET-ILW, the averaged OT electron temperature, $\langle T_{\mathrm{e,OT}}\rangle$, has been observed to be a key parameter in correlating changes in the divertor recycling regime with the OMP separatrix density, $\mathrm{n}_{\mathrm{e,sep}}$ [209]. Whereas the deuterium gas valve fluxes and localised neutral pressure measurements in the divertor (see e.g. [210]) are suitable engineering parameters for correlating detachment evolution to $n_{\mathrm{e,sep}}$ changes via increasing edge particle inventory for a particular divertor geometry, $\langle T_{\mathrm{e,OT}}\rangle$ is shown to reconcile changes in pumping efficiency in different JET-ILW divertor configurations. Hence, previously reported [211, 212] divertor geometry influence on plasma performance is reconciled by mapping $n_{\mathrm{e,sep}}$ as well as global performance parameters such as H_{98}, density peaking to $\langle T_{\mathrm{e,OT}}\rangle$ thus yielding robust correlations, and more clearly linking changes in the edge plasma recycling and neutral dynamics to the confined plasma fuelling and observed performance degradation.

Clearly other ingredients are found to play a role in setting $\mathrm{n}_{\mathrm{e,sep}}$, namely the divertor recycling, the neutral leakage clearly influenced by divertor geometries [183, 213, 214], the FW materials and the main chamber recycling. The latter is hard to be properly modelled since it depends on far SOL transport which, as previously mentioned, is strongly anomalous.

ITER divertor design simulations for type-I ELMy H-mode detached scenarios usually assume diffusive radial transport coefficients to be set in the numerical model to identify the specific heat decay parameter λ_q in the near-SOL (i.e. for the ITER type-I H-mode simulations [215] anticipating additional widening $\lambda_q \approx 3\,\mathrm{mm} > \lambda_q^{\mathrm{Eich}}$) independently of how the divertor dissipates the heat-flux downstream [16]. The argumentation follows by the fact that upstream λ_q is essentially set by the assumptions for the ratio radial to parallel heat conductivity and thus λ_q in high-power H-modes is barely affected by the divertor transport itself (cf section 2.2). SOLPS-ITER simulations have confirmed this for unseeded JET H-modes [216] and also with low- to medium-Z seeding (e.g. with Nitrogen) using EDGE2D-EIRENE [217, 218]. With the impurities acting mainly on the level of dissipation in the divertor, there is no impact on the upstream conditions or the confined plasma region itself observed [85].

Along the field, parallel SOL plasma transport in high density conditions competes with dissipation driven by radial losses (e.g. turbulence or classical drifts) and the interactions with the neutrals and impurities. A rigorous attempt to identify and collect all relevant ion-neutral interactions and neutral collisional and transport processes for the ITER divertor design is summarised by Kotov and Kukushkin [215, 219] (and references therein). It is now widely accepted that for the overall ionisation-recombination balance in high density divertors, additional processes such as ion-neutral elastic collisions, charge-exchange (CX, resonant and non-resonant, including CX with impurities [220]), molecular assisted processes for enhanced recombination, ionisation and dissociation (MAR, MAI and MAD, respectively, [221–224]), neutral viscosity effects (neutral-neutral collisions) [225] and radiative excitation from opaque Lyman photons [226–228] must be considered. Spectroscopic investigation of N and Ne seeded induced detachment in JET ITER-like wall L-modes combining experiment and EDGE2D-EIRENE modelling demonstrated an enhanced ionisation at the OT is caused by high Lyman series opacity [229]. Here, and in contrast to experiment, EDGE2D-EIRENE simulations using optically thin divertor plasma assumptions show a larger impact of volume recombination and a factor of two shortfall in the LFS divertor n_e.

Various authors have demonstrated that the full inclusion of all aforementioned processes help to improve comparative studies of the divertor conditions in various devices (AUG [76, 230], JET [225, 231], Alcator C-Mod [74, 227] to cite only a few and a summary is given in [72]).

Although the recycling cloud peaks close to the strike-lines of the SOL plasma on the targets (with particle fluxes of the order $10^{23}\,\mathrm{s}^{-1}$ being dominant compared to the applied gas throughput), the neutral particles become less and less confined in the divertor PFR and flow disconnected from the magnetic field in the divertor volume and between sub-divertor structures. As a consequence, neutrals can equilibrate any occurring in-out asymmetries in the heat-flux that might be existing at lower density due to outward ballooning transport and/or combined poloidal and radial $\mathbf{E} \times \mathbf{B}$ drift-flows. A drawback is the loss of particles into the main-chamber and thus a closed divertor like a vertical-target (VT) configuration is beneficial to minimise the detrimental geometrical effect on neutral compression as foreseen in the ITER divertor design. Various numerical studies have been pursued to demonstrate the advantage of a closed divertor compared to a more open divertor for various devices (JET [232, 233], DIII-D [234], TCV [75]). Also the impact on the recirculation of particles below the divertor volume through sub-divertor structures up to the pump has been assessed by using a DSMC model approach for ITER [235] and JET [236]. The results were compared to previous benchmarks with EIRENE on JET [236, 237] demonstrating that the measured sub-divertor pressure can be matched for a given particle throughput in the experiment. The relevance of isotope effects in neutral transport has been demonstrated at JET ILW in H, D, DT and T campaign experiments for the onset of detachment [238]. Heavier isotopes due to their reduced speeds at otherwise fixed energies during recycling (assuming sheath conditions with $T_\mathrm{e} < 2\,\mathrm{eV}$) seem more confined in the divertor region causing less leakage and thus allow an earlier achievement of detachment at similar upstream densities [238]. The observations support previous results obtained on JET in C-wall era where detachment onset was observed at lower density for heavier isotope in Vertical divertor configuration in L-mode plasmas [239].

All the divertor processes described so far can be ascribed to some extent to interaction between charged and neutral particles or classical drifts (cf section 2.3). Nonetheless experimental evidences of divertor turbulence, not necessarily connected to the mid-plane turbulence previously described, have been reported [108, 240–242] for a long time with some theoretical predictions of the role of the X-point [243] geometry or divertor leg turbulence [244]. Despite this the amount of the information and the level of understanding of plasma turbulence in the tokamak divertor (including X-point region, divertor legs, and the PFR), is by far less advanced with respect to main SOL investigations. However, turbulent plasma transport in the private region along with drift effects might play an important role in the filling of the PFR with plasma, which forms the *baffle* preventing the penetration of neutrals from divertor to the core in the vicinity of the X-point. On the other hand, anomalous cross-field plasma transport in the divertor legs could be an important player in widening of the heat flux footprint on divertor targets, in particular important for the cases of advanced divertor configuration with additional X-points [245, 246] or long leg divertors [132].

Indeed, largely motivated by the interest towards Alternative Divertor Configurations, the amount of experimental and theoretical studies dedicated to divertor turbulence greatly increased in the recent years. Experimentally, information has been gathered using optical imaging diagnostic and reciprocating or wall mounted Langmuir probes [119, 128, 130, 131, 133, 247–249], focusing primarily on the dynamics of blobs, arising as non-linear evolution of plasma turbulence in both inner and outer divertor leg, as shown for example in figure 6 where divertor filaments as observed on NSTX are shown. It was found that similar to the blobs in the SOL, the blobs in the divertor region (in both inner and outer legs) move radially outwards towards the main-chamber wall. This

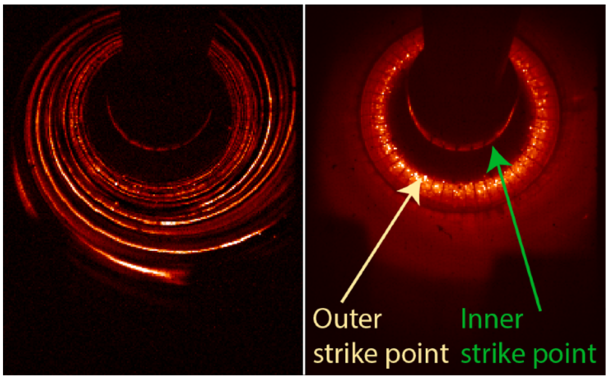

Figure 6. Li I imaging of divertor fluctuations in NSTX: fluctuating (left) and average (right) components. Reproduced from [131]. © 2018 IAEA, Vienna.

indicates that the *interchange drive* is the main mechanism propelling blobs in both SOL and divertor, although other mechanisms (e.g. Kelvin–Helmholtz instability) might originate similar structures. The velocities of the blobs in the divertor region are a few hundred m/s and also close to that in the SOL (e.g. see [130, 249]). The role played by divertor turbulence and divertor leg geometrical factors in the broadening of the density and particle fluxes at the target in inner and outer divertors is presently under investigation [134, 249]. As theoretically predicted [243], the level of correlation between main SOL and divertor blobs in the vicinity of the separatrix is low, implying the disconnection of the SOL and divertor turbulence due to X-point induced magnetic shear. An increase of such a correlation is on the contrary observed further toward the outer wall (e.g. see [248]).

2.7. Conclusions

Proper understanding of SOL physics and transport still represents a major challenge on the path towards reliable extrapolation of edge plasma characteristics to future devices. As stated, while the dynamics of parallel transport is reasonably well understood, including kinetic corrections and possible boundary conditions at the sheath, perpendicular and binormal transport is strongly influenced by turbulent processes which require complex 3D multi-scale simulations to be properly treated. Nevertheless in the past 15 years significant progresses have been achieved which increase confidences on physics understanding. A multi machine database of the heat flux decay has been established, providing a robust dependence of the heat-flux decay length for stationary inter-ELM period in attached Type-I ELMy H-mode with the inverse of the poloidal field strength at the OMP has been established. The scaling has been tested up to the magnetic field strength of the order of the one foreseen for ITER, projecting for ITER a value below 1 mm. Nevertheless, numerical simulations of ITER 15 MA operations suggest a bifurcated behaviour with rapid increase of λ_q for ITER likely due to a change on the type of anomalous transport foreseen across the separatrix in ITER. Unfortunately, none of the present running devices will be in the position to test the predictive transport modification and next step devices or further numerical independent modelling are mandatory to increase confidence on the expected behaviour. Concerning anomalous transport, which proved to be the main driver of far SOL heat and particle fluxes, it has been universally recognised to be dominated by macroscopic filaments, which propagate due to an internal polarisation. This mechanism has been modelled by electrical circuit-like models which have been reasonably well validated experimentally mostly in L-mode, but without substantial differences observed so far with inter-ELM filaments in H-mode low density scenarios. Although substantially less experimental evidence exists, these structures have been observed as well below the X-point, driving transport into the PFR. They seem to have similar drift-curvature drives, with possible additional mechanisms (such as Kelvin–Helmholtz instabilities along the shear layers close to the separatrix) at play.

High separatrix density with high gas throughput is envisaged for future burning plasmas. In these operational regimes all present devices exhibit a SOL density profile broadening known also as shoulder formation. While an overall understanding of such a mechanism has not been fully established, multiple investigations both in L and H-mode reveal that several ingredients are likely required, including increased turbulent transport, ensuring enough power flowing in the far SOL, reduced parallel flow and an increase of local neutral source coming either from main wall or divertor recycling. On H-mode, present understanding suggests that the increased transport is determined by the more resistive interchange unstable plasma close to the separatrix caused by an higher edge collisionality α_t. Extrapolation to future devices such as ITER is nevertheless still missing: whilst the conditions for increased transport in terms of edge collisionality might be met for ITER it is unclear if higher neutral divertor compression and pellet-dominated fuelling will provide sufficient ionisation source to produce a flattening of the density profile. In this respect, the choice of FW material may be particularly relevant, determining both the recycling coefficient as well as the average temperature of recycled neutrals. In case all the aforementioned conditions will be met, a potential increase of the FW heat fluxes will be envisaged with a possible enhancement of the erosion rates at the main wall.

Specific uncertainties remain in the upscaling of the SOL transport towards reactor scale exist. Those might be resolved by further experimental investigations as well as extended validated numerical simulations. Whereas in 2D the numerical assessment of SOLPS physics has matured to its main features, a complete treatment of edge plasma transport in full 3D geometry is still lacking. Technically, required tools have emerged but are still computationally very demanding for large devices such as like ITER: physical ingredients that are standard in 2D simulations, like multi-species interactions as well as full retention of kinetic effect for neutrals are presently being included in a full self-consistent approach also in 3D. Irrespectively of the remaining uncertainties in the physics models (e.g. far-SOL transport) it seems now feasible to have an integrated approach available that allows consistent predictions of the exhaust scenario in ITER from the wall to the core plasma including transport of impurities.

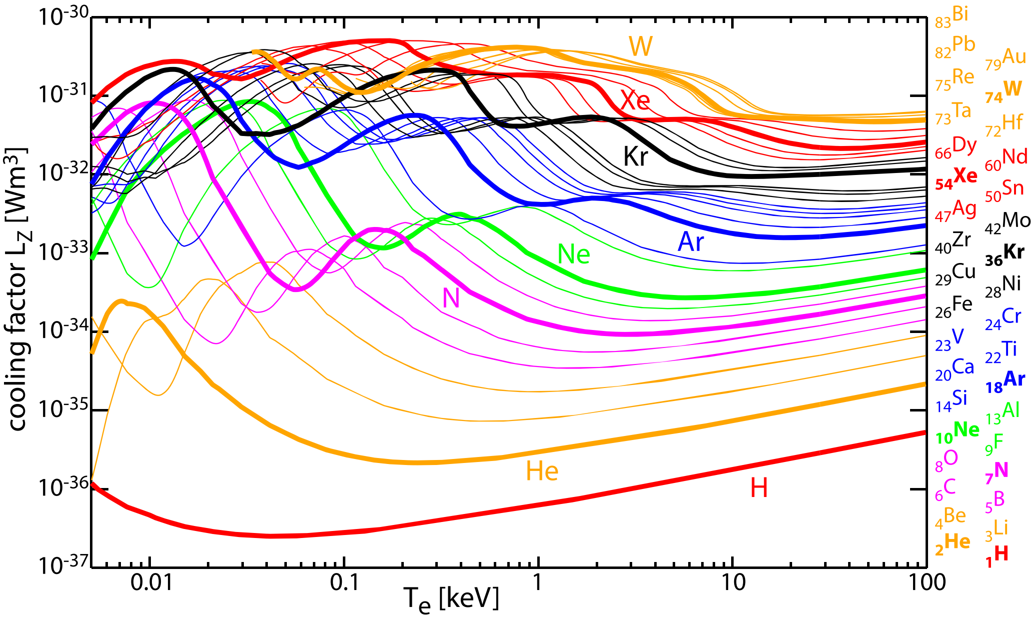

Figure 7. Radiative loss function L_z for a number of elements calculated for coronal equilibrium. Reproduced from [253]. © 2019 EURATOM. All rights reserved.

3. Stationary power dissipation

3.1. Introduction

With the introduction of high-Z elements such as tungsten as PFMs, and the subsequent loss of self-regulating carbon erosion/radiation, the use of impurity seeding became necessary for the attainment of at least partially detached divertor conditions [250], which is the foreseen operational scenario for ITER [16, 251]. Partial detachment is required for the limitation of the peak heat flux to about 10 MW m^{-2} in discharges with high heating power in present day machines as well as in ITER. The role of the seed impurity is to radiate a major fraction of the power entering the SOL and to cool down the plasma to electron temperatures of a few eV in order to allow momentum loss processes like CX and recombination to become effective [221, 252].

Figure 7 shows recent calculations of the radiative loss function for a large range of elements [253]. As a consequence of the temperature dependence of the radiative loss function L_z, N, Ne and Ar are considered as divertor radiators for the expected ITER parameter range while maintaining low core radiation. A quantitative calculation and prediction of radiative losses turned out to be complicated by the presence of non-coronal conditions, caused by sources and transport [254] as well as CX with neutral deuterium [220]. The underlying key challenge is to minimise the amount of core dilution and central radiation losses which are caused by the divertor seeding required for the achievement of the aspired detachment level. This condition can be expressed by the divertor enrichment parameter, usually taken as the ratio of the divertor- and the core impurity concentrations. A prediction of the enrichment by 2D modelling turned out to be a very difficult task, since a number of physics effects and a delicate balance between parallel forces are involved [255].

An open question regards the impact of the near SOL parallel heat flux width λ_q, as introduced in the previous section. Small values of λ_q have a negative impact on the achievement of acceptable power fluxes at the divertor: First, they lead to a higher heat flux for given conducted power. Second, they reduce the divertor volume available for radiative power dissipation, and thus require a higher impurity content for the achievement of detachment.

ITER divertor modelling uses an intermediate value of $\lambda_q = 3.4$ mm for 15 MA Q = 10 plasmas, between that of the Eich scaling (1 mm) and of edge turbulent transport models (≈6 mm); an in-depth discussion on this topic is given in [16]. Additional effects, such as wall pumping and, in the case of N_2 seeding, ammonia production [256–259] further complicate the prediction of required seeding fluxes. While nitrogen is in principle a possible divertor radiator for ITER, the use of other gases would be preferred due to implications of tritiated ammonia formation for the duty cycle and the design of the tritium plant [16]. The optimal impurity mix is defined by:

- maintaining detachment and buffer transients
- allow control of the detachment state
- minimise fuel dilution, radiation and confinement losses in the plasma core
- keep $P_{\mathrm{sep}} > P_{\mathrm{LH}}$
- minimise erosion and fuel retention.

This chapter is organised as follows: the first section describes divertor seeding experiments in current tokamaks aiming at partial detachment in H-mode. Following, more

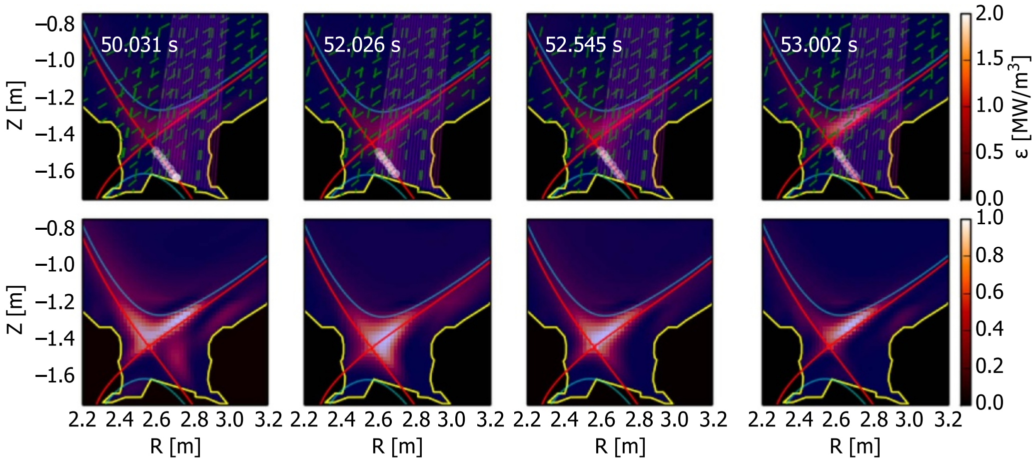

Figure 8. Distribution of the inter-ELM radiated emissivity from bolometer tomography of the nitrogen seeded JET H-mode discharge #89241 (top row plots normalised to identical scale, bottom row plots normalised to respective maximum values). The temporal development follows a ramp-up of the seeding rate. Reproduced from [260]. © 2017 CCFE. All rights reserved.

pronounced detachment scenarios and the XPR regime are addressed. Next, the integration with no-ELM scenarios is discussed before detachment control techniques are summarised. Empirical detachment scalings are briefly reviewed as well as the status of 2D modelling of high power H-mode. Finally, the impact of seeding on the pedestal and core performance and future work and steps beyond ITER are addressed. Some conclusions are drawn at the end of the chapter.

3.2. Divertor impurity seeding for partial detachment

Impurity seeding for the attainment of partially detached conditions in H-mode, as foreseen in ITER, has been developed in various devices, including Alcator C-Mod [261, 262], AUG [80, 192], DIII-D [214, 263, 264], EAST [265], JET [266–269], JT-60U [270, 271] and TCV [180, 272]. Detachment is understood here as a substantial pressure loss along a flux tube in the divertor, which is accompanied by a strong reduction of the target heat load. Seeding has been applied successfully with various divertor configurations, while a closed divertor is supposed to deliver the highest power dissipation rate for a given core plasma impurity pollution [214]. However, a quantitative assessment of the effect of the divertor closure is not available yet, and additional parameters effect the power dissipation. The combination of impurity seeding and tungsten PFCs also brought up the problem of tungsten sputtering by the seed impurity. The increase of the sputtering yield due to the presence of a heavier species can be compensated by a sufficient reduction of the electron temperature in front of the target [273], thus an optimisation of the seeding rates is required.

With increased seeding, plasma parameters such as ELM frequency, divertor temperature and ion and power fluxes to the target are changing, partly with different time scales. In JET with increasing nitrogen puff rate, a continuous movement of the radiation front, measured inter-ELM as shown in figure 8, from the OT up to the X-point region is observed, accompanied by a quite steady reduction of the total ion fluxes to the inner and OT [260]. More steady phases of X-point radiation are obtained in JET ILW compared to carbon walls.

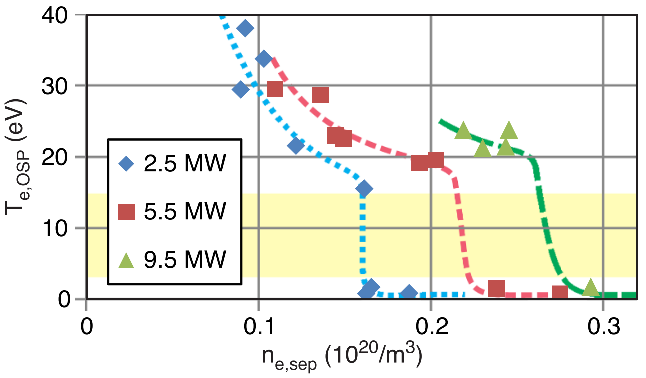

Figure 9. Bifurcation of the divertor temperature near the outer SP, $T_{e,OSP}$, in DIII-D during detachment in a density scan (here represented by the upstream separatrix density, $n_{e,sep}$) at different heating powers. Reprinted from [274], Copyright (2015), with permission from Elsevier.

In DIII-D, a quite steep dependence of the divertor T_e, measured by TS, on the upstream separatrix density has been found [274, 275]. This manifests in a very quick reduction of the (inter-ELM) T_e during the detachment process from 10 down to 2 eV, called detachment cliff, as shown in figure 9. The possible explanation of this bifurcation is given by the interdependence of $\mathbf{E} \times \mathbf{B}$-drift fluxes, divertor electric potential structure and divertor conditions [63].

The divertor neutral pressure has been identified as an important parameter for the power exhaust by impurity seeding, both in modelling [276] and in experiment [192]. A high neutral deuterium pressure leads to a better impurity compression in the divertor, and, thus, usually to a higher ratio of divertor radiation to core impurity contamination. A combination of neutral pressure and detachment control has been implemented in AUG [277], but most experiments use a fixed deuterium puff leading to quite constant divertor neutral pressure conditions. On the other hand, increased neutral pressure is generally associated with reduced energy confinement/H-factor [278]. Therefore, combining deuterium with impurity puffing presents, broadly speaking, an optimisation task to achieve a balance between core impurity level and energy confinement.

Most experiments in mid-size tokamaks employed nitrogen seeding to increase the divertor radiation. Compared to neon, nitrogen has a higher radiative loss function L_z at low electron temperatures around $T_e = 10\,\mathrm{eV}$ (see figure 7) and leads to higher divertor radiation levels [268]. Nevertheless, detachment can also be achieved with neon [269], but the radiating zone is located more upstream, and a higher core pollution is observed. Argon also exhibits a peak in L_z between 10–20 eV. Its contribution to the divertor radiation is often masked by argon radiative losses in the pedestal and core regions, which reduce the divertor input power. An important parameter is the neutral impurity mean free path, which has a strong influence on the divertor impurity retention at least in mid-size tokamaks [279, 280]. Nitrogen, neon and argon are the main divertor cooling candidates for ITER, while for a future DEMO with a conventional ITER-like divertor, a core radiating species like krypton or xenon needs to be added to dissipate sufficient energy already inside the separatrix and reduce the power flux to be just above the LH power threshold [281]. The important aspects of different impurity divertor enrichment will be discussed in subsection 3.7.

3.3. Pronounced detachment and XPR

If seeding is further increased under partially detached condition, pronounced detachment [192] and an XPR regime [282–285] are obtained. In the XPR regime, the radiation concentrates in a small region at the X-point or inside of the confined plasma region (see figure 10), from where up to 40% of the exhaust power are dissipated by radiation. Similar radiation patterns are observed e.g. in JET [286], JT-60U [287, 288] and KSTAR with an open divertor geometry [289]. The radiation patterns are comparable to a MARFE [290]. They were rather stably maintained, but the peak location was not actively controlled.

An XPR has been observed at AUG with N_2 and Ar seeding [80, 283], at JET with N_2, Ne, Ar and Kr seeding [268, 269], and at EAST with Ne seeding [284]. For AUG, this radiator is observed to move inside the confined region, up to 15 cm above the X-point. With a high location of the radiator ($\geqslant$7 cm above the X-point), ELMs are suppressed. Position control of the XPR was demonstrated by, e.g. nitrogen seeding as actuator [283]. The XPR is connected to a strong local density increase inside the X-point area and a corresponding electron temperature reduction to a few eV, therefore a parallel T_e gradient towards the OMP is present [291]. Due to the very large flux expansion close to the X-point, the affected field lines on which parallel T_e gradients appear inside the plasma are very close to the separatrix, at the foot of the pedestal. This is regarded as key ingredient to make high confinement and highly radiating plasmas compatible [262].

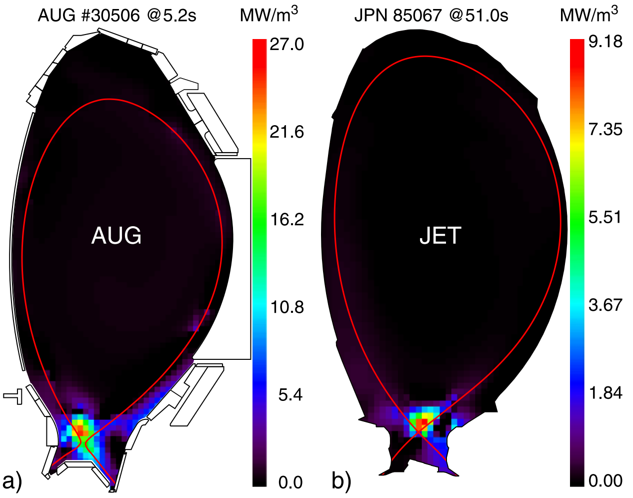

Figure 10. Radiation distribution of nitrogen seeded discharges at (*a*) AUG (#30506) and (*b*) JET (#85067) in the pronounced/fully detached state. Reproduced with permission from [268]. CC BY-NC-ND 4.0.

With the access to partial or pronounced detachment, an increase of the line averaged electron density and a reduction of the energy confinement are observed. With the access to the ELM suppression via an XPR the pedestal parameters are affected, leading to a density reduction of 10%–15% while keeping the confinement (with respect to the ITERH98P(y,2) scaling) about constant [283]. For JET, impurities, such as Ne, can have a stabilising effect on core ITG modes, leading to higher core electron temperature gradients and, thus, an increased core confinement while having the pedestal reduced [269]. In EAST, Ne seeding induced detachment is usually accompanied by a significantly increased radiation near the X-point [284] in grassy ELMy H-mode plasmas. The radiation in EAST was measured by the absolute extreme ultraviolet (AXUV) radiation diagnostic. The chord-integrated radiation peaks far away from X-point before neon seeding, while it peaks around the X-point region after neon seeding. The AXUV measurements are corroborated by spatially resolved measurements of the Ne II line emission at 421.97 nm in the divertor. While X-point radiation is not the foreseen operational regime for the ITER divertor, the unambiguous observations in metal wall tokamaks indicate that such a regime might also be accessed at ITER and could potentially provide a suitable scenario to alleviate transient power fluxes by ELMs.

According to an analytical model [285], which has been corroborated by SOLPS modelling [84] the penetration of neutrals is important for the formation of the XPR. In this context, recent detachment studies in the HL-2A tokamak are of interest [292]. With its very closed divertor configuration, detachment is observed without formation of a radiation zone in the X-point region, and no accompanying rise of the core density. In the current understanding of the XPR, this is expected to be caused by the geometrical screening of the neutrals.

3.4. Integration with no-ELM scenarios

In ITER as well as in a future DEMO, divertor detachment needs to be integrated with a no-ELM scenario for material fatigue avoidance. Work on this has started on several devices, but no-ELM scenarios are often achieved under conditions of low separatrix density and divertor neutral pressure, where higher values around $p_0 = 10\,\mathrm{Pa}$ are expected in ITER [16]. The XPR scenario described before generally works at high divertor densities, but requires further understanding and predictive modelling for extrapolation. The simultaneous achievement of low pedestal collisionality, as required for some no-ELM scenarios like QH-mode and RMP ELM suppression, and high divertor collisionality as favourable for detachment is—for standard fields and currents—only possible in large devices like ITER or DEMO.

A number of seeding studies have been performed in the type-III ELMy scenario [266, 270]. This ELM type exhibits more benign power load characteristics in comparison to type-I ELMs in present day devices. However, extrapolation to ITER is still unclear due to the temperature dependence of type-III ELMs.

Seeding into I-modes revealed an issue with the integration of detachment [293], namely an I-L transition occurring during nitrogen seeding before detachment of the outer divertor is achieved. Detachment of the inner divertor could be achieved with N_2 seeding in AUG [294].

In the EDA H-mode [295], very high pedestal pressures have been achieved in the final experiments on Alcator C-Mod [296]. A quite straightforward integration of a no-ELM regime and partial detachment has been obtained in the EDA H-mode [297] in AUG. Figure 11 shows time traces of an EDA H-mode discharge in AUG with a double feedback of Ar for pedestal radiation, required to maintain the EDA H-mode at high heating power, and nitrogen seeding to achieve partial divertor detachment. No-ELM conditions are supposed to be maintained by additional transport caused by a QCM in the pedestal region [298], see also section 5.5 in chapter *Pedestal and Edge Physics* [11].

Extending the EDA H-mode to higher gas puff and separatrix density, the QCE regime is obtained in AUG at high triangularity close to double-null. Here, a strong broadening of the power width is measured at the target by IR thermography, with λ_q a factor of 4 larger than the inter-ELM value in a standard H-mode at the same B_p [35]. The ballooning mode activity close to the separatrix linked to an increased filament frequency is supposed to be the origin of the widening of the power carrying layer.

Radiative L-modes sometimes exhibit improved energy confinement, partly due to a stabilisation of ITG modes by increased Z_eff and dilution [300]. But these improvements are assumed not to be sufficient to run a reactor-grade device under L-mode conditions [301]. RMP effects on the power load will be discussed in section 5.

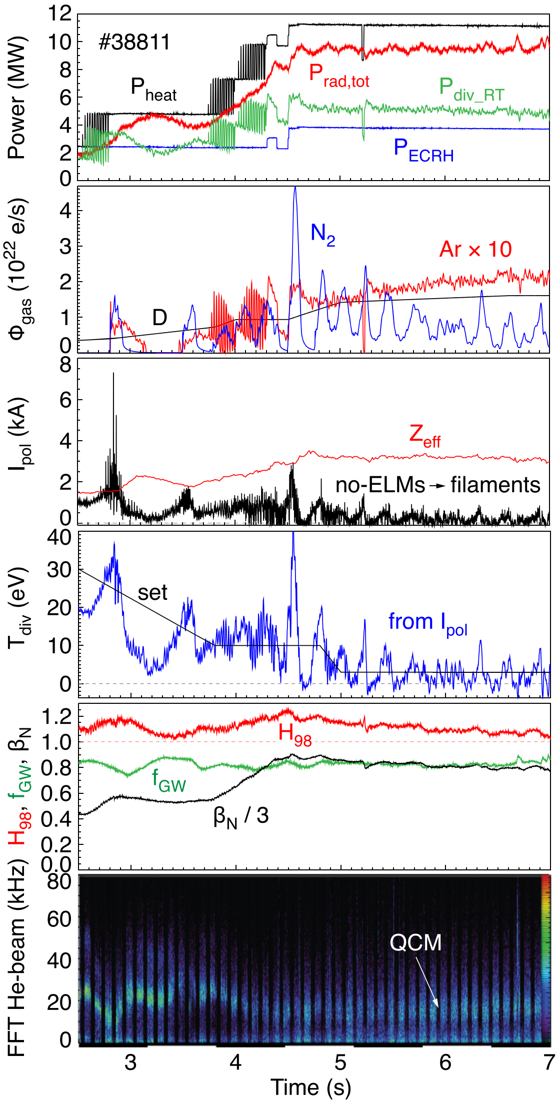

Figure 11. Time traces of a partially detached no-ELM discharge in EDA H-mode with double seeding feedback of nitrogen and argon in ASDEX Upgrade. Reproduced with permission from [299].

3.5. Detachment control: sensors and application

A large number of sensors have been introduced for radiative divertor control, mainly based in the outer divertor. Measurements of the divertor radiation, aiming at the difference of $P_\mathrm{sep} - P_\mathrm{rad,div}$, and/or direct measures for the power impinging the target plates are used [302]. For partially detached conditions at the target, passive thermoelectric current measurements by shunts can be used as the most simple and robust diagnostic [303]. The measurement itself is sufficiently fast to distinguish between ELM and inter-ELM periods, although the variation in the divertor current itself is limited by the current redistribution time of the considered section of the divertor [304]. Foil bolometry has also been used

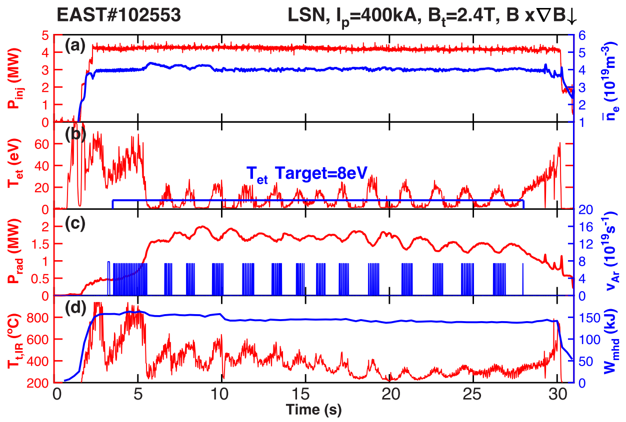

Figure 12. Active detachment feedback control in a 30 s long-pulse H-mode plasma with W divertor on EAST. (*a*) Line averaged density and heating power, (*b*) feedback controlled T_{et} around the strike point at lower outer plates, (*c*) radiative power in the bulk plasma and Ar seeding rate, (*d*) plasma stored energy and IR-camera measured peak surface temperature. Reproduced from [312]. © 2022 IAEA, Vienna. All rights reserved.

successfully [305, 306]. However, due to high significant noise levels, time averaging is required reducing the final temporal resolution to several milliseconds [307]. AXUV diodes [308] allow fast measurements of divertor radiation [283, 284], but the strong energy dependence of their sensitivity hinders the evaluation of absolute values of the radiated power.

More demanding with regard to real time evaluation are Langmuir probes, either for the ion saturation current j_{sat} [309, 310] or the electron temperature at the target $T_{\mathrm{e,t}}$ [265, 311]. The latter allowed at EAST the control of detachment for more than 25 s [312], as shown in figure 12. Before full detachment, at target temperatures $T_{\mathrm{e,t}}$ in the range 5–8 eV, the detachment control can be applied while maintaining good confinement. For strongly detached plasmas, where $T_{\mathrm{e,t}}$ and j_{sat} are at minimal values, Langmuir probes do not allow a detailed control. Similarly, near-surface thermocouples [313] and infrared thermography [314] appear less useful for detached conditions. This caveat is due to the low power fluxes, where the former suffer from a poor temporal resolution through the significant (0.1 s for ITER) thermal response time [315] and the latter is additionally disturbed by low surface emission and by volumetric emission of the detached divertor plasma in the infra-red spectrum. For deeper than partial detachment, control of the spatial location of the detachment front is achieved by camera measurements (MANTIS [316, 317]) or arrays of AXUV diodes, either in the divertor volume or just inside the X-point (XPR). TS can provide direct measurements of n_{e} and T_{e} in the divertor volume and is applied to control the onset of detachment [275], but due to the limited time resolution of TS measurements, ELM filtering remains a challenge. Volumetric radiation losses derived from line-integrated bolometer measurements are used on various devices and are mainly used to determine the net power into the divertor.

The combination of several diagnostics in one control scheme has been demonstrated such as $T_{\mathrm{e,t}}$ guided $P_{\mathrm{rad,X-point}}$ control [284], or simultaneous divertor and main chamber radiation feedback [305]. A scheme where multiple complementary diagnostics are used to control one detachment state is not shown yet and constitutes a task for the following years. Not only redundancy is important but also diagnostics that complement each other in terms of resolution allowing the observation of a larger operating space with a higher temporal and spatial resolution. This also requires the development of control-oriented models of the exhaust which can integrate those diagnostics and enable *a priori* controller development or more advanced model predictive control approaches. An issue for the operation of high power devices such as ITER with detachment control is a transient re-attachment, e.g. caused by a power excursion [16]. This is expected to be easily detectable by the diagnostics mentioned above. The long time scales related to the large volumes and core impurity confinement times in reactor grade devices will challenge the controlled buffering of fast transient events. Predicable events can be dealt with by predictive control schemes, while unpredictable events require a faster method of actuation than gas injectors, e.g. the injection of impurity doped pellets [318].

3.6. Empirical scalings

A number of empirically based analytical scalings have been developed for the prediction of the onset of detachment under impurity seeded conditions [319–321]. The prediction of the divertor radiation is based on the two-point model, using Spitzer–Härm conductivity for the electron temperature variation along the field lines and pressure conservation. The radiation is obtained by the weighted integral of the radiative loss function L_z over the SOL temperature range from the mid-plane to the target, as originally proposed by Lengyel [322] and recently re-derived in [254] for comparisons to SOLPS-4.3. These comparisons reveal a general over-prediction of the divertor impurity concentration at target ion flux rollover by the Lengyel model, but a correct capture of parameter dependencies. Since the analytical scalings are usually obtained for vanishing heat flux at the target, most of the models associate detachment with 100% radiation of P_{sep}. The plasma parameters inferred by the (modified) two-point model could be quite well corroborated for unseeded H-modes in DIII-D by experimental measurements in the mid-plane, the divertor volume and at the target [323]. This supports the procedure of calculating the power width λ_q from mid-plane temperature and density decay lengths assuming Spitzer–Härm conductivity for detached conditions, where inference via target profiles is not possible. The scalings are gauged on experimental measurements and cannot predict effects during detachment, since recombination and neutral particle interactions are neglected.

For the calculation of the divertor radiated power based on impurity concentrations, non-coronal effects need to be included in the calculation of L_z. Radiation enhancement by non-coronal effects can be calculated from atomic data. For the simulation of divertor conditions, e.g. in ADAS [324], neutral atoms are exposed to a plasma with the specified n_{e}, T_{e} and the emitted radiation is integrated for the residence time τ_{div}, resulting in an averaged loss power. The increased radiation is emitted during the ionisation of the impurity, while lower radiation levels are usually obtained from the equilibrium ionisation stage. Therefore long residence times lead to lower radiated power per atom, see also [325]. Often the non-coronal parameter $n_e\,\tau_{\text{div}}$ is used for parametrisation of the radiation loss function L_z. This parameter represents the ratio of the divertor residence time τ_{div} and the ionisation time which is $\propto 1/n_e$. In reality, additional effects may also lead to deviation from coronal equilibrium, such as CX with D atoms [220] or recombination of higher charged impurity ions in combination with transport effects [288].

The analytical models [319–321] predict a strong rise of the divertor radiation with the upstream separatrix density or separatrix Greenwald fraction, $P_{\text{rad,div}} \propto n_{\text{e,sep}}^{2-3}$. For the divertor neutral flux based model [321] this relation is recovered by the strong dependence of the divertor neutral flux $p_0 \propto n_{\text{e,sep}}^3$. It should be noted that the (weak) rise of $n_{\text{e,sep}}$ with p_0 has been observed to saturate in 2D ITER divertor modelling [16] due to effects related to the SOL ionisation power balance [250]. The favourable effect of a high TF has been emphasised for conditions where the mid-plane density is limited to a fraction ($\approx$0.5) of the Greenwald density [320].

A problem in comparing the models to experimental data is the lack of direct measurements of impurity concentrations in the divertor. These have been recently established for nitrogen [326] and carbon [327], and a corresponding detachment scaling has been developed [328]. While the predicted impurity concentration levels at detachment onset bear significant uncertainties due to the atomic physics effects and the neglect of 2D effects in the divertor geometry, the strong rise of divertor radiation with $n_{\text{e,sep}}$ squared or even stronger can be regarded as being robust. This favours high density scenarios for benign exhaust, as foreseen for ITER, and suggests an issue for scenarios which require lower $n_{\text{e,sep}}$ and also a challenge for larger machines that tend to have a lower Greenwald density which require other approaches to divertor power dissipation beyond that provided by an ITER-like divertor (i.e. super-X, snowflake, etc).

3.7. 2D modelling of impurity seeding and enrichment for divertor detachment

Divertor simulations, involving 2D modelling in the poloidal plane under the assumption of toroidal symmetry, have been developed to reproduce experimental results, particularly for impurity seeded divertor detachment. Identification of the crucial physics mechanisms to produce the energy and momentum losses [329], control of the detachment onset (rollover of the particle flux), and further improvement of their modelling are the most important tasks for a reliable extrapolation to ITER divertor conditions. At the same time, impurity penetration into the core plasma while increasing the divertor radiated power is an important issue for selection of the seeding species. A relevant parameter is the divertor enrichment η_z [330], which measures the ratio of divertor (either ion or neutral) and core impurity concentrations. Among the divertor radiating species nitrogen, neon and argon, neon exhibits comparatively low divertor enrichment values (using n_{imp} at outer divertor separatrix and mid-plane SOL), experimentally shown in AUG [297] and DIII-D [331] as well as in ITER SOLPS 4.3 modelling such as $c_{\text{imp}}^{\text{OSP}}/c_{\text{imp}}^{\text{OMP}} = 0.5\text{–}1$ in the detached divertor [254]. For the medium size tokamaks, the assumed cause for the low enrichment of neon is its high neutral ionisation energy, which leads to a long ionisation mean free path. The reported low helium enrichment values well below 1 [2] are at least partly explained by its long ionisation mean free path, a further reduction of helium enrichment has been observed during divertor detachment [332]. Comprehensive measurements of the divertor enrichment will provide important input and benchmark for the modelling of impurity transport in the SOL and divertor, i.e. the ionisation length of impurity atoms, and the parallel force balance between the thermal (temperature-gradient driven) and friction forces from the bulk plasma. Another important aspect for the core density of the seeded impurity is the pedestal neoclassical transport, particularly for the higher Z seeded impurities [333]. Altogether, this will help to make an informed decision on the best divertor radiating species for ITER.

Physics modelling of the detached divertor for high power heating scenarios is challenging work at this stage. One reason is the very high computational costs for H-mode plasma profiles with steep radial and parallel gradients of T_e and n_e, and, in particular, for activating drifts. ITER divertor modelling has been mainly based on SOLPS4.3, which did not include a drift description. Recent calculation results with SOLPS-ITER, albeit for a limited parameter set for the ITER divertor [16, 280, 334] confirmed the general trends of these calculations such as the reduction of the total peak heat load at the target ($q_{\perp\text{pk}}$) with increasing divertor neutral pressure (p_n). Effects of activating drifts appear in systematic enhancements of divertor in-out asymmetries of impurity concentrations as well as the plasma density, which in turn cause asymmetries of the radiation loss and power load.

Figure 13 shows SOLPS calculations for the OT peak heat flux versus the neutral pressure for different code settings [334]. Effects of the drifts on the plasma and impurity (Ne) transport in both SOL and divertor are significant under attached divertor conditions (neutral pressure $p_0 = 2\text{–}6$ Pa), such as an $\approx$2 times enhancement of the outer $q_{\perp,\text{pk}}$. Since these values of the outer $q_{\perp,\text{pk}}$ become larger than 10 MW m^{-2}, the drift effect may have a large impact on the ITER operational scenario. On the other hand, the effect becomes smaller under detached divertor conditions ($p_n \geqslant$ 7 Pa) and the inner and outer $q_{\perp,\text{pk}}$ become similar (difference less than 20%) and less than 10 MW m^{-2}. The in–out asymmetry of $q_{\perp,\text{pk}}$ is mainly produced by that of the divertor radiation $P_{\text{rad}}^{\text{div}}$. With inclusion of drifts, enhancement of the inner divertor radiation and reduction of the outer divertor radiation are observed under attached conditions ($p_0 \approx 5$ Pa). The asymmetry effects are small under detached conditions. The high penetration of seeded neon into the main plasma as observed in AUG and DIII-D experiments and modelling is not predicted for ITER in SOLPS modelling due to the shorter mean-free-path of impurity ionisation and larger divertor size.

Quantitative validations of the impurity screening and enrichment factors are still not available because strong spatial variations of the divertor impurity concentrations are often

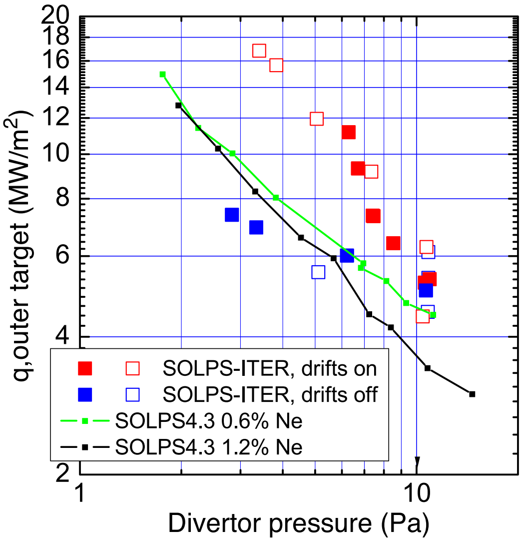

Figure 13. Peak heat flux at the outer ITER divertor versus neutral pressure from SOLPS-ITER with and without drifts (filled points at $c_{\mathrm{Ne}} = 0.8\%–1.1\%$, all points in the range $c_{\mathrm{Ne}} = 0.35\%–2\%$) and from the SOLPS4.3 database at two different values of c_{Ne}. Reproduced from [334]. © 2020 IAEA, Vienna. All rights reserved.

found in modelling [334] and measurements usually provide line-integrated values. 2D measurements of impurity ion concentrations near the divertor target are required, and so far only available for N and C, albeit with approximations for the plasma parameters along the lines of sight [326, 327]. A more global divertor concentration parameter such as the ratio of impurity and deuterium neutral fluxes in the sub-divertor appears therefore appropriate for model validation [328]. On the contrary, impurity concentration measurements in the core and edge plasma are generally available from CX recombination spectroscopy (for fully ionised N and Ne, and some Ar ionisation states).

3.8. Impact of seeding on pedestal and core performance

Strong impurity seeding affects the pedestal and core performance. Generally, a high separatrix density, as required for maximising the divertor radiated power with acceptable level of the core impurity pollution, is observed to lead to a reduction in the pedestal top pressure, i.e. to a weakening of the ETB. Furthermore, it is difficult to obtain H-mode plasmas with a high Greenwald density fraction ($f_{\mathrm{GW}} = 0.9–1$) only by external gas fuelling, as was seen in metal wall experiments of JET-ILW and AUG [335]. On the positive side, the confinement degradation at high $n_{\mathrm{e,sep}}$ is accompanied by a broadening of the power width [34, 336, 337]. Plasma shaping may be an optimising parameter in this respect [263]. The reduction of the pedestal top pressure with increased fuelling has been explained by an outward shift of the density profile leading to a subsequent reduction of the pedestal stability in AUG [338]. A pedestal reduction can also be attributed to the high collisionality reduction of the edge bootstrap current resulting in lower edge MHD stability [339]. The two effects are related and both scale positively to larger tokamaks and lower collisionality pedestals. The higher density in the separatrix region is related to the formation of a HFSHD region [82, 340] in combination with radial particle transport. The HFSHD is partly driven by the power flow in the SOL, which can be counteracted by nitrogen radiation. Therefore, nitrogen seeding mitigates the HFSHD leading to a density profile inward shift and energy confinement recovery [338, 341, 342]. A similar trend, in particular, for nitrogen seeding has been confirmed in JET-ILW [342] [343] and Alcator C-Mod [262, 344]. For Ne seeding this effect is weaker and can lead to unstable regimes, while for Ar no confinement improvement is observed [268]. With increasing core Z_{eff} and radiation loss inside the separatrix, an improvement of core energy confinement produced inside the pedestal may be attributed to (partial) stabilisation of ITG turbulence by the impurity related ion dilution [269, 301]. This effect may also be responsible for the limited impact of the XPR regime on the confinement, as observed at AUG [283], and resembling the original findings of the completely detached H-mode [345].

High integrated plasma performances with a detached divertor relevant to the ITER inductive scenario were demonstrated so far with fuel gas puff and nitrogen seeding, where the main plasma radiation fraction ($f_{\mathrm{rad}}^{\mathrm{main}} = P_{\mathrm{rad}}^{\mathrm{main}}/P_{\mathrm{heat}}$) was at ITER level. In AUG, with plasma parameters in the range of $I_{\mathrm{p}} = 1–1.2\,\mathrm{MA}$, $q_{95} = 3.7–4.3$, $P_{\mathrm{heat}} = 14–25\,\mathrm{MW}$ and a normalised separatrix power flux, $P_{\mathrm{sep}}/R_{\mathrm{p}}$, of up to $10\,\mathrm{MW\,m^{-1}}$ (where P_{sep} denotes the total power flow across the separatrix and R_{p} denotes the plasma major radius), a plasma performance in terms of $H_{98} = 0.95–1$, $\beta_{\mathrm{N}} \sim 3$, $f_{\mathrm{rad}}^{\mathrm{main}} \sim 0.3$ and $f_{\mathrm{GW}} \sim 0.8$ could be achieved with a partially-detached divertor [192]. In subsequent experiments, $H_{98} \sim 0.95$ could be maintained with pronounced divertor detachment and ELM suppression using a controlled XPR [283].

In JET-ILW discharge #85425 with plasma parameters $I_{\mathrm{p}} = 2.5\,\mathrm{MA}$, $B_t = 2.7\,\mathrm{T}$, $q_{95} \approx 3.3$, $P_{\mathrm{heat}} = 18\,\mathrm{MW}$ and $P_{\mathrm{sep}}/R_{\mathrm{p}} \approx 5\,\mathrm{MW\,m^{-1}}$, a performance in terms of $H_{98} \approx 0.85$ was achieved with a high radiated fraction $f_{\mathrm{rad}}^{\mathrm{total}} = (P_{\mathrm{rad}}^{\mathrm{main}} + P_{\mathrm{rad}}^{\mathrm{div}})/P_{\mathrm{heat}} \approx 0.65$ at $f_{\mathrm{GW}} = n_{\mathrm{e}}/n_{\mathrm{GW}} \approx 0.85$ [282]. These radiative plasmas were restricted to high $f_{\mathrm{rad}}^{\mathrm{total}}$ (0.6–0.7 in AUG and 0.60–0.65 in JET-ILW), where the radiation peak near the X-point was located inside the confined plasma as shown in figure 10 [268]. Recently, JET obtained high plasma performance with neon seeding, reaching $H_{98} \approx 0.9$ and $f_{\mathrm{GW}} \approx 0.94$ at 30 MW heating power with low power deposition on the W divertor [346].

Recovery of confinement degradation during mainly N_2 seeding with nearly full detachment has recently been demonstrated in DIII-D by combination of detachment control with an ITB in high H_{98} ($\approx$1.5), β_{N} ($\approx$3) and β_{p} ($>$2) discharges [264, 311, 347, 348], which were achieved in a collaboration with similar EAST experiments. This integrated high performance scenario aims for the ITER steady-state conditions with a reduced disruption probability at high $q_{95} = 7–8$, and better core plasma performance and controllability. The appropriate N_2 seeding rate for nearly full detachment was so far set via the ion saturation current (particle flux) at the target,

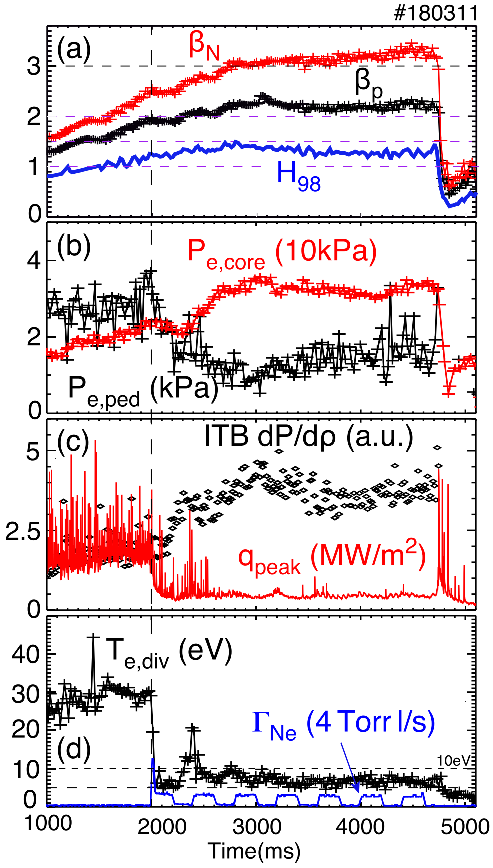

Figure 14. Time traces of a Ne-seeded discharge with internal transport barrier and ELM suppression in DIII-D. Reproduced from [347]. CC BY 4.0.

and the X-point radiation (inside separatrix) was dominated by intrinsic carbon ions rather than by the seeded nitrogen. This may contribute to produce a relatively low pedestal top pressure and ELM mitigation but also a large ITB inside $\rho \sim 0.8$. Control of ETB and ITB by seeding and fuel gas puffing has also been reported. Extrapolation of the integrated scenario and control method to ITER edge and SOL plasma conditions with higher temperature and lower collisionality is an important challenge for high power experiments and integrated modelling.

Neon injection was also applied to this scenario, which can lead to a partially detached divertor with $T_{\mathrm{e,t}} < 10\,\mathrm{eV}$. ELM suppression was achieved due to further reduction of the pedestal height [264, 347]. Even with a strong pedestal degradation, a high confinement core is still achieved, with $H_{98} = 1.3$–1.4, $\beta_{\mathrm{N}} > 3$, and $\beta_{\mathrm{p}} > 2$ at $q_{95} \sim 7$, as shown in figure 14.

Due to the synergy of an ITB and the pedestal, an even stronger ITB forms with the pedestal reduction. This regime with high confinement high β core, detached divertor, and no/small ELMs may open a path for core-edge integration without the intermittent HHF from ELMs. On the other hand, neon results in a strong fuel dilution and increasing of Z_{eff}, which would be unacceptable in a fusion reactor. Pedestal and core impurity transport studies are required to understand the extrapolation of the experimental impurity levels to a fusion reactor.

3.9. Future work and steps beyond ITER

Power exhaust becomes more challenging in DEMO compared to ITER, due to higher absolute heating power, possibly even more tight fuel dilution limits, steady state requirements (lower separatrix/divertor density) and neutron irradiation resulting in both higher material degradation and strong limitations for diagnostics resulting in a sparsely diagnosed device. Several power exhaust scenarios and conventional divertor concepts for a future reactor (DEMO) have been developed in ITER Member countries.

Divertor modelling and scenario development for power exhaust in a divertor larger than that of ITER ($P_{\mathrm{fus}} = 1$–$2\,\mathrm{GW}$, $R_{\mathrm{p}} = 7$–$9\,\mathrm{m}$) are ongoing for the European DEMO (2 h pulsed) operation [349, 350], as well as for steady-state DEMO concepts, such as the Japanese DEMO [351, 352], the Chinese CFETR [353, 354], the Korean K-DEMO [355] and the US FNSF [356].

Optimising future DEMO designs will face different challenges; for example (i) $f_{\mathrm{rad}}^{\mathrm{main}}$ should be increased if aiming at the same $P_{\mathrm{sep}}/R_{\mathrm{p}}$ value as ITER, (ii) the divertor design should be simplified and (iii) $f_{\mathrm{rad}}^{\mathrm{div}}$ should be raised above ITER values if we accept designs showing $P_{\mathrm{sep}}/R_{\mathrm{p}} \geqslant 25\,\mathrm{MW\,m^{-1}}$. Power exhaust simulations with larger $P_{\mathrm{sep}} = 150$–$300\,\mathrm{MW}$ have been performed using integrated divertor codes considering an ITER-based divertor geometry with longer leg length (1.6–1.7 m), as in a common baseline design. Simulation results also demonstrated that diffusion coefficients of the heat and particle fluxes are critical parameters for DEMO divertor design, and that effects of various drifts on outboard-enhanced asymmetry of the heat flux might imply the need for a longer divertor leg to ensure the existence of a detached divertor operation window. At the same time, integrated design of the water cooled divertor target, CB and cooling pipe routing has been developed for each DEMO concept, based on the ITER-like tungsten MB (W-MB) and Cu-alloy pipe. These DEMO approaches [357, 358] provide important case-studies of the DEMO divertor, and will significantly contribute to future reactor designs.

Since the compatibility of the core impurity pollution connected to sustainable power exhaust in the above conventional divertor concepts is currently not fully certain for DEMO conditions, alternative strategies are followed for risk mitigation. To meet these requirements, alternative divertor configurations (X-divertor, snowflake divertor) are investigated which aim at a higher dissipation fraction with better pedestal and core performance and a lower core dilution by the divertor seeding species [359, 360]. Liquid divertor targets offer a reduction of solid material erosion and a better handling of short power excursions [361, 362]. For a close-to-standard divertor geometry, the use of liquid tin in a tungsten CPS is regarded as a promising set-up [363]. Such alternative power exhaust strategies are currently being developed. Two small liquid metal targets based on a CPS structure and filled by Li and a LiSn alloy were exposed to the COMPASS divertor plasma and subsequently analysed [364]. First tests of a liquid-tin W-CPS in the AUG divertor under high-power H-mode conditions highlighted the necessity of further design improvement to reduce the loss of liquid tin from the tungsten matrix [365].

3.10. Conclusions

Impurity seeding is successfully used to facilitate benign power dissipation. Core/pedestal radiation by argon or heavier species reduces the separatrix power P_{sep}, while lower Z species enhance the divertor radiation. While for ITER the focus is on the divertor radiating species N, Ne and possibly also Ar, the higher heating power in a reactor will require additional core/pedestal radiators, like Kr or Xe when the power exhaust solution is based on a conventional ITER-like divertor. Divertor cooling and radiative power exhaust, which must amount to a large fraction of the power entering the SOL, also support the conditions required for hydrogenic momentum losses becoming effective. Core plasma penetration by the seeded species and corresponding radiative losses and fuel dilution will reduce the fusion rate. Strong variations of the divertor impurity enrichment are observed in mid-size tokamaks, with particularly low values for neon, leading to a high neon core pollution at a given divertor radiation level. A leading parameter for this effect appears to be the impurity ionisation mean free path, which is large for neon due to its high first ionisation potential. Modelling suggests this effect to weaken for ITER conditions, which is also expected for drift induced effects leading to in-out divertor asymmetries. Further modelling work is required to answer the question about the most appropriate ITER divertor radiating species. Both experiments and modelling find a positive effect of a high divertor neutral pressure on the plasma impurity pollution associated with the achievement of detachment. While 2D modelling shows continuous progress in reproducing current experimental results, uncertainties in turbulent transport and the heat flux width λ_q hamper the extrapolation to ITER and DEMO. The decreased neoclassical impurity inward transport remains a favourable and robust effect in the pedestal region which suggests comparatively lower core impurity concentrations in devices with a large pedestal ion temperature gradient [366–368].

4. ELM transients

4.1. Introduction

Section 4 describes progress since the 2007 PIPB in the understanding of ELMs in the context of power exhaust and their projection to future devices. High intensity transient heat fluxes due to ELMs can severely limit the lifetime of PFCs since they can exceed the thermo-mechanical limits of the PFC materials. Frequent excursions of a material's surface from its baseline operating temperature can lead to degradation from melting, ablation and/or cracking. The limits on surface temperature rise and its frequency are summarised in sections 8 and 9. Additionally, ELMs can cause significant erosion of high-Z PFCs, leading to unacceptable contamination of the core plasma. Enhanced erosion occurs when energetic particles released from the pedestal during an ELM strikes PFCs with energy above the material sputtering threshold. Erosion of tungsten divertor surfaces due to ELMs is summarised in section 6. An accurate scaling of ELM heat flux will be necessary to project the operational space over which ITER sized tokamaks will require ELM mitigation or complete suppression as described in section 4 of chapter *Pedestal and Edge Physics* [11].

A transient heat flux will cause a material surface temperature to rise as $\Delta T = \alpha\varepsilon t^{-1/2}$, where ΔT is the surface temperature rise from its steady-state value, ε is the deposited ELM energy density ($\mathrm{J\,m^{-2}}$), t is the duration of the heat pulse and α is the thermal diffusivity of the PFC material. Note that this relation is derived for square heat pulses and can deviate significantly for other temporal shapes [369]. Quantitative prediction of the ELM impulse parameter, $\varepsilon t^{-1/2}$, has improved significantly since the original IPB, in both qualitative understanding and predictive capability. As described in more detail in section 4.2, the Type I ELM energy deposition can be modelled as an MHD instability that connects the pedestal plasma to the divertor target with a path parallel to the magnetic field. Multi-tokamak data is found to be consistent with this model as further described in section 4.2. The time dependence for ELM energy deposition, the other important parameter in the ELM impulse parameter, has been accurately described by parallel transport models as described in section 4.3. The models include Particle-in-cell (PIC) codes that include sheath formation, ion orbits and other effects to accurately determine deposition time-dependence and other characteristics such as deposition to tile gaps and corners. This model of ELM deposition has also proved useful in describing high-Z divertor target erosion due ELMs as described in section 6.3. Several techniques, including 3D fields, pellets, and axisymmetric displacements have been developed to reduce ELM energy loss from the pedestal to a tolerable level. However, the energy deposition from these mitigated Type I ELMs is still consistent with the deposition model as described in section 4.4. Operational regimes with inherent small tolerable ELMs and potential for ELM heat flux dissipation through radiative processes is also summarised in section 4.4. In addition to the divertor target, ELMs can also impact the lifetime of main chamber structures when magnetic flux tubes in the pedestal reconnect and break away to travel radially in the SOL. Measurements of main chamber ELM deposition, their scaling, and models describing these characteristics are discussed in section 4.5.

4.2. Type I ELM target heat flux scaling

A model of parallel ELM energy transport along field lines reconnecting the pedestal top volume to the divertor target during the MHD ELM instability process is presented in [370]. Here, the target deposited ELM energy fluence is described successfully with a reduced number of plasma edge quantities. Utilising the major radius R_{geo}, an edge safety factor evaluated at the OMP by

$$q_{\text{edge}} = \sqrt{\frac{1+\kappa^2}{2}}\,\frac{a_{\text{geo}}}{R_{\text{geo}}}\,\frac{B_{\text{tor}}}{B_{\text{pol}}} \tag{4}$$

and the pedestal top electron pressure $p_{\text{e,ped}}$ a prediction for the peak parallel ELM energy fluence $\varepsilon^{\text{peak}}_{\|,\text{ELM}}$ is given by

$$\varepsilon_{\|,\text{model}} = 6\pi\, R_{\text{geo}}\, q_{\text{edge}}\, p_{\text{e,ped}} \tag{5}$$

In this model, the peak parallel deposited energy density, $\varepsilon_{\|}$, is equated with the energy density ($3\times p_{\text{e,ped}}\,[\text{J}\,\text{m}^{-3}]$) in the reconnected flux tube, where the length of the reconnected flux tube is given by the magnetic equilibrium quantities, $L_{\text{c}} = 2\pi\, R_{\text{geo}}\, q_{\text{edge}}$. The effect of the volumetric expansion of the flux tube in the confined region (about a factor of 1.7–2) compensates for the power sharing of the two inner/OT plates (factor $1/2$). It should be noted that the model only connects the peak value of the energy fluence profile with the pedestal top electron pressure value.

An ELM energy fluence spatial profile is calculated according to

$$\varepsilon_{\|}\left(s\right) = \frac{1}{\sin\alpha_s}\int_{t=t_0}^{t=t_{\text{ELM}}} q\left(s\right) - q_0\left(t_{\text{ELM}} - t_0\right)\mathrm{d}t \tag{6}$$

with $q(s)$ being the ELM induced heat fluxes for a given divertor target coordinate s, q_0 the background target heat flux at that location before t_0 and field line inclination angle α_s. The choice of $t = t_0$ and $t = t_{\text{ELM}}$ is given by measurement constraints: Typically the onset of ELM induced power loadings with 10% above background is used as t_0 and for t_{ELM} the fall-off to $1/\text{e}$ from the peak power value. For more details see [371, 372]. The peak ELM energy fluence is then a single value corresponding to the maximum of the fluence profile $\varepsilon_{\|,\text{measured}} = \max(\varepsilon_{\|}(s))$.

The reader may note that the time scale is not explicitly included in the ELM fluence model. The reason is that the temporal evolution of the parallel heat flux is mainly driven by the ion transit time, which is discussed in detail in section 4.3. The ion transit time is defined as

$$\tau_{\|} = \frac{L_{\text{c}}}{c_{\text{s}}} = \frac{2\pi\, R_{\text{geo}}\, q_{\text{edge}}}{c_{\text{s}}} \tag{7}$$

with $c_{\text{s}} = \sqrt{2T_{\text{e}}/m_{\text{D}}}$ (assuming $T_{\text{e}} = T_{\text{i}}$ and m_{D} the Deuteron mass) being the plasma sound speed. This typical transport time does not vary much when comparing the different devices as shown in table 1. Also, slight differences in t would lead to only modest changes in material risk due to the square root dependence for the material limit as $\Delta T = \alpha\,\varepsilon\, t^{-1/2}$.

The ELM fluence model presented in this part will serve as a basis for evaluating the following issues in this chapter. Figure 15 compares this model with the latest database including data from JET, AUG, MAST, COMPASS and HL-2A [373]. Further work that falls in line with this is reported from DIII-D [374]. Also we note that recent JET studies for (a) Tritium plasmas and (b) inner divertor target data also report agreement with the ELM energy fluence model [36].

Table 1. The ELM parallel transport time is similar for operating major tokamaks and ITER and thus the critical energy fluence w.r.t. the material limit is the dominant parameter.

	AUG	DIII-D	JET	ITER
L_{c} (m)	40	44	66	120
T_{e} (eV)	500	750	1500	4700
$\tau_{\|}$ (μs)	185	161	170	176

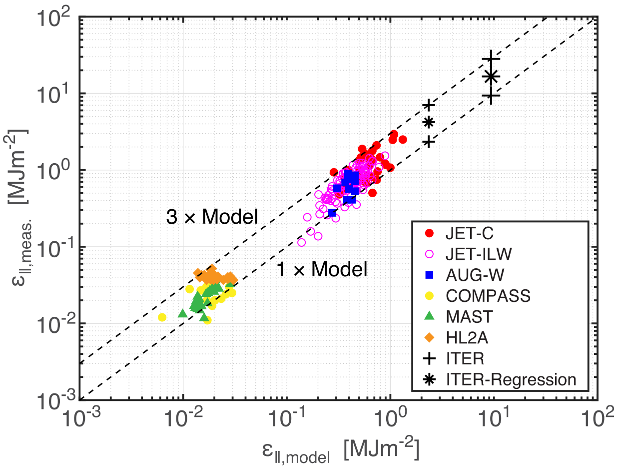

Figure 15. Comparison of measured versus predicted ELM energy fluence on the outer divertor target for JET, ASDEX Upgrade, MAST, COMPASS and HL-2A. Also included is the prediction for ITER full and half field operation from the model (+) and based on data regression (*). Reprinted from [370], Copyright (2017), with permission from Elsevier.

Figure 15 also include the result of a multi-machine scaling performed with data from JET, AUG and MAST [370] for ITER, both for the *half field* 7.5 MA/2.65 T scenario and the full inductive $Q = 10$ at a plasma current of 15 MA and 5.3 T TF, labelled as *ITER regression*. For the pedestal parameters, an electron temperature of 2350 eV and density of $4 \times 10^{19}\,\text{m}^{-3}$ and 4700 eV and $8 \times 10^{19}\,\text{m}^{-3}$ was used for the half and full current cases respectively.

A variation in ELM size, as defined by $\Delta E = E_{\text{loss}}/W_{\text{plasma}}$ is contained in the data base with a mean value of 5.4%, as shown in figure 16. Including ELM size in the fitted scaling of JET, AUG and MAST data ($R^2 = 0.82$) results in

$$\varepsilon^{\text{peak}}_{\|,\text{reg}} = 0.28\,\text{MJ}\,\text{m}^{-2} \times n^{0.75}_{\text{e,ped}}\, T^{0.98}_{\text{e,ped}}\, \Delta E^{0.52}_{\text{ELM}}\, R^{1}_{\text{geo}} \tag{8}$$

with the pedestal density $n_{\text{e,ped}}$ expressed in units of $[10^{20}\,\text{m}^{-3}]$, $T_{\text{e,ped}}$ in [keV], ΔE_{ELM} in [%] and R_{geo} in [m]. Error bars for the pre-factor and the exponents are found in [370]. The regression law resembles the proportionality between the product of the pedestal energy density times pedestal volume projected onto a target surface ($\propto n_{\text{e}}\, T_{\text{e}} R^3/R^2$) and motivated the model development. However, the dependence on the square-root on the relative ELM size is likely a numerical artefact due to the nature of the statistical approach used in the analysis.

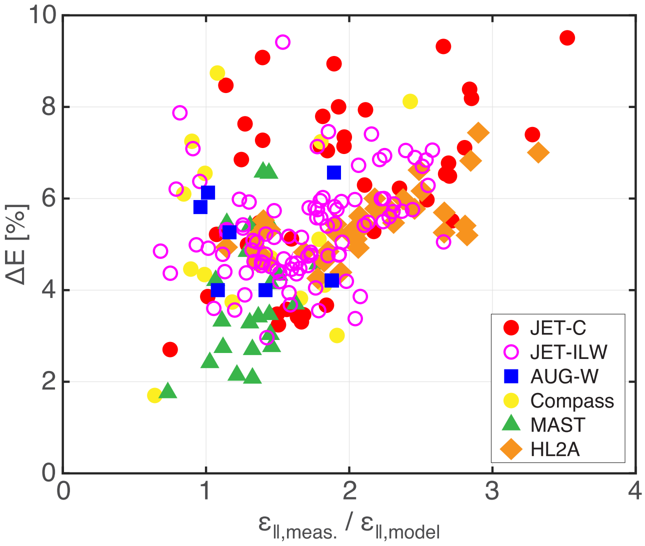

Figure 16. The deviation from the ELM energy fluence model from the 1:1 to 3:1 value is constrained by the normalised ELM energy loss for all analysed data bases in a complex, non-understood, manner. For smallest type-I ELMs in the 2% region the 1:1 line is found to describe the expected ELM energy fluence within the experimental scatter. Reprinted from [370], Copyright (2017), with permission from Elsevier.

There are hidden parameters in the discussed model well visible through the scatter in the scaling ranging up to approximately a factor of three. To date, any specific hidden parameters have not yet been identified, though various attempts give some indication that proximity to the H-Mode threshold, peeling vs. ballooning character of the actual ELM instability or conduction vs. convective losses may play a significant role [374]. However, as shown in figure 16 the actual scatter between the 1:1 and 3:1 line is correlated with the normalised ELM energy loss. In plasma scenarios utilising ELM sizes at the lower boundary of observed values here and thus about 2%, the hidden parameters appear to be of less importance for the prediction based on the simple model and the ELM energy fluence is thought to be close to equation (5), i.e. the 1:1 line.

The projected data points for ITER as presented in figure 15 need to be compared to the target material limits and perpendicular projection of the actual divertor tile geometry in ITER. This is done in sections 8 and 9 which refer to the results presented here.

4.3. ELM parallel transport

Over the past decades, several models of ELM parallel transport in the SOL have been developed to study the ELM particle and heat loads on the divertor plates and the associated PSI processes. They can be divided into analytical, (gyro-)kinetic PIC and Vlasov, fluid and MHD models, which are described below.

4.3.1. FSM. The simplest model of ELM parallel transport is the so-called FSM. The original version of the FSM is based on the 1D propagation of an ensemble of ELM ions, initially localised in time and space in the empty SOL (see equation (4.3) in [375]):

$$\begin{gathered} S\left(s, V_\parallel, V_\perp, t\right) = S_0\,\delta\left(s\right)\,\delta\left(t\right) f_{\mathrm{M}}\left(V_\parallel, V_\perp\right) \\ f_{\mathrm{M}}\left(V_\parallel, V_\perp\right) = \exp\left(-\left(V_\parallel^2 + V_\perp^2\right)/2V_T^2\right) \\ V_T = \sqrt{T/m} \end{gathered} \tag{9}$$

where S denotes the ion source function, S_0 is the integral ion source and s, $V_\parallel$ and $V_\perp$ are the parallel coordinate and the parallel and cross-field components of the ion velocity, respectively. Despite its simplicity, when electron dynamics as well as the parallel electric field are neglected, the FSM well reproduces the evolution of the divertor heat loads of the average ELM in different machines [371, 376] (see figure 17).

Later, in [377, 378], the FSM was updated by the inclusion of electron dynamics, electric field and more realistic spatial and temporal distributions of the initial ELM particle burst in the SOL. The resulting profiles of the SOL density, n, the particle parallel temperature, $T_\parallel$, and the divertor target particle flux, F_{div}, and heat flux, Q_{div}, during the ELM are given by:

$$\begin{aligned} n\left(s,t\right) &= \frac{n_0}{\sqrt{1+\left(t/\tau_\lambda\right)^2}} \\ &\quad \times \exp\left(-\frac{s^2}{2\lambda^2\left(1+\left(t/\tau_\lambda\right)^2\right)}\right) \\ T_{\text{e,i}}^{\parallel}\left(t\right) &= \frac{T_{0,\text{e,i}}}{1+\left(t/\tau_\lambda\right)^2} \\ F_{\text{div}}\left(t\right) &= n_0\,c_{\text{s}}\,\frac{L_\parallel}{\lambda}\,\frac{t/\tau_\lambda}{\left(1+\left(t/\tau_\lambda\right)^2\right)^{3/2}} \\ &\quad \times \exp\left(-\frac{\left(L_\parallel/\lambda\right)^2}{2\left(1+\left(t/\tau_\lambda\right)^2\right)}\right) \\ \tau_\lambda &= \frac{\lambda}{c_{\text{s}}}, \quad c_{\text{s}} = \sqrt{\frac{T_{\text{i}}+Z_{\text{i}}T_{\text{e}}}{m_{\text{i}}}} \\ Q_{\text{div,e,i}}\left(t\right) &= F_{\text{div}}\left(t\right)\,T_{0,\text{e,i}}\left(\frac{c_s^2}{2\,V_{T_{\text{e,i}}}^2}\right. \\ &\quad \left. \times \frac{\left(L_\parallel/\lambda\right)^2\left(t/\tau_\lambda\right)^2}{\left(1+\left(t/\tau_\lambda\right)^2\right)^2} + \frac{3/2}{1+\left(t/\tau_\lambda\right)^2} + 1\right). \end{aligned} \tag{10}$$

Here, λ, $L_\parallel$ and Z_{i} are the initial ELM width in the SOL, the parallel collection length and the ion charge state, respectively; the sub-index 0 denotes initial values.

The divertor heat loads obtained from the original and updated FSM are practically indistinguishable, but the latter also allows estimation of the divertor temperature during the ELM and has been validated against full kinetic codes including Coulomb collisionality [378]. Further attempts have been made in [379, 380] to extend the FSM to explain the low electron divertor temperature measurements during the ELMs at

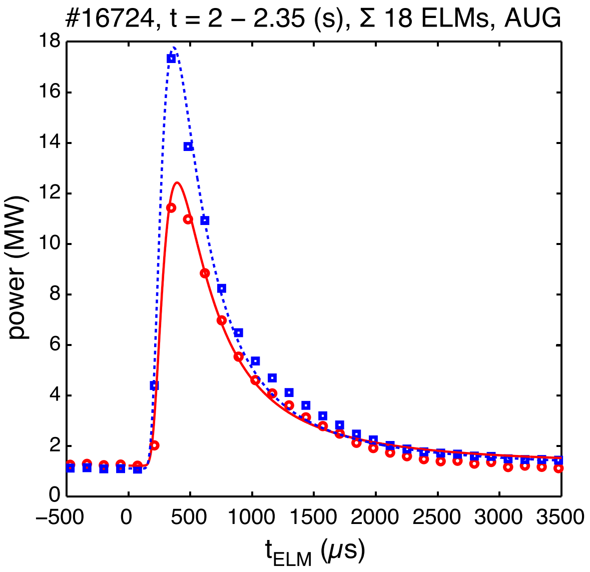

Figure 17. ELM power loads to the ASDEX Upgrade divertor (blue inner and red outer) averaged over 18 ELMs. The points correspond to the experimental values and the solid and dashed lines correspond to the FSM. Reprinted from [371], Copyright (2009), with permission from Elsevier.

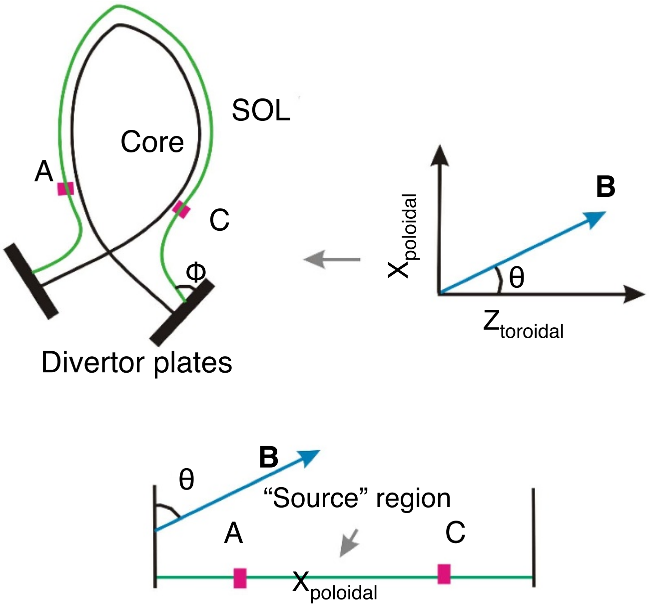

Figure 18. Geometry of 1D PIC simulations of the SOL. Reproduced with kind permission of Società Italiana di Fisica. Copyright [382] by the Italian Physical Society.

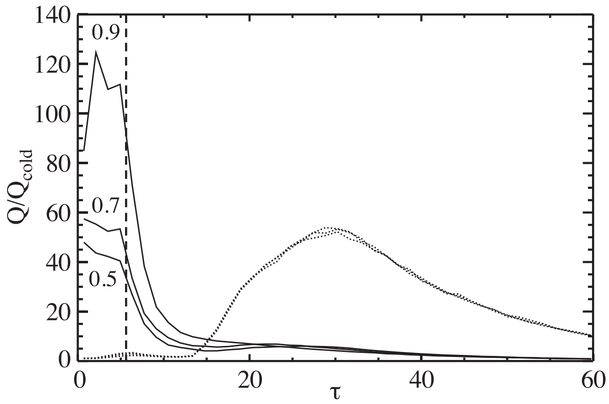

Figure 19. ELM electron (solid line) and ion (dashed line) power loads to the divertor plates for different secondary electron emission rates. $\tau = tV_{T_e}/L_{\parallel}$ is the normalised time from the onset of the ELM. Reproduced from [384]. © Published under licence by IOP Publishing Ltd. All rights reserved.

JET. The FSM is a 1D model and leads only to the cooling of the electron-parallel temperature component at the divertor. To explain the total electron divertor temperature cooling, the authors in [379, 380] included Coulomb collisionality in the FSM, leading to isotropisation and cooling of the electron divertor temperature. Recently, however, the above-mentioned Langmuir probe measurements have been re-evaluated and it has been shown that electron divertor temperatures during ELMs at JET can exceed 100 eV [381]. These results were also confirmed by full kinetic modelling of the ELM transport in the JET SOL. Therefore, the hypothesis of strong ELM electron cooling via Coulomb collisionality does not seem to be valid.

The main advantage of the FSM is its simplicity. The model assumes 1D ELM transport in the SOL with unperturbed magnetic field configuration (to match the experiment, $L_{\parallel}$ has sometimes been artificially increased); it also neglects ELM-thermal plasma and ELM-wall interactions, but nevertheless the FSM predicts average ELM particle and heat loads on the divertor plates and provides qualitative estimates of particle temperatures in the divertor.

4.3.2. Kinetic modelling. The first kinetic model of ELM parallel transport in the SOL was reported in [383]. Due to limitations of computing power in the 1990s, the Fokker–Planck model of ELM transport used in that work was too simplified to obtain reasonable quantitative results. Increased computing power in the early 2000's allowed more realistic kinetic modelling of ELM transport in the SOL. The majority of these models have been developed using PIC codes, with the simulation geometry corresponding to a 1D SOL bounded by inner and outer divertor plates (figure 18). ELM reconnection is modelled by injecting high-temperature ELM particles into the source region. The first PIC-ELM-SOL transport model was relatively simplified without magnetic field and Coulomb interactions [384]. As a result, there was virtually no electron-ion coupling, and the power loads to the divertor exhibit two peaks corresponding to the electron and ion SOL transit time scales. Secondary electron emission effects were also overestimated (see figure 19).

Different results were obtained by more complex PIC models taking into account the magnetic field and plasma recycling at the divertor plates [382, 385–387]: here the main ELM energy was carried by the ions propagating at the ELM ion sound speed (see figure 20). The effects of emitted secondary electrons have been neglected as they do not affect the ELM divertor power loads due to their prompt reabsorption. These

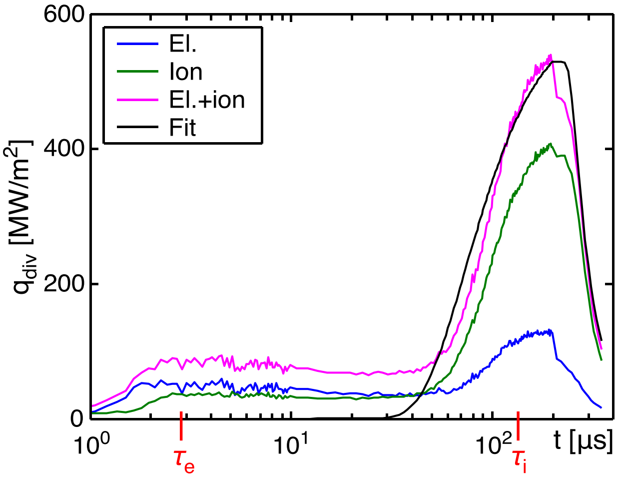

Figure 20. Heat loads to the JET outer divertor during 0.4 MJ type-I ELMs. τ_e and τ_i correspond to electron and ion transit times, respectively. Reproduced with permission from [387].

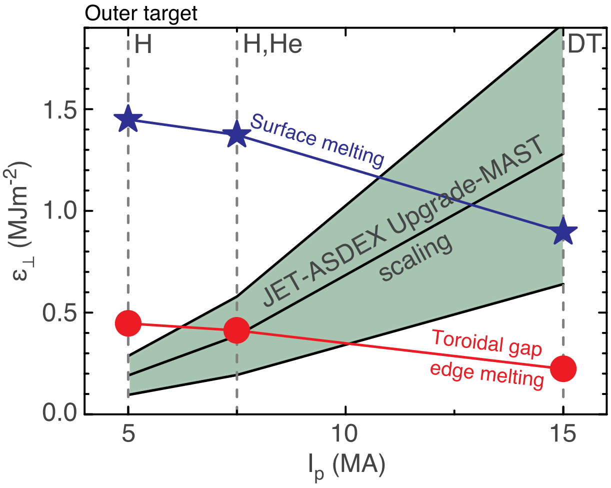

Figure 21. Predicted melting of the outer vertical divertor tiles in ITER during an ELM. The shaded area indicates the range of expected ELM energy fluences, $\varepsilon_\perp$, in ITER based on the empirical scaling law in [370]. The dashed lines indicate the operating points for the pre-nuclear (H and D/He) and DT nuclear burning scenarios. Reproduced from [398]. © 2017 IAEA, Vienna. All rights reserved.

results are in agreement with FSM results and experimental measurements. The ELM simulation in these models typically shows three distinct phases: i. pre-ELM; ii. intra-ELM with increased source particle temperature and injection rate; and iii. after-ELM with the same injection parameters as in the pre-ELM phase. The best agreement with the experiment was obtained by assuming instantaneously switched on and switched off ELMs [388].

Despite the simplified assumption of 1D ELM propagation along the unperturbed field lines, the 1D kinetic models show remarkable agreement with the ELM divertor heat loads measured in different machines, such as JET [387–389], JT60-U [390], TCV [391] and COMPASS [376]. Furthermore, this agreement improves with increasing model fidelity, which is achieved by including more physical processes such as plasma-neutral and plasma-impurity interactions in the model [388]. The existence of two-time scales of ELM parallel transport, electron and ion transit times, also well agrees with the experiment [392]. A 2D kinetic model of the ELM transport in ITER has been developed in [393]. 2D simulations indicate a strong influence of cross-field drifts on the ELM divertor heat loads, although the greatly reduced SOL size (more than a factor of 100) used in this model may have led to an overestimation of the cross-field drifts.

For completeness, we mention examples of ELM kinetic transport models other than PIC—the Vlasov [394] and the gyro-kinetic [395] approaches. They are significantly faster than PIC approach, but contrary to the latter do not include the divertor sheath and related processes in the simulation domain (for a detailed discussion see e.g. [396]).

An important extension of the ELM parallel transport study is provided by combined PIC and test particle simulations of the ELM loads on the divertor tiles (see [397, 398] and references therein). In these studies, the authors estimate the ELM heat loads on the divertor elements, such as the divertor tile face, the gaps between the tiles and the gap edges. Simulations predict possible melting of the toroidal gap edges of the ITER vertical divertor during the ELMs (see figure 21). It should be noted that these models do not include plasma-neutral interactions in front of the divertor plates. Due to this interaction, a significant fraction of the plasma energy is expected to be transferred to the charge-exchanged neutrals, thus reducing the plasma divertor heat loads. Divertor heat loads due to charge-exchanged neutrals will be more evenly distributed across the divertor plate surface, resulting in lower melting rates.

4.3.3. *Fluid models of ELM transport in the SOL.*

At present, kinetic models of the SOL are unable to simulate the true multi-dimensional nature of ELM transport in the SOL and also cannot reproduce the detailed power load pattern at the plasma-facing components wetted by the ELMs. These effects are partially covered by fluid SOL simulation codes. The latter do not include the deformation of the SOL magnetic field surfaces during the ELMs, but consider the 2D plasma transport in a static equilibrium magnetic field. This corresponds to an averaged transport of the ELM in the SOL. Fluid codes, unlike kinetic codes, can simulate repeated ELMs and study cumulative effects. The ELMs are triggered by repetitively increasing the transport coefficients with frequency and duration taken from experiment [399]. This is typically done by increasing the cross-field diffusivity and heat conductivity near the separatrix region, and by invoking artificial convective radial transport [400]. These fluid models are used to study ELM divertor power loads [401–403], and to estimate the associated W erosion rates [400, 404].

The validity of the ELM fluid SOL transport model was investigated in [405]. The authors showed that the 1D fluid model of convective ELM transport agrees reasonably well with the kinetic model, but requires the appropriate introduction of kinetic corrections. Typical examples of kinetic

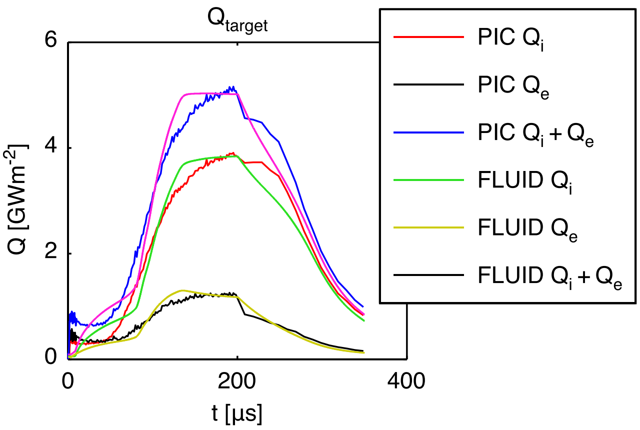

Figure 22. Comparison of PIC and fluid (convective) ELM divertor heat loads. No heat flux limiters were used, i.e. $\alpha \to \infty$ in equation (11), viscosity limited by $\beta = 0.1$ and the total energy source due to the ELM is prescribed to be shared by ions and electrons at a ratio of 3:1. Plasma–neutral and plasma-impurity particle interactions are not included in the model. Reproduced from [405]. © IOP Publishing Ltd. All rights reserved.

corrections are the constrained expressions for the parallel heat flux, $q_\parallel$, and for the viscosity $\pi_\parallel$,

$$q_\parallel = \left(\frac{1}{q_{\mathrm{SH}}} + \frac{1}{\alpha n T V_T}\right)^{-1}, \quad \pi_\parallel = \left(\frac{1}{\pi_{\mathrm{BR}}} + \frac{1}{\beta n T}\right)^{-1} \tag{11}$$

where $q_{\mathrm{SH}} = -\chi_\parallel \partial T/\partial s$ is the Spitzer–Härm heat flux density and $\pi_{\mathrm{BR}} = -4/3\,\eta_\parallel\,\partial V_\parallel/\partial s$ is the Braginskii parallel viscosity, with $\chi_\parallel$ and $\eta_\parallel$ the classical parallel electron thermal conductivity and collisionality, respectively; α and β are free parameters called flux LIMs. These expressions are often used to limit the classical parallel transport for low collisional SOL plasmas, which might otherwise predict unrealistically high values.

In [405] it was shown that for convective ELMs, when the ELM enters the SOL from the pedestal via convective transport, it is not the ion and electron heat fluxes that need to be limited, but the ion parallel viscosity ($\beta = 0.1$). In addition, although the total ELM divertor heat loads agree with the kinetic values, an artificial increase in the ion to electron ELM source energy ratio to 3:1 is required for the electron and ion heat load fractions to agree separately. Under these conditions, the 1D fluid model of the ELM well describes the divertor heat loads (see figures 22 and 23). In contrast, the transport of the conductive ELMs was not reproduced in the fluid simulations; particularly, the ELM propagation velocity in the SOL exceeded the speed of sound (figure 24). Such supersonic ELM transport contradicts the kinetic picture as well as experimental observations. Limiting the parallel heat flux slightly improved the results, but the authors were convinced that spatially uniform and time-constant limiting factors used in fluid models do not seem to be able to match quantitative PIC simulation results of conductive ELMs.

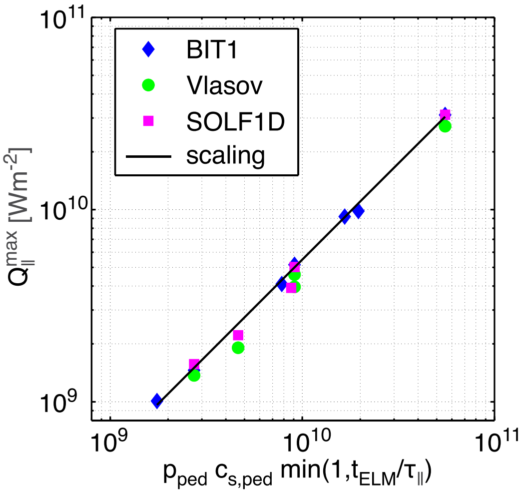

Figure 23. Peak values of the ELM divertor heat loads from PIC (BIT1), Vlasov and Fluid (SOLF1D) simulations. The kinetic factors in the fluid model are as described in figure 22. The scaling is given by $Q_\parallel^{\max} = 0.55\,(nTc_s)_{\mathrm{ped}} \times \min(1, t_{\mathrm{ELM}}/\tau_\parallel)$, $\tau_\parallel = L_\parallel/c_{s,\mathrm{ped}}$. Reproduced from [405]. © IOP Publishing Ltd. All rights reserved.

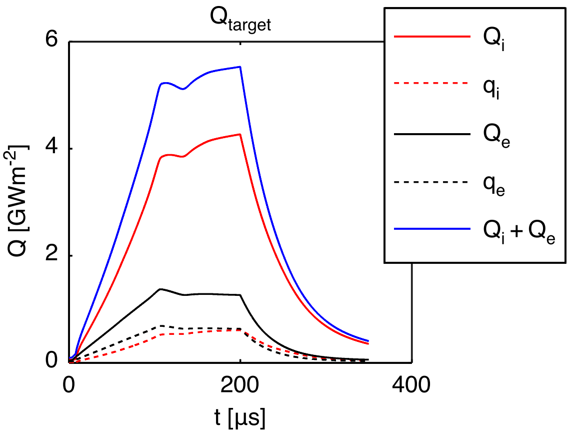

Figure 24. Conductive ELM divertor heat load from fluid simulation. The kinetic factors in the fluid model are as described in figure 22. Reproduced from [405]. © IOP Publishing Ltd. All rights reserved.

Similar results for conductive ELMs have been obtained from 2D fluid modelling using SOLPS [406] and EDGE2D-EIRENE [401]. In [406], where type-III ELMs in TCV were simulated, the authors used a strong heat flux LIM ($\alpha \geqslant 0.5$) to partially compensate for the discrepancy between the fluid and kinetic results. This observation of supersonic ELM transport in fluid models is a consequence of keeping only the conductive heat flux contribution in the ion energy conservation equation

$$\frac{3}{2}\frac{\partial}{\partial t}(nT_{\mathrm{i}}) = -\frac{\partial}{\partial s}\chi_\parallel^{\mathrm{i}}\frac{\partial}{\partial s}T_{\mathrm{i}} \tag{12}$$

and assuming $\partial/\partial t \approx 1/\tau_{\mathrm{cond}}$ and $\partial/\partial s \approx 1/L_\parallel$. By simple transformations, one obtains $t_{\mathrm{cond}} \approx \tau_\parallel^2/t_{\mathrm{coll}}$ where $t_{\mathrm{coll}} \approx 2 \times 10^{12} T_{i,\mathrm{ped}}^{3/2}/n$ is the ion-ion collision time; t, T and n are in

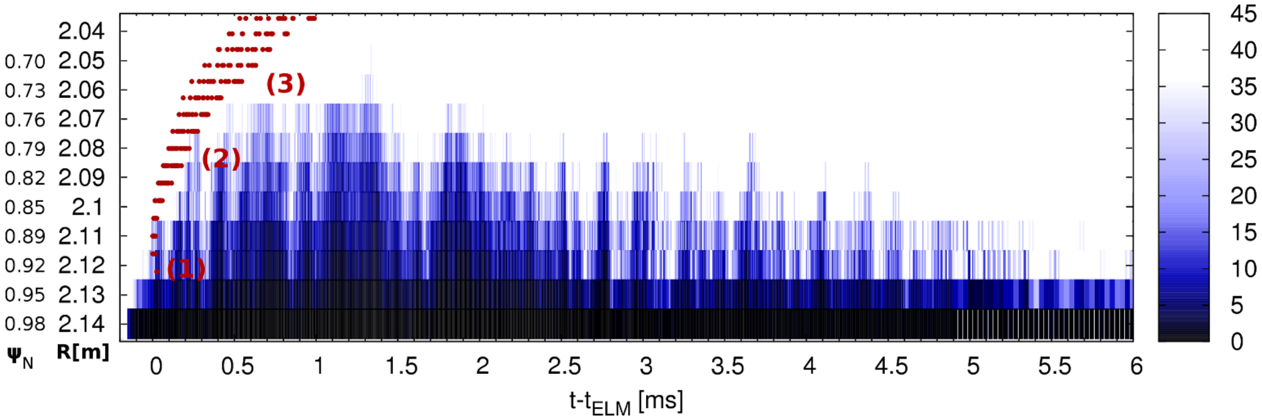

Figure 25. Parallel connection length (in km) at various radial positions, R, from the mid-plane to the divertor targets along the magnetic field lines plotted over time from the onset of an ELM. Red dots with numbers represent different phases of magnetic field ergodisation and formation of islands. Reproduced from [413]. © EUROfusion Consortium, 2018.

s, eV and m^{-3}, respectively. From $\tau_{\|} < t_{\mathrm{coll}}$, it follows that $t_{\mathrm{cond}} < \tau_{\|}$. A further improvement of the ELM fluid model was achieved in [403] by applying kinetic divertor sheath boundary conditions during the ELM.

These results indicate that the validity of the fluid ELM model is questionable when the ELM parallel transport is dominated by heat conduction. However, there are processes that do not require the exact time history of the ELM particle and heat loads on the divertors, but rather their integrated values. One such process is the sputtering of tungsten, which was studied in [404] and [400]. In [404], the W transport in the JET-ELMy H-mode was studied with the Monte-Carlo code DIVIMP using background plasma and neutral profiles from the fluid/kinetic code suite EDGE2D/EIRENE. During the intra-ELM phase, the simulations show an increase in the tungsten core contamination rate by two orders of magnitude, while during the ELM recovery divertor densities up to five times the pre-ELM values were obtained, strongly enhancing divertor retention via increased friction with the main ions. However, the simulations did not include W prompt redeposition and W rates were probably overestimated.

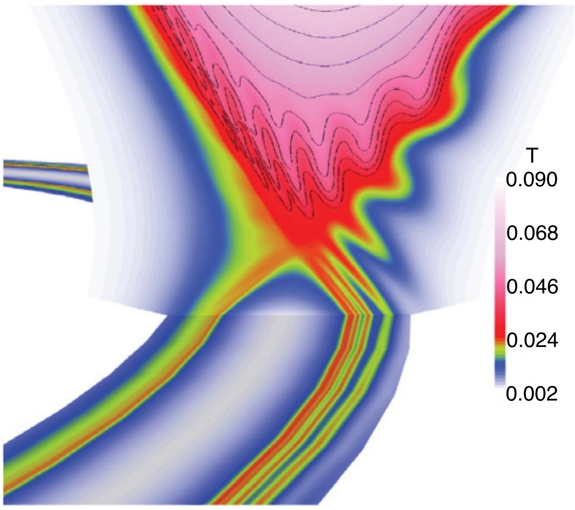

Figure 26. Poloidal and toroidal cross-section of the plasma temperature, T, in relative units, for JET-like plasma conditions, illustrating the ELM induced striations forming spirals on the target. Reproduced from [414]. © IOP Publishing Ltd. All rights reserved.

4.3.4. MHD models. The first MHD models of an ELM crash and transport in the SOL were developed more than a decade ago [407–409]. They represent single-fluid visco-resistive MHD models capable of self-consistently reproducing linear and nonlinear phases of ELM dynamics, although anomalous cross-field transport coefficients are the ad hoc inputs of these models. Subsequently, the MHD codes for ELM modelling were updated with two-fluid models (for electrons and major plasma ions) including neutral and impurity particle transport modules [410–412].

Although the ELM transport in the SOL is rather simplified in MHD models by using reduced fluid plasma and neutral particle models, a number of remarkable results concerning the ELM parallel transport have been obtained. The MHD simulations using the JOREK code indicate an ergodisation of the magnetic field in the entire ELM-affected region, leading to an increase in the parallel connection length [413–415]. There is a clear separation of two regions magnetically connected to the divertor plates during the ELM crash: the inner region (up to the pre-ELM separatrix), with connection lengths of up to a few tens of km (see figure 25), and the SOL, where the connection length does not increase significantly. As a result, the ELM particle and energy parallel transport time is defined by the effective connection length $\tau_{\|} = \alpha L_{\|}/c_{\mathrm{s}}$ where $\alpha \leqslant 5$ [411, 414, 415].

The MHD models reproduce well the filamentary structure of the ELMs and the resulting heat loads on the divertor plates (see figure 26), as well as the broadening of the ELM wetted area there (see figure 27). The latter has been explained in [416] as a consequence of two mechanisms leading to the

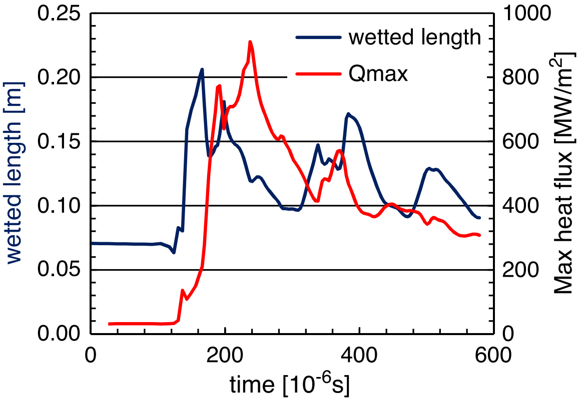

Figure 27. Time evolution of the peak divertor heat flux and the ELM wetted length on the ITER OT during a convective 1.6 MJ ELM in ITER. Reproduced from [416]. © 2013 IAEA, Vienna. All rights reserved.

radial broadening of the ELM divertor footprint: the creation of an ergodic magnetic field at the plasma edge and the formation of the filaments, which also propagate radially.

JOREK modelling has been used to investigate ELM divertor heat loads for the advanced divertor configurations. In [411] it was shown that the peak (outer) divertor heat flux and fluence for a super-X divertor configuration are reduced by a factor of 10 and 8, respectively, compared to a conventional divertor configuration. Simulations also indicated that the ELM plasma can still burn through the detached super-X divertor plasma, but will cause lower heat loads than predicted by the empirical scaling of section 4.2.

Finally, we mention recent attempts to explain experimental results where dominant ELM energy deposition is found at the inner divertor. In [417], a significant increase in the ratio of inner to outer divertor ELM heat loads was demonstrated due to diamagnetic drifts, although the obtained value was still below 1. The implementation of kinetic effects and more advanced neutral and impurity transport modules may improve the agreement with the experiment [410].

4.4. Mitigation of divertor ELM heat flux

A major topic of ELM research has been the development of mitigation tools to eliminate ELMs, or at least reduce their magnitude to tolerable levels [418, 419]. From the scaling described in section 4.2, ELM energy deposition needs to be reduced roughly an order of magnitude in a reactor-scale tokamak such as ITER to be tolerable over many pulses. Investigations of experimental actuators and operational regimes that produce small, or mitigated ELMs is summarised in section 4 of chapter *Pedestal and Edge Physics* [11].

Summarised here is the efficacy of these techniques to reduce divertor target ELM energy deposition. These techniques include RMPs, rapid pellet injection, vertical displacements of the core plasma, and naturally occurring small ELM regimes. In general, these techniques reduce ELM deposition only to the extent they modify ELM energy transport as outlined in section 4.2, i.e. parallel transport from the pedestal high pressure region.

An encouraging prospect for the elimination of ELMs is the application of RMPs. Short of full ELM suppression, RMPs have also produced mitigated ELM regimes with greatly reduced ELM energy loss from the core plasma. Experimental measurements of divertor heat flux from RMP mitigated ELMs in DIII-D [420], ASDEX-Upgrade [421], and MAST [422], have shown reduced ELM divertor heat flux with the application of RMPs. However, these results can still be interpreted in the context of the conceptual model of section 4.2. An example from ASDEX-Upgrade is shown in figure 28 [370], where in figure 28(*a*) the blue shaded region of the time trace highlights the reference conditions and the yellow the RMP ELM mitigation phases. The RMP application, see figure 28(*b*), results in a factor of several reduction in ELM energy loss, ΔE_{ELM}, with a more modest reduction in ELM peak energy deposition, $\varepsilon_{||}$. However, $\varepsilon_{||}$ still follows the model scaling figure 28(*c*) due to the concomitant reduction in pedestal pressure, figure 28(*a*). The lesser reduction of $\varepsilon_{||}$ compared to ΔE_{ELM} was also measured in DIII-D [420] and attributed to a narrower deposition pattern. This is consistent with RMP ELM mitigation reducing the fraction of the pedestal plasma magnetic flux tubes that are reconnected to the divertor target and associated plasma that is transported via parallel processes to the divertor target. For a detailed discussion of the application of RMPs the reader is referred to the following section 5.

Another approach to achieve a reduction in $\varepsilon_{||}$ is to increase the ELM frequency. This approach is motivated by the experimental observation [423], that the time-averaged energy loss from the core plasma due to ELMs across a range of ELM frequency is roughly 20%–30% of the total power across the separatrix, or $P_{\mathrm{ELM}} \sim f_{\mathrm{ELM}} \times \Delta E_{\mathrm{ELM}}$. A promising technique for increasing ELM frequency is rapid periodic injection of hydrogenic pellets. With the observation that fuelling pellets may also trigger ELMs, studies on DIII-D [424–427], ASDEX-Upgrade [428, 429] and JET [430, 431] have demonstrated pellet injection at a higher frequency than that of naturally occurring ELMs can reduce the peak heat flux incident on the divertor target. Injected pellets are understood to trigger ELMs by deposition of plasma density to locally increase the pedestal pressure beyond the MHD stability limit [432–435]. A comprehensive study of pellet size and frequency in DIII-D [436] has found significant limitations to this technique as shown in figure 29 with the maximum ELM energy deposition to the inner and outer divertor targets as a function of pedestal collisionality. Small pellets, that may be less perturbative to overall particle throughput and core plasma operational scenarios, are found to trigger ELMs only when the pedestal pressure nears the MHD stability limit. This results in ELMs triggered by small pellets to produce divertor deposition nearly identical to naturally occurring ELMs. Larger pellets are found to trigger ELMs with the pedestal well below the MHD stability limit, reducing ELM deposition above the inboard divertor by approximately a factor of two. However, the outboard divertor deposition remains unchanged. Consistent with dominant

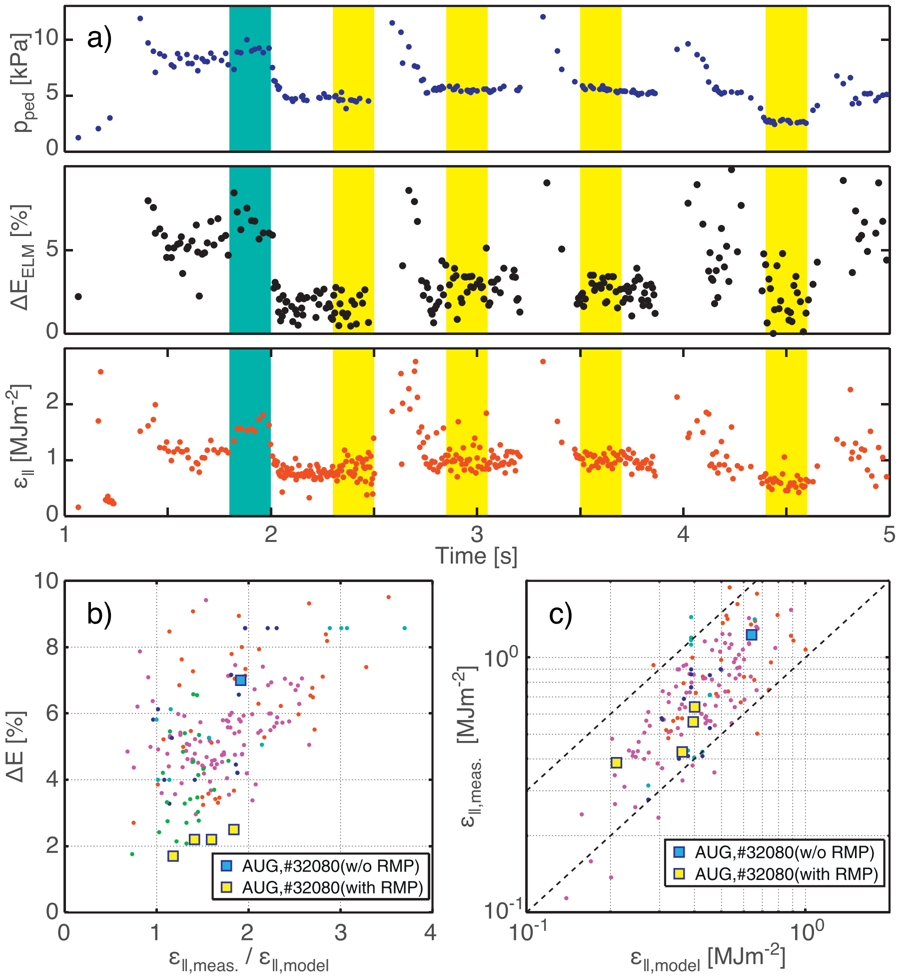

Figure 28. (*a*) Influence of external magnetic perturbation on the pedestal pressure and ELM energy fluence in ASDEX-upgrade discharges. Light blue denotes the reference time before RMPs are applied, yellow denotes the intervals used for analysis with RMPs switched on. (*b*) Reduction of ELM loss size, ΔE_{ELM}, and (*c*) reduction of the divertor ELM peak energy fluence, $\varepsilon_{\|}$. Reprinted from [370], Copyright (2017), with permission from Elsevier.

Low-Field-Side transport is the appearance of significant far SOL deposition with large pellet triggered ELMs. Similarly pellet injection was able to achieve only modest reduction in ELM deposition in JET [431], though this technique did significantly help to control core impurity accumulation.

An approach conceptually similar to ELM pellet injection is SMBI. SMBI seeks to increase the ELM frequency by localised particle deposition into the pedestal steep gradient region. In application of SMBI on the HL-2A tokamak, ELM frequency was increased a factor of 2–3, and similar reduction in ELM energy lost from the pedestal. The localised particle source from SMBI increased the density gradient at the foot of the pedestal just inside the separatrix to produce more frequent and smaller transport events compared to large ELMs. Further work is needed to quantify the reduction in ELM target heat flux and scaling to larger tokamaks [437].

Another technique to increase ELM frequency, the application of periodic vertical displacements of the magnetic equilibrium has been explored in a number of tokamaks [438–441]. A detailed study of this technique on JET [442] was able to increase the ELM frequency up to a factor of 5. Fast vertical displacements were found to induce a current near the separatrix that triggers the ELM instability. However, this technique has also produced only a modest reduction in peak ELM divertor deposition, consistent with the conceptual model of section 4.2, though it may be useful for core impurity control.

Although the use of techniques such as RMPs and pellet injection to reduce ELM energy loss have not resulted in similar reductions in peak surface energy deposition, the integrated ELM deposition on surfaces has been significantly mitigated by these techniques. And while the potential for divertor surface damage may only be modestly reduced, the reduced integrated deposition implies a reduction in deposition area and integrated surface material erosion. The potential of these ELM mitigation techniques to reduce core contamination from ELM induced high Z divertor material erosion has not yet been fully explored and remains an area of active research.

An additional ELM divertor heat flux mitigation option that has been explored is ELM-buffering, whereby a detached divertor plasma dissipates the ELM flux through impurity radiation and neutral collisions. Initial studies of ELM dissipation in JET [443] in seeded detached plasmas found ELM heat

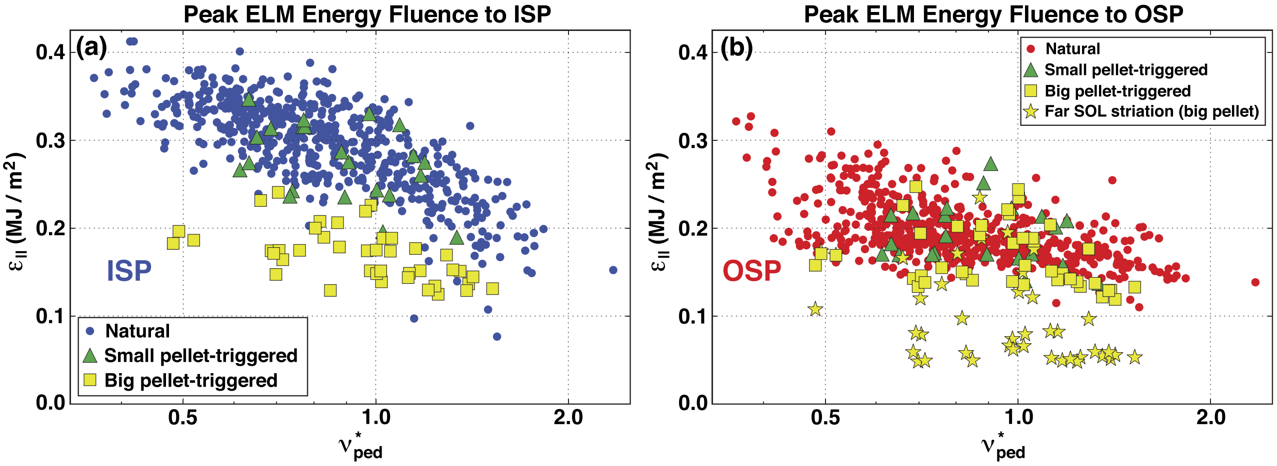

Figure 29. Peak parallel ELM energy fluence as a function of ν^*_{ped} at the (*a*) inner and (*b*) outer strike points. Natural ELMs are plotted as (*a*) blue and (*b*) red circles, ELMs triggered by small pellets are plotted as green triangles, and ELMs triggered by big pellets are plotted as yellow squares. Striations in the far SOL are also plotted in (*b*) as yellow stars for ELMs triggered by big pellets. Collisionality on the *x*-axis is on a log scale. Reproduced from [436]. © 2021 IAEA, Vienna. All rights reserved.

flux reduction only for small ELMs, with larger ELMs quickly ionising divertor neutrals and impurity ions to more weakly radiating charge states. Plasma fluid modelling has supported these findings with conclusions that only smaller ELMs may be sufficiently dissipated through atomic physics processes in future reactor scale tokamaks [443]. More recent work at AUG has found that impurity seeding can enhance ELM buffering, with up to 80% of the ELM heat flux dissipated through impurity radiation [444]. Pedestal pressure and core confinement remained high during the impurity seeding though an increase in ELM frequency and decrease in ELM amplitude was observed. Further work on scaling of ELM buffering is needed to project its efficacy in ITER and DEMO.

Finally, naturally occurring small ELM regimes may be possible as described in section 5 of *Pedestal and Edge Physics* [11]. These regimes include Type II ELM [445, 446], grassy ELMs [284, 447, 448] and QH-mode [449, 450] amongst others. Transient divertor deposition in these regimes has not yet been adequately studied to predict their tolerability in future tokamaks. As studies determine the applicability of these regimes to reactor-scale tokamaks, their transient divertor deposition characteristics will become a focus of future research.

4.5. Main chamber heat flux from type I ELMs

Besides the divertor target, type I ELMs can also reduce the lifetime of the main chamber wall and other PFCs. The source of this concern can be seen in main-chamber images of ELMs in the MAST spherical tokamak as shown in figure 30 [451, 452]. An overall picture of ELM far-SOL has emerged where in the initial stage of the ELM MHD instability the pedestal plasma is magnetically reconnected to the divertor target where it delivers a majority of the ELM energy through parallel transport. As the magnetic field lines evolve during the magnetic turbulence, plasma filaments eventually disconnect from the pedestal plasma and travel radially outward by $\mathbf{E} \times \mathbf{B}$ convection. As the filaments propagate radially they dissipate their particles and energy through parallel transport to material surfaces as described by a parallel loss model [375]. This model includes dissipation of the filament through parallel conduction and convection and plasma sheath boundary conditions at vessel surfaces. This description of parallel transport is a simplification of the processes described in more detail in section 4.3. The footprint of the filament maps out a spiral pattern on the divertor target as it moves radially due to the changing pitch of the magnetic field lines that the filament is aligned with.

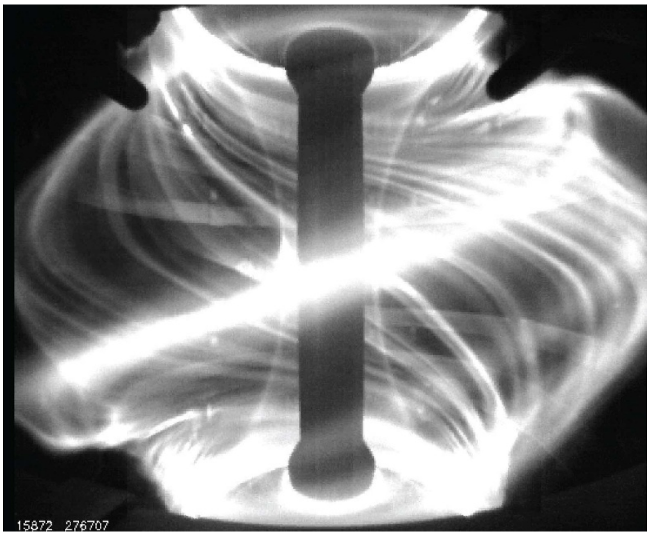

Figure 30. High speed video image in visible light of the MAST plasma obtained at the start of an ELM. The bright filaments are parallel to the background magnetic field. Reprinted from [453], with the permission of AIP Publishing.

A number of experimental measurements have been found to be consistent with this model of ELM filamentary transport. As the filaments propagate radially and remain aligned

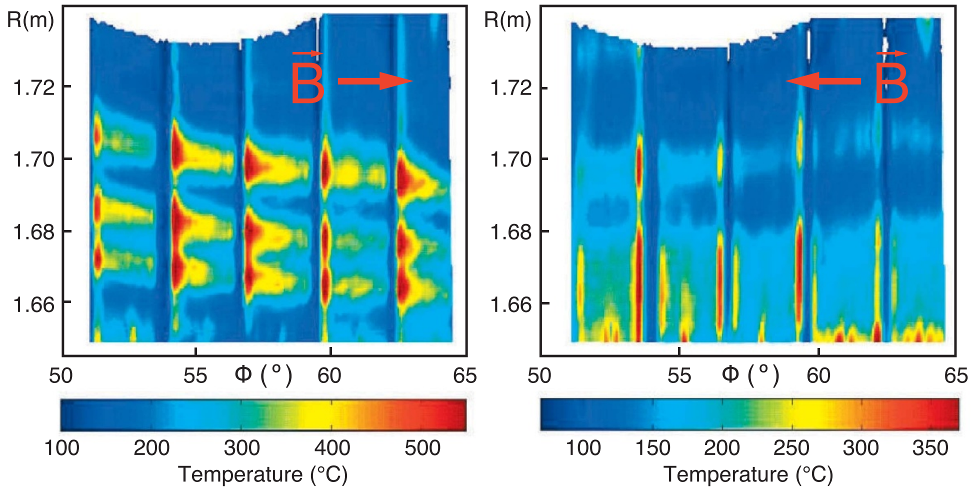

Figure 31. The ELM heat flux pattern in ASDEX-Upgrade during an ELM. The region shown is just outside the outboard strike point peak heat flux. In the left image the $\mathbf{B} \times \nabla B$ direction points away from the X-point, while the right image the $\mathbf{B} \times \nabla B$ points towards the X-point. Reproduced from [454]. © IOP Publishing Ltd. All rights reserved.

to the background magnetic field they map out a spiral pattern onto the divertor target as observed in the far SOL of ASDEX-Upgrade [454, 456]. The deposition profiles, figure 31, were found to be consistent with an ELM instability toroidal mode number of $n = 12$–14, consistent with pedestal stability analysis. The ELM filaments responsible for the radial transport have also been directly measured in the main chamber with insertable Langmuir probes in DIII-D [455], ASDEX-Upgrade [99, 457], JET [458], KSTAR [459] and MAST [460]. The ELM filaments in the SOL are generally measured to be a few, in the range of 3–8, centimetres in diameter at the mid-plane and traveling radially by $\mathbf{E} \times \mathbf{B}$ convection at velocities in the range of 0.1–1 km s^{-1}. Parallel losses from the propagating filaments result in a radial decay length of the electron temperature in the range of $\Delta_{T_e} \sim 1$–2 cm, with a longer decay length of the density in the range of $\Delta_{n_e} \sim 3$–8 cm. An example of such decay from DIII-D is shown in figure 32.

The ion temperature, however, exhibits a significantly longer decay length. RFA measurements exhibited T_i up to, and in excess of 400 eV reaching the far SOL and main chamber walls in JET [386, 461]. These measurements of ELM filament propagation and decay have been shown to be consistent with both simplified analytic models and more detailed PiC computational models that include the physics of parallel conduction and convection as well as plasma sheath interactions with material surfaces [375, 386].

While ELM filaments propagating in the far-SOL are typically found to carry no more than 10% of the Type I ELM energy lost from the core plasma [168, 455, 462–464], the parallel deposition onto LEs of main chamber PFCs can be significant. Infra-red camera measurements in ASDEX-Upgrade [465] revealed ELM-induced perpendicular heat flux transients of up to 30 MW m^{-2} onto outboard main chamber protection LIMs. Similarly, JET has also observed intense heat flux to main chamber LIM LEs due to ELMs [463]. Though the measurements were of insufficient time resolution to resolve instantaneous heat flux, surface temperature rises of several hundred °C were observed. The observed levels of main chamber heat flux and filament radial velocity were also found to be consistent with the parallel loss model.

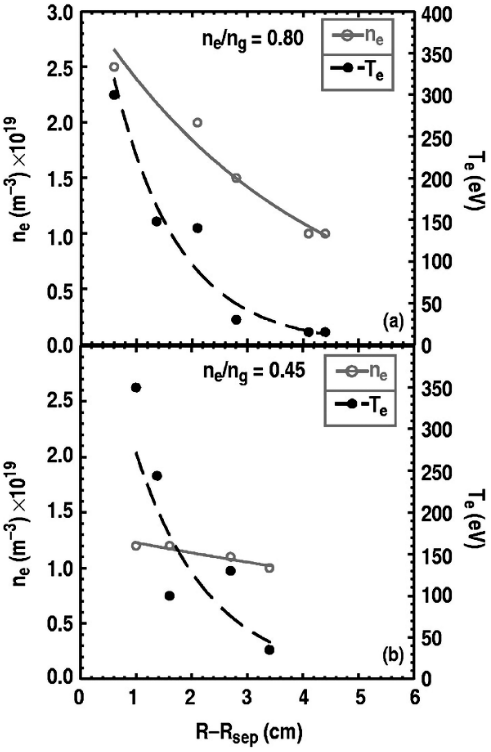

Figure 32. Radial variation of the ELM peak density and temperature values obtained from inserted probes in DIII-D for (*a*) high density and (*b*) low density discharges. The temperature decays quickly with radius in both cases, but the density decay length is much longer at low density. Reprinted from [455], with the permission of AIP Publishing.

The ELM heat flux to the PFCs is also expected to depend on the shape and configuration of the tokamak magnetic equilibrium. In highly shaped plasmas designed for improved core performance, a secondary separatrix with associated x-point and divertor may be formed in the upper half of the tokamak chamber. As the ELM filaments propagate past the primary separatrix, heat flux is deposited to both the outer and inner divertors. However, upon crossing the secondary separatrix the ELM filament is magnetically mapped to the upper outer divertor, where ELM deposition takes place. The decay length of ELM heat flux to the secondary divertor is generally found to continue that observed in the primary divertor, in accordance with the parallel loss model [466, 467]. However, ELM heat flux to PFCs has also been observed in regions that do not magnetically map to filaments propagating at the OMP. These magnetically isolated regions include the upper inner secondary divertor, the lower inner primary divertor outside the secondary separatrix, and even the PFRs of the primary and secondary divertor. Further work is needed to understand the transport mechanisms to these unmapped regions to adequately design PFCs outside of the primary steady-state heat flux regions.

Projecting main chamber ELM heat fluxes to future devices is challenging due to uncertainty in scaling of the ELM filament size and radial velocity. Rough estimates of what might be expected in ITER have been made for the design of main chamber PFCs [12, 468]. Limited data suggest Type I ELM filament size and radial decay length scales linearly with device size [468]. This would be consistent with filament size scaling with pedestal width and radial velocity in turn scaling with filament size. However, theoretical considerations of interchange driven filament formation would suggest a radial velocity in ITER similar to existing devices [386]. Based on these scalings combined with the parallel transport model [375], projections to ITER estimate up to 20 MJ m^{-2} of parallel deposition could be expected for unmitigated Type I ELMs at the upper secondary X-point protection LIMs [12]. While this level of deposition is concerning for enhanced erosion, the intermittency and toroidal localisation and distribution of individual filaments indicates the time-averaged heat flux to be tolerable with appropriate wall/LIM design. Another mitigating consideration is that unmitigated Type I ELMs are unlikely to be allowed in future reactor-scale tokamaks due to divertor target considerations. Mitigated ELMs, or small-ELM regimes would likely lead to smaller deposition on main chamber PFCs due to ELM filaments. Given the uncertainty in ELM filament formation and propagation further work on this topic is warranted.

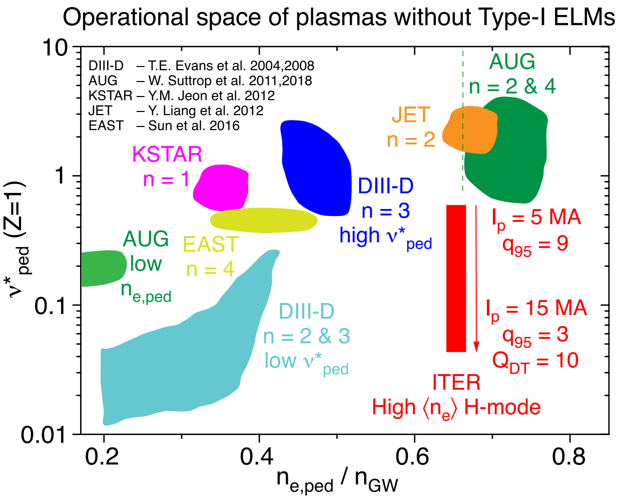

Figure 33. Operational range over which H-modes without type-I ELMs have been achieved in present experiments by the application of 3D fields with various toroidal symmetries. © 2014, The ITER Organization [419]. This image is hereby used courtesy of the ITER Organization

5. Application of RMPs for ELM control

The unfavourable scaling of type-I ELMs with machine size (see previous section) requires the development and verification of concepts for ELM control (mitigation or suppression) in ITER [418, 419]. An overview of various types of ELM control techniques has been presented in an earlier review along with a discussion of the requirements for ITER [469]. An update is given in the chapter on *Pedestal and Edge Physics* of this Special Issue [11]. The focus of this section is on application of RMPs fields by dedicated in-vessel coil systems, which have successfully demonstrated to mitigate (lower ELM energy at higher frequency) or completely suppress ELMs across several present day tokamaks such as AUG [421, 470], DIII-D [471, 472], EAST [473, 474] JET [475, 476], KSTAR [477], MAST [422, 478]. Based on this success, RMP application will be one of the two main strategies for ELM control in ITER [419] (controlled triggering of ELMs with reduced energy loss per cycle by pellet injection [479, 480] is the other, and vertical plasma movements [481] are considered as a back-up option during the initial low current H-mode operation). Nevertheless, research into alternative high confinement regimes without or with small ELMs is still ongoing [265, 283, 347, 482, 483].

The operation space for plasmas without type-I ELMs is shown in figure 33 in terms of pedestal collisionality ν^*_{ped} and electron density $n_{\mathrm{e,ped}}/n_{\mathrm{GW}}$ (normalised to the Greenwald limit), and it can be seen that present experiments can either cover the range of pedestal collisionalities or densities expected in ITER—but not both at the same time (see also review [484]). The pedestal density and collisionality relation is further discussed in section 4.1.3.2 of the chapter on *Pedestal and Edge Physics* [11]. Several possible designs of ex-vessel and in-vessel coils have been evaluated for ITER [485–487], which ultimately resulted in a configuration with 3 rows of 9 window-frame type coils [488, 489] as shown in figure 34. This setup makes it possible to operate with toroidal base mode $n = 3$ and $n = 4$ perturbations, both with operational flexibility to optimise the spectrum of the applied field by adjusting the relative phase between each row of coils. Furthermore, $n = 3$ perturbations can be smoothly rotated in ITER while holding the relative phase between each row of coils constant and thus maintaining ELM control. This is useful to toroidally time-average non-axisymmetric

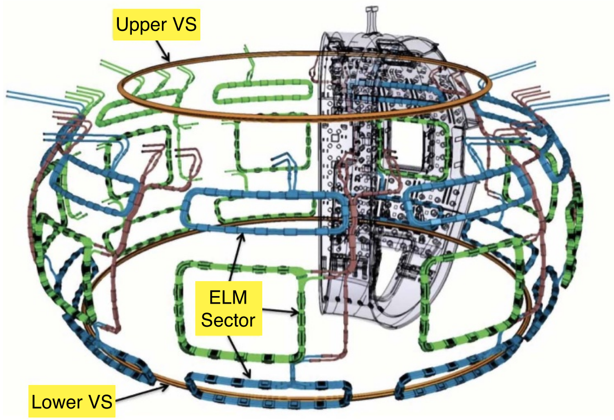

Figure 34. Geometry of the in-vessel ELM control coils in ITER. The set consists of three toroidal rows with nine sectors of window-frame type coils (green/blue). Also shown are the upper and lower vertical stability (VS) control coils (brown). [488] [2011], reprinted by permission of the publisher (Taylor & Francis Ltd. www.tandfonline.com.).

heat and particle fluxes onto the ITER divertor, if needed. If no rotation is required, the set of 27 coils provides a sufficient level of redundancy in case of malfunctions in individual window-frame coils. For an overview of RMP coil geometries in present experiments see figure 15 of the chapter on *Pedestal and Edge Physics* [11].

One observation in many ELM control experiments is the reduction of pedestal density and gradient when RMPs are applied (known as *density pump-out*). For a discussion of this see the chapters on *Pedestal and Edge Physics* (e.g. table 1 in section 4.1) [11] and *Transport and Confinement* (section 6) [8] of this special issue. However, while application of RMPs offers a promising strategy to remove transient heat loads (or at least reduce them to an acceptable level), it remains to be demonstrated that this is compatible with required solutions for stationary power dissipation in ITER (see section 3 stationary power dissipation). The ITER divertor [16, 490] has been designed to operate in a partially detached state based on extensive plasma boundary modelling with SOLPS, but these simulations assume a toroidal symmetry that is no longer present once RMPs are applied. In particular, it has been found that particle and heat loads can split into non-axisymmetric striations when RMPs are applied. This is evident in figure 35 by the striated C III emission pattern in the DIII-D divertor as a result of carbon being eroded from the divertor plates by the incident ion flux. Therefore, it is important to re-evaluate the impact of RMPs on recycling and power exhaust in ITER in extension of sections 2 scrape-off-layer and divertor transport and 3 stationary power dissipation, and in support of section 6 erosion of PFCs and impurity migration (see in particular section 6.6.4).

Presently, two different approaches are pursued to develop a 3D physics model for RMP ELM control: (1) full MHD simulations of the complete ELM cycle in the presence of RMPs [492], and (2) steady state simulations of the perturbed plasma boundary during RMP ELM suppression (or between mitigated ELMs akin to 2D plasma boundary modelling). The former approach is significantly more challenging because it requires (among other things) to account for a large variation of time scales, which range from the Alfvén time scale ($\tau_A \sim \mu$s) to the ELM repetition rate ($1/f_{\mathrm{ELM}} \sim 100$ ms). Nevertheless, such time dependent non-linear MHD simulations are required in order to capture the unstable peeling-ballooning modes responsible for ELMs without RMPs, and to evaluate their stabilisation when RMPs are applied. The second approach, on the other hand, is focused on the evaluation of the resulting heat loads on the divertor targets when RMPs are successfully applied to suppress ELMs. Different from the first approach, RMP application is here considered from the divertor and SOL point of view in which the plasma boundary is typically understood as a fluid problem in a given magnetic field (although kinetic effects may be included for the neutral particles interacting with the plasma, and/or by corrections to the fast parallel transport along field lines). This is essentially an extension of the traditional 2D (axisymmetric) framework for the steady-state plasma boundary into 3D, and it is the approach followed by EMC3-EIRENE [493–495] with its extension to poloidal divertor geometry [496].

In the following we will begin with a qualitative discussion of the perturbed magnetic geometry in section 5.1. While such a magnetic field structure is input for 3D fluid modelling of the plasma boundary, it is also utilised for the interpretation of experimental observations, and it may guide the characterisation of intermediate states in time dependent MHD modelling. Based on this introduction, we will then discuss ELM mitigation and suppression in attached plasmas in section 5.2 with a focus on resulting particle and heat loads on the divertor targets. We will also discuss optimisation of the applied RMP field through phase rotation and mixed mode application in this section. Afterwards, we will address the impact of RMPs on detachment in section 5.4 with a review of different observations in present machines and predictions for ITER. Finally, we will summarise aspects from stellarators relevant for RMP application in section 5.5.

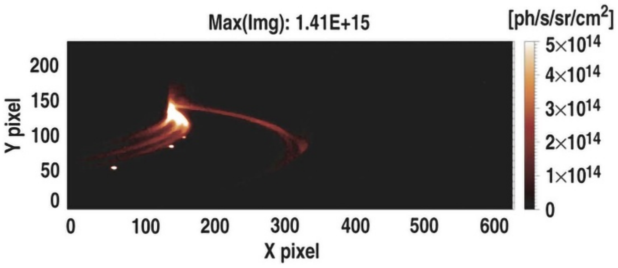

Figure 35. Tangential view of divertor C III (465 nm) emission during RMP ELM suppression in an ISS (ITER similar shape) plasma discharge in DIII-D. Tokamak centre post on the left—strong emission seen near inner and outer strike point regions. Reproduced from [491]. © 2008 IAEA, Vienna. All rights reserved.

5.1. Characterisation of magnetic perturbations

This section introduces qualitative aspects of the perturbed magnetic geometry that are relevant for power exhaust. Characteristic parameters are described in section 5.1.1 and implications for heat loads are discussed in section 5.1.2. The concepts developed below aim at a description of the properties of the configuration, and can be applied regardless of the source of the magnetic perturbations. On should note, however, that an important aspect of RMPs are the changes related to the rearrangement of the currents flowing inside the plasma volume, and we will explicitly touch upon plasma response effects in section 5.1.3. A full review of the history of RMPs in toroidal devices is beyond of the scope of this review, and we refer the reader to [497–499] instead for more details.

5.1.1. Figures of merit. In poloidal divertor tokamaks, the confined plasma is separated from dedicated material surfaces by a magnetic separatrix. A radial density and temperature gradient results in small transport across the magnetic separatrix, and fast transport along field lines deposits particles and energy onto divertor targets in a narrow region determined by the separatrix SP (in the R-Z cross-section or strike line in 3D). Heat loads are characterised by the upstream width λ_q of the transport channel at the mid-plane (also known as power fall-off length), the flux expansion factor f_x between mid-plane and divertor target, and the divertor (downstream) spreading factor S (see also section 2 scrape-off-layer and divertor transport).

By introducing RMPs, however, the magnetic separatrix splits into a pair of invariant manifolds with field lines connecting to the X-point either in forward or backward direction [500–504]. These so called homoclinic tangles are illustrated in figure 36(*a*). They still separate *traditional* SOL field lines from field lines inside the plasma, but they now form helical lobes which oscillate with increasing amplitude on their approach towards the X-point. The spacing between crossing points along the equilibrium separatrix is determined by the toroidal mode number and the asymptotic behaviour of the poloidal field at the X-point [505]. The extension of the lobes increases with perturbation strength. Direct evidence of this helical lobe structure is shown in figure 37 from visible light imaging of the X-point region in MAST and is confirmed for other toroidal mode numbers [506, 507].

Wherever helical lobes stretch far enough to intersect with divertor targets, field lines can escape from the plasma and carry particles and energy with them. The footprint of the spiralling perturbed separatrix [508–510] is illustrated in blue in figure 36(*b*) where the dark shaded region corresponds to this new type of exhaust channel. Outside, field lines do not enter the plasma and connect to the other divertor target within one poloidal turn. Inside, field lines enter the plasma and stay there for at least two poloidal turns. First observation of the heat flux striations due to RMPs have been reported from COMPASS-D [511], where magnetic perturbations with the two main modes $m/n = 1/1$ and $m/n = 2/1$ have been applied to poloidal divertor plasmas. Also, LIM devices such as TEXTOR [512–514] reported a strong influence of a chaotic boundary on the structure of power deposition with strike line splitting. The structure of the strike line is also governed by intersecting lobes of the invariant manifolds [515]. Since then, SP/line splitting has been observed at DIII-D [420, 516, 517] (evident by the striation pattern in figure 35), JET [518, 519],

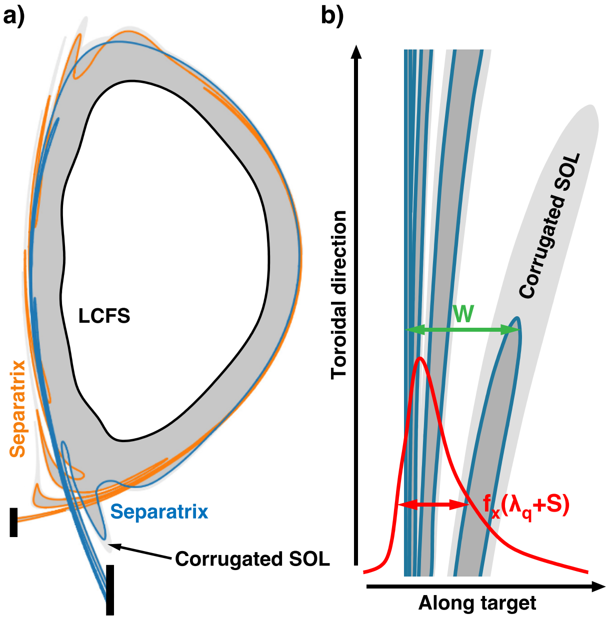

Figure 36. Illustration of the perturbed magnetic separatrix of a single null tokamak configuration: (*a*) cross-section in R–Z plane, and (*b*) intersection with outer divertor target. Dark grey regions indicate perturbed field lines outside the LCFS that can escape from the main plasma to the divertor targets, and light grey regions highlight the scrape-off layer which is corrugated by the perturbed separatrix. The shape of a typical unperturbed heat flux profile is displayed in red for a reference width f_x $(\lambda_q + S)$.

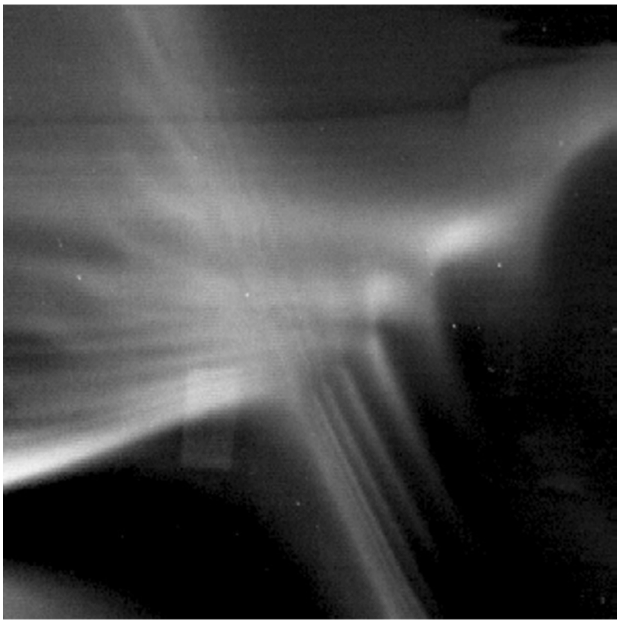

Figure 37. Image of the He^{1+} emission from the X-point region captured during an inter-ELM period of a MAST lower single null H-mode discharge with RMPs in an $n = 6$ configuration. Reproduced from [507]. © 2013 IAEA, Vienna. All rights reserved.

MAST [518, 520, 521], AUG [522–524], EAST [525, 526] and KSTAR [527–529].

One characteristic parameter for this striation pattern is the footprint width W: the maximum distance along the target between the perturbed separatrix and the equilibrium separatrix. For particle and heat loads, however, such a sharp pattern cannot be expected because of the competition with cross-field transport into the traditional SOL. The traditional SOL is wrapped around the helical lobes of the perturbed separatrix and thus extends the striation pattern on the target as highlighted in light grey in figure 36(*b*). Both upstream (λ_q) and downstream (S) cross-field transport will have to be considered in relation to the footprint width W in order to evaluate the impact of RMPs on head loads.

5.1.2. Ad hoc heat load model. Without dissipation, one may approximate heat loads by a convolution of the heat flux arriving at the divertor entrance with a Gaussian representing divertor spreading (see section 2 scrape-off-layer and divertor transport and equation (1) in [24]). Simple models have been proposed which include RMP effects by tracing perturbed field lines from the divertor target to the outboard midplane for determination of the upstream heat flux. Figure 38 shows a comparison between IR measurements in an AUG L-mode discharge and such an ad hoc model, and it can be seen that the nature of RMPs is well captured by this naive combination of magnetic geometry and transport effects. In particular, the model reproduces the experimental observation that the toroidally averaged heat flux in this discharge is not affected by RMPs [523], suggesting that there is no additional cross-field transport from RMPs. However, a similar approach has been applied to a DIII-D H-mode plasma with $n = 3$ RMPs in good agreement with more sophisticated heat load modelling [530], and those models do suggest a broadening and change of shape of the toroidally averaged profiles [531, 532] (similar observations are found in KSTAR, as shown in figure 41 in section 5.2.1). This might be related to a relatively larger footprint width in DIII-D, and due to subtle differences in how the upstream heat flux q_u is selected in the ad hoc models. Specifically, q_u may no longer exhibit an exponential shape inside the perturbed separatrix. Also, non-uniform divertor broadening (S) [523] or partial screening [524, 533] may explain the more pronounced peaks in the modelling further away from the equilibrium strike line in figure 38.

5.1.3. Plasma response effects. Another aspect is the radial connection of perturbed field lines. Resonances within the plasma are located where the helical pitch (safety factor) $q = m/n$ is equal to a ratio of integer numbers for poloidal vs. toroidal turns before an equilibrium field line connects back to itself. Perturbations result in the formation of magnetic island chains at these resonances, and in regions with chaotic field line paths—often attributed to the overlap of neighbouring island chains—from resonant tangle interactions between islands [501, 502]. These regions are interchangeably referred to as stochastic [499, 534]. With RMPs for ELM control, the chaotic/stochastic layer forms at the plasma edge between a LCFS and the perturbed separatrix, which is indicated by the shaded region in figure 36(*a*). Even though the vacuum RMP approximation (i.e. in which the external RMP field is superimposed on the equilibrium field) may capture the general nature of the magnetic footprint, it can largely overestimate the radial width of the chaotic/stochastic layer. In rotating plasmas, the generation of currents on rational flux surfaces can result in screening of RMPs [535–537] which substantially reduces the width of the stochastic layer. According to recent two-fluid nonlinear MHD simulations with TM1, ELM suppression is linked to RMP penetration and island formation at the pedestal top together with strong screening of resonant fields in the steep gradient region [538, 539]. This confirms earlier quasi-linear MHD modelling [540], and it implies that the chaotic/stochastic region is restricted to the narrow region near the separatrix at the bottom of the pedestal where RMP penetration can occur due to higher resistivity.

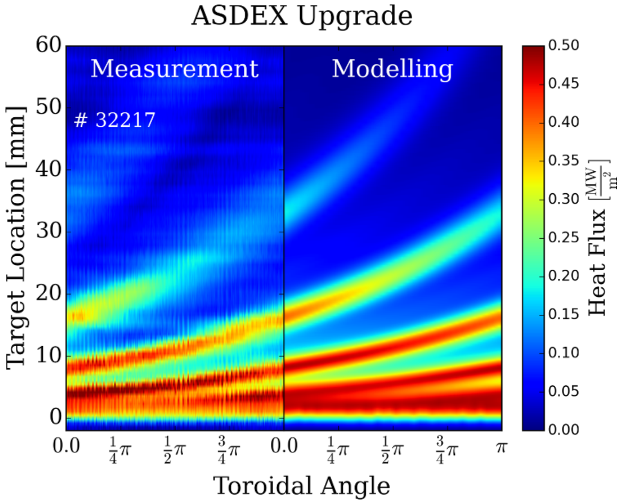

Figure 38. Heat loads on the outer divertor target in an ASDEX upgrade L-mode discharge with $n = 2$ RMPs: (*a*) obtained by IR measurements, and (*b*) from an ad hoc model based on field line tracing and a convolution between upstream heat flux and divertor spreading. Reproduced from [523]. © IOP Publishing Ltd. All rights reserved.

An approximation of the plasma response has been presented in [541] which mimics screening of RMPs by introducing helical current sheets on selected resonances. These current sheets suppress magnetic islands and reduce the amount of strike-point splitting with increasing number of screening surfaces. At AUG, strong screening of resonances is required to match experimental observations for low density L-mode discharges [533, 542]. At DIII-D, it has been shown that screening is required to mitigate the collapse of the modelled temperature profile [543] although too much screening suppresses the splitting of the measured downstream T_e profile [544].

The ad-hoc screening model completely neglects a possible amplification of non-resonant field components (kink/edge-peeling response) [545, 546] and poloidal harmonic coupling to the pitch aligned component [547, 548]. More advanced numerical models can be used to compute the plasma

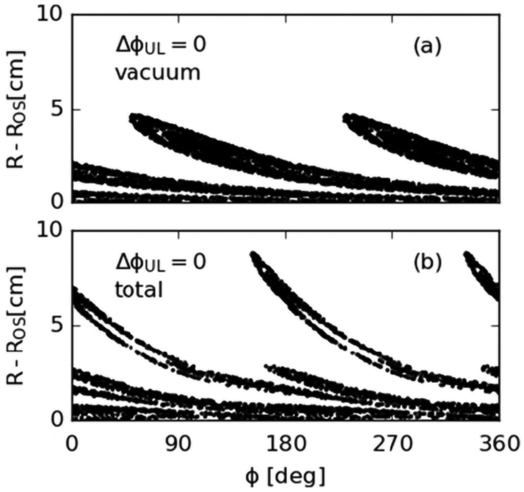

Figure 39. Magnetic footprint at the lower outer divertor target in DIII-D from $n = 2$ RMPs with upper and lower row of coils in phase: (*a*) vacuum RMP approximation, (*b*) with plasma response computed by linear M3D-C1. Reproduced from [561]. © 2021 IAEA, Vienna. All rights reserved.

response such as IPEC [549, 550], GPEC [551], HINT [552], JOREK [412, 548, 553], M3D-C1 [554, 555], or MARS-F [556, 557]. For a review and benchmark of these models (ideal vs. resistive MHD, linear vs. nonlinear, single fluid vs. two fluid) we refer to [558–560] and to section 4.1.2 in [11]. In particular, a comparison of different plasma response models for DIII-D H-mode plasmas with $n = 3$ RMPs shows that presently no single model can simultaneously reproduce upstream and downstream observations in both even and odd parity RMP configurations [544]. One noteworthy finding is highlighted in figure 39 where M3D-C1 simulations for a DIII-D H-mode plasma show that the magnetic footprint on the outer divertor target leads to thinner and longer main lobes compared to the vacuum case (as well as the presence of smaller secondary lobes) [561] confirming earlier predictions for DIII-D of similar nature [562]. Also, it should be noted that MARS-F predicts that with finite resistivity, the outermost pitch aligned component can be comparable to the vacuum value in AUG [547], which would imply that some striations remain.

5.2. Focus on ELM control

ELM mitigation by RMPs aims at a decrease of the ELM-related energy density at the target plates by reducing the ELM size while maintaining at the same time compatibility with sufficient plasma performance for a sustained fusion reaction. Widening of the ELM footprint by RMPs, on the other hand, does not appear to contribute much to power load reduction [563]. The impact of RMPs on transient fluxes have been discussed in section 4, and our focus is now on the impact on steady state divertor loads—either during ELM mitigation or suppression by RMPs. Observations from experiments are summarised in section 5.2.1 and implications for impurity exhaust are addressed in section 5.3. Optimisation strategies are then reviewed in section 5.3.1, and predictions for ITER are discussed in section 5.3.2.

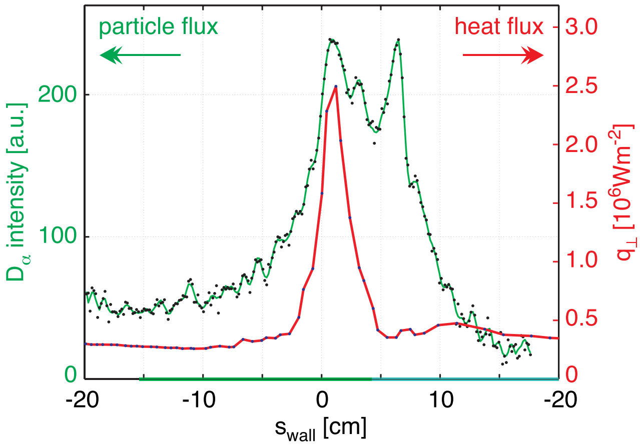

Figure 40. Measured profiles of the D_α intensity (as a proxy for the particle flux) and the heat flux to the outer target in a DIII-D H-mode plasma during ELM suppression with $n = 3$ RMPs in even parity. Reproduced from [517]. © IOP Publishing Ltd. All rights reserved.

5.2.1. Steady state particle and heat loads with RMPs. At DIII-D, slitting of the divertor target heat flux into several distinct peaks has been observed when an $n = 3$ magnetic perturbation from the I-coils is applied [516]. Plasma response may result in wider splitting and higher heat deposition through outer lobes at high collisionality [420, 564], which suggests some amplification effect of the plasma response. The heat flux is of the same order as in the inter-ELM phase without RMPs. At low collisionality, on the other hand, a moderate increase of the total power flux to the divertor targets is observed when RMPs are applied. This is consistent with a reduction in the total radiation measured by the bolometer system, and using gas puffing to return the core density to the pre-RMP levels more than eliminates the increase in inter-ELM heat flux [565]. Clear splitting, however, is then only observed for the particle flux while the outer peak of the heat flux is barely detectable (see figure 40)—although in some cases the opposite was seen with an amplification of the strike line. Numerical modelling with EMC3-EIRENE based on full screening of the $m = 7$–11 resonances (located at the edge) has shown that a reduction of the outer heat flux peak is consistent with screening of the RMP field [543]. Nevertheless, this goes together with a similar reduction of the outer particle flux peak which implies that screening cannot be too strong. Instead (or in combination with weak screening), recycling conditions may play a key role for the qualitative difference between the particle and heat flux profile [566]. Toroidally resolved measurements [563] showed that without the RMP fields, ELMs display a variety of different heat load dynamics and a range of toroidal variability coming from their 3D structure. On average, however, there is no asymmetry in the deposited energy between two toroidal locations. With RMP-mitigated ELMs, the variability in the radially averaged power loads is significantly reduced and toroidal asymmetries up to 30% in power loads are introduced. Observations from other experiments are summarised below.

In NSTX, the measured heat flux profile shows that the radial location and spacing of the striations are qualitatively consistent with a vacuum field tracing calculation in H-mode plasma with $n = 3$ RMPs [567]. Multiple heat flux peaks are reproduced in EMC3-EIRENE simulations [568]. Higher q_{95} produces finer striations and increased heat flux peaks (figure 7 in [569]). Local peaks in the D_α profile become more pronounced for higher collisionality ($\nu^*_{\mathrm{ped}} = 2.4$ compared to $\nu^*_{\mathrm{ped}} = 5.5$ in figure 8 in [569]).

In JET, a clear splitting of the strike-point is observed in L-mode plasmas in agreement with field line tracing in vacuum RMP approximation [518, 519], but not in ELM mitigated H-mode plasmas for identical applied $n = 2$ perturbations [518]. The latter is attributed to partial screening of the RMP field.

In MAST, the position of the second heat flux SP is reproduced by vacuum RMP field line tracing in L-mode plasmas with $n = 3$ RMPs and $n = 1$ error field correction [518]. In [521], however, the weaker second heat flux peak is attributed to screening from which a reduced radial excursion of field lines is expected. Splitting is not clearly observed in H-mode plasmas which is considered to be caused by stronger screening effects there [518].

In AUG [522, 523, 570, 571], the divertor heat load traces for L-mode discharges with $n = 2$ RMPs show that toroidal peaking is largest for the resonant configuration (differential phasing of $\Delta\Phi = -\pi/2$ which is field aligned at the $q = 5$ surface at the edge).

In EAST, splitting of the particle flux with $n = 1$ RMPs has been observed with divertor probes on the outer upper (and lower) target, especially in L-mode [525]. Observations are consistent with field line tracing based on vacuum RMPs. Splitting of the divertor heat flux has been observed in ELM suppressed H-mode plasmas with $n = 3$ and $n = 4$ RMPs, respectively, using an upgraded infrared diagnostic system, and it is found that the stationary heat flux is increased by 37% at the original SP (see figure 6(*a*) in [572]). MHD response modelling using the MARS-F code shows that the observed q_{95} window (3.6–3.75) for ELM suppression is consistent with the peak of the edge magnetic field stochasticity at $q_{95} \approx 3.65$ for the odd parity $n = 4$ configuration [474].

In KSTAR [527, 528, 573–575], (mostly) robust striation patterns exist throughout the ELM suppression phase for $50\,\tau_{\mathrm{E}}$ (energy confinement times) as shown in figure 5 in [528] for $n = 1$ RMPs. However, significant increase of the stationary peak heat load on the outer divertor target is observed, as can be seen in figure 41. This is thought to be related to strong density pump-out and associated reduction of radiation losses [529]. It has been found in JOREK simulations coupled with PENTRC (NTV) that RMP response can increase the heat flux on the lower outer divertor by redistributing the heat transport between the divertor plates, and thereby reproducing experimental observations [576]. It is suggested that this is a result of strong shaping with large lower triangularity of $\delta_{\mathrm{low}} = 0.87$.

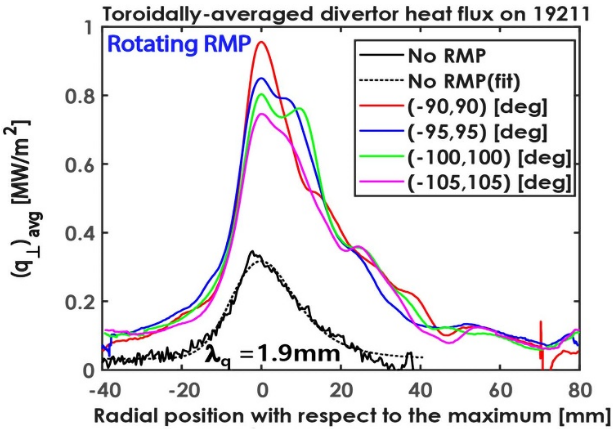

Figure 41. Divertor heat flux measurements in KSTAR with $n = 1$ RMPs in 90° phasing and with increased phasing (i.e. shifted towards kink-resonance): toroidally averaged heat flux profiles from re-aligned IR camera measurements. Reproduced from [574]. © 2019 IAEA, Vienna. All rights reserved.

5.3. *Implications for impurity exhaust*

Radiative cooling by impurity accumulation in the core is problematic, especially for high Z impurities. While ELMs can increase impurity sources by sputtering wall material, they also provide an efficient method of removing impurities from the H-mode plasma. In addition, the ability to exhaust helium is a critical requirement for burning plasmas.

When applying RMPs for ELM suppression, this mechanism is replaced by enhanced transport along perturbed magnetic field lines. Experiments on DIII-D with tungsten laser blow-off show that RMPs reduce the impurity confinement time in the H-mode pedestal below that of natural ELMy plasmas, suggesting that RMPs are beneficial for controlling impurity build-up in the pedestal region of the plasma [577].

This is consistent with observations in EAST where reduced line emission from the core region is found for both low and high Z impurities [578]. Analysis of helium puffing experiments on DIII-D using a multi-reservoir model has also shown a reduction in impurity confinement times in the core, edge and pumping plenum when RMPs are applied for ELM suppression [579]. A reduction in helium confinement time with RMPs has also been reported in TEXTOR and edge magnetic island configurations in LHD [580].

5.3.1. Optimisation strategies. The multi-row, multi-coil setup of the external RMP field allows tailoring or fine tuning of the RMP spectrum for ELM control. Several figures of merit for ELM suppression have been proposed (see also section 4.1.5 of the chapter on *Pedestal and Edge Physics* [11]): vacuum island overlap width [487, 581], X-point displacement [478, 560], HFS response [582, 583], peeling/edge-kink response [546, 548, 584]. Of particular interest here is how those figure of merit are linked to the plasma boundary geometry and resulting exhaust characteristics.

Optimisation strategies include mixing of toroidal modes and phase rotation of the current waveform for the coils of a selected row. Rotation of the global phase implements toroidal (time) averaging of particle and heat loads, and at MAST this has been found to double the ELM frequency with $n = 3$ RMPs [129]. For diagnostic purposes, global phase rotation facilitates measurement of the spiralling load pattern from toroidally localised probes. On the other hand, rotation or adjustment of the relative/differential phase between rows affects the spectrum of the RMP field, and this is explored both for maximising the beneficial impact (i.e. ELM suppression) and/or minimising the detrimental impact on core performance. Figure 42(*a*) shows that the area and extent of the magnetic footprint is linked to the predicted HFS response in DIII-D. These predictions are confirmed in figure 42(*b*) by measurements of the low and HFS plasma response compared to the width of IR emission profiles in related experiments. This suggests that it will be challenging to decouple the magnetic footprint from the resonant coupling for RMP ELM-control [561].

At KSTAR, it is found that balancing core and edge perturbations is required for viable ELM suppression scenarios [585]. Nevertheless, recent numerical studies for KSTAR showed that there may be room for fine tuning due to the more flexible three-row setup of the RMP coils [586] (even though these studies showed that uncertainties remain related to equilibrium truncation in the GPEC plasma response). Figure 41 shows that reduced peak heat fluxes and broadened profiles (15%–20% wider area) are observed with intentionally misaligned RMPs towards the kink-resonance (>90°) [574]. Nevertheless, broadening has also been reported for the opposite direction of misalignment (figure 6 in [529]), which is considered to reduce the risk of mode-locking.

Optimisation of the relative phase $\Delta\Phi_{\mathrm{UL}}$ between the upper and lower row of RMP coils has also been explored in AUG [587]. It has been found that an optimal phase Φ_{opt,n_e}, which maximises the density pump-out effect, is shifted upwards relative to the phase $\Delta\Phi_{\mathrm{opt,ELM}}$, which maximises the mitigated ELM frequency, by about 60° (see figure 5 in [587]). However, these findings have been attributed to a lag in density evolution relative to the ELM frequency, and therefore the observed shift may not occur in static (or rigidly rotating) RMP fields.

ELM suppression over one full cycle of a rotating $n = 2$ RMP field that is superimposed on a static $n = 3$ RMP field has been achieved at low collisionality in DIII-D [588, 589]. Prominent heat flux splitting on the outer divertor target has been observed with a secondary peak at around 3 cm distance from the equilibrium SP. The full width at half maximum value of the time averaged heat flux profiles is increased once the rotating $n = 2$ harmonic is superimposed on the static $n = 3$ one, and figure 5(*a*) in [588] shows that the amplitude of the additional heat flux peak is decreased with shifting current from the $n = 3$ harmonic to the $n = 2$ harmonic. One should note, however, that the overall heat flux is increased by about 10% during mixed mode operation, but this may be attributed to a change in power balance (radiation vs. deposition on IT vs. deposition on OT) as a result from increased edge stochasticity from mode mixing. Regarding the amplitude of the secondary heat flux peak, it is found that it can be controlled by the phase of the $n = 2$ harmonic as shown in figure 7 in [588] (*a*) and (*b*) in reasonable agreement with field line tracing results in (*c*).

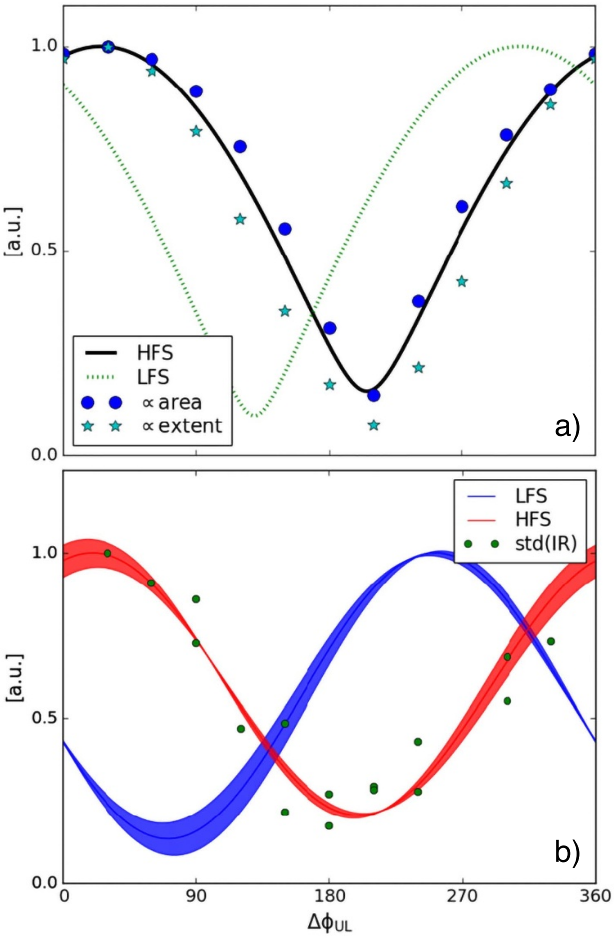

Figure 42. Impact of the RMP spectrum (relative phase between upper and lower row of coils) in a DIII-D H-mode plasma with $n = 2$ RMPs on the magnetic plasma response and the consequences for the scrape-off layer: (*a*) M3D-C1 predictions of the normalised high and low field side response compared to the normalised area and extent of the magnetic footprint, (*b*) measurements of the high and low field side response compared to the width of IR emission profiles in related experiments. Reproduced from [561]. © 2021 IAEA, Vienna. All rights reserved.

In EAST, a differential phase scan with $n = 1$ RMPs has identified a range $\Delta\Phi_{\mathrm{UL}} = 0°–50°$ for ELM mitigation and a range $\Delta\Phi_{\mathrm{UL}} = 50°–120°$ for ELM suppression (see figure 43). Particle flux splitting appears to be roughly consistent with magnetic footprint modelling based on vacuum RMPs, with a somewhat larger spiraling pattern during mitigation compared to suppression (see also figure 10 in [526]). Nevertheless, the phase dependence of the vacuum island overlap width Δ_{VIOW} in figure 43(*a*) shows a clear offset with respect to the ELM mitigation and suppression time windows highlighted in yellow and pink, respectively. For $n = 2$ RMPs, an offset between the externally applied RMP field and the total field has been predicted by MARS-F (see figure 6 in [526]), resulting in either screening ($\Delta\Phi_{\mathrm{UL}} = 90°$)

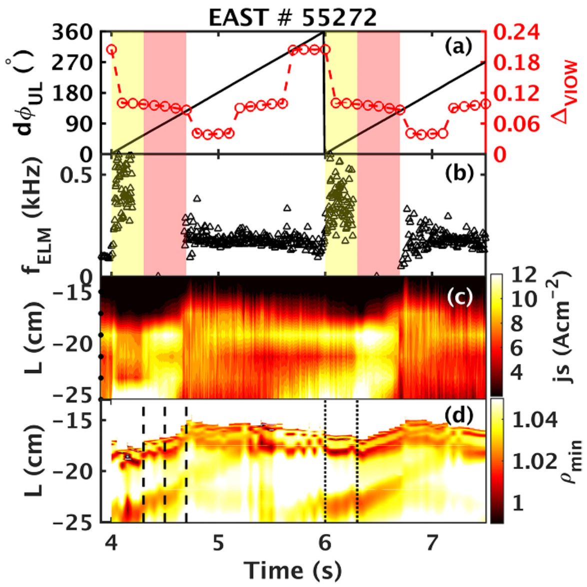

Figure 43. Differential phase scan for $n = 1$ RMPs in EAST. Temporal evolution of (*a*) $\Delta\Phi_{UL}$ (black solid line) and the associated edge stochastic width as measured by the vacuum island overlap width Δ_{VIOW} (red dashed line with circles), (*b*) ELM frequency, (*c*) particle flux on the upper outer divertor measured at $\phi = 327°$, and (*d*) the magnetic footprint at the same location. In (*a*) and (*b*), the time windows of ELM mitigation and suppression are shaded with yellow and pink colours, respectively. Reproduced from [526]. © 2018 IAEA, Vienna. All rights reserved.

or amplification ($\Delta\Phi_{UL} = 270°$). Consistent with that, a clear SP splitting is observed for $\Delta\Phi_{UL} = 270°$ together with density pump out and ELM mitigation, but not for $\Delta\Phi_{UL} = 90°$ (see figure 5 in [526]).

5.3.2. Predictions for ITER. Recently, non-linear resistive MHD simulations with JOREK have been conducted for ITER H-mode discharges with selected RMPs with the aim of demonstrating ELM suppression while heat and particle fluxes onto divertor targets remain below divertor material limits [590]. These simulations pick up on a previous optimisation study [591] which has identified the relative phase combination ($\Delta\Phi_{UM}, \Delta\Phi_{LM}$) for the upper, middle and lower rows of RMP coils which maximises the displacement near the X-point in MARS-F linear resistive MHD approximation as a proxy for ELM suppression. With this setup, JOREK simulations show that the threshold RMP coil current for ELM suppression in the 15 MA/5.3 T, $q = 10$ scenario is at around 45–60 kAt (i.e. well below the capacity of 90 kAt).

Figure 44 shows a comparison between results for the unperturbed case and for RMP application with toroidal mode number $n = 3$. Splitting of stationary heat (and particle) fluxes is found with a maximum radial extension of ≈20 cm on the inner divertor target and ≈40 cm on the outer divertor target. It can be seen in figure 44(*b*) that the peak heat flux with RMPs does not exceed 5 MW m^{-2}, and that it reduces to ≈1 MW m^{-2} towards the outer part of the striations. This is within the design limits of the divertor targets (<10 MW m^{-2}) and the baffle (<5 MW m^{-2}). It should be noted, however, that (*a*) transient fluxes when RMPs are switched on can be much larger, and (*b*) these results have been scaled to a total power of 50 MW into the divertor (i.e. half of the anticipated 100 MW). This may underestimate the expected heat loads in ITER, but it should also be noted that the current JOREK model does not include divertor physics such as recycling and radiation, and that it can therefore not yet give an accurate prediction of the magnitude of heat loads. The extent and shape of the heat load striations, on the other hand, is determined by non-linear MHD and can provide a valuable reference for linear MHD plasma response models coupled to dedicated SOL models. We will follow up with a discussion of detachment under RMP application in section 5.4.2.

5.4. Focus on power dissipation

Access to detached plasmas with RMPs while maintaining ELM suppression remains challenging because of the upper critical density at which ELM suppression is lost. The emphasis of this section is on the impact of RMPs regardless of ELM control, and the aim is to establish what the changes to the magnetic geometry (upstream to downstream link) imply for particle and energy exhaust.

5.4.1. Observations from present experiments. In AUG, it is found that the initially non-axisymmetric heat flux at low density becomes increasingly axisymmetric towards higher density in both L-mode and ELM mitigated H-mode plasmas [524]: toroidal variations of up to 50% in attached conditions are reduced to below 20% in partially and strongly detached conditions. This is attributed to the increase of the divertor broadening factor S by an order of magnitude at high density. The decrease of the toroidal heat flux variation can be reproduced by EMC3-EIRENE simulations—even though those simulations did not include volume recombination. In particular, no *burn-through* of the lobes has been observed, and no significant change of the power fall-off length λ_q and broadening S has been found for the toroidally averaged profiles with RMPs compared to the case without RMPs [523, 524, 533]. This suggests that the radial width of open field lines extending from within the equilibrium separatrix is relatively narrow, with the observed toroidal variations arising solely from corrugations in the SOL plasma induced by the RMP.

In NSTX, on the other hand, it has been found that a partially detached divertor plasma can re-attach when $n = 3$ RMPs are applied [569, 592, 593]. This is shown in figure 45(*a*): the plasma is detached before RMP application and after divertor gas puffing (blue), but then the peak heat flux increases to the level of the attached case without RMPs and gas puffing (red) when RMPs are applied (green). It should be noted, however, that ELMs are triggered here by RMPs applied to an ELM-free H-mode (which has been achieved with Li wall coatings of the PFCs), i.e. the ELMs burn through the detachment and re-attach the plasma which then stays attached during the inter-ELM period. It is shown in figure 45(*b*) that this can be avoided with additional gas puffing in the divertor.

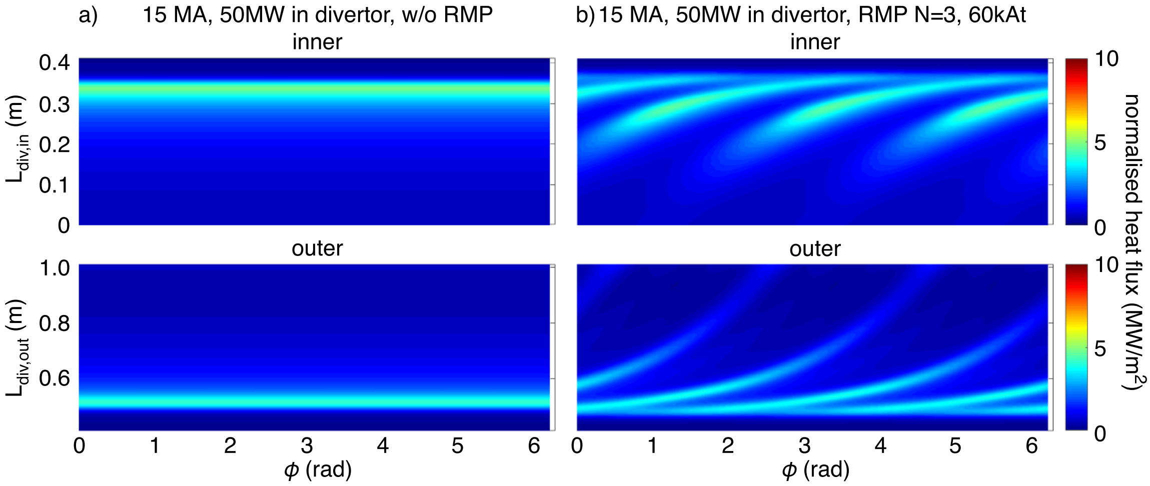

Figure 44. JOREK predictions of stationary heat flux onto the inner divertor (upper row) and outer divertor (lower row) in ITER normalised to a total power of 50 MW: (*a*) without RMPs, (*b*) with RMP application in $n = 3$ configuration at 60 kAt. Reproduced from [590]. © 2022 IAEA, Vienna. All rights reserved.

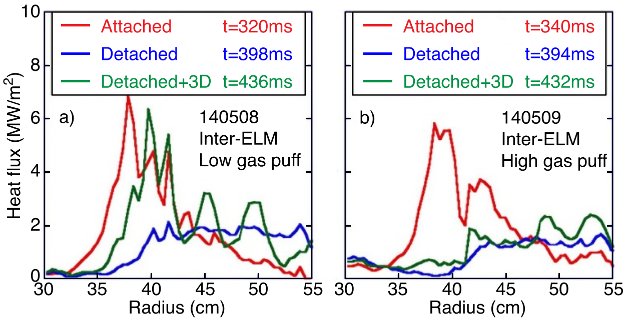

Figure 45. Measured divertor heat flux profiles in a NSTX discharge with $n = 3$ RMPs (green) compared to the reference without RMPs with (blue) and without gas puff (red): (*a*) for low gas puff rate of $\approx 7 \times 10^{21}$ D s^{-1}, and (*b*) for high gas puff rate of $\approx 11 \times 10^{21}$ D s^{-1}. Reproduced from [592]. © IOP Publishing Ltd. All rights reserved.

Radiating divertor experiments at DIII-D with deuterium and argon gas injection have shown that complete ELM suppression by RMPs is accessible only in a limited range in pedestal density and collisionality [594]. Nevertheless, significant ELM mitigation with heat flux reduction has been found to be possible over a much wide range. A radiation fraction of up to 75% has been achieved with RMPs, which is significantly higher than for standard ELMing H-mode plasma at the same $n_{\mathrm{e,ped}}$. Measurements have shown that at sufficiently high densities (i.e. above the onset of divertor detachment), the inter-ELM heat flux striations on the open outer divertor target induced by RMP fields can be eliminated, and that the target heat flux profile is nearly identical to that measured without RMPs (see figure 4 in [595]). Furthermore, an increase in the divertor detachment threshold as a function of density is found in cases where the core electron temperature is increased by 10%–20% after RMP application [565], which has been attributed to the presence of a rotating MHD mode in the reference case without RMPs. Divertor TS measurements have shown that local secondary peaks in the electron temperature near the OT plate are reduced and move away from the target as the core density increases, while in turn peaks in the divertor electron density are increased. These trends haven been qualitatively reproduced by scanning the upstream density in EMC3-EIRENE simulations.

More recently, integrated ELM and divertor flux control experiments have been carried out in EAST [474, 596]. Figure 46 shows that ELM suppression by $n = 4$ RMPs is successfully maintained up to a line average density of $0.6 n_{\mathrm{GW}}$ (with n_{GW} denoting the Greenwald density) when deuterium gas puffing is increased to mitigate the heat flux at the primary (equilibrium) SP and the RMP generated secondary off-separatrix power lobes under high recycling conditions. Nevertheless, mitigated ELMs return at higher density. Reduction of the primary heat flux peak has also been achieved with $n = 2$ RMPs, however, no impact of gas puffing on the secondary heat flux peak has been found in that configuration. This is found to be consistent with modelling of the magnetic footprint (taking into account the plasma response computed by MARS-F) which shows that field lines at the secondary peak have only a shallow radial connection in the $n = 4$ RMP configuration. Furthermore, a 33% reduction of the primary heat flux peak has also been achieved by neon seeding in $n = 2$ configuration—again, however, without beneficial impact on the secondary heat flux peak.

A significant reduction of the divertor heat flux by gas puffing has also been achieved in KSTAR plasmas with $n = 2$ RMP application and fairly good ELM suppression. Figure 47 shows the reduction of the peak heat flux from 2.1 MW m^{-2} to 0.9 MW m^{-2}, yet Langmuir probe measurements show that the plasma is still attached. Further reduction of the heat flux has been achieved in argon seeding experiments in KSTAR with ELM suppression by $n = 1$ RMPs [597]. The ion saturation current begins to decrease when argon seeding is introduced, but it should be noted that the radiation zone

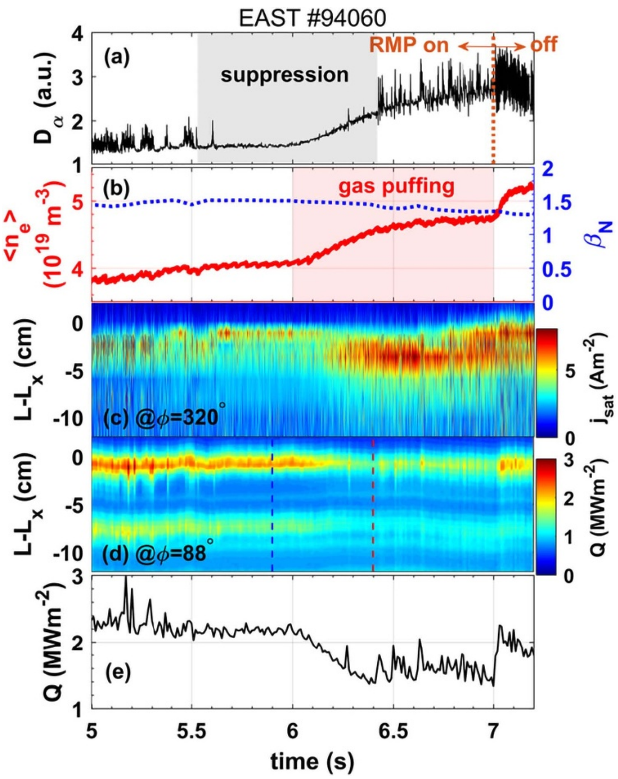

Figure 46. Time evolution of an EAST discharge with $n = 4$ RMPs: (*a*) D_α emission, (*b*) line averaged density (red) and β_N (blue), (*c*) ion flux j_{sat} on the upper outer divertor, (*d*) heat flux Q on the upper outer divertor, and (*e*) its value at the equilibrium strike point at $L = L_x$. Reproduced from [596]. © 2021 IAEA, Vienna. All rights reserved.

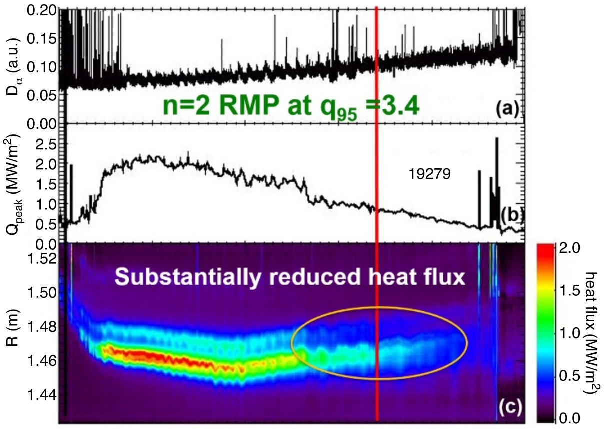

Figure 47. High density, $n = 2$ RMP-driven, ELM suppression with substantially reduced divertor heat flux in KSTAR: time evolution of (*a*) the D_α signal, (*b*) the peak divertor heat flux, and (*c*) the heat flux profile along the target. Reproduced from [529]. © 2019 IAEA, Vienna. All rights reserved.

moves towards the X-point and that core radiation substantially increases at the same time. When the radiation zone detaches from the IT (last two panels in figure 5 in [597]), ELM suppression is lost and mitigated ELMs return.

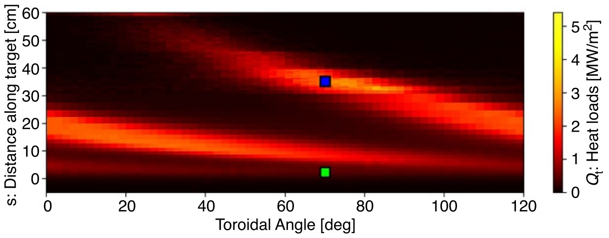

Figure 48. EMC3-EIRENE predictions for heat loads on the outer divertor target in ITER during $n = 3$ RMP application in the pre-fusion power operation (PFPO-I) phase. The distance s along the target is taken from the equilibrium strike point. Reprinted figure with permission from [598], Copyright (2020) by the American Physical Society.

5.4.2. Predictions for ITER.

Based on linear, resistive, single-fluid MHD plasma response (MARS-F) studies [591], plasma boundary simulations with EMC3-EIRENE [598, 599] have been conducted for the pre-fusion power operation (PFPO-I) phase in ITER with hydrogen H-mode plasmas at reduced field (1.8 T) and current (5 MA) for 30 MW of ECH power. At this power level, dissipation from seeded impurities is not required to achieve partial detachment. The RMP coil phasing for maximal X-point displacement (see discussion in section 5.3.2) in toroidal mode number $n = 3$ has been applied. Despite partial screening of the resonant fields (which results in a much narrower stochastic edge region compared to the vacuum RMP approximation), the plasma response includes field amplification near the separatrix. As a result, the magnetic footprint on the divertor target can still be quite large, and it has been found to be sensitive to the assumptions that determine the toroidal rotation profile as input for the plasma response calculation. Nevertheless, significant striations are consistent with full MHD (JOREK) modelling as discussed earlier in section 5.3.2. Therefore, linear MHD plasma response can still be suitable as input for plasma boundary modelling, with the advantage that EMC3-EIRENE does include divertor physics such as recycling and volumetric recombination [600].

Simulation results from EMC3-EIRENE are shown in figure 48 where it can be seen that the extent of the striation pattern on the outer divertor target is similar to the one obtained by JOREK in figure 44(*b*). However, the difference is that the EMC3-EIRENE predictions show a substantially reduced heat load within about 8 cm from the equilibrium SP. A simulated density scan by gas puffing has shown that the reduced heat loads in the main strike area (green dot) are connected to an earlier roll-over of the particle flux compared to the reference case without RMPs (figure 3 in [598]). The earlier roll-over point is consistent with a lower upstream heat flux that results from distributing power exhaust over the relatively large lobes in ITER compared to the power fall-off length λ_q.

The far SOL SP (blue dot), on the other hand, remains attached. Here, the difference from a partially detached state without RMPs is that the upstream heat flux is substantially higher due to the magnetic connection into the edge plasma.

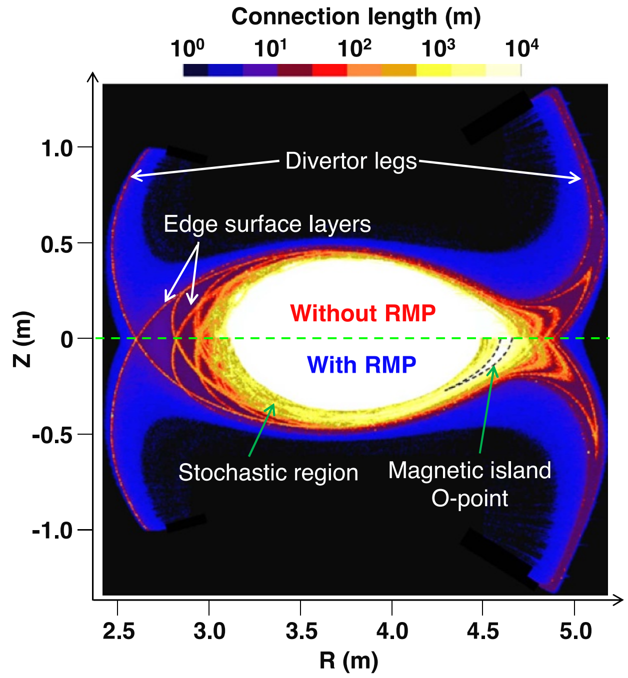

Figure 49. Magnetic field connection length in a poloidal cross section at the horizontally elongated section in LHD, without (upper half) and with (lower half) RMP field. The RMP field with main mode $m/n = 1/1$ creates a remnant island in the edge stochastic region with the O-point located at the outboard side in this cross section. Reproduced from [602]. © 2013 IAEA, Vienna. All rights reserved.

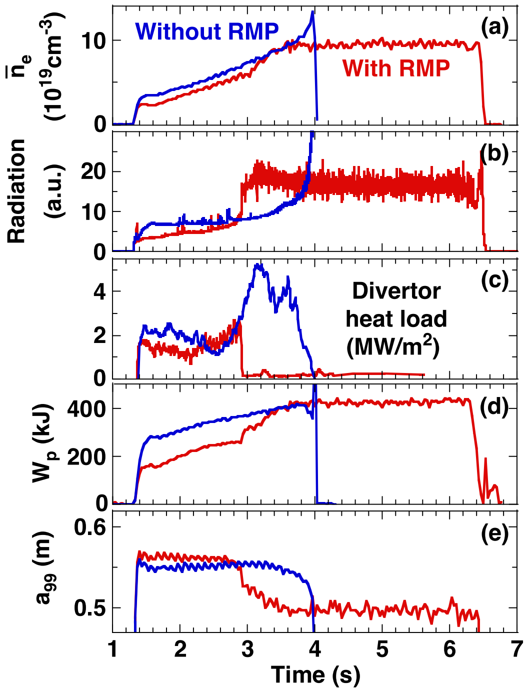

Figure 50. Time traces of (*a*) line averaged density, (*b*) radiated power measured by AXUV, (*c*) divertor heat load, (*d*) plasma stored energy, (*e*) plasma minor radius, for the cases with RMP (red) and without RMP (blue), respectively. a_{99} is defined as a radius that contains 99% of the stored energy. Reproduced from [602]. © 2013 IAEA, Vienna. All rights reserved.

The peak heat load still remains tolerable for the 30 MW of power during PFPO-I. Preliminary impurity seeding studies suggest that dissipation is less efficient in the attached outer lobe SP [599], but this could be connected to the lower density during PFPO-I. Nevertheless, first EMC3-EIRENE simulations for partial detachment with RMPs at FPO with 100 MW of power exhaust through the SOL suggest that sufficient dissipation is possible despite significant heat loads to secondary SPs [601]. However, validation against recent studies at EAST [596] and KSTAR [597] for dissipation with RMPs has yet to be demonstrated, and predictions for ITER remain challenging because of the qualitative differences expected from the relatively larger lobe size.

5.5. Relevant aspects from stellarators

In LHD, the perturbation field from coils at the top and bottom of the torus creates a $m/n = 1/1$ magnetic island in the edge stochastic layer as shown in figure 49. The island separatrix is stochastisised in this region, resulting in a clear flattening of the electron temperature. It has been found that the $m/n = 1/1$ edge magnetic island has a critical impact on detachment stabilisation in LHD [602, 603]. This was first found in a density ramp-up experiment as shown in figure 50, where the main radiator is carbon from graphite divertor plates. The detachment threshold density becomes lower with the island than the case without the RMP field, and the impurity radiation is stabilised around the island [604]. Without the edge island, on the other hand, it is very difficult to avoid the impurity radiation from penetrating to the confinement region and leading to radiation collapse, as shown by the blue profiles in figure 50. The easier access to the detachment with the edge island is interpreted as due to the selective cooling of the X-point of the island, where the energy transport is inhibited in the perpendicular direction by the flux expansion and in the parallel direction by the resonant feature of the field line trajectories. The geometrical effects on the impurity radiation distribution are analysed in experiments [605, 606] and in numerical simulations [607, 608], while a complete understanding of the mechanism of the radiation stabilisation is not yet made.

The divertor heat load patterns during the attached and detached states exhibit a mode structure with $n = 1$, but with a phase shift between the two states [609]. The phase shift of the $n = 1$ mode pattern is considered due to the plasma response to the RMP field, where the field tends to be attenuated in the attached state while it is amplified in the detached state, respectively [609, 610]. The core plasma confinement during the detachment phase with the RMP is maintained without a significant degradation as shown in figure 50(*d*). It is found that the edge density gradient at the inner edge of the island becomes steeper as the detachment transition occurs.

Recently, auxiliary impurity seeding experiments, such as neon, have been conducted with the edge island and a stable detachment is obtained, too [611]. In the neon seeding experiments, the divertor heat load decreases at all toroidal sections, which is different from the case with carbon as dominant

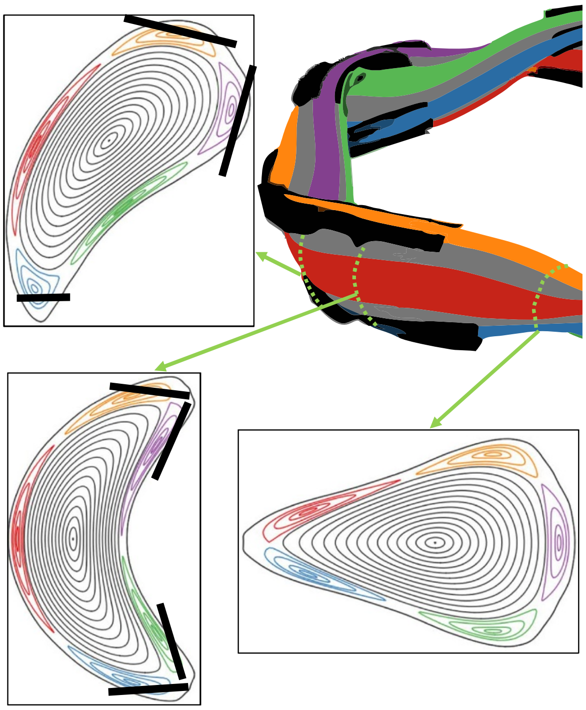

Figure 51. Island divertor formed by five independent islands in W7-X. These islands are established by 50 non-planar coils on a rational flux surface with $1/q = 1/1$. Reproduced from [612]. The Author(s). CC BY 4.0.

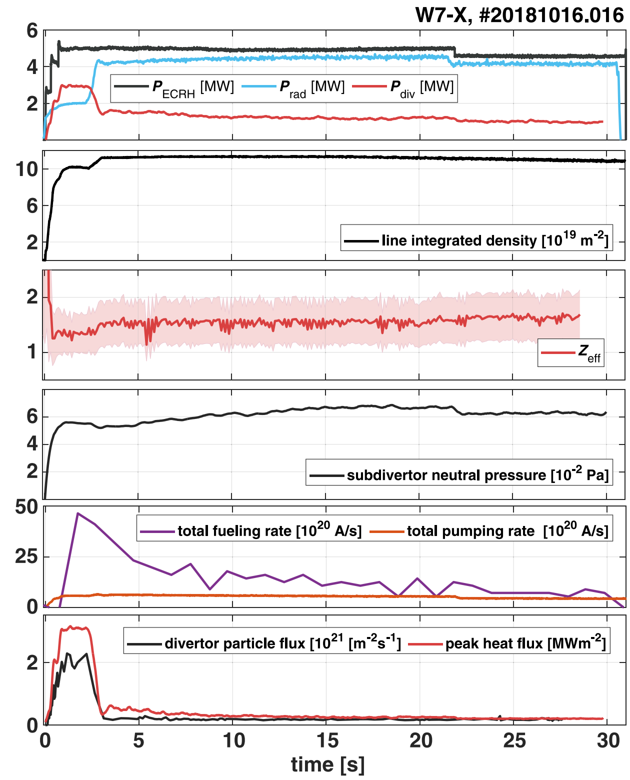

Figure 52. Time traces of the W7-X discharge with detached phase from $t \geqslant 3$ s. From top to bottom: ECR heating power (PECRH), total divertor loads (P_{div}) and total radiated power (P_{rad}); line integrated density and central electron density; neutral pressure at the entrance to the pumping gap; total fuelling and pumping rate and peak heat and particle fluxes to the divertor. Reproduced from [612]. The Author(s). CC BY 4.0.

radiator in the density ramp-up discharges as described above. Neon seems to be more effective in radiating uniformly in toroidal direction than carbon due to the higher temperature of the maximum of a cooling function (see also figure 7 in section 3).

In Wendelstein 7-X (W7-X), an optimised stellarator, a so-called island divertor is installed, which allows to create an efficient exhaust concept for the low-shear, helically shaped plasma of a HELIAS-type magnetic fusion device [613]. The island divertor is inherently three-dimensional (see figure 51) with field lines of different connection lengths forming the SOL. Due to low rational number of the resonant flux surface at which islands are formed, they are rather sensitive to the external perturbations. Therefore additional sets of coils were placed around W7-X. Field errors of limited amplitude can be partly balanced by an asymmetric operation of the so-called island control coils placed behind each divertor. Additionally five so-called trim coils were built equidistantly around the torus to balance b_{11} error fields (i.e. error fields with poloidal and toroidal mode number $m = n = 1$) [614].

Detachment is routinely achieved at W7-X either through intrinsic impurities (mostly carbon) [612, 615] or be seeding external impurities (e.g. Ne or N_2 [616]). Raising plasma radiated fraction f_{rad} above 0.8 leads to a full, thermal detachment with peak heat loads reduced up to an order of magnitude. This regime provides also a significant reduction of recycling flux across the whole divertor surface, while providing neutral pressure in the sub-divertor volume and neutral compression in SOL adequate for density control at W7-X. Numerical studies of the transition to detachment process in W7-X are routinely performed with EMC3-EIRENE. The simulations show that plasma radiation in the attached state is localised within the magnetic island, with a radiation band extending from the strike line to the O-point. When the radiation fraction is increased, either by raising the plasma density or by seeding external impurities, the radiation layer shifts closer to the separatrix [617]. Such a scenario is very robust and could be extended up to 27 s with inertially cooled divertor [612] as presented in figure 52. In contrast to LHD, the detachment scenario does not need to be stabilised with the external fields. As most of the power reaching divertor is coming from plasma radiation asymmetries due to error fields perturbing 5/5 islands are also strongly minimised.

5.6. Conclusions

Splitting of the divertor heat flux by application of RMPs has been verified experimentally across machines. Striations are found to be larger when the perturbation field (including plasma response) is more resonant. This suggests that it will be challenging to decouple the magnetic footprint from optimisation of ELM suppression when larger magnetic footprints result in less efficient dissipation in the far SOL peaks in ITER. The three-row setup of the RMP coils in ITER may open up room for fine tuning, and this can already be explored in

KSTAR—although perhaps with less flexibility related to the stronger core perturbation from $n = 1$ RMPs that are applied in this tokamak compared $n = 3$ or 4 in ITER.

Plasma response can include competing effects from screening of resonances and their amplification through mode coupling to non-resonant components, both of which determine the magnetic footprint. Therefore, validation of plasma response models with particular focus on the plasma edge towards the separatrix is key for the interpretation of experiments and predictive modelling with regard to particle and power exhaust. Linear plasma response models may be sufficient to capture the nature of RMPs and provide trends, but non-linear models are likely necessary to resolve the sudden differences observed at the transition between ELM mitigation and suppression.

Extrapolations of ELM suppression by RMPs and detachment to ITER remain difficult because present machines struggle to simultaneously achieve the anticipated electron pedestal collisionality for ELM suppression in ITER and the high density for effective divertor radiation. Predictions for ITER are further complicated by opposite trends of key figures: larger striations are expected from RMPs for ELM suppression in larger machines with smaller (or possibly similar) heat flux widths λ_q. Integration of RMP effects (including plasma response) into the 3D plasma boundary code EMC3-EIRENE follows the *fluid plasma in a magnetic field* approach of 2D models (such as SOLPS and UEDGE). Validation of EMC3-EIRENE against recent radiative divertor experiments with RMPs will be essential for improving the reliability of predictions for ITER and beyond.

6. Erosion of PFCs and impurity migration

6.1. Introduction

This section is focused on new insights in the material migration cycle [618, 619], comprising erosion, transport and deposition of FW materials, gained since the last ITER physics reviews on PWIs processes and exhaust [329, 620]. Since then, carbon has been abandoned as a PFM for ITER due to unacceptable high erosion [621–623] and associated tritium retention in deposited layers [624–626]. Instead, as outlined in the 2018 research plan [3] ITER would operate with tungsten for divertor plasma-facing components and beryllium for PFCs in the main chamber wall with the option to convert ITER to a full-W device in later phases of operation. As mentioned in the introduction section, the option of using a full-W FW configuration from start will be discussed in 2024 [4] while this contribution deals predominantly with the original concept of ITER with a Be/W material mix, discussing extrapolation to full-W where appropriate and changes between Be and W FW are crucial. The decision to replace graphite-based materials by metallic PFCs in 2013 has been accompanied with an extensive PSI research programme regarding the qualification of W as a divertor material [627, 628] and either Be [629] or W [630] as main chamber material. The associated key experimental findings related to material migration in tokamaks operating with metallic PFCs are presented in section 6.2 for JET [618], AUG [631], EAST [632], WEST [633], and DIII-D [634].

In the following we will define gross erosion as the number of primarily removed atoms from the plasma-facing surface which can typically be quantified by in-situ OES. The sputtered atoms can be ionised on their way through the plasma, influenced by the magnetic and electric fields and by collisions with the plasma ions, and finally return to the surface and become redeposited there. The material lifetime and the impurity level are determined by the net erosion of materials, which is defined as the difference between gross erosion and re-deposition [635]. Net erosion can be measured in most situations by post-mortem analysis of specific marker wall components. The transfer from graphite towards metallic components results in a drastic reduction of main chamber erosion due to the absence of chemical erosion at low impact energies by residual ion fluxes and CXN [636, 637] in the envisaged metallic PFMs. In addition fuel retention by co-deposition in the divertor [638, 639] has been decreased (for a detailed discussion see section 7 HI inventory and recovery), and dust formation from deposited layers is less prominent [640]. The underlying physical and chemical processes at the surface brought in perspective to the adaptation in the divertor plasmas and SOL conditions with metallic PFCs is addressed in more detail in section 6.3. This section addresses the most advanced descriptions of the sputtering process of the selected ITER materials Be and W (as well as C for comparison) by hydrogenic and impurity atoms or ions as a function of the projectile energy, impact angle, and surface roughness.

Updated atomic, molecular, and surface data since the last review is used in the state-of-the-art PSI and transport codes, which are utilised to simulate global, covering the full device, and local, considering a limited volume like a divertor leg, experimental migration results obtained in tokamak experiments. Section 6.4 introduces the main modelling codes applied for the interpretative material migration simulations in the different tokamak devices and different FW materials mentioned before: WallDYN [641], ERO [642] or ERO2.0 [643], and DIVIMP [644]. These codes are coupled to plasma boundary codes like SOLPS-ITER [67], EDGE2D-EIRENE [645], SOLEDGE-EIRENE [646], and EMC3-EIRENE [494] all with the neutral particle solver EIRENE [647]. Section 6.5 discusses the comparison between experiments and modelling subdivided into first-wall limited and diverted magnetic configurations to address the phases relevant to the standard single null configuration foreseen in ITER. The specific role of JET as the closest tokamak in size and PFM selection to ITER is stressed in this section as it lays the foundation for direct extrapolation towards the foreseen ITER plasma operation phases [4] and is used to benchmark the simulation codes. Predictions of material erosion, impurity transport, material deposition, and ultimately dust formation in steady-state conditions on the basis of experimental results and predictive modelling for ITER are summarised in section 6.6. Finally, the paper concludes with a brief outlook to the remaining challenges in the global migration analysis that needs to be tackled.

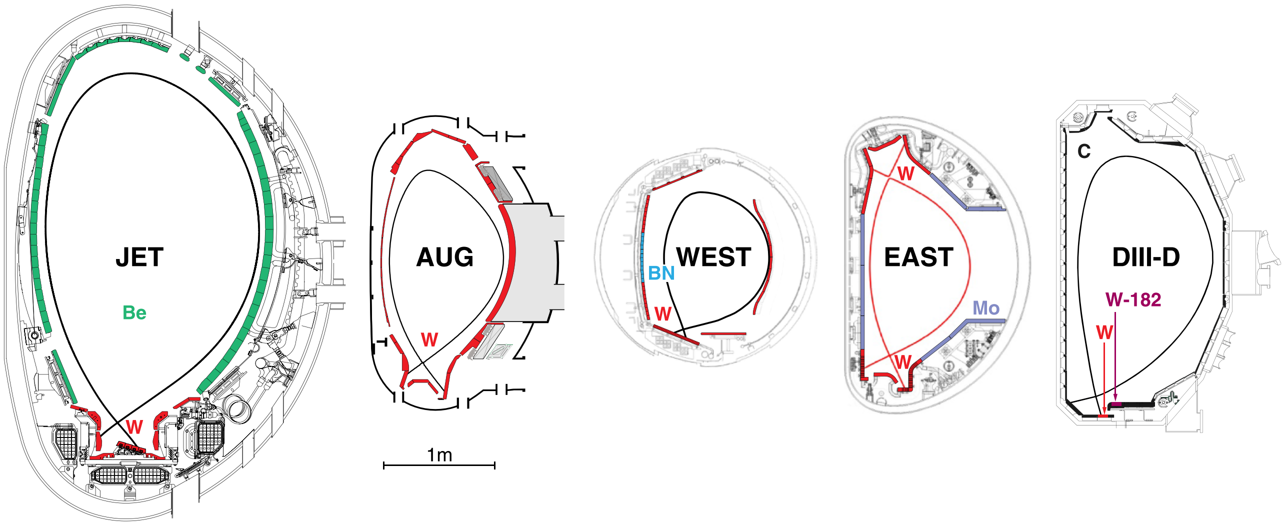

Figure 53. Poloidal cross-section of key tokamak devices (JET, ASDEX Upgrade, WEST, EAST, DIII-D) with metallic plasma-facing materials providing specific experimental input to the first wall selection in ITER.

6.2. Key experimental findings: material migration in all-metal divertor tokamaks

Material migration, thus the cycle of material erosion from plasma-facing surfaces, material transport in plasma, and material deposition on in-vessel surfaces, has drastically changed in magnetically-confined devices upon switching from full-carbon walls, assessed in previous reviews for ITER [620] and beyond [625], to all-metallic machines either in a single step transformation like JET and WEST [648, 649], in a gradual exchange of PFCs over campaigns like AUG and EAST [631, 650], or in dedicated experimental periods with application of metallic PFCs like DIII-D and the pioneering experiment TEXTOR with W LIMs [651, 652]. The most notable tokamak experiments (figure 53) from which experimental data regarding material migration for ITER originates are JET with its ITER-like wall (ILW) configuration, thus Be FW and W divertor [618], AUG [653] and WEST [633] with full-W environment, and EAST [632] with a mixture of different metallic components, i.e. Molybdenum (Mo) FW and upper W divertor. DIII-D operating with graphite (C) PFCs in the FW was used to study W migration starting from the lower divertor during its metallic ring campaign (MRC) [634]. It should be explicitly noted, that also C-Mod equipped with metallic PFCs from day one of operation has studied W migration [654] in the otherwise Mo environment

The complete exchange of FW components from graphite to metallic PFCs in a single step allows the most clear comparison of material migration paths in a toroidal facility as the magnetic configurations, the design or geometry of the plasma-facing components, and the plasma operational window are either identical or comparable before and after the exchange. JET with its transfer from a full-C to a Be/W device reveals the key experimental findings representative also for other metallic toroidal facilities regarding the cycle of material erosion, transport and deposition or in other words: the global material migration.

The global PFC material migration is the sum of four principal *migration paths* namely (i) PFM erosion at the FW, transport, and deposition in the divertor, (ii) PFM erosion at the FW, transport, and deposition at the FW, (iii) PFM erosion in the divertor, transport, and deposition in the main chamber, and (iv) PFM erosion in the divertor, transport, and deposition in the divertor. The strengths of the individual migration paths vary with the applied magnetic configurations and plasma operation regime. Campaign-integrated post-mortem analysis provides information on the overall balance of these four mechanisms after component removal. Often specific operations before tile removal are applied to obtain a benchmark for one set of specific magnetic configuration and plasma condition. Most relevant for JET-ILW is the plasma operation before the first removal of tiles, which consists of 151 identical H-mode plasma discharges in deuterium reaching a fluence comparable to ITER PFPO discharges [655–657]. These plasmas were in the standard lower single null configuration with the inner strike-line on the vertical target at the onset of semi-detachment and the outer strike-line on the bulk-W divertor target plate under fully attached and ionising conditions.

Figure 54(*a*) shows the poloidal cross-section of JET equipped with the Be/W material mix with the present understanding of the dominant material migration paths. The main chamber erosion, namely Be erosion (see section 6.3.1), is dominated by the impinging plasma flux and by the charge-exchange neutral flux of HI species. As in the case of JET-C plasmas, SOL flows [658] lead to a preferred transport of the FW material from the OMP, at the stagnation point, towards the inner divertor leg [622]. Net deposition of Be in the order of tens of micrometres occurs preferentially on the apron of the inner divertor (figure 54(*b*)), whereas the apron of the outer divertor is in balance without significant W net erosion or Be deposition. Line-of sight transport of re-eroded or reflected Be from the vertical W target plate was measured in-situ on the high-field side (HFS) below the bulk-W tile as a function of the strike-line position [659]. The main differences between

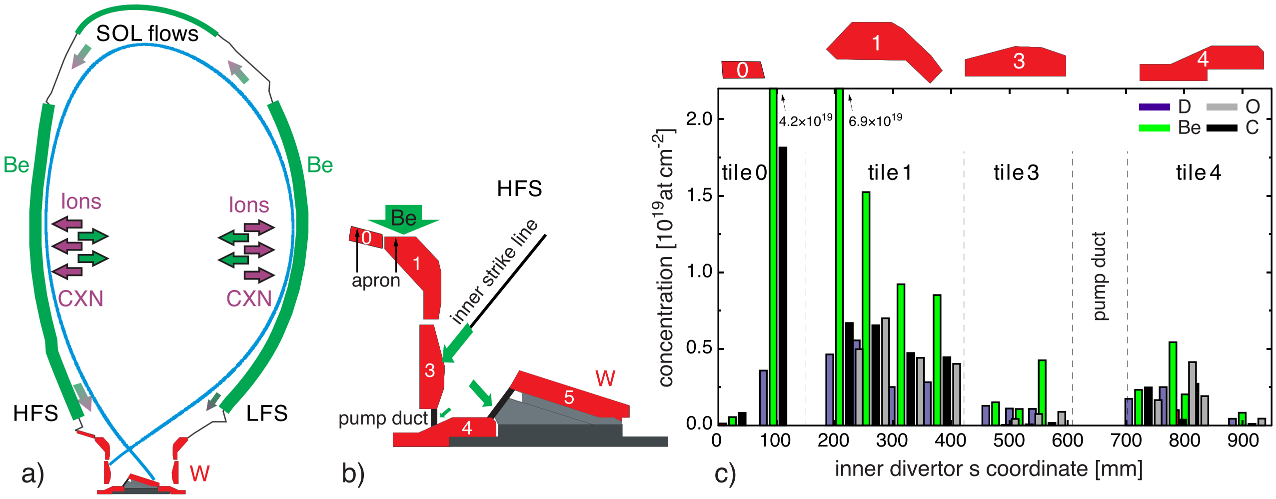

Figure 54. JET: (*a*) poloidal cross-section of JET with the main material migration path indicated. (*b*) Enlarged view in the inner divertor. (*c*) Deposition of Be and other intrinsic impurities in the inner divertor of JET after the first period of operation. Reprinted from [618], Copyright (2015), with permission from Elsevier.

C and Be migration in JET-C and JET-ILW, respectively, are the significantly lower overall main chamber erosion source in the case of Be (factor 5), the reduced deposition rate on the inner divertor apron (factor 10) with higher Be layer stability, the strong reduction of step-wise transport of Be from the deposits towards the pump duct entrance [618], and the associated massive reduction of Be dust formation from layer conversion (factor 100) deduced from extensive post-mortem analysis [640]. Chemical erosion, thus, the material erosion at lowest impact energies or even room temperature-induced material release as volatile molecule, which is present in the case of graphite, is absent in the case of Be due to an impact energy threshold $E_{\mathrm{imp,th}}$ for Be sputtering by plasma particles. The sputtering threshold is the main cause for the different behaviour in material migration between JET-C and JET-ILW, or in other words, between carbon and metals. The absence of chemical erosion reduces in particular the number of erosion and deposition cycles in the SOL and subsequent net-transport from the apron and the vertical target towards the inner divertor pump-duct entrance in multiple steps [656] as observed in C and described by e.g. the walking process [660]. Figure 54(*c*) shows the typical deposition on W-PFCs in the divertor after the first phase of operation with pre-dominant Be deposition above the inner strike-line position in the SOL [639]. The usage of the described migration paths along the poloidal coordinate in figure 54(*a*) is a simplification as shadowing and 3D plasma effects impose in reality a non-uniformity in toroidal direction as seen in post-mortem analysis [638] and interpretative modelling of the JET-ILW [643].

To summarise, the dominant global migration path in JET with ITER-like wall mix is from the Be main chamber into the inner divertor equipped with W PFCs. This causes with rising operational time, Be deposition by the impinging Be ion flux in the range of 1% [637] with respect to the total ion flux approaching this location. The resulting Be layers contain besides Be and D, the plasma fuel, significant amounts of C and O, the typical intrinsic impurities present in the JET edge plasma [661], in the order of 5–10 at% [638, 639]. Sputtering of W at the strike-line location of the inner divertor leg has been documented in intra-ELM phases of H-mode plasmas [662], but was usually below the detection level in the inter-ELM phases and high density L-mode plasmas. This underlines that high impact energy is required to sputter physically W by both, HI ions and Be ions, or in general, low-Z impurities present in JET (section 6.3.2) as well as that W must be present at the PFC surface and not (partially) covered by Be deposits. Inter-ELM sputtering of W is regularly switched off in the inner divertor of JET due to cold or semi-detached/detached divertor operation.

The Be flux to the outer leg amounts approximately to half of Be flux to the inner leg one and is in general insufficient for a homogenous Be deposition; the local erosion/deposition balance is shifted towards erosion. The outer divertor in the near-SOL is in general a net erosion source of W under attached divertor conditions. In H-mode both inter- and intra-ELM sputtering of W takes place at the strike-line location. The intra-ELM phase dominates under attached conditions and is the sole source of W under detached conditions as the ELMs burn through the SOL plasma to the target [663, 664]. Moderate Be deposition occurs several centimetres away from the strike-line in the SOL, but neither erosion nor deposition is detectable at the apron region. Eroded W is to a large extent locally redeposited owing to a high prompt re-deposition fraction of above 95% [657, 665]. This results in an overall low net erosion of W and the so-called W leakage from the divertor is in general moderate and not compromising plasma operation in hydrogen or deuterium in JET. Significant deposition of leaked W on Be in the main chamber has not been observed.

The overall W source in both divertor legs is very low in comparison with the C source in the previous graphite divertor in JET-C and largely determined by intra-ELM sputtering by HIs and low-Z impurities with impact energies above the threshold for physical sputtering. CXNs can in particular in H-mode contribute to the overall W sputtering [666]. It should be noted, that after several years of operation and change of the dominant magnetic configuration, i.e. averaged inner strike-line position now on the inner horizontal target plate, also deposits with thickness of several μm are formed on the horizontal target plates [667].

These JET-ILW observations are in general consistent with results from AUG, WEST, and EAST plasma operation in deuterium where light impurities have been determined to dominate the erosion of W PFCs in the divertor [619, 632, 668]. Application of a medium-Z (Mo) or high-Z (W) main chamber wall is further decreasing the primary erosion source in L-mode and inter-ELM phases due to the higher sputtering threshold energy of those materials in comparison with the low-Z materials C and Be. Thus, with the decrease of the primary erosion source also the global material migration from the main chamber into the divertor is further decreasing. But, spectroscopic data at the AUG main chamber reveal significant W gross erosion with lower screening induced in particular by ELM impact. Indeed intra-ELM sputtering is responsible for 70% of the source at the outboard LIMs and in the relatively inert inboard around 40% [669]. In the case of JET and Be FW intra-ELM phases have only a minor contribution to the overall global Be erosion in the inter-ELM phase due to the very localised impact area of ELM filaments as well as the lower sputtering threshold energy for Be than for W. Moreover, 3D effects in recessed areas from ripple, shadowing, LIMs etc impose a challenge in plasma edge diagnosis and interpretation of PWI processes. Similar experimental observations are made in EAST [632], AUG [670], and WEST [671] though for other metallic FW materials than Be.

Finally, it is important to indicate that the mentioned metallic devices usually operate with the aid of low-Z conditioning techniques to reduce the intrinsic impurity content. In the case of JET, Be is acting as low-Z wall conditioning species to reduce in particular the Oxygen (O) content, whereas in the case of AUG and WEST, the half-metal Boron (B) is used to suppress oxygen and condition the machine via boronisations [672] or B powder injections [673–675]. In the case of EAST, the alkali-metal Lithium (Li) is regularly applied to condition the FW in the form of Li-evaporation or in-operando by Li powder injection [676]. Similarly to JET, thick co-deposited layers can be formed in the presence of these impurities which complicate determining the actual erosion rates of the original wall materials. Therefore, it is relevant to indicate that Li and B participate in general into the material migration processes in these tokamaks, though the low-Z layer thickness and its FW surface coverage homogeneity is less defined as in the case of Be, which is used as low-Z plasma-facing material in JET.

6.3. Principles of W and Be erosion and deposition processes

6.3.1. Beryllium erosion and deposition processes. Beryllium (atomic number $Z = 4$) has until recently been foreseen as the FW material in ITER due to its good oxygen getter properties, providing permanent in-situ wall conditioning, the lower HI content in resulting co-deposits than is the case with C, the good metallic properties with a relatively high melting point of 1278 °C in comparison to other low-Z or medium-Z metals, and reduced impact on core performance than what would be the situation with high-Z materials. The impact energy threshold for physical sputtering by deuterium is approximately $E_{\mathrm{th}} = 10\,\mathrm{eV}$ (see figure 55(*a*)). This points to a high primary erosion source at the FW and indeed disqualifies Be as material for a reactor at high duty cycle of more than 0.7, but makes Be still a good candidate for the fusion test facility ITER. Dedicated experimental studies related to the qualification of Be for fusion application were carried out in different ion beam facilities, in the linear plasma-device PISCES-B [677], at the JET tokamak, in laboratory analysis stations like e.g. FREDIS [678] as well as in the material modelling by e.g. MD. The overall present-day knowledge about Be properties, the erosion and deposition characteristic as well as the retention behaviour in co-deposits has been recently reviewed in [679]. In the following, we will focus on a few specific properties and processes relevant in the nuclear fusion context and linked primarily to PISCES-B and JET-ILW studies and associated modelling.

A key difference between the sputtering of the low-Z materials C and Be is the chemical erosion of C which is associated with a release of hydrocarbons at thermal impact energies of HIs, thus, no effective sputtering energy threshold exist as depicted in (figure 55(*a*)). Though Be has a clear threshold energy as measured in ion beam experiments and shown in the same figure [680], the measured sputtering yield shows a dependence on the surface temperature indicating an additional release process next to pure physical sputtering. Experiments in PISCES-B under deuterium plasma bombardment have revealed this process as CAPS, which vanishes at high surface temperatures of Be [681]. A clear signature of the release mechanism is the spectroscopic detection of the so-called BeD A-X band indicating a molecular release with the product BeD along its dissociation chain [682]. The sputtering requires a minimum energy and therefore is an ion-induced damage process in contrast to the thermal release in the chemical erosion of graphite. Complementary experiments in laboratories indicated a high deuterium concentration in the near surface related to supersaturation and formation of a BeD$_x$ complex [683]. MD studies, with more than ten orders higher impinging flux compared to the laboratory studies, modelled successfully the release mechanism and provided a description of the BeD and BeD$_2$ molecule release, the fraction of CAPS to the ordinary physical sputtering process as well as the underlying energy dependence [684]. Furthermore, a temperature dependence of the yield was found and related to the D content in the interaction zone [685], explaining the absence of CAPS at high surface temperatures with the absence of D in the surface (figure 55(*b*)). The question remained whether the process was associated with changes in surface morphology specific to perpendicular and monoenergetic plasma incidence, characteristic for high flux linear plasma devices at low magnetic field, as described in detail in [686] for a large number of projectile and target materials. This study showed a

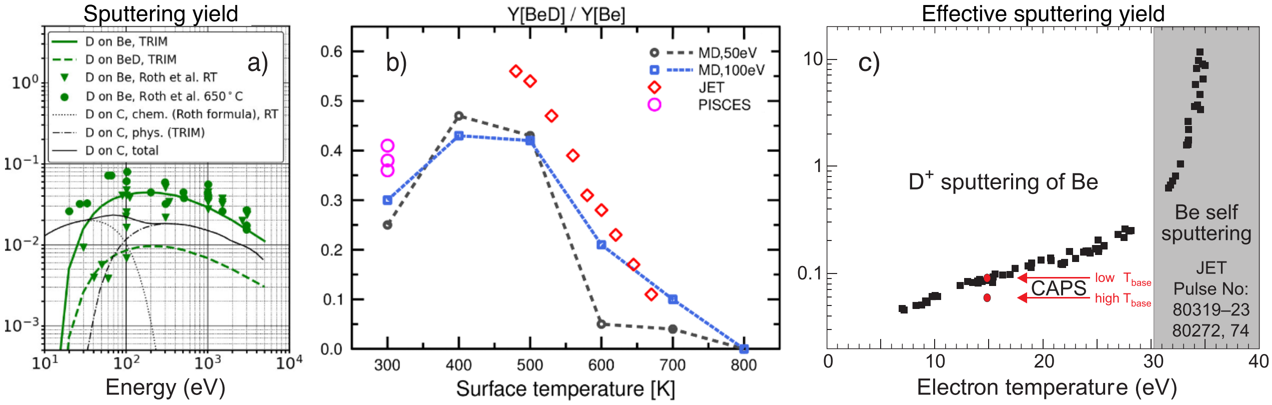

Figure 55. (*a*) Be sputtering yield by D bombardment from SDTRIM.SP simulations [687, 688] and yields measured in D ion beam experiments for Be [680, 689] and C [690]. (*b*) Temperature-dependent contribution of BeD to the total Be sputtering in PISCES-B, JET and MD simulations. Reproduced from [685]. © IOP Publishing Ltd. All rights reserved. (*c*) Spectroscopically determined effective Be sputtering yield at JET limiters. Reproduced from [691]. © 2014 EURATOM. All rights reserved.

systematically lower sputtering yield for low-*Z* materials in linear plasma devices compared to simulations with SDTRIM based on the binary collision approximation, with the discrepancy ascribed to the formation of cone-like surface structures in the experiment.

In JET-ILW using limited plasma configuration in conjunction with OES the Be sputtering yield was investigated under tokamak conditions at a high magnetic field, with a thermal impact energy distribution as well as variations in the impact angle. Moreover, because the JET PFCs are not actively cooled, the surface temperature was in subsequent discharges ratcheting up beyond the expected maximum of CAPS [691]. Indeed CAPS was verified and about 1/3 of the total effective Be sputtering yield (gross erosion) at an impact energy of $E_{\mathrm{in}} = 75\,\mathrm{eV}$ for deuterons was attributed to the process at the peak value of appearance. Moreover, a decay of CAPS with almost complete disappearance was measured at Be surface temperatures of about 520 °C [691] with parallel desorption of deuterium from the Be LIM measured spectroscopically by the molecular release of D_2. Successful modelling of the experiment was carried out with the ERO code [692, 693] under consideration of the molecular release and modifying the sputtering yields by inclusion of the D content in the Be matrix.

Variation of the impact energy by D_2 fuelling and local plasma cooling demonstrated that in JET three different sputtering processes take place: physical sputtering by hydrogenic impact, chemical assisted physical sputtering by hydrogenic impact at moderate impact energies while at high impact energies self-sputtering by Be ions takes finally over. The self sputtering is in particular critical in the start-up phase of a tokamak plasma with Be main chamber PFCs. Figure 55(*c*) shows the gross Be sputtering yield at the LIM as a function of the local electron temperature and associated ERO2.0 simulation (see section 6.4.2) boundary for the two Be sputtering yield data sets mentioned before [694]. Comparison between post-mortem analysis performed at the end of the first phase of operation [695] and campaign-integrated spectroscopic data provided a factor two difference between gross and net erosion of Be at the LIMs [637] at the location of the observation spot. Normalised to the LIM phase a net erosion of about 10% of the original Be thickness was measured at the LIM apex mainly due to the self-sputtering phase in the LIM configuration [696]. A complex erosion-deposition pattern of Be was recorded in the toroidal and poloidal directions and linked to the shadowing effects by neighbouring LIMs, thus, to 3D effects.

Finally, no significant increase of Be sputtering in the main chamber was observed in simulations of H-mode discharges with inter- and intra-ELM phases in contrast to studies with full-W FW. This is caused by the overall low impact energy sputtering threshold for Be and the sputtering of the FW by residual impurity ions and charge-exchange neutrals [637] which overlays the enhanced sputtering during a short ELM-impact at a very localised area of an ELM-filament reaching the LIM PFCs [663]. However, RF-sheath induced Be sputtering can lead to significant Be impurity production [697] and associated W sputtering in the divertor. Optimisation of the RF antenna design as performed in AUG can reduce the sputtering and is envisaged for ITER.

6.3.2. *Tungsten erosion and deposition processes.*

The key erosion process of W material (atomic number $Z = 74$) is physical sputtering, which has a much lower sputtering yield compared to the low-*Z* materials. The W sputtering threshold energy due to the incidence of main plasma species D and T are around $E_{\mathrm{th}} = 210\,\mathrm{eV}$ and approximately $E_{\mathrm{th}} = 140\,\mathrm{eV}$, respectively. Therefore, W erosion by background ions is almost negligible for thermal steady-state divertor plasma conditions [657]. Since the larger mass of the projectiles leads to higher sputtering yield and lower sputtering threshold, the majority of W erosion is normally caused by impurity bombardments even at a low impurity concentration, in particular at low plasma temperatures [664, 698, 699]. The higher charge state of the ion can gain higher kinetic energy in the plasma sheath near the material surface.

Figure 56(*a*) shows the sputtering yield for W for different intrinsic and extrinsic impurity species present in current day devices under perpendicular impact. The corresponding

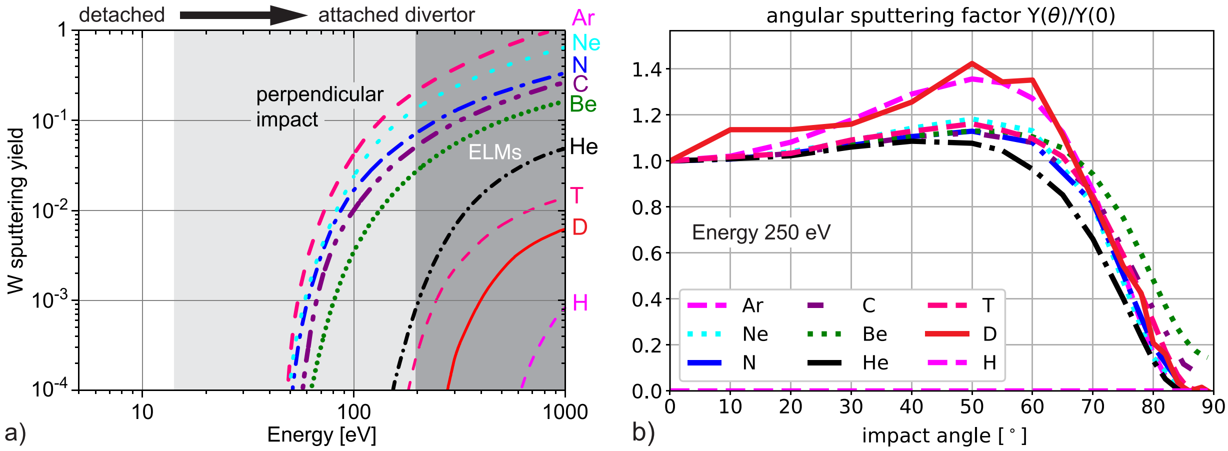

Figure 56. (*a*) W sputtering yield calculated with SDTRIM.SP [687, 688] for perpendicular impact of different singly ionised species. The light grey area indicated detached divertor conditions and the dark grey area the region of intra-ELM projectile energies. (*b*) Angular dependence of the W sputtering yield normalised to yield at perpendicular incidence for different ionising species at an impact energy of 250 eV calculated with SDTRIM.SP.

angular distribution is depicted in figure 56(*b*). The typical impact angle for the ions lays effectively between 40° and 60° [693, 700, 701] as in the case of Be despite a characteristic length for the impact of the magnetic pitch angle of only a few centimetres due to sheath effects as well as surface roughness. Surface roughness reduces erosion of metallic wall components like tungsten PFCs. An extensive database has been collected from W PFCs from AUG and from linear devices like MAGNUM-PSI [702] and PSI-2 [703], indicating several times reduced net erosion as roughness changes from atomically smooth surfaces to technical ones (roughness up to 10 μm) [619, 704–706]. In general, the effective sputtering yield decreases for rough surfaces in comparison to smooth ones, which may be due to the higher capturing probability of eroded W due to the local geometry in the μm-scale.

W erosion by HIs can play an important role during transient events. In H mode plasmas, the ELMs burst periodically energetic particles out of the confined region towards the target plate (see section 4) and cause intra-ELM sputtering of W. The W sputtering in the intra-ELM phase is determined by both impurity and high energetic fuel particle ions [653, 663, 707, 708]. However, for the inter-ELM phase, the sputtering of W is dominated by the impinging impurities, since the plasma conditions are comparable to the situation of L mode operation. By operation in the (semi-)detached divertor regime, W erosion in the inter-ELM phase can be mitigated since the incident energy of the ions can be reduced to below the sputtering threshold. For the intra-ELM phase, the W gross erosion cannot be suppressed by the detached operation because the energetic ions are expelled from the pedestal. According to the experiments in current tokamaks, W gross erosion can be dominated by the intra-ELM phases in H-mode plasmas [707]. The ratio between inter- and intra- ELM erosion depends on the local plasma conditions, impact energies of impinging ions, the impinging flux to the targets, the impurity concentration, and indeed on the ELM frequency and magnitude [657, 709]. In addition to the physical sputtering process, W material would also be eroded due to CAPS during plasma bombardment with the release of tungsten hydride molecules like WH and isotopologues [710, 711]. The W erosion due to CAPS is very low in comparison to physical sputtering, but has likely a lower threshold for the sputtering process and is one potential explanation for W erosion below impact threshold energies and associated transport in remote areas. Quantification analysis of the process is still on going.

The W gross erosion can be quantified spectroscopically with the help of W I emission using the inverse photon efficiency (S/XB values), which converts photon fluxes into particle fluxes of the eroded W atoms. The sputtered W particles may transport globally in the main and SOL plasma or locally transport in the divertor region dominated by the so-called prompt re-deposition [712], which is defined as the deposition during the first gyration after being ionised. The prompt re-deposition fraction can be experimentally characterised by comparing spectral emission lines of neutral W and ionised W. Since W has large number of electrons and large mass, it has rather large ionisation probabilities and also large gyration radii which increase the probability of prompt re-deposition [713–715]. It has been found that the resulting W net erosion rate is much lower compared to the gross erosion rate due to the high local re-deposition of eroded W [657]. The eroded W returned to the surface leads also to self-sputtering of the bulk material, which is an important contribution to W erosion. The respective fraction of total erosion is implicitly included in the experimental results and can therefore only be determined by modelling.

Unlike the gaseous elements such as HIs, solid elements such as Be sputtered from the FW or boron from wall conditioning procedures will deposit on an initially clean W surface and lead to formation of mixed-material layers [716]. This will decrease the W concentration at the surface and thus the effective W erosion rate in comparison with the pristine W surface. Under conditions where the deposition rate of the non-volatile material will exceed its re-erosion rate or its diffusion rate into the bulk material at elevated temperatures, closed deposited layers will grow on the target material [717]. The synergistic interplay of simultaneous erosion by volatile and non-volatile incident species was first studied by TRIDYN [718] and EDDY [719] code simulations and subsequently validated in ion beam experiments [720, 721] and divertor erosion studies in DIII-D [635].

Seeding impurities such as N_2, Ne, Ar etc used for radiative cooling will per se cause additional sputtering contributions, which is counter balanced by the radiative cooling of the divertor plasma [267, 367]. Therefore, the concentration of the seeding impurities must be carefully controlled and optimised for maximal radiation cooling fraction while avoiding extensive W sputtering and simultaneously maintaining good plasma performance in the core region (see section 3).

Other important channels enhancing the W erosion are the (i) acceleration of plasma and impurity ions in the rectified sheath with RF in use [722, 723] and (ii) arc erosion [724]. The W influxes can be increased by about a factor of ten during the operation of RF with the main W source contributed by the LIM source. The local erosion in the divertor of AUG can be dominated by the arc erosion occurring at high density operation at the inner divertor apron. Further studies are required here to assess the impact on the global scale for long-pulse operation devices with actively cooled PFCs.

Finally, the impact of He on W and associated morphology changes has been identified to be potentially critical [725] with significant impact on the W erosion-deposition balance. Detailed studies in linear plasma devices [726, 727] and tokamaks [728, 729] were carried out under the ITPA framework in order to validate model predictions for ITER [730].

6.4. State of the art codes to simulate material migration in tokamaks

In this section we will discuss the different simulation codes that are presently being used to model migration of the different wall materials and impurities in the edge and SOL plasmas of tokamaks. Typically, the first step is to reproduce the background plasma that will subsequently be used as an input to the actual migration codes. Several advances since the previous ITER Physics Review will be reported including the 3D nature of the migration process, extension of the simulation grids to the tokamak walls, improved atomic and molecular data used by the codes, as well as elaborated treatment of transient phenomena like ELMs.

6.4.1. The WallDYN simulation code. WallDYN [641] is a code that describes the FW evolution based on erosion/deposition and global impurity transport. In the WallDYN code, the FW is subdivided into different elements, and each contains a reaction zone located on an infinite bulk. Material erosion and deposition processes occur within the reaction zone, and an appropriate material exchange with the bulk is allowed to compensate for the material loss and gain. The redistribution of these impurity sources, by erosion and reflection, is described by a matrix which describes the influx onto the wall elements due to the impurity source from all the other wall elements. This coupling of surface evolution and plasma transport allows for a self consistent description of both the surface composition evolution and the corresponding evolution of the impurity influxes from the plasma. The code describes this coupled evolution as a differential algebraic equation system that is solved time dependently and maintains a global material balance for all eroded/reflected and migrating particles. The reflection and erosion rate coefficients are parameterised from the simulation results of SDTRIM.SP [687, 688] or MD codes [731]. To determine the impurity redistribution probabilities among different wall elements, test particles are launched homogeneously in a trace impurity transport calculation, and then a redistribution matrix for a given background plasma condition is generated. WallDYN can also provide the growth rate of a deposition layer which can be used to calculate the fuel retention by co-deposition [732].

6.4.2. The ERO simulation code. The ERO code is a 3D Monte–Carlo code which simulates material erosion, impurity transport and deposition in magnetic fusion devices [642]. Originally, the code could only focus on localised wall components with sizes in the range of centimetres to meters, such as the divertor target plates, LIM tiles or samples exposed in tokamaks or linear machines. The ERO source code has been recently rewritten and updated to the ERO2.0 version with massive parallelisation, which is capable of performing modelling for much larger 3D volumes, even the entire dimensions of tokamaks with divertor and main chamber walls [643]. The physics models and main features are similar for the two versions of the code. In addition to benchmarking simulations with existing experiments, predictive modelling of the erosion and deposition of wall components for future fusion devices can also be performed. The main features of the code are described in the following. Impurity particles are originated from the material surface by physical sputtering, chemical erosion, external gas puffing or evaporation. The particles are released from the surfaces as neutrals, and then can be ionised or dissociated on their way through the plasma. The movement of charged particles is determined by the magnetic and electric fields, friction force, thermal force and (anomalous) cross-field diffusion. Full Larmor gyration or guiding centre approximation of the charge particles can optionally be chosen to be used in the code. The eroded particles can return to the material surface where they can be reflected or re-deposited. In addition, the returned particles themselves can erode further the material surface. The background plasma parameters are taken as input parameters in the ERO code, which can be either provided by plasma transport modelling or constructed based on the experimental measurements. The databases on sputtering yields, reflection coefficients and rate coefficients for atomic processes are used in the code. Sputtering and reflection data are based on the SDTRIM.SP [687, 688] or MD simulations [731]. Ionisation, recombination and photon emission rates for atoms are typically taken from ADAS [733]. The surface composition for ERO calculations can be considered by coupling with the SDTRIM.SP code or alternatively by using a homogeneous mixing material model.

6.4.3. The DIVIMP simulation code.

The DIVIMP code [734] is a two–dimensional divertor impurity transport code which follows the transport of sputtered or injected impurities in the edge plasma. The background plasma as well as computational meshes used by DIVIMP can be extracted from other widely used fluid codes such as SOLPS [735] and UEDGE [736] or experimental based simple models like the OSM [644, 737]. With a given background plasma condition, impurities are followed in a Monte-Carlo way until they finally deposit on a solid surface. The influence of impurity distribution on the background plasma is ignored in the code, so DIVIMP is usually applied to impurities with a small concentration. DIVIMP has obvious advantages on W transport simulation compared to other fluid codes, because the possible high charge states of W bring large amount of calculations for the convergence of fluid equations. Therefore, DIVIMP has been used for edge W erosion and transport simulations for fusion devices with W PFCs in recent years. According to a specified erosion model in the DIVIMP code, W erosion can be calculated based on the impinging particles flux density and energy derived from the background plasma. The sputtered neutrals are launched and followed until ionisation or re-deposition. A predefined cross-field diffusion coefficient is considered. For the parallel transport, collisions with the background plasma and various forces including friction, electrostatic force and temperature gradient forces are included. The self-sputtering cascades are self-consistently calculated and followed as well. After the DIVIMP simulation, the 2D spatial distributions of impurities for each charge state can be provided.

6.4.4. The SDTRIM.SP simulation code.

SDTRIM.SP [687, 688] is a modern implementation of the binary collision approximation description of the transport of ions in matter: TRIM. It describes the transport of fast (primary-)projectiles impinging on amorphous target structures by a sequence of binary collisions. During these collisions also target recoil atoms are created, which are followed in the same way as the primary projectile is, thereby also potentially creating new recoils. This gives rise to a so called *collision cascade* and all particles in this cascade are followed until their energy is dissipated by inelastic energy loss to the target electrons. If during this collision cascade the primary projectile leaves the target, it contributes to the reflection yield of the projectile whereas if a target atom leaves the surface it contributes to the partial sputter yield of the respective element type from the target surface. SDTRIM.SP can be used in two modes: static or dynamic. In the dynamic mode the target composition and thickness is modified according to the material transport during the collision cascade which allows to simulate surface recession and ion beam mixing. In the static mode the target composition is fixed and in this mode sputter and reflection yields are computed and also range distribution and displacement damage events are recorded.

6.5. Material migration in tokamaks: experiment and simulation

6.5.1. Specific experimental and modelling contributions from JET.

PSI processes between Be and H isotopes have been studied in-situ in inner-wall limited discharges in JET with the contact point on the high-field side of the torus with dedicated OES lines-of-sight. The effective Be gross erosion yields can be determined via measurements of Be II at 527 nm and D_β as well as the application of known S/XB values (see figure 55(c)) in JET covering all three Be erosion processes (physical sputtering, CAPS and Be self sputtering) as a function of the ion impact energy and the Be surface temperature [691]. The 3D ERO2.0 code was benchmarked with this set of effective Be sputtering yields employing toroidally symmetric onion-skin-based circular plasma backgrounds as input [694]. The experimental and modelled effective Be sputtering yields are in general in good agreement as depicted in figure 57(a). The D content in the Be surface decreases with rising surface temperature. The rising temperature has been achieved by decreasing the central plasma density as the PFCs are only inertially cooled. Therefore, the experimental values lay within the boundaries of the two SDTRIM.SP Be sputtering yield data sets (w and w/o D content in the Be surface) applied. ERO2.0 reproduces successfully the strong Be self-sputtering branch at the highest impact energies, or corresponding to the lowest central plasma densities as used as abscissa in figure 57(a). This modelling in the LIM configuration gives confidence in the global Be source term simulation under tokamak conditions, thus in the first step of the Be migration modelling.

Diverted magnetic configurations were assessed initially in 2D simulations with the WallDYN code assuming a toroidally symmetric FW and plasma in the applied standard configuration in JET (see figure 54(a)) with the inner strike-line positioned on the vertical target plate. The WallDYN impurity migration matrices calculated for JET by DIVIMP suggested that a large fraction of Be from the main chamber wall would impact the top of the inner divertor baffle or the apron region. Combining this migration matrix for deriving the material ion flux, with the dynamic surface evolution model in WallDYN, resulted in Be layer growth rates on the apron, that were close to the experimentally observed values [732]. These can be converted into the measured thickness of about 20 μm after 13 h of plasma operation in the divertor configuration [637, 738], which was predominantly in the first years in the standard single null configuration. Figure 57(b) shows the result of the WallDYN simulations at the inner divertor leg for the typical H-mode plasma prior to the first tile removal [655] and can directly be compared with the deposition pattern from post-mortem analysis [639] shown in figure 54(c). The main pathway of Be migration in JET H-mode plasmas with erosion at the FW and predominant deposition on the inner divertor apron could be reproduced in these 2D simulations.

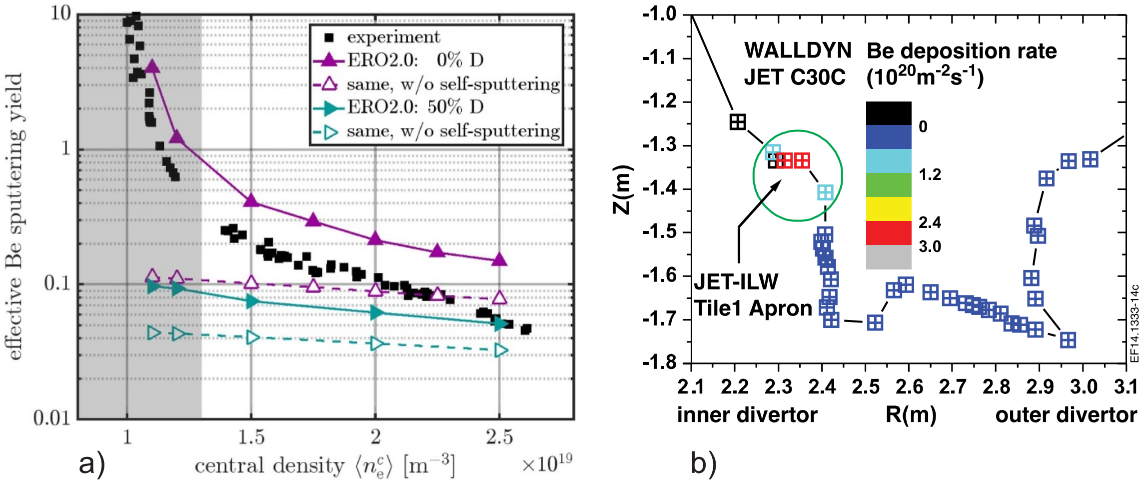

Figure 57. (*a*) Comparison of global Be erosion in JET-ILW discharges in limiter configuration with ERO2.0 simulations. Reproduced from [694]. CC BY 4.0. (*b*) WallDYN simulations for JET in the first year of ILW operation reproducing the deposition pattern on the inner divertor apron during diverted plasma configuration. Reproduced from [637]. © 2015 EURATOM. CC BY 3.0.

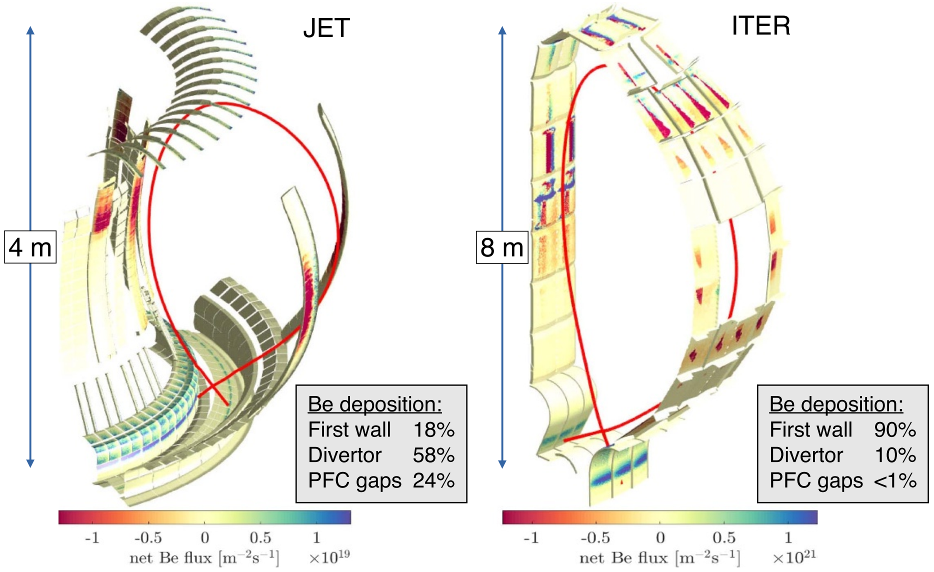

Figure 58. The global Be erosion/deposition pattern interpretative modelled with ERO2.0 for JET-ILW in divertor configuration and a predictive simulation for ITER for H-mode plasma conditions. Plots created by J. Romazanov from simulation results published in [694] and [739]. Reproduced with friendly permission by J. Romazanov. © 2024 J. Romazanov.

Finally, full 3D simulations of H-mode plasmas were carried out with ERO2.0 to include, in particular, the shadowing effects of FW PFCs and dedicated synthetic diagnostic simulations to improve the accuracy of the simulations. Figure 58(*a*) shows the net Be erosion-deposition pattern in JET simulated with ERO2.0 [694] for the very same plasma described before in the 2D WallDYN case. The generic material transport from the main chamber into the inner divertor is reproduced, but now the spatial variation of Be erosion in the main chamber and the distribution of Be sources at the inner and outer wall are resolved. Moreover, in the global simulation also the net re-deposition of Be at the FW can be estimated. In fact, in the diverted magnetic configuration, only a small 18% fraction of Be is redeposited on the FW elements while 58% is redeposited in the divertor, with the remaining 24% being redeposited in the gaps of the 3D PFC structures. However, the dominant migration path changes in predictive simulations for ITER when ERO2.0 is applied to the standard $Q = 10$ H-mode plasma with much higher density in the SOL than in current JET plasma simulations [739]. A much larger fraction of Be eroded at the first-wall PFCs remains at the FW (figure 58(*b*)), namely 90%, as described in more detail in the next section addressing predictive ITER simulations with full 3D wall shaping. The change of the dominant Be migration path will have a vital impact on the subsequent PSI-processes like tritium co-deposition with Be and Be dust formation as well as the lifetime of the wall components.

The previously introduced simulations were performed assuming quasi-steady-state plasma conditions excluding ELMs. Though this is an acceptable approach for the Be FW simulation, it is insufficient for modelling the W erosion-deposition pattern in the divertor due to the important role of the intra-ELM phase on the sputtering process (see section 6.3.2). In the first step, local ERO simulations were carried out modelling inter- and intra-ELM phases of W erosion and deposition in the divertor with experimental plasma parameters as input and compared with OES [665, 740]. Thereby, the FSM, tested experimentally against different types of ELMs, was implemented in a dedicated module in ERO and benchmarked against single ELM events [663, 741]. The intra-ELM sputtering is governed by the impinging energetic hydrogen fuel ions and by the dominant impurity ion fraction in the pedestal. However, the Be concentration in the JET pedestal is low and amounts typically to less than 1.5%, thus deuterons are dominating [663].

The (prompt) re-deposition of W at the outer strike-line was determined experimentally for the series of 151 discharges prior to the first bulk-W tile removal under attached conditions ($T_e = 35\,\mathrm{eV}$) in deuterium. The gross erosion of W was measured in-situ by OES on the W I line at 400.9 nm whereas the net erosion of W was determined by post-mortem analysis of bulk W lamellae with a Mo marker layer [638]. The combined analysis provided with good spatial resolution: (i) inter- and intra-ELM W source distribution (only OES), (ii) gross and net erosion of W, and (iii) the re-deposition factor of more than 95% [657]. Interpretative ERO modelling reproduced these observations and disentangled the net W erosion into inter- and intra-ELM phases, the poloidal distribution of W gross erosion and deposition along the OT plate as well as the leakage paths of W out of the divertor. At the inner strike-line on the vertical target leakage towards the apron occurs, whereas at the outer strike-line on the bulk-W plate W remains in the corner region. ERO revealed the importance of W self-sputtering in the source estimation with about 25% of the total W sputtering which cannot be studied experimentally. Moreover, ERO interpreted also the behaviour at the IT plate with $T_e = 7\,\mathrm{eV}$ and confirmed the absence of inter-ELM sputtering in the cold divertor and burn-through of energetic D and Be ions in the intra-ELM phase overcoming the impact energy sputtering threshold.

Most recent JET simulations are global ERO2.0 simulations for different ELMy H-mode plasmas with inter- and intra-ELM phases by adaptation of transport coefficients in the background plasmas associated with the pedestal drop during an ELM crash and expulsion of highly energetic D as well as Be ions [666]. The key observations of the initial ERO simulations could be reproduced, but additionally the role of charge-exchange neutrals during the inter- and intra-ELM phase has been identified to be critical at the upper part of the outer divertor [666] and on the main chamber [742]. Further studies are required to quantify the impact of this far-SOL W source in the W leakage and W plasma contamination.

6.5.2. Specific experimental and modelling contributions from AUG. On AUG, material migration has been addressed both via dedicated experiments using its divertor manipulator system [743–745], allowing exposure of marker samples at the LFS (outer) strike-point region of the torus, and via analysis of marker tiles removed from the torus after completing an experimental campaign [746, 747]. Data is available from both D and He plasmas, performed in various L- and H-mode scenarios, as well as for different geometries, materials, and surface roughnesses of the marker samples or tiles. The erosion profiles of the markers and the migration patterns of light (C, N, B) and heavy (W and its proxies) elements, both globally and locally, have been extensively modelled using ERO/ERO2.0, DIVIMP, WallDYN and ASCOT [670, 748, 749]. At the divertor, combination of spectroscopic and PM data indicate net-erosion rates of W to remain below $0.1\,\mathrm{nm\,s^{-1}}$, excluding the exact strike-point areas. Re-deposition is generally >90% and even in low-density plasma scenarios, it can reach values of 50%–60% [744]. Erosion of W PFCs is also strongly dependent on local plasma conditions and transients impinging on them, which is evidenced by W sputtering in H-mode to exceed the corresponding L-mode values by 1–2 orders of magnitude [619]. Net erosion, however, is not amplified that strongly. The main contribution on W erosion in H-mode comes from intra-ELM sputtering, except in clearly attached plasmas with high electron temperatures when comparable inter- and intra-ELM erosion of W could be measured [653].

Main-chamber erosion of W remains at low levels, based on data integrated over full-length experimental campaigns. In most regions, the determined erosion rates are 1–2 orders of magnitude lower than the corresponding divertor values except for specific LIM structures at the outboard mid-plane [747]. Here, W erosion may become equally noticeable as in the divertor, but with stronger impact on the W core concentration due to poorer screening, and thus contribute strongly to the observed erosion-deposition patterns everywhere in the tokamak. In the global scale, distinct 3D migration patterns have been observed to be formed particularly on protruding surface features in the main chamber. Modelling, for its part, has revealed that besides the local plasma conditions and surface morphology, material migration on AUG is largely governed by flows in the SOL plasma, successive erosion and re-deposition steps, but also in the case of light elements by the chemistry of the surface, leading to enhanced re-erosion [670].

Surface morphology contributes significantly to the balance between gross and net erosion of W as one can see in figure 59. At the divertor, increasing the roughness by an order of magnitude (in terms of the mean arithmetic roughness: Ra) results in the reduction of net W erosion by a factor of 5–10 [619, 744, 745]. Simultaneously, thicker co-deposited layers are formed on the surface. Noticeable, however, is that in H-mode the conclusions are not that clear than in more benign L-mode conditions due to possible competition between erosion and deposition throughout the affected area [745]. Even for gross erosion the picture changes qualitatively with roughness since

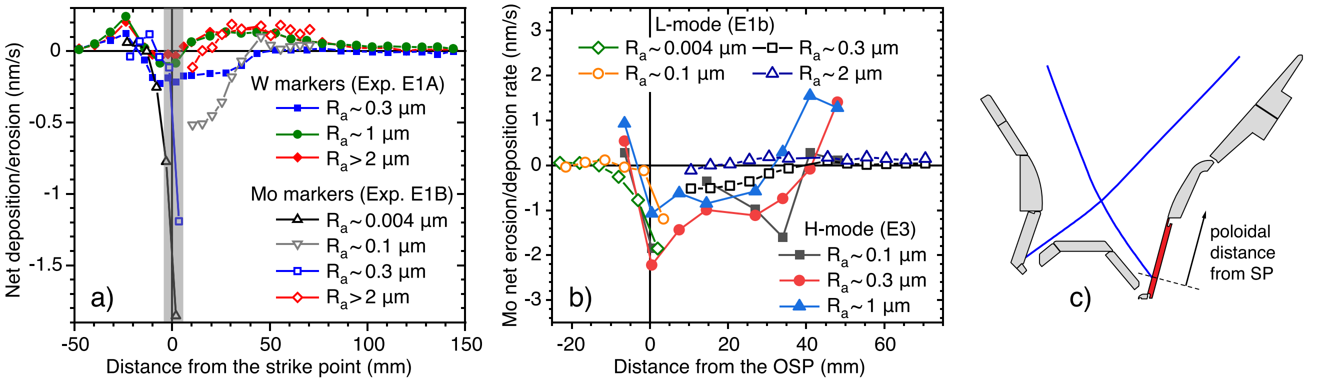

Figure 59. AUG: (*a*) poloidal net erosion/deposition (negative/positive values) of W and Mo marker coatings with different surface roughness exposed to deuterium L-mode plasmas in the outer strike-point region. Reproduced from [619]. The Author(s). CC BY 4.0. (*b*) Poloidal net erosion/deposition (negative/positive values) profiles for samples with different surface roughness, exposed in the outer strike-point region to both L- and H-mode plasmas. Reprinted from [745], Copyright (2022), with permission from Elsevier. (*c*) Illustration of the AUG divertor geometry and the position of the divertor-manipulator tiles in the experiments presented in [619].

sputtering preferentially starts to occur more and more at the tips of the surface peaks. Net erosion and deposition should thus be considered at the microscopic level.

6.5.3. Specific experimental and modelling contributions from WEST. Material migration was studied in the full-W environment of WEST (figure 53(*c*)). WEST operation was phased, with a full ITER grade W actively cooled divertor implemented in the second phase from the end of 2022. In the first phase reported here, the lower divertor was equipped with a mix of actively cooled W ITER grade PFUs and inertially cooled PFUs, made of W-coatings ($\simeq 10\,\mu$m) on a graphite substrate. Specific inertially cooled PFUs, the so called erosion marker tiles, were implemented on the lower divertor to assess material migration. These erosion markers feature an additional W layer (1–2 μm) and a thin Mo layer (100 nm) on top of the standard W coating. They were retrieved from WEST for PM analysis throughout phase 1, which included five experimental campaigns (C1 to C5): 2 tiles after the C3 campaign (7300 s of plasma exposure in D), 4 tiles after the C4 campaign, which ended with a He campaign (3000 s) after long exposure in D (9700 s), 2 tiles after the C5 campaign with 4600 s of plasma exposure in D. The heating power and pulse duration of the applied L-mode plasmas was progressively increased during phase 1, leading to a maximum surface temperature of the inertial PFU in the OSP area up to 500 °C for C3 and 900 °C for C4 and C5 [750]. Finally, boronisations were regularly carried out for vessel conditioning.

The analysis of visual range spectroscopic line emission in phase 1 of WEST operations revealed that the W sputtering in the divertor is dominated in L-mode conditions by residual light impurities such as O, B, C [668]. The main chamber W gross erosion sources, originating from the RF systems protection LIMs, the outer bumper, the upper divertor or the baffle (see figure 53(*c*)) were found to be generally lower in absolute magnitude compared to the divertor source, but not as strongly screened as the divertor sources [723, 751]. The contributions of the various W sources (divertor vs. main chamber) to the plasma core W contamination could be quantitatively investigated by global analysis of W migration across the WEST discharge data base using fully 3D SOLEDGE-ERO2.0 W transport simulations [671, 752, 753]. Post exposure analysis of divertor tiles equipped with erosion markers showed net erosion both at the inner and outer strike line areas with a more pronounced erosion zone at the OT. Deposited layers of several μm thickness were measured on the HFS [754], with a sharp transition between the erosion-dominated area around the inner strike line and the deposited layers. Thin deposition with a few 100 nm was found further away from the strike line area on both the inner and outer divertor surface. The radial extent of the net erosion area around the outer strike-line grew after C4 and also was shifted further out towards the LFS [754, 755]. The thick deposited layers on the HFS exhibit a complex morphology, with a stratified layout alternating locally with spherical or elongated structures. In the up to 30 μm thick layers found after the C5 campaign, significant fractions of B, C, and O were identified in addition to the PFU material tungsten [754, 756]. This is consistent with VIS range divertor spectroscopy, where B, C and O emission lines are generally observed during plasma operation. Finally, it should be noted that these deposited layers did not hamper operation under phase 1 plasma conditions, as no increase of layer delamination and ‘UFO’ related disruptions was observed. There are, however, concerns that deposited layers might become unstable with increasing thickness leading to transient impurity ingress due to delaminated flakes as discussed in [757, 758]. Indeed recent experiments in WEST [759], accumulating high plasma fluence by multiple plasma discharges in attached L-mode conditions, revealed layer formation and spallation of deposits by stress relief.

Based on PM analysis of the erosion marker tiles, a net campaign integrated erosion rate can be inferred for the SP area in the C3 campaign, with a lower range of 0.1 nm s^{-1}

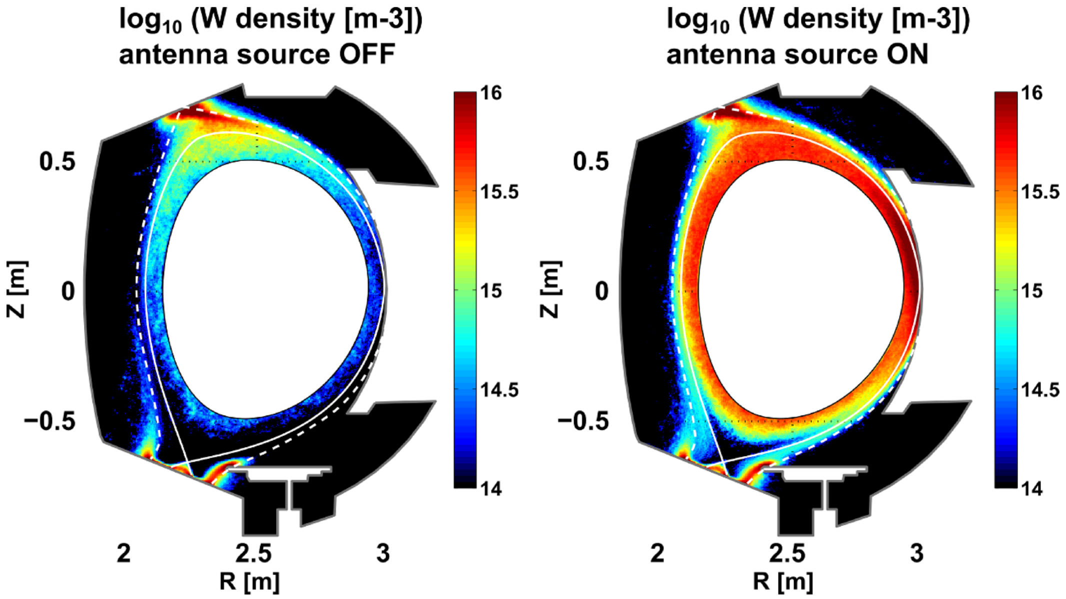

Figure 60. WEST: (*a*) SOLEDGE-ERO2.0 simulation with toroidally symmetric plasma without outboard W antenna limiters included in the model. (*b*) Full 3D SOLEDGE-ERO2,0 simulation with four discrete limiters made of W determining the W concentration in the plasma. Reprinted from [671], Copyright (2023), with permission from Elsevier.

up to 0.5 nm s^{-1} when taking into account the various experimental uncertainties [754]. In contrast, the campaign integrated growth rate of the thick deposited layers on the HFS is of the order of 1 nm s^{-1}. This can be compared with simulations of W migration in WEST using the ERO2.0 code [753], for conditions representative of an Ohmic plasma or an RF heated plasma, respectively. Preliminary modelling results indicate that the overall erosion-deposition pattern can be recovered (net erosion in the SP area, deposition elsewhere), but simulations cannot reproduce the experimental asymmetry with a strong deposition on the HFS, which might be related to flows not covered in the plasma background with SOLEDGE-EIRENE.

Modelling also tends to underestimate the net erosion rate, but it should be noted that results are very sensitive to the local W re-deposition fraction, which is higher than 95% and not considering surface roughness enhancements observed e.g. in AUG. The material migration path seems consistent with other tokamaks, namely strong main chamber W sources (FW, upper divertor, and RF antennas) and subsequent transport to the HFS where deposition is observed. Efforts are ongoing to better describe the WEST main chamber configuration in 3D with inclusion of LIMs [671]. The modulation of the magnetic field due to the ripple, which is with 8% significant in WEST, can further modulate heat and particle fluxes on the divertor but this is not yet taken into account. Figure 60 shows the W density maps computed by ERO2.0 for a non axisymmetric set up with toroidally localised LIMs on the LFS, using a 3D plasma background generated by the SOLEDGE code (simulation with fluid neutrals and a constant 3% O concentration). Two cases are compared: not taking into account the W sources from the discrete LIMs (a) and taking it into account (b). This results in significant differences in the computed W core contamination. Those preliminary simulations suggest that taking into account toroidally localised objects are required to accurately simulate W migration in WEST discharges.

6.5.4. Specific experimental and modelling contributions from EAST. Material erosion and migration with a ITER FW panel proxy was studied on EAST [632]. A specially designed test LIM with the ITER-like first-wall panel geometry was exposed to the boundary plasma in helium discharges by using the OMP Material and Plasma Evaluation System (MAPES). Net erosion and deposition patterns of the carbon-coated Mo plates on the LIM front surface were estimated using IBA. The Helium plasma was used to reduce the contribution of carbon chemical erosion. As shown in figure 61, no net deposition was found on the proxy wall element even in the shadowed regions. The erosion profiles from the 3D ERO simulations with magnetic shadowing model showed excellent agreements with the experimental data. No net deposition in the central magnetically shadowed area indicated that the CXN-induced erosion playing an important role in this experiment at EAST.

A high time resolution spectroscopy system has been developed in EAST to provide a real-time measurement of W erosion in the upper and lower W divertor installed in 2014 and 2021, respectively. Both Li and silicon (Si) are used for the wall conditioning in EAST, and experimental results reveal that compared to Si, Li coating is more effective on W source suppression [760]. Li aerosol injection into the upper divertor can dramatically reduce divertor W erosion by cooling the edge plasma. The intra-ELM W sputtering yields is found to have a positive correlation with the pedestal electron temperature as in the case of JET [657], and a negative correlation with the ELM frequency [761]. Unlike the results on DIII-D, W erosion mitigation is achieved by applying RMPs (RMP described in 5), and the mitigation effect on the outer divertor

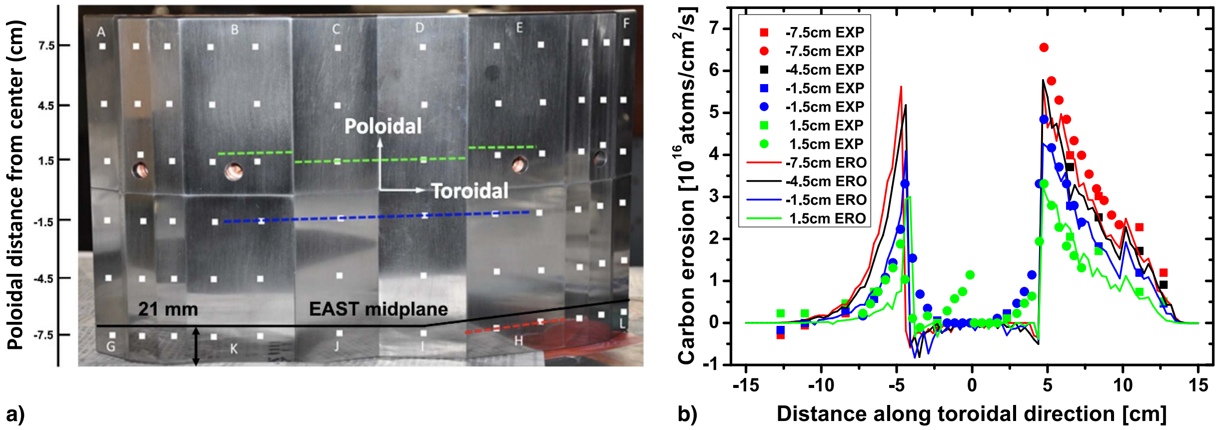

Figure 61. EAST: (*a*) photograph of the proxy for the ITER-like first-wall panel. (*b*) Experimental and modelled C net erosion profiles at different poloidal positions on the panel along the toroidal direction, as indicated by the dashed blue and green lines in (*a*). Reproduced from [632]. © 2015 IAEA, Vienna. All rights reserved.

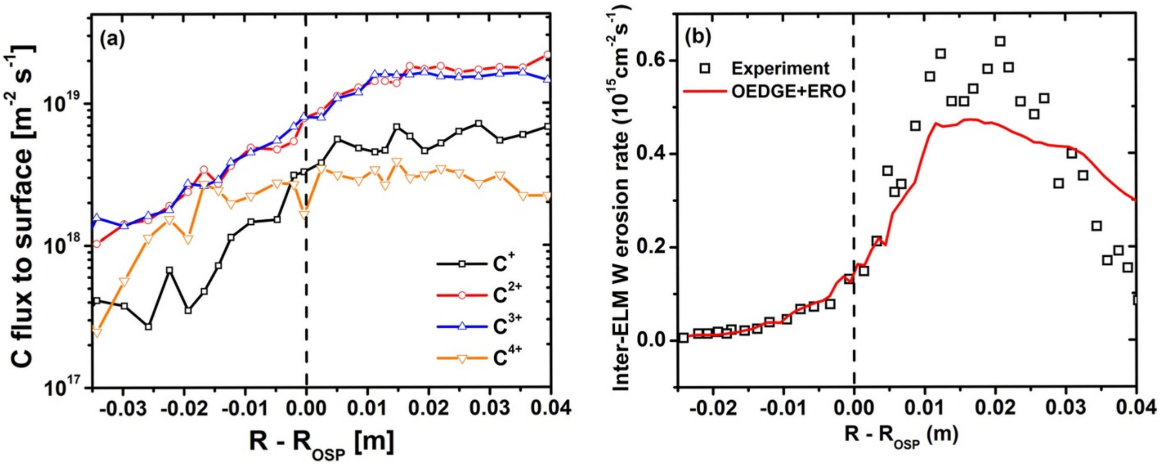

Figure 62. DIII-D: (*a*) OEDGE calculated carbon fluxes in different charge states as a function of radial position. (*b*) Spectroscopic measurements of the inter-ELM W erosion rate as a function of radial position in comparison with OEDGE and ERO modelling. Reproduced from [712]. © 2017 IAEA, Vienna. All rights reserved.

target is stronger than that on the IT. Simulation results of W erosion profiles from the ERO code agree well with the experimental data for EAST L-mode discharges [762]. Modelling results indicate that W erosion is mainly determined by the local C impurity concentration in the background plasma. The recycling C flux is proved to be non-negligible on the W erosion calculation.

6.5.5. Specific experimental and modelling contributions from DIII-D. By leveraging the divertor material evaluation system (DiMES), W samples with different sizes are exposed to the DIII-D plasma to evaluate the W gross erosion, net erosion, and re-deposition [763] as well as effective S/XB-values for W I at 400.9 nm [764]. Model validation to the dedicated experiments improved the understanding of erosion and re-deposition of high-Z materials in a mixed material environment [635, 712]. The W net erosion rate is significantly reduced compared to observations in JET and AUG due to the high local re-deposition probability and explained earlier in section 6.3.2. The local re-deposition is mainly controlled by the electric field and plasma density within the magnetic pre-sheath according to the applied interpretative modelling. Reducing the potential drop can increase the plasma density inside of the sheath, and thus the W re-deposition rate will not be reduced.

The role of background low-Z impurities in determining high-Z material erosion was also identified. Spectroscopically measured radial profiles of inter-ELM W erosion rates at DIII-D divertor were well reproduced by the ERO modelling taking into account charge-state-resolved C ion flux in the background plasma calculated using the OEDGE code (figure 62). Different methods, suggested by predictive modelling such as the application of local electric biasing and gas injection, successfully suppressed the high-Z material erosion in DIII-D experiments [712, 765].

A metal ring campaign [634] was carried out on DIII-D in 2016 to investigate W erosion and transport in a global scale. Two toroidally symmetric rings of W tiles were inserted in the lower outer divertor of DIII-D (figure 53(*d*)) with all other

PFCs remaining graphite. The inter-ELM W erosion profiles along the radial direction of the W ring can be well reproduced by OEDGE simulations with a carbon–tungsten (C–W) mixed material model [766]. Under the C–W mixed material environment, W erosion is mainly caused by the local recycled C flux, most of which is originated from the erosion of the C deposited temporarily on the W surface. The deposited C fraction on the W surface is proved to have a nonlinear effect on W erosion. A higher C surface fraction increases the C flux to the target and thus promotes W erosion, but the deposited C can act as a protection layer against W sputtering at the same time. With the use of isotopic W sources and a dual-faced collector probe, the W leakage ability from different divertor locations was studied [767]. The W leakage ability from the OSP location shows a positive correlation with power across the separatrix (P_{sep}), which is caused by the increase of the parallel ion temperature gradient force in the near-SOL region. Whereas for the far-SOL region, W leakage ability shows a negative correlation with P_{sep} and a positive correlation with the ELM size, indicating that the ELM plays a role in the W transport. The first experimental evidence of the near-separatrix W accumulation between the plasma top and the OMP was obtained from the collector probe data. DIVIMP-3DLIM code package simulations demonstrate that both the TF direction and the parallel ion temperature gradient force strongly affect the flow pattern in the SOL, and thus determine the existence of W crown accumulation [768].

Based on the ELM-resolved 400.9 nm W I spectroscopy during the MRC, intra-ELM W erosion was quantitatively analysed. The W erosion was found to be strongly reduced during the ELM mitigation phase by pellet pacing, but no reduction of W source is observed during the RMP application [769]. For typical type-I ELMs, a strong correlation between the intra-ELM W sputtering source and ELM frequency is observed. With the increase of the ELM frequency, the W sputtering source increases first and then rolls over at sufficiently high ELM frequency. At JET a similar behaviour was linked to the transition from type-I to type-III ELMy H-mode [707]. ELM transport characteristics were obtained by using an interpretive plasma FSM [375, 379] to fit the divertor ion saturation current and heat flux density for different flux tubes in the SOL [766]. Unlike the inter-ELM W erosion, the intra-ELM W erosion is dominated by both the energetic C^{6+} originated from the pedestal and the local recycling C^{2+}.

6.6. Conclusions for ITER operation in the Be/W plasma-facing material mix

The different experiments in metallic devices presented before have provided vital information about the global material migration process, thus the cycle of erosion, transport, and deposition. Moreover, dedicated benchmarking for the two key modelling tools for global PWI namely WallDYN and ERO2.0 for the current ITER material mix Be/W as well as for the full-W option for a potential future phase of operation was successfully done. Both codes complement each other and have been applied in different evolution stages, e.g. 2D to 3D in case of WallDYN or polished to rough surfaces in case of ERO2.0, to predict ITER steady-state plasma conditions covering the PFPO in H and He and the FPO in DT [4]. Key input for both codes are reliable plasma background simulations for the different operational phases in 2D or 3D as well as the exact FW geometry. The shape of the ITER FW evolved in the recent decade to ensure compatibility with the expected heat load pattern on the main chamber PFCs [53]. Moreover, the plasma backgrounds and the physics included evolved to gain accuracy in the prediction by inclusion of e.g. flows and drifts in the divertor [334]. However, none of the 2D plasma backgrounds were initially up to the FW limiting surface and also excluded *a priori* 3D shadowing and shaping effects, thus, individual plasma extrapolations for each case up to the FW and in toroidal direction are required. These extrapolations for the different envisaged plasmas in L- and H-mode at variable input power, magnetic field strength, plasma species, and outer divertor shoulder permit predictions beyond direct experimental extrapolation with the highest possible accuracy in order to map out the operational space and potential limitations in ITER.

6.6.1. ERO2.0 predictive simulations for ITER. As reported in [739, 770, 771], ERO2.0 has been used to predict steady-state Be FW erosion in ITER in different PFPO and FPO plasma conditions. The variations included the magnetic configuration, the far-SOL conditions (density, temperature, flow velocity), the power and fuel (H, He, DT) species, the cross-field diffusion and the impact angles of sputtering ions and neutrals. As input, the simulations used wide-grid plasma backgrounds provided by OEDGE [772], which in turn are based on SOLPS-4.3 modelling [490]. Note that as an approximation in both OEDGE/SOLPS and ERO2.0, the plasma in DT cases is approximated by a pure D plasma. Figure 63(*a*) shows the Be net flux (i.e. the Be gross deposition minus gross erosion) for two selected $Q = 10$ cases. The FW erosion is dominated by ion impact (in particular by Be impurities) in plasma-wetted areas. These constitute about 10% of the 760 m^2 FW area and they were obtained by numerical tracing of magnetic field lines with similar assumptions as used for power flux predictions with SMITER [773] and are in good agreement with the latter.

The impact of neutrals, in particular the highly energetic charge-exchange neutrals, leads to an additional erosion channel which amounts to roughly 1/3rd of the total Be source. However, this channel is characterised by low erosion fluxes covering the entire FW area, and is thus not relevant for FW armour lifetime which is limited by the erosion in wetted areas. The highest net erosion rate is found at the inner wall (panel 5) with 0.057 $\mathrm{mm\,h^{-1}}$ Be layer depletion, which is close to previous predictions by local LIM [774] and ERO modelling [693, 775]. It should be noted that the simulations were performed with an old magnetic equilibrium which assumed a wall contour that protrudes by 4 cm into the plasma at the HFS, thus it does not match the (correct) 3D wall geometry. Although this was mitigated by morphing the grid at the high-field side to match the correct wall contour, the erosion in that location is likely still overestimated.

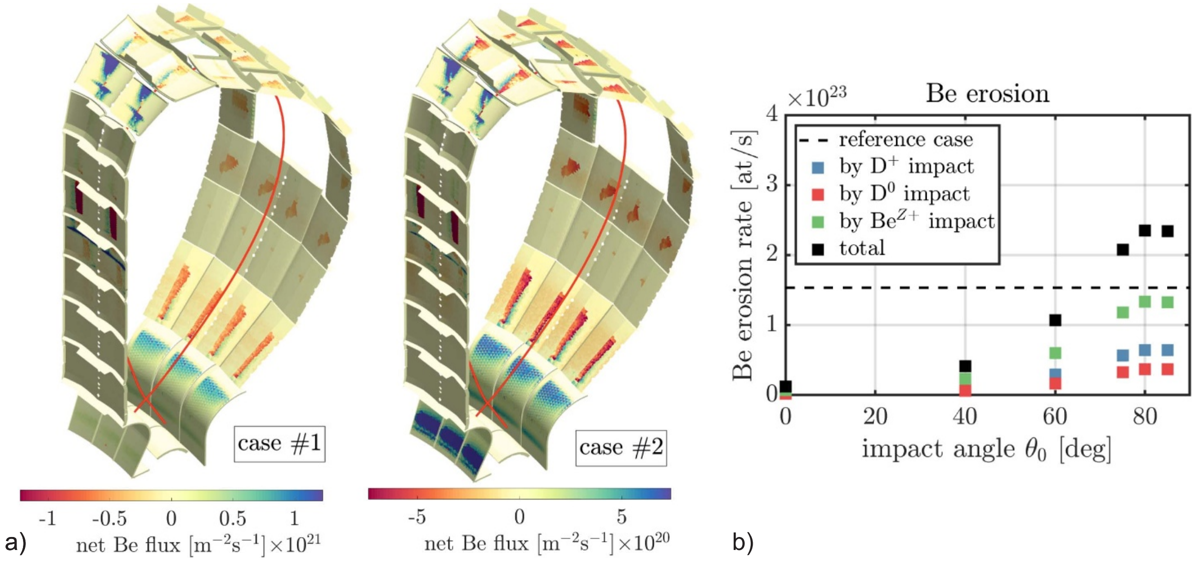

Figure 63. (*a*) ERO2.0 results for Be net erosion/deposition flux (positive: net deposition, negative: net erosion) in a $Q = 10$ ITER discharge. Two simulations are shown for different OEDGE plasma background: left (case #1): no imposed SOL flow, right (case #2): high imposed SOL flow of $M = 0.5$. For better visibility, each colour map is cropped at the 99th percentile of main chamber flux. (*b*) Variation of projectile impact angle for case #1 and resulting Be gross erosion rate (i.e. the gross erosion flux integrated over the FW area). Plot created by J. Romazanov from data presented in [739] (figure 1 therein). (a) and (b) Reproduced from [739]. © 2022 The Author(s). Published on behalf of IAEA by IOP Publishing Ltd. CC BY 4.0.

The major fraction of Be eroded from the FW is again redeposited on the FW, while a smaller fraction is deposited in the divertor. The ERO2.0 simulation results are highly sensitive on the assumptions concerning the background deuterium ion flow velocity used in the input OEDGE plasma backgrounds. ‘Case #1’ in figure 63(*a*) uses only source-sink driven flows and no drifts, resulting in a Be fraction of 10% depositing in the divertor. ‘Case #2’ uses an imposed SOL flow of $M = 0.5$ to study the effect of a very high flow, in this case the Be fraction in the divertor is doubled to 21% and leads to a higher deposition in the inner divertor, which is more in line with the findings at JET. The high SOL flow in case #2 also leads to a reduction of FW erosion, with a gross Be erosion rate (i.e. the gross erosion flux integrated over the FW area) of 1.1×10^{23} Be s^{-1}, compared to 1.5×10^{23} Be s^{-1} in case #1.

Part of the study was devoted to characterising the impact of modelling uncertainties on the prediction of the total Be source (using case #1 as reference). Variation of the anomalous diffusion coefficient for Be impurities in the range $D_\perp = 0.3$–$10\ \mathrm{m}^2\ \mathrm{s}^{-1}$ leads to a variation of the Be gross erosion rate in the range $(0.97$–$1.96) \times 10^{23}$ Be s^{-1}, due to the changes in the Be self-sputtering contribution. A slightly larger uncertainty is introduced by the radially outward extrapolation of plasma parameters between the OEDGE grid boundary and the shaped FW surfaces. Here, variation between a strong radial decay (with a constant decay length of $\lambda = 1$ mm) and radially constant plasma profiles $\lambda \rightarrow \infty$, corresponding to strong convective/turbulent transport) leads to a variation of the Be gross erosion rate in the range $(0.55$–$1.53) \times 10^{23}$ Be s^{-1}. Finally, the largest variation was found when varying the assumed impact angle of background D ions and neutrals within the range 0–85°, resulting in a variation of the Be gross erosion rate in the range $(0.13$–$2.35) \times 10^{23}$ Be s^{-1}, as shown in figure 63(*b*). For comparison, the reference case #1 erosion rate of 1.5×10^{23} Be s^{-1} is obtained with $D_\perp = 1\ \mathrm{m}^2\ \mathrm{s}^{-1}$, constant plasma extrapolation $\lambda \rightarrow \infty$ and the following assumptions for projectile impact angles: (1) ions have angular distributions numerically obtained from tracing their gyration through the sheath before impacting on a perfectly smooth surface, (2) CXN are assumed to impact along the local magnetic field angle, since they originate from ions following field lines before undergoing the charge-exchange process. Especially the latter assumptions on the impact angles are somewhat arbitrary. This can be improved in the future if angular distributions become available from the EIRENE code [647] and the influence of roughness on the distributions is accounted for using models such as [776].

6.6.2. *WallDYN predictive simulations for ITER.*

The WallDYN code is applied to ITER to make predictions on the location and growth rate of Be layers on the FW [732, 777]. The formation of these layers can potentially limit ITER operation since they can retain large amounts of the D/T fuel and form tritiated dust when they delaminate and disintegrate in the plasma. The formation of these layers is determined by the balance of the Be influx onto the wall from the plasma Γ_{in} and the source flux back into the plasma due to erosion and reflection: $\Gamma_{\mathrm{src}} = \Gamma_{\mathrm{ero}} + \Gamma_{\mathrm{refl}}$. Both the erosion and reflection flux depend on the local surface composition. Γ_{in} is determined by the plasma transport of Be atoms emitted by the sources Γ_{src} into the plasma. This leads to a coupling of the FW composition and Be influx on all plasma wetted surfaces throughout the ITER FW. At locations where $\Gamma_{\mathrm{in}} > \Gamma_{\mathrm{src}}$, Be layers are

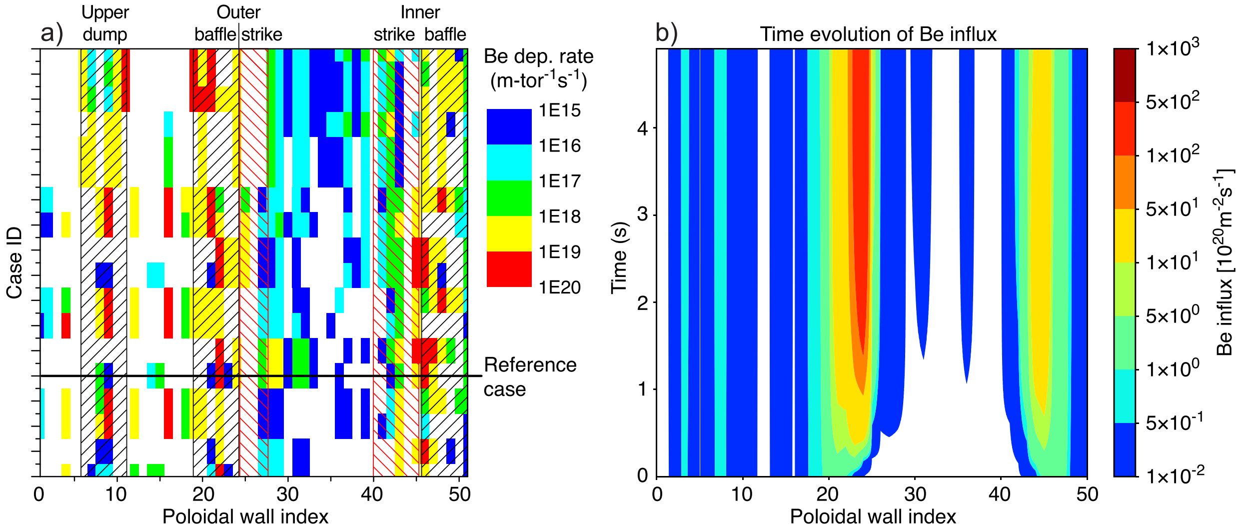

Figure 64. (*a*) Net Be layer growth rate for the different ITER background plasma assumptions vs poloidal wall index. See text for explanation of units. Plot re-created by K. Schmid from figure 3 in [778]. (*b*) Time evolution of the Be influx for a typical ITER background plasma case (taken from plot (*a*)). Plot created by K. Schmid from data published in [778]. (*a*) and (*b*) Reproduced from [778]. © 2015 EURATOM. All rights reserved.

formed, whereas for $\Gamma_{\text{in}} < \Gamma_{\text{src}}$, the Be FW is continuously eroded. This coupling is modelled in WallDYN, applying a dynamic FW composition model where the local impurity influx is coupled, by plasma transport, to the impurity source fluxes Γ_{src} from all wall areas.

Before applying WallDYN to ITER it was first benchmarked against Be layer formation results obtained from JET in the ITER-like wall configuration as shown in figure 57(*b*). The so validated code, was then applied to a large number of ITER background plasma scenarios, differing in input power, divertor density and far-SOL transport assumptions. The resulting migration matrices all look qualitatively similar, whereas the wall plasma parameters (D-fluxes, plasma temperatures) vary significantly and span a large range of possible operating scenarios. The resulting net Be layer growth rates for the different scenarios vs. poloidal wall index are shown in figure 64(*a*). The colour scale denotes the layer deposition rate per area ($\text{m}^{-2}\,\text{s}^{-1}$) integrated over the poloidal length of each wall tile, i.e. in units of m-tor^{-1} s^{-1} where m-tor^{-1} stands for *per meter in toroidal direction*.

While in figure 64(*a*) the details and absolute layer growth rates vary across the different background plasma scenarios, qualitatively most deposition takes place in the divertor, mainly at the baffles. In figure 64(*b*) the time evolution of the Be influx is shown vs. poloidal wall index location for a reference ITER case indicated in figure 64(*a*) by a horizontal line. The influx onto the inner (wall indices 40–50) and outer (wall indices 20–30) divertor W baffles, which initially at $t = 0$ have pure W surfaces, increases strongly and equilibrates after $\approx$3 s. Initially the only source of Be is the erosion of the main chamber Be wall, which is transported by the plasma into the divertor where it is partially deposited or reflected from the W surfaces. This continuous (re-)erosion and reflection results in Be recycling in the divertor and thus gives rise to new local Be sources. These new sources evolve over time and result in an increase of the Be influx locally in the divertor. This highlights the afore mentioned need for a wall dynamics model, that describes the surface modification by Be deposition and the resulting Be-sources due to re-erosion, to correctly describe the poloidal distribution of the Be influx. The details of the co-deposition of fuel resulting from the so calculated Be layer growth rates are summarised in sub-section 7.6.1.2 of section 7 HI inventory and recovery.

In [732] the Be FW was assumed to be perfectly toroidally symmetric whereas in reality it is a 3D shaped wall to avoid LEs as mentioned before. This shaping results in a large number of weakly plasma wetted surface areas which cannot be described by a 2D code but require a 3D version of WallDYN. In [779] the Be layer growth in ITER is revisited using EMC3-EIRENE [495] to derive the impurity migration matrices. When averaged over the toroidal direction the migration matrices in 2D and 3D look qualitatively the same. However, the full 3D WallDYN simulation for ITER with shaped Be wall predicts up to a factor 5 more deposition at the main chamber wall compared to the 2D calculation with a toroidally symmetric wall. The reason for this difference is that the 3D results include deposition in the recessed areas of the main chamber, which reduces the material available for deposition in the divertor since in both calculations the total Be source is comparable. Still this shift in the deposition location had no significant impact on the fuel retention, but might have impact on applicable fuel recovery schemes.

The dynamic surface model in WallDYN also includes self-sputtering by the impurities that return to their source wall location. If for a surface location a fraction γ of Γ_{src} returns back to it, then the influx Γ_{in} of the impurity in equilibrium can be derived from the equation

$$\Gamma_{\text{in}} = \gamma \times \left(\Gamma_{\text{in}} \times \left(Y^{\text{self}} + R^{\text{self}}\right) + \Gamma_{\text{BG}} \times Y^{\text{BG}}\right)$$

which yields

$$\Gamma_{\text{in}} = \frac{\gamma \times \Gamma_{\text{BG}} \times Y^{\text{BG}}}{1 - \left(\gamma \times \left(Y^{\text{self}} + R^{\text{self}}\right)\right)} \tag{13}$$

where $\Gamma_{\text{BG}} \times Y^{\text{BG}}$ represents the erosion flux due to impact of the main background (BG) plasma species and Y^{self} and R^{self} denote the self-sputtering and reflection yields, respectively.

When in the denominator of equation (13) the term $\gamma \times \left(Y^{\text{self}} + R^{\text{self}}\right)$ becomes close to unity, the influx and therefore also the source flux back into the plasma become infinite. This is commonly referred to as *run-away self-sputtering*. Since γ and R^{self} are both $\leqslant 1$, for this condition to be met the self-sputter yield has to be $Y^{\text{self}} > 1$. While this is not commonly the case for Be, for W the self-sputtering yield quickly reaches values >1 as a function of energy. In combination with oblique impact angles the problem becomes even more severe. Due to its large number of electrons, W quickly reaches charge states of $+5$ and higher in ITER, which for the high plasma temperatures at the wall results in strong sheath acceleration and thus W impact energies of several 100 eV. For instance from the SDTRIM.SP sputter yield database used by WallDYN, the W self-sputtering yield exceeds unity at $\approx$800 eV for impact along the surface normal and at $\approx$400 eV at 40° relative to the surface normal. At $q = +5$ the 400 eV threshold is reached for $T_{\text{e}} = T_{\text{i}} \approx 20$ eV, a condition readily met in the hot far SOL at the ITER divertor baffles. The occurrence of run away self-sputtering manifests itself in WallDYN in the form of negative values for Γ_{in}. As discussed in [778] run-away self-sputtering was encountered for some of the ITER background plasma scenarios where the distance between the primary and secondary separatrices was very small (4 cm). In these cases the far-SOL close to the wall becomes in the simulated plasma backgrounds very hot. It should be noted that to detect excessive W-self-sputtering without WallDYN's matrix based description of impurity migration, in a Monte-Carlo code like DIVIMP or ERO2.0 is computationally expensive. Since the self-sputtering flux builds up further and further with each generation of self-sputtered particles, many generations have to be followed. Finally, either an equilibrium influx is found or the self-sputtering run-away continues. Of course run-away self-sputtering cannot be observed experimentally since the strong impurity influx will lead to a radiative collapse.

6.6.3. Conclusions for ITER. A comprehensive set of simulations with ERO2.0 [739] and WallDYN [779] have been carried out to predict the expected ITER lifetime, the integrated material migration behaviour in steady-state conditions starting with PFPO-1 and currently ending with FPO-3. The aim of these simulations was to determine the scenario compatibility with regard to the initial wall erosion at the Be LIMs and at the W divertor target plates, the tritium inventory determined by co-deposition with Be in the divertor and main chamber and, finally, the Be dust formation. By combining both codes, a fully compatible path from the L-mode to the reference H-mode with $Q = 10$ at 15 MA has been identified, demonstrating the compatibility of PWIs for the Be/W material mix in the steady-state plasma scenarios of the different ITER operational phases. Uncertainty remains in the extrapolation of charge-exchange neutral fluxes and residual ion fluxes during the so-called shoulder formation, hence worst-case scenarios with high electron and ion temperatures in the SOL up to the apex of the shaped wall with $T_{\text{e}} = 20$ eV were included in the analysis. Certain H-mode scenarios with very low wall clearance and low distance between the primary and secondary separatrices have been identified as being incompatible with the specified lifetime of FW components and may only be used for a limited time. Moreover, the high re-deposition of Be in the main chamber requires more attention in areas beyond the material migration to properly understand e.g. fuel retention, wall conditioning and layer stability, as well as to interpret infrared diagnostic data.

However, the Be dust formation is not only a result of regular material erosion-deposition processes, but more governed by transients like disruptions or VDEs. These processes and their contribution to the dust formation are not included in the predictions and the assessment presented here. Secondary effects of damaged Be and W PFCs have also not been considered regarding enhanced erosion of e.g. LEs by melting or RE impact and require e.g. ERO2.0 simulations in the future which include the surface topology of damaged PFCs.

6.6.4. Outlook. Finally, a brief outlook to the remaining challenges in the global migration analysis, namely (a) the coverage of three-dimensional effects of the plasma, which are e.g. imposed to mitigate fast transients, and (b) the research needs associated with ITER operation with all-W PFCs as foreseen for the later phase of exploitation.

Although the application of RMP field is the preferred method to control the type-I ELMs in ITER, RMP can break the symmetry of the edge plasma and form a 3D helical plasma transport, which makes the associated PWI processes 3D. The impact of RMP on the W gross erosion for L-mode discharges has been investigated in DIII-D [780]. With the RMP applied, the SP splits into separatrix lobes and the plasma can impact the divertor target through the individual helical figure-like magnetic structures. The W gross erosion rate is found to be increased in the far-SOL and decreased in the private-flux region by several tens of percent compared to the case without RMP. Since the RMP can break the original flux surface, it can influence the pathway of W transport and therefore the W screening. EMC3-EIRENE has been used earlier to simulate the 3D divertor particle and heat flux footprints for ITER standard 15 MA $Q = 10$ H-mode plasmas with attached divertor [781] with RMP. A heat flux spreading is achieved by using the RMP and the corresponding peak heat flux density arriving on the divertor target is reduced by 30%. However, data from other devices is not fully consistent with the DIII-D observations and generally the impact of RMP on divertor W erosion and transport in ITER remains largely unknown. Additional work including model development and experimental verification on the 3D effects is therefore required.

ITER has the option to exchange the first-wall PFCs and change from Be towards W once the main scientific goals are achieved and routine plasma operation is established. The transformation would be in a single step like in JET from C to W, but now from Be to W. The experimental studies in full-W devices presented in this review are providing vital scientific input for such a transition, but modelling with the established tools ERO2.0 and WallDYN are required to predict the conditions and W source terms in the main chamber and divertor. Initial studies were carried out with ERO2.0 [782] by replacing in the code simply the PFM and keeping the plasma conditions for different FPO plasmas. Clearly, the FW erosion drops several orders of magnitude in comparison with a Be FW. However, significant W erosion at the FW which is dominated by charge-exchange neutrals and seeding impurity ions like Ar or Ne takes place and their impact on the W contamination needs to be critically assessed.

7. HI inventory and recovery

7.1. Introduction: fuel retention from carbon to metallic FW configurations

The influence of the plasma-facing materials on the in-vessel retention of hydrogen fuel isotopes (HI), i.e. D and T, has attracted particular attention since the first designs of ITER [783] because of the radiological safety issue related to tritium. For this reason, the T inventory in ITER is limited to 1 kg of mobilisable T in the vessel, of which 120 g corresponds to the maximum expected cryopump inventory. Taking into account the measurement uncertainty (estimated at 180 g), this limits the in-vessel T inventory to a limit of 700 g [784, 785]. Therefore, T retention in the vessel must be minimised to avoid the need for frequent, time-consuming cleaning procedures, but also to maximise the tritium breeding ratio, a key issue for future self-sufficient fusion plant operation. The choice of PFM remains the most important factor in keeping fuel retention at an acceptable level.

Due to its good thermo-mechanical properties and compatibility with high plasma performance, carbon was primarily used as a PFM in tokamaks until the early 2000s. However, large retained fuel fractions have been observed in all-carbon devices, particularly confirmed by the first experiments with a DT fuel mix in both JET and TFTR, which showed that prior to cleaning procedures or dedicated subsequent fuel removal campaigns, up to 40% (JET [786]) and 51% (TFTR [787]) of the injected T was retained in the vessel. Moreover, even after intensive cleaning campaigns, 16% (JET [788]) and 17% (TFTR [789]) of the injected T was still retained in the vessel. The main mechanism responsible for fuel retention in carbon devices has been identified as co-deposition of fuel with the eroded carbon, which cannot be suppressed as the carbon erosion source remains significant even at low plasma temperature due to chemical erosion (see for example the reviews in [790, 791]).

Extrapolation to ITER [624, 625], based on a nominal burning $Q = 10$ plasma of 400 s, shows that in an all-carbon wall configuration the T inventory limit would be reached after only 20–30 discharges. For the initial ITER choice of PFM (CFC on the divertor HHF area, W for the rest of the divertor and a Be FW), the retention was predicted to be lower and about 250 discharges would be possible. An additional gain of 10 was predicted if all CFC components were removed, allowing up to 20 000 discharges [778].

Encouraged by the success of AUG in operating a full W device including the divertor [792], the *JET programme in support of ITER* [793, 794] was established to investigate an all-metal ITER-like wall (JET-ILW) configuration. In addition to JET, also WEST [649] and EAST [795] have since made the transition from carbon to full metal PFC. For cross-sections of these devices, see figure 53 in section 6.

The first experiments carried out with AUG in its full W configuration and prior to any wall conditioning by boronisation, showed during the steady state plasma phase an equilibrium between D injection and exhaust within the error bars [796, 797], confirming a significant reduction in fuel retention during plasma operation compared to the carbon configuration [798]. Post-campaign analysis of the D content in removed divertor plates [799] confirmed that the transition to a full W machine without boronisation reduced the in-vessel D inventory by a factor of 5–10 compared to the carbon-dominated machine.

Experiments performed at the end of 2011 with the JET-ILW also showed a strong reduction of the long-term retention rate by a factor of 10–20, depending on the confinement regime, compared to JET-C [655, 800]. These results were confirmed by analysis of samples retrieved after the first two ILW campaigns [638, 801], which showed that the total deposition rate in the divertor decreased by a factor of 4–9 compared to the carbon deposition rate in JET-C.

Together with the unacceptable T retention rate predicted for a CFC divertor target, the encouraging AUG and JET results were key factors in the ITER decision to install a single full W divertor from Day 1 through the early nuclear phases [14].

Consequently, this section will focus on fuel retention and recovery for W and Be as PFMs, with carbon related processes only discussed for comparison. Section 7.2 describes the methods used to measure fuel retention in tokamaks. Section 7.3 gives an overview of the processes involved in fuel retention in W and Be. The main findings on fuel retention in metal PFC fusion devices are summarised in section 7.4 while section 7.5 deals with fuel recovery and wall conditioning methods. Finally, section 7.6 presents the state of the art of modelling tools in this field, before section 7.7 looks ahead to open questions and implications for ITER and future fusion devices.

7.2. Methods to quantify fuel retention

Gas balance and post-mortem analysis are complementary methods for assessing fuel retention in fusion devices. The former is a global measurement of how much fuel is retained, obtained by comparing the amount of fuel injected and exhausted on a per-discharge basis. It also provides information on the post-discharge outgassing phase in the time window between discharges (typically ∼10 min). The latter, based on the retrieval of wall samples after tokamak exposure for ex-situ analysis, is a local measurement that allows the amount and location of trapped fuel and the main retention processes to be identified. However, it reflects the local retention integrated over a complete experimental campaign, including many different plasma scenarios, but also conditioning phases, disruptions and long duration outgassing phases (overnight, weekend, etc over months of operation).

7.2.1. Gas balance procedures. Gas balance analysis [790, 798] is based on the measurement of injected and pumped particle fluxes during and between plasma discharges. The particle balance can be described as:

$$\int_0^t Q_{\text{Gas}}\,\mathrm{d}t + \int_0^t Q_{\text{NBI}}\,\mathrm{d}t + \int_0^t Q_{\text{Pellet}}\,\mathrm{d}t = N_{\text{e}} + \int_0^t \Phi_{\text{p,Vessel}}\,\mathrm{d}t + \int_0^t \Phi_{\text{p,Divertor}}\,\mathrm{d}t + N_{\text{Wall}} \quad (14)$$

where Q_{Gas}, Q_{NBI} and Q_{Pellet} are the particle injection rates associated with gas feed, NBI and pellet injection respectively, N_{e} is the plasma particle content, $\Phi_{\text{p,Vessel}}$ is the particle flux pumped by the vessel pumping systems (turbo pumps, neutral beam boxes and/or diagnostics), $\Phi_{\text{p,Divertor}}$ is the particle flux exhausted by the divertor pumps and N_{Wall} is the number of particles trapped or released by the wall.

Particle balance has been shown to be a reliable method for retention analysis of specific plasma scenarios typically with discharge durations from ≈10 s to 6 min [655, 791, 798, 802].

The particle balance studies have revealed characteristic regimes of retention, identified as *dynamic* or *short-term* retention and *long-term* retention. Dynamic retention is attributed to the ability of the exposed material to store fuel, even when saturated, under large particle fluxes. It acts as a pump in the early stages of a discharge and contributes to plasma density control. The retained inventory is released by neutral outgassing after the discharge. Long-term retention is related to other processes, such as co-deposition, and corresponds to trapped fuel that is not released after the discharge.

The respective contributions of short and long term retention can be separated during a plasma discharge when both the discharge and the vessel wall have reached a steady state regime. This typically requires long discharges performed in actively cooled devices, where the surface temperature of the PFCs remains constant, resulting in a constant outgassing flux over the entire discharge duration [655, 790, 791, 796–798, 800, 802].

For longer timescales of the order of a day(s) and/or for devices without dedicated diagnostics, dedicated particle balance discharges are not routinely used. In fact, assuming that the pumping rate is well known/calibrated, the accuracy of the exhausted flux based on neutral pressure measurements can lead to significant errors when integrated over days or weeks. Under these conditions, an *integral gas balance* can be performed by collecting the gas pumped by the divertor (accumulated during the experiments/sessions/days or regenerated when cryopumps are used) in a calibrated volume. The amount of gas collected corresponds to all the particles pumped during the plasma operation and also to the gas released by outgassing between pulses. This is a routine procedure in JET [786, 791], which has been used in particular for the quantification of fuel retention with the JET-ILW [655]. It should be noted that gas balance measurements rely on very careful and regular calibration. This is particularly the case with the integral method, because the fuel retention is in the range of only a few percent of the injected flux and is derived from the tiny difference between the large quantities of the total amount of injected and recovered particles. In this context, on AUG, the gas inlet and pumping systems have been recalibrated [796], achieving an accuracy of ≈3%, mainly dominated by uncertainties of the gas temperature. At JET-ILW, dedicated sessions for the calibration of the collected gas volume, using JET's AGHS, provided an accuracy in the range of 1% [655].

7.2.2. Post-exposure ex-situ analysis of retrieved components. Complementing the gas balance measurements, which provide a global retention value for the entire vessel, the contribution of the different PFC regions to the overall retention is assessed by analysis of samples taken from PFCs during shutdowns following experimental campaigns. Such *PM* analysis only provides campaign integrated data and therefore cannot be linked to a specific plasma scenario.

A number of techniques are used for near surface analysis of samples, such as IBA (see [803] for further details) or imaging plate techniques for detecting the local distribution of T retention [804]. Depending on the technique used, these methods can probe different depths in the sample, from a few nm to μm, and can detect different materials with some being especially suitable for light or heavy elements, respectively. By their combination it is possible to obtain a detailed picture of the fuel content in the sample, the surface material composition and the material morphology resulting from plasma exposure.

It should be noted, however, that material samples are generally exposed to air during retrieval and storage (from a few days up to months) prior to their analysis, which can further complicate the interpretation of the measurements. This point is discussed in [803] particularly for IBA measurements. It is concluded that the main effects of sample exposure to the ambient atmosphere are related to: (1) isotopic exchange of deuterium or tritium by hydrogen from water vapour present in humid air and (2) reaction of oxygen with surfaces.

In contrast to the generally non-destructive IBA methods, in TDS the samples are heated while measuring the rate of the different species desorbed as a function of temperature [805]. The measured TDS spectra allow to determine the amount of released species but also include information on the energy of their respective trapping sites in the material. In contrast to the IBA methods, such as the mainly used NRA, which probes only the first few microns depth below the sample surface, TDS provides information on the whole sample volume, provided the maximum temperature was sufficient to fully desorb all trapped species. Hence, fuel retention values measured by NRA are generally smaller than those from TDS measurements.

7.2.3. Laser-based in-situ surface diagnostics. To overcome the limitation of the integral in-situ gas balance measurements, a number of laser based methods were developed for local in-situ measurements of the composition and particularly the HI retention on PFCs in between plasma discharges without breaking the vessel vacuum. The basis for these methods is a laser of sufficient power to heat up or ablate small spots on PFCs. It is generally combined with a steerable optics to access specific locations. LIBS detects spectral line emission from ablated material while LID detects species desorbed from the heated laser spot by QMS of the in-vessel atmosphere (LID-QMS). For details on both methods see e.g. [806]. A LID-QMS system was recently installed and commissioned at JET for measurements in and after the DTE3 campaign [805, 807] and will also be used for further studies during the JET clean-up and decommissioning campaigns.

7.2.4. Comparison of principal results obtained by the various methods. To be representative, post-campaign sample analysis requires the analysis of a large number of specimens from the various components in the vessel, both from plasma wetted surfaces as well as from remote areas, including collected dust particles. However, it turned out that fuel retention determined by gas balance is generally by a factor of 10–20 higher than that determined by PM analysis [791]. Moreover, although the total fuel retention in devices with metallic PFCs decreased by a factor of 10–20 compared to carbon PFCs [655, 796, 797], the retention determined by gas balance was always 10–20 times higher than that estimated by analysis of retrieved samples [638, 808–810]. However, even with the absolute retention fractions from both methods differing by more than an order of magnitude, the results of the two methods are still consistent, showing the same decrease of fuel retention for devices with metallic PFC compared to those with carbon PFC.

7.3. Main processes involved in the formation of H inventories in W and Be

The retention of HIs in the FW and divertor of ITER is driven by two different processes. Firstly, the impact of energetic HI leads to implantation in the PFM, followed by diffusion to and trapping in defects in the bulk material [811] (see 7.3.1). This process is limited by the diffusion into the bulk so that the inventory of HIs evolves $\propto t^{1/2}$. Secondly, for wall materials with a high erosion yield (i.e. Be or C), the redeposition of eroded material together with HIs (co-deposition) leads to the formation of HI-containing layers that grow continuously [812] (see 7.3.2). These layers may break and detach from the surface above a certain thickness, forming HI-containing dust that can accumulate at remote locations, further contributing to the in-vessel HI inventory (see 7.3.3). For both mechanisms the uptake of HIs is determined by the local growth rate of the HI-containing layers and thus the HI inventory increases continuously with time. The amount of HI that can be retained by either process is limited by the number of HI sites and their equilibrium occupancy at the local temperature.

7.3.1. Bulk retention by implantation, diffusion and trapping. For implantation, diffusion and trapping, HIs are trapped at lattice imperfections. The HI solubility in W and Be is very low, but the HI concentration in these materials under plasma irradiation can still be significant, exceeding 1%, due to the presence of intrinsic and induced defects such as displacement damage from fusion neutrons or He from decay of activated isotopes. Therefore, bulk retention of HI in PFCs can potentially become an issue if a high trap concentration develops throughout the volume of the PFC. However, HI diffusion is greatly reduced at high trap concentrations and the operating time required to fill all the traps is correspondingly increased.

7.3.1.1. Bulk retention in tungsten—trapping sites including neutron damage. Since ITER will operate with much larger ion and neutron fluxes to the PFCs compared to all existing tokamaks, laboratory experiments and theoretical analyses are very important for correct predictions of the T retention. HI retention in W has been intensively studied over the last decades and most of the key results are reviewed in [813]. In particular, the HI interaction with different types of lattice defects has been analysed. Tungsten materials always have a certain amount of intrinsic defects. Their concentration depends on the manufacturing process and the initial heat treatment of the material. Polycrystalline tungsten can have more than 0.01 at.% of trap sites even after high temperature annealing, but most traps (dislocations, grain boundaries, etc) have a relatively low binding energy below 1 eV [814].

Plasma irradiation, even with low energy ions ($<$100 eV), produces an increased concentration of defects in a limited subsurface layer, which can be much larger than the implantation range, up to several microns [815]. This is possible due to extreme stresses caused by HI concentrations exceeding the solubility value by orders of magnitude. Under these conditions, blister-like structures can form on the surface. The most intense blistering was found for temperatures around 500 K, correlating with the highest D retention of $\approx 10^{22}$ m^{-2} for an incident fluence of 10^{27} m^{-2} [815]. Above 700 K no blisters were formed and the D retention decreased accordingly. Helium seeding of the D plasma also prevented blistering and resulted in reduced total D retention at elevated temperatures (400–700 K). A more detailed discussion of this process can be found in [813].

Irradiation by 14 MeV neutrons produces defects (vacancies, interstitials, dislocation loops, etc) with rather high binding energies in all PFC materials and thus will be the main source of trap sites for HI in the case of DT plasma operation. Intensive investigations have been carried out to characterise such radiation damage and the binding energies of HI with expected defects. The characteristics of the trapping sites are usually derived from TDS data or from theoretical approaches. However, most of these experiments have used ion irradiation as proxy and results from experiments using neutron irradiation of W are still very limited. Neutron irradiation to 0.01–1 dpa in the High Flux Isotope Reactor (HFIR) at Oak Ridge National Laboratory resulted in a significant increase in HI retention in W [816]. The near surface D concentration increased with decreasing plasma exposure temperature, reaching a value of ~1 at.% at 200 °C after irradiation to 0.3 dpa, an order of magnitude above typical values for non-irradiated W. After exposure at 760 °C, the D concentration was $\sim10^{-2}$ at.% at 0.1 dpa. The TDS measurements for neutron-irradiated W showed broad peaks extending from the plasma exposure temperature to 1000 °C [817] corresponding to a trapping energy of 1.4–2 eV [817]. This range is consistent with many experimental data obtained for ion-induced traps in W, for example with data on D trapping in W damaged by MeV W ions [818], which, as noted above, is used as a proxy for the characteristic displacement damage pattern created by the 14 MeV fusion neutrons. A similarly high concentration of traps can be expected in ITER, since the damage level at the end of operation will reach 0.54 dpa [819].

The most energetic traps are usually attributed to vacancy clusters and voids. Large vacancy clusters consisting of about 40 vacancies have also been detected after neutron irradiation in the HFIR at 300 °C, with an accumulated 0.3 dpa and D trapping in these vacancy clusters confirmed by positron annihilation spectroscopy [820].

7.3.1.2. Bulk retention in tungsten—filling rates of trapping sites. The filling of trapping sites in the bulk is a diffusive process and its rate depends on the incident flux and energy of the ions, temperature and material properties. A detailed analysis of the HI filling process in W is given in [821]. In particular, based on a set of experimental data and modelling, it has been shown that the steady-state HI concentration in the traps increases with the increase of the incident flux and the energy of the ions.

The penetration depth and total HI retention typically grow as the square root of the fluence. Such a dependence was observed, for example, for polycrystalline W elements exposed in the divertor of the ASDEX-Upgrade tokamak [822]. These results were in good agreement with the extrapolation from laboratory experiments. The square root dependence was also observed for the D retention in neutron-irradiated W after plasma exposure at 300 °C–500 °C [823]. According to modelling of experiments with neutron-irradiated W [824], the penetration depth is in the range of 50–100 μm after plasma exposure for 10^4 s at a temperature of 500 °C and a flux of (5–7) $\times 10^{21}$ $\mathrm{m}^{-2}\,\mathrm{s}^{-1}$.

The presence of impurities in the incident flux to the wall can significantly modify the morphology and composition of the PFC on and below the surface. This can create additional trapping sites in the subsurface region and influence the HI diffusion flux into the bulk and hence the overall HI bulk retention.

The effect of He impurities on HI retention in W is generally benign. Although at low fluence He induced defects in the surface layer can increase the HI retention, in the He saturated layer it decreases significantly [825]. HI diffusion into the bulk also decreases significantly. In D-ion driven permeation experiments an up to ten-fold decrease was observed in the case of He seeding [826]. A reduced D retention in the case of He seeding was also found in high fluence plasma experiments for temperatures in the range of 400–700 K in [815, 827]. The mechanism is not entirely clear, but it has been suggested that He bubbles may form interconnected channels increasing HI transport towards the front surface, and thereby causing a reduced HI flux into the bulk. In [828] the influence of He on D trapping and transport was investigated by implanting He deep into the bulk to avoid the influence of these surface effects. It was shown that He implantation creates additional trap sites even in self-damaged W, but the presence of He does not affect the propagation of the D diffusion front beyond what is expected from diffusion trapping theory: Once the He generated traps are filled, the He does not further affect the D transport.

Simultaneous irradiation of W with D and Ne (Ne/D = 2.5%) in ion beam experiments also showed a reduced D retention in the temperature range of 300–700 K [829]. The mechanism of this behaviour is not yet clear, but it is thought that implanted Ne atoms create some stress in the subsurface layer and influence the diffusion process. In [830], the D ion-driven permeation flux through tungsten also decreased in the temperature range of 500–1000 K in the case of Ne seeding. Finally, a reduction of D retention by a factor of four in the case of Ne seeding was observed in high flux plasma irradiation experiments at the Pilot-PSI facility [831].

In contrast to He and Ne, the presence of C and N impurities in the incident flux can increase D bulk retention. For N seeded plasmas this was demonstrated in [832]. For a systematic study of the influence of He, Ne, Ar and N seeding on the deuterium retention in tungsten in the linear plasma devices PSI-2 and PISCES-A see [833].

Apart from HI-retention, also the permeation of HI through W is affected by the presence of impurities. In [826], the addition of carbon as an impurity increased the D ion-driven permeation flux through tungsten up to 200 times compared to pure D experiments. In similar experiments with nitrogen [834], the ion-driven permeation flux was increased by a factor of 20. In both cases the increase was attributed to changes of diffusivity and recombination rate in the subsurface layer.

The currently available data suggest that T permeation through the W bulk material into the coolant system is not expected to be a serious problem for ITER, although recent predictive studies [835] indicate that the potential consequences for future fusion reactor operation at much longer run times could be significant. In this context, an additional problem may arise from the gaps between adjacent MBs in the poloidal direction and the possibility of direct penetration into the coolant tubes in the gaps. It has been shown experimentally [836] that direct HI penetration into the coolant tubes in the gaps can significantly exceed the absorption flux from the working gas due to the generation of hot HI atoms in the plasma discharge.

7.3.1.3. Bulk retention in beryllium. The number of experiments investigating HI retention in Be is small. A comprehensive review of experimental data from ion and plasma irradiation experiments over a wide range of temperatures, ion energies and fluences has been published by Anderl *et al* [837]. The HI retention in Be showed a maximum at room temperature and decreased with increasing temperature. It was concluded that the HI retention under ITER relevant conditions ($\Gamma_{\mathrm{HI}} > 10^{20}\,\mathrm{m}^{-2}\,\mathrm{s}^{-1}$, $E > 100\,\mathrm{eV}$) saturates at about $10^{21}\,\mathrm{m}^{-2}$. The saturation was attributed to a strongly increased outflow of implanted plasma ions and atoms to the surface due to bubble formation in the subsurface layer and the resulting increasing porosity.

The T retention in the bulk of Be PFC is therefore expected to be a small contribution to the total inventory in ITER. In recent experiments at the linear plasma facility PISCES-B, Be samples were exposed to pure D and He seeded D plasma up to D fluence of $2 \times 10^{27}\,\mathrm{m}^{-2}$ [838]. More classical dependencies, similar to those for W, were observed for pure D irradiation. D retention increased with D ion energy and fluence. The maximum D retention was up to $2 \times 10^{22}\,\mathrm{m}^{-2}$ for irradiation at 330 K and decreased by two orders of magnitude at 650 K. Helium seeding reduced D retention for exposure temperatures below 473 K and saturation was observed at about $10^{21}\,\mathrm{m}^{-2}$. At higher temperatures (>650 K) the effect of He was negligible.

In summary, although the bulk HI retention in Be could be slightly higher than concluded in [837], it is still not expected to be a major mechanism of T retention in ITER.

7.3.2. Retention by co-deposition. With co-deposition, the HIs are retained at trap sites or chemical bonds in the amorphous co-deposits up to a certain HI/X ratio, where X is the primary redepositing impurity, i.e. Be in ITER with a Be FW [812]. The HI/Be ratio depends on the local temperature T (K), the HI incidence energy E_{HI} (eV) and the layer growth rate r_d ($\mathrm{m}^{-2}\,\mathrm{s}^{-1}$). The resulting retention rate Γ_{ret} ($\mathrm{m}^{-2}\,\mathrm{s}^{-1}$) is given by $\Gamma_{\mathrm{ret}} = \mathrm{HI}/\mathrm{Be}(T, E_{\mathrm{HI}}, r_d) \times r_d$. To make predictions for future devices, the necessary input parameters must be obtained from modelling: edge plasma simulations [839] provide particle energies E_{HI} and power fluxes from which the wall temperature T can be calculated using thermo-mechanical simulations [840]. The determination of the layer growth rate r_d requires coupled surface evolution and plasma transport simulations as discussed in section 7.6.

The parametrisation of the co-deposition fraction as $\mathrm{HI}/\mathrm{X}(T, E_{\mathrm{HI}}, r_d)$ for a given impurity species X, originally developed for Be [812], has since been extended to co-deposition with W [841–843] and C [844]). Co-deposition of D with W was found to be 1–2 orders of magnitude lower than co-deposition with Be. From this result and the lower erosion rate of W, it was concluded that HI retention by co-deposition with W can be neglected in the presence of large amounts of Be. However, with the recent plans to remove Be as PFM from ITER, these results have become essential for the evaluation of fuel retention by co-deposition with W alone.

A limitation of the original scaling law in [812] was that the accessible parameter values for T, E_{HI} and r_d did not cover the range of these parameters expected in ITER. In a subsequent study [845], co-deposited layers were produced on a biased target in a magnetron sputtering device with a Be cathode, which provides higher bias voltages and deposition rates. In addition to confirming the validity of the scaling law from [812] over a wider parameter range, the results in [845] also suggest that the HI/Be dependence on E_{HI} varies strongly with ambient gas pressure D_2: At low pressures (≈0.3 Pa) no energy dependence was seen and only at higher pressures of ≈1 Pa did it appear. This was attributed to the emergence of a low temperature (450 K) HI binding state (≡T0-state) at high D_2 pressure with a pronounced dependence of HI retention on E_{HI}. This pressure dependence of Be co-deposition was further investigated in [846].

In [847] all available data were re-fitted to the original scaling function. A comparison with the original scaling parameters in [812] showed a much weaker dependence on E_{HI} when the data from [845] were included. This was mainly attributed to the weaker dependence on E_{HI} associated with the pressure dependent low temperature T0-state in the data from [845]. Therefore, an extended pressure-dependent HI/Be scaling law has been proposed in [847] which takes into account the pressure, temperature and energy dependence of the T0-state. For pressures $\geqslant 0.135$ Pa and temperatures $\leqslant 470$ K, the T0 state contributes to the HI/Be scaling law with a strong dependence on E_{HI}. However, most of the deposition sites in ITER are predicted to be outside this parameter range, resulting in a weak energy dependence of Be co-deposition in ITER. This has implications for current predictions [732] based on the original scaling in [812], which yielded HI/Be values larger in ITER than in JET-ILW due to the higher average particle energies. Therefore, a weaker dependence on E_{HI} leads to lower retention by Be co-deposition in ITER.

In both JET-ILW and ITER, W is also eroded and contributes to the co-deposited layers, although at a small fraction due to the lower W erosion rate compared to that of Be. In [848] the co-deposition of D with Be and W was studied using the same setup as in [845]. The W concentration (4.4–28.4 at.%) and the D_2 pressure (0.8–8 Pa) were varied at a constant temperature of 373 K. At low W concentrations, the same pressure dependence of D/Be as in [845] was found, but it disappeared at W concentrations $\geqslant 10$ at.%. Overall, D retention initially increased with W concentration up to 10 at.% and then decreased. This was attributed to the formation of additional low temperature trap sites, which are not expected to contribute much to D retention at deposition temperatures above 450 K. Consequently, the admixture of W to the Be layers formed in ITER is expected to further reduce the HI retention.

7.3.3. Contribution of dust to fuel retention. There are two main sources of dust formation in tokamaks. Re-deposited layers can delaminate due to internal stress or transient thermal loads and form so-called flakes. In addition, transient high energy deposition, e.g. due to disruptions, arcing, VDEs, ELMs or REs, can cause melting of metallic PFMs with splashing and droplet formation. Both flakes and agglomerations of emitted droplets often have a corrugated surface with a large effective area [849], which can provide an additional mechanism for fuel retention by adsorption. In [850], T sorption by tokamak relevant W particles at 743 K was analysed and found to be linearly dependent on the specific surface area.

In addition to the previous mechanisms, the growth of *fuzz* fibre-structures on W surfaces exposed to He containing plasmas (see 8.2.2.2 in section 8) can contribute to dust formation by fibres breaking off from the surface. The W fibres contain He bubbles, which are trapping sites for HI. However, experiments showed only a moderate concentration of HI in the fuzzy layer and a gradual erosion of the fibres even at pulsed high heat loads [851], so their effect on the overall HI inventory is negligible.

In summary, dust formation does not appear to be critical with respect to the retained fuel inventory in ITER. However, its contribution could become significant in future fusion reactors with much longer operating times.

7.4. Main findings in fusion devices with metallic PFC

7.4.1. Results from gas balance analysis. The first gas balance experiments in a full metallic PFC configuration were performed in AUG after the final removal of all carbon tiles. With full W-PFC coverage, particle flux analysis shows saturation of the retention during the steady state phase of a standard H-mode discharge [796, 797], as shown in figure 65 [797]. Although these experiments were performed with inertially cooled PFCs with potential outgassing at high temperatures, the equilibrium between total gas input (gas feed and NBI injection at a rate of 2.75×10^{22} s^{-1}) and exhaust was reached after ≈2 s in the high power phase. Based on the calibrated gas input and exhaust measurements, the retention rate during this phase is in the range of $(1.5 \pm 3.2)\%$ [796]. The balance between gas feed and exhaust is a clear signature of greatly reduced retention due to co-deposition in the W device, although there were still residual traces of carbon in the plasma. It is worth noting that no boronisation was performed prior to this series of experiments to avoid a possible contribution of boron to the retention.

In JET-ILW, dedicated fuel retention experiments were performed for different plasma conditions (L-mode and H-mode with type I and type III ELMs) with gas balance analysis based on the integral method [655]. The main objective of these experiments was to quantify the expected reduction in the long-term retention rate when going from a full carbon device to the ILW. All experiments were carried out by performing a series of identical plasma discharges to obtain good statistics through the maximum feasible plasma duration. The results are summarised in figure 66, which shows the retention averaged over the pulse duration. The ILW values of the total retention rate with an upper limit of 1.5×10^{20} s^{-1} are consistent with fuel co-deposition with Be as the main mechanism for the remaining long-term retention. By the overall decrease in retention of at least one order of magnitude for all scenarios, the elimination of CFC as PFM in ITER to limit T retention could be experimentally confirmed.

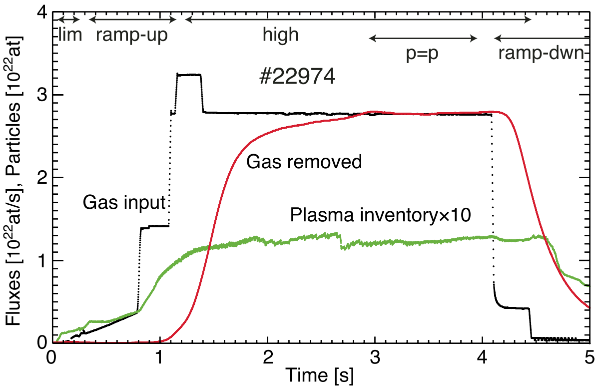

Figure 65. Gas input and removed gas for a standard H-mode shot in AUG in a full W configuration and prior to any boronisation. The different phases of the discharges (limiter, density ramp-up, high power flat-top and ramp-down) are indicated. Reproduced from [797]. © 2009 IAEA, Vienna. All rights reserved.

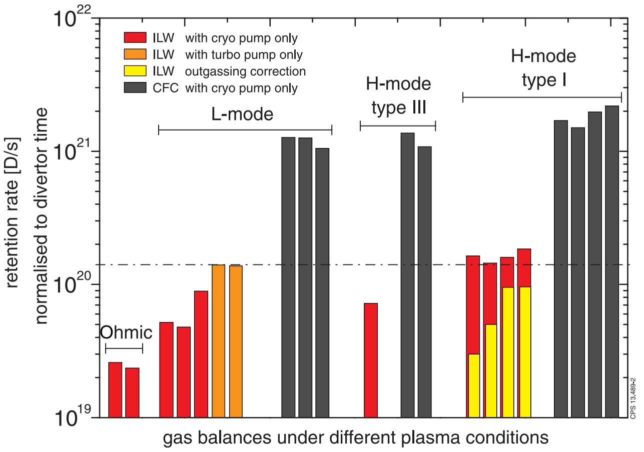

Figure 66. Measured D retention rates (log scale) for different plasma and confinement conditions in JET with the ILW and related to JET-C references. Global balances are performed in the JET-C case with cryogenic pumping only (■), and in the JET-ILW case with either the use of the turbo-molecular (🟧) or cryogenic pumping (🟥). The longer inter-shot outgassing period after H-mode discharges with the JET-ILW in comparison with JET-C leads to a reduction in the retention rate (🟨) owing to pumping of neutrals by the NBI cryogenic system. Reproduced from [655]. © 2013 IAEA, Vienna. All rights reserved.

Gas balance analysis in both the AUG and JET-ILW experiments has shown that the HI fuel retention for an all-metal device is reduced by at least one order of magnitude compared to carbon devices. Although by a factor of ∼10 lower than the gas balance results, the PM analysis in AUG also showed a similar reduction of the deuterium content in the divertor deposits by a factor of 13 [797]. In JET-ILW, the results obtained for the different plasma scenarios show a reduction by a factor of 20 compared to the carbon configuration. The retention rate increases with the ion flux to the main PFCs (divertor, guard LIM and main chamber), starting with Ohmic

Table 2. Main characteristics of plasmas during ILW-1, ILW-2 and ILW-3 campaigns [696, 809].

	# of pulses	Limiter plasma time (h)	X-point plasma time (h)	Total plasma time) (h)	Injected energy (GJ)	Glow disch. time (h)
ILW-1	3812	6	13	19	150.6	564
ILW-2[a]	4150	5.2	14.2	19.4	200.5	517
ILW-3[b]	3725[c]	4.9	18.5	23.4	245	1027
Total	**11 687**	**16.1**	**45.7**	**61.8**	**596.1**	**2108**

[a] ILW-2 ended with 0.6 h of H_2 experiments.

[b] ILW-3 ended with N_2 seeded H-mode pulses of accumulated 15 min.

[c] Only $I_p > 0.5$ MA and $\Delta t_{plasma} > 0.5$ s.

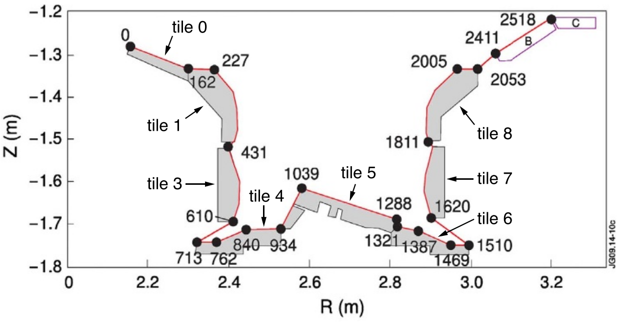

Figure 67. JET-ILW divertor cross section showing the tiles numbers and the poloidal S coordinate along the tile surfaces. Reprinted from [854], Copyright (2015), with permission from Elsevier.

and ending with H-mode confined plasmas. At the highest wall fluxes the results suggest saturation at high input power and density. Modelling of the experiments in JET-ILW with the WALLDYN [732] and ERO codes [739], as well as post-mortem analysis of deposited layers on retrieved tiles [810], are also consistent with the lower retention predicted for ITER.

In this context, further studies on the influence of seeding impurities on fuel retention are required. To date, only a few dedicated experiments have been performed in the three devices JET-ILW [257], AUG [256, 258] and WEST [259] to investigate the potential effect of N_2 on the overall retention and also on the fraction of HI outgassing with nitrogen in the form of ammonia. Ammonia was detected in AUG, where the strongest N_2 injection was performed, whereas in JET-ILW the ammonia release was close to the detection limit and in the WEST experiments no ammonia was detected at all. No accurate data on the potential effect on fuel retention could be obtained for either AUG or WEST. In JET-ILW [257] the gas balance measurements indicate a very strong N_2 retention (>30%) with a clear N_2 legacy from pulse to pulse. In addition, a higher D_2 retention of up to 2% was estimated, attributed to a conversion of about 15% of the injected N atoms into ND_3.

7.4.2. Results from JET PM analysis. In the JET-ILW configuration, three experimental campaigns, ILW-1–3, were carried out mainly with pure D plasma [809]. The PM analysis of samples from these campaigns provides a detailed picture of both material erosion/deposition and associated fuel retention for the ILW. As summarised in table 2, both integrated plasma time and injected energy increased from ILW-1 to ILW-2 and finally to ILW-3. ILW-2 ended with a H-fuelled campaign (300 pulses) and ILW-3 ended with N_2 seeded H-mode discharges with an accumulated plasma time of 15 min [809].

7.4.2.1. Main chamber Be LIM tiles. In the JET-ILW 1–3 campaigns, the central parts of the PFS of the inner wall guard LIMs and the outer poloidal LIMs at/near the mid-plane position were subjected to high thermal loads and showed significant erosion as discussed in [691], while deposition was dominant near the toroidal edges of the tiles, inferred from analysis of marker layers [696] (for the location of the analysed Be LIM tiles see figure 1 in [696]). The distribution of D on the PFS of the inner wall guard LIMs and outer poloidal LIMs measured by NRA indicates that the local D retention is anti-correlated with the campaign-averaged local heat/particle flux. The significant increase in D towards the toroidal edges of the tiles suggests co-deposition of D with Be, O and trace metallic impurities with a D concentration of ∼1% in the co-deposited layers [696].

Co-deposits containing D and T (with T traces originating from D-D fusion reactions) were also observed in the gaps of castellated PFC [852, 853]. The concentrations of D and T were highest at 1–2 mm depth from the entrance of the gaps and decreased further down into the gaps [852, 853], in agreement with modelling [852]. The fraction of fuel inventory in these less accessible regions is an important factor in the evaluation of the various removal methods discussed in section 7.5 H inventory recovery methods.

The fuel inventory measured in the main chamber during the ILW-1–3 campaigns shows that the LIMs and the UDP account for only 0.01% of the total D-fuel injected [696]. Global fuel retention in ILW-2 was lower than in ILW-1 and ILW-3 which is attributed to the H-fuelling campaign at the end of ILW-2. The main factor for the main chamber fuel retention was identified in the plasma time in the LIM configuration, which contributes up to 25%–30% of the total plasma operating time. In the LIM configuration, the effective Be sputtering yield is higher than in the divertor, and the eroded material is also predominantly redeposited in the main chamber [691] with corresponding fuel co-deposition.

7.4.2.2. Divertor tungsten tiles. The near-surface compositions of divertor tiles retrieved after ILW-1 [801] and ILW-2 [638] were investigated using IBA. As reported in [638, 801], most of the D in the divertor region was present in thick layers of Be containing some C formed on the upper part of the inner divertor (tiles 0 and 1, see figures 67 and 68, $S = 0$–227 mm). After ILW-1, these two tiles retained more than 70% of the D retained in the divertor region [854]. The D/Be ratio in the deposited layers was $\lesssim 0.1$ [801]. The deposition layer on the inner floor tile (tile 4) was much thinner than those on tiles 0 and 1, but with a higher D/Be ratio, close to unity [808], except near the ISPs. D retention in the outer divertor tiles (7 and 8)

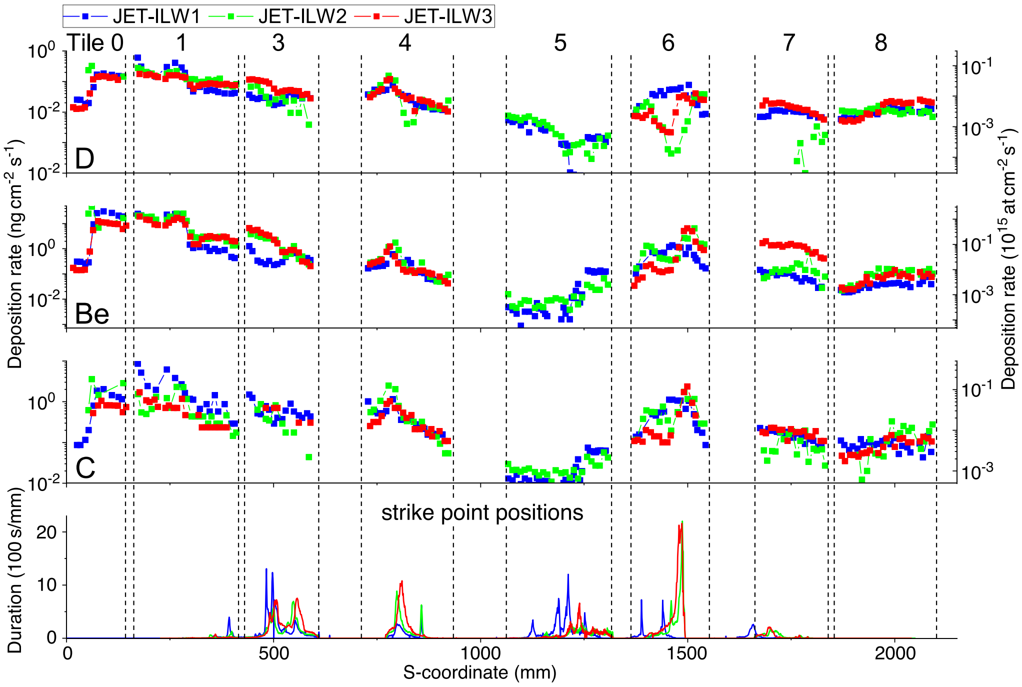

Figure 68. Top to bottom: distributions of D, Be and C deposition rates (in logarithmic scale), and distribution of strike point positions (linear scale) in the first three JET-ILW campaigns. Blue: ILW-1, green: ILW-2, red: ILW-3. Vertical dashed lines indicate borders of the divertor tiles. Numbers on top of the figure denote JET tile numbers. For tile 5, data is shown for the lamellae in row 13. Reproduced from [809]. © IOP Publishing Ltd. All rights reserved.

was much lower than in the inner divertor, with the bulk W lamellae (tile 5) showing the lowest D retention [638, 808]. These results confirm that fuel retention is strongly reduced in regions exposed to HHF leading to increased diffusion outflux and desorption.

The amount of D injected during ILW-2 was about twice that of ILW-1 [808]. Nevertheless, the amount of D accumulated in the divertor region during ILW-2 was comparable to that during ILW-1 [638, 801]. The average C/Be ratio in the divertor region was 0.18 after ILW-1 [801] and 0.084 after ILW-2 [638]. This can be attributed to a higher average heat flux (inferred from the higher total injected energy, see table 2) and enhanced desorption, the H campaign at the end of ILW-2, and decreasing C content in the deposits. However, depth profiling of D in the layers on tile 1 using SIMS showed that Be:H layers formed on top of the Be:D layers during the H discharges, with no significant depletion of D in these underlying deposits [808], confirming that isotope exchange (D to H) by plasma operation [855] is insufficient as a fuel removal method in deposition-dominated regions, even with SP sweeping. However, operating plasmas with the ISP raised to regions with the thickest Be layers and fuel content allowed the co-deposits to be heated to surface temperatures where desorption becomes efficient, as discussed in 7.5.

Similar to the castellated Be main chamber LIMs, fuel retained in co-deposited layers was found at 1–2 mm depth from the entrance of divertor castellation gaps and bulk W lamella gaps, together with a gradual decrease further into the gaps [852, 853, 856]. Similar co-deposition in the gaps between MBs can also be expected in ITER with a Be main chamber FW.

The combined results of the post-mortem analysis in JET-ILW (figure 68) show only small variations of the poloidal deposition distribution over the subsequent campaigns. The strong correlation of the distribution of D in the divertor with the distribution of Be deposition confirms Be-D co-deposition as the most important fuel retention process [809].

7.4.2.3. Integral fuel retention from JET PFC data. The most comprehensive fuel retention data set was obtained from the post-mortem PFC analysis following the ILW-3 campaign [810]. The global fuel retention was determined to be $(0.19 \pm 0.08)\%$ of the injected fuel. This is consistent with the PM analysis after ILW-1 which showed that $\approx 0.2\%$ of the injected D was retained in the wall [639, 854]. The inner divertor also had the highest fuel retention in ILW-3 with 46.5% of the total fuel retention, mainly in co-deposits on tile 0 and tile 1. However, the retention in the divertor corners as a fraction of the divertor retention was reduced by a factor of >2 for ILW-3 compared to ILW-1, mainly due to the further reduction of residual C.

These results show, similarly to the gas balance analysis discussed in 7.4.1, that the total fuel retention in the ILW all-metal configuration decreased by a factor of 10–20 compared to the JET-C configuration [696], although, as mentioned in the introduction 7.1, the campaign integrated retention fraction derived from post-mortem PFC analysis is 3–24 times lower in absolute value than the gas balance evaluation in individual plasma scenarios [655, 810]. However, the largest discrepancies correspond to scenarios that were rarely run during the ILW campaigns. A narrower range between 3 and 6 was found in a study involving several fusion devices [791]. Part of the discrepancy between the two methods is attributed to the storage of retrieved samples in air for a typical period of several days to several months prior to analysis. During this period, up to $\sim 1/3$ of the PFC fuel inventory can be lost through outgassing and isotope exchange prior to analysis [810]. Furthermore, results from post-mortem samples always represent only a fraction of the total internal surface area of the vessel. It is therefore expected that as more PFC are analysed, current estimates from post-mortem data will come closer to those from gas balance studies.

7.4.2.4. Fuel retention in dust. The most relevant information for ITER regarding the expected fuel retention in dust was obtained from the analysis of dust samples after the JET-ILW campaigns, summarised in [640]. The total amount of dust collected by vacuum cleaning after each of the three JET-ILW campaigns was estimated to be 1–1.4 g per campaign (with 19.1–23.5 h plasma operation per campaign). This amount is over 100 times less than the corresponding amounts in JET-C, consistent with the reduced Be erosion and redeposition compared to C. Tungsten made only a minor contribution to the dust, attributed to erosion of the W coatings used. The average D retention in dust particles from the inner divertor was estimated by TDS to be 1.2×10^{21} atoms per gram of dust (giving D/Be ≈ 0.02, assuming the dust to be pure Be). The total D retained in the dust particles in the inner divertor after the ILW-1 campaign was only $\approx$0.4% of the retention in the co-deposited layers on the divertor tiles. From these results it can be concluded that only a small fraction of the co-deposits delaminates in JET experiments, although this fraction is expected to increase in devices with longer operating times such as ITER. Similar conclusions on D retention have been drawn in [857] on the basis of IBA of the elemental composition of dust particles collected after the ILW-3 campaign.

TDS analysis showed that D release from the Be-rich dust particles started at 800 K and peaked at 1050 K [640], which is higher than in laboratory Be-D co-deposition experiments [845], where the peak release occurred around 750 K. Consequently, complete removal of T from dust requires heating to relatively high temperatures ($>$1050 K), and it may be easier to remove the tritiated dust than to remove T from the *in situ* dust deposits.

7.4.3. Results from AUG PM analysis. Post-mortem analysis of PFC samples from AUG during the stepwise transition from an all-C to a full-W PFC configuration confirmed that D retention is strongly correlated with the amount of residual C in the machine available for co-deposition with D. C deposition in the divertor decreased by a factor of 15 with the transition to the full-W FW [799]. At the same time, the amount of D retained in the divertor decreased by a factor of 8–14 [799]. Co-deposition of D with B can also contribute significantly to D retention, particularly when the total B source becomes comparable to or exceeds the residual C source. For example, after covering the ICRH LIM with W, C deposition decreased by a factor of 4–6 in the subsequent campaign, but D retention in deposited layers in the divertor decreased by only a factor of 2 due to co-deposition with B, as can be seen in figure 3 in [799] for the step from the 2004/5 to the 2005/6 AUG campaigns.

While the amount of C deposited in the divertor decreased by a factor of 15 with the transition to a fully W-covered FW, the amount of C in the plasma from spectroscopy decreased by only a factor of 2–3. The accepted explanation for this discrepancy is that a small residual source of C is recycled more efficiently from the W surfaces. This increase in recycling is due to higher re-erosion of low-Z elements from high-Z surfaces as described in [858]. There remain several different sources of residual C even with a fully W-covered FW [799]. Most parts of the FW PFC in the AUG still consist of graphite with W coatings. This allows for chemical erosion of the tile backs by atomic hydrogen or oxygen. There are also many electrical arc tracks in the divertor, which remove the W coating and erode the C underneath. In devices such as ITER with all-metal bulk PFC, the amount of residual carbon is expected to decrease to the limit given by the C impurity fraction in the PFM.

In contrast to co-deposition with C in the inner divertor, retention in the outer divertor is dominated by retention in W since the AUG transition to a full W FW [822, 859, 860]. A comparison of the amount retained in the near surface region by NRA depth profiling with the total amount from full outgassing by TDS showed that most D is retained beyond the depth range accessible to NRA. As discussed in 7.3.1, D diffuses deep into the material and is retained at trapping sites in the W bulk. The near surface depth profiles of NRA of D in different W grades are very different, but the total amounts are generally similar [859]. A detailed comparison of retention in different types of W exposed at the OT in AUG is given in [822]. In general, the W coatings produced by either vapour plasma spraying or combined magnetron sputtering and ion implantation have a higher defect density, including pores, compared to solid polycrystalline W tiles. These pores result in additional high temperature peaks in the TDS spectra (see figure 3 in [822]). The increase in D retention in bulk W tiles showed a square root dependence on the accumulated D fluence, also suggesting diffusion limited filling of trap sites in the bulk W with D.

Overall, the change from a C to a full W FW reduced the D retention by a factor of 5–10. This finding encourages the use of a full W FW in future fusion devices, now also planned for ITER.

7.5. H inventory recovery methods

7.5.1. ITER fuel removal methods. As identified in previous sections, co-deposition with beryllium drives the tritium inventory build-up in ITER. The maximum allowed retention in the in-vessel components in ITER is set at 700 g. At a JET-like retention fraction of the injected fuel of 0.14%–0.19% [810], without recovery methods, ITER could potentially reach this limit already within the first FPO campaigns of the ITER research plan [3]. Retention should therefore be monitored closely, and fuel recovery techniques must be applied at the required time intervals.

Fuel removal methods aim to release HIs from PFCs by relying on thermal desorption of tritium and isotope exchange, replacing tritium with hydrogen or deuterium at trapping sites. For both processes, the temperature of the materials is important as it determines the hydrogen transport rates by Arrhenius terms, while isotope exchange moreover depends on the particle fluence.

This section reviews recent results on ITER fuel removal methods applied with and without magnetic fields in present devices. ITER's TF, B_t, generated by superconducting coils, remains active for multiple weeks continuously. GDC which requires the magnetic field to be off, is therefore limited to the regular short-term maintenance periods lasting up to several days. Baking which requires considerable additional time and effort, is restricted to long-term maintenance periods between operations campaigns. To mitigate the tritium inventory build-up throughout an experimental day or week, conditioning discharges created at the ion cyclotron and EC range of frequencies (ICWC and ECWC) are being developed, as well as tokamak plasmas optimised for clean-up purposes. The first section describes baking and GDC, applied without B_t, and the second ICWC, ECWC and tokamak discharges, applied with B_t. An outlook to the T-recovery strategy in ITER is presented in the last section including recommendations for further research.

7.5.2. Conditioning without toroidal magnetic field.

7.5.2.1. Baking. In the Baseline 2016 of ITER [3] the Be FW and the W divertor are baked to 240 °C and 350 °C respectively by circulating hot water or gas through their cooling circuit. These temperatures are found sufficient for fuel removal from bulk Be and W while for thick co-deposited layers higher temperatures are required as described below. It is estimated that about 100 h are needed to heat up the divertor and cool it back down, to which the actual baking duration needs to be added. Recent experience of JET, equipped with the ITER-like beryllium main chamber wall and tungsten divertor, showed that a 4 days main chamber bake at 320 °C removed an equivalent of 23% of the estimated long term inventory [861]. Baking is thus effective, and a few tens of cycles for fuel removal during DT operations are presently planned in ITER.

In ITER, similar to the JET-ILW experience [810], the majority of the tritium will be retained in co-deposited beryllium layers. At the divertor baffles these layers may grow to several tens of microns thick under $Q = 10$ burning plasma conditions between baking cycles [785]. Outgassing tests from PFCs exposed in JET-ILW at ITER-relevant baking temperatures, suggest that fuel depletion from such thick deposits might require significant baking durations (>1 month) [785, 862]. Only 13% of embedded fuel could be removed from 40 μm thick co-deposit layers on the W coated CFC divertor tiles by 15 h of baking at 350 °C [862]. This is true also for removal of implanted fuel from the JET Be main chamber samples in the deposit-free erosion zones of LIM tiles on the mid-plane, where baking at 240 °C was even less time-efficient [862] showing a fuel recovery range of 10%. From these and similar studies, it is known that all fuel (whether or not in co-deposited layers) is recovered when the surfaces are heated to temperatures of at least 800 °C for several minutes [785, 862, 863]. The latter temperatures may be obtained at the divertor deposits by plasma scenarios with raised divertor SPs (see section 7.5.3.3).

Performing baking experiments early during PFPO in preparation for FPO will allow for checking the fuel removal efficiency and confirm whether additional techniques would be required. The pulse duration, and resultant divertor fluence, during these early phases will however be limited, so that a full validation of the baking efficiency can only be obtained when sufficient co-deposition has occurred in the machine [864]. With increased material exposure, their retention and outgassing characteristics change. For instance, helium irradiation is shown to influence the thermal desorption behaviour of tritium from tungsten, requiring higher temperatures for thermal release at He fluencies of up to 10^{17} cm^{-2}, before bubble connections lead to the formation of surface-connected pores [865, 866].

7.5.2.2. Glow discharge conditioning. Glow discharges in tokamaks behave as hollow cathode discharges where the cathode is represented by the grounded wall surfaces [867]. The discharge is sustained by fast electrons emitted from the cathode by ion impact. Being accelerated and subsequently trapped in the potential well formed by the cathode fall surrounding the plasma these electrons are responsible for the creation of a nearly uniform ion current all over the vessel surfaces. The efficiency of H_2-GDC for isotope exchange at the ILW was assessed after the first six-month deuterium campaign [868]. The reservoir accessible for isotopic exchange by GDC was found to be one order of magnitude lower than in prior JET studies with carbon based PFC. Recent experiments in JET-ILW combined FW baking at 320 °C with GDC, doubling the fuel removal rate compared to baking alone [861]. Also in laboratory studies it is shown that irradiation of ITER proxy materials at 500 K by hydrogen atoms and hydrogen plasma ions at 50 eV accelerates isotope desorption [869].

A new design of the ITER GDC system based on a fixed electrode concept replaces the previous design which had movable electrodes integrated with the ITER In-Vessel-Viewing-System [870]. The new system for the ITER Baseline 2016 consists of 7 anodes distributed in the OMP and upper lateral port plugs, forming an integral part of the diagnostic shield modules mounted on the port plug front ends, directly facing the plasma. GDC in ITER will be run at a discharge current up to 30 A per anode, in the steady pressure range of 0.3–0.8 Pa. A study of the JET glow discharge as a function of the number of electrodes, glow current and pressure indicates that the GDC system for ITER will provide sufficient toroidal and poloidal homogeneity [868].

The distribution of glow plasma current density on the in-vessel PFCs was simulated using a self-consistent 2D axisymmetric multi-species fluid model [871, 872], benchmarked against experimental data from glow discharges produced both on a small scale laboratory experiment and in toroidal devices JET and RFX, with reasonable agreement [873]. The model describes the two populations of electrons by separate sets of fluid equations: one for the thermalised electrons of the plasma and one for the fast secondary electrons that are accelerated in the cathode sheath. The ion current distribution and glow homogeneity is found optimal at or below pressures of 0.5 Pa [867]. While the uniformity improves little at lower pressures, the increased heating of the water-cooled anodes must be considered if the pressure is too low, particularly when applying GDC during baking. Finally, the wall ion current density is most uniform and highest when all planned 7 anodes are used simultaneously at 0.21 A m^{-2}. This value is comparable to the ion fluxes in GDC in JET (0.10 A m^{-2}), RFX and Tore Supra (0.06 A m^{-2}), and ASDEX-upgrade (0.20 A m^{-2}).

From the broad operational experience of GDC in present tokamaks, several issues for GDC must be considered for ITER. The first relates to GDC operation with He and applies more generally to the use of He in devices with metallic PFCs. He GDC has been observed to form dense bubbles of size 2–20 nm, dislocation loops and cracks connecting the bubble's metallic surfaces [874]. Such damage may increase trapping sites for the plasma fuel, potentially increasing T-retention as a consequence [875]. The effect of He irradiation is discussed in paragraph 7.3.1.2. He GDC is also shown to sputter Fe from the steel panels in W7-X [876] and led to He retention in W PFCs in AUG [877]. The second issue regards the initiation of the GDC which in the absence of a separate electron source such as in AUG [878] and ADITYA upgrade [879], as is the case in ITER, relies on a *Paschen breakdown* which requires a tenfold pressure increase. At such higher pressures, the GDC exists in ports and gaps and care must be taken to avoid strong local erosion or arcs.

7.5.3. Conditioning with toroidal magnetic field. The need for conditioning techniques that work in the presence of the TF in superconducting devices was already mentioned in [672]. Analysis of the conditioning cycle on JET with the ITER-Like Wall evidenced a reduced need for wall cleaning in-between pulses compared to JET–CFC [867]. However, at ITER these techniques will be needed to control the Tritium inventory, as well as to recondition the device after the use of the ITER DMS and to assist in fuelling gas changes. The magnetised conditioning discharges in ITER, namely ECWC, ICWC and diverted plasmas with raised SPs, will be applied using the plasma control system and require a number of ITER plant systems, including the heating systems as well as gas input, poloidal field and diagnostics. The techniques are, as their non-magnetised counterpart, aimed at inducing a known and optimal flux of particles to the PFCs, to initiate the release of impurities and/or HIs. The preferred transport of charged particles along the magnetic field lines affects however the uniformity of the conditioning flux for different wall components [880]. For charged particles, the interaction occurs via the inevitable wall intersection points of the outer magnetic field lines. At the divertor surfaces it is characterised by the shallow angle between the field lines and surface, spreading the parallel flux along a large surface area. In ICWC and ECWC discharges this flux is evidently lower (≈100 times) than in diverted plasmas, affecting their efficiency for fuel removal from these surfaces. Therefore, diverted plasmas with equilibria other than the baseline magnetic equilibrium are proposed for removal at the divertor. The LIMs and main wall in diverted plasma are located in the far SOL with much reduced plasma density. ECWC and ICWC, with optimised duty cycle are aimed to target these areas. Their ion flux is highest at the LIMs due to the toroidally localised interaction and larger impact angles. This will be the case also for the shaped FW panels in ITER where the parallel ion heat flux will be dissipated on about 10% of its surface area. The recessed surfaces (>10–20 cm from the separatrix in ITER) receive a greatly reduced ion flux due to the strong plasma density decay (≈1 cm) behind the first field line interesting components. Neutrals, not affected by the magnetic field, can be the dominant flux component at such recessed locations. This is also the case for the gaps and castellations where impurities are known to co-deposit with plasma fuel [881].

7.5.3.1. ECWC. ECRH conditioning discharges are produced by coupling RF waves at the ECR condition (1st harmonic) or its 2nd harmonic at a gas pressure of typically 1–50 mPa. In tokamaks these plasmas are substantially different from their counterpart in stellarators [882] due to their strongly reduced plasma confinement. The current-less ECWC plasma exists without equilibrium in tokamaks and remains typically partially ionised. It was first carried out in JFT-2 by using the 2.45 GHz LH system and a magnetic field of 87.5 mT [883]. Since then it has been tested on many other devices in studies on reactive and non-reactive cleaning, thin film deposition and removal of co-deposited layers. ITER will operate ECWC at the half or full magnetic field (2.65 and 5.3 T respectively) and the 170 GHz frequency of the ECRH heating and current drive system.

Experiments in TCV assessed the applicability of EC conditioning in helium at the second EC harmonic to de-saturate the carbon-based PFSs from deuterium [884]. The work was part of the preparations for the first operations campaign on JT-60SA. A vertical field of about 0.5% of the TF was found to be necessary to minimise the breakdown time and increase the steady plasma density. The radial discharge uniformity can be improved by the addition of a small horizontal field component. This was previously demonstrated in JT-60U [885] and KSTAR [886], at both the fundamental and second harmonic ECRH frequency, and in Tore Supra [867] at the fundamental ECR The improved wall coverage resulted in increased removal of hydrogen in the 50 ms long helium fuelled discharges on Tore Supra [867]. However, the operational space of the additional pure radial field is limited to low amplitudes alone (0.2% of B_t in the TCV case [884]), above which breakdown is too slow or simply not possible. Combining a radial and vertical field component, resulting e.g. in a quadrupolar poloidal field map maximised the ion currents at the TCV inner wall in X2 ECWC, yielding a local perpendicular He ion flux of up to $6 \times 10^{19}\,\mathrm{m^{-2}\,s^{-1}}$ (to be compared to $\approx 6 \times 10^{17}\,\mathrm{m^{-2}\,s^{-1}}$ for the 0.1 A m^{-2} range for GDC), as measured with wall probes on the central column [884].

Directing ion flux from the resonance layer to inner wall surfaces is found less effective in D_2 ECWC in the larger AUG with full W PFCs, due to magnetic mirror effects and outward convective flows [887]. The discharges were produced using X2 waves launched horizontally from the equatorial ports. While the efficiency of ECWC for fuel and impurity removal from metallic surfaces has been less investigated so far, modelling predicts the presence of an intense flux of low energy atoms produced at the ECH absorption layer. This atom flux reaches all PFCs uniformly and may be effective for conditioning the HFS surfaces also.

The high electron densities and temperatures in ECWC plasmas (of order $10^{19}\,\mathrm{m^{-3}}$ and 40 eV respectively) result in significant re-ionisation and re-implantation of wall desorbed species affecting fuel and impurity exhaust [885]. This can be mitigated by pulsing ECWC discharges with an appropriate duty cycle. Recovery from disruptions using pulsed ECWC was successfully demonstrated in KSTAR [886]. Pulsed ECWC also minimises the possible absorption of EC energy on in-vessel components as the single pass absorption is typically below 50% in a tokamak ECRH plasma [885]. To minimise EC stray radiation, the plasma breakdown phase, without measurable density and hence negligible EC absorption by plasma, needs to be short, and more importantly the absorption during the longer plasma phase needs to be high. The breakdown time and absorption in a tokamak ECWC plasma depend sensitively on the gas and its pressure, the ECRH power, polarisation and launch angle, the location of the EC resonance relative to the magnetic axis and the applied poloidal field [880, 888, 889].

Predicting the ECWC plasma parameters and power requirements for ITER requires estimates of the power absorption and transport mechanisms of the toroidal magnetised plasmas. The 1D transport oriented model for magnetised toroidal RF discharges, TOMATOR-1D, provides a practical means to validate scalings for transport or power absorption modules against experimental data sets [887, 890]. The model simulates self-consistent radial density and temperature profiles for magnetised plasma mixtures of hydrogen and helium with a detailed description of the collisional processes. Using conventional assumptions on transport and EC power absorption, it reproduces the density profiles of X2 ECRH plasmas on TCV and AUG in parametric scans of the launched ECRH power and the applied vertical magnetic field. A poloidal magnetic field dependent scaling for anomalous diffusion is proposed based on Bohm diffusion, with a numerical coefficient of the same order as the Bohm and Spitzer coefficients. Outward convection is implemented as to result from drifts in the toroidal magnetic field configuration.

7.5.3.2. Ion cyclotron wall conditioning in tokamaks. ICWC uses the standard ICH antennas for producing low density, partially ionised and current-less conditioning plasma. In addition to the TF, a small ($<1\%$ of B_t) shaped vertical magnetic field is applied to obtain a uniform discharge. Similar to ECWC, ICWC will be applied in series of short repetitive pulses to mitigate re-ionisation and re-deposition of particles released from the wall. Compared to GDC in JET-ILW, ICWC has a similar removal efficiency as a function of the coupled energy to the plasma [861]. Hence in ITER, at a low ICWC duty cycle of 10%, the time averaged energy throughput of ICWC will be similar or slightly higher than that of GDC.

ICRF plasma production is robust in present devices and possible in a broad range of heating scenarios be it at the fundamental, higher harmonic or subharmonic frequencies of the discharge gas [888, 891]. The breakdown phase has been described by 1D PIC simulations [892]. The appearance of an antenna loading at higher density is triggered by the occurrence of the LH resonance near the antenna [893]. The steady plasma is sustained by coupling ICH power to both electrons and ions, mainly via non-resonant processes. Toroidal monopole phasing of the poloidal strap arrays improves RF coupling and uniformity of the ICWC discharges by reducing the cut-off density for Fast Wave propagation [891].

In ITER, ICWC is envisaged to control the T-inventory build-up, assist fuelling gas changes and remove impurities, e.g. after DMS activation. Gas balance experiments in JET with the ITER-like wall show that 630 s of ICWC plasma removes an amount of fuel (8.6×10^{22} atoms [888]) which corresponds to 573 s of plasma operations at a worst case retention rate of $1.5 \times 10^{20}\,\mathrm{s^{-1}}$ [655]. Higher removal rates can be obtained by combining ICWC with main chamber baking [861]. While these results indicate the efficacy of ICWC for fuel recovery in-between pulses in ITER, it is to be noted that the removal stems from both long term as well as transient retention, as is the case also for the other T recovery techniques. Fuel removal in ITER needs to address the long term retention as the transient retention will be quickly refilled up to 50% T in a subsequent DT discharge [855].

A main energy loss mechanism of ions in ICWC plasma is charge-exchange reactions with neutrals. Due to resonant and collisional ICH power absorption, the neutral particle energy distributions show high energy tails above 1 keV in Tore Supra [894], AUG [892] and JET [895]. These represent about 1% to the total neutral flux to the PFC [894]. First measurements in the energy range below 500 eV are obtained in TOMAS for discharges at 25 MHz and 125 mT, showing an integral neutral flux of $(0.2\text{–}1.1) \times 10^{19}\,\mathrm{m^{-2}\,s^{-1}}$ [896], confirming earlier estimates of 0D ICWC modelling [897]. This flux can be compared with the aforementioned typical wall ion current density in GDC of $\sim 10^{18}\,\mathrm{m^{-2}\,s^{-1}}$. The ion flux parallel to the field lines is much higher, reaching $10^{21}\,\mathrm{m^{-2}\,s^{-1}}$ at the LFS in ICWC discharges in Tore Supra [867], but decays however strongly behind the diagnostic protection LIM. The applicability of He-ICWC to assist a changeover from hydrogen to helium plasmas has been demonstrated at AUG [898] where 20 He-ICWC pulses, including outgassing between discharges, removed more D atoms than two H-mode plasma discharges in helium before ICWC and 25 H-mode discharges after ICWC ($\approx$13 Pa m^3 vs. 3 Pa m^3). Fuel removal by He-ICWC in JET-C, operating with carbon based PFC mostly, was found to be less efficient than in hydrogen [895]. Moreover, significant He retention is reported in these experiments, as well as in AUG with tungsten PFC. The presence of Be as constituting materials of RF antenna protection LIMs in JET-C is suspected to be responsible for the 80% retained fraction of the He injected in the ICWC discharges. This retention and the possible impact of helium as conditioning gas on subsequent plasma operation needs to be assessed for ITER.

Further experiments show the applicability of ICWC for wall cleaning, for instance to help recover operation after DMS activation. Amounts of argon implanted in the W surfaces of AUG could be removed in 6 He-ICWC discharges [899]. Pulsed He-ICWC discharges have been successfully applied on Tore Supra to recover from unmitigated disruptions [895]. Operation recovery after exposure to reactive gases was shown in EAST [900] and TEXTOR [901]. Inter-shot ICWC in KSTAR allowed to suppress the water partial pressure during operational days [902].

7.5.3.3. Raised SP scenarios.

Post-mortem analysis of components removed from the vessel after operation campaigns show that fuel retention in JET is dominated by co-deposition with Be. The thickest deposits, up to a few tens of μm, are found at the inner divertor baffle area and account for 46.5% of the retained fuel in the 3rd ILW campaign [810]. This will be the same in ITER, where several tens of microns thick layers can build up between baking cycles [785].

The efficiency of the planned 350 °C divertor bake appears limited for such thick co-deposits. Tokamak plasma with raised inner divertor strike-point is proposed to heat the co-deposits directly and enhance tritium desorption [903]. In laboratory it is shown that 200 s of D plasma exposure at 600 °C removes 84% of D from 3 μm co-deposited layers [863]. The highest D removal is achieved at higher temperature, longer exposures and using H plasma instead of D plasma. In order to deplete thick surface layers by thermal outgassing alone, they must be heated above 800 °C for several minutes, based on TDS spectra [863].

JET demonstrated the raised inner divertor SP scenario by heating the uppermost accessible point to at least 800 °C throughout the stationary diverted phase of 18 s [861]. As the bulk material temperature increased only by about 100 °C per pulse and reached a maximum temperature by ratcheting of about 200 °C overall, the high temperature is limited to the thin resistive deposit layer only. Spatially-resolved high-resolution H_α spectroscopy in the hydrogen fuelled discharges showed consistently a higher D content at the upper inner divertor compared to other divertor locations, confirming the locally stimulated thermal outgassing. For comparison, isotopic exchange experiments on the JET-ILW using plasmas with a LIM phase followed by high and low triangularity phases report removal from implanted areas mostly with a very weak access to the long term retention reservoir by co-deposition [855].

The desorbed isotopes released above the ISP will be re-ionised. While a major part of the isotopes will eventually be evacuated through the divertor pumps, a non-negligible part will be further retained in co-deposited layers in areas that are likely inaccessible through plasma operations, even for the raised SP configuration. The too frequent application of such a plasma scenario may therefore contribute to an increase of the long term retention elsewhere in the vessel [855]. In addition, if the isotopic ratio is reduced after this partial cleaning, particularly if the pulse is performed without T, additional T injection will be required for the following pulse to reach the T concentration target. Since the retention is shown to increase with the gas throughput [655], the cleaning through diverted plasma scenarios may lead, and this is a paradox, to an increased T retention compared to the absence of cleaning. It is therefore proposed to apply fuel removal by *pure* (D_2-fuelling) diverted plasmas only at the end of an experimental campaign [855] and/or to combine it with techniques such as ICWC to recover the fuel that is made accessible.

The possibility of running ITER plasmas with raised strike-points was first examined in [904] and recent SOLPS-ITER simulations were conducted to assess the feasibility of this approach for detritiation from Be co-deposits [905]. The study found that for SPs raised to just below the current transition region from the straight to curved parts of the vertical W divertor targets, L-mode plasmas up to 14 MA would be controllable in terms of vertical stability, well above the maximum plasma currents envisaged to be attempted in PFPO-1. However, even higher strike-point positions might be required based on predicted deposition patterns in ITER [739].

7.5.4. T removal after JET T&DT campaigns.

An optimised tritium recovery sequence was applied in JET-ILW after the second Deuterium–Tritium Campaign (DTE2) and full T campaigns that preceded and followed after the DTE2 [906]. Baking, superimposed with ICWC and GDC cleaning cycles in D, and diverted plasma operation in D with different SP configurations, including raised ISP pulses, and with different plasma heating allowed reducing the residual T content in D NBI-heated plasmas to about 0.1% as deduced from neutron rate measurements, below the 1% target set by the allocated 14 MeV fusion neutrons budget for the following D campaigns. Access to the T-rich Be deposits at the inner divertor baffle region was clearly evidenced from the increased neutron rate and elevated surface temperatures in plasmas with the ISP raised onto this area. The measured removed T amount, 0.67 g T was comparable to the in-vessel T inventory assessed from past D retention data and T fuelling into the vacuum vessel (252 g T), ranging between 0.48 g T (post-mortem D data [810]) and 5.04 g T (gas balance D data [655]), indicating the effectiveness of the combination of fuel removal techniques that are being developed for ITER.

7.5.5. Outlook to T-recovery in ITER.

This section summarised the development of the fuel removal techniques under consideration in the ITER Research Plan [3]. This plan foresees the development of the ITER fuel recovery strategy from the pre-fusion operation phases. The different techniques will be used complementary in ITER, weighing the specific strengths and limitations of each. Studies in present devices and the development of models, as presented in this section, are needed to identify these and should continue to prepare ITER operations. In ITER, baking and GDC can be applied between operation cycles, when the toroidal magnetic field is off. To mitigate the accumulation of the inventory during experimental periods when the TF is continuously present, ICWC, ECWC and diverted plasmas with raised SPs are foreseen. GDC and ICWC provide a uniform conditioning flux to the PFCs, however this flux may be less effective in depleting thick Be co-deposit layers. Diverted plasmas with raised SPs can strongly heat the thick Be deposits at the inner divertor, effectively depleting the co-deposited layer inventory through thermal outgassing. Alternating this method with pulsed ICWC or ECWC discharges is proposed to minimise retrapping of the released fuel in co-deposits. Finally, after removing T from the PFCs, extra T fuelling will be needed to obtain optimal T concentrations in the next DT pulse. Care must be taken not to increase the overall T throughput and hence retention by the application of fuel removal techniques [855].

7.6. Modelling

As detailed in section 7.3.2 the HI-retention by co-deposition of HI with impurities depends on the growth rate of the deposited layer, on the local HI impact energy and on the surface temperature. In order to predict retention by co-deposition, a model is needed that calculates the location and growth rate r_d of the co-deposited mix such that based on the HI/X ratio the local retention can be calculated as $\Gamma_{\mathrm{ret}} = \mathrm{HI/X} \times r_d$. The formation of these layers is inevitable in particular when low-Z elements with a high erosion rate are present. This necessitates the application of T-removal methods as detailed in section 7.5.

7.6.1. Modelling of material migration. Co-deposition is a consequence of impurity migration in magnetic confinement fusion devices: The wall material is eroded by the impinging plasma through physical sputtering and/or chemical erosion. The impurities created by the erosion processes enter the plasma, are ionised and then transported parallel and perpendicular to the magnetic field. Eventually the impurities are re-deposited on the wall at some potentially distant location from their origin. They may be re-eroded to again undergo plasma transport and be re-deposited. This re-erosion/re-deposition cycle continues until the impurities deposit at a location where the re-erosion/reflection rate is lower than the incident flux and co-deposited layer starts to form and grow. Therefore to describe the formation of co-deposits a coupled description of the surface processes (deposition/reflection/erosion) and transport of impurities in the plasma is needed.

7.6.1.1. Description of migration codes. For ITER predictions, three codes were used to model the above processes: the ERO code [642] is a sophisticated impurity plasma transport code that has a simple surface dynamics model attached to it. It follows the gyro-motion of the impurities and due to this complex plasma transport model it is usually only applied to a small sub-volume of the plasma requiring ad-hoc assumptions about losses and influx of impurities to/from its limited simulation region. To remedy this limitation the massive parallel ERO2.0 code [694] was developed which can perform 3D global gyro-orbit resolved impurity transport calculations but so far has not been run with a surface dynamic model to make predictions about co-deposition and is mainly used to predict Be erosion.

The WallDYN [732] code was developed from the start to describe the coupled nature of surface processes and plasma transport to describe co-deposition. It uses the well benchmarked global impurity transport code DIVIMP. Originally WallDYN, due its use of DIVIMP [907], was limited to toroidally symmetric geometries but it was recently extended to perform global 3D impurity migration calculations [908]. WallDYN features a surface dynamics model similar to that in ERO but uses composition dependent reflection and sputter yields. All three codes require as input the background HI-plasma and operate under trace approximation: The migration of impurities and resulting impurity plasma densities are assumed to be low enough such that the plasma solution is not affected.

ERO and ERO2.0 are Monte-Carlo codes that follow virtual particles until they are no longer re-emitted. In contrast WallDYN describes impurity migration and surface dynamics as DAE system [732]: The impurity migration is described by a re-distribution matrix1determined once using DIVIMP for a given background plasma solution and then allows to compute the local influx of impurities as a simple matrix multiplication of the source flux from the wall. The time evolution of surface composition of impurity is calculated as a simple flux balance of influx minus reflection and erosion flux. In this approach directly couples the change in the surface composition with the impurity influx into and back from the plasma.

7.6.1.2. Code validation based on experiments. The predictive codes require validation of their underlying models and assumptions against the available experimental data as described in section 6.5, typically comparing layer thicknesses measured during PM analysis or using synthetic diagnostics for direct comparison to e.g. measured spectroscopic data.

In [740] the ERO code was used to compare deposition in remote areas for different FW configurations of JET: be deposition in JET-ILW and C deposition in JET-C. The simulation volume was limited to the inner divertor target area and the inner divertor floor. The calculated values for deposition were compared to measured deposition on a rotating collector probe located under the divertor dome. ERO was able to reproduce the measured Be deposition rates assuming an ad-hoc influx fraction of 0.1% of Be in the D-plasma flowing into the inner divertor. The calculations also showed that the plasma transport of C and Be leads to similar deposition patterns for both species. Therefore the observed difference in the deposited amount: 5–10 times more C in JET-C compared to Be in JET-ILW has to stem from a higher influx of C compared Be. In [740] also the W erosion rate was investigated showing that W erosion is dominated by ELMs during H-mode plasma operation in JET-ILW and is 2–3 orders of magnitude lower than the erosion of Be. In [909] Be migration in JET-ILW configuration was investigated by ERO modelling of a larger simulation volume spanning from the inner divertor to inner upper mid-plane. The calculations were compared to the BeII spectroscopic signals measured intra- and inter-ELM. However the modelled spectroscopic intensities could not match the experimental values even qualitatively which was attributed to too high plasma temperatures in the background plasma used for performing the migration calculations. Still the deposition patterns qualitatively matched the PM measured values of Be deposition: The thickest deposits were found on top of the inner divertor entrance baffle. The patterns even matched quantitatively when adjusting the upstream Be source in an ad-hoc fashion similar to the approach in [740]. The ERO2.0 code has been used extensively to predict Be erosion and transport but due to the lack of a surface dynamics module it cannot be used to predict co-deposition since it cannot describe impurity recycling. In [739] Be erosion from the 3D shaped Be FW in ITER and migration to the divertor is simulated. The authors also give *net deposition* numbers in the W divertor but these need to be understood only as the difference between influx and reflection since re-erosion cannot be calculated without a surface dynamics model.

In [732] the Be and C migration and co-deposition in JET-ILW and JET-C respectively was investigated using the WallDYN code. For JET-C the FW composition is constant and erosion depends on energy (physical sputtering) and temperature (chemical erosion/sputtering). With the so calculated C source flux and a DIVIMP based migration matrix M the Be-flux fractions into the inner divertor are of the order of 0.1% as was required by [740] to match the deposition data. However this flux fraction varies strongly radially across the entrance of the divertor and cannot be described by a single value, highlighting the need for a global calculation. From the calculated Be and C layer growth rates r_d, D-retention rates (D s^{-1}) were calculated using scaling laws for the D/C and D/Be-ratio from [844] and [812] respectively. Using the WallDYN approach it was possible to quantitatively reproduce the long term fuel retention in JET-ILW and JET-C as determined by gas balance from [655]: JET-C retains 10 times more D than JET-ILW. Also, the poloidal distribution of the Be deposition was qualitatively in line with PM analysis: In the divertor Be deposited mainly on the entrance baffles with the thickest layer predicted on the HFS. The fact that all models predict similar poloidal deposition patterns despite different underlying background plasma solutions suggests that Be deposition can probably also be expected at similar locations in ITER.

7.6.1.3. Extrapolation to ITER. Using the same code-settings as for the JET-ILW cases but with background plasma solutions for ITER, WallDYN was in [732, 777] used to make predictions for the T-retention in ITER by co-deposition. Various different background plasma solutions, covering the operation range of ITER, were used. The T co-deposition rates based on [812] resulting from these different background plasmas showed a strong scatter of almost an order of magnitude.

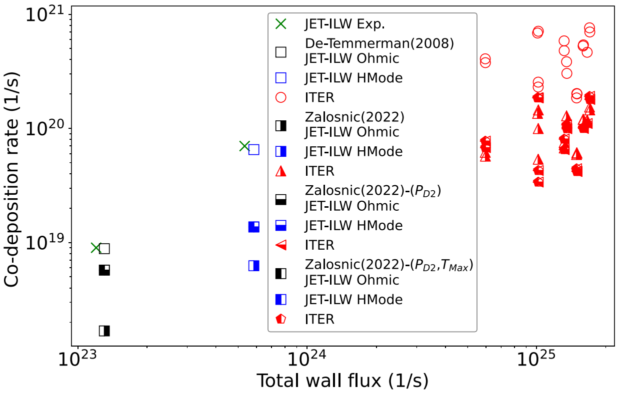

Figure 69. Recalculating the D retention rates via co-deposition using the same parameters as in [732] but using the new scaling laws from [847]. The label Zalosnik(2022) refers to equation (3), the label Zalosnik(2022)-(P_{D_2}) refers to equation (5) and the label Zalosnik(2022)-(P_{D_2}, T_{max}) refers to equation (6) in [847].

Therefore, the resulting number of full power ITER discharges that can be run before the T inventory limit is reached varies from 3000 to 20 000. As outlined in section 7.3.2, the fit parameters in the D/Be-ratio scaling law have rather wide confidence bands and are thus rather uncertain. In particular the energy dependence has been modified significantly since the original work by [812]. Therefore in figure 69, the D retention rate is re-computed using both the original [812] and the new model in [847]. In general the new scaling laws from [847] underestimate the retention by co-deposition in JET-ILW by a factor of 4–7 and yields almost an order of magnitude less retention for ITER compared to the original scaling law from [812]. The main reason for this difference is the reduced energy dependence of the D/Be-ratio in [847]. The new predictions based on the scaling laws in [847] seem to alleviate the challenge of co-deposition in ITER. However, large uncertainties remain for retention by co-deposition in ITER.

7.6.2. Modelling bulk retention.

7.6.2.1. Basic concepts. Rough estimates of the HI accumulation rate in the bulk of PFCs can be obtained by extrapolation of fluence dependences on the base of existing experimental data from laboratories and current fusion devices. However, operation conditions in ITER will be very different from current fusion devices and, as shown in the section 7.3.1 on the main processes involved in H inventory in W and Be, many factors may influence HI behaviour. An advanced prediction can be done using so-called *rate equation modelling* (or diffusion-trapping models) describing HI transport in the bulk of PFCs, HI implantation and release, generation of radiation induced lattice defects, and HI interaction with these defects.

The method is rather straightforward, and general equations can be found, for example, in [821, 910, 911]. The HI transport is described by the Fick's second law with an additional source of particles due to implantation and a sink to trapping sites. In parallel, the heat transfer equation should be solved to provide the temperature distribution in the material. Several kinds of trapping sites corresponding to different lattice defects (vacancy, dislocations, etc) are introduced by providing trapping and de-trapping rates. The dynamic production of traps due to ion and neutron bombardment can be also included like in [912].

7.6.2.2. Determining material input parameters. Diffusion trapping codes require a large number of input parameters, which should be either experimentally measured or theoretically calculated. A discussion of reliable experimental data can be found in [813, 913]. Due to the low HI solubility in W and Be, experimental data for basic transport parameters are strongly affected by presence of defects. Surface oxidation is an additional issue in the case of Be. Therefore, a very limited number of experiments provides an adequate data. *Ab initio* calculations using the DFT provide the most confident theoretical data for HI diffusion barriers and HI interaction with defects. The results for Be are reviewed, for example, in [914], and in [915] for W. The DFT predicted diffusivities for the HI in W and Be are generally higher than the experimental data. This may be due to the influence of defects even for the most accurate data, as it was shown in [916] for W. The influence of existing uncertainties in the HI diffusivity in W on predictions of global T retention was considered in [917], where it was shown that the T accumulation rate can be 2–3 times higher when using the values calculated by DFT.

7.6.2.3. Predictions for ITER. The most general prediction for tritium retention in ITER with different configurations of PFMs was done by Roth *et al* [624]. A small rate of T accumulation in the bulk of W divertor plates was obtained in these calculations, providing the administrative 700 g T limit after 5000 400 s ITER discharges, as a maximum, including the effect of neutrons. However, many simplifying assumptions were used for this analysis. In particular, a 1D model was used with constant PFC temperature excluding transient events. An expected reduction of the T accumulation rate due to presence of He impurities in the plasma was later included in the modelling presented in [832]. In reality, PFCs in ITER have a complex 3D shape with strong temperature gradients due to active cooling. In addition, transient events with different time scales will occur and the surface layer will be significantly modified under plasma irradiation. It is very difficult to simultaneously take into account all these effects due to an enormous growth of the computational cost and a variety of possible plasma operation regimes, but some efforts to estimate their influence have been done.

7.6.2.4. Transient events. Different transient events are expected in ITER. Firstly, slow ramp-up and ramp-down processes are unavoidable. Continuous (10 000 s) and cycled plasma (100 s ramp-up, 400 s steady-state, a 100 s ramp-down and 1000 s waiting phase) irradiation were compared in [918]. Only some local deviations in the dynamics of HI retention during transients have been observed, but there were no remarkable differences in the long term fluence dependence of the HI retention.

During fast transient events, such as ELMs, there is an increased ion incident flux to the surface, but the surface temperature also increases, leading to an increased D release. The effect of ELMs has been analysed for JET conditions in [919, 920]. According to these simulations, the surface temperature increased by only about 100 K during ELMs and the total D retention was reduced in comparison to calculations of the base plasma load. Interestingly, the recycling coefficient was also almost unaffected and was close to $R \approx 1$ even during the ELMs. An advanced modelling including defect dynamics in [920], demonstrated that the temperature increase during the ELMs leads to agglomeration of defects and an enhanced concentration of complex defects with a higher binding energy in the surface layer.

However, the heat load and particle fluxes during the ELMs in ITER will be larger than in JET. In such conditions, their effects on the HI retention can be more serious. As discussed in section 7.3.1, the experiments in the QSPA-T facility [921] demonstrated a substantial HI retention in W after powerful pulsed plasma irradiation (1 ms, 0.4–3.7 MJ m^{-2}). According to modelling of these data, an increased temperature of the surface layer strongly accelerates HI diffusion and HI can reach the depth up to tens of microns after one pulse already. The high particle flux to the surface during the pulse lead to the significant HI accumulation rate even at very high surface temperature up to melting. Thus, the effect of ELMs may strongly depend on their characteristics and should be analysed in more details.

7.6.2.5. 2D/3D modelling. 2D simulations of HI retention in W MBs with the ITER geometry have been performed in [911, 922, 923] using the code FESTIM. Comparison with 1D simulations at various irradiation conditions demonstrated differences in the range of 20%–95% [911]. An inhomogeneous temperature distribution in the MB and desorption from toroidal edges in 2D geometry are the main sources of the difference with 1D simulations. The temporal evolution of HI inventory was close to the square root dependence in a wide range of parameters in both 1D and 2D cases.

2D calculations need much more computational time, however, using a parametric approach [923], it was possible to make an estimation for the HI retention in the full W divertor taking into account different particle and heat fluxes on each MB. The predicted total HI inventory after 107 s was only 8 g, neglecting saturation effects this would allow for 25 ITER discharges of 400 s before hitting the T inventory limit of 750 g. The maximum of the HI retention was shifted by 5 cm from the SP in the poloidal direction. To simplify the calculations the trap parameters remained fixed, in reality a time evolution of the trap parameters could influence the results.

7.6.2.6. Multiple occupation of traps and boundary conditions/subsurface layer. DFT calculations predict trapping of several hydrogen atoms in a single vacancy [915] and, therefore, the possibility of multiple occupation of traps is introduced now in codes [924, 925]. For single isotope experiments no qualitative difference to the classic single occupancy picture can be found. However, for multiple isotopes, the fill level dependence of the de-trapping energies predicted by the DFT calculations needs to be taken into account. This requires a different trapping model which describes the coupling between the different fill levels [924]. Only then the experimentally observed low temperature isotope exchange, where the standard model predicts no exchange, can be modelled.

Modification of the subsurface layer due to high plasma irradiation and implantation of various impurities is a very complex process, and it is impossible to include all possible effects in the modelling. Therefore, the simplest assumptions are often used and the HI concentration at the surface is usually fixed to zero that is reasonable in many cases [813].

Fortunately, many effects demonstrate a decreased HI accumulation rate in comparison to standard assumptions due to reduction of the HI diffusion flux into the bulk. This is the case for the presence of He and Ne impurities in the plasma [826, 829] and HHF plasma irradiation of Be [837], as discussed in 7.3.1. An increase of the trapping sites concentration in the thin subsurface layer does not contribute significantly in the total retention. This was demonstrated, for example, in [849], where formation of the so-called supersaturated layer was implemented in the modelling.

7.7. Conclusions and outlook

During the design and construction of ITER, the T inventory in the vessel has had a major impact, driving many important design decisions with respect to PFMs, choice of impurity seeding species and design of the T handling facility. Foremost among these was the decision to remove carbon-based PFMs from the machine entirely, but also the recently considered change from a Be-based main chamber armour to an all-Tungsten machine was partly motivated by the much reduced T retention without continuous Be co-deposition.

With co-deposition virtually eliminated, T retention in ITER is now mainly due to bulk retention of HI by implantation, diffusion and trapping in lattice defects. As discussed in section 7.3.1, this process does not contribute significantly to the total fuel inventory in current fusion devices and is not expected to do so for ITER. However, because of the much higher levels of neutron radiation damage, He induced defects and higher T fluence expected over the longer lifetime of a fusion reactor, the study of this mechanism and its consequences remains an important R&D issue. Although the modelling of T-retention processes has made significant progress, as discussed in section 7.6, the reliability of the predictions depends heavily on an improved data base for code validation. While some of this research can be carried out using proxy defect generation processes, it ultimately requires the availability of irradiation facilities for 14 MeV fusion neutrons such as IFMIF/EVEDA [926], IFMIF-DONES [927] or dedicated tokamak devices as volumetric neutron sources [928].

Finally, the prospect of ITER operation with a full-W FW has introduced a new issue, as boronisation may be required for wall conditioning, which could have a significant impact on T retention. This has motivated further R&D on this topic within the ITPA.

On the diagnostic side, monitoring of T retention in ITER will continue to be essential, firstly to comply with radiation safety regulations, and secondly to optimise the use of the limited amount of T fuel available.

8. Evolution of PFMs under sustained plasma exposure

8.1. Introduction

As part of the DIVSOL ITPA activities, since the implementation of the ITER physics basis [2] and the design of the ITER plasma-facing components [12], major changes have been made in the choice of materials for ITER, including the exclusive use of tungsten in the divertor [14]. In this section, we therefore seek to elaborate the consequences of these choices and the additional understanding gained for the long-term use of the new material mix under high fluence plasma exposure, and to identify gaps in the current knowledge base.

The structure of this section is as follows: We start with an introduction 8.1, followed by three subsections on studies based on laboratory studies 8.2, on work on fusion devices 8.3 and on modelling 8.4. Implications and open issues are discussed in the summary 8.5.

For the discussion in this section, a range of exposure conditions needs to be taken into account with brief references included where overview and review materials already exist. For an introduction to the material issues in fusion with respect to material parameters, the main challenges have already been elaborated in detail in [929], with figure 70 giving a rough overview of the synergistic loading conditions. Please take note that when discussing loading condition also the cooling conditions of the tested materials play a significant role—with either actively cooled setups or inertially cooled samples or components, for the latter temperature evolution is only defined by thermal mass, radiation while for the active cooling heat is removed.

ITER will be one of the first facilities to truly expose materials not only to high steady-state and transient thermal loads, hydrogen and helium bombardment, but also to 14 MeV neutrons, placing high demands on the selection of PFMs and the manufacture of actively cooled components with long expected lifetimes. ITER, as all long pulse devices, needs actively cooled components in contrast with inertially cooled components which were still used in a majority of tokamaks at the time of the release of [2]. Operating actively cooled PFC has been pioneered with carbon PFC in Tore Supra, and is now being explored in superconducting devices such as WEST, EAST, KSTAR in W as well as W7-X in carbon.

With this in mind, further discussion in this section will focus on the issues arising from synergistic effects such as high thermal loads under plasma exposure or simultaneous thermal and neutron wall loads as summarised in [929]. An overview of the ITER PFCs and the established design of the FW and divertor is given in section 1 and figure 1. The main focus of this

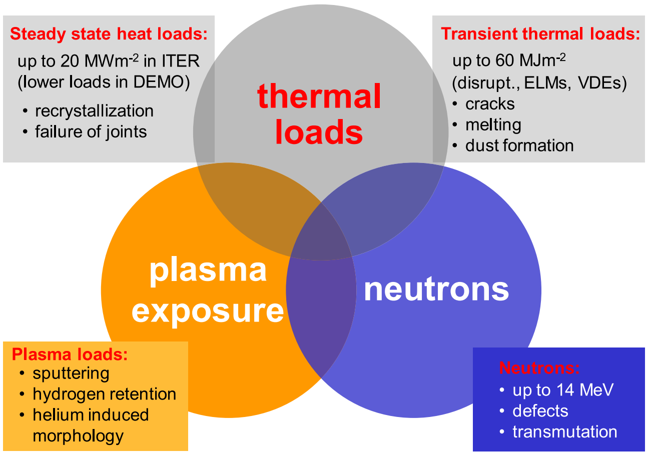

Figure 70. Synergistic loads and their main consequences for the first wall armour in thermo-nuclear (DT) operation of magnetic confinement devices. Reproduced from [929]. CC BY 4.0.

section is on tungsten materials, with references to e.g. beryllium where appropriate.

8.1.1. Materials. Materials are one of the major challenges for the operation of ITER and any future fusion device [930]. Initially, the PFC material selection strategy for ITER, as described in [12], included an all-beryllium FW, together with divertor targets that would have used both CFC and tungsten in the high power regions in a stepwise approach eventually changing to all tungsten. Since the release of [2] a full tungsten divertor is now the baseline option and a full tungsten wall has been chosen.

This material combination was subsequently modified by removing carbon due to its unacceptably high fuel retention (see discussion in section 7) and updating the HHF divertor area to a full tungsten design [14]. Tungsten was always considered for the later phase of operation, as it was clear that carbon in particular would have limitations in the nuclear phase, e.g. thermal conductivity reduction [929].

The successful high power operation of AUG with an all tungsten wall [931, 932] showed a clear path towards an all metal, all tungsten reactor for power generation. Nevertheless detailed consideration on the issues of PFC material evolution as discussed here are were still to be dealt with.

For an overview of considerations on the use of tungsten before and after the 2013 decision [14] see [628, 933] and [934–937] respectively. Since then, research on material damage resulting from HHF and high fluence exposure has focused mainly on tungsten. For a review of related results and conclusions drawn in support of the ITER full W divertor see [15].

In parallel, issues related to beryllium as FW material were also addressed. With regard to the engineering challenges and the development of the ITER blanket system and divertor, the wide range of challenges and solutions are discussed in detail in [938–940].

For a summary on the topic of the beryllium FW, recent work can be found in [679], focusing mainly on erosion and retention issues, while a summary of the overall ITER blanket design challenge can be found in [941]. In particular, lifetime issues [942] due to erosion and melting are challenges that have been addressed in recent years (see section 6) as well as the issue of HHF performance [943] and melting (see section 9). More recently, a critical re-evaluation of the ITER design baseline led to the proposal to abandon beryllium and to redesign the FW of the main vessel with tungsten armour. The R&D issues arising from this new approach are outside the scope of this review and will not be discussed here.

8.1.1.1. ILW project. In the years leading up to the publication of the 2007 PIPB, a decision was taken to upgrade the Joint European Torus to address many of the issues of ITER, and here in particular the materials issues arising from beryllium and tungsten as plasma cladding materials were highlighted [793]. Therefore, the work carried out under the ILW project are highly relevant also to the discussions the section on retention (see section 7), erosion (see section 6) and melting (see section 9).

8.1.2. Synergistic loads. When considering synergies between thermal loads and plasma exposure, plasma-induced processes—such as blister or bubble formation, hydrogen embrittlement, and the growth of He nano-bubble layers or fuzz on plasma-exposed surfaces—must be taken into account, as they adversely affect resistance to intense thermal loads. For details, particularly on PWI and synergistic loads, see [929, 944], where an in-depth analysis of the response of tungsten (W) materials to plasma particle and thermal loads is presented, with a particular focus on the relevant processes in the ITER divertor, characterised by high fluxes of low-energy particles and resulting elevated surface temperatures. Their analysis reveals various effects such as changes in surface morphology, changes in mechanical and thermal properties, and damage induced by thermal shocks. Specific conditions under which phenomena such as blistering and fuzz formation are likely to occur are identified, and their implications for ITER operation are discussed.

The following discussions in this section focus on the synergistic interplay between thermal loads and neutron effects on material performance. Neutron-induced phenomena—such as decreased thermal conductivity, embrittlement and an increase in the ductile-to-brittle transition temperature but also material transmutation—critically influence the thermomechanical performance of wall components at HHF under both steady-state conditions and during high-power transient loads. The third synergistic interaction, involving the combined effects of plasma exposure and neutron damage, is not explored in detail here. Future research will need to focus particularly on understanding mechanisms such as hydrogen and helium trapping in neutron-induced defects, as well as the formation and implications of transmutation products in these contexts.

8.1.2.1. Power loads. In ITER, the divertor is exposed to a HHF from the edge plasma with typical loads around 10 MW m^{-2} for nominal operation (5000 cycles) as well as

20 MW m^{-2} for slow transients (10 s with a limited number of 300 cycles [15]. Under these HHF conditions, the temperature gradient from the plasma-exposed surfaces of the HHF components to the coolant channels can become very large, e.g. of the order of 10^6 K m^{-1} for tungsten with a thermal conductivity of 100 W m^{-1} K^{-1} (value at a temperature around 1000 °C) [16, 935].

For the agreed design [16], it is still a challenge to keep the power loads on the divertor surfaces within tolerable limits with respect to the parallel power loads expected for unmitigated Type I ELM loads in ITER, which are given in [370]. For some additional details on surface heat loads, see [398] where a detailed discussion on the effect of shaping on the heat load distribution can be found, including also specific issues of the exposure of PFC edges to power loads, which can lead to overheating and melting.

For the main chamber FW armour made of beryllium grade S-65 (S-65 has the lowest impurity levels of commonly made grades of beryllium, which reduces the amount of transuranic elements, so that the material needs less storage time after being removed from reactors), there are two types of FW panels, depending on the expected steady-state heat loads. A *normal* heat flux design capable of withstanding up to 2 MW m^{-2} and an *enhanced* heat flux design capable of withstanding up to 4.7 MW m^{-2} are employed [679]. Modelling of the FW heat loads due to ELMs has shown that controlled ELMs in ITER during burning plasma operation ($\Delta W_{\mathrm{ELM}} \approx 0.6$ MJ) will not lead to melting or significant evaporation of the beryllium surfaces [945]. For transient events such as edge-localised modes, these transient power fluxes rise to 1 GW m^{-2} for a duration of typically 0.5–0.75 ms in the divertor region, and a significant fraction of this power flux is also expected to be deposited on the FW.

As a consequence of these results, the issue of surface protection has also gained considerable importance. This mainly concerns the PFC on the FW and the divertor. For the FW the main loading condition arise in part during startup, where the default start-up configuration for ITER prioritises the inner wall LIM plasma ramp-up, with power fluxes on the shaped beryllium FWP being particularly sensitive to misalignments between the central column and the TF. Depending on the shaping parameters, the current alignment requirement may result in power fluxes exceeding the inner wall's capacity. To address this, a reduced alignment target is proposed, though challenges persist even with this adjustment. Ensuring proper shaping through precise alignment control is essential for maintaining flexibility in current ramp-up scenarios. Additionally, detailed analysis of coil locking and TF, along with a comprehensive TF mapping diagnostic using NMR sensors, will guide shaping efforts during assembly and operation phases, supported by metrology data for accurate alignment adjustments [946].

With respect to the divertor ITER's plasma-facing component design has advanced significantly, with a particular focus on shaping to control power loads. The integration of shaping into the divertor concept has reached a mature stage, allowing for remote handling replacement and addressing the challenges of transient and steady-state loads. This shaping design, informed by comprehensive heat load specifications, draws from the latest understanding of plasma physics. However, the magnitude of energy deposition during transient events poses a significant challenge, surpassing the capability of any shaping design or material to ensure component lifetime. Thus, reliable schemes for ELM control and disruption mitigation are imperative. The eventual transition to a full-W divertor underscores the importance of robust shaping strategies for edge misalignment protection. Moreover, careful consideration of materials like beryllium, especially in high PWI areas such as the secondary divertor, is crucial for erosion lifetime and tritium retention [12, 14, 16].

8.1.2.2. Plasma particle loads. In addition to the power loads, one of the main drivers for changes in the exposed materials is the exposure to high fluence plasma particle loads such as the fuel isotopes (D, T), the He ash fraction, as well as residual impurities (e.g. C, O) and intentionally introduced impurities for wall conditioning (B) and power load reduction (e.g. N, Ne, Ar, …). Boronisation, although not originally envisaged for the original Be/W wall, is now being considered for wall conditioning in ITER following the decision to go for an all-W FW.

An important consideration is that the particle fluence for ITER and beyond will be orders of magnitude higher than in current facilities, and will therefore introduce new effects on plasma-facing materials. For expected quantitative fluence values, see [944] and figure 71.

Studies of the interaction of the FW and the divertor with the plasma are grouped under the term PWI [703] and have been studied both in linear plasma devices and in tokamaks and stellarators. The understanding of the actual plasma conditions is derived from modelling and scaling experiments based on e.g. JET, AUG and JT-60U as well as WEST, EAST and DIII-D. Typical divertor particle fluxes are given in [16] at some 10^{23} m^{-2} s^{-1}, details of the divertor plasma conditions are discussed in section 2 Scrape-off-layer and divertor transport.

8.1.2.3. Neutron irradiation. The production of He in a burning D/T plasma is accompanied by the production of neutrons, which strike the materials facing the plasma. The neutrons create collision cascades within the lattice, leaving defects in the material. The measure of the damage caused by the collision cascades is called displacement per atom (dpa). One of the main differences between ITER and future DEMO-like devices is the much higher neutron fluence to the components of the FW and the divertor. It is well established for ITER [819] that the displacement damage will not cause any relevant engineering limits for the divertor and the FW, since even at the end of life the expected transmutation and embrittlement are insignificant, due to the predicted damage being well below 1 dpa for the divertor [819]. There is currently no high-flux fusion neutron source available (IFMIF-DONES under construction [950]), so researchers have used a variety

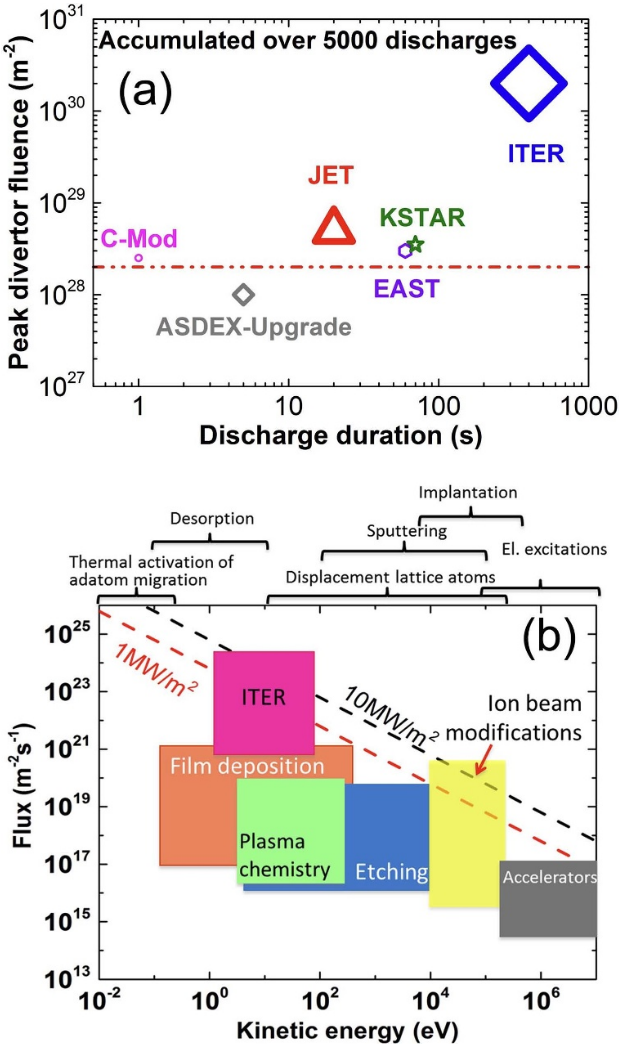

Figure 71. (*a*) Comparison of the ion fluence to the divertor for three different devices calculated for 5000 typical plasma discharges. Symbol size is proportional to the device size. Horizontal dashed line indicates the highest ion fluence reported from a laboratory experiment [947]. (*b*) Typical experimental conditions for various ion-assisted processing techniques; also indicated are the typical conditions expected at the ITER divertor vertical target. © 2018, The ITER Organization [944]. This image is hereby used courtesy of the ITER Organization. Reproduced with permission from [948]. Copyright [2011], by the AVS. Reproduced with permission from [949]. Copyright [1984], by the AVS.

of techniques to simulate the expected damage, such as W self-damage [951] and proton irradiation [952]. Such issues have been part of the assessment of both the divertor materials [953] and the FW [954]. In particular, the use of unalloyed tungsten, as in ITER, has been studied using irradiation with fission neutrons [955]. The known effects of irradiation in W, again based on experiments using irradiation with fission neutrons, are void swelling, hardening ductility degradation, a shift in the DBTT [956] and a decrease in thermal conductivity [957]. More recently, the latter has also been reproduced for W dislocation damage typical of 14 MeV fusion neutrons induced by MeV ion bombardment [958].

8.2. Laboratory experiments under well controlled conditions

For the investigation of long-term plasma exposure effects when using beryllium or tungsten as PFMs, linear plasma devices provide a unique opportunity by allowing plasma exposure at high fluxes and fluences. In recent years, many devices have been used to study the effects relevant to the ITER FW and divertor. A detailed overview of the test facilities is given in [959]. Due to the high toxicity of beryllium, related studies have been performed in a dedicated facility, PISCES-B [677], with studies also addressing mixed material issues [716, 960, 961]. For the study of neutron irradiated samples, the JULE-PSI facility is currently being commissioned [962]. In addition, Japanese linear plasma facilities have pioneered the study of tungsten fuzz, as discussed below.

8.2.1. PFMs under high sustained and transient thermal loads. Linear plasma devices and electron beams, as well as lasers, have been extensively used to study the impact of different transient effects on tungsten and beryllium. Cracking and the evolution of crack networks have been identified as one of the major issues when considering the lifetime of components for ITER, as it is not yet clear how these might evolve under relevant operating conditions and how this might affect the operation of the FW and the divertor in the long term.

Tests under ITER-relevant conditions, combining high fluence and high cycle number transient loading of ITER-like MBs, were performed in Magnum-PSI [702, 963]. These showed that fatigue cracking is expected to be a problem in ITER, especially when approaching ITER lifetime-integrated levels of particle fluence, and that understanding the extent to which this effect can be tolerated is essential for predicting divertor lifetime and reliability [963]. Apart from the singular load case, also synergistic loading conditions, i.e. the combined loading by sustained plasma heat load and transients were investigated [964–967].

To gain a more detailed understanding of the damage induced by repeated transients, various studies have been carried out, focusing in particular on the issue of high cycle numbers [968] and the shape of the transients [369, 969–971]. Overall, it was found that there is no clear damage threshold with respect to the size of the transients, as in almost all cases the fatigue damage increases with high cycles, leading to cracking and subsequent local melting, even for transients below the cracking threshold found for single transients for tungsten [968]. The typical cracking threshold is below 0.55 GW m^{-2} which is significantly below the value for an unmitigated ITER ELM (2 GW m^{-2} [419]).

In ITER, the issue of transient heat fluxes is not limited to the divertor, but is also a potential problem for the main chamber FW. In particular, recent electron beam experiments have revealed further details of the behaviour beyond what was known at the start of the ITER project. ITER-qualified S-65 beryllium has been subjected to up to 10^7 transient heat pulses [972–977]. A strong decrease of the melting threshold was observed during the experiments due to fatigue effects, with damage saturation after 10^5 pulses [973].

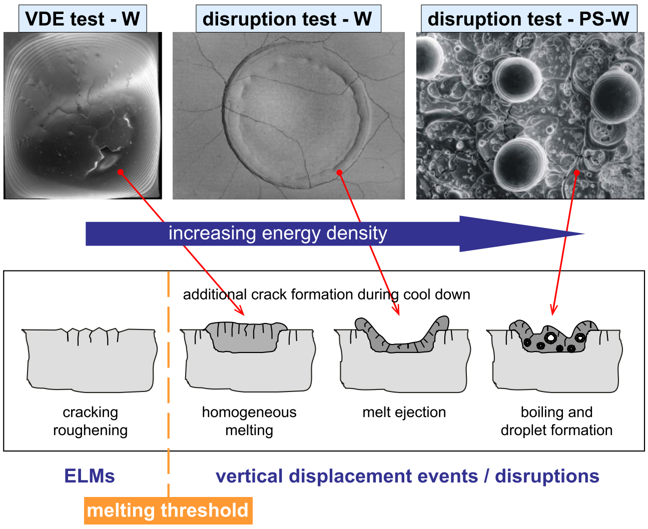

Figure 72. Schematic representation of the degradation of tungsten-based armour tiles with increasing transient thermal loads below and above the melting threshold [978]. The top row shows photographs of test samples exposed to off-normal events that could occur in ITER if appropriate mitigation techniques are not applied. Reproduced from [929]. CC BY 4.0.

8.2.1.1. Cracking. On of the most concerning issues for use of tungsten as a PFM in ITER is its behaviour under power load transients with respect to cracking. Much of the experimental history and recent results are summarised in [929]. Therefore, only the highlights and conclusions are summarised below.

The typical damage progression of tungsten under increasing power load is shown in figure 72, starting with cracking and ending with deep melting. For melting related damage processes see section 9 PFC damage by excessive heat loads.

In an attempt to understand what damage can be expected in terms of crack development under repeated transient power loading such as ELM exposure, studies of the resilience of different PFMs to ELM-like heat fluxes have been carried out using systematic thermal loading tests in electron beam and laser beam experiments [979]. Typical damage thresholds and damage maps have been generated with an example shown in figure 73.

In general, cracking due to fatigue damage is an almost universal phenomenon so that apart from limiting exposure, no material can overcome this problem, especially at high cycle numbers, as discussed in detail in [968, 981–983]. Based on these publications (see [929]), it is evident that for devices of ITER size and beyond, transient heat fluxes must be drastically reduced. To prevent component failure caused by high-cycle fatigue damage due to frequent ELMs, the heat flux factor should not exceed 6 $\mathrm{MW\,s^{1/2}\,m^{-2}}$. The heat flux factor, defined as the product of power density and the square root of the pulse duration Δt, is motivated by the temperature increase of a semi-infinite body under a constant heat load.

A significant limitation of these findings is that they do not yet incorporate the synergistic effects of combined hydrogen fuel, helium and neutron bombardment, which remain an area of active investigation.

Additionally, thermally induced surface damage of the FW armour, such as cracking or grain boundary separation, could compromise the safe operation of a fusion device. Deep cracks, in particular, can significantly affect the transfer of heat from the plasma-facing surface to the heat sink. Cracks that develop perpendicular to the thermal gradient in the armour material are especially problematic, as they severely impair heat transport, potentially leading to isolated hot spots that may exceed tungsten's melting point.

Facilities such as GLADIS have also played an important role in the study of whole plasma-facing components [984]. The capabilities of this and similar facilities have been used in particular by the European Materials Programme [936, 985]. For an overview of the test facilities used in this collaboration see [959].

8.2.1.2. Recrystallisation. A major factor affecting the lifetime of the W divertor components in ITER is the potential degradation of the thermo-mechanical performance of tungsten under cyclic high steady state heat loading conditions due to recrystallisation. It was found that the original tungsten material specification for the W MBs delivered to ITER did not sufficiently take into account that cyclic transients can lead to a variety of crack behaviours [986]. The macro-cracks observed in the MBs after cyclic loading tests varied between different suppliers, although they all met the ITER material specification. The main property that appeared to affect the HHF test performance was the resistance to recrystallisation in terms of recrystallisation temperature. The actual value of the recrystallisation temperature depends on the initial state of the material and its entire processing history, e.g. the initial grain size, the plastic strain achieved during deformation and, not least, the annealing time span applied [987]. With the aim of improving the material specification for tungsten, several tungsten materials have been subjected to a material characterisation programme [988] to potentially include the hardness in the specifications of the material [988] in relation to recrystallisation. Recrystallisation kinetics were studied in particular detail to understand the synergistic effects of temperature, thermal loading and other effects [987, 989, 990]. In addition, the relationship between the presence of helium and hydrogen in the material and the recrystallisation behaviour has been studied. For the hydrogen fuel isotopes no definitive effects could be observed [991], with some indications for changes in recrystallisation kinetics [992], whereas helium seems to be able to cause retarded recrystallisation [993].

8.2.2. Evolution of material properties due to plasma ion exposure. Plasma-facing surfaces are simultaneously exposed to both heat and particle fluxes. Well-controlled experiments in linear plasma devices have been conducted to investigate the effects of the associated PSIs in fusion devices. This section briefly presents the results of these studies and the implications of these effects for ITER plasma-facing materials. In particular, we discuss changes in surface morphology due to plasma irradiation, which depend mainly

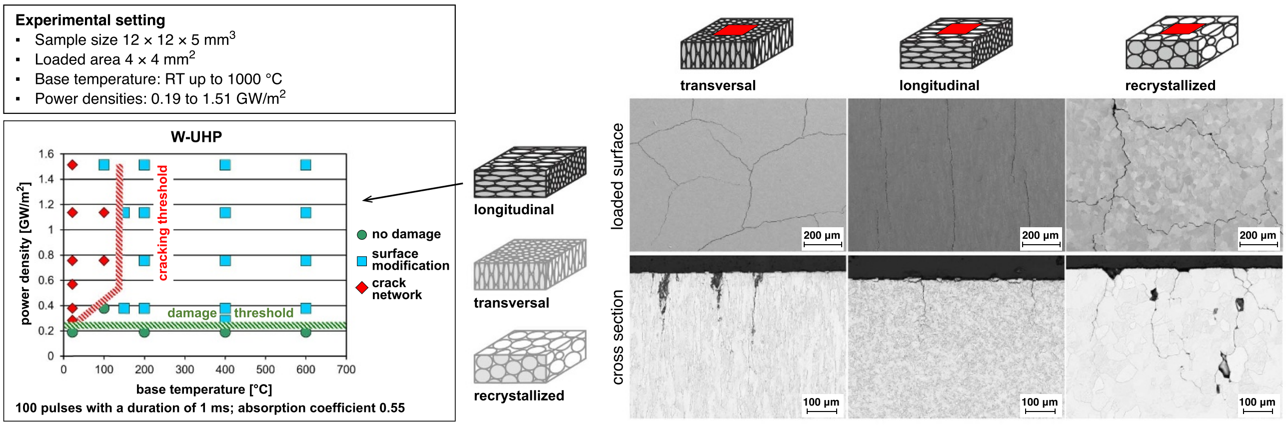

(a) (b)

Figure 73. (*a*) Generation of a typical damage map for an ultra-high purity tungsten grade with longitudinal grain orientation under intense transient thermal loading applied at the JUDITH 1 electron beam test facility. Each data point represents a single test sample exposed to 100 electron beam pulses at different base temperatures and power densities (green circles, no damage; blue squares, surface modifications; red diamonds, crack network)) (*b*) Micrographs taken by scanning electron microscopy (top row) and after metallographic sectioning by optical microscopy (bottom row) on tungsten test samples exposed to a particular load scenario plotted in the damage map in (*a*). The three different test samples (transverse, longitudinal and recrystallised) were exposed to 100 repeated electron beam pulses under identical conditions: a power density level of 0.38 GW m^{-2}($F_{\mathrm{HF}} = 12$ MW s$^{1/2}$ m^{-2}) and a base temperature of room temperature [980]. Reproduced from [929]. CC BY 4.0. Reprinted from [980], Copyright (2017), with permission from Elsevier.

on the amount of implanted ions and the surface temperature. These include blistering and the formation of tungsten nano-structures and beryllium cone-like structures. In addition, embrittlement related to recrystallisation as described in section 8.2.1.2 and its suppression is discussed here. Finally, the effect of changes in surface morphology on material loss is also discussed.

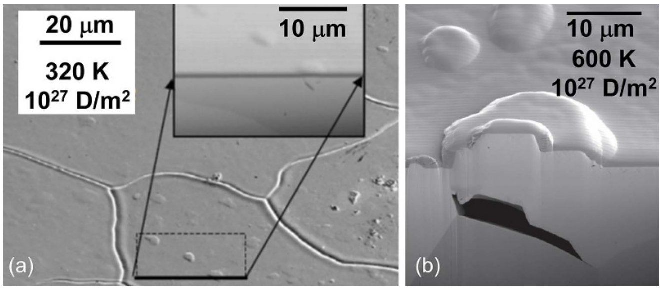

Figure 74. Tungsten surfaces exposed to a D fluence of 10^{27} m^{-2} at 320 K (*a*) and 600 K (*b*). The inserts in (*a*) show the cross-section through one of the sparse blisters. In (*b*), the cross-section is also shown. A focused ion beam was employed for the cross-sectioning with a Pt–C film coating for protection. Reproduced from [994]. © IOP Publishing Ltd. All rights reserved.

8.2.2.1. Blistering. A *blister* on a metal surface is a surface morphological modification caused by atoms of a gaseous element such as HIs and helium implanted in the surface. The implanted atoms locally aggregate at grain boundaries and/or vacancies, and the surface layer rises due to the local high pressure, forming the blister. The blisters can take two forms: shallow blisters with thin dome caps (figure 74(*a*)) and large irregularly shaped blisters with much deeper gas-filled cavities beneath (figure 74(*b*)). The shallow blisters form below the DBTT as gas atoms agglomerate at near-surface defects and plastically deform the tungsten at the surface, causing it to rise. The large irregular blisters form at temperatures above the DBTT when gas atoms accumulate at much deeper lattice defects or grain boundaries, causing the large volume of tungsten above the gas-filled void to relax the stress by dislocations moving along lattice planes through the crystalline grain [994].

The conditions for blistering by HIs have been studied for tungsten and summarised in [933, 934]. The formation of blisters on a target is determined by the competition between the flux of ions impinging on the surface and the diffusion of corresponding atoms in the bulk of the target. Experiments on blistering have been carried out in linear plasma devices, which showed that blistering occurs even with ions impinging at low energies such as 7 eV [995]. The experiments also showed that blistering disappears above a threshold temperature, which depends itself on the ion flux [996–999]. The roughness of the material exposed can play a significant role when studying blistering on industrial surfaces.

Suppression of blister formation has been observed in D/He [1000], D/Be [1001] or D/Ne [1002] mixed plasmas. This is attributed to a reduced hydrogen retention due to the deposited or implanted impurity species. On the other hand, increased blister formation was observed in D/C [1003] or D/N [831, 834, 991] mixed plasmas where hydrogen retention is increased compared to pure hydrogen plasmas. Suppression of blistering has also been observed on rough surfaces produced by mechanical polishing and subsequent chemical etching [1004, 1005].

The appearance of blistering was found to depend not only on the plasma conditions and composition, but also on the grain orientation of the material [801, 1006]. The most and least pronounced blistering was observed on grains with [111] and [001] orientations, respectively. A possible mechanism for

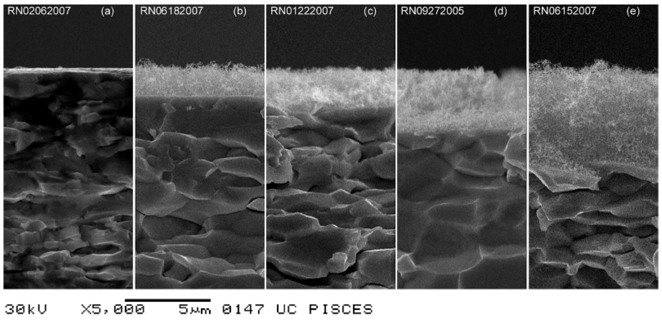

Figure 75. Cross-sectional SEM images of tungsten targets exposed to pure He plasma at 1120 K for exposure times from (*a*) 300 s to (*e*) 22 000 s with a He flux of (4–6) × 10^{22} m^{-2} s^{-1}. Reproduced from [1008]. © 2008 IAEA, Vienna. All rights reserved.

this effect is the orientation dependence of the plastic deformation coefficient of tungsten, which results in the [111] surface layer being more easily deformed by the gas pressure [1007].

8.2.2.2. He induced damage and modification of surface morphology of tungsten. Following the publication of the 2007 PIPB, dedicated research has been carried out into the effects of helium on the material properties of tungsten. Helium induces damage such as helium bubbles and changes in surface morphology such as fibrous nano-structures called *fuzz*. These strongly influence erosion and fuel retention properties. The impact of helium plasma exposure on plasma-facing materials is a crucial issue, firstly because He, as a product of the DT fusion reactions, is an inevitable plasma species in a thermonuclear plasma, and secondly because dedicated helium plasma experiments were part of the originally foreseen early non-nuclear experimental campaigns of ITER.

Helium is a unique element due to its high mobility and high binding energy of helium defect structures in metals. Because of this, implanted He atoms strongly affect the near-surface properties of tungsten plasma-facing components, such as surface morphology. The most drastic change in surface morphology induced by He irradiation is the formation of the fibrous *fuzz* nanostructure shown in figure 75 [1008], discovered in 2006 [1009]. Helium bubble formation is the dominant cause of the change in surface morphology and also affects fuel retention. This section summarises the understanding of the effects of helium plasma irradiation on tungsten gained from experiments with linear plasma devices.

Figure 75 shows the operational regions in terms of surface temperature and incident ion energy where bubble formation and nanostructure formation (fuzz) have been observed in helium plasma experiments conducted in NAGDIS-II and PISCES-B [1010]. Helium ion incidence energy, ion flux, ion fluence and surface temperature have been studied to find the conditions under which these helium-induced effects are relevant. Typically, the impact energy of helium ions on a material sample in linear plasma experiments is well below the threshold energy for displacement damage in tungsten of ≈0.5 keV. Nevertheless, it has been observed that bubbles and voids are produced by an incident low energy helium flux.

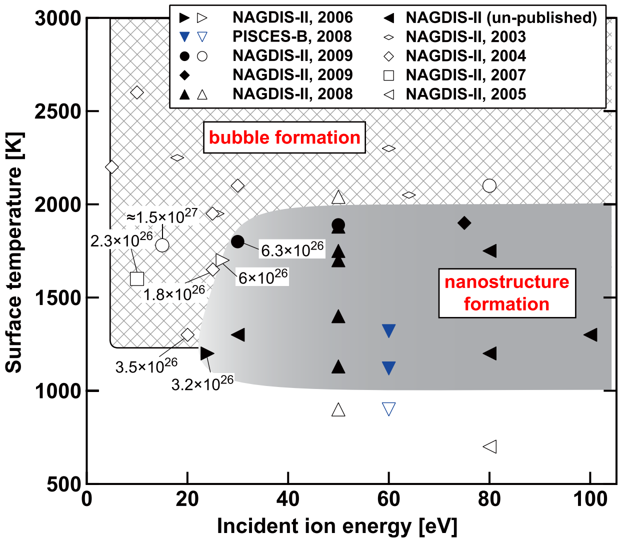

Figure 76. Surface temperature versus incident energy parameter space of fuzz formation in the NAGDIS-II and PISCES-B helium plasma experiments. Reproduced from [1010]. © 2009 IAEA, Vienna. All rights reserved.

The threshold energy for bubble formation is approximately 5 eV at a tungsten surface temperature of 2200 K. [1011]. This energy corresponds to the surface barrier potential of a helium atom to penetrate tungsten, with values obtained e.g. from first-principles calculations [1011, 1012]. This experimental result suggests that bubbles are formed when helium atoms penetrate a tungsten surface at a sufficiently high temperature. Helium atoms can be trapped by vacancies, where they become precursors of helium bubbles. Vacancies are not created by displacements at the low impact energy of helium, but exist naturally and can also be created thermally if the surface temperature of the tungsten is high enough. In addition, a process called *trap mutation* can occur when implanted helium atoms cluster together at interstitial sites within the tungsten lattice and eventually achieve sufficient pressure to eject the tungsten atom from its normal lattice position [1013].

In the higher impact energy range of about 20 eV at a surface temperature higher than 900–1000 K, W-fuzz is formed at helium ion fluences above about 10^{25} m^{-2}. [1008, 1010]. Microscopic analysis by TEM has shown that helium bubbles are present in each fibre [1014, 1015]. As shown in figure 75, the thickness of the fuzz increases with time proportional to the square root of the plasma exposure time, suggesting that the growth is dominated by a diffusion-like process under the same conditions of ion flux and surface temperature [1008]. The growth is also enhanced by further increasing the W surface temperature [1008], although no W fuzz is formed in the temperature range above 2000 K as shown in figure 76. [1010]. It has been confirmed that W fuzz is also formed in D-He mixed plasma exposure, suggesting that ionised deuterium does not affect the formation mechanism [1016].

On the other hand, it has been observed that existing fuzz is annealed or reintegrated into the bulk when the surface temperature rises above 1600–2000 K. [970, 1017–1019]. Annealing of fuzz is also observed without sufficient or any helium ion flux even in the temperature range of fuzz formation [1016, 1020]. The helium ion flux threshold for the transition between fuzz growth and annealing is not sharp, but has been observed to be in the range of 10^{21}–10^{22} $\mathrm{m}^{-2}\,\mathrm{s}^{-1}$ [1020]. Changes in the microstructure of the fuzz as a function of temperature under vacuum conditions were studied using an in-situ TEM [1021]. In this experiment, the fuzz structure changed drastically and many helium bubbles in the fuzz disappeared at 1273 K, where at the same time strong helium desorption was observed.

Because of the drastically altered surface morphology, the physical properties of tungsten fuzz, such as physical sputtering and thermal conductivity, are different from bulk tungsten with a smooth surface. Physical sputtering of the fuzz was investigated using argon plasma exposure and a significant reduction in sputtering yield up to 10%–20% of the yield of a smooth surface was observed [1022, 1023]. This effect diminished with exposure time and the sputtering yield returned to the value for a smooth surface. This is attributed to the reduction of porosity by the sputtering process itself. Regarding the thermal conductivity of the fuzz, the large porosity leads to a lower thermal conductivity in the fuzz compared to that of a smooth surface, with the reduction depending on the porosity of the fuzz [1020, 1024].

Based on the above experimental results, a growth/annealing equilibrium model for the fuzz, including the changes in sputtering and thermal conductivity with the thickness of the fuzz layer, was proposed and applied to the expected conditions at the tungsten divertor target in ITER under H-mode burning plasma conditions with attenuated type I ELMs [730]. It is worth noting that there is a narrow operational window for W fuzz to occur on the ITER divertor, resulting in a potential narrow region to be affected. Experiments in various tokamaks were performed, showing the complex interplay between fuzz formation and erosion by ELMs/impurities etc in tokamak conditions compared to linear devices see section 8.3

The results show that the fuzz is annealed by the ELM-induced heating, and an equilibrium thickness determined by the inter-ELM growth and annealing during the ELMs exists depending on the conditions of the ELMs, although the thickness of the fuzz increases with the discharge time in the case of no ELMs. It should be noted that this study does not include the effect of impurities which may lead to increased erosion of the fuzz.

Some of the most consequential changes that can occur during He plasma exposure are a change in the surface thermal conductivity making it more difficult to handle the extreme heat flux associated with controlled fusion confinement devices, embrittlement of the surface due to the presence of He atoms making transient heat loads more likely to result in surface cracking and morphology changes to the surface. Any modification to the originally designed surface has the potential to alter the loss rate of material from the plasma-facing component which could adversely affect the confinement properties of the core plasma, therefore, it is essential to have an accurate picture of how the plasma and its surrounding material interact [1025].

The formation of fuzz-like structures by helium irradiation has also been observed in metals other than tungsten such as molybdenum and rhenium [1026–1028]. Experimental results on fuzz formation in several metals point to the influence of surface temperature, helium mobility, and shear modulus on the nanostructure formation mechanism [1026]. To investigate the material transport during bubble and fuzz growth, plasma exposure of molybdenum (or tungsten) thin film (35–135 nm) on tungsten (or molybdenum) bulk substrate was conducted [1029, 1030]. The result shows that if the conditions for fuzz formation in one material are met, fuzz is formed including both materials. For example, in the case of a molybdenum thin film on bulk tungsten at 838 K, a molybdenum and tungsten mixture fuzz is formed, though the temperature is too low for pure tungsten fuzz growth. With elevating the surface temperature, the degree of the mixture increased. This result suggests that fuzz grows by material transport from the bubble layer in the bulk to the fibre tips by diffusion of punched dislocation loops in the bulk toward the fuzz base followed by diffusion of ad-atoms along the fuzz base and fibre surface, with effective transport of ad-atoms upwards due to trapping of ad-atoms at curved fibre tips and/or due to a gradient in ad-atom concentration along the length of fibres [1030]. The observed fuzz height or thickness is at most a few microns with a few hours of plasma irradiation, but in the presence of impurities in the helium plasma or simultaneous tungsten deposition on a tungsten target, nano-fibre structures much larger than the fuzz have been observed, and the related studies were reviewed in [726]. Isolated fibre form structures, called NTB (figure 77(*a*)), are formed instead of dense structures like fuzz in experiments where the incident He energy is modulated by the application of a high-frequency potential [1031] or when the operating gas contains impurities such as carbon, nitrogen, neon, and argon in addition to helium. In low energy (300 eV) helium ion beam experiments, the addition of 0.01% carbon suppressed fuzz formation and NTBs were observed [1032]. In helium plasma experiments, NTBs have been observed with the addition of a few to 10% nitrogen, neon, and argon [1033]. The surface temperature at which NTBs are formed is 870–1220 K in the modulated helium ion energy case and 1400–1600 K in the case of plasma exposure. In experiments in which tungsten is deposited simultaneously with helium plasma irradiation to form co-deposited layers, it has been observed that LFN (figure 77(*b*)) of several millimetres in size is formed at a growth rate about two orders of magnitude faster than fuzz [1034, 1035]. The temperature range of the LFN growth is higher than 1100 K, and the minimum temperature is higher than that of fuzz. A sufficient supply of additional tungsten is also necessary for the growth of LFN [1034, 1035].

Effects of low-energy helium plasma irradiation on tungsten surface morphology at the temperatures below the temperature threshold of fuzz formation have been investigated in the PSI-2 device [1036]. With helium plasma irradiation in which the ion impinging energy is less than the threshold energy of physical sputtering, a nanoscale undulating surface structure having a periodic arrangement is formed with a height of approximately 8 nm. The formation of the structure depends on the crystal grain orientation, and it has been pointed out in [1028] that this can relate to the morphology change in

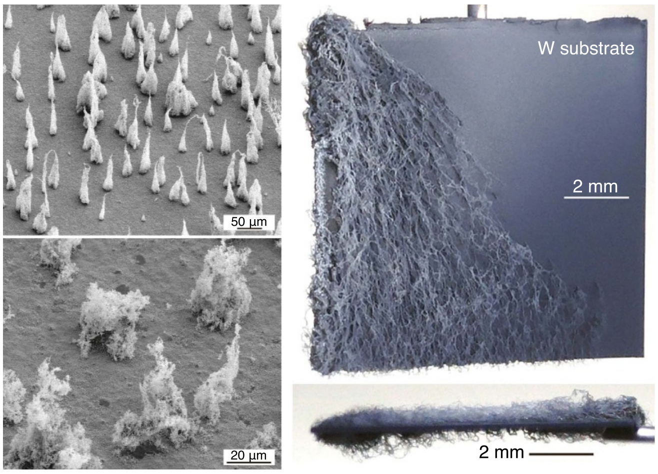

a) b)

Figure 77. (*a*) Nano tendril bundles, (*b*) Large-scale fibre-form nanostructure generated in NAGDIS-II. Reprinted from [726], Copyright (2020), with permission from Elsevier.

the initial phase of the fuzz growth in which the orientation dependence has been observed [1037, 1038].

8.2.2.3. Embrittlement of tungsten. When using tungsten as PFM, its operational window to prevent defects related to unfavourable thermo-mechanical properties such as low-temperature brittleness, high DBTT and recrystallisation embrittlement needs to be considered [1039] as discussed in more detail in section 8.2.1.2. In the case of plasma exposure, the effects of HIs and helium particle loads also must be taken into account. One of the effects of corresponding particle loads is hydrogen-induced embrittlement which lowers the critical stress thresholds for crack formation and propagation [1040, 1041]. Furthermore, surface embrittlement caused by plasma exposure can generate dust by exfoliation, which may also shorten the lifetime of W plasma-facing components. It has been observed, however, that under helium irradiation tungsten recrystallisation is retarded in both ion beam experiments with an impact energy range from 10 keV to 50 MeV [1042–1045] and in plasma exposure experiments with an impact energy range of 25–60 eV [993, 1046, 1047]. The retarding effect occurs even at low helium concentrations such as $(1–2) \times 10^{-5}$ in the ion beam experiments. At a such low density of helium, helium clusters could retard grain boundary migration by the impurity drag effect of the clusters [1044]. In the case of helium plasma irradiation, the effect has been observed above an ion fluence of $10^{24}\,\mathrm{m}^{-2}$ without significant variation in the fluence range from $3 \times 10^{24}\,\mathrm{m}^{-2}$ to $1 \times 10^{25}\,\mathrm{m}^{-2}$. The retarding effect is larger at 573 K than at 1073 K. This can be attributed to the slower grain boundary migration by Zener drag, which is inversely proportional to helium nano-bubble radius and proportional to the volume fraction of helium nano-bubbles. The saturation of the retarding effect with increasing ion fluence is attributed to the saturation of helium nano-bubble formation at high ion fluence above $10^{23}\,\mathrm{m}^{-2}$ [1046]. It should also be noted that there is no significant retarding effect by hydrogen plasma exposure [1048].

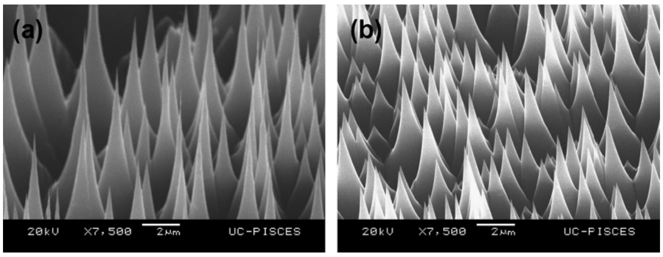

Figure 78. Cone-like structure formed on Be as a result of (*a*) deuterium plasma and (*b*) helium plasma exposure. Reprinted from [1052], Copyright (2014), with permission from Elsevier.

8.2.2.4. Roughness of beryllium induced by ion irradiation. Initially smooth plasma-facing material surfaces can be roughened by ion and neutral atom bombardment from the plasma. One such case is the fuzz formation on tungsten surfaces due to helium ion irradiation discussed above in section 8.2.2.2. For beryllium, formation of grassy cone-like structures is observed (figure 78), caused by both HIs and/or helium ion irradiation in ion beam [1049] and plasma [686] experiments at ion fluence values larger than $\approx 10^{24}\,\mathrm{m}^{-2}$ [837] below a surface temperature of 573 K [1050]. The height of the cone-like features is up to a few μm, and increases at constant fluence with increasing incident ion energy. However, once the structure is formed, no more significant morphology changes occur if the fluence is increased further [1051].

The effective sputtering yield for Be surfaces with cone-like structures are reduced compared to yields computed by SDTRIM.SP [687, 688] with the assumption of a smooth surface. However, irradiation with heavier impurity species such as argon does not lead to formation of such structures and the experimental sputtering rates are in this case consistent with SDTRIM.SP results [1051]. Although the mechanism of the cone-like structure formation is not necessarily clear, it is thought to be the growth of randomly existing bumps on the surface due to the angular dependence of the sputtering yield [1052]. As the sample temperature increases, cone-like structures do not form because of the correspondingly increasing mobility of the atoms [1052]. The effect of deuterium ion irradiation at relatively high temperatures up to about 773 K on the Be surface is similar to that observed in high-energy low-fluence ion beam experiments, where pores appear on the surface. Their depth is deeper than the range of the ions and the porous region has been observed to become deeper with increasing fluence with many damage sites growing together and interconnect [960].

8.2.2.5. Effects of surface modifications on the erosion of W and Be. The erosion of tungsten and beryllium by the plasma ion and atom bombardment is discussed in section 6 Erosion of PFCs and impurity migration. Here we discuss additional erosion processes and connected effects linked to the nano structure surface modifications discussed above.

For shallow blisters, once the local pressure exceeds the critical stress of the material, the blister ruptures with ejected debris contributing to material erosion and dust generation [1053, 1054]. The reduced effective sputtering yield of nano structures such as tungsten fuzz and beryllium cone-like structures has been explained as a result of the deposition of sputtered atoms on adjacent fuzz [1022] or cone-like structures [1052]. However, as discussed in [726, 944], the decrease of thermal conductivity by the fuzz formation can lead to significantly increased erosion due to initiation of arcing, enhanced vaporisation and melting.

8.3. Experiments in fusion devices

Before the large scale introduction of tungsten as PFM replacing low-Z elements, dedicated experiments to study its suitability were carried out using exposure of W samples in specific discharges (see for example [628]), however, studies of the long term behaviour of W PFCs under realistic exposure conditions became only possible when tokamak devices began to install W PFCs. AUG completed its transformation to all W PFCs [630, 792] in 2007, initially using W VPS coatings in the divertor, but finally switching to bulk W divertor target plates [1055]. Alcator C-Mod operated from 2007–2008 with one full toroidal row of bulk tungsten tiles in the HHF area of the lower outer divertor [1056]. In JET, with the ILW project starting in 2011, bulk W as well as W coated PFCs were installed in the divertor whereas in the main chamber bulk Be as well as Be and W coatings were used [648, 1057]. With that, JET became the only fusion device where the behaviour of Be PFCs could be studied. EAST installed an actively cooled W upper divertor in 2014 [1058] and finally also moved to a full actively cooled W lower divertor in 2021 [795]. Finally Tore Supra was converted from an all carbon LIM device to the all W divertor device WEST in 2017 [1059]. Initially, the WEST lower divertor included a mix of ITER grade actively cooled bulk tungsten components and inertially cooled W coated components. Since 2021/2022, WEST is equipped with a full ITER grade actively cooled W lower divertor [1059].

8.3.1. Effects of power loads. In all devices with metal PFCs, surface damage by thermal overloading of bulk PFCs is an issue. Specifically, LEs facing the full parallel power flux of the edge plasma are prone to melting, but even below the melting point of the used metals, both micro and macro cracking is observed. To study the behaviour of so pre-damaged surfaces under further plasma loading, dedicated experiments were performed. In this subsection results related to micro- and macro-cracking will be discussed along with dust production and effects of sustained exposure of pre-damaged PFCs. Melting and vaporisation processes are discussed in detail in section 9.

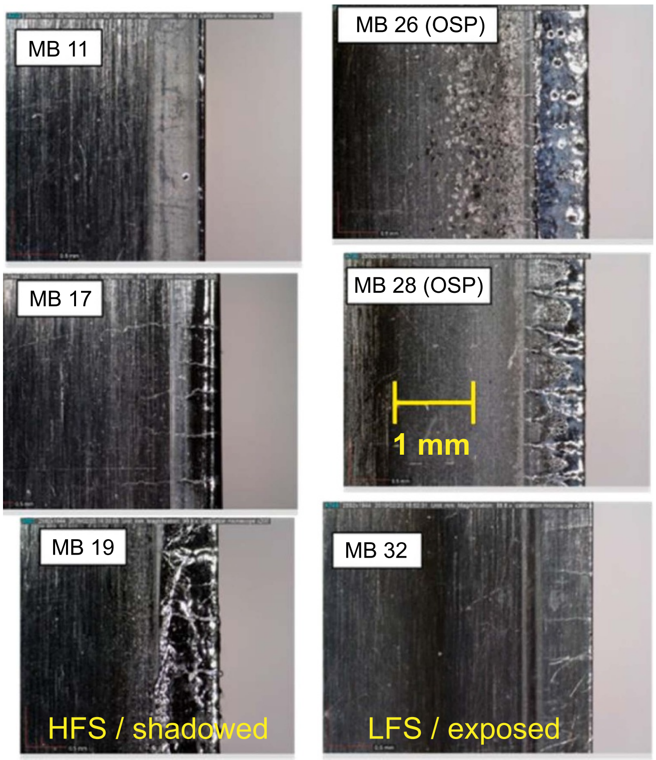

Figure 79. Post exposure photographs of monoblocks retrieved after a WEST campaign with visible cracks (mostly vertical) and deformation. The 0.8 mm wide discoloured band at the side surfaces of the monoblocks corresponds to an intentionally introduced misalignment of the plasma facing unit (PFU) with respect to its neighbour. Reprinted from [1060], Copyright (2021), with permission from Elsevier.

8.3.1.1. Micro-cracking. In the WEST tokamak, actively cooled unshaped ITER-like divertor targets consisting of tungsten MBs were installed for the 2018 experimental campaign and operated at moderate peak power loads ($\leqslant 2.5\,\mathrm{MW\,m^{-2}}$) [755, 1060].

Inspections after the campaign revealed a wide variety of small scale damage (cracking, deformation and melting) at both leading and trailing MB edges and at the end points of magnetic field lines passing between toroidal gaps between MBs onto the poloidal LEs of the adjacent downstream MBs. The typical damage patterns with micro-cracks and surface deformations due to an intentional misalignment of 0.8 mm are shown in figure 79. Modelling of the MB thermo-mechanical response suggest that the cracks are due to brittle fracture attributed to disruptions with MBs being still below the DBTT [1061].

For unprotected LEs, micro cracking is expected to occur from the cooling phase following transients, in particular for *cold* MB below DBTT. This should be avoided by using shaping to protect LEs, provided the stringent alignment specifications between neighbouring PFU are met (0.3 mm maximum misalignment). It should be noted however that given the transient loads expected in ITER, the same micro cracking phenomena could occur on the top surface, in contrast with WEST. In part this cannot be avoided in ITER, and is expected to cause local melting at every ELM in particular [1060].

In EAST, the upper divertor was equipped with actively cooled W PFCS in 2014 [937] and finally the lower divertor in 2021 [1062, 1063]. Due to LEs of the W mono-blocks at the upper divertor PFCS caused by initial assembly tolerances and EM force during operation, edge melting and micro-cracks developed, with a similar appearance to those in WEST [1064]. Whereas operation of EAST was partially hampered by droplets of molten W, which fell into the plasma causing high radiation and strong cooling of the plasma, no direct impact of the micro-cracks was observed. The locations of the damaged mono-blocks were strongly correlated with the position of the SP and the number of cracked W mono-block PFUs increased from campaign to campaign finally reaching 28 at the inner divertor and 40 at the outer divertor target after the 2019 campaign. Recent microstructural investigation confirmed that the cracks are concentrated on the LE of the mono-blocks [1065]. The maximum crack depth was observed to be up to 2.4 mm and with increased absorbed heat flux, the crack width was getting wider. The crack propagation mode is intergranular and extends from the recrystallised region to the area with initial grain structure.

8.3.1.2. Macro-cracking. Besides superficial micro-crack networks, macroscopic cracks were observed in AUG on a large fraction of the bulk-W outer divertor target tiles [1066]. This particular behaviour could be traced back to the specific situation in AUG with large (≈20 cm vertical extent) W tiles held only at two points at the lower and upper edges. Because of that, substantial stresses can be induced by electromagnetic forces (during disruptions) as well as thermo-mechanical forces, creating a cyclic loading pattern in successive discharges. As remedies for the avoidance of these deep cracks, a reduction of the toroidal dimension (splitting into two narrower tiles [1066]) and alternatively the use of a more ductile W heavy alloys [1067] were successfully applied.

Besides actively cooled mono-blocks EAST is also using actively cooled W/Cu bevelled flat tile components in the newly installed lower divertor [1063]. In post-mortem inspections severe melting and even delamination of edge-bevelled W plates on the W/Cu flat-type PFCs was found at the horizontal targets. Due to the larger inclination angle, the bevelled area receives about three times the power load compared to the flat part of the plasma facing unit. Obviously, the cyclic loading led to cracking in the W/CuCrZr joint leading to a reduced heat removal capability. Consequently, this led to strong overheating of the W armour, resulting in macro-cracking, melting or even complete detachment [1068]. All of the defected components of the horizontal targets had to be replaced after the experimental campaign [1063].

8.3.1.3. Effects of pre-damaged PFCs. Specific experiments with pre-damaged tiles were performed using the divertor manipulator (DIM-II) in AUG [743] for exposure under well defined loading conditions. For this purpose TZM-tiles were exposed in GLADIS (to simulate a slow transient thermal overload) and JUDITH (to simulate crack damage by cyclic fast transients) up to surface melting. The so prepared tiles were then exposed in a series of identical AUG Type-I ELM H-mode discharges with substantial local power deposition [1069]. Post-exposure analysis showed that no significant progression of the initial damage structures had occurred. In another experiment, pre-damaged actively cooled W-MB targets were exposed in WEST [1070]. The damage, which was produced in the JUDITH facility, ranged from light roughening and small cracks over stronger roughening with a crack network up to melt droplets. Similar to the behaviour in AUG, none of these damage types showed a significant deterioration under the power load conditions prevailing during the exposure in WEST with $P_{\mathrm{surf}} < 0.4\,\mathrm{MW\,m^{-2}}$ [1071]. For further studies of damaged components self-castellated W MB are being exposed to WEST.

8.3.1.4. Dust production. The microscopic damage of PFCs created by high power, high fluence plasma exposure will also lead to dust formation, e.g. by melt droplet ejection during fast transients, exfoliation of deposited layers, grain losses due micro- and macro-cracking, fuzz release and electrical arcing. Although the transition to all-metal PFC devices led to a large reduction of the overall dust formation rate, models of dust formation during long term operation of next step devices still predict accumulation of hundreds of kilograms of metallic dust in the vacuum vessel over time [1072]. Presently, dust mostly plays a subordinate role during the operation of magnetic fusion devices, but mobilised dust originating from high-Z PFCs can negatively impact plasma performance. In addition, activated and tritiated dust could pose a serious safety risk in ITER and future nuclear devices in the case of air ingress into the vacuum chamber and the subsequent mobilisation of dust inventories. It is therefore important to identify the dust sources, quantify their production rate and characterise their morphology and migration properties. A recent review on activities related to dust in present day fusion is presented in [1073], aiming at quantitative predictions for ITER and fusion power plants. In this respect production and release conditions such as arcing and cracking with the subsequent delamination of surface layers as well as dust grain size and velocity distributions are important input parameters. The still limited information available on these parameters and the difficulty to assess them in present day fusion devices, has motivated accompanying experiments in laboratory devices.

After the transition to full W PFCs in AUG, dust was collected in five consecutive experimental campaigns (2007–2011) on installed sets of Si witness samples, by filtered vacuum sampling and with adhesive tapes (2009) [1074]. The majority of the ≈50 000 analysed particles (2009 campaign) contain tungsten and show basically two appearances: spheroids and irregularly shaped particles. Most of the W-dominated spheroids consist of a solid W core, which indicates their origin as solidified W droplets. A fraction of these particles is coated with low-Z material. In addition, some conglomerates of B, C and W appear as spherical particles, which is attributed to plasma contact after their initial formation. Most of the particles classified as irregularly shaped particles consist of the same constituents with a varying fraction of embedded W in a B–C matrix and a porous morphology, which can exceed 50%. The fragile structures of many conglomerates hint at the absence of intensive plasma contact. Arcing is proposed as the main source of both the conglomerates and the spheres. The size distribution of the dust particles could be described by a log-normal distribution allowing extrapolation to the total dust volume and surface area. The maxima of these distributions are found for radii between 0.3 and 1 μm. From the amount of particles and their distribution the amount of W-containing dust produced during the 2009 campaign was extrapolated to be less than 300 mg. In a dedicated series of discharges, substrates prepared with adhered μm-sized dust grains were exposed in the outer divertor of ASDEX-Upgrade to ELMy H-mode discharges [1075]. The dust grains consisted of Be proxy elements (chromium, copper) and of refractory metals (tungsten, molybdenum) and were deposited on the plasma-facing and plasma-shadowed sides of the substrates as well as on the bottom of gaps. Interaction with time-averaged transient heat loads of up to 5 MW m^{-2} led to dust remobilisation, clustering, melting and droplet coagulation. It turned out that gaps efficiently trap adhered dust, but dust does not seem to preferentially move and collect inside the gaps. In accordance to theoretical expectations it was found that the remobilisation activity was higher for larger grains and dust clusters while no systematic dependency on the morphology and composition was observed. Clustering was identified for all dust species. Whereas cluster melting and subsequent coagulation were observed after exposure, no melting of isolated dust grains was seen.

First studies of dust collected in WEST after the second operational campaign with ≈1800 s of plasma could identify a low amount of W dust mainly in spherical form [850, 1076], most probably coming from off normal events such as disruption and runaway impact but these are not necessarily the same events as the ones impacting the divertor and causing the micro-cracks discussed in section 8.3.1.1.

JET in its ITER-Like Wall configuration with Be (main chamber) and W (divertor and main chamber) PFCs provided a unique opportunity for studies of dust generation relevant to ITER. Using a comprehensive set of complementary techniques, e.g. microscopy methods, electron and ion spectroscopy, liquid scintillography and thermal desorption the following results could be achieved [640]: the total amount of dust collected by vacuum cleaning after three campaigns is about 1–1.4 g per campaign with a total plasma operating time of 19.1–23.5 h, which is about 100 times lower than the dust accumulation rate in JET operated with carbon walls. Two major categories of Be dust were identified: flakes of co-deposits formed on PFCs and droplets with a diameter in the range from 2–10 μm. A smaller fraction, below 1 g of Be droplets and splashes are associated mainly with the melting of beryllium LIMs. Figure 80 shows some micrographs of typical Be deposits found in the divertor dust sampling carrier.

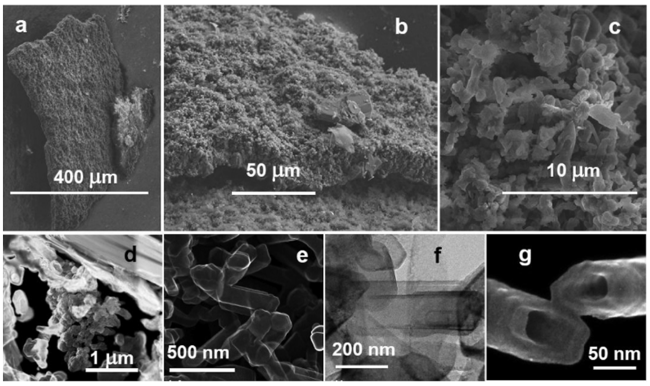

Figure 80. Dust in JET-ILW: thick Be deposits retrieved from the divertor carriers: (*a*)–(*c*) surface topography recorded by SEM and (*d*)–(*g*) internal structure recorded by STEM from the FIB-produced lamellae. Reprinted from [640], Copyright (2018), with permission from Elsevier.

Tungsten dust was identified mainly as partly molten flakes with their origin attributed to the W coated tiles of the vertical divertor targets, baffles and some highly loaded areas in the main chamber.

It must be noted that the source process of microscopic delamination of coatings will be absent in ITER as no coatings are being used.

In Alcator C-Mod, less than 1% of molten tungsten was found re-deposited on surfaces, the rest is assumed to have been converted to dust, e.g. by ejection of melt as droplets [1056]. Indeed, a subsequent detailed investigation of dust in Alcator C-Mod, revealed that W dust was mostly found as spheres or splashes with a rather large size (40–150 μm) indicating that they originated from accidental W melt damage processes [1077].

8.3.2. Surface modifications by H and He plasma exposures.

8.3.2.1. Surface modification by hydrogen irradiation. Blistering by hydrogen plasma exposure is regularly observed in lab devices but seldomly reported in fusion devices. Partly this is due to the fact, that on technical surfaces blisters are difficult to be identified. In AUG a polished W sample was exposed to 510 discharges in the campaign 2011 by using the divertor manipulator system. This exposure led to the formation of blisters with sizes, areal density and inner structures comparable to those found in laboratory experiments on polished W surfaces under similar exposure conditions. Only recently blistering has been observed by differential microscopy on technical surfaces in a lab experiment already after exposure to a rather low fluence of deuterium 1.5×10^{23} m^{-2} [1078], hinting to the fact the technical W surfaces in fusion devices will also undergo blistering. However, its role for macroscopic surface modification and dust production in present day fusion devices seems to be limited due to the rather low plasma fluence.

8.3.2.2. Fuzz formation. He plasma experiments have been performed in several fusion devices in order to investigate the production/behaviour of W fuzz under conditions typical for fusion plasmas, namely oblique magnetic field, high steady state and transient power load as well as plasma impurities. The main work on fuzz however is part of laboratory studies (see 8.2.2.2).

The general observation is that W fuzz growth is rarely observed and it seems that it appears in a rather narrow operational window in present day fusion devices. The most prominent example for fuzz formation was found in CMOD [1079]. The observed nano-tendril morphology and layer thickness was almost identical to the layers grown under similar conditions in the linear device Pilot-PSI [1080]. However, in an earlier experiment at the LIM of TEXTOR [725] no clear indication of W fuzz growth was found. At that time the authors concluded that probably the erosion rate under LIM plasma conditions was larger than the W-fuzz growth rate which was supported by the fact, that preformed W-fuzz exposed in a similar location was strongly eroded. More recently dedicated experiments were performed in AUG [728], DIII-D [1081], LHD [1082] and WEST [729].

In WEST a dedicated helium campaign was performed accumulating about 2000 s of repetitive L-mode discharges. Despite the fact that conditions for tungsten fuzz formation were met (see section 8.2.2.2) no visible signs of He-fuzz were observed at the inertially cooled tungsten divertor elements, indicating a complex interplay between W fuzz formation and erosion in tokamak conditions.

In a first experiment in AUG, samples with pre-made He-fuzz as well as polished W samples were exposed with the divertor manipulator to a series of He plasma discharges. However, instead of observing fuzz growth or erosion, the fuzz was buried under a deposited layer which consisted mainly out of boron [728], attributed to the high boron fraction in the plasma and low divertor electron temperatures favouring impurity deposition at the strike-point. In a second experiment with more optimised discharge conditions [1083], growth of W nano-structures but also erosion under *growing conditions* was observed in ELMy H-modes (see figure 6 in [1083]), whereas no W fuzz formation was seen in L-mode discharges, attributed to surface temperatures below the fuzz formation threshold.

In LHD, bulk tungsten samples were exposed at the divertor during long pulse helium discharges with 10 190 s total plasma time. The incident ion energy and total He fluence were 100–200 eV and $\approx 5 \times 10^{25}$ m^{-2}, respectively. The typical surface temperature was estimated to be in the range from 1900–2300 K. After exposure, analysis of PFC surfaces revealed an early stage of W-fuzz formation [1082].

In DIII-D experiments W fuzz growth was not observed, with pre-formed W fuzz surviving plasma exposure without significant changes of the exposed surface [1081] except for areas with arcs which appear to be more easily triggered on W-fuzz.

8.3.3. Migration. Work on migration is directly related to section 6 thus only brief mention on some of the effects is given here.

In Alcator C-Mod, which was equipped with a single toroidal row of W tiles at the strike-point in the outer divertor, results of W migration studies were published in [654]. As main areas of deposition originating from this defined source, the surface below the outer strike-point as well as around the inner strike-point were identified. Towards the entrance of the outer as well as of the inner divertor the W deposition decreased significantly. The deposition pattern at the outer divertor could be explained by REDEP/WBC code simulations as a superposition of local erosion and deposition [1084], pointing to a large fraction ($\approx$90%) of local redeposition.

In DIII-D, where two tungsten coated rings were installed similar to the first W-divertor in AUG [1085]. The long range migration of W was investigated in 25 repeated attached L-mode plasma discharges in the reverse-B_t configuration with the OSP located on the outboard tungsten ring. The modelling and analysis of these experiments were carried out using the ERO and ERO2.0 code. Besides the complex interaction with carbon erosion and co-deposition, the analysis and modelling of W deposition suggest that the W radial migration is mainly induced by $\mathbf{E} \times \mathbf{B}$ drifts outside of the sheath, similarly to long-range carbon radial transport in the outer divertor [1086]. Consequently, most of the eroded tungsten not locally redeposited migrates further away and redeposits predominantly in the far-SOL region.

In WEST, ERO2.0 simulations highlighted the lower and upper divertor, baffle and VDE protection as zones of W gross erosion/deposition with a typical flux of the order of 10^{19} m^{-2} s^{-1}. In particular, the lower divertor was found to be a region of adjacent net erosion/deposition zones with the strike lines identified as net erosion areas and surrounded by net deposition areas in both private and common flux region [633].

JET in its ILW offered unique conditions for migration studies close to those expected in ITER. During LIM discharges, the main fraction of eroded Be stays within the main chamber [637]. In the divertor configuration, the eroded Be is transported by SOL flows towards the inner divertor with net deposition of plasma impurity species. The amount of Be eroded at the FW (21 g) and the Be amount deposited in the inner divertor (28 g) are in fair agreement [637]. The primary impurity source in the JET-ILW is a factor of 5.3 smaller than that for JET with C-based PFCs, resulting in a lower divertor material deposition, by more than one order of magnitude. Within the divertor, Be is subject to far fewer re-erosion and transport steps than C due to the higher energetic threshold for Be sputtering. As a result its transport to the divertor floor and the pump duct entrance is negligible [637]. Since according to spectroscopy measurements and post exposure PFC surface analysis and confirmed by ERO1.0 modelling, the local redeposition of W in the divertor is 94% (experimental data) and >99% (modelling), respectively, no strong long range migration is observed [657]. The simulations predict that the small fraction of W not locally re-deposited escapes upstream to the SOL, and, for the JET geometry, to the outer corner region.

8.4. Modelling and simulation

For the modelling activities we highlight here the recent work on the shaping of the tungsten PFU MBs in the ITER divertor [1087], as the lifetime requirements of the divertor PFC were still a significant design and optimisation issue. It has been shown in [398, 1088] that a detailed study of the MB shape of the ITER target is essential to understand the actual loading conditions. In order to avoid excessive power loads on the toroidal gap edges and the formation of OHSs during ELMs, a redesign was carried out based on the analysis in [398, 1088], resulting in a MB geometry with a simple 0.5 mm toroidal chamfer, complemented where necessary by more complex planar toroidal-poloidal chamfer geometries.

The analysis of the design solutions also showed that in the inner divertor, even when a planar toroidal-poloidal bevel is applied to shadow the LEs, the orientation of the toroidal MB gaps relative to the magnetic flux surfaces still results in strong heat loads on geometrically shadowed MB edges and side faces by hot ELM-related ions, which can reach these areas due to the orientation and size of their gyration orbits. This leads to edge temperatures significantly higher than the top surface temperature, especially during ELM pulses. In contrast, the OT surface has a reverse orientation to the flux surfaces, so that both ions and electrons hit only the lower MB edges, allowing these corners to be fully protected by suitable shaping [1087].

A key finding from the analysis is the viability of a shallow toroidal-poloidal bevel, with a depth of 0.5 mm in both dimensions, as a compromise solution to improve overall heat handling at the OT. This configuration ensures full shadowing of the top toroidal edge, significantly mitigating edge heating during inter-ELM periods and limiting temperature spikes during ELMs to levels that do not exceed the top surface temperature. However, the reduction in ELM heating at the top edge comes at the cost of increased heating at the bottom edge, which, however, still remains within acceptable limits.

The effectiveness of the shallow toroidal-poloidal bevel shaping is closely related to maintaining sufficient accuracy of poloidal alignment between toroidally adjacent PFUs. The analysis in [1087] also ventures into the challenges posed by potential PFU poloidal misalignment and proposes as a solution the introduction of additional PFU variants, with the caveat of further increasing the complexity of the ITER divertor design.

Further, the feasibility of a deep toroidal-poloidal bevel is explored as a means to ensure comprehensive shadowing of the poloidal LE and the upper toroidal edge while also eliminating OHSs. Although this design variant offers significant advantages in thermal management, it necessitates an adjustment in the magnetic field line angle, leading to an increased heat flux and associated design challenges.

The decision on the optimal shaping strategy involves a careful consideration of the trade-offs between mitigating extreme ELM heating and OHS formation against the backdrop of increased main surface loading. Despite the complexities involved, the findings suggest a balanced approach, where edge ELM heating remains within manageable levels, albeit requiring precise poloidal alignment. The complexity of implementing a refined shaping strategy at the OT, coupled with the inability to address ELM-induced edge overload at the IT, informs the decision towards adopting a simpler toroidal bevel design for the first ITER divertor vertical targets.

In addition to this work tests of actual components in WEST highlighted the progress in understanding heat loading and damage mechanisms of components for ITER. Here the results presented in [1089] is summarised. In the WEST tokamak's initial experimental campaigns (phases I and II, C1-C7), a comprehensive evaluation was conducted on ITER-grade Plasma-Facing Units (PFUs) and tungsten (W) blocks to understand their performance under various plasma conditions. This assessment covered different block geometries (shaped and unshaped) and assembly configurations, including vertical and radial misalignments. High spatial resolution infrared (IR) imaging (0.1 mm per pixel) was utilised to measure temperature and heat load distributions across individual blocks, requiring sophisticated photonic modelling to account for the complex, highly reflective thermal scene. Specular reflections were predominantly observed in toroidal gaps, trailing edges, and chamfered surfaces.

Interestingly, OHSs, expected in ITER due to plasma impacts on PFU poloidal edges through toroidal gaps, were not detected in-situ. This absence was attributed to their location in magnetically shadowed areas, not directly exposed to plasma, with the current heat load conditions in WEST ($\approx 6\,\mathrm{MW\,m^{-2}}$ on the MB's top surface) being insufficient to raise the thermal signature of OHS above the IR detection threshold (typically 300 °C).

Various damage mechanisms to tungsten were identified based on heat load exposure. Misaligned/unshaped PFUs within specified assembly tolerances showed regularly spaced cracking on LEs, with crack patterns consistent with brittle failure due to transient heat loads simulated using the TREX code [1090]. Additionally, ductile failure was observed, with crack formation on the LE directly detected under extremely high power loads, highlighting the impact of tungsten recrystallisation.

Post-mortem analysis of unshaped blocks generally showed no evidence of cracking, except for a pre-damaged block that exhibited a micro-crack network pattern, where exposure in WEST led to the broadening of cracks and the formation of new ones. This study, alongside ongoing post-mortem activities and future experimental campaigns, aims to further elucidate the behaviour of ITER-grade PFUs under various plasma and heat load conditions, contributing valuable insights into their durability and performance.

Regarding the understanding of cracking and recrystallisation further modelling was undertaken [1061, 1091].

When analysing the simultaneous effects of recrystallisation and recovery on the softening of tungsten during high-temperature annealing (1450 °C–1800 °C) various parameters involved in these processes for two types of tungsten were assessed. A mean field model is utilised to predict the evolution of grain radius and dislocation density, incorporating factors like grain-boundary migration and static recovery. This approach allows for a quantitative analysis of recrystallisation and recovery, as confirmed by hardness reduction and EBSD techniques, highlighting significant discrepancies between softening and recrystallisation kinetics as previously noted by Richou *et al* [1092].

The study compares two tungsten types, A and B, revealing initial dislocation densities and assessing their recovery parameters, which vary with temperature. An Arrhenius analysis indicates an apparent activation energy close to 391 kJ/mol for both types. EBSD maps facilitate the identification of initial grain distributions, showing differences in median and standard deviation between types A and B, particularly in not recrystallised grains.

Recrystallisation and softening kinetics were reliably predicted at various temperatures for both tungsten types. The findings suggest that material softening can outpace recrystallisation, allowing for full softening even when only partially recrystallised. This study enhances understanding of the competition between softening and recrystallisation, with implications for optimising tungsten's microstructure and improving the lifetime of tungsten-armoured plasma-facing components. The mean field model's parameters are now set for further exploration of the effects of mobility, recovery activation energies, dislocation density, and initial grain size distributions on tungsten's annealing behaviour. Future work could leverage this model to define ideal tungsten microstructures for plasma-facing applications.

8.5. Summary and outlook

The evolution of PFMs and their properties under sustained plasma exposure can be summarised in terms of the synergistic effects on the materials as outlined in figure 81. However final answers to the magnitude and relevance of some of these effects still remain open. As part of the work performed within the ITPA DivSOL various issues of importance have been identified as part of the activities related to the ITER Research Plan—here various priority items with relevance to the operation of PFCs have been identified and partly addressed by the ITPA DivSOL.

8.5.1. Remaining issues and open questions. For improved assessment of the properties and evolution properties of PFMs under sustained plasma exposure, the following open issues require further detailed studies, particularly with the planned change of the ITER design to a full-W FW:

8.5.1.1. He plasma modification of W mechanical properties at high fluencies. Experiments performed with He plasmas e.g. at JET, WEST and AUG [898, 1083], still cannot reach the He fluence range expected during an originally planned extended He campaign in the non-nuclear ITER operation phase. However, the fluence due to He ashes in DT phases is still presumably significantly above what was achieved in tokamaks so far. Partly work on linear machines has filled in the gap but more dedicated studies on the evolution of W mechanical properties under He exposure are required extending the currently investigated He fluence range.

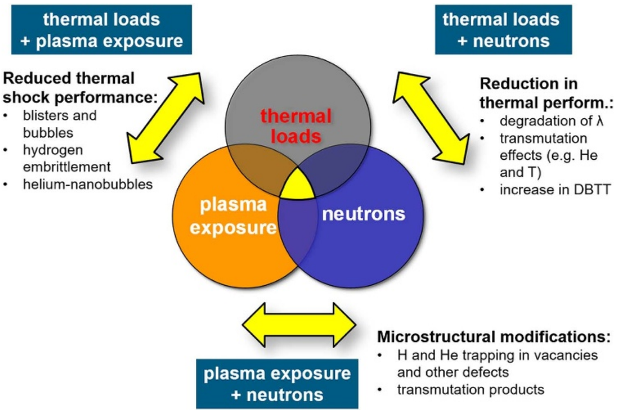

Figure 81. Synergistic loading scenarios and important parameters with a strong impact on performance and lifetime of PFCs in future fusion reactors. Reproduced from [929]. CC BY 4.0.

8.5.1.2. Formation of fuzz by He exposure of W and critical fuzz thickness. This issue was initially investigated mainly by exposure of W PFCs to He plasmas in linear devices. Therefore, regarding W-fuzz production under tokamak divertor conditions there are still open questions with respect to a possible saturation of fuzz growth and long term consequences on plasma operation and dust formation. After the detailed discussion in [730], further experimental studies were carried out, by exposure of the innermost W divertor lamella stack at JET to a dedicated He campaign and by exposure of dedicated W samples to series of He plasma discharges in AUG [1083] with subsequent surface analysis of the retrieved samples. Interpretative modelling of the AUG experiments is still ongoing whereas for the analysis of the JET experiment, retrieved PFCs will only become available in the next years in the frame of the decommissioning activity at JET.

8.5.1.3. Power flux to castellated PFCs. With respect to utilisation of PFCs in ITER it is crucial to understand that due to the shaping and castellation of the PFCs power flux can reach both top surfaces and side surfaces, while previous studies concentrated on loads on the top PFSs. Hence work is ongoing to determine the power fluxes to castellated structures in stationary plasmas and during ELMs over a range of conditions and to identify dominant physics processes. This work is performed in tokamaks such as COMPASS [1093], AUG [1094] and WEST [1060] as well as on linear devices such as Magnum-PSI [1095] and complemented with modelling [1087, 1088].

8.5.1.4. Tolerable W damage on surface and macro-brush edges for tokamak operation. This topic is among the most difficult to assess and at the same time the most urgent issue. It aims to experimentally determine the type and severity of edge, surface and bulk damage on divertor PFC subcomponents such as mono-blocks and how these damage types might affect tokamak operation. Early related work is summarised in [929]. For results from more recent and ongoing studies see [1069–1071] for AUG and WEST. Further experiments in HHF test facilities such as Judith [968, 980, 981, 988] and GLADIS [1096, 1097] aimed at elucidating the general impact of cracking on the lifetime of the W-divertor. However, a coherent set of criteria for the evaluation of PFC thermo-mechanical ageing and the prediction of ITER divertor lifetime is still not available and requires further dedicated experiments and validation of involved modelling codes.

8.5.1.5. W operation above recrystallisation and implications for tokamak operation. With respect to recrystallisation it is essential to understand the evolution of W divertor material properties after sustained operation above the recrystallisation temperature and assess possible synergistic effects with plasma exposure and consequences for tokamak operation. Here work both on tokamaks and linear plasma devices is ongoing [265, 988, 1089, 1091]. Looking forward to DEMO or a Fusion Power Plant it also has been stated [1098–1100] that careful design can overcome most issues with tungsten recrystallisation.

8.5.1.6. W surface modification by high plasma fluence exposure and implications for tokamak operation. As discussed in [702] as well as in the overview above, the modification of W PFC surfaces by plasma exposure to ITER-like fluences at relevant power flux may have consequences for tokamak operation and operational boundary conditions. Relevant results are expected from ongoing and planned dedicated high-fluence WEST campaigns.

Overall it is evident that there are limits to what can be assessed without access to materials exposed to all three drivers of material evolution and degradation, i.e. plasma particle flux, heat flux and neutron flux at relevant flux levels. Although planning of ITER operation depends on the knowledge of damage types and levels to be expected, in the end, the complete picture might ultimately require analysis of PFC evolution during plasma operation in ITER itself.

9. PFC damage by excessive heat loads

Since the publication of the PIPB 2007, a major new development has been the replacement of HHF CFC divertor components with tungsten-based components. While tungsten has the advantage of a much lower sputtering yield than CFC for typical plasma conditions at the divertor target plates, the use of a metal as a PFM introduces the problem of melting by excessive power loads, e.g. by accidentally large ELMs. Despite the much lower nominal power flux range to the main chamber FW and LIMs, this is still a problem for metallic main chamber components, particularly when using metals with low melting point such as beryllium, because of the possibility of large power transients. Section 9 discusses new insights into the formation and progression of surface damage, both from repeated superficial melting and from sustained deep melting. In addition to substantial progress in understanding the dynamics of melt motion and potential splashing and material release, this includes new insights into the beneficial influence of vapour shielding.

A detailed discussion of the physics processes determining the load conditions and ultimately the design of the ITER FW and divertor armour was published in [12, 1101]. The specific transient power load conditions due to disruptions and strategies for their control and mitigation are discussed in detail in [1102, 1103]. After the decision to eliminate CFC for the divertor HHF areas, the technology and the physics issues determining the plasma and material boundary conditions for the new full-W divertor design were presented in [14]. Further optimisation steps were published in [15] with the final design presented in [16].

The local power flux to the surface of PFCs exposed to the edge plasma or divertor plasma can be computed from the radial profile of the parallel power flux, $q_{||}$, by following the magnetic field lines towards their intersection with the material surfaces at a given location. In addition to the pure geometric considerations, variations due to transport and radiation losses need to be taken into account. With that, the surface heat flux is given by the projection of the local parallel heat flux, $q_{||}\sin(\alpha)$, where α is local B-field inclination angle. For PFC designs with castellated surface structures at length scales of the ion's Larmor radius and below, the heat flux distribution at castellation gaps and corners is modified by ion gyro effects, which had been predicted by ion orbit and PIC simulations [398, 1104]. Experimental evidence for these effects was obtained by IR observations at high spatial resolution in COMPASS [1093, 1105] and KSTAR [1106] and later directly confirmed by analysis of divertor erosion samples exposed to H-mode discharges in AUG [1094].

9.1. Empirical evidence

This subsection presents melting observations mainly from tokamaks though results from linear machines are briefly reviewed as well. The empirical evidence is grouped under two major categories *accidental/unintentional* and *designed experiments*. Particular attention is paid to evidence concerning the dynamics and stability of molten layers.

The dedicated experiments presented in this subsection are summarised in table 3, along with the modelling results which are discussed in the following subsections.

9.1.1. Accidental PFC melting in tokamaks. Most of the current operational experience with all-metal divertor PFCs emerged after publication of the 2007 PIPB. Despite the generally very favourable performance of the new divertor technology demonstrated in AUG, Alcator Cmod, JET, EAST and WEST, several cases of accidental melting of W-PFCs have

Table 3. Overview table of the dedicated experiments on PFC melting and melt dynamics in tokamaks and the respective modelling. All simulations listed have reproduced basic evidence—final deformation profiles and displaced melt volumes, this table highlights only additional contains which were also matched by the modelling with MEMOS-U and MEMENTO codes.

Type/Material	Machine /	Geometry	Power load	Splashing	Evidence	Modelling results
Sustained 2 mm W plate [1114, 1115]	TEXTOR	Limiter Sloped 20°	$\approx 17\,\frac{\mathrm{MW}}{\mathrm{m}^2}$ for 2.17 s	Spill from edge to side face	$\mathbf{J}\times\mathbf{B}$ due to TE Melting at ≈1.9 s	
Sustained W MB [1115]	TEXTOR	Limiter spherical	exposure for ≈4.2 s	Gap bridging no gap wetting	$\mathbf{J}\times\mathbf{B}$ due to TE	
Sustained 2 mm W plate [1116–1118]	TEXTOR	Sloped 36°	$(20\text{–}30)\,\frac{\mathrm{MW}}{\mathrm{m}^2}$ for several s	Spray ($\sim\mu$m) Droplet ejection $\sim 10\,\mu$m	$\mathbf{J}\times\mathbf{B}$ due to TE Melting at ≈1 s Boiling?	
Sustained W MB [1109]	AUG	LE	$\approx 80\,\frac{\mathrm{MW}}{\mathrm{m}^2}$ ELM avg	Spill from edge Droplet ejection	$\mathbf{J}\times\mathbf{B}$ due to TE	
Transient W [1120–1123]	JET	LE	Intra-ELM $(0.5\text{–}1.5)\,\frac{\mathrm{GW}}{\mathrm{m}^2}$ Inter-ELM $(50\text{–}200)\,\frac{\mathrm{MW}}{\mathrm{m}^2}$ ≈30 Hz	None	$\mathbf{J}\times\mathbf{B}$ due to TE	$\mathbf{J}\times\mathbf{B}$ with TE scaling as [1119] Pool $h\sim 100\,\mu$m at ~ 1 m s^{-1}
Transient W [1122, 1124]	AUG	LE	Intra-ELM $(0.5\text{–}1)\,\frac{\mathrm{GW}}{\mathrm{m}^2}$ Inter-ELM $(30\text{–}100)\,\frac{\mathrm{MW}}{\mathrm{m}^2}$ ≈70 Hz	Spill from edge No droplets	$\mathbf{J}\times\mathbf{B}$ due to TE	$\mathbf{J}\times\mathbf{B}$ with TE scaling as [1119] Pool $h\sim 100\,\mu$m at ~ 1 m s^{-1} Melt crossed edge
Transient W [1124–1126]	AUG	Sloped ≈18°	Intra-ELM $\lesssim 1\,\frac{\mathrm{GW}}{\mathrm{m}^2}$ Inter-ELM $\lesssim 50\,\frac{\mathrm{MW}}{\mathrm{m}^2}$ ≈70 Hz	None	$\mathbf{J}\times\mathbf{B}$ due to TE	$\mathbf{J}\times\mathbf{B}$ with TE scaling as [1119] Pool striations by varying local $\mathbf{n}$
Sustained Be [1122, 1127]	JET	Sloped UDP ≈20°	VDE CQ few 10's ms $\approx 100\,\frac{\mathrm{MW}}{\mathrm{m}^2}$	Splashing from edge Large droplets $\sim 100\,\mu$m	$\mathbf{J}\times\mathbf{B}$ due to halo current Melt moves from wetted side over corner to shadowed side	$\mathbf{J}\times\mathbf{B}$ with exp. $J_{\mathrm{halo}} = 50\,\mathrm{kA\,m^{-2}}$ Pool $h\sim 500\,\mu$m at ~ 1 m s^{-1} Profiles matched on wetted & shadowed
Sustained W *electrically insulated* [1128]	AUG	LE	Intra-ELM $\approx 1\,\frac{\mathrm{GW}}{\mathrm{m}^2}$ Inter-ELM $(20\text{–}40)\,\frac{\mathrm{MW}}{\mathrm{m}^2}$ ≈50 Hz	None	No replacement current 30% more absorbed energy compared to grounded sample	Gravity driven long-lived deep pool $h\sim 1\,\mathrm{mm}$ Matched deposited energy and temperature rise
Sustained W ITER-like MB with *active cooling* [1129, 1130]	WEST	LE	$150\,\frac{\mathrm{MW}}{\mathrm{m}^2}$ for 5 s	None	$\mathbf{J}\times\mathbf{B}$ due to TE due to TE Melting at ≈1 s Deform. at 1.7 s	$\mathbf{J}\times\mathbf{B}$ (main) + Marangoni Pool $h\sim 10\,\mu$m at ~ 1 cm s^{-1} Matched onsets of melt & deform.
Sustained Nb and Ir *simultaneous exposure* [1130]	AUG	Sloped ≈18°	Intra-ELM $\approx 600\,\frac{\mathrm{MW}}{\mathrm{m}^2}$ Inter-ELM $\approx 70\,\frac{\mathrm{MW}}{\mathrm{m}^2}$ ≈70 Hz	None	Small Ir pool and much stronger melting and flow on Nb sample	$\mathbf{J}\times\mathbf{B}$ + gravity + Marangoni Matched response of two materials under same load

been reported. These events were generally a consequence of misaligned PFCs, either by excessive EM forces during disruptions or failure to meet required tolerances during installation, with varying consequences on machine operation, depending on the severity of the misalignment and the evolving damage pattern.

In the first experimental campaign with a full tungsten FW configuration in AUG, the divertor target consisted of graphite plates with a 200 μm W-coating. During the campaign, partial layer delamination on two out of 128 OT tiles by thermal overloading caused partial melting with subsequent disruptions requiring an unscheduled vent of the machine for tile exchange [1107]. The disruptions were, however, caused by spallation of solid W flakes from the delaminated parts of the W layer and not by ejection of molten W. In the remaining part of the campaign, despite further melt damage with droplet formation occurring on 10 tiles and partial layer delamination on another six tiles, plasma operation was not impaired over several weeks until the scheduled end of the campaign [1107]. For risk mitigation and for extending the plasma operational parameter space, the W-coated graphite tiles in the outer divertor were subsequently replaced by solid W-tiles (AUG Divertor-III [1055]). In the following campaign, electromagnetic forces due to a disruption caused a slight displacement of four divertor sector assemblies, creating LEs at the W-tiles on the plasma upstream side of the sector assemblies with up to 0.6 mm height. Despite severe melting with removal of W to a depth of ~1 mm and displacement over several cm poloidal length by melt flow and ejection of molten W, further plasma operation was possible over 800 discharges without severe detrimental effects, such as increased W core concentration [1055, 1108].

In Alcator C-mod, failure of tile mounting bolts led to the loss of several W lamellae in one outer divertor stack during subsequent plasma operation, which created a gap of about 16 mm toroidal circumference. This, together with the protrusion of the remaining loose stack above the nominal target plate surface created a LE of 3 mm height on the lamella downstream of the gap [1056] which repeatedly melted during subsequent plasma exposure leading to an overall material loss of 15 g. Ejected tungsten melt was partly entering the confined plasma leading to frequent disruptions, which could only be avoided in the remaining campaign by positioning the strike line above the damage zone [1056]. Post-campaign inspection and analysis of the damaged lamellae surface topology revealed that the damage zone finally extended over all protruding lamellae, attributed to repeated strong melt motion across the damage zone and gradual pile up of material [1109]. No indications for self-healing effects by *plasma machining* of elevated surface areas and filling up of depressed areas with melt could be found.

In EAST, accidental melting was observed after installation of a full-W upper divertor with ITER-like cooled W MB stacks. Slight misalignment of the sector cassettes created LEs at the MB stacks downstream of the gap between adjacent cassettes with heights in some instances exceeding 1 mm [1110, 1111]. Similar to the observations in Alcator Cmod, W-melting at the overloaded LEs led to ejection of melt droplets. In EAST, because melting occurred in the upper divertor, ejected melt droplets would generally follow gravity and often led to disruptions when they reached the confined plasma [1110, 1112]. Despite the resulting increase of disruption occurrence rate in the respective experimental campaigns, plasma operation during stable discharges was not severely impaired [1110, 1112]. Post-campaign analysis of the melt area topology showed, like in AUG and Alcator Cmod, displacement of material along the LEs by melt motion with gradual pile up of material at the gap side faces of MBs in adjacent cooler surface areas [1111]. Moreover, the sharp corner of the LEs developed into a chamfered geometry by the melt losses, which indicates that self-healing of overloaded edges might be possible in case of small <1 mm misalignments [1111]. In more severe cases of misalignment, repeated melt events led in some cases to debonding of W-MBs from their CuCrZr cooling tubes and ultimately developed into a coolant leak, which highlights the dangers of thermal overloading of cooled MB PFCs [1113].

9.1.2. Dedicated experiments on PFC melting and melt dynamics in tokamaks. The principal possibility of melt events in tokamaks with metal divertor PFCs and their potential negative consequences for plasma operation, particularly during the later thermo-nuclear operation phases of ITER with restricted accessibility and hence more difficult repair options motivated dedicated experiments to better understand the melt displacement during a melt event, the resulting short and long term modification of surface topology and structural properties and corresponding consequences on power handling capabilities and finally the ejection of melt droplets and re-solidified debris into the plasma including their consequences for plasma operation.

In what follows, the terms *sustained* and *transient* melting refer to the nature of the liquid pools and not to the type of heat loads. In this context, *sustained* means that a molten pool, once formed, does not re-solidify until the end of plasma exposure.

9.1.2.1. Sustained melting. First tungsten related melt studies in AUG focused on the transport of ejected W melt droplets in the divertor plasma. In these experiments tungsten pins protruding out of the nominal outer divertor target plate surface were exposed in H-mode discharges to a local parallel power flux of 60 MW m^{-2} using the AUG divertor manipulator [1131]. Droplets ejected from the melting pins were observed using two high speed VIS range camera systems with crossed lines of sight. The ejected droplets were visible for ~0.1 s travelling over distances of $\gtrsim$1 m in the divertor plasma along the OT plate and vertically upwards [1132, 1133] with initial droplet sizes estimated in the range from 60–100 μm. The W source due to their evaporation led to an observable transient increase of tungsten core concentration although the magnitude always remained below $c_W = 10^{-4}$ and therefore without significant decrease of energy confinement or loss of H-mode. An analysis of c_W versus time evolution of droplet emission intensity showed that the screening of the droplet W-source in the divertor was similar to that of the W sputter source at the target plates [1132]. The outcome of the experiment suggested that the additional W source by a small scale melt event at the OT plate would only have comparably mild and transient consequences on plasma performance.

In a following experiment, sustained melting was studied at a castellated W sample with a LE created by intentional misalignment. The sample was exposed in the outer divertor of AUG to a local parallel power flux of 80 MW m^{-2} in high power H-mode discharges by means of the divertor manipulator. Ejection of melt droplets was again observed by a fast VIS range camera. These led to measurable transient increase of W core concentration but again at a level where plasma performance was not significantly affected. In the following discharge, however, a large amount of material was ejected into the confined plasma region leading to a disruption. Subsequent analysis of the retrieved sample showed, similar to the observations in accidental melt events, that at the LE material had been removed to a depth of ~1 mm with molten W spilling from the lower edge of the castellation onto the adjacent flat area of the W-sample. The re-solidified melt was found to be only loosely attached to the surface, which led to the conclusion that the observed material ejection perpendicularly from the surface was caused by spallation of solid debris rather than molten W during the actual melt phase [1109].

W melting at main chamber PFCs was studied by exposure of dedicated test LIMs in the TEXTOR tokamak [1114–1118]. Melting of bulk tungsten LIMs with a castellated and lamella configuration, respectively, were discussed in [1114, 1115] while the other studies [1116–1118] used 2 mm thick W plates embedded in a carbon LIM (see detailed discussion in section 9.1.3). In the experiments with W inserts, melting was induced shortly after the first second of several seconds long exposure to a power flux in the range of 20–30 MW m^{-2} with surface temperatures reaching up to 6000 K [1116].

Sustained melting of actively cooled ITER-like PFCs under steady-state loads was subsequently investigated in WEST on a dedicated outer divertor PFU with a poloidal LE created on one tungsten MB [1129]. By exposure to a parallel heat flux of ≈150 MW m^{-2}, the tungsten melting point was reached after 1 s, whereas deformation of the LE due to the melt displacement was first detected *in-situ* at ≈1.7 s by high spatial resolution IR imaging [1130]. Because of the active cooling, the measured surface temperature was only marginally above the melting point throughout the 5 s long exposure. There was no noticeable effect of melting on plasma operation. Stable radiated power and tungsten impurity content were reported in this experiment [1129].

Transient heat loads can induce sustained melting. This has been investigated on the beryllium UDPs in JET by deliberate melting induced by the impact of VDEs [1127]. An instance of UDP damage is presented in figure 82(*a*). Figure 82(*b*) features a zoomed-in image of castellation gaps that are filled in with melt. Only the total UDP conducted energy is known experimentally [1127], but estimates [1122] revealed that energy deposition over the CQ timescale of few tens of ms, translating to a heat flux of ≈0.1 GW m^{-2}, would suffice to generate the observed melt volume.

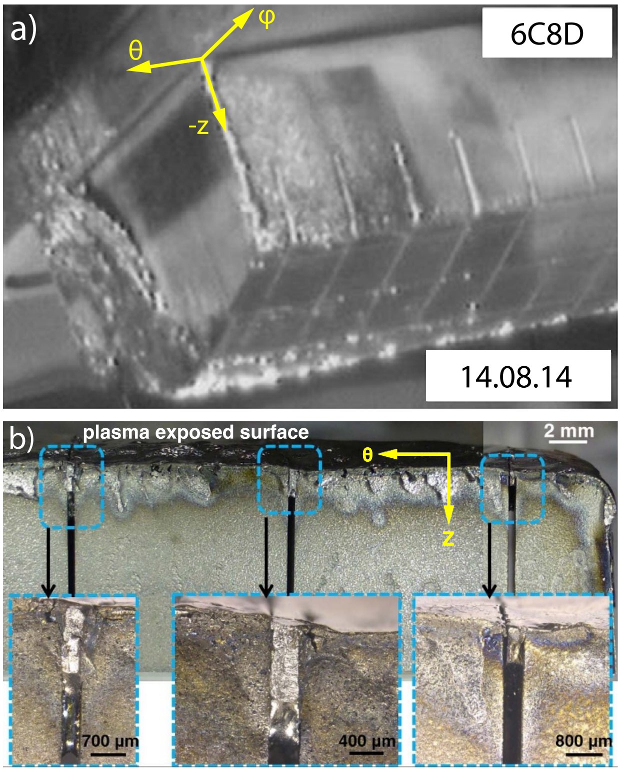

Figure 82. (*a*) Image of a Be UDP tile (DP-8) at the end of the JET ILW2 campaign. (*b*) 3D optical microscopy image showing melt damage to the tile castellations and melt infiltration of the castellation gaps. The grooves are randomly filled with molten Be to depths between 0.2 mm and 3.5 mm. The original figures have been amended to include arrows indicating the vessel coordinate system directions φ (toroidal), θ (poloidal) and z (vertical). Reproduced from [1127]. © 2019 EURATOM. All rights reserved.

Short ~ ms power load transients such as ELMs can also ultimately result in sustained melting under certain conditions. Documented examples include the ELM-induced melting of an electrically insulated tungsten LE [1128] and the ELM-induced melting of refractory metal proxies [1130], both achieved in dedicated exposures to H-mode AUG plasmas. The experiment with the floating W LE featured an unusual energy deposition; in the presence of intense thermionic emission (TE), the sheath heat transmission factor increased due to the direct electron contribution so that the floating sample absorbed 30% more energy compared to the identical grounded sample exposed to the same plasma (max intra-ELM values of ≈1 GW m^{-2}, inter-ELM values of 20–40 MW m^{-2}, a typical ELM duration <3 ms with an ≈50 Hz average ELM frequency) [1128]. Thus, the incident heat flux during these exposures resulted in pronounced melting and surface modifications for the floating sample, but was insufficient to cause substantial melting of the grounded W sample.

In the poor-versus-efficient thermionic emitter experiment in AUG; niobium (Nb, melting at 2745 K) and iridium (Ir, melting at 2719 K) samples were simultaneously exposed with both forming sustained melt pools [1130]. The AUG experiment was designed to contrast the deformation and thermal

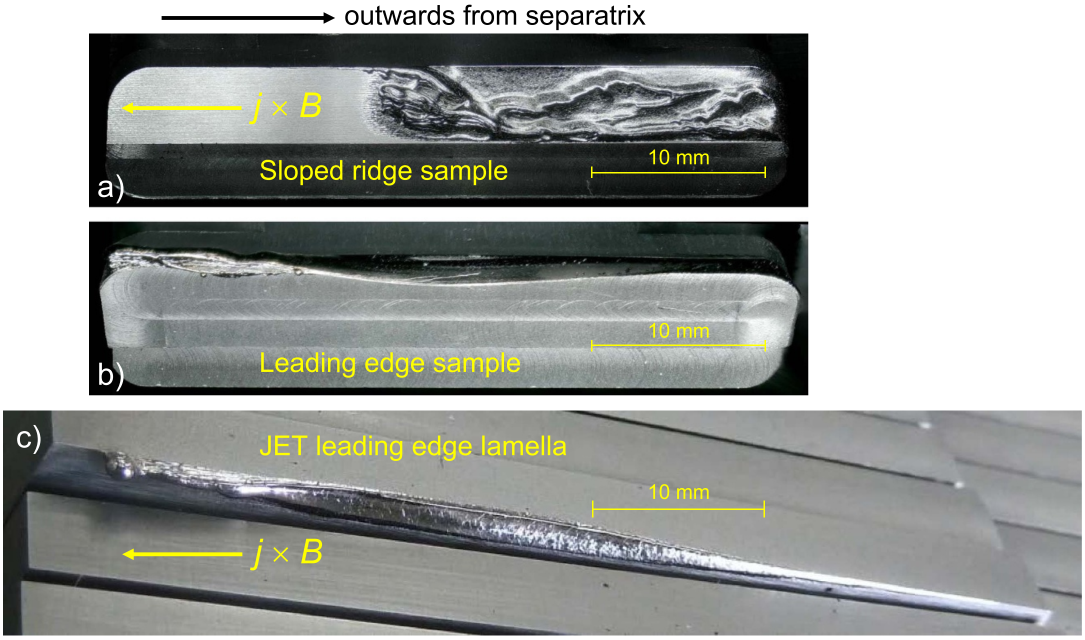

Figure 83. Post exposure melt patterns of the ASDEX Upgrade sloped melt sample (*a*) and leading edge melt sample (*b*). The melt pattern after the JET leading edge lamella study [1121] is shown (*c*) with identical length scale for the sake of comparison. (*a*) and (*b*) Reproduced from [1124]. © 2018 EURATOM. All rights reserved. (*c*) Reproduced from [1121]. © 2016 EUROfusion. All rights reserved.

response of poor and efficient emitters, which otherwise have similar thermo-physical properties [1130]. When exposed to the same heat load, the melt displacement in two identical samples should then vary drastically owing to the different escaping thermionic fluxes. Ir and Nb were selected as sample materials because of their different work functions (5.3 eV and 4.2 eV respectively), but nearly identical melting points. The experiment design was guided by MEMOS-U [1126, 1128] modelling; the simulation predictions of modest material excavation on the Ir sample and of gross material erosion with possible ejection from the Nb sample were confirmed in the AUG exposures [1130]. In this experiment, the samples were exposed to ELMy H-mode plasmas with peak intra-ELM values of ≈600 MW m^{-2}, peak inter-ELM values of ≈70 MW m^{-2}, an ELM duration of ≈3 ms with ≈70 Hz average ELM frequency.

9.1.2.2. Transient melting. Repeated transient melting due to ELMs is typically achieved with grounded tungsten samples (in contrast to the above examples). ELM-induced transient pools have been reported in the JET tungsten LE experiments [1120, 1121] and, later on, a similar picture was confirmed in the AUG LE and sloped lamella experiments [1124, 1125]. The respective surface deformation profiles are shown in figure 83.

The heat flux in JET LE W experiments [1120, 1121], as reconstructed from IR thermographic data [1134], featured inter-ELM values of 50–200 MW m^{-2} and peak intra-ELM values of 0.5–1.5 GW m^{-2}, the typical ELM duration was <3 ms with a 30 Hz average ELM frequency. Comparable heat loads were realised in the AUG LE exposures [1124] with a heat flux of 30–100 MW m^{-2} and 0.5–1 MW m^{-2} for the inter-ELM and intra-ELM phases, but with a twice higher average ELM frequency of 72 Hz. In such repetitive-ELM melting of W samples, nearly 99% of the incident energy is expended to raise the base bulk temperature close enough to the melting point, so that superimposed ELM-driven temperature excursions will suffice to initiate melting and create transient pools towards the end of a few second long exposures [1122, 1123].

To study the influence of the intersection angle between magnetic field and PFC surface on melt dynamics, samples with a sloped elevated feature were exposed both in AUG and JET. In the AUG experiments sloped samples with the exposed surface intersecting the B-field at 18° were exposed [1124, 1125]. In JET, a W lamella with similar geometry was installed for a comparison study [1135]. Compared to the LE geometry, the shallower incidence angle reduces the projected parallel heat flux but also the escaping thermionic current, with both effects leading to much smaller and slower surface modification than at LEs [1126, 1128]. To compensate, the exposure duration in the AUG experiment was prolonged so that transient melting was achieved at the end of 5.5 s exposures. Another aspect of heat loading, particular to sloped geometry and absent in the LE case, concerns local surface normal variations due to surface modifications induced by melt motion, which can significantly affect the surface projected area and enhance the absorbed heat flux.

9.1.3. Evidence of melt layer splashing in tokamaks and its effect on plasma operation. The majority of the controlled experiments discussed above featured predominant melt flow direction and no evidence of liquid pool disintegration or splashing, as documented by the post-exposure analysis (see figure 83 for typical examples). The distinct exception is melt ejection due to presence of geometrical obstacles, as realised when the flow reaches the edge of the PFC. Material ejection from molten W LE was observed in the 2013 [1109] and 2018 [1109, 1124] AUG experiments with post-mortem images revealing liquid jets emerging from the edge of elevated samples and spilling when in contact with components aligned with the divertor surface, see an example in figure 84. Note that liquid W ejection was not observed in the JET W LE experiment [1120], where the melt did not reached the edge, since the re-solidified material piled-up ≈7 mm away.

MEMOS-U modelling of the 2018 LE exposure [1122, 1128] and modelling of melt splashing from the edge [1136] have guided the design of a recent controlled ejection experiment in AUG. An open edge and an ITER-like gap have been embedded in W LE samples. The SP was positioned on the samples in a manner that allowed the ELM-induced transient pools to reach the gap or edge within their life-time, i.e. prior to re-solidification [1137]. The experiment demonstrated that the melt bridges a 0.5 mm gap with no signs of flow disintegration or splashing and also that the melt jets off from the edge's open side.

A similar scenario of melt splashing owing to a geometrical obstacle was realised in the VDE-induced melting of the JET Be UDP where droplets, ejected when liquid Be crossed the UDP edge, impacted onto the nearby vacuum vessel wall [1127]. Only a fraction of the melt pool was ejected in the form of droplets from the edge of Face 1 (figure 84(*b*)). The remaining melt has reached the plasma-shadowed UDP face (Face 2 in figure 84(*b*)) and re-solidified into a so-called *inverse waterfall* structure, see figure 82(*a*). The dynamics of the flow in such regimes is discussed in details in section 9.3.4.

We also mention experiments with unconventional PFC dimensions, namely thin W plates [1116] and W wires [1131, 1132], specifically designed to elucidate the effect of W material loss on the plasma operation. TEXTOR experiments [1116, 1117] with 2 mm thick W plates inserted in a carbon LIM, also discussed in section 9.1.2.1, had an atypical thermal response due to the thermal insulation and spatial/temporal time scales involved. Since the characteristic heat diffusion length becomes of the order the plate thickness within a fraction of second, the in-depth temperature profile becomes uniform earlier on during exposure followed by formation of deep melt pools. PM analysis revealed that melt did not move over the surrounding colder graphite surface with the material piling up at the borders of the W plate. Surface temperatures up to 6000 K were reported together with evidence of boiling and evidence of the ejection of fine (μm size) as well as larger, 30–100 μm, droplets.

The AUG experiment [1131, 1132] used a W pin protruding 3 mm above the plasma exposed outer divertor tile surface. The onset of melting, induced by moving the SP towards the pin position, was followed by the release of W droplets. Analysis of their observed trajectories showed that droplets ejected in the outer divertor generally do not reach the confined plasma. In addition, dedicated experiments in TEXTOR and AUG [1109] have addressed the consequences of progressive melt-induced damage. There, after several successive melting events, spallation of solid melt debris was observed, some of which penetrated into the plasma core in sufficient quantities to cause disruptions.

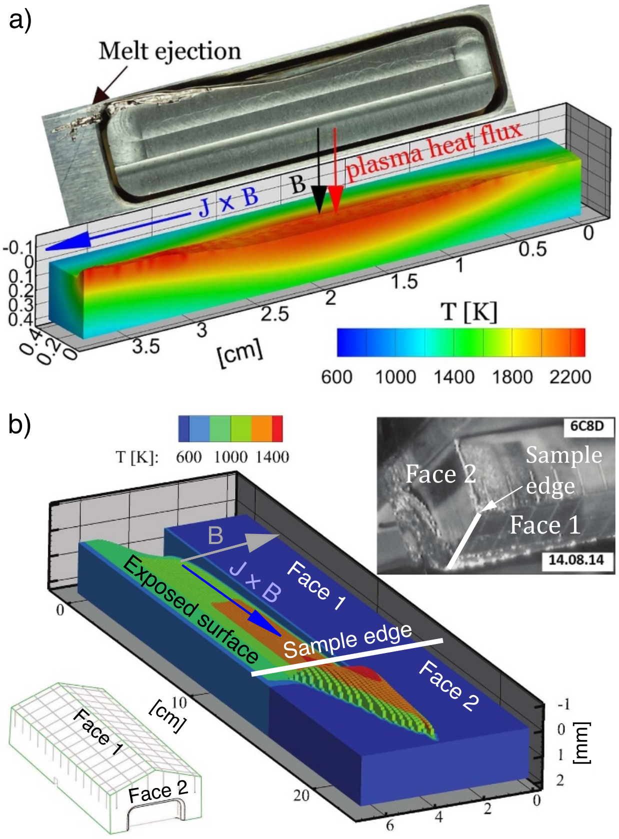

Figure 84. (*a*) Deformed 3D domain simulated by MEMOS-U for the W leading edge exposure in AUG ELMy H-mode pulses #33504, #33508 and #33509 (3.5 s total exposure time with 2 s constant strike point position). The W sample dimensions are 9 mm × 38 mm × 10.1 mm. The final profile is compared to the experimental post-exposure profile (view on top of sample) which includes molten material ejected from the edge. Reproduced from [1122]. CC BY 3.0. (*b*) Bottom left: sketch of the UDP plate geometry. Top: image of a Be UDP tile (DP-8) at the end of the ILW2 campaign showing the plasma-wetted side where melt is produced (Face 1) and the shadowed side over which melt can traverse prior to re-solidification (Face 2). The magnified image is shown in figure 82(*b*). Main: MEMOS-U deformed 3D domain after a 35 ms exposure to the heat flux specified in the caption to figure 5 in [1122]. Reproduced from [1127]. © EURATOM 2019. All rights reserved.

9.1.4. Other machines (linear devices, QSPAs).

In addition to the evidence from contemporary fusion devices, there are many experiments in other machines that are devoted to the investigation of the response of metallic PFCs under high heat loads that emulate ITER-relevant transient events. Sample exposures in linear machines, multiple mirror magnetic confinement and Quasi-Steady-State Plasma Accelerators (QSPAs) have yielded vast data concerning the behaviour of not only W but also Be targets, see e.g. in [1095, 1138–1147], the latter constituting a valuable addition to the unique evidence obtained from the Be UDP melting in

JET. The experimental design and diagnostic access in these machines often allows the direct observation of melt splashing events and also vapour cloud characterisation, giving such experimental data a particular value for model validation and code benchmarking. Projection of the respective results to tokamaks and to ITER, should be done with caution, since, while the heat flux loading in these machines is usually fusion relevant, the specifics of plasma production and plasma parameters that dictate the forces which drive the melt motion are generally not (see the current closure through the end plate in linear machines [1095] or the high plasma pressures in QSPAs [1147]).

9.2. Main mechanisms and processes governing the thermal response, dynamics and stability of molten layers

This subsection introduces the main processes that control the PFC thermal response, the melt formation and the melt dynamics. The description is primarily qualitative, but the main dependences on the plasma parameters as well as on the PFC geometry and on the magnetic field inclination are provided.

9.2.1. Thermal response, phase transitions, surface cooling and convective cooling. For typical steady-state and transient loads, the total material thickness that is traversed by plasma particles, which impinge with energies below few keV, prior to their thermalisation (the depth range) lies well in the nanometre range. For a specific example of 10 keV incident energy, the electron, proton and helium depth ranges are ≈300 nm, ≈150 nm, ≈100 nm in Be and ≈80 nm, ≈40 nm, ≈20 nm in W [1148]. The situation is different for REs, where for 1 MeV the electron depth range is ≈3 mm in Be and ≈0.4 mm in W [1149]. Thus, plasma incidence leads to surface heating while RE-induced melting events are characterised by volumetric heating. In the case of relativistic REs, the energy deposition profile is defined by not only by electronic and nuclear stopping but also by internal photon and secondary (delta ray) electron transport [1150]. In some scenarios, RE-induced melting events can be of the explosive type and can be accompanied by the release of fast solid ejecta [1073, 1151, 1152].

The PFC cooling is mediated through surface fluxes, convection due to melt motion and, in the case of actively cooled components, convective flux at the coolant-pipe interface. The surface cooling fluxes due to thermal radiation and vaporisation are present for PFCs of any material composition. On the other hand, cooling owing to TE is mostly important for W PFCs, since TE is governed by the Richardson–Dushman law whose exponential surface temperature dependence makes the emitted electron fluxes negligible for Be due to its low melting point. For every escaping thermionic electron, not only its kinetic energy is lost from the material but also an energy equal to the work function (4.55 eV for atomically clean polycrystalline W), since the replacement electron is pulled from the bulk material to fill the thermal vacancy, driving a current through the PFC volume. Away from the normal boiling point vicinity, where vaporisation takes over, TE constitutes the dominant cooling channel for W PFCs and plays a decisive role in restricting the melt production [1122, 1123, 1128]. In fact, in ELMy H-mode plasma exposures, the TE flux is comparable to the incoming inter-ELM heat flux and leads to the re-solidification of transient pools that are induced during the ELM. Other emission processes are discussed in section 9.2.3.

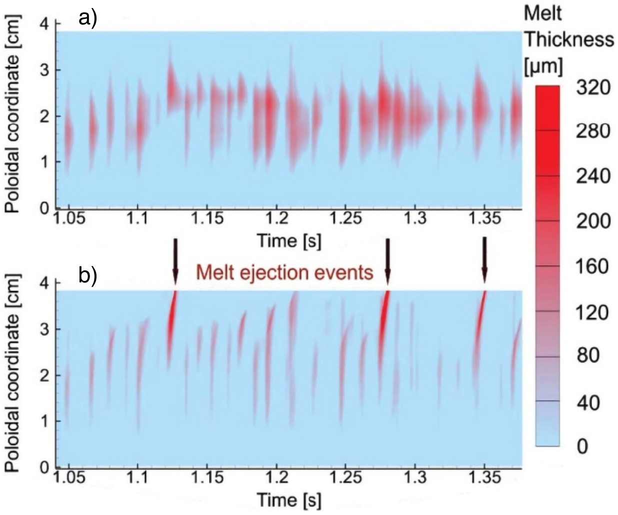

Figure 85. MEMOS-U simulations of the AUG W leading edge melting during pulse #33509 (1.4 s total exposure time with 1.1 s constant strike point position). Melt thickness as function of the exposure time and poloidal coordinate, for the uppermost part of the sample corner (where deepest melting occurs) near the end of the exposure time interval. Results for (*a*) heat transfer independent of fluid motion, (*b*) fully coupled heat transfer and motion. Reproduced from [1122]. CC BY 3.0.

Convective heat transfer is another powerful cooling mechanism given the localised nature of the incident heat flux. Due to the melt motion, the heat is transported from the induced pool onto the adjacent surface which, being much colder, provides an efficient conduction channel for the deposited energy. The thermal response of the W LE in JET exposures [1120] constitutes a characteristic example of the role of the convection cooling, since neglecting convective heat transfer leads to sustained melt pools in contradiction to the observations [1123, 1128]. A similar conclusion is deduced from the AUG LE exposure [1124]; figure 85(*a*) shows sustained pools that are formed when convection is neglected and figure 85(*b*) demonstrates that transient pools reaching the sample edge, in accordance with experimental evidence of material ejection, are formed only when the full coupling between heat transfer and fluid dynamics is enabled.

Melt generation is naturally controlled by the fraction of the absorbed energy that is expended on the phase transition, which is strongly dependent on the exposure scenario. In the W LE exposures in AUG and JET, the absorbed energy was in the range of 10 kJ while only 30 J is needed to produce a melt volume of 6 mm^3, as observed in the experiments. A similar situation is encountered in the WEST exposures of active cooled PFCs, where out of the ≈14 kJ of plasma deposited (≈5 kJ absorbed) energy only ≈1 J is expended on the formation of the observed 0.3 mm^3 melt volume. Such energy partition between sensible and latent heat during exposures results in the high sensitivity of melt production; small variations in the incident heat flux can lead to significant variations in the produced melt volume [1122, 1123, 1128]. The WEST experiment [1129] provided the first direct empirical evidence of such dependence [1130]; in three exposures with identical discharge parameters, a detectable melt build-up was formed only in one discharge. This is in contrast to disruption-induced Be melting, where a larger fraction of the energy is consumed for latent heat and melt formation, that does not exhibit such a threshold-like behaviour [1122].

9.2.2. Free-surface effects and main driving forces acting on the molten metallic layers. The acceleration experienced by a molten layer is due to the combined action of hydrostatic effects (fluid pressure gradient), shear stress divergence (viscous damping) and external volumetric forces. Among the latter, the Lorentz force density is typically dominant, where the nature of the current flowing through the melt layer is dictated by the scenario. In the case of disruption CQ induced melting, this is the halo current. In the case of melting driven by steady-state, ELMs or disruption TQ heat loads, this is the replacement current triggered by the electron emission (when incoming plasma fluxes remain ambipolar due to the localisation of the wetted area, see section 9.2.3). Gravity can also play a role, when the Lorentz force is particularly weak [1130] or when it is the only external force, as in the case of electrically insulated components [1128].

Given the dominance of the Lorentz force, the magnitude of the driving current density (along with the tokamak B-field) is crucial to the melt dynamics. The magnitude is defined by the current paths inside the molten layer and the electromagnetic boundary condition on the plasma-PFC interface which involves total current density that is normal to the metallic surface, J_s. As mentioned before, in melting induced by the disruption CQ, $J_\mathrm{s} = J_\mathrm{halo}$. In melting induced by steady-state, ELM or disruption TQ heat fluxes, $J_\mathrm{s} = J_\mathrm{em}$, where J_em is the local *escaping* current density that is determined by the temperature field, incident plasma flux and B-field inclination angle, see detailed discussion in section 9.2.3.

The charge continuity equation inside the metal implies that the current density variation should be nearly the same in each spatial direction near the PFC surface. For sloped geometries, where the B-field is at very shallow or at modest angle with respect to the surface tangent, in-depth variations can be neglected when the tangential gradient scales are much larger than the melt thickness. Since the extent of the melt pool is dictated by the wetted area, it is typically much larger than the melt thickness, which ranges from hundreds of μm in contemporary machines up to millimetres in ITER-disruption scenarios. Therefore, at such exposure geometry, the Lorentz force is simply $\mathbf{J}_\mathrm{halo} \times \mathbf{B}$ or $\mathbf{J}_\mathrm{em} \times \mathbf{B}$, depending on the scenario. In case of the LE geometry, due to the bending of the current paths, both tangential and normal components exhibit strong variations. Detailed numerical solution revealed that the depth-averaged current density component gives rise to a tangential Lorentz force that is four times smaller than $\mathbf{J}_\mathrm{em} \times \mathbf{B}$ for the LE AUG exposure [1153].

During the disruption TQ phase, there is also the Lorentz force density that is associated with the eddy current present in PFCs [1102]. Since the eddy currents flow along the PFC (within some skin depth, typically larger than the characteristic melt depth), the resulting $\mathbf{J} \times \mathbf{B}$ force density is normal to the pool surface and it does not lead to a tangential melt displacement. Such force, however, when directed towards the plasma, i.e. away from the melt surface, can be responsible for melt pool disintegration due to the Rayleigh- Taylor instability [1154], see also section 9.2.5.

The interaction with the surrounding environment, that is the plasma-plus-metal vapour, is governed by the kinematic, dynamic, thermal and electromagnetic boundary conditions on the ambient-liquid metal interface—the free surface. For the kinematic boundary conditions see e.g. [1123], the thermal response was outlined above, thus below we focus on the latter two boundary conditions to highlight their main effects on melt dynamics.

The stress balance condition normal to the surface generally includes the thermodynamic pressure jump and the magnetic pressure jump. Due to the negligible induced magnetic field and the non-ferromagnetic nature of typical PFCs (the stainless steel employed in fusion applications is typically of austenitic grade and thus paramagnetic), the magnetic pressure jump can be omitted. This implies that the difference between the fluid pressure at the free surface and the ambient pressure balances the surface tension force. Surface tension plays an important role in the stability and the disintegration of melt layers, see 9.2.5. In case of *bulk* motion with small deformations, variations of the ambient (plasma and/or metal vapour) pressure essentially translate to a force acting on the melt layer. Order of magnitude estimates reveal that typical tangential (along the melt surface) plasma pressure gradients are small compared to the Lorentz force density both in contemporary tokamaks and in ITER scenarios. For example, in the AUG and the JET W LE exposures [1120, 1124], pressure gradients of $<1\,\mathrm{kPa\,cm^{-1}}$ ($<10^5\,\mathrm{N\,m^{-3}}$), are two orders of magnitude smaller than the $\mathbf{J} \times \mathbf{B}$ force density with a replacement current density of several $\mathrm{MA\,m^{-2}}$ [1122] and with $B = 3\,\mathrm{T}$. In the JET Be UDP melting events [1127], pressure gradients of $<0.1\,\mathrm{kPa\,cm^{-1}}$ ($<10^4\,\mathrm{N\,m^{-3}}$) are at least one order of magnitude smaller than the $\mathbf{J}_\mathrm{em} \times \mathbf{B}$ force density with a halo current density of $100\,\mathrm{kA\,m^{-2}}$ [1122] and $B = 3\,\mathrm{T}$. For the ITER worst case scenario of a disruption in a 15 MA/5.3 T discharge, with parallel plasma pressure gradients from JOREK simulations of $<5 \times 10^3\,\mathrm{N\,m^{-3}}$ and halo current densities of a few tens of $\mathrm{kA\,m^{-2}}$ [1155], the Lorentz force is again about two orders of magnitude larger. Tangential gradients of the vapour pressure are defined by the surface temperature variations which result from the PFC thermal response under a given heat load. Vapour pressure gradients along the surface might be non-negligible compared to other forces for scenarios with highly elevated, well beyond melting point, surface temperatures. Their exact effect on the macroscopic melt motion in such cases, however, needs to be considered in the light of the vapour shielding that is present in such scenarios (see section 9.2.4).

The jump in the tangential components of the hydrodynamic stress at the free surface is balanced by the stress due to the tangential gradients in the surface tension, $\nabla_t\gamma$. The tangential component of the stress exerted by plasma on the melt is the plasma drag force per unit area, which depends on the magnetised plasma viscosity and the plasma flows along the metal surface. Treating plasma as an ordinary fluid in contact with the metal pool faces a conceptual issue: the near-surface dynamics of magnetised plasmas is driven by electromagnetic processes of kinetic origin that cannot be described by standard fluid models and boundary conditions. To estimate the order of magnitude of the volumetric drag force, the force per unit area value from the fluid dynamics drag equation (with skin friction or drag coefficient for high Reynolds numbers) [1156] can be divided by the melt thickness. For the ITER worst case scenario of a disruption in a 15 MA/5.3 T discharge [1155], employing a D plasma density of 10^{20} m^{-3}, a temperature of 10 eV and assuming a Mach number $M = 1$ and a rather thin melt layer of 100 μm, such estimates yield $\sim 10^3$ N m^{-3}—at least two orders of magnitude smaller than the $\mathbf{J}\times\mathbf{B}$ force with the current and B field values cited above. The empirical evidence from present day machines also shows that the plasma drag does not play any significant role in the melt bulk motion because in all relevant experiments the observed melt displacement was in the direction of the $\mathbf{J}\times\mathbf{B}$ force and thus perpendicular to the main plasma flow. However, it is worth emphasising that very high velocity flows might be responsible for shear-driven (Kelvin–Helmholtz) destabilisation of the melt layer on short time scales, see sections 9.2.5 and 9.3.

The stress balance conditions also imply that a non-zero $\nabla_t\gamma$ at the interface will drive melt motion. Gradients in γ arise due to variations in the surface temperature or interfacial chemical composition. For the uniform material composition relevant to fusion applications, $\nabla_t\gamma$ generates the thermo-capillary term $(\partial\gamma/\partial T)\nabla_t T_s$. Since the surface tension decreases with increasing temperature, this leads to an effective force on the melt layer which pushes the liquid metal from the hot regions towards the colder areas, i.e. the Marangoni effect. In fusion-relevant melt events, the importance of thermo-capillary acceleration varies with the specifics of the plasma wetting (heat profile) which controls the tangential gradients. In the LE geometry, the magnitude of the thermo-capillary accelerations might be weak compared to the Lorentz acceleration mechanism [1122, 1123], yet, in the direction that is perpendicular to the main $\mathbf{J}\times\mathbf{B}$ force, they can provide a non-negligible contribution to the pool displacement [1130]. Similarly, within the weak Lorentz force regime, the Marangoni flows can make essential contributions to the melt dynamics [1130]. Such a weak $\mathbf{J}\times\mathbf{B}$ regime is of relevance to ELM-induced FW plasma-facing component castellation edge melting in ITER, since Be is a relatively poor thermionic emitter.

Finally, there is one aspect of melt dynamics that is particular to tokamaks; the fact that resolidification effectively controls the overall melt displacement as well as the final surface modification profile [1122]. This is due to the localised nature of wetted areas (melt pools are surrounded by a progressively colder solid) combined with the typical accelerations of melt layers which are such that the lifetime melt displacements are of the order of the pool extension. When liquid moves out of the induced pool a few effects take place; (i) the melt heats the adjacent surface thus enabling further displacement of the sequent fluid parcel and promoting some spreading of the displaced material, (ii) bottom-up propagation of the resolidification front reduces the melt thickness and enhances the viscous damping, hence impeding acceleration, (iii) the arrest of motion due to the resolidification is responsible for the commonly observed surface modification profiles featuring a crater and amassment near its edge. At this point, it is illuminating to recall that liquid metals wet their own solid excellently due to the strong interfacial bonding that has metallic nature [1157, 1158]. This signifies that essentially solidification counteracts spreading and wetting, leading to the observed surface deformation profiles (see section 9.1 and figures 83–84), with *apparent* large contact angle instead of thin films expected under good wetability conditions. More detailed discussion of wetting dynamics in the presence of large temperature differences between the liquid and solid phases in tokamak relevant scenarios can be found in [1137].

9.2.3. Electron emission processes (thermionic, field-assisted thermionic, electron-induced and ion-induced). Electron emission processes from PFC surfaces play a crucial role in the melt formation and its dynamics, as they are not only responsible for melt acceleration but also constitute effective cooling channels. Each emission process is characterised by its own energy distribution and it thus contributes differently to the heat balance. Thermionic and field-assisted thermionic electrons (extended Schottky regime) follow a (half) Maxwellian distribution at the surface temperature [1159, 1160]. The chemical contribution, namely the work function W_f of about 4−5 eV per escaping thermionic electron, is the main contribution to the cooling flux, as discussed above. In case of electron-induced emission processes, the chemical contribution is less dominant compared to the mean exit energies which are; (i) 2 W_f in secondary electron emission, (ii) of the order of the incident electron energy in low energy electron reflection, (iii) a significant fraction of the incident electron energy in electron backscattering [1161–1163]. Ion-induced electron emission [1164, 1165] for high energy plasma ions, noble gases or multiply charged impurity ions might also be of importance for some ITER scenarios [1166, 1167].

As already mentioned in section 9.2.2, the electron emission processes can be also responsible for the origin of the current (non-ambipolar current density escaping from the sheath) flowing though the melt layer which gives rise to the volumetric Lorentz force. Both the cooling fluxes and the Lorentz force density scale with the escaping emitted electron current density whose analytical evaluation is not feasible given the presence of several emitted populations [1167, 1168], the formation of space charge (non-monotonic potential due to virtual cathode) in case of intense TE [1169, 1170] as well as the prompt re-deposition of the emitted species in the presence of inclined magnetic fields [1171, 1172]. This complex problem has been addressed in recent dedicated PIC simulations where the emergence of SCL thermionic sheaths for inclined magnetic fields has been established [1119, 1173, 1174]. A semi-empirical expression, $J_{\mathrm{em}} \simeq 0.43\, e n_{\mathrm{e}} v_{\mathrm{T_e}} \sin^2(\alpha)$, has been determined for the thermionic current saturation limit as a function of the plasma parameters in front of the target surface and the B-field inclination angle, α, that is accurate for both the inter—and intra-ELM plasmas of present-day tokamaks [1119]. In current devices, the SCL transition generally occurs at surface temperatures below the W melting point so that molten W PFCs are nearly always surrounded by SCL sheaths. However, for high, ITER ELM-relevant, electron temperatures and plasma densities, large incident plasma fluxes push the formation of the virtual cathode to higher surface temperatures and intense normal wall electrostatic fields lead to the strong coupling of TE with field electron emission (primarily in the Schottky regime) in the monotonic potential profile regime [1168].

The above picture is valid for W PFCs electrically connected to the large grounded vessel and localised wetted areas, so that the emissive sheath is unable to affect the global plasma potential or alter the classical Bohm pre-sheath potential structure, irrespective of the TE strength. As a consequence, the incident plasma fluxes remain nearly ambipolar and a non-ambipolar current density (the escaping current) triggers a replacement current density that flows through the melt volume and generates the $\mathbf{J} \times \mathbf{B}$ volumetric force. The above picture has been validated in multiple dedicated melt experiments in tokamaks, not only for W LEs [1122, 1123] but also in more complex sloped geometries where the emission depends on the B-field inclination angle [1126] as well as in specially designed melting experiments within the weak Lorentz force regime, such as the exposure of low melting point materials and the exposure of actively cooled W components [1130]. All the experiments have been successfully reproduced by the MEMOS-U physics model, whose boundary conditions are based on such a current density description and the aforementioned J_{em} scaling (for further details see section 9.3).

In the opposite limit, when the emitting area is large enough to affect the global plasma potential and the pre-sheath conditions, 1D kinetic simulation results suggest the formation of a so-called inverse sheath, where the surface is positive with respect to the plasma potential. This is facilitated by ionisation and CX collisions that trap cold ions near the surface, which then progressively destroy the virtual cathode [1175–1177]. In such a floating case, since all particle fluxes, including the emitted electron fluxes, are ambipolar, there is no replacement current density and hence no associated Lorentz force density acting on the melt layer. The inverse sheath potential profiles are such that the incident electron and ion energy fluxes change drastically compared to the SCL regime, resulting in a significantly reduced heat load on the emitting surface due to the formation of a target plasma with a much lower temperature [1178]. Combined with the absence of ion acceleration in the pre-sheath (inhibiting the contribution of recombination heat flux and limiting damage due to sputtering), this constitutes the main motivation for the proposed innovative divertor operating scenario of emission-induced detachment [1178, 1179]. At present, inverse sheaths have not been yet demonstrated in realistic (multi-dimensional) simulations for tokamak conditions, where the newly formed trapped ions can possibly escape from the SCL potential well before the transition to an inverse sheath is realised.

9.2.4. Vapour shielding. Under high transient heat loads, the PFC surface temperatures can reach very elevated values at which intense vaporisation takes place. Interaction of the cold dense vapour with the incident plasma includes numerous processes through which the plasma loses energy; collisions, ionisation, radiation. Moreover, the vapour cloud and the secondary plasma also expand and diffuse. Detailed modelling of plasma-vapour interaction requires simulations by dedicated numerical tools is discussed in section 9.3, here we briefly discuss consequences of shielding on the PFC thermal response.

Vapour production is very sensitive to the surface temperature owing to the evaporation flux scaling with the vapour pressure (Hertz-Knudsen equation [1180]) and the exponential vapour pressure dependence on the surface temperature (Antoine equation [1181]). As a result, surface temperature changes of a few hundred K can lead to a many-fold increase of the evaporation flux which, upon interaction with the incident plasma, leads to reduction of the energy eventually absorbed by the surface, i.e. vapour shielding.

As a consequence of the exponential dependence of the evaporation rate on the surface temperature, the effect of plasma-vapour interaction details on the absorbed energy is effectively masked [1182, 1183]. This picture was firmly confirmed in [1183], where calculations for three vastly different vapour cloud regimes revealed that the absorbed energy dependence on the radiation properties and the dynamics of the cloud is logarithmically weak. The resulting maximum absorbed energy depends only on the thermo-physical properties of the target (specific isobaric heat capacity, thermal conductivity, mass density) and the exposure duration as $\sqrt{t}$. As soon as the surface temperature reaches a maximum value that yields a sufficiently strong vaporisation flux for efficient shielding, its value stabilises and decays very slowly. This indicates that the incident heat flux should scale as $1/\sqrt{t}$. In fact, if one postulates an ad hoc constant surface temperature and uses the well known solution for the spatiotemporal temperature profile (see e.g. [1184]) to calculate the heat flux at the boundary, the same temporal and material property dependence emerges [1185]. As pointed out in references [1182, 1183], such low sensitivity to any other details of the exact scenario largely explains the observed experimental fact that for both CFC and W targets the absorbed energy is very similar in spite of the significantly different radiation capabilities of the two materials. It is worth emphasising that such robust estimates of the absorbed energy do not apply to vapour mass loss which is highly sensitive to details of the shielding cloud processes [1182, 1183].

9.2.5. Stability of melt layers.

A summary of experimental evidence of melt splashing in present day machines is provided in section 9.1.3 and a brief account of the modelling of such events is given in sections 9.3.3 and 9.3.4. Here we point out some general characteristic of relevance to the fusion melting scenarios.

One important aspect is that estimates of the most unstable wavelength and corresponding growth time should be viewed in light of the spatial dimensions of the melt pool and its lifetime [1152]. In case of typically extended shallow melt layers driven by forces parallel to their free surface, the linearly unstable free-surface modes with wavelength much larger than the melt depth are prone to saturate once the nonlinear regime is achieved, settling in a quasi-steady perturbation that does not result in splashing [1186]. Hence, the modes leading to splashing are those whose wavelength is smaller than the melt pool depth and whose growth time is shorter than the duration of the melt-inducing transient heat load and the associated melt lifetime.

General types of instabilities of relevance to fusion applications are shear-, buoyancy- or geometry-driven. Shear-driven instabilities can arise due to plasma flows or body forces acting along the melt pool. Gravity and the Lorentz force due to eddy currents are body forces normal to the surface that can trigger buoyancy-driven instabilities. Geometry-driven instabilities are consequences of either sloping bathymetry effects or obstacles present on the path of the melt. Given the characteristic melt thickness, typical plasma flows, the Lorentz force due to halo current magnitudes and the gravity magnitude, it appears that geometry-driven instability is most likely to lead to the melt pool destabilisation and material ejection [1152]—in line with the present empirical evidence. Other candidates, both of relevance to the TQ phase of disruption, where definite conclusions have not been reached yet, concern the buoyancy-driven instability caused by the Lorentz force due to eddy currents (which can reach values up to $10^7\,\mathrm{N\,m^{-3}}$) and recoil pressure destabilisation in the case of intense vaporisation from the pool surface. A final comment is due on the peculiarity of fusion relevant melting scenarios, i.e. the stabilising role of the resolidification, see section 9.3.4.

9.3. Modelling of experiments and predictive studies

This subsection summarises results of numerical modelling focusing first on the simulations of existing experiments which provide empirical input concerning the heat loads, the PFC geometry and the magnetic field inclination. The modelling outcome is compared to observed post-exposure surface modifications but also to additional empirical constrains available in specially designed experiments. This is followed by discussion of predictive numerical studies which employ ITER-specified input for loading, PFC geometry and magnetic field inclination. The subsection is structured by the nature of the heat loads.

9.3.1. Modelling approaches and numerical tools.

PFC melting scenarios fall under the category of MHD free-surface flows coupled with heat transfer and phase transitions. PFC melt events are characterised by vast spatial scale separation: the extent of the typical melt motion along the PFC (that is defined by the wetted area) is up to a fraction of a meter, the melt depth is $\sim 100\,\mu\mathrm{m}$ and nonlinear free-surface instabilities (that are responsible for splashing) develop on even smaller scales. In addition, the melt domain is bounded by two evolving interfaces: the solid-liquid boundary and the plasma-side free-surface that might deform rapidly and severely, leading to material ejection. Brute force numerical modelling of such multi-scale problems is prohibitively expensive computationally, thus different approaches and simplifications have been sought and employed.

The scale separation allows the use of the shallow water approximation [1187] that is based on the depth-integration of the Navier–Stokes equations. The depth-averaging leads to a drastic reduction of the computational cost and opens up the possibility to simulate the actual size of PFCs (including active cooling) and wetted areas over prolonged exposure times, while retaining sufficient physics details for adequate description of large-scale melt motion. The MEMOS-U [1122, 1123, 1128] and MEMENTO [1130, 1188, 1189] codes are former and new numerical implementations of the MEMOS-U physics model, respectively. Both codes solve the 3D heat and phase transfer problem coupled with the incompressible Navier–Stokes equations (for the metal phase) in the shallow water approximation and with 3D current propagation equations on the domain with time-evolving and deforming metal-plasma interface. The PSI processes are incorporated through the boundary conditions on the free surface. In particular, the escaping emission current density is evaluated on the basis of scalings derived from comprehensive 2D 3V SPICE2 PIC simulations of reactor-relevant multi-emissive magnetised sheaths [1119, 1167, 1168, 1173, 1174].

In investigations focusing on melt instabilities and splashing, naturally smaller scales must be resolved, typically at the cost of limiting the size of the simulated domain to a small fraction ($\mathcal{O}(1\,\mathrm{mm})$) of the transient load induced melt pool extension ($\mathcal{O}(1\,\mathrm{m})$) and the exposure to few tens of ms. Such modelling of *multiphase* flows with severely deforming free surface has been carried out thus far only in 2D geometry with customised set-ups in commercial or open-source software, where the Navier–Stokes equations can be solved together with the heat transfer and field equations. Fusion relevant simulations have been carried out with customised set-ups in OpenFOAM [1190–1192] where the plasma medium above the metal surface was modelled as a fluid with realistic properties and in ANSYS Fluent [1136, 1193] where the plasma was modelled as a so-called ghost fluid, adopting the method that has been successfully applied to pressure-driven flows occurring at cathode spots in vacuum arcs [1194–1196].

In the case of highly elevated surface temperatures and intense vaporisation, the detailed modelling of vapour shielding requires that various atomic processes and MHD effects are considered. There are mainly two tools that are capable of such simulations. TOKES [1197] is a full-scale tokamak simulation platform for the modelling of multi-fluid plasma processes in core and SOL plasmas that accounts for the evolution of the magnetic field as well as of the currents in the plasma and the poloidal field coils. Models include fuelling, transport of radiation and neutrons as well as transport of vapour atoms in the vessel along with their ionisation and charge-exchange collisions. The HEIGHTS simulation package [1198] has been developed to study intense energy deposition on target materials in various applications and has also been employed to simulate fusion relevant scenarios under transient loads [1199–1201]. The integrated models and packages include MHD model of the secondary plasma, coupled with plasma heat conduction, radiation transport, magnetic diffusion and core plasma energy deposition. In case low collisionality does not warrant the validity of fluid descriptions, PIC simulations offer the possibility to treat energetic particles and sheath formation. The PIXY code [1202] is a weighted (1D 3V) PIC code simulating interaction of the plasma particles with the vapour released from the surface. It is coupled to the 1D heat conduction equation and allows to model vapour shielding effects in the PFC thermal response by accounting for radiation cooling and ion-neutral collisions, which dissipate the electron and ion fluxes, respectively.

9.3.2. Modelling of melting under steady state loading. The WEST experiment on the melting of an ITER-like actively cooled W MB [1129] was modelled by the MEMENTO code employing the experimental heat flux. The modelling revealed surface temperatures of only few degrees above the melting point and an instantaneous melt pool depth $h < 10\,\mu$m [1130]. In spite of the sustained nature of melting and, thus, the extended melt lifetime, for such ultra-thin layers, the viscous damping (scaling with $1/h^2$) is highly efficient in preventing significant melt acceleration and displacement, which is further restricted by the prompt resolidification of the melt layer in contact with the surrounding colder solid surface. While the $\mathbf{J} \times \mathbf{B}$ force was responsible for the major melt displacement along the LE, the contribution from thermo-capillary effects was also discerned in the modelling of the final deformation profile. The resulting speeds of $v \sim 1\,\mathrm{cm\,s^{-1}}$ led to a modest, ~1 mm, overall displacement of the melt pool and, hence, to a small mass excavation and material build-up. A unique experimental constraint of these WEST exposures, that concerned the time resolved detection of the LE deformation due to the melt displacement, was also closely reproduced by the MEMENTO simulations [1130].

9.3.3. Modelling of ELM-induced melting. Simulations of the LE W exposures in JET [1120, 1121] and AUG [1124, 1125] with the MEMOS-U code [1122, 1123], highlighted major aspects of the transient W melt pool dynamics. Detailed modelling of these exposures with the experimental heat fluxes revealed the importance of convective cooling, TE and resolidification on the melt formation and dynamics (effects discussed in detail in section 9.2). The depth of the transient pools for the uppermost part of the sample corner (where the deepest melting occurs), as a function of the exposure time and the poloidal coordinate, is presented in figure 85(*b*). In contrast to the aforementioned WEST experiment, in these exposures of inertially cooled samples, the deeper $h \sim 200\,\mu$m melt pools experienced much less efficient viscous damping so that the dominant $\mathbf{J} \times \mathbf{B}$ force accelerated the liquid metal up to $v \sim 1\ \mathrm{m\ s^{-1}}$ over the transient pool life time of ~10 ms. The observed final deformation profiles were closely matched by the simulations (see figure 84); material build-up is a cumulative effect of displacement of several transient melt pools. An additional observation concerned the material ejection shown in figure 83 that was also successfully replicated in the MEMOS-U modelling, where some of the transient melt pools reached the sample edge and were expelled from the domain [1122]. These events are depicted by the arrows in figure 85(*b*).

In order to model the experimentally observed W ejection, the main characteristics of macroscopic melt motion emerging from such MEMOS-U simulations (melt thickness, speed and temperature) were applied as boundary conditions in customised FLUENT set-ups [1136]. This numerical tool combination allows for the resolution of smaller-scale flow features such as strong free-surface deformations and melt ejection (FLUENT), while enforcing large-scale flow characteristics (MEMOS-U). Navier–Stokes simulations in FLUENT revealed that the stability of the melt layer flowing over the PFC edge is governed by critical values of the Weber number, which quantifies the relative strength of fluid inertia and surface tension, $\mathrm{We} = \rho_\mathrm{m} h v^2/\gamma$ [1136]. The critical curves of We, separating three hydrodynamic regimes characterised by various degrees of downstream flow attachment to the underneath solid surface, are depicted in figure 86. In particular, with the MEMOS-U predictions of the ELM-induced transient tungsten pool depths h and velocities u [1122], the melt ejection event shown in figure 84 corresponds to $\mathrm{We} = 2\text{–}8$. Such values of the Weber number place it mostly in the quasi-steady jetting regime, in agreement with the observations. The simulations [1136] also revealed that at the intermediate and attached regimes (domain below $\mathrm{We} = 3.4$ in figure 86), the size of melt bulge forming when melt is turning over the edge is about several h. This implies that a layer can easily bridge a gap several times larger than its thickness. Such a hydrodynamic picture is valid for inviscid fluids with Weber numbers $\mathrm{We} \geqslant 1$. Thinner and/or slower layers characterised by small We will not bulge as much. Still, the resolidification can assist in the bridge formation even in such regimes, as clearly demonstrated in the AUG gap experiment [1137].

In the above LE experiments, the melt surface temperature well exceeded the W melting point so that the thermionic sheath was in the SCL regime and obeyed the plasma parameter scaling, as discussed in section 9.2.3 and as employed in the modelling [1122, 1123]. The dependence of the escaping TE current on the magnetic field inclination angle was further tested in the modelling of the sloped geometry W exposure in AUG [1124]. MEMOS-U simulations revealed that variations of the surface normal, affecting both the deposited heat flux and the local escaping TE current density, were responsible for the experimentally observed material build-up along thin ridges on one side of the sample [1126].

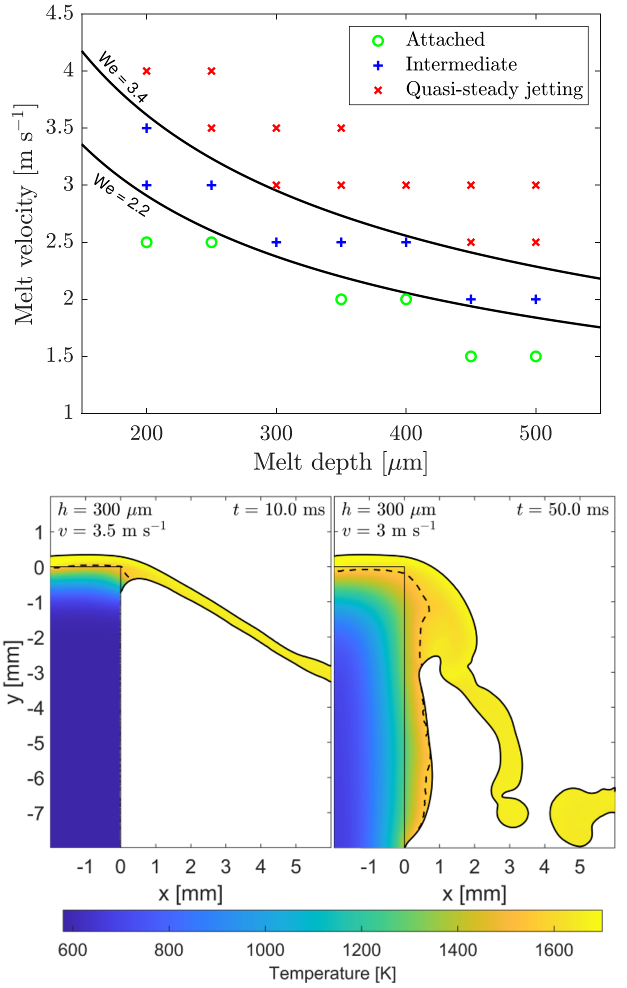

Figure 86. Upper: parametric map of the flow regimes for liquid Be in the depth-velocity plane. The three main flow behaviours that emerged in pure hydrodynamic simulations can be separated by curves of constant Weber (We) number. Reproduced from [1136]. © 2022 The Author(s). Published on behalf of IAEA by IOP Publishing Ltd. CC BY 4.0. Lower: coupled heat transfer and hydrodynamic simulations of Be flows over a straight edge, displaying two different ejection regimes: quasi-steady jetting [1136] (left) and the so-called intermediate regime [1136] accompanied by detached material (right). The melt front is plotted as the dashed line; the injected melt depth h and velocity v are indicated. Reproduced from [1152]. © The Author(s). Published by IOP Publishing Ltd. CC BY 4.0. Reproduced from [1136]. © 2022 The Author(s). Published on behalf of IAEA by IOP Publishing Ltd. CC BY 4.0.

The specially designed experiment of sloped Nb and Ir samples in AUG had accessed a previously unexplored regime allowing to evaluate the impact of TE prior to the transition to space charge limitation [1130]. Given the low melting points (below 2750 K for Ir and Nb vs 3695 K for W), the Nb and Ir TE current densities were about two and four orders of magnitude lower, respectively, than for W. Modelling with the MEMENTO code revealed that in this weak Lorentz force density regime, gravity and thermo-capillary effects were responsible for the bulk melt displacement. Under the same experimental heat flux, simulations managed to reproduce the thermal responses and deformation profiles of two refractory metals with diametrically opposite thermionic properties. Additional experimental constraints that were related to the observed onset of melting for these two materials were also reproduced.

Finally, modelling of the electrically insulated, i.e. floating, W LE exposure in AUG [1128] confirmed the role of the replacement current density. MEMOS-U simulation results revealed that in absence of the replacement current and the associated (typically dominant) $\mathbf{J} \times \mathbf{B}$ force, gravity acceleration was sufficient to displace the melt pool over the observed distance. The reason is that unusual energy deposition (see section 9.1.2) led to the formation of a deep ($\sim$1 mm) sustained pool which experienced weak viscous damping and was accelerated over a long ($\mathcal{O}(1\,\mathrm{s})$) time.

MEMENTO [1188, 1189], tailored to modelling melt motion problems characterised by a large spatio-temporal scale separation, has also recently been used for predictive studies of ITER divertor MB damage [1203]. In this study, the ELM energy density thresholds and the acceptable number of uncontrolled ELM transients before damage occurs, which could affect the long-term performance of the MBs, were investigated. The MEMENTO simulations [1203] revealed the importance of the coupling between heat flux loading and surface deformation, which is present for all shallow incidence angle cases. It results from the reduction of the projection area for the parallel flux due to surface deformation and leads to a positive feedback loop where already deformed surfaces are subjected to even stronger heat fluxes. Such coupling implies that safe ELMy operating windows depend on past surface deformations, i.e. ITER ELMs that would not melt an undamaged MB could exacerbate damage to one already deformed by previous overloading.

9.3.4. Modelling of disruption-induced melting. The deliberate VDE campaign carried out in JET led to unique experimental evidence for the disruption-induced melting of Be PFCs. The observed melting of the Be UDP as well as the formation of the *inverse waterfall* structure [1127] have been modelled with the MEMOS-U code employing the heat flux as reconstructed from available thermocouple data and empirical CQ halo current densities [1122]. The continuous VDE heat fluxes deposited over few tens of ms resulted in the formation of a sustained melt pool whose depth reached 500 μm. The VDE-induced $\mathbf{J} \times \mathbf{B}$ force (counteracted by viscous damping) accelerated the melt to a few m s^{-1} displacing it over distances of $\sim$10 cm. The importance of convection and re-solidification is highlighted here by the fact that the melt was created on the UDP wetted face but moved over the corner onto shadowed side, where it re-solidified into a structure resembling an *inverse waterfall*. Detailed modelling revealed that the balance between the resolidification rate and the uninterrupted melt supply (dictated by heat transfer in the wetted area) determines the moving layer thickness and final deformation profile [1122].

Similar to the aforementioned modelling of transient W melting events, the macroscopic melt motion characteristics from these MEMOS-U simulations were employed as boundary conditions in customised fluent set-ups [1136] aiming to model the experimentally observed splashing of Be flows over the UDP straight edge [1127]. The predictive capability of such a modelling approach was tested by comparing the output of the Navier–Stokes simulations with the JET data published in [1127] concerning the frozen melt layer morphology and the location of Be droplets that splashed onto the nearby vessel surfaces [1136]. These simulations reconfirmed that accounting for the coupling between fluid dynamics and heat transfer results in a stabilisation due to the progressive re-solidification of the melt layer downstream of the corner, which reduces the downstream melt depth and leads to higher viscous damping, as discussed in section 9.2.2. Two examples of such coupled hydrodynamic and heat transfer simulations are depicted in figure 86 for different melt layer speeds leading to full jetting (left) or partial detachment and ejection of material (right).

The above tools, validated in the modelling of multiple dedicated melt experiments, have been employed in predictive ITER studies concerning VDE-induced melt damage of the FWPs [1155, 1204, 1205]. In these studies, the spatio-temporal profiles of heat flux deposition were calculated employing the SMITER field-tracing software [1206] which utilised time-dependent magnetic flux maps, the radial parallel heat flux distribution in the halo region and the total energy deposited on the FW simulated by the disruption code DINA [1207, 1208]. Initial calculations, performed for the CQ phase of the unmitigated 5 MA/1.8 T upward VDE, revealed that the highest load occurs on the upper FWP #9 and #8, the latter receiving a surface normal heat flux of 187 MW m^{-2} at the end of the ≈200 ms long deposition time [1204]. These were reassessed in [1205] following updates to the DINA disruption model, in particular the model's calculations of the radial parallel heat flux distribution in the halo region and its characteristic decay length. For the same scenario of an unmitigated 5 MA/1.8 T upward VDE, the new simulations predicted a maximum surface normal heat flux of 83 MW m^{-2} at the end of the 75 ms long deposition time. Similarly, for the 15 MA case, the new maximum heat flux value of ≈320 MW m^{-2}, was almost three times smaller compared to the original. As a consequence, while, for the original 5 MA case, MEMOS-U modelling predicted 0.5 mm deep deformation as a result of the poloidal melt displacement by the Lorentz force, the heat load in the new 5 MA case proved to be too small to bring the FW temperature to the melting point even when accounting for the large uncertainty in the starting Be impurity density [1205]. Simulations for the new 15 MA case showed that the induced melt pool, with surface temperatures approaching 2500 K, can be displaced by up to 0.5 m, leaving an ≈2 mm deep excavation behind.

In a further extension of this study [1155], the FW energy deposition and melt damage were assessed for 38 (out of the 84) cases present in the DINA disruption database. The latter includes both downward and upward VDEs as well as MDs for the three scenarios that are envisaged for the ITER PFPO: 5 MA/1.8 T, 7.5 MA/2.65 T and 15 MA/5.3 T where for each case at least two choices for the perpendicular transport coefficient were assumed. The vapour shielding has been included in the MEMOS-U modelling though a tabulated input extracted from the PIXY code [1202]. The PIXY simulations with the DINA plasma parameters provided the vapour shielding efficiency (reduction coefficient for the incident heat flux) as a function of the surface temperature and the initial heat flux. The use of such coefficient at every time step of the MEMOS-U simulations relies on the assumption that the vapour shield stays above the mesh grid over the time step, i.e. no expansion parallel to the FW occurs. MEMOS-U calculations of the final deformation profiles showed no damage for all the 5 MA VDEs and MDs as well as for nearly all of the 7.5 MA cases. Substantial melt damage was found for all 15 MA cases, with a similar deformation caused by VDE and MD. Concerning the material excavation depth, the upwards 15 MA VDE presents the worst case scenario, where results, with vapour shielding included, predicted a 2 mm deep deformation, about 30% lower compared to the 3 mm predictions without shielding.

This worst case of an unmitigated upward VDE at 15 MA/5.3 T, striking FWP #8 [1155] has been selected as a concrete ITER CQ scenario for the simulation of Be melt instabilities and material splashing [1193]. MEMOS-U calculations [1155] showed that up to half of the liquid Be volume present on the surface of FWP #8 reaches the chamfered edge of the panel towards the end of the CQ. Similar to the JET Be UDP case discussed above, the presence of a 45° chamfer at the edge of the FW panels causes disturbances in the liquid layer, seeding free-surface instabilities. The FLUENT software has been employed to simulate the evolution of a flowing Be layer injected with the spatio-temporal profiles of the main melt characteristics (height, velocity and temperature) as adopted from the corresponding MEMOS-U simulations [1155]. The FLUENT results [1193] suggest that, although the liquid layer is significantly destabilised, only 5% of the total melt mass created on the FWP surface is lost through ejection. Since the ejection is found to be parallel to the FWP chamfer, it is anticipated that most of the liquid ejecta moves towards remote, plasma-shadowed surfaces such as inter-panel gaps. There, similarly to the JET observations [1127], it will likely splash and remain as a frozen spatter. Owing to their extended contact area and strong metallic bonding such splats are unlikely to convert to solid dust [1130].

The ITER divertor damage caused by the earlier phase of disruptions has been addressed in [1185], where the 2D dynamics of the vapour shield layer has been simulated by the TOKES code [1197] for the MD of a full TF/full plasma current H-mode (DT) 350 MJ discharge. It was shown that during a few ms load, the unmitigated heat flux on the outer divertor leg can reach 40–80 GW m^{-2}, while the heat load is reduced below 8 GW m^{-2} when vapour shielding is taken into account. The heat flux maximum is at the separatrix SP where intensely vaporised tungsten is ionised in front of the target. The cross-field diffusion of such a secondary W plasma shields the rest of the target so that vaporisation and the melt region become confined to a 1.5 cm stripe. Without shielding accounted for, the extent of the melt and intense vaporisation region would have been about ten times larger.

9.3.5. Modelling of RE induced-melting. The interaction of REs at energies of a few MeV with PFCs leads to volumetric heating, because the respective penetration depth range is of the order of millimetres. Up to date, modelling has been limited to the thermal response, neglecting the mechanical solid response or the hydrodynamic melt response. In the literature, no numerical tools are able to simulate solid-fluid and solid-solid interactions necessary to describe all possible damage mechanisms that could arise during RE-PFC interaction [1073, 1151, 1152].

The common methodology comprises calculations of relativistic electron transport into matter with a Monte Carlo code that computes the energy deposition profile. Thus, the volumetric heat flux can be obtained which can be used in heat transfer modelling. Early works which follow such approach are a few decades old, see e.g. the references [1209–1211]. Already in 1993, a work employing GEANT for electron transport highlighted the two-fold effect of a strong shallow inclined magnetic field on the energy deposition; return of reflected electrons to the surface and gyration of electrons inside the material [1209]. Typically, simplifying assumptions have been employed for RE impact properties such as the current density, energy distribution and transverse to parallel energy ratio, see [1211] (employing the FLUKA code for electron transport) and [1212] (employing the ENDEP code for electron transport). Parametric studies with the HEIGHTS code [1150] revealed that the melt depth is sensitive to the incident energies and angles, highlighting that the knowledge of the RE velocity distribution is critical for accurate predictions and emphasising again the role of the magnetic field. Indeed, gyration increases the electron path, contributing to enhanced slowing down rates and resulting in reduced penetration depths [1209].

The most recent evaluations concerning PFC damage upon RE impact has been carried out with the disruption code DINA [1207, 1208] for the time-dependent plasma equilibria, the SMITER field line tracing code [1206] for 3D RE footprints, the GEANT4 tool-kit [1213] for electron transport (neglecting the B-field) and the MEMOS-U code [1122, 1123] for heat transfer. The workflow has undergone preliminary testing against observations of RE-induced Be melting in JET, with further studies underway.

9.3.6. Other simulation efforts. Metallic melt layer stability has been addressed in several studies [1190–1192, 1214] that employed customised OpenFoam set-ups in order to simulate multiphase free-surface flows. The latest of these works [1214] numerically investigates the stability of W melt under prescribed parallel plasma flows and concludes that plasma flow velocities of a few km s^{-1} are sufficient to trigger violent free-surface instabilities, which ultimately lead to the complete disintegration of the liquid pool into droplets within sub-millisecond time scales, i.e. before any noticeable bulk melt motion can develop (see figure 3(*c*) in [1214]). These results can be also extrapolated to Be using analytical Kelvin–Helmholtz scalings [1214], leading to the prediction that almost all macroscopic melts (Be or W) produced in current tokamaks should disintegrate into droplets. This has not been confirmed by post-mortem observations of transient PFC melt events in present tokamaks, see section 9.1. The discrepancy is most likely due to unrealistically high plasma viscosity values assumed in these simulations [1152]. The most recent modelling with the OpenFoam set-ups [1215] have addressed vapour-driven Be melts and also predicted pool disintegration. The simulations assumed an arbitrary combination of pool and vapour parameters even though the vaporised flux is defined through the surface temperature by the Hertz-Knudsen relation.

The simulation package HEIGHTS has been employed for the assessment of ITER armour damage due to transient heat loads [1199–1201]. However, the assumed scenarios of the temporal and spatial scales characteristic for energy deposition are outside the parameter range relevant for ITER. Consequently, so the presented results are not immediately applicable for predictive simulations of armour damage under loading conditions according to ITER specifications.

9.4. Summary

Significant progress has been achieved in the development of methodology and modelling tools for simulations of the PFC response and melt dynamics under *surface* plasma heat loads. Continuing extensive validation activity through dedicated EUROfusion experiments, specially designed to maximise experimental constraints, has allowed to gain confidence in the physics models developed and demonstrated that we are well on our way to high fidelity cost-effective modelling.

The situation is rather different for the *volumetric* loading scenarios realised under RE-impacts. The physics of damage is not understood, the tokamak evidence is limited and modelling of RE-induced damage at its infancy. To realistically model such scenarios, it is crucial to go beyond heat transfer to include thermal expansion, internal phase transitions, shock-wave propagation and material fragmentation. Finally, there is a clear need for controlled experiments on damage by RE impact in order to test developed work-flows.

10. Summary

Scrape-off-layer and divertor transport

A comprehensive description of the SOL physics is currently still lacking. While the parallel transport on the magnetic field surfaces is relatively well understood, the perpendicular transport across the flux surfaces is not understood to a level that would allow sound predictions for ITER. The parallel transport can be well described by classical conduction and convection, with some corrections for kinetic effects. The perpendicular transport is largely anomalous in nature. However, enormous efforts have been made in the last decade to reduce the uncertainties. An ITPA multi-machine comparison of divertor heat fluxes has revealed the strong dependence of the radial heat decay length on the inverse of the poloidal magnetic field. The so-called *Eich scaling* predicts a power decay length of

$\lambda_q < 1\,\mathrm{mm}$ for ITER at full current operation. However, several computational approaches predict this power decay length to be longer, mainly because the transport regime in ITER is thought to be different from that in current devices. BOUT simulations claim that ITER will be dominated by turbulent radial transport, in contrast to the drift-dominated transport in current devices. XGC simulations predict a longer radial correlation length of edge turbulence due to the lower $\mathbf{E} \times \mathbf{B}$ shearing rate of the neoclassical flow for ITER. All numerical exercises have been carried out for attached plasmas. The same applies to the Eich scaling. Significant radiation in the partially detached divertor operation will spread the power.

Classical drifts have been further characterised, but the various results from experimental devices are controversial. While in DIII-D prompt losses can have a significant effect on the radial electric field and hence turbulence suppression in H modes, in AUG the effects seem to be small. However, it appears that drifts in the SOL and PFR could be responsible for the asymmetries in the fluxes to the inner and OTs. Measurements showed that drifts are essential for the overall plasma solution and the distribution of neutral particle sources in the divertor, and are responsible for the feeding of the confined plasma from the high-field side. Drifts are more pronounced in smaller devices, leading to greater asymmetries in the divertor plasma. In larger devices, such as ITER, these asymmetries are expected to decrease. This tendency towards symmetry is further enhanced in strongly radiating plasmas, where larger devices are expected to have a more symmetric divertor, both in terms of plasma parameters and detachment characteristics.

The anomalous turbulent transport in the SOL is still not fully understood. This is particularly true for the interplay between broadband electromagnetic turbulence and blobby transport. Some progress has been made in characterising the blobby transport using fast camera systems, but this has mostly been limited to L modes. It is generally understood that the anomalous transport and the corresponding structures (blobs) are generated at the separatrix, driven by curvature effects.

The far SOL transport is less understood and predictions of plasma parameters far into the SOL are still subject to large error bars. This is particularly true for H modes and ELM suppressed H modes. Neutral leakage from the divertor into the main chamber complicates the study of far SOL transport, especially in the current smaller devices. The situation may be different in ITER, where the ionisation mean-free path is much shorter and the divertor is effectively decoupled from the main chamber. In that case, recycling at the main chamber wall will be the more determining factor of the far-SOL plasma profiles.

Stationary power dissipation

Steady state power dissipation is required to reduce the peak power load on the divertor to $10\,\mathrm{MW\,m^{-2}}$. Recent predictions of the unmitigated power load profile in the divertor with $\lambda_q \sim 1\,\mathrm{mm}$ have further emphasised the need for efficient power dissipation by seeding impurities. Over the past 40 years, power dissipation by various seeded impurities has been studied. The most promising for ITER are N_2, Ne and Ar. Nitrogen has been shown to be the best coolant, mainly due to its radiative cooling curve, which exhibits high cooling rates at 10 eV. This is consistent with the requirement that the divertor must be cooled to $T_e < 10\,\mathrm{eV}$ to reduce the physical sputtering of tungsten by the seeded light impurities to acceptable levels. However, nitrogen may have severe limitations for use in ITER due to the by-product, tritiated ammonia, which will have an impact on the duty cycle and the tritium plant. Impurity enrichment, the ratio of divertor to plasma core impurity concentrations, is a good criterion for the selection of impurity species. In medium-sized tokamaks, neon has been found to have a particularly low enrichment, resulting in high neon core contamination for a given divertor radiation. Nitrogen and argon are much better in this respect. Predictions for ITER suggest that in this case there is not an issue for neon due to its shorter ionisation mean free path. The effect of seeding on pedestal and core confinement has been studied extensively over the last decade. Neon and nitrogen have been found to stabilise ITG instabilities due to the higher Z_{eff} in the core and lead to improved core confinement. Impurity seeding can have a detrimental effect on the pedestal pressure, which is explained by an outward movement of the density profile leading to an increased separatrix density. This increased separatrix density results in a high density region on the HFS, which fuels the confined plasma and degrades confinement. This can be counteracted by nitrogen seeding, which reduces the power flow into the divertor and restores energy confinement. Highly radiative plasmas by nitrogen seeding with high confinement ($H_{98(\mathrm{y},2)} \sim 1$) have been obtained on AUG in type III ELMy H modes.

Most of the data on steady-state power dissipation by seeding impurities were not obtained in the relevant ITER regimes. High-density operation at low pedestal collisionality is not possible with current devices. This is also true for relevant no-ELM regimes, such as the QH mode. Seeding impurities into type III ELMy H modes was successful. Seeding into I-mode revealed a problem with the integration of detachment. I-mode to L-mode transitions were observed before detachment of the outer divertor was achieved with nitrogen seeding.

Detachment control has been achieved using various techniques. The most reliable are thermoelectric current measurements using shunts, radiation measurements using metal foil bolometers and AXUV diodes. Langmuir probes are inherently difficult to use at low divertor electron temperatures, and surface temperature measurements by thermocouples or IR thermography suffer from poor signal-to-noise ratios in these partially or completely detached plasmas. Control systems have become more sophisticated, including multi-parameter and multi-variable control to take into account not only the degree of detachment and radiation level, but also the effect on confinement.

There are still many open questions in the modelling of the impurity seeding and detachment process, which has not progressed much beyond what was known three decades ago.

ELM transients

The understanding of ELM physics in the context of power exhaust has improved significantly since the formulation of the ITER Physics Basis. In particular, the quantitative prediction of the ELM impulse parameter, $\varepsilon\, t^{-1/2}$, has improved both in terms of qualitative understanding and predictive confidence. The ELM energy footprint can be described as the result of an MHD instability connecting the pedestal plasma to the divertor target. Multi-device data are found to be consistent with this model. The simple model depends only on the electron pedestal pressure, the major radius, q at the edge and the ion transit time. However, for practical reasons, the ion transit time is always assumed to be the same. The model describes energy deposition without dissipation by radiation, for which regression analysis of the multi-device data set yields the scaling law $\varepsilon^{\mathrm{peak}}_{\|,\mathrm{reg}} = 0.28\,\mathrm{MJ\ m}^{-2} \times n^{0.75}_{\mathrm{e,ped}}\, T^{0.98}_{\mathrm{e,ped}}\, \Delta E^{0.52}_{\mathrm{ELM}}\, R^{1}_{\mathrm{geo}}$. The as yet unresolved scatter of the experimental data in this scaling suggests the influence of hidden parameters, thought to be related to the different regimes of conductive and convective ELMs.

The time dependence of the ELM energy deposition, the other important parameter in the ELM impact, was accurately described by parallel transport models. A 1D free steam model, where ions propagate through the SOL from the pedestal to the targets, showed remarkable agreement with the experimental data, despite its simplicity. Recent Langmuir probe data during ELMs indicate that strong ELM electron cooling by Coulomb collisions does not occur. Electron temperatures during ELMs have exceeded 100 eV on JET. More computationally intensive models such as particle-in-cell codes, which include sheath formation, ion orbits and other effects, accurately describe the time dependence of deposition and other features such as deposition in tile gaps and corners. However, plasma neutral interactions are not included in these models and predictions may be pessimistic if CX processes lead to a smoother deposition profile. The kinetic ELM modelling was complemented by fluid modelling of the ELMs. The fluid model, with kinetic corrections, can be used to predict the full radial deposition profile and can also be used to investigate recurrent events for cumulative effects. Good agreement was found between the fluid model and the kinetic model for convective ELMs. However, for conductive ELMs, the fluid model was not appropriate, resulting in supersonic ELM transport. MHD simulations of the ELM dynamics revealed two regions with separate effects. The first region is the ELM affected region in the plasma edge, where magnetic ergodisation takes place, resulting in very long connection lengths of up to tens of km. The second region is the SOL, where ELM filaments propagate radially and simultaneously lose energy to the divertor by parallel losses with standard SOL connection lengths.

Several techniques including 3D fields, pellets and axisymmetric displacements have been developed to reduce ELM size to a tolerable level. However, the energy deposition from these mitigated ELMs is still consistent with the deposition model. Complete suppression of ELMs by RMPs has been observed in many tokamaks. Increasing the ELM frequency is another approach to mitigate the heat load from ELMs. This can be done using hydrogen pellets or supersonic molecular beams. Comprehensive studies have shown the limitations of these techniques. The maximum thermal load is not reduced as much as hoped, and the pellet size has to be tuned depending on the proximity of the pedestal to the MHD stability limit.

Operating regimes with small tolerable ELMs and potential for ELM heat flux removal by radiative processes have been identified but further research is needed to assess their utility for ITER-size devices.

Application of RMPs for ELM control

Due to the unfavourable scaling of Type I ELMs with machine size, effective control strategies are essential. RMPs, successfully tested in tokamaks such as AUG, DIII-D, EAST, JET, KSTAR and MAST, have shown promise in mitigating or suppressing ELMs, making them a primary ELM control strategy for ITER. However, it remains to be demonstrated that this is compatible with the steady-state power dissipation requirements of ITER. The inherent dilemma is that optimal plasma boundary solutions for steady-state heat load removal (e.g. high divertor density, high impurity radiation) in current devices have been found to be mostly incompatible with the requirements for full ELM suppression, since they require lower pedestal collisionality. As current experiments can only cover either the range of pedestal collisionalities or densities expected in ITER, an integrated solution cannot be demonstrated before ITER operation. This highlights the need for further exploration of the currently accessible operational space to further optimise the ELM control strategies envisaged for ITER.

A common observation in current ELM control experiments is the reduction in pedestal density and gradient when RMPs are applied, known as density pump-out. While RMPs can effectively reduce transient local heat loads, their compatibility with ITER's steady-state power dissipation solutions remains to be demonstrated. Predictive SOLPS modelling, on which the design of the ITER divertor is based, makes the assumption of toroidal symmetry. However, this basic assumption becomes invalid with the application of RMPs, which break the toroidal symmetry: Particle and heat loads can split into non-axisymmetric striations.

This suggests that it will be challenging to decouple the magnetic footprint from the optimisation of ELM suppression, complicating the management of the power dissipation and its predictive modelling. The resulting 3D heat and particle flux structure may require a rotating RMP field to distribute the steady state power loads. Experiments to optimise the RMP spectrum by phase rotation have shown that the average heat load can be reduced by more than a factor of two. Radiative cooling by seeded impurities has the potential to further smoothen the heat flux profiles, as indicated by detachment experiments.

Codes such as EMC3-EIRENE, which extend 2D plasma boundary modelling to fully 3D simulations, are used to assess the impact of RMPs on heat loads, in particular the effect of the striated footprint patterns. Initial simulations for partial detachment with RMPs at ITER FPO with 100 MW of power output through the SOL suggest that sufficient dissipation is possible despite significant heat loads on secondary SPs. Validation of such simulations against radiative divertor experiments with RMPs will be essential to improve the reliability of predictions for ITER and beyond.

Erosion of PFCs and impurity migration

Since the publication of the PIPB, many tokamaks around the world have moved from graphite to metallic walls. In particular, the transition of JET from CFC to an ITER-like wall of Be tiles in the main chamber and a W divertor has provided great insight into the erosion and impurity migration expected for ITER. In JET, the overall main chamber erosion with Be was greatly reduced compared to the C main chamber wall. The overall picture of impurity migration remained the same, with the main source of erosion being the main chamber wall and the transport of eroded material mainly to the inner divertor. The strong reduction in stepwise transport from the main deposition zone of the inner divertor to remote areas due to the absence of Be chemical erosion resulted in a massive reduction in Be dust formation compared to carbon. It was also found that no significant net deposition of Be occurs in the outer divertor due to the factor two lower Be flux to the outer divertor compared to the inner divertor.

The erosion of W in the divertor in both the JET and AUG H-mode scenarios is mainly due to the ELMs. Between the ELMs the divertor is detached and the erosion of W is much lower, mainly due to sputtering by light impurities, either residual or seeded, while during the ELMs sputtering by the fuel ions also becomes significant. Because of 95% prompt gyro orbit redeposition of sputtered W, the overall net W erosion in the divertor is greatly reduced compared to low-Z PFM. High energy CX neutrals can further contribute to the total W source, both in the divertor and in the main chamber, with experimental evidence e.g. from EAST. In the case of W main chamber LIMs, the incident intra-ELM fluxes contribute up to 70% to the average local W sources, while in LIM plasma configurations during start-up and shutdown, W self-sputtering can also become important. In AUG and WEST with a full W wall configuration, the divertor was identified as the strongest W source. However, the W core concentration is determined more by the W source from the main chamber PFC. To understand the screening of localised W sources, such as from LIMs or due to RMP application for ELM mitigation, studies in WEST highlighted the need for full 3D simulations, which are still an open area of research.

Over the last decade, significant progress has been made in modelling erosion, impurity migration and redeposition. ERO2.0 and WALLDYN have been successfully used to predict material migration for ITER. The main findings are that the erosion of a Be FW is dominated by ion impact (in particular Be self-sputtering) on the plasma wetted areas, which account for $\sim$10% of the total wall area. The CX neutrals contribute only $1/3$ of the total Be source. The highest erosion rate is found on the inner wall, but with a large uncertainty in the absolute value depending on the transport models used. Detailed investigations with 3D WALLDYN predict a factor of 5 higher redeposition in the main chamber compared to simpler 2D models. Simulations of material migration with WALLDYN and ERO2.0 for ITER $Q = 10$ scenarios predict up to 90% redeposition on the FW due to the opaque SOL. Modelling of intra-ELM W erosion predicts that sputtering of W by energetic deuterons is the dominant erosion process at typical light impurity concentrations. ERO simulations predict that W self-sputtering contributes up to 25% of the total W source and also revealed significant contributions from CX neutrals.

It should be noted that the envisaged transition of ITER from a Be to a full W FW will have a strong impact on the main chamber impurity source. This is of particular concern for the ITER ramp-up phase, when the plasma will be in direct contact with the W FW. Additional R&D is required to determine the relative contributions of impurity sputtering from boronisations and from seeding gases compared to sputtering from CX neutrals and tungsten self-sputtering, and their dependency on the plasma scenario.

HI inventory and recovery

In devices with carbon PFC, H isotope retention was found to be too high with respect to the T inventory limit in a thermonuclear device, mainly due to continuous HI co-deposition with C. Therefore, ITER was designed with a Be FW, retaining C (CFC) only in the HHF areas of the divertor and W elsewhere, with a plan to install a full W divertor before thermonuclear operation. Encouraged by the success of AUG in operating a full W device, the JET ILW project was undertaken to confirm the material choice for ITER, with further devices (WEST, EAST) subsequently moving to all-metal PFC configurations.

With detailed gas balance studies of fuel retention and post-campaign analysis of retrieved PFC samples, JET-ILW demonstrated a reduction in deuterium retention by a factor of 10–20 compared to the all-C JET, mainly due to the lack of chemical erosion of Be. However, T inventory growth rates due to fuel co-deposition with Be in the divertor were still a concern. Although the retained fuel fraction in Be deposits is significantly lower than in C, in-vessel fuel removal techniques would still be required to recover the T retained in the deposited layers. In comparison, fuel retention in the main chamber LIMs and UDPs in the JET-ILW was negligibly small (0.01%). Similar to the JET-ILW results, in the first campaign with an all-W AUG without boronisation, D retention was found to be reduced by a factor of 5–10 compared to an all-carbon AUG. With both measurement methods, gas balance and post-campaign sample analysis, comparable reduction factors were observed from all-C to all-metal PFC configurations. It should be noted that post-mortem studies typically yield values 3–6 smaller in absolute terms than gas balance, with the difference attributed to not fully representative wall coverage of samples taken from the vessel, losses due to storage of samples in air, and missing contributions e.g. from dust.

The encouraging results from AUG and JET were the main driver for the ITER decision to use a full W divertor from Day 1. More recently, the still significant growth rate of the Be-related T inventory has been one of the factors behind the plan to abandon Be altogether in ITER and switch to a full W device.

Even in full-W PFC devices, fuel recovery and wall conditioning methods are still required to maintain optimum discharge performance and in-vessel T inventory. Vessel baking is an effective method for removing residual impurities after pump-down and for fuel removal, particularly at high temperatures, but requires longer times for outgassing of thick co-deposited layers. GDC can be used to enhance isotope exchange and fuel removal, especially when combined with baking. However, it is not applicable in the presence of a toroidal magnetic field. In this case, electron/ion cyclotron wall conditioning can be used instead, but these methods still require future R&D efforts for optimisation and code validation.

While great progress has been made in understanding hydrogen retention for metallic wall materials, there are still open questions, e.g. the influence of seeded impurities (e.g. N_2, Ne, Ar etc) on fuel implantation. This also applies to the effect of implanted impurities on the formation of trap sites and on fuel diffusion in the PFM. For devices with reactor-relevant operating times and correspondingly high neutron irradiation fluence, the created trap sites can increase fuel retention by an order of magnitude. While sophisticated modelling tools have been developed for predictive simulations of fuel trapping, diffusion and permeation in the PFM over a wide range of parameters, most of the experimental results required for code validation have been obtained with materials exposed to fission neutrons or proxy ion irradiation, while studies with 14 MeV fusion neutrons will only become available with new dedicated irradiation facilities such as IFMIF and VNS.

Evolution of PFMs under sustained plasma exposure

The evolution of PFMs under sustained plasma exposure is a critical issue for future tokamaks. PFMs in tokamaks are subjected to synergistic loads combining thermal, plasma particle and neutron fluxes. Thermal and plasma particle loads scale strongly with device size, e.g. in ITER, the divertor must be designed for steady state thermal loads of up to $10\,\mathrm{MW\,m^{-2}}$, transient loads of up to $20\,\mathrm{MW\,m^{-2}}$ for 10 s transients, and cycling ELM transient loads at heat flux factors of up to $6\,\mathrm{MW\,s^{1/2}\,m^{-2}}$. Loading conditions above these limits will result in problems such as cracking, melting and dust formation, but even below these limits will result in long-term deterioration of the PFM.

Laboratory experiments, such as HHF test stands and linear plasma devices, provide controlled environments to study PFM behaviour under high fluence and high cycle conditions. For example, studies of the properties of W MBs at high fluence in Magnum-PSI, have shown that fatigue cracking is an important issue under ITER-relevant conditions. These and similar experiments have shown that cracking thresholds are significantly lower than the unmitigated ELM loads expected in ITER. Under these high cycle transient loads, cracks may also grow and propagate after their onset, potentially leading to local melting and component failure. Further experiments also focused on W recrystallisation under cyclic thermal loading, which can degrade the thermomechanical properties and performance of W PFCs. Future R&D is required to better define the safety margins for PFC loads, which, together with the margins for crack formation, will set boundary conditions for the plasma operational space of ITER and beyond.

Experiments in fusion devices complement laboratory studies by providing *real world* exposure conditions. The long-term behaviour of tungsten and beryllium PFMs has been studied in tokamaks such as AUG, WEST, EAST and JET-ILW. These studies reveal micro- and macro-cracking, dust formation and the effects of long-term plasma exposure on pre-damaged components. For example, AUG's transition to all-tungsten PFCs highlighted issues such as macroscopic cracking due to electromagnetic and thermomechanical forces, leading to design adjustments and the optional use of a more ductile W-heavy alloy to reduce crack formation. The occurrence of cracking and local melting on the W MB divertor PFCs in EAST highlighted the need for optimised shaping to avoid local overheating. Observations on the W divertor PFU in WEST highlighted the problem of cracking during transients when the total steady-state heat load is low enough to keep the W surface temperature below the DBTT, leading to brittle fracture.

Plasma exposure also induces surface modifications such as embrittlement, blistering and fuzz formation. Blistering, caused by hydrogen or helium implantation, can potentially degrade material integrity in the surface region. Fuzz formation on W under helium plasma exposure changes the surface morphology, erosion properties and thermal conductivity. The complex interplay between fuzz formation and erosion by ELMs/impurities has been studied experimentally both in linear plasma devices and in various tokamaks, concluding that W fuzz will only occur within a narrow operational window under ITER divertor conditions.

Dust formation as a result of surface damage and plasma interactions is a major challenge, particularly for future reactors with long operating times. In devices with metallic PFCs, dust is formed by processes such as melt droplet ejection, exfoliation and micro-cracking. The management of dust accumulation and migration is crucial to maintain plasma performance and safety. Studies in fusion devices and laboratory setups have aimed to quantify dust production rates, characterise particle properties and understand migration patterns to inform mitigation strategies. However, there are still significant gaps in the understanding of the respective processes, motivating future R&D efforts.

Another important issue is the interaction of plasma exposure with neutron-induced defects due to neutron wall loads in thermonuclear devices. Identified knowledge gaps highlight the need for further research into the trapping of hydrogen and helium in neutron-induced defects, the formation and influence of transmutation products, and towards a comprehensive understanding of the behaviour of PFMs under the combined effects of plasma, thermal and neutron loading. Advanced neutron sources providing 14 MeV fusion neutrons will be essential for these studies and for the validation of related modelling tools.

PFC damage by excessive heat loads

Transient heat loads that exceed the heat flux capabilities of metallic PFCs, such as those caused by unmitigated ELMs, VDEs and disruptions, can cause significant damage due to severe cracking and melting. The resulting metallic melt is subject to plasma-induced forces that displace material, causing large-scale surface deformation that can severely compromise power handling.

Since the publication of the PIPB, a coordinated effort by the ITPA and the EUROfusion consortium has been undertaken to plan and execute a series of carefully designed intentional melting experiments. These multi-machine studies have established a robust model validation base for PFC melting due to excessive plasma thermal loads, covering a range of devices with different material compositions, cooling methods (active and inertial), geometries, plasma scenarios and bulk current sources affecting the melt zones. Beyond standard damage metrics—such as displaced melt volume and final deformation profiles—these experiments have also introduced previously unattainable experimental constraints. Key advances include simultaneous exposure of materials with different thermal responses, high-resolution IR camera detection of melt onset and displacement, melt splashing from sample edges, and melt motion on PFCs with complex geometries such as tiles with gaps.

Model validation against the new extended empirical database has confirmed the critical role of TE in the melt damage of W components and has allowed confidence to be gained in the physical models developed to describe macroscopic melt motion and melt splashing. The validation process and model refinement led to the development of new simulation tools, MEMOS-U and MEMENTO, which have been used for ITER predictive studies of Be and W armour melting under transient heat loads.

For disruption transients, apart from CQ thermal loads at high plasma currents, the potential formation of high energy, high current RE populations constitutes the main threat to the ITER FW armour. REs are of particular concern due to their ability to penetrate deeper into the material bulk than typical plasma transient thermal loads, thereby endangering the integrity of the final actively cooled FW panels. As such, unmitigated REs represent a critical challenge for ITER, irrespective of the main chamber armour material selected.

In contrast to melting under plasma thermal loads, the understanding of PFC evolution under volumetric heat loads by RE-related power fluxes remains limited. Currently, no computational tools are available to reliably model the complex processes of RE-PFC interaction associated with volumetric heating, compressive flows, shock wave propagation and fragmentation. The main reason for this is the lack of controlled experiments on RE-induced damage, as experimental evidence of accidental damage does not provide sufficient experimental input. Since it is not possible to generate fusion-relevant electron beams in external facilities (due to the extreme intensity and high degree of localisation), experiments in tokamaks will be necessary to provide the missing data.

Conclusions

Since the *Progress of the ITER Physics Basis* (PIPB) in 2007, significant advances in scrape-off-layer (SOL) and divertor physics have been made, partly driven by ITER design modifications, such as the installation of RMP coils for ELM suppression and the decision to adopt a full tungsten divertor from day one of ITER operation. ELM mitigation and suppression have now been demonstrated across several tokamaks, and substantial progress has been achieved in integrating ELM suppression with detached divertor regimes.

Over the past decade, a great deal of research has been devoted to a better understanding of near-SOL transport. A multi-machine comparison of divertor heat fluxes coordinated by the ITPA revealed a strong radial heat flux decay length dependence on the inverse of the poloidal magnetic field, leading to the so-called Eich scaling, which predicts a decay length of $\lambda_q < 1\,\mathrm{mm}$ for ITER at full current operation. This scaling has shown quantitative agreement with a heuristic drift-based model of the heat flux decay length in low-gas-puff H-mode, although advanced simulations suggest a longer decay length under ITER-like parameters.

The decision to use a full tungsten divertor from day one initiated extensive studies on plasma detachment and its control. High power discharges with impurity seeding in AUG have demonstrated effective detachment control while maintaining high confinement in a full tungsten FW configuration. Similar results have been reproduced in other medium-sized tokamaks, reinforcing the design choice of tungsten PFCs for ITER.

Since the PIPB, JET's upgrade to an ITER-like wall with a beryllium main chamber and a full tungsten divertor has allowed extensive fuel retention studies to be carried out, demonstrating a tenfold reduction in fuel retention compared to carbon-based walls, which has also been demonstrated in medium-sized tokamaks with full W-wall armour. These results support the selection of the FW and divertor materials for ITER with respect to the safety margins for the tritium in-vessel fuel inventory.

Experiments at JET, AUG and WEST have further advanced the understanding of tungsten erosion, screening of tungsten sources and tungsten migration. Advanced in-situ and ex-situ diagnostics, combined with detailed simulations, have provided a robust parametrisation of the tungsten erosion sources in the divertor, providing detailed insights into the impact of these processes expected in ITER.

Significant progress has also been made in modelling the response of tungsten to excessive transient heat loads, particularly in resolidification dominated melt dynamics. Numerical simulation models, validated against data from JET, AUG and WEST, now provide high confidence predictions of how tungsten will behave under extreme plasma conditions.

Research outcomes from this period have led to multiple impactful publications, six of which have received the Nuclear Fusion Award.

The recent decision to move from a beryllium to an all-tungsten design for the ITER main chamber armour has opened up new areas of research. Key questions include the properties of the tungsten sources in the main chamber, in particular those induced by ICRH, the transport of tungsten through the SOL and boundary plasma to the pedestal, and the utilisation criteria of wall conditioning by boronisation, including its impact on fuel retention and removal. In addition, the quantification of tungsten and mixed material dust formation during long pulse plasma operation and the scaling of these results to ITER will be crucial for future operational planning. Finally, unmitigated REs remain a critical challenge for ITER, irrespective of the main chamber armour material selected, with predictive modelling still in its infancy.

Acknowledgments

The author team would like to acknowledge the tremendous effort and help of the Nuclear Fusion guest editors in charge of this chapter, Alberto Loarte (ITER Organization) and Emmanuelle Tsitrone (CEA Cadarache) and the entire team of guest editors for this special issue.

In addition, we would like to thank the following experts of ITPA TG DivSOL for their valuable comments and suggestions: M. van Berkel (DIFFER), X. Bonnin (ITER Organization), L. Cai (Southwestern Institute of Physics), S. Krat (MEPhI), J.-S. Park (Oak Ridge National Laboratory), M. Patino (University of California San Diego), M. Wischmeier (Max-Planck-Institut für Plasmaphysik), W. Zholobenko (Max-Planck-Institut für Plasmaphysik).

Authors from institutes in the EU (M. Bernert, S. Brezinsek, D. Carralero, J.W. Coenen, D. Douai, A. Hakola, M. Jakubowski, A. Kallenbach, K. Krieger, T. Loarer, R. Neu, S. Ratynskaia, K. Schmid, E. Tsitrone, D. Tskhakaya, N. Vianello, S. Wiesen) received funding within the framework of the EUROfusion Consortium, funded by the European Union via the Euratom Research and Training Programme (Grant Agreement No. 101052200—EUROfusion). Views and opinions expressed are however those of the author(s) only and do not necessarily reflect those of the European Union or the European Commission. Neither the European Union nor the European Commission can be held responsible for them.

D. Carralero received funding by the Spanish Ministry of Science, Innovation and Universities under Grant No. PID2021-125607NB-I00.

H. Frerichs received funding by the US Department of Energy under Award Nos. DE-SC0020284 and DE-SC0020357.

M. Kobayashi received funding by the Japan Society for the Promotion of Science (JSPS), KAKENHI Grant No. 19H01878.

A. Leonard received funding by US Department of Energy under DE-FC02-04ER54698.

S. Ratynskaia received funding by the Swedish Research Council under Grant No. 2021-05649.

The views and opinions expressed herein do not necessarily reflect those of the ITER Organization.

Chairs of Topical Group Scrape-Off-Layer and Divertor Physics (DivSOL)

A substantial fraction of the work presented in this chapter was carried out as part of collaborative projects planned and organised in the ITPA Topical Group Scrape-Off-Layer and Divertor Physics, chaired by: N. Asakura (QST, 2001–2008), B. Lipschultz (University of York, 2009–2011), E. Tsitrone (CEA Cadarache, 2012–2014), H.-Y. Guo (General Atomics, 2015–2017), K. Krieger (Max-Planck-Institut für Plasmaphysik, 2018–2020), T. Nakano (QST, 2021–2023), J. Rapp (Oak Ridge National Laboratory, 2024–2026).

ORCID iDs

K. Krieger https://orcid.org/0000-0003-0427-8184
S. Brezinsek https://orcid.org/0000-0002-7213-3326
J.W. Coenen https://orcid.org/0000-0002-8579-908X
H. Frerichs https://orcid.org/0000-0002-3527-5106
A. Kallenbach https://orcid.org/0000-0003-0538-2493
A.W. Leonard https://orcid.org/0000-0001-9356-1074
T. Loarer https://orcid.org/0000-0002-5688-7988
S. Ratynskaia https://orcid.org/0000-0002-6712-3625
N. Vianello https://orcid.org/0000-0003-4401-5346
N. Asakura https://orcid.org/0000-0002-8393-7311
M. Bernert https://orcid.org/0000-0003-1131-0867
D. Carralero https://orcid.org/0000-0002-7824-3307
R. Ding https://orcid.org/0000-0003-2880-9736
D. Douai https://orcid.org/0009-0002-6980-9927
T. Eich https://orcid.org/0000-0003-3065-8420
Y. Gasparyan https://orcid.org/0000-0003-0003-0579
A. Hakola https://orcid.org/0000-0003-1385-1296
Y. Hatano https://orcid.org/0000-0001-5084-5931
M. Jakubowski https://orcid.org/0000-0002-6557-3497
M. Kobayashi https://orcid.org/0000-0002-0990-7093
S. Krasheninnikov https://orcid.org/0000-0002-0786-5440
S. Masuzaki https://orcid.org/0000-0003-0161-0938
T. Nakano https://orcid.org/0009-0002-1031-0013
R. Neu https://orcid.org/0000-0002-6062-1955
R.A. Pitts https://orcid.org/0000-0001-9455-2698
J. Rapp https://orcid.org/0000-0003-2785-9280
O. Schmitz https://orcid.org/0000-0002-9580-9149
D. Tskhakaya https://orcid.org/0000-0002-4229-0961
L. Wang https://orcid.org/0000-0002-8373-117X
T. Wauters https://orcid.org/0000-0002-2941-7817
S. Wiesen https://orcid.org/0000-0002-3696-5475

References

[1] ITER Physics Basis Editors, ITER Physics Expert Group Chairs and Co-Chairs and ITER Joint Central Team and Physics Integration Unit 1999 ITER Physics Basis Chapter 1: Overview and summary *Nucl. Fusion* **39** 2137–74

[2] Ikeda K. 2007 Progress in the ITER Physics Basis *Nucl. Fusion* **47** E01

[3] ITER Organization 2018 ITER research plan within the staged approach (level III—provisional version) *Technical Report* ITR-18-003 (ITER Organization)

[4] ITER Organization 2024 ITER research plan within the staged approach (level III—final version) *Technical Report* ITR-24-005 (ITER Organization)

[5] Barabaschi P. 2023 Progress on ITER manufacturing, construction, commissioning and plans *29th IAEA Fusion Energy Conf.—Programme, Contributions and Conf. Material (London, UK, 16–21 October 2023)* (International Atomic Energy Agency (IAEA)) OV 1–3

[6] Stangeby P.C. 2000 *The Plasma Boundary of Magnetic Fusion Devices* (Institute of Physics Publishing)

[7] ITPA TG MHD Author Team 2025 MHD, disruptions and control physics Chapter 4 of the Special Issue: On the path to tokamak burning plasma operation *Nucl. Fusion* (submitted)

[8] Yoshida M. *et al* (The Transport and Confinement Group) 2025 Transport and confinement physics Chapter 2 of the Special Issue: On the path to tokamak burning plasma operation *Nucl. Fusion* **65** 033001

[9] Kallenbach A. *et al* 1999 Scrape-off layer radiation and heat load to the ASDEX Upgrade LYRA divertor *Nucl. Fusion* **39** 901–17

[10] Goetz J.A. *et al* 1999 High confinement dissipative divertor operation on Alcator C-Mod *Phys. Plasmas* **6** 1899–906

[11] ITPA TG PEP Author Team 2025 Pedestal and edge physics Chapter 3 of the Special Issue: On the path to tokamak burning plasma operation *Nucl. Fusion* (submitted)

[12] Pitts R.A. *et al* 2011 Physics basis and design of the ITER plasma-facing components *J. Nucl. Mater.* **415** S957–64

[13] Stangeby P. and Mitteau R. 2009 Analysis for shaping the ITER first wall *J. Nucl. Mater.* **390–391** 963–6

[14] Pitts R.A. *et al* 2013 A full tungsten divertor for ITER: physics issues and design status *J. Nucl. Mater.* **438** S48–S56

[15] Pitts R.A. *et al* 2017 Physics conclusions in support of ITER W divertor monoblock shaping *Nucl. Mater. Energy* **12** 60–74

[16] Pitts R.A. *et al* 2019 Physics basis for the first ITER tungsten divertor *Nucl. Mater. Energy* **20** 100696

[17] Zweben S.J., Terry J.L., Stotler D.P. and Maqueda R.J. 2017 Invited Review Article: Gas puff imaging diagnostics of edge plasma turbulence in magnetic fusion devices *Rev. Sci. Instrum.* **88** 041101

[18] Michels D., Stegmeir A., Ulbl P., Jarema D. and Jenko F. 2021 GENE-X: a full-*f* gyrokinetic turbulence code based on the flux-coordinate independent approach *Comput. Phys. Commun.* **264** 107986

[19] Romanelli M. *et al* 2014 JINTRAC: a system of codes for integrated simulation of tokamak scenarios *Plasma Fusion Res.* **9** 3403023

[20] Parail V. *et al* 2009 Integrated modelling of ITER reference scenarios *Nucl. Fusion* **49** 075030

[21] Wiesen S., Köchl F., Belo P., Kotov V., Loarte A., Parail V., Corrigan G., Garzotti L. and Harting D. 2017 Control of particle and power exhaust in pellet fuelled ITER DT scenarios employing integrated models *Nucl. Fusion* **57** 076020

[22] Garzotti L. *et al* 2012 Simulations of density profiles, pellet fuelling and density control in ITER *Nucl. Fusion* **52** 013002

[23] Hayashi N., Takizuka T., Aiba N., Oyama N., Ozeki T., Wiesen S. and Parail V. 2009 Integrated simulation of ELM energy loss and cycle in improved H-mode plasmas *Nucl. Fusion* **49** 095015

[24] Eich T. *et al* 2013 Scaling of the tokamak near the scrape-off layer H-mode power width and implications for ITER *Nucl. Fusion* **53** 093031

[25] Brunner D., LaBombard B., Kuang A.Q. and Terry J.L. 2018 High-resolution heat flux width measurements at reactor-level magnetic fields and observation of a unified width scaling across confinement regimes in the Alcator C-Mod tokamak *Nucl. Fusion* **58** 094002

[26] Chang C.S. *et al* 2017 Gyrokinetic projection of the divertor heat-flux width from present tokamaks to ITER *Nucl. Fusion* **57** 116023

[27] Xu X.Q., Li N.M., Li Z.Y., Chen B., Xia T.Y., Tang T.F., Zhu B. and Chan V.S. 2019 Simulations of tokamak boundary plasma turbulence transport in setting the divertor heat flux width *Nucl. Fusion* **59** 126039

[28] Chang C.S., Ku S., Hager R., Churchill R.M., Hughes J., Köchl F., Loarte A., Parail V. and Pitts R.A. 2021 Constructing a new predictive scaling formula for ITER's divertor heat-load width informed by a simulation-anchored machine learning *Phys. Plasmas* **28** 022501

[29] Goldston R.J. 2012 Heuristic drift-based model of the power scrape-off width in low-gas-puff H-mode tokamaks *Nucl. Fusion* **52** 013009

[30] Xia T.Y., Xu X.Q., Wu Y.B., Huang Y.Q., Wang L., Zheng Z., Liu J.B., Zang Q., Li Y.Y. and Zhao D. 2017 Divertor heat flux simulations in ELMy H-mode discharges of EAST *Nucl. Fusion* **57** 116016

[31] Tang T.F., Shi H., Wang Z.H., Zhong W.L., Xia T.Y., Xu X.Q., Sun J.Z. and Wang D.Z. 2018 Quasi-coherent mode simulation during inter-ELM period in HL-2A *Phys. Plasmas* **25** 122510

[32] Charidakos I.K., Myra J.R., Ku S., Churchill R.M., Hager R., Chang C.S. and Parker S. 2020 Comparison of edge turbulence characteristics between DIII-D and C-Mod simulations with XGC1 *Phys. Plasmas* **27** 072302

[33] Sun H.J., Wolfrum E., Eich T., Kurzan B., Potzel S. and Stroth U. 2015 Study of near scrape-off layer (SOL) temperature and density gradient lengths with Thomson scattering *Plasma Phys. Control. Fusion* **57** 125011

[34] Eich T., Manz P., Goldston R.J., Hennequin P., David P., Faitsch M., Kurzan B., Sieglin B. and Wolfrum E. 2020 Turbulence driven widening of the near-SOL power width in ASDEX Upgrade H-mode discharges *Nucl. Fusion* **60** 056016

[35] Faitsch M., Eich T., Harrer G.F., Wolfrum E., Brida D., David P., Griener M. and Stroth U. 2021 Broadening of the power fall-off length in a high density, high confinement H-mode regime in ASDEX Upgrade *Nucl. Mater. Energy* **26** 100890

[36] Faitsch M., Balboa I., Lomas P., Silburn S.A., Tookey A., Kos D., Huber A., de la Luna E., Keeling D. and Kappatou A. 2023 Divertor power load investigations with deuterium and tritium in type-I ELMy H-mode plasmas in JET with the ITER-like wall *Nucl. Fusion* **63** 112013

[37] Xu X.Q., Nevins W.M., Rognlien T.D., Bulmer R.H., Greenwald M., Mahdavi A., Pearlstein L.D. and Snyder P. 2003 Transitions of turbulence in plasma density limits *Phys. Plasmas* **10** 1773–81

[38] Zhu B., Francisquez M. and Rogers B.N. 2017 Global 3D two-fluid simulations of the tokamak edge region: turbulence, transport, profile evolution and spontaneous $E \times B$ rotation *Phys. Plasmas* **24** 055903

[39] Giacomin M. and Ricci P. 2020 Investigation of turbulent transport regimes in the tokamak edge by using two-fluid simulations *J. Plasma Phys.* **86** 905860502

[40] Tatali R., Serre E., Tamain P., Galassi D., Ghendrih P., Nespoli F., Bufferand H., Cartier-Michaud T. and Ciraolo G. 2021 Impact of collisionality on turbulence in the edge of tokamak plasma using 3D global simulations *Nucl. Fusion* **61** 056002

[41] Ulbl P., Body T., Zholobenko W., Stegmeir A., Pfennig J. and Jenko F. 2023 Influence of collisions on the validation of global gyrokinetic simulations in the edge and scrape-off layer of TCV *Phys. Plasmas* **30** 052507

[42] Riva F., Militello F., Elmore S., Omotani J.T., Dudson B. and Walkden N.R. 2019 Three-dimensional plasma edge turbulence simulations of the Mega Ampere Spherical Tokamak and comparison with experimental measurements *Plasma Phys. Control. Fusion* **61** 095013

[43] Oliveira D.S. *et al* 2022 Validation of edge turbulence codes against the TCV-X21 diverted L-mode reference case *Nucl. Fusion* **62** 096001

[44] Zholobenko W., Stegmeir A., Griener M., Conway G.D., Body T., Coster D. and Jenko F. 2021 The role of neutral gas in validated global edge turbulence simulations *Nucl. Fusion* **61** 116015

[45] Eich T. and Manz P. (The ASDEX Upgrade Team) 2021 The separatrix operational space of ASDEX Upgrade due to interchange-drift-Alfvén turbulence *Nucl. Fusion* **61** 086017

[46] Stagni A. *et al* 2022 Dependence of scrape-off layer profiles and turbulence on gas fuelling in high density H-mode regimes in TCV *Nucl. Fusion* **62** 096031

[47] Brown A.O. and Goldston R.J. 2021 Generalization of the Heuristic Drift SOL model for finite collisionality and effect on flow shearing rate vs. interchange growth rate *Nucl. Mater. Energy* **27** 101002

[48] Eich T., Goldston R.J., Kallenbach A., Sieglin B. and Sun H.J. 2018 Correlation of the tokamak H-mode density limit with ballooning stability at the separatrix *Nucl. Fusion* **58** 034001

[49] Faitsch M., Eich T. and Sieglin B. 2020 Correlation between near scrape-off layer power fall-off length and confinement properties in JET operated with carbon and ITER-like wall *Plasma Phys. Control. Fusion* **62** 085004

[50] Stangeby P., Canik J. and Whyte D. 2010 The relation between upstream density and temperature widths in the scrape-off layer and the power width in an attached divertor *Nucl. Fusion* **50** 125003

[51] Maurizio R., Duval B.P., Labit B., Reimerdes H., Faitsch M., Komm M., Sheikh U. and Theiler C. (The TCV Team and The EUROfusion MST1 Team) 2021 H-mode scrape-off layer power width in the TCV tokamak *Nucl. Fusion* **61** 024003

[52] Arnoux G. *et al* 2013 Scrape-off layer properties of ITER-like limiter start-up plasmas in JET *Nucl. Fusion* **53** 073016

[53] Kočan M. *et al* 2015 Impact of a narrow limiter SOL heat flux channel on the ITER first wall panel shaping *Nucl. Fusion* **55** 033019

[54] Horacek J. *et al* 2016 Multi-machine scaling of the main SOL parallel heat flux width in tokamak limiter plasmas *Plasma Phys. Control. Fusion* **58** 074005

[55] Nespoli F. *et al* 2017 Understanding and suppressing the near scrape-off layer heat flux feature in inboard-limited plasmas in TCV *Nucl. Fusion* **57** 126029

[56] Hinton F.L. and Chu M.S. 1985 Neoclassical ion transport through the separatrix in divertor tokamaks *Nucl. Fusion* **25** 345–58

[57] Krasheninnikov S.I. and Yushmanov P.N. 1994 The influence of a radial electric field on neoclassical orbits and ion prompt losses from tokamak edge plasmas *Phys. Plasmas* **1** 1186–94

[58] Chang C.S. and Ku S. 2008 Spontaneous rotation sources in a quiescent tokamak edge plasma *Phys. Plasmas* **15** 062510

[59] Viezzer E., Pütterich T., Angioni C., Bergmann A., Dux R., Fable E., McDermott R.M., Stroth U. and Wolfrum E. 2014 Evidence for the neoclassical nature of the radial electric field in the edge transport barrier of ASDEX Upgrade *Nucl. Fusion* **54** 012003

[60] deGrassie J.S., Boedo J.A. and Grierson B.A. 2015 Thermal ion orbit loss and radial electric field in DIII-D *Phys. Plasmas* **22** 080701

[61] Boedo J.A. *et al* 2016 Experimental evidence of edge intrinsic momentum source driven by kinetic ion loss and edge radial electric fields in tokamaks *Phys. Plasmas* **23** 092506

[62] Rozhansky V., Kaveeva E., Senichenkov I. and Vekshina E. 2018 Structure of the classical scrape-off layer of a tokamak *Plasma Phys. Control. Fusion* **60** 035001

[63] Jaervinen A.E. *et al* 2018 $E \times B$ flux driven detachment bifurcation in the DIII-D tokamak *Phys. Rev. Lett.* **121** 075001

[64] Wensing M., Loizu J., Reimerdes H., Duval B.P. and Wischmeier M. (The TCV Team) 2020 X-point potential well formation in diverted tokamaks with unfavorable magnetic field direction *Nucl. Fusion* **60** 054005

[65] Senichenkov I.Y., Kaveeva E.G., Rozhansky V.A., Voskoboynikov S.P., Veselova I.Y., Shtyrkhunov N.V., Coster D.P. and Bonnin X. 2021 Approaching the radiating X-point in SOLPS-ITER modeling of ASDEX Upgrade H-mode discharges *Plasma Phys. Control. Fusion* **63** 055011

[66] Tsui C.K., Boedo J.A., Février O., Reimerdes H., Colandrea C. and Gorno S. 2022 Relevance of $E \times B$ drifts for particle and heat transport in divertors *Plasma Phys. Control. Fusion* **64** 065008

[67] Wiesen S. *et al* 2015 The new SOLPS-ITER code package *J. Nucl. Mater.* **463** 480–4

[68] Bonnin X., Dekeyser W., Pitts R., Coster D., Voskoboynikov S. and Wiesen S. 2016 Presentation of the new SOLPS-ITER code package for tokamak plasma edge modelling *Plasma Fusion Res.* **11** 1403102

[69] Simonini R., Corrigan G., Radford G., Spence J. and Taroni A. 1994 Models and numerics in the multi-fluid 2-D edge plasma code EDGE2D/U *Contrib. Plasma Phys.* **34** 368–73

[70] Wiesen S. 2006 ITC project report 2006 *Technical Report* (Forschungszentrum Jülich) (available at: www.eirene.de/old_eirene/e2deir_report_30jun06.pdf)

[71] Groth M. *et al* 2011 Influence of cross-field drifts and chemical sputtering on simulations of divertor particle and heat loads in Ohmic and L-mode plasmas in DIII-D, AUG and JET using UEDGE *J. Nucl. Mater.* **415** S530

[72] Wiesen S., Groth M., Wischmeier M., Brezinsek S., Jarvinen A., Reimold F. and Aho-Mantila L. (JET Contributors, The EUROfusion MST1 Team, The ASDEX Upgrade Team and The Alcator C-Mod Team) 2017 Plasma edge and plasma-wall interaction modelling: lessons learned from metallic devices *Nucl. Mater. Energy* **12** 3–17

[73] Groth M. *et al* 2014 Steps in validating scrape-off layer simulations of attached and detached plasmas in the JET ITER-like wall configuration *25th IAEA Fusion Energy*

Conf.—Programme, Abstracts and Contributions (St. Petersburg, Russian Federation, 13–18 October 2014) vol CN-221 (International Atomic Energy Agency (IAEA)) TH P5–35 (available at: https://nucleus.iaea.org/sites/fusionportal/Shared%20Documents/FEC%202014/fec2014-preprints/518_THP535.pdf)

[74] Dekeyser W., Bonnin X., Lisgo S.W., Pitts R.A., Brunner D., LaBombard B. and Terry J.L. 2017 SOLPS-ITER study of neutral leakage and drift effects on the Alcator C-Mod divertor plasma *Nucl. Mater. Energy* **12** 899–907

[75] Wensing M. *et al* 2021 SOLPS-ITER validation with TCV L-mode discharges *Phys. Plasmas* **28** 082508

[76] Wu H., Subba F., Wischmeier M., Cavedon M. and Zanino R. 2021 SOLPS-ITER modeling of ASDEX Upgrade L-mode detachment states *Plasma Phys. Control. Fusion* **63** 105005

[77] Aho-Mantila L., Bonnin X., Coster D.P., Lowry C., Wischmeier M., Brezinsek S. and Federici G. 2015 Model-based radiation scalings for the ITER-like divertors of JET and ASDEX Upgrade *J. Nucl. Mater.* **463** 546–50

[78] Aho-Mantila L. *et al* 2017 Assessment of SOLPS5.0 divertor solutions with drifts and currents against L-mode experiments in ASDEX Upgrade and JET *Plasma Phys. Control. Fusion* **59** 035003

[79] Potzel S., Wischmeier M., Bernert M., Dux R., Müller H.W. and Scarabosio A. 2013 A new experimental classification of divertor detachment in ASDEX Upgrade *Nucl. Fusion* **54** 013001

[80] Reimold F., Wischmeier M., Bernert M., Potzel S., Kallenbach A., Müller H.W., Sieglin B. and Stroth U. 2015 Divertor studies in nitrogen induced completely detached H-modes in full tungsten ASDEX Upgrade *Nucl. Fusion* **55** 033004

[81] Reimold F. *et al* 2015 Experimental studies and modeling of complete H-mode divertor detachment in ASDEX Upgrade *J. Nucl. Mater.* **463** 128–34

[82] Reimold F., Wischmeier M., Potzel S., Guimarais L., Reiter D., Bernert M., Dunne M. and Lunt T. 2017 The high field side high density region in SOLPS-modeling of nitrogen-seeded H-modes in ASDEX Upgrade *Nucl. Mater. Energy* **12** 193–9

[83] Korving S.Q., Huijsmans G.T.A., Park J.-S. and Loarte A. 2023 Development of the neutral model in the nonlinear MHD code JOREK: application to $E \times B$ drifts in ITER PFPO-1 plasmas *Phys. Plasmas* **30** 042509

[84] Pan O., Bernert M., Lunt T., Cavedon M., Kurzan B., Wiesen S., Wischmeier M. and Stroth U. (The ASDEX Upgrade Team) 2023 SOLPS-ITER simulations of an X-point radiator in the ASDEX Upgrade tokamak *Nucl. Fusion* **63** 016001

[85] Kaveeva E., Rozhansky V., Veselova I., Senichenkov I., Giroud C., Pitts R.A., Wiesen S. and Voskoboynikov S. 2021 SOLPS-ITER drift modelling of JET Ne and N-seeded H-modes *Nucl. Mater. Energy* **28** 101030

[86] Rozhansky V., Kaveeva E., Senichenkov I., Veselova I., Voskoboynikov S., Pitts R.A., Coster D., Giroud C. and Wiesen S. 2021 Multi-machine SOLPS-ITER comparison of impurity seeded H-mode radiative divertor regimes with metal walls *Nucl. Fusion* **61** 126073

[87] Meier E.T., Goldston R.J., Kaveeva E.G., Makowski M.A., Mordijck S., Rozhansky V.A., Senichenkov I.Y. and Voskoboynikov S.P. 2016 Analysis of drift effects on the tokamak power scrape-off width using SOLPS-ITER *Plasma Phys. Control. Fusion* **58** 125012

[88] Krasheninnikov S.I., Sigmar D.J. and Yushmanov P.N. 1995 Effect of E×B drift on divertor plasma flows *Phys. Plasmas* **2** 1972

[89] Chankin A.V., Delabie E., Corrigan G., Harting D., Maggi C.F. and Meyer H. 2017 EDGE2D-EIRENE modelling of near SOL E-r: possible impact on the H-mode power threshold *Plasma Phys. Control. Fusion* **59** 045012

[90] Chankin A.V. and Corrigan G. (JET Contributors) 2021 EDGE2D-EIRENE modeling of the impact of wall materials on core edge, scrape-off layer and divertor parameters *Plasma Phys. Control. Fusion* **63** 035010

[91] Senichenkov I., Kaveeva E., Rozhansky V. and Coster D. 2021 Features of radial electric field in impurity-seeded, detached plasma in a tokamak *Phys. Plasmas* **28** 062507

[92] Brida D., Conway G.D., Adamek J., Silvagni D., David P., Eich T., Grenfell G., Komm M. and Plank U. 2022 Physics of the electric field in the scrape-off layer in ASDEX Upgrade L-mode discharges and comparison to experiments *Nucl. Mater. Energy* **33** 101262

[93] Doyle E.J. *et al* (ITPA Transport Physics Topical Group, ITPA Confinement Database and Modelling Topical Group and ITPA Pedestal and Edge Topical Group) 2007 Chapter 2: Plasma confinement and transport *Nucl. Fusion* **47** S18–S127

[94] Viezzer E. *et al* 2017 Investigation of inter-ELM ion heat transport in the H-mode pedestal of ASDEX Upgrade plasmas *Nucl. Fusion* **57** 022020

[95] Krasheninnikov S.I., D'Ippolito D.A. and Myra J.R. 2008 Recent theoretical progress in understanding coherent structures in edge and SOL turbulence *J. Plasma Phys.* **74** 679–717

[96] D'Ippolito D.A., Myra J.R. and Zweben S.J. 2011 Convective transport by intermittent blob-filaments: comparison of theory and experiment *Phys. Plasmas* **18** 060501

[97] Garcia O.E., Horacek J., Pitts R.A., Nielsen A.H., Fundamenski W., Naulin V. and Rasmussen J.J. 2007 Fluctuations and transport in the TCV scrape-off layer *Nucl. Fusion* **47** 667–76

[98] Silva C., Gonçalves B., Hidalgo C., Pedrosa M.A., Fundamenski W., Stamp M. and Pitts R.A. 2009 Intermittent transport in the JET far-SOL *J. Nucl. Mater.* **390–391** 355–8

[99] Müller H.W. *et al* 2011 Latest investigations on fluctuations, ELM filaments and turbulent transport in the SOL of ASDEX Upgrade *Nucl. Fusion* **51** 073023

[100] Boedo J.A. 2009 Edge turbulence and SOL transport in tokamaks *J. Nucl. Mater.* **390–391** 29–37

[101] Ionita C. *et al* 2013 Radial transport in the far scrape-off layer of ASDEX Upgrade during L-mode and ELMy H-mode *Nucl. Fusion* **53** 043021

[102] Boedo J.A. *et al* 2014 Edge transport studies in the edge and scrape-off layer of the National Spherical Torus Experiment with Langmuir probes *Phys. Plasmas* **21** 042309

[103] Carralero D., Artene S., Bernert M., Birkenmeier G., Faitsch M., Manz P., de Marne P., Stroth U., Wischmeier M. and Wolfrum E. 2018 On the role of filaments in perpendicular heat transport at the scrape-off layer *Nucl. Fusion* **58** 096015

[104] Hong R., Tynan G.R., Diamond P.H., Nie L., Guo D., Long T., Ke R., Wu Y., Yuan B. and Xu M. 2018 Edge shear flows and particle transport near the density limit of the HL-2A tokamak *Nucl. Fusion* **58** 016041

[105] Kube R., Garcia O.E., Theodorsen A., Brunner D., Kuang A.Q., LaBombard B. and Terry J.L. 2018 Intermittent electron density and temperature fluctuations and associated fluxes in the Alcator C-Mod scrape-off layer *Plasma Phys. Control. Fusion* **60** 065002

[106] Maqueda R., Stotler D. and Zweben S. (The NSTX Team) 2011 Intermittency in the scrape-off layer of the National

Spherical Torus Experiment during H-mode confinement *J. Nucl. Mater.* **415** S459–62

[107] Asakura N., Ohno N., Tanaka H., Kawashima H. and Nakano T. 2009 Statistical analysis to the SOL plasma fluctuation in JT-60U *J. Nucl. Mater.* **390** 364–7

[108] Tanaka H., Ohno N., Asakura N., Tsuji Y., Kawashima H., Takamura S. and Uesugi Y. 2009 Statistical analysis of fluctuation characteristics at high- and low-field sides in L-mode SOL plasmas of JT-60U *Nucl. Fusion* **49** 065017

[109] Walkden N.R., Wynn A., Militello F., Lipschultz B., Matthews G., Guillemaut C., Harrison J. and Moulton D. 2017 Interpretation of scrape-off layer profile evolution and first-wall ion flux statistics on JET using a stochastic framework based on fillamentary motion *Plasma Phys. Control. Fusion* **59** 085009

[110] Tsui C.K. *et al* 2018 Filamentary velocity scaling validation in the TCV tokamak *Phys. Plasmas* **25** 072506

[111] Elmore S., Allan S.Y., Fishpool G., Kirk A., Thornton A.J., Walkden N.R. and Harrison J.R. 2016 Scrape-off layer ion temperature measurements at the divertor target during type III and type I ELMs in MAST measured by RFEA *Plasma Phys. Control. Fusion* **58** 065002

[112] Kočan M., Gennrich F.P., Kendl A. and Müller H.W. (ASDEX Upgrade Team) 2012 Ion temperature fluctuations in the ASDEX Upgrade scrape-off layer *Plasma Phys. Control. Fusion* **54** 085009

[113] Kočan M. *et al* (The ASDEX Upgrade Team) 2013 Intermittent transport across the scrape-off layer: latest results from ASDEX Upgrade *Nucl. Fusion* **53** 073047

[114] Elmore S., Allan S.Y., Kirk A., Fishpool G., Harrison J., Tamain P., Kočan M., Gaffka R., Stephen R. and Bradley J.W. 2012 Upstream and divertor ion temperature measurements on MAST by retarding field energy analyser *Plasma Phys. Control. Fusion* **54** 065001

[115] Adamek J. *et al* 2021 Ion temperature measurements in the tokamak scrape-off layer with high temporal resolution *Nucl. Fusion* **61** 036023

[116] Carralero D. *et al* 2017 Recent progress towards a quantitative description of filamentary SOL transport *Nucl. Fusion* **57** 056044

[117] Cipciar D., Adamek J., Horacek J., Cavalier J. and Hron M. 2022 Statistical properties of ion and electron temperature fluctuations in the edge of the COMPASS tokamak *Plasma Phys. Control. Fusion* **64** 055021

[118] Terry J., Zweben S.J., Umansky M.V., Cziegler I., Grulke O., LaBombard B. and Stotler D.P. 2009 Spatial structure of scrape-off-layer filaments near the midplane and X-point regions of Alcator-C-Mod *J. Nucl. Mater.* **390** 339–42

[119] Grulke O., Terry J.L., Cziegler I., LaBombard B. and Garcia O.E. 2014 Experimental investigation of the parallel structure of fluctuations in the scrape-off layer of Alcator C-Mod *Nucl. Fusion* **54** 043012

[120] Offeddu N. *et al* 2022 Cross-field and parallel dynamics of SOL filaments in TCV *Nucl. Fusion* **62** 096014

[121] Spolaore M. *et al* 2017 Electromagnetic ELM and inter-ELM filaments detected in the COMPASS Scrape-Off Layer *Nucl. Mater. Energy* **12** 844–51

[122] Grenfell G. *et al* 2020 Turbulent filament properties in L- and H-mode regime in the RFX-mod operating as a tokamak *Nucl. Fusion* **60** 126006

[123] Ayed N.B., Kirk A., Dudson B., Tallents S., Vann R.G.L. and Wilson H.R. 2009 Inter-ELM filaments and turbulent transport in the Mega-Amp Spherical Tokamak *Plasma Phys. Control. Fusion* **51** 035016

[124] Zweben S.J., Myra J.R., Davis W.M., D'Ippolito D.A., Gray T.K., Kaye S.M., LeBlanc B.P., Maqueda R.J., Russell D.A. and Stotler D.P. 2016 Blob structure and motion in the edge and SOL of NSTX *Plasma Phys. Control. Fusion* **58** 044007

[125] Fuchert G., Birkenmeier G., Carralero D., Lunt T., Manz P., Müller H.W., Nold B., Ramisch M., Rohde V. and Stroth U. 2014 Blob properties in L- and H-mode from gas-puff imaging in ASDEX Upgrade *Plasma Phys. Control. Fusion* **56** 125001

[126] Griener M. *et al* 2020 Continuous observation of filaments from the confined region to the far scrape-off layer *Nucl. Mater. Energy* **25** 100854

[127] Vianello N. *et al* 2020 Scrape-off layer transport and filament characteristics in high-density tokamak regimes *Nucl. Fusion* **60** 016001

[128] Harrison J.R., Fishpool G.M., Thornton A.J. and Walkden N.R. 2015 The appearance and propagation of filaments in the private flux region in Mega Amp Spherical Tokamak *Phys. Plasmas* **22** 092508

[129] Thornton A.J., Fishpool G. and Kirk A. (MAST Team and EUROfusion MST1 Team) 2015 The effect of L mode filaments on divertor heat flux profiles as measured by infrared thermography on MAST *Plasma Phys. Control. Fusion* **57** 115010

[130] Terry J.L., Ballinger S., Brunner D., LaBombard B., White A.E. and Zweben S.J. 2017 Fast imaging of filaments in the X-point region of Alcator C-Mod *Nucl. Mater. Energy* **12** 989–93

[131] Scotti F., Zweben S., Soukhanovskii V., Baver D. and Myra J. 2018 Divertor leg filaments in NSTX-U *Nucl. Fusion* **58** 126028

[132] Gallo A. *et al* 2018 Impact of the plasma geometry on divertor power exhaust: experimental evidence from TCV and simulations with SolEdge2D and TOKAM3X *Plasma Phys. Control. Fusion* **60** 014007

[133] Walkden N.R., Riva F., Harrison J., Militello F., Farley T., Omotani J. and Lipschultz B. 2022 The physics of turbulence localised to the tokamak divertor volume *Commun. Phys.* **5** 139

[134] Walkden N.R., Riva F., Dudson B.D., Ham C., Militello F., Moulton D., Nicholas T. and Omotani J.T. 2019 3D simulations of turbulent mixing in a simplified slab-divertor geometry *Nucl. Mater. Energy* **18** 111–7

[135] Diamond P.H., Itoh S.-I., Itoh K. and Hahm T.S. 2005 Zonal flows in plasma—a review *Plasma Phys. Control. Fusion* **47** R35–R161

[136] Fujisawa A. 2009 A review of zonal flow experiments *Nucl. Fusion* **49** 013001

[137] Fujisawa A. 2014 Turbulence in toroidal plasma *Proc. 12th Asia Pacific Physics Conf. (APPC12) (Makuhari, Chiba, Japan, 14–19 July 2013)* (Journal of the Physical Society of Japan) (https://doi.org/10.7566/jpscp.1.015005)

[138] Kim C.-B., Min B. and An C.-Y. 2018 Localization of the eigenmode of the drift-resistive plasma by zonal flow *Phys. Plasmas* **25** 102501

[139] Zhang Y. and Krasheninnikov S.I. 2020 Influence of zonal flow and density on resistive drift wave turbulent transport *Phys. Plasmas* **27** 122303

[140] Dif-Pradalier G. *et al* 2015 Finding the elusive E × B staircase in magnetized plasmas *Phys. Rev. Lett.* **114** 085004

[141] Qi D., Majda A.J. and Cerfon A.J. 2019 A flux-balanced fluid model for collisional plasma edge turbulence: numerical simulations with different aspect ratios *Phys. Plasmas* **26** 082303

[142] Rogers B.N., Drake J.F. and Zeiler A. 1998 Phase space of tokamak edge turbulence, the L-H transition and the formation of the edge pedestal *Phys. Rev. Lett.* **81** 4396–9

[143] Scott B.D. 2005 Drift wave versus interchange turbulence in tokamak geometry: linear versus nonlinear mode structure *Phys. Plasmas* **12** 062314

[144] Scott B.D. 2007 Tokamak edge turbulence: background theory and computation *Plasma Phys. Control. Fusion* **49** S25–S41
[145] Thrysøe A.S., Løiten M., Madsen J., Naulin V., Nielsen A.H. and Rasmussen J.J. 2018 Plasma particle sources due to interactions with neutrals in a turbulent scrape-off layer of a toroidally confined plasma *Phys. Plasmas* **25** 032307
[146] Russell D.A., Myra J.R., Militello F. and Moulton D. 2021 Reduced-model scrape-off layer turbulence (nSOLT) simulations comparing three fueling scenarios *Phys. Plasmas* **28** 092305
[147] Wiesen S., Fundamenski W., Wischmeier M., Groth M., Brezinsek S. and Naulin V. 2011 Relevance of collisionality in the transport model assumptions for divertor detachment multi-fluid modelling on JET *J. Nucl. Mater.* **415** S525
[148] Li Z.-Y., Xu X.Q., Li N.-M., Chan V.S. and Wang X.-G. 2019 Prediction of divertor heat flux width for ITER using BOUT++ transport and turbulence module *Nucl. Fusion* **59** 046014
[149] Zholobenko W., Body T., Manz P., Stegmeir A., Zhu B., Griener M., Conway G.D., Coster D. and Jenko F. 2021 Electric field and turbulence in global Braginskii simulations across the ASDEX Upgrade edge and scrape-off layer *Plasma Phys. Control. Fusion* **63** 034001
[150] Hakim A.H., Mandell N.R., Bernard T.N., Francisquez M., Hammett G.W. and Shi E.L. 2020 Continuum electromagnetic gyrokinetic simulations of turbulence in the tokamak scrape-off layer and laboratory devices *Phys. Plasmas* **27** 042304
[151] Giacomin M., Ricci P., Coroado A., Fourestey G., Galassi D., Lanti E., Mancini D., Richart N., Stenger L.N. and Varini N. 2022 The GBS code for the self-consistent simulation of plasma turbulence and kinetic neutral dynamics in the tokamak boundary *J. Comput. Phys.* **463** 111294
[152] Bufferand H. *et al* 2021 Progress in edge plasma turbulence modelling–hierarchy of models from 2D transport application to 3D fluid simulations in realistic tokamak geometry *Nucl. Fusion* **61** 116052
[153] Pan Q., Told D., Shi E.L., Hammett G.W. and Jenko F. 2018 Full-f version of GENE for turbulence in open-field-line systems *Phys. Plasmas* **25** 062303
[154] Boesl M., Bergmann A., Bottino A., Coster D., Lanti E., Ohana N. and Jenko F. 2019 Gyrokinetic full-f particle-in-cell simulations on open field lines with PICLS *Phys. Plasmas* **26** 122302
[155] Dorf M. and Dorr M. 2021 Continuum gyrokinetic simulations of edge plasmas in single-null geometries *Phys. Plasmas* **28** 032508
[156] Pigarov A.Y., Krasheninnikov S.I. and Rognlien T.D. 2011 New approach in two-dimensional fluid modeling of edge plasma transport with high intermittency due to blobs and edge localized modes *Phys. Plasmas* **18** 092503
[157] Pigarov A.Y., Krasheninnikov S.I. and Rognlien T.D. 2012 Time-dependent 2-D modeling of edge plasma transport with high intermittency due to blobs *Phys. Plasmas* **19** 072516
[158] Pigarov A.Y., Krasheninnikov S.I., Rognlien T.D., Hollmann E.M., Lasnier C.J. and Unterberg E. 2014 Multi-fluid transport code modeling of time-dependent recycling in ELMy H-mode *Phys. Plasmas* **21** 062514
[159] Manz P. *et al* 2020 The diffusion limit of ballistic transport in the scrape-off layer *Phys. Plasmas* **27** 022506
[160] Dekeyser W., Bonnin X., Lisgo S.W., Pitts R.A. and LaBombard B. 2019 Implementation of a 9-point stencil in SOLPS-ITER and implications for Alcator C-Mod divertor plasma simulations *Nucl. Mater. Energy* **18** 125–35
[161] Baschetti S., Bufferand H., Ciraolo G., Ghendrih P., Serre E. and Tamain P. (The WEST Team) 2021 Self-consistent cross-field transport model for core and edge plasma transport *Nucl. Fusion* **61** 106020
[162] Carli S., Dekeyser W., Coosemans R., Dejarnac R., Komm M., Dimitrova M., Adámek J., Bílková P. and Böhm P. 2020 Interchange-turbulence-based radial transport model for SOLPS-ITER: a COMPASS case study *Contrib. Plasma Phys.* **60** e201900155
[163] Coosemans R., Dekeyser W. and Baelmans M. 2020 A new mean-field plasma edge transport model based on turbulent kinetic energy and enstrophy *Contrib. Plasma Phys.* **60** e201900156
[164] Coosemans R., Dekeyser W. and Baelmans M. 2021 Turbulent kinetic energy in 2D isothermal interchange-dominated scrape-off layer E × B drift turbulence: governing equation and relation to particle transport *Phys. Plasmas* **28** 012302
[165] Zohm H., Militello F., Morgan T.W., Morris W., Reimerdes H. and Siccinio M. 2021 The EU strategy for solving the DEMO exhaust problem *Fusion Eng. Des.* **166** 112307
[166] Asakura N. *et al* 1997 SOL plasma profiles under radiative and detached divertor conditions in JT-60U *J. Nucl. Mater.* **241–243** 559–63
[167] LaBombard B., Boivin R.L., Greenwald M., Hughes J., Lipschultz B., Mossessian D., Pitcher C.S., Terry J.L. and Zweben S.J. 2001 Particle transport in the scrape-off layer and its relationship to discharge density limit in Alcator C-Mod *Phys. Plasmas* **8** 2107–17
[168] Rudakov D.L. *et al* 2005 Far SOL transport and main wall plasma interaction in DIII-D *Nucl. Fusion* **45** 1589–99
[169] Carralero D., Manz P., Aho-Mantila L., Birkenmeier G., Brix M., Groth M., Müller H., Stroth U., Vianello N. and Wolfrum E. 2015 Experimental validation of a filament transport model in turbulent magnetized plasmas *Phys. Rev. Lett.* **115** 215002
[170] Militello F., Garzotti L., Harrison J., Omotani J.T., Scannell R., Allan S., Kirk A., Lupelli I. and Thornton A.J. 2016 Characterisation of the L-mode scrape off layer in MAST: decay lengths *Nucl. Fusion* **56** 016006
[171] Vianello N. *et al* 2017 Modification of SOL profiles and fluctuations with line-average density and divertor flux expansion in TCV *Nucl. Fusion* **57** 116014
[172] Wynn A. *et al* (JET Contributors) 2018 Investigation into the formation of the scrape-off layer density shoulder in JET ITER-like wall L-mode and H-mode plasmas *Nucl. Fusion* **58** 056001
[173] Kuang A.Q., LaBombard B., Brunner D., Garcia O.E., Kube R. and Theodorsen A. 2019 Plasma fluctuations in the scrape-off layer and at the divertor target in Alcator C-Mod and their relationship to divertor collisionality and density shoulder formation *Nucl. Mater. Energy* **19** 295–9
[174] Carralero D., Birkenmeier G., Müller H.W., Manz P., deMarne P., Müller S.H., Reimold F., Stroth U., Wischmeier M. and Wolfrum E. 2014 An experimental investigation of the high density transition of the scrape-off layer transport in ASDEX Upgrade *Nucl. Fusion* **54** 123005
[175] Yan N. *et al* 2021 Dependence of upstream SOL density shoulder on divertor neutral pressure observed in L-mode and H-mode plasmas in the EAST superconducting tokamak *Nucl. Fusion* **61** 076018

[176] Tsui C.K. *et al* 2022 Evidence on the effects of main-chamber neutrals on density shoulder broadening *Phys. Plasmas* **29** 062507

[177] Agostini M., Terry J.L., Scarin P. and Zweben S.J. 2011 Edge turbulence in different density regimes in Alcator C-Mod experiment *Nucl. Fusion* **51** 053020

[178] Nishizawa T., Manz P., Grenfell G., Griener M., Wendler D., Brida D., Kriete D.M., Dux R., Kobayashi T. and Sasaki M. 2022 Characterizing the flow and turbulence structure near the last closed flux surface in L-mode plasmas of ASDEX Upgrade *Phys. Plasmas* **29** 072304

[179] Grenfell G. *et al* 2022 Turbulence in the near scrape-off layer towards the L-mode density limit in ASDEX-Upgrade *Nucl. Mater. Energy* **33** 101277

[180] Février O. *et al* 2020 Nitrogen-seeded divertor detachment in TCV L-mode plasmas *Plasma Phys. Control. Fusion* **62** 035017

[181] Myra J.R., Russell D.A. and D'Ippolito D.A. 2006 Collisionality and magnetic geometry effects on tokamak edge turbulent transport. I. A two-region model with application to blobs *Phys. Plasmas* **13** 112502

[182] Lunt T., Carralero D., Feng Y., Birkenmeier G., Müller H.W., Müller S. and Wischmeier M. 2015 EMC3-Eirene simulations of particle- and energy fluxes to main chamber- and divertor plasma facing components in ASDEX Upgrade compared to experiments *J. Nucl. Mater.* **463** 744–7

[183] Zito A., Wischmeier M., Carralero D., Manz P., Paradela Pérez I. and Passoni M. 2021 Numerical modelling of an enhanced perpendicular transport regime in the scrape-off layer of ASDEX Upgrade *Plasma Phys. Control. Fusion* **63** 075003

[184] Agostini M., Vianello N., Carraro L., Carralero D., Cavedon M., Dux R., Naulin V., Spolaore M. and Wolfrum E. 2019 Neutral density estimation in the ASDEX Upgrade divertor from deuterium emissivity measurements during detachment and shoulder formation *Plasma Phys. Control. Fusion* **61** 115001

[185] Mancini D., Ricci P., Vianello N., Giacomin M. and Coroado A. 2021 Investigation of the density shoulder formation by using self-consistent simulations of plasma turbulence and neutral kinetic dynamics *Nucl. Fusion* **61** 126029

[186] Zholobenko W., Pfennig J., Stegmeir A., Body T., Ulbl P. and Jenko F. 2023 Filamentary transport in global edge-SOL simulations of ASDEX Upgrade *Nucl. Mater. Energy* **34** 101351

[187] Boedo J.A. *et al* 2001 Transport by intermittent convection in the boundary of the DIII-D tokamak *Phys. Plasmas* **8** 4826–33

[188] Müller H.W., Bernert M., Carralero D., Kallenbach A., Kurzan B., Scarabosio A., Sieglin B., Tophøj L., Vianello N. and Wolfrum E. 2015 Far scrape-off layer particle and heat fluxes in high density—high power scenarios *J. Nucl. Mater.* **463** 739–43

[189] Carralero D. *et al* 2017 A study on the density shoulder formation in the SOL of H-mode plasmas *Nucl. Mater. Energy* **12** 1189–93

[190] Lunt T. *et al* 2020 Near- and far scrape-off layer transport studies in detached, small-ELM ASDEX Upgrade discharges by means of EMC3-EIRENE *Plasma Phys. Control. Fusion* **62** 105016

[191] Vianello N. *et al* 2021 SOL profile and fluctuations in different divertor recycling conditions in H-Mode plasmas *28th IAEAFusion Energy Conf.—Programme, Contributions and Conf. Material (10–14 May 2021)* (International Atomic Energy Agency (IAEA)) EX P3–14 (available at: https://nucleus.iaea.org/sites/fusionportal/Shared%20Documents/FEC%202020/fec2020-preprints/preprint1051.pdf)

[192] Kallenbach A. *et al* 2015 Partial detachment of high power discharges in ASDEX Upgrade *Nucl. Fusion* **55** 053026

[193] Redl A., Eich T., Vianello N. and David P. 2023 Energy load on first wall components in high density, small ELM regimes in ASDEX Upgrade *Nucl. Mater. Energy* **34** 101319

[194] Park J.-S., Bonnin X. and Pitts R. 2021 Assessment of ITER divertor performance during early operation phases *Nucl. Fusion* **61** 016021

[195] Harrer G.F. *et al* 2018 Parameter dependences of small edge localized modes (ELMs) *Nucl. Fusion* **58** 112001

[196] LaBombard B., Umansky M.V., Boivin R.L., Goetz J.A., Hughes J., Lipschultz B., Mossessian D., Pitcher C.S. and Terry J.L. (Alcator Group) 2000 Cross-field plasma transport and main-chamber recycling in diverted plasmas on Alcator C-Mod *Nucl. Fusion* **40** 2041

[197] Lomanowski B. *et al* 2022 Parameter dependencies of the separatrix density in low triangularity L-mode and H-mode JET-ILW plasmas *Nucl. Fusion* **63** 036019

[198] Lunt T., Reimold F., Wolfrum E., Carralero D., Feng Y. and Schmid K. 2017 Influence of the first wall material on the particle fuelling in ASDEX Upgrade *Plasma Phys. Control. Fusion* **59** 055016

[199] Sun H.J. *et al* 2023 The broadening of SOL profiles in JET tritium plasma and its impact on machine operation *Nucl. Fusion* **63** 016021

[200] Birkenmeier G. *et al* 2015 Filament transport, warm ions and erosion in ASDEX Upgrade L-modes *Nucl. Fusion* **55** 033018

[201] Stotler D., Lang J., Chang C., Churchill R. and Ku S. 2017 Neutral recycling effects on ITG turbulence *Nucl. Fusion* **57** 086028

[202] Pitcher C.S. and Stangeby P.C. 1997 Experimental divertor physics *Plasma Phys. Control. Fusion* **39** 779–930

[203] Stotler D.P., Bell R.E., Hill K.W., Johnson D.W. and Levinton F.M. 2007 Atomic physics in ITER—the foundation for the next step to fusion power *AIP Conf. Proc.* **901** 95–104

[204] Krasheninnikov S.I., Kukushkin A.S., Pshenov A.A., Smolyakov A.I. and Zhang Y. 2017 Stability of divertor detachment *Nucl. Mater. Energy* **12** 1061–6

[205] Stangeby P.C. 2018 Basic physical processes and reduced models for plasma detachment *Plasma Phys. Control. Fusion* **60** 044022

[206] Stangeby P.C. 2020 The roles of power loss and momentum-pressure loss in causing particle-detachment in tokamak divertors: I. A heuristic model analysis *Plasma Phys. Control. Fusion* **62** 025012

[207] Wischmeier M. *et al* 2009 Current understanding of divertor detachment: experiments and modelling *J. Nucl. Mater.* **390–391** 250–4

[208] Wischmeier M. *et al* 2011 Assessment of edge modeling in support of ITER *J. Nucl. Mater.* **415** S523–9

[209] Lomanowski B. *et al* 2022 Experimental study on the role of the target electron temperature as a key parameter linking recycling to plasma performance in JET-ILW *Nucl. Fusion* **62** 066030

[210] Kallenbach A., Sun H.J., Eich T., Carralero D., Hobirk J., Scarabosio A. and Siccinio M. 2018 Parameter dependences of the separatrix density in nitrogen seeded ASDEX Upgrade H-mode discharges *Plasma Phys. Control. Fusion* **60** 045006

[211] Joffrin E. *et al* 2017 Impact of divertor geometry on H-mode confinement in the JET metallic wall *Nucl. Fusion* **57** 086025

[212] Tamain P. *et al* 2015 Investigation of the influence of divertor recycling on global plasma confinement in JET ITER-like wall *J. Nucl. Mater.* **463** 450–4

[213] Casali L., Eldon D., Boedo J.A., Leonard T. and Covele B. 2020 Neutral leakage, power dissipation and pedestal fueling in open vs closed divertors *Nucl. Fusion* **60** 076011

[214] Casali L., Osborne T.H., Grierson B.A., McLean A.G., Meier E.T., Ren J., Shafer M.W., Wang H. and Watkins J.G. 2020 Improved core-edge compatibility using impurity seeding in the small angle slot (SAS) divertor at DIII-D *Phys. Plasmas* **27** 062506

[215] Kukushkin A.S., Polevoi A.R., Pacher H.D., Pacher G.W. and Pitts R.A. 2011 Physics requirements on fuel throughput in ITER *J. Nucl. Mater.* **415** S497–500

[216] Wiesen S. *et al* 2018 On the role of finite grid extent in SOLPS-ITER edge plasma simulations for JET H-mode discharges with metallic wall *Nucl. Mater. Energy* **17** 174–81

[217] Jaervinen A. *et al* 2015 Interpretation of radiative divertor studies with impurity seeding in type-I ELMy H-mode plasmas in JET-ILW using EDGE2D-EIRENE *J. Nucl. Mater.* **463** 135

[218] Jaervinen A. *et al* 2016 Comparison of H-mode plasmas in JET-ILW and JET-C with and without nitrogen seeding *Nucl. Fusion* **56** 046012

[219] Kotov V., Reiter D. and Kukushkin A.S. 2007 Numerical study of the ITER divertor plasma with the B2-EIRENE code package *Technical Report* Juel-4257 (Forschungszentrum Jülich)

[220] Dux R., Cavedon M., Kallenbach A., McDermott R.M. and Vogel G. (The ASDEX Upgrade Team) 2020 Influence of CX-reactions on the radiation in the pedestal region at ASDEX Upgrade *Nucl. Fusion* **60** 126039

[221] Verhaegh K. *et al* 2021 The role of plasma-molecule interactions on power and particle balance during detachment on the TCV tokamak *Nucl. Fusion* **61** 106014

[222] Akkermans G.R.A., Classen I.G.J., Perillo R., van der Meiden H.J., Federici F. and Brezinsek S. 2020 The role of hydrogen molecular effects on detachment in Magnum-PSI *Phys. Plasmas* **27** 102509

[223] Wischmeier M. *et al* 2004 The influence of molecular dynamics on divertor detachment in TCV *Contrib. Plasma Phys.* **44** 268–73

[224] Groth M. *et al* 2019 EDGE2D-EIRENE predictions of molecular emission in DIII-D high-recycling divertor plasmas *Nucl. Mater. Energy* **19** 211–7

[225] Kotov V., Reiter D., Pitts R.A., Jachmich S., Huber A. and Coster D.P. 2008 Numerical modelling of high density JET divertor plasma with the SOLPS4.2 (B2-EIRENE) code *Plasma Phys. Control. Fusion* **50** 105012

[226] Reiter D., Wiesen S. and Born M. 2003 Radiation transfer in dense edge plasmas and divertors: experimental and recent computational results *J. Nucl. Mater.* **313–316** 845–51

[227] Lisgo S. *et al* 2005 OSM-EIRENE modeling of neutral pressures in the Alcator C-Mod divertor *J. Nucl. Mater.* **337–339** 139–45

[228] Pshenov A.A., Kukushkin A.S., Gorbunov A.V. and Marenkov E.D. 2023 Divertor plasma opacity effects *Nucl. Mater. Energy* **34** 101342

[229] Lomanowski B. *et al* 2019 Spectroscopic investigation of N and Ne seeded induced detachment in JET ITER-like wall L-modes combining experiment and EDGE2D modeling *Nucl. Mater. Energy* **20** 100676

[230] Aho-Mantila L., Wischmeier M., Müller H.W., Potzel S., Coster D.P., Bonnin X. and Conway G.D. 2012 Outer divertor of ASDEX Upgrade in low-density L-mode discharges in forward and reversed magnetic field: I. Comparison between measured plasma conditions and SOLPS5.0 code calculations *Nucl. Fusion* **52** 103006

[231] Guillemaut C. *et al* 2013 EDGE2D-EIRENE modelling of divertor detachment in JET high triangularity L-mode plasmas in carbon and Be/W environment *J. Nucl. Mater.* **438** S638–42

[232] Groth M. *et al* 2015 Divertor plasma conditions and neutral dynamics in horizontal and vertical divertor configurations in JET-ILW low confinement mode plasmas *J. Nucl. Mater.* **463** 471

[233] Jaervinen A. *et al* 2016 Impact of divertor geometry on radiative divertor performance in JET H-mode plasmas *Plasmas Phys. Control. Fusion* **458** 045011

[234] Sang C.F., Stangeby P.C., Guo H.Y., Leonard A.W., Covele B., Lao L.L., Moser A.L. and Thomas D.M. 2016 SOLPS modeling of the effect on plasma detachment of closing the lower divertor in DIII-D *Plasma Phys. Control. Fusion* **59** 025009

[235] Gleason-González C., Varoutis S., Hauer V. and Day C. 2014 Simulation of neutral gas flow in a tokamak divertor using the direct simulation Monte Carlo method *Fusion Eng. Des.* **89** 1042–7

[236] Varoutis S., Gleason-González C., Moulton D., Kruezi U., Groth M., Day C., Wiesen S. and Harting D. 2017 Simulation of neutral gas flow in the JET sub-divertor *Fusion Eng. Des.* **121** 13–21

[237] Moulton D., Groth M., Harting D., Wiesen S. and Gleason-Gonzalez C. 2015 Pumping in vertical and horizontal target configurations on JET in L-mode; an interpretive study using EDGE2D-EIRENE *Proc. 42nd European Physical Society Conf. on Plasma Physics (EPS 2015) (Lisbon, Portugal, 22–26 June 2015)* ed R. Bingham vol 39E O-4.119 (available at: https://info.fusion.ciemat.es/OCS/EPS2015PAP/pdf/O4.119.pdf)

[238] Groth M. *et al* 2023 Characterisation of divertor detachment onset in JET-ILW hydrogen, deuterium, tritium and deuterium-tritium low-confinement mode plasmas *Nucl. Mater. Energy* **34** 101345

[239] Maggi C. *et al* 1999 The isotope effect on the L mode density limit in JET hydrogen, deuterium and tritium divertor plasmas *Nucl. Fusion* **39** 979–91

[240] García-Cortés I., Hidalgo C., n-Solís J.R.M., Ali-Arshad S., Clement S., Davies S.J., Lingertat J., Loarte A., Matthews G.F. and Monk R.D. 1996 Characterization of fluctuations in the JET divertor plasmas with Langmuir probes *Plasma Phys. Control. Fusion* **38** 2051–62

[241] Antar G.Y., Counsell G., Ahn J.-W., Yang Y., Price M., Tabasso A. and Kirk A. 2005 The poloidal distribution of turbulent fluctuations in the Mega-Ampère Spherical Tokamak *Phys. Plasmas* **12** 032506

[242] Maqueda R.J. and Stotler D.P. 2010 Intermittent divertor filaments in the National Spherical Torus Experiment and their relation to midplane blobs *Nucl. Fusion* **50** 075002

[243] Farina D., Pozzoli R. and Ryutov D.D. 1993 Effect of the magnetic field geometry on the flute-like perturbations near the divertor X point *Nucl. Fusion* **33** 1315

[244] Ryutov D.D. and Cohen R.H. 2004 Instability driven by sheath boundary conditions and limited to divertor legs *Contrib. Plasma Phys.* **44** 168

[245] Ryutov D.D. and Soukhanovskii V.A. 2015 The snowflake divertor *Phys. Plasmas* **22** 110901

[246] Giacomin M., Stenger L.N. and Ricci P. 2020 Turbulence and flows in the plasma boundary of snowflake magnetic configurations *Nucl. Fusion* **60** 024001

[247] Ballinger S.B., Terry J.L., Baek S.G., Tang K., von Stechow A., Killer C., Nicolai D., Satheeswaran G., Drews P. and Grulke O. 2018 Fast camera imaging of

plasmas in Alcator C-Mod and W7-X *Nucl. Mater. Energy* **17** 269–73

[248] Scotti F., Zweben S., Myra J., Maqueda R. and Soukhanovskii V. 2019 Disconnection of scrape off layer turbulence between the outer midplane and divertor target plate in NSTX *Nucl. Fusion* **60** 026004

[249] Wüthrich C. *et al* 2022 X-point and divertor filament dynamics from gas puff imaging on TCV *Nucl. Fusion* **62** 106022

[250] Krasheninnikov S.I. and Kukushkin A.S. 2017 Physics of ultimate detachment of a tokamak divertor plasma *J. Plasma Phys.* **83** 155830501

[251] Loarte A. and Neu R. 2017 Power exhaust in tokamaks and scenario integration issues *Fusion Eng. Des.* **122** 256–73

[252] Verhaegh K. *et al* 2022 Spectroscopic investigations of detachment on the MAST Upgrade Super-X divertor *Nucl. Fusion* **63** 016014

[253] Pütterich T., Fable E., Dux R., O'Mullane M., Neu R. and Siccinio M. 2019 Determination of the tolerable impurity concentrations in a fusion reactor using a consistent set of cooling factors *Nucl. Fusion* **59** 056013

[254] Moulton D., Stangeby P.C., Bonnin X. and Pitts R.A. 2021 Comparison between SOLPS-4.3 and the Lengyel model for ITER baseline neon-seeded plasmas *Nucl. Fusion* **61** 046029

[255] Senichenkov I.Y., Kaveeva E.G., Sytova E.A., Rozhansky V.A., Voskoboynikov S.P., Veselova I.Y., Coster D.P., Bonnin X. and Reimold F. 2019 On mechanisms of impurity leakage and retention in the tokamak divertor *Plasma Phys. Control. Fusion* **61** 045013

[256] Neuwirth D., Rohde V. and Schwarz-Selinger T. 2012 Formation of ammonia during nitrogen-seeded discharges at ASDEX Upgrade *Plasma Phys. Control. Fusion* **54** 085008

[257] Oberkofler M. *et al* 2013 First nitrogen-seeding experiments in JET with the ITER-like wall *J. Nucl. Mater.* **438** S258–61

[258] Drenik A. *et al* 2019 Evolution of nitrogen concentration and ammonia production in N2-seeded H-mode discharges at ASDEX Upgrade *Nucl. Fusion* **59** 046010

[259] Loarer T. *et al* 2020 Long discharges in a steady state with D-2 and N-2 on the actively cooled tungsten upper divertor in WEST *Nucl. Fusion* **60** 126046

[260] Field A.R. *et al* 2017 Dynamics and stability of divertor detachment in H mode plasmas on JET *Plasma Phys. Control. Fusion* **59** 095003

[261] Reinke M.L., Hughes J.W., Loarte A., Brunner D., Hutchinson I.H., LaBombard B., Payne J. and Terry J.L. 2011 Effect of N2, Ne and Ar seeding on Alcator C-Mod H-mode confinement *J. Nucl. Mater.* **415** S340–4

[262] Loarte A. *et al* 2011 High confinement/high radiated power H-mode experiments in Alcator C-Mod and consequences for International Thermonuclear Experimental Reactor (ITER) Q(DT) = 10 operation *Phys. Plasmas* **18** 056105

[263] Petrie T.W. *et al* 2019 High performance double-null plasmas under radiating divertor and mantle scenarios on DIII-D *Nucl. Fusion* **59** 086053

[264] Wang H.Q. *et al* 2021 Observation of fully detached divertor integrated with improved core confinement for tokamak fusion plasmas *Phys. Plasmas* **28** 052507

[265] Li K.D. *et al* 2021 Sustained radiative divertor in high-performance grassy-ELM regime with metal wall towards long-pulse operation in EAST *Nucl. Mater. Energy* **26** 100867

[266] Rapp J. *et al* 2009 Integrated scenario with type-III ELMy H-mode edge: extrapolation to ITER *Nucl. Fusion* **49** 095012

[267] Giroud C. *et al* 2013 Impact of nitrogen seeding on confinement and power load control of a high-triangularity JET ELMy H-mode plasma with a metal wall *Nucl. Fusion* **53** 113025

[268] Bernert M. *et al* 2017 Power exhaust by SOL and pedestal radiation at ASDEX Upgrade and JET *Nucl. Mater. Energy* **12** 111–8

[269] Glöggler S. *et al* 2019 Characterisation of highly radiating neon seeded plasmas in JET-ILW *Nucl. Fusion* **59** 126031

[270] Asakura N., Nakano T., Oyama N., Sakamoto T., Matsunaga G. and Itami K. 2009 Investigations of impurity seeding and radiation control for long-pulse and high-density H-mode plasmas in JT-60U *Nucl. Fusion* **49** 115010

[271] Nakano T., Asakura N. and Kubo H. 2013 Contribution of Ne ions to radiation enhancement in JT-60U divertor plasmas *J. Nucl. Mater.* **438** S291–6

[272] Harrison J.R. *et al* 2019 Progress toward divertor detachment on TCV within H-mode operating parameters *Plasma Phys. Control. Fusion* **61** 065024

[273] Kallenbach A. *et al* 2011 Plasma surface interactions in impurity seeded plasmas *J. Nucl. Mater.* **415** S19–S26

[274] McLean A.G. *et al* 2015 Electron pressure balance in the SOL through the transition to detachment *J. Nucl. Mater.* **463** 533–6

[275] Eldon D. *et al* 2017 Controlling marginally detached divertor plasmas *Nucl. Fusion* **57** 066039

[276] Kukushkin A.S., Pacher H.D., Pacher G.W., Janeschitz G., Coster D., Loarte A. and Reiter D. 2003 Scaling laws for edge plasma parameters in ITER from two-dimensional edge modelling *Nucl. Fusion* **43** 716–23

[277] Lang P.T. *et al* 2005 Integrated exhaust scenarios with actively controlled ELMs *Nucl. Fusion* **45** 502–11

[278] Ryter F., Angioni C., Tardini G., Birkenmeier G., David P., Dunne M., Fischer R., Pütterich T., Schweinzer J. and Stober J. (The ASDEX Upgrade Team and The EUROfusion MST1 Team) 2021 The upgraded ASDEX Upgrade contribution to the ITPA confinement database: description and analysis *Nucl. Fusion* **61** 046030

[279] Hitzler F., Wischmeier M., Reimold F. and Coster D.P. 2020 Impurity transport and divertor retention in Ar and N seeded SOLPS 5.0 simulations for ASDEX Upgrade *Plasma Phys. Control. Fusion* **62** 085013

[280] Sytova E. *et al* 2019 Comparing N versus Ne as divertor radiators in ASDEX-Upgrade and ITER *Nucl. Mater. Energy* **19** 72–78

[281] David P., Bernert M., Cavedon M., Harrer G. and Eich T. (The ASDEX Upgrade Team) 2022 Influence of pedestal radiation on the L-H transition using krypton seeded discharges at AUG *Nucl. Fusion* **62** 106012

[282] Wischmeier M. (ASDEX Upgrade Team and JET EFDA Contributors) 2015 High density operation for reactor-relevant power exhaust *J. Nucl. Mater.* **463** 22–29

[283] Bernert M. *et al* 2021 X-point radiation, its control and an ELM suppressed radiating regime at the ASDEX Upgrade tokamak *Nucl. Fusion* **61** 024001

[284] Xu G.S. *et al* 2020 Divertor impurity seeding with a new feedback control scheme for maintaining good core confinement in grassy-ELM H-mode regime with tungsten monoblock divertor in EAST *Nucl. Fusion* **60** 086001

[285] Stroth U., Bernert M., Brida D., Cavedon M., Dux R., Huett E., Lunt T., Pan O. and Wischmeier M. (The ASDEX Upgrade Team) 2022 Model for access and stability of the X-point radiator and the threshold for marfes in tokamak plasmas *Nucl. Fusion* **62** 076008

[286] Matthews G.F. *et al* 1999 Studies in JET divertors of varied geometry. II: impurity seeded plasmas *Nucl. Fusion* **39** 19–40

[287] Nakano T., Kubo H., Asakura N., Shimizu K., Kawashima H. and Higashijima S. 2009 Radiation process of carbon ions in JT-60U detached divertor plasmas *J. Nucl. Mater.* **390–391** 255–8

[288] Nakano T. and Asakura N. 2019 Spatial distribution of Ne ions in detached divertor plasmas of JT-60U *Nucl. Mater. Energy* **18** 356–9

[289] Park J.-S., Pitts R., Jang J., Han Y.S., Choe W., Lore J., Hwang J., Bak J.-G., Juhn J.-W. and Hong S.-H. 2023 Bifurcation-like transition of divertor conditions induced by X-point radiation in KSTAR L-mode plasmas *Nucl. Fusion* **63** 086018

[290] Lipschultz B., LaBombard B., Marmar E.S., Pickrell M.M., Terry J.L., Watterson R. and Wolfe S.M. 1984 Marfe: an edge plasma phenomenon *Nucl. Fusion* **24** 977–88

[291] Cavedon M. *et al* 2022 Experimental investigation of L- and H-mode detachment via the divertor Thomson scattering at ASDEX Upgrade *Nucl. Fusion* **62** 066027

[292] Gao J. *et al* 2023 The effect of impurity seeding into the closed divertor on plasma detachment in the HL-2A tokamak *Nucl. Fusion* **63** 036006

[293] Reinke M.L. *et al* 2019 Radiative heat exhaust in Alcator C-Mod I-mode plasmas *Nucl. Fusion* **59** 046018

[294] Happel T. *et al* 2021 Approaching detachment in I-mode—response of core confinement and the edge pedestal in the ASDEX Upgrade tokamak *Nucl. Fusion* **61** 036026

[295] Greenwald M. *et al* 1999 Characterization of enhanced D-alpha high-confinement modes in Alcator C-Mod *Phys. Plasmas* **6** 1943–9

[296] Hughes J.W. *et al* 2018 Access to pedestal pressure relevant to burning plasmas on the high magnetic field tokamak Alcator C-Mod *Nucl. Fusion* **58** 112003

[297] Kallenbach A. *et al* 2021 Developments towards an ELM-free pedestal radiative cooling scenario using noble gas seeding in ASDEX Upgrade *Nucl. Fusion* **61** 016002

[298] Gil L. *et al* 2020 Stationary ELM-free H-mode in ASDEX Upgrade *Nucl. Fusion* **60** 054003

[299] Kallenbach A. *et al* 2021 Developments towards an ELM-free DEMO pedestal radiative cooling scenario in ASDEX Upgrade *28th IAEA Fusion Energy Conf.—Programme, Contributions and Conf. Material (10–14 May 2021)* vol CN-286 (International Atomic Energy Agency (IAEA)) EX 2–5 (available at: https://nucleus.iaea.org/sites/fusionportal/Shared%20Documents/FEC%202020/fec2020-preprints/preprint0741.pdf)

[300] Tokar M.Z., Jaspers R., Weynants R.R., Koslowski H.R., Krämer-Flecken A., Messiaen A.M., Ongena J. and Unterberg B. 1999 Evidence of suppression of ITG-instability in the radiatively improved mode in TEXTOR-94 *Plasma Phys. Control. Fusion* **41** L9–L15

[301] Fable E., Kallenbach A., McDermott R.M., Bernert M. and Angioni C. (The ASDEX Upgrade Team) 2022 High-confinement radiative L-modes in ASDEX Upgrade *Nucl. Fusion* **62** 024001

[302] Terry J. and Reinke M. 2017 Diagnostic tools for studying divertor detachment: bolometry, spectroscopy and thermography for surface heat-flux *Plasma Phys. Control. Fusion* **59** 044004

[303] Kallenbach A. *et al* 2010 Divertor power load feedback with nitrogen seeding in ASDEX Upgrade *Plasma Phys. Control. Fusion* **52** 055002

[304] Orrico C., Ravensbergen T., Pitts R.A., Bonnin X., Kaveeva E., Park J.S., Rozhansky V., Senichenkov I., Watts C. and de Baar M. 2023 Evaluation of ITER divertor shunts as a synthetic diagnostic for detachment control *Nucl. Fusion* **63** 086002

[305] Kallenbach A., Bernert M., Eich T., Fuchs J.C., Giannone L., Herrmann A., Schweinzer J. and Treutterer W. 2012 Optimized tokamak power exhaust with double radiative feedback in ASDEX Upgrade *Nucl. Fusion* **52** 122003

[306] Eldon D., Kolemen E., Humphreys D.A., Hyatt A.W., Järvinen A.E., Leonard A.W., McLean A.G., Moser A.L., Petrie T.W. and Walker M.L. 2019 Advances in radiated power control at DIII-D *Nucl. Mater. Energy* **18** 285–90

[307] Lovell J., Reinke M.L., Field A.R. and Lomanowski B.A. 2023 Overview and first measurements of the MAST Upgrade bolometer diagnostic *Rev. Sci. Instrum.* **94** 023509

[308] Bernert M., Eich T., Burckhart A., Fuchs J.C., Giannone L., Kallenbach A., McDermott R.M. and Sieglin B. 2014 Application of AXUV diode detectors at ASDEX Upgrade *Rev. Sci. Instrum.* **85** 033503

[309] Guillemaut C. *et al* 2017 Real-time control of divertor detachment in H-mode with impurity seeding using Langmuir probe feedback in JET-ITER-like wall *Plasma Phys. Control. Fusion* **59** 045001

[310] Wang L. *et al* 2019 Advances in plasma-wall interaction control for H-mode operation over 100 s with ITER-like tungsten divertor on EAST *Nucl. Fusion* **59** 086036

[311] Eldon D. *et al* 2021 An analysis of controlled detachment by seeding various impurity species in high performance scenarios on DIII-D and EAST *Nucl. Mater. Energy* **27** 100963

[312] Wang L. *et al* 2022 Achievements of actively controlled divertor detachment compatible with sustained high confinement core in DIII-D and EAST *Nucl. Fusion* **62** 076002

[313] Brunner D. *et al* 2017 Surface heat flux feedback controlled impurity seeding experiments with Alcator C-Mod's high-Z vertical target plate divertor: performance, limitations and implications for fusion power reactors *Nucl. Fusion* **57** 086030

[314] Chen M.W. *et al* 2020 Detachment plasma achieved based on active temperature feedback system in EAST *Nucl. Fusion* **60** 076009

[315] Kitazawa S., Yamamoto T., Kawano Y. and Itami K. 2014 Progress of preparation for ITER divertor thermocouple in JADA *Plasma Fusion Res.* **9** 3405049

[316] Ravensbergen T. *et al* 2021 Real-time feedback control of the impurity emission front in tokamak divertor plasmas *Nat. Commun.* **12** 1105

[317] Koenders J., Perek A., Kool B., Février O., Ravensbergen T., Galperti C., Duval B.P., Theiler C. and van Berkel M. (The TCV Team and The EUROfusion MST1 Team) 2023 Corrigendum: Model-based impurity emission front control using deuterium fueling and nitrogen seeding in TCV (2023 *Nucl. Fusion* 63 026006) *Nucl. Fusion* **63** 069501

[318] Kallenbach A. *et al* 2022 Argon doped pellets for fast and efficient radiative power removal in ASDEX Upgrade *Nucl. Fusion* **62** 106013

[319] Goldston R.J., Reinke M.L. and Schwartz J.A. 2017 A new scaling for divertor detachment *Plasma Phys. Control. Fusion* **59** 055015

[320] Reinke M.L. 2017 Heat flux mitigation by impurity seeding in high-field tokamaks *Nucl. Fusion* **57** 034004

[321] Kallenbach A., Bernert M., Dux R., Reimold F. and Wischmeier M. 2016 Analytical calculations for impurity seeded partially detached divertor conditions *Plasma Phys. Control. Fusion* **58** 045013

[322] Lengyel L.L. 1981 Analysis of radiating plasma boundary layers *Technical Report* (Max-Planck-Institut für Plasmaphysik)

[323] Leonard A.W., McLean A.G., Makowski M.A. and Stangeby P.C. 2017 Compatibility of separatrix density scaling for divertor detachment with H-mode pedestal operation in DIII-D *Nucl. Fusion* **57** 086033

[324] Summers H.P. 2004 The ADAS user manual *Technical Report* v2.7 2nd edn (University of Strathclyde Glasgow) (available at: www.adas.ac.uk/manual.php)

[325] Xiang L., Wischmeier M., Coster D., Bernert M., Guo H.Y. and Luo G.N. (ASDEX Upgrade Team) 2017 Modeling of argon seeding in ASDEX Upgrade H-mode plasma with SOLPS5.0 *Nucl. Mater. Energy* **12** 1146–51

[326] Henderson S.S., Bernert M., Brezinsek S., Carr M., Cavedon M., Dux R., Lipschultz B., O'Mullane M.G., Reimold F. and Reinke M.L. 2018 Determination of volumetric plasma parameters from spectroscopic N II and N III line ratio measurements in the ASDEX Upgrade divertor *Nucl. Fusion* **58** 016047

[327] Fenstermacher M.E. (DIII-D Team) 2022 DIII-D research advancing the physics basis for optimizing the tokamak approach to fusion energy *Nucl. Fusion* **62** 042024

[328] Henderson S.S. *et al* 2021 Parameter dependencies of the experimental nitrogen concentration required for detachment on ASDEX Upgrade and JET *Nucl. Mater. Energy* **28** 101000

[329] Loarte A. *et al* 2007 Chapter 4: Power and particle control *Nucl. Fusion* **47** S203–63

[330] Goetz J.A., Pitcher C.S., LaBombard B., Lipschultz B., Rice J.E. and Terry J.L. 2001 The relation between impurity neutral and impurity ion compression in the Alcator C-Mod divertor *Nucl. Fusion* **41** 1751–4

[331] Casali L., Eldon D., McLean A., Osborne T., Leonard A., Grierson B. and Ren J. 2022 Impurity leakage and radiative cooling in the first nitrogen and neon seeding study in the closed DIII-D SAS configuration *Nucl. Fusion* **62** 026021

[332] Zito A. *et al* 2023 Investigation of helium exhaust dynamics at the ASDEX Upgrade tokamak with full-tungsten wall *Nucl. Fusion* **63** 096027

[333] Angioni C. 2021 Impurity transport in tokamak plasmas, theory, modelling and comparison with experiments *Plasma Phys. Control. Fusion* **63** 073001

[334] Kaveeva E. *et al* 2020 SOLPS-ITER modelling of ITER edge plasma with drifts and currents *Nucl. Fusion* **60** 046019

[335] Huber A. *et al* 2017 Comparative H-mode density limit studies in JET and AUG *Nucl. Mater. Energy* **12** 100–10

[336] Leonard A., Jaervinen A., McLean A. and Scotti F. 2020 MHD stability constraints on divertor heat flux width in DIII-D *Nucl. Mater. Energy* **25** 100869

[337] Faitsch M., Eich T., Harrer G.F., Wolfrum E., Brida D., David P., Dunne M., Gil L., Labit B. and Stroth U. 2023 Analysis and expansion of the quasi-continuous exhaust (QCE) regime in ASDEX Upgrade *Nucl. Fusion* **63** 076013

[338] Dunne M.G. *et al* 2017 The role of the density profile in the ASDEX-Upgrade pedestal structure *Plasma Phys. Control. Fusion* **59** 014017

[339] Leonard A., Makowski M., McLean A., Osborne T. and Snyder P. 2015 Compatibility of detached divertor operation with robust edge pedestal performance *J. Nucl. Mater.* **463** 519–23

[340] Potzel S. *et al* 2015 Formation of the high density front in the inner far SOL at ASDEX Upgrade and JET *J. Nucl. Mater.* **463** 541–5

[341] Schweinzer J. *et al* 2011 Confinement of 'improved H-modes' in the all-tungsten ASDEX Upgrade with nitrogen seeding *Nucl. Fusion* **51** 113003

[342] Beurskens M.N.A. *et al* 2013 The effect of a metal wall on confinement in JET and ASDEX Upgrade *Plasma Phys. Control. Fusion* **55** 124043

[343] Giroud C. *et al* 2015 Progress at JET in integrating ITER-relevant core and edge plasmas within the constraints of an ITER-like wall *Plasma Phys. Control. Fusion* **57** 035004

[344] Hughes J.W. *et al* 2011 Power requirements for superior H-mode confinement on Alcator C-Mod: experiments in support of ITER *Nucl. Fusion* **51** 083007

[345] Gruber O. *et al* 1995 Observation of continuous divertor detachment in H-mode discharges in ASDEX Upgrade *Phys. Rev. Lett.* **74** 4217–20

[346] Giroud C. *et al* 2021 High performance ITER-baseline discharges in deuterium with nitrogen and neon-seeding in the JET-ILW *28th IAEAFusion Energy Conf.–Programme, Contributions and Conf. Material (10–14 May 2021)* (International Atomic Energy Agency (IAEA)) EX/P3–9 (available at: https://nucleus.iaea.org/sites/fusionportal/Shared%20Documents/FEC%202020/fec2020-preprints/preprint0977.pdf)

[347] Wang L. *et al* 2021 Integration of full divertor detachment with improved core confinement for tokamak fusion plasmas *Nat. Commun.* **12** 1365

[348] Ding S. and Garofalo A.M. 2022 Progress in the development and understanding of a high poloidal-beta tokamak operating scenario for an attractive fusion pilot plant *Rev. Mod. Plasma Phys.* **7** 4

[349] Wenninger R. *et al* 2016 The physics and technology basis entering European system code studies for DEMO *Nucl. Fusion* **57** 016011

[350] Subba F., Coster D.P., Moscheni M. and Siccinio M. 2021 SOLPS-ITER modeling of divertor scenarios for EU-DEMO *Nucl. Fusion* **61** 106013

[351] Asakura N. *et al* 2017 Studies of power exhaust and divertor design for a 1.5 GW-level fusion power DEMO *Nucl. Fusion* **57** 126050

[352] Asakura N., Hoshino K., Homma Y. and Sakamoto Y. 2021 Simulation studies of divertor detachment and critical power exhaust parameters for Japanese DEMO design *Nucl. Mater. Energy* **26** 100864

[353] Liu X.J. *et al* 2020 Simulation studies of divertor power exhaust with neon seeding for CFETR with GW-level fusion power *Phys. Plasmas* **27** 092508

[354] Si H., Ding R., Senichenkov I., Rozhansky V., Molchanov P., Liu X., Jia G., Sang C., Mao S. and Chan V. (The CFETR Team) 2022 SOLPS-ITER simulations of high power exhaust for CFETR divertor with full drifts *Nucl. Fusion* **62** 026031

[355] Kwon S., Im K., Hong S.-H., Lee H., Rognlien T.D., Meyer W. and Kim K. 2020 Recent progress in the design of the K-DEMO divertor *Fusion Eng. Des.* **159** 111770

[356] Rognlien T.D., Rensink M.E. and Stotler D.P. 2018 Scrape-off layer plasma and neutral characteristics and their interactions with walls for FNSF *Fusion Eng. Des.* **135** 380–93

[357] Asakura N. *et al* 2021 Power exhaust concepts and divertor designs for Japanese and European DEMO fusion reactors *Nucl. Fusion* **61** 126057

[358] Asakura N., Hoshino K., Kakudate S., Subba F., You J.-H., Wiesen S., Rognlien T.D., Ding R. and Kwon S. 2023 Recent progress of plasma exhaust concepts and divertor designs for tokamak DEMO reactors *Nucl. Mater. Energy* **35** 101446

[359] Kotschenreuther M., Valanju P.M., Mahajan S.M. and Wiley J.C. 2007 On heat loading, novel divertors and fusion reactors *Phys. Plasmas* **14** 072502

[360] Reimerdes H. *et al* 2020 Assessment of alternative divertor configurations as an exhaust solution for DEMO *Nucl. Fusion* **60** 066030

[361] Goldston R.J., Hakim A., Hammett G.W., Jaworski M.A. and Schwartz J. 2017 Recent advances towards a lithium vapor box divertor *Nucl. Mater. Energy* **12** 1118–21

[362] Pericoli R.V., Chmielewski P., Ivanova-Stanik I., Poradziński M., Zagórski R., Ambrosino R. and Crisanti F. 2020 Comparison between liquid lithium and liquid tin targets in reactor relevant conditions for DEMO and I-DTT *Phys. Plasmas* **27** 112506

[363] Rindt P., Korving S., Morgan T. and Cardozo N.J. 2021 Performance of liquid-lithium-filled 3D-printed tungsten divertor targets under deuterium loading with ELM-like pulses in Magnum-PSI *Nucl. Fusion* **61** 066026

[364] Horacek J. *et al* 2020 Modeling of COMPASS tokamak divertor liquid metal experiments *Nucl. Mater. Energy* **25** 100860

[365] Scholte J. *et al* 2023 Performance of a liquid Sn divertor target during ASDEX upgrade L-mode and H-mode operation *Nucl. Mater. Energy* **37** 101522

[366] Dux R., Loarte A., Fable E. and Kukushkin A. 2014 Transport of tungsten in the H-mode edge transport barrier of ITER *Plasma Phys. Control. Fusion* **56** 124003

[367] Dux R., Loarte A., Angioni C., Coster D., Fable E. and Kallenbach A. 2017 The interplay of controlling the power exhaust and the tungsten content in ITER *Nucl. Mater. Energy* **12** 28–35

[368] Field A. *et al* 2022 Peripheral temperature gradient screening of high-Z impurities in optimised ‘hybrid’ scenario H-mode plasmas in JET-ILW *Nucl. Fusion* **63** 016028

[369] Yu J.H., De Temmerman G., Doerner R.P., Pitts R.A. and Van D.B.M.A. 2015 The effect of transient temporal pulse shape on surface temperature and tungsten damage *Nucl. Fusion* **55** 093027

[370] Eich T., Sieglin B., Thornton A.J., Faitsch M., Kirk A., Herrmann A. and Suttrop W. 2017 ELM divertor peak energy fluence scaling to ITER with data from JET, MAST and ASDEX Upgrade *Nucl. Mater. Energy* **12** 84–90

[371] Eich T., Kallenbach A., Fundamenski W., Herrmann A. and Naulin V. 2009 On the asymmetries of ELM divertor power deposition in JET and ASDEX Upgrade *J. Nucl. Mater.* **390–391** 760–3

[372] Eich T., Thomsen H., Fundamenski W., Arnoux G., Brezinsek S., Devaux S., Herrmann A., Jachmich S. and Rapp J. 2011 Type-I ELM power deposition profile width and temporal shape in JET *J. Nucl. Mater.* **415** S856–9

[373] Gao J.M. *et al* 2021 Type-I ELM power loads on the closed outer divertor targets in the HL-2A tokamak *Nucl. Fusion* **61** 066024

[374] Knolker M. *et al* 2018 Investigation of the role of pedestal pressure and collisionality on type-I ELM divertor heat loads in DIII-D *Nucl. Fusion* **58** 096023

[375] Fundamenski W. and Pitts R.A. (JET EFDA Contributors) 2006 A model of ELM filament energy evolution due to parallel losses *Plasma Phys. Control. Fusion* **48** 109–56

[376] Adamek J. *et al* 2020 On the transport of edge localized mode filaments in the tokamak scrape-off layer *Nucl. Fusion* **60** 096014

[377] Moulton D., Ghendrih P., Fundamenski W., Manfredi G. and Tskhakaya D. 2013 Quasineutral plasma expansion into infinite vacuum as a model for parallel ELM transport *Plasma Phys. Control. Fusion* **55** 085003

[378] Moulton D., Fundamenski W., Manfredi G., Hirstoaga S. and Tskhakaya D. 2013 Comparison of free-streaming ELM formulae to a Vlasov simulation *J. Nucl. Mater.* **438** S633–7

[379] Guillemaut C. *et al* 2015 Ion target impact energy during Type I edge localized modes in JET ITER-like Wall *Plasma Phys. Control. Fusion* **57** 085006

[380] Guillemaut C., Metzger C., Moulton D., Heinola K., O’Mullane M., Balboa I., Boom J., Matthews G.F., Silburn S. and Solano E.R. 2018 Experimental validation of an analytical kinetic model for edge-localized modes in JET-ITER-like wall *Nucl. Fusion* **58** 066006

[381] Horacek J. *et al* 2023 ELM temperature in JET and COMPASS tokamak divertors *Nucl. Fusion* **63** 056007

[382] Tskhakaya D. 2004 Kinetic simulations of the tokamak scrape-off layer *ISPP-21 Joint Varenna-Lausanne Int. Workshop on Theory of Fusion Plasmas (Proc. Int. School of Plasma Physics Piero Caldirola) (Varenna, Italy, 30 August–3 September 2004)* (Societa Italiana di Fisica) pp 97–109

[383] Sigmar D.J., Batishcheva A.A., Batishchev O.V., Krasheninnikov S.I. and Catto P.J. 1996 Kinetic models of ELMs burst *Contrib. Plasma Phys.* **36** 230–4

[384] Bergmann A. 2002 Transport of edge-localized mode energy in a scrape-off layer in the presence of collisionless fast electrons *Nucl. Fusion* **42** 1162–7

[385] Takizuka T. and Hosokawa M. 2006 Particle simulation of the transient behavior of one-dimensional SOL-divertor plasmas after an ELM crash *Contrib. Plasma Phys.* **46** 698–703

[386] Pitts R.A., Andrew P., Arnoux G., Eich T., Fundamenski W., Huber A., Silva C. and Tskhakaya D. 2007 ELM transport in the JET scrape-off layer *Nucl. Fusion* **47** 1437–48

[387] Tskhakaya D. *et al* 2007 PIC simulations of ELM particle and heat loads to the JET divertor targets *Proc. 34th EPS Conf. on Controlled Fusion and Plasma Physics* (*Europhysics Conf. Abstracts* vol 31F) *(Warsaw, Poland, 2–6 July 2007)* (European Physical Society) O–2.002 (available at: https://info.fusion.ciemat.es/OCS/EPS2007/pdf/O2_002.pdf)

[388] Tskhakaya D., Pitts R.A., Fundamenski W., Eich T. and Kuhn S. (JET EFDA Contributors) 2009 Kinetic simulations of the parallel transport in the JET scrape-off layer *J. Nucl. Mater.* **390–391** 335–8

[389] Tskhakaya D., Jachmich S., Eich T. and Fundamenski W. 2011 Interpretation of divertor Langmuir probe measurements during the ELMs at JET *J. Nucl. Mater.* **415** S860–4

[390] Takizuka T., Oyama N. and Hosokawa M. 2008 Effect of radial transport loss on the asymmetry of ELM heat flux *Contrib. Plasma Phys.* **48** 207–11

[391] Marki J., Pitts R.A., Horacek J. and Tskhakaya D. 2009 ELM induced divertor heat loads on TCV *J. Nucl. Mater.* **390–391** 801–5

[392] Loarte A. *et al* 2002 Characteristics and scaling of energy and particle losses during Type I ELMs in JET H-modes *Plasma Phys. Control. Fusion* **44** 1815–44

[393] Hosokawa M., Loarte A., Huijsmans G.T.A., Takizuka T. and Hayashi N. 2016 Kinetic modelling of divertor fluxes during ELMs in ITER and effect of in/out divertor plasma asymmetries *Plasma Fusion Res.* **11** 1403104

[394] Manfredi G., Hirstoaga S. and Devaux S. 2010 Vlasov modelling of parallel transport in a tokamak scrape-off layer *Plasma Phys. Control. Fusion* **53** 015012

[395] Shi E.L., Hakim A.H. and Hammett G.W. 2015 A gyrokinetic one-dimensional scrape-off layer model of an edge-localized mode heat pulse *Phys. Plasmas* **22** 022504

[396] Tskhakaya D., Subba F., Bonnin X., Coster D.P., Fundamenski W., Pitts R.A. and EFDA Contributors J. 2008 On kinetic effects during parallel transport in the SOL *Contrib. Plasma Phys.* **48** 89–93

[397] Dejarnac R., Komm M., Tskhakaya D., Gunn J.P. and Pekarek Z. 2010 Detailed particle and power fluxes into ITER castellated divertor gaps during ELMs *IEEE Trans. Plasma Sci.* **38** 1042–6

[398] Gunn J.P. *et al* 2017 Surface heat loads on the ITER divertor vertical targets *Nucl. Fusion* **57** 046025

[399] Kallenbach A. *et al* 2004 EDGE2D modelling of edge profiles obtained in JET diagnostic optimized configuration *Plasma Phys. Control. Fusion* **46** 431–46

[400] Coster D.P. *et al* 2015 SOLPS modelling of W arising from repetitive mitigated ELMs in ITER *J. Nucl. Mater.* **463** 620–3

[401] Wiesen S., Brezinsek S., Järvinen A., Eich T., Fundamenski W., Huber A., Parail V., Corrigan G. and Hayashi N. 2011 Integrated modelling of a JET type-I ELMy H-mode pulse and predictions for ITER-like wall scenarios *Plasma Phys. Control. Fusion* **53** 124039

[402] Rognlien T.D., Cohen R.H., Ryutov D.D. and Umansky M.V. 2013 Comparison of ELM heat loads in snowflake and standard divertors *J. Nucl. Mater.* **438** S418–21

[403] Harting D.M. *et al* 2015 Intra-ELM phase modelling of a JET ITER-like wall H-mode discharge with EDGE2D-EIRENE *J. Nucl. Mater.* **463** 493–7

[404] Järvinen A.E. *et al* 2013 Simulations of tungsten transport in the edge of JET ELMy H-mode plasmas *J. Nucl. Mater.* **438** S1005–9

[405] Havlíčková E., Fundamenski W., Tskhakaya D., Manfredi G. and Moulton D. 2012 Comparison of fluid and kinetic models of target energy fluxes during edge localized modes *Plasma Phys. Control. Fusion* **54** 045002

[406] Gulejová B., Pitts R.A., Tskhakaya D. and Coster D. 2011 Benchmark of fluid and kinetic simulations of type III ELMing H-mode on TCV *Fusion Sci. Technol.* **60** 48–55

[407] Pankin A.Y., Bateman G., Brennan D.P., Kritz A.H., Kruger S., Snyder P.B. and Sovinec C. (The NIMROD Team) 2007 Modelling of ELM dynamics for DIII-D and ITER *Plasma Phys. Control. Fusion* **49** S63–S75

[408] Huysmans G.T.A. and Czarny O. 2007 MHD stability in X-point geometry: simulation of ELMs *Nucl. Fusion* **47** 659–66

[409] Sugiyama L.E. 2012 Intrinsic stochasticity in fusion plasmas *Phys. Scr.* **86** 058205

[410] Huijsmans G.T.A., van Vugt D.C., Franssen S., Korving S.Q. and Becoulet M. 2019 Non-linear MHD simulations of ELMs in a high recycling divertor *Proc. 46th EPS Conf. on Controlled Fusion and Plasma Physics* (*Europhysics Conf. Abstracts* vol 43C) *(Milan, Italy, 8–12 July 2019)* (European Physical Society) P1.1059 (available at: https://info.fusion.ciemat.es/OCS/EPS2019PAP/pdf/P1.1059.pdf)

[411] Smith S.F., Pamela S.J.P., Fil A., Hölzl M., Huijsmans G.T.A., Kirk A., Moulton D., Myatra O., Thornton A.J. and Wilson H.R. 2020 Simulations of edge localised mode instabilities in MAST-U Super-X tokamak plasmas *Nucl. Fusion* **60** 066021

[412] Hoelzl M. *et al* 2021 The JOREK non-linear extended MHD code and applications to large-scale instabilities and their control in magnetically confined fusion plasmas *Nucl. Fusion* **61** 065001

[413] Hoelzl M. *et al* 2018 Insights into type-I edge localized modes and edge localized mode control from JOREK non-linear magneto-hydrodynamic simulations *Contrib. Plasma Phys.* **58** 518–28

[414] Huysmans G.T.A., Pamela S., van der Plas E. and Ramet P. 2009 Non-linear MHD simulations of edge localized modes (ELMs) *Plasma Phys. Control. Fusion* **51** 124012

[415] Pamela S. *et al* 2015 Non-linear MHD simulations of ELMs in JET and quantitative comparisons to experiments *Plasma Phys. Control. Fusion* **58** 014026

[416] Huijsmans G.T.A. and Loarte A. 2013 Non-linear MHD simulation of ELM energy deposition *Nucl. Fusion* **53** 123023

[417] Orain F. *et al* 2015 Resistive reduced MHD modeling of multi-edge-localized-mode cycles in tokamak X-point plasmas *Phys. Rev. Lett.* **114** 035001

[418] Lang P.T. *et al* 2013 ELM control strategies and tools: status and potential for ITER *Nucl. Fusion* **53** 043004

[419] Loarte A. *et al* 2014 Progress on the application of ELM control schemes to ITER scenarios from the non-active phase to DT operation *Nucl. Fusion* **54** 033007

[420] Jakubowski M.W. *et al* 2009 Overview of the results on divertor heat loads in RMP controlled H-mode plasmas on DIII-D *Nucl. Fusion* **49** 095013

[421] Suttrop W. *et al* 2011 First observation of edge localized modes mitigation with resonant and nonresonant magnetic perturbations in ASDEX Upgrade *Phys. Rev. Lett.* **106** 225004

[422] Kirk A. *et al* 2015 Effect of resonant magnetic perturbations on low collisionality discharges in MAST and a comparison with ASDEX Upgrade *Nucl. Fusion* **55** 043011

[423] Herrmann A. 2002 Overview on stationary and transient divertor heat loads *Plasma Phys. Control. Fusion* **44** 883–95

[424] Baylor L.R. *et al* 2013 Reduction of edge-localized mode intensity using high-repetition-rate pellet injection in tokamak H-mode plasmas *Phys. Rev. Lett.* **110** 245001

[425] Baylor L.R. *et al* 2013 Reduction of edge localized mode intensity on DIII-D by on-demand triggering with high frequency pellet injection and implications for ITER *Phys. Plasmas* **20** 082513

[426] Bortolon A. *et al* 2016 High frequency pacing of edge localized modes by injection of lithium granules in DIII-D H-mode discharges *Nucl. Fusion* **56** 056008

[427] Bortolon A. *et al* 2017 Mitigation of divertor heat flux by high-frequency ELM pacing with non-fuel pellet injection in DIII-D *Nucl. Mater. Energy* **12** 1030–6

[428] Lang P.T. *et al* 2004 ELM pace making and mitigation by pellet injection in ASDEX Upgrade *Nucl. Fusion* **44** 665–77

[429] Wenninger R.P., Eich T.H., Huysmans G.T.A., Lang P.T., Devaux S., Jachmich S. and Köchl F. 2011 Scrape-off layer heat transport and divertor power deposition of pellet-induced edge localized modes *Plasma Phys. Control. Fusion* **53** 105002

[430] Lang P.T. *et al* 2011 ELM pacing investigations at JET with the new pellet launcher *Nucl. Fusion* **51** 033010

[431] Lang P.T. *et al* 2013 ELM pacing and trigger investigations at JET with the new ITER-like wall *Nucl. Fusion* **53** 073010

[432] Futatani S., Pamela S., Garzotti L., Huijsmans G.T.A., Hoelzl M., Frigione D. and Lennholm M. 2019 Non-linear magnetohydrodynamic simulations of pellet triggered edge-localized modes in JET *Nucl. Fusion* **60** 026003

[433] Futatani S., Cathey A., Hoelzl M., Lang P.T., Huijsmans G.T.A. and Dunne M. (The JOREK Team, The ASDEX Upgrade Team and The EUROfusion MST1 Team) 2021 Transition from no-ELM response to pellet ELM triggering during pedestal build-up—insights from extended MHD simulations *Nucl. Fusion* **61** 046043

[434] Wingen A., Lyons B.C., Wilcox R.S., Baylor L.R., Ferraro N.M., Jardin S.C. and Shiraki D. 2021 Simulation of pellet ELM triggering in low-collisionality, ITER-like discharges *Nucl. Fusion* **61** 126059
[435] Hayashi N., Aiba N., Takizuka T. and Oyama N. 2013 Reduction of ELM energy loss by pellet injection for ELM pacing *Nucl. Fusion* **53** 123009
[436] Wilcox R.S. *et al* 2022 Pellet triggering of edge localized modes in low collisionality pedestals at DIII-D *Nucl. Fusion* **62** 026017
[437] Xiao W.W. *et al* 2012 ELM mitigation by supersonic molecular beam injection into the H-mode pedestal in the HL-2A tokamak *Nucl. Fusion* **52** 114027
[438] Degeling A.W., Martin Y.R., Lister J.B., Villard L., Dokouka V.N., Lukash V.E. and Khayrutdinov R.R. 2003 Magnetic triggering of ELMs in TCV *Plasma Phys. Control. Fusion* **45** 1637
[439] Lang P.T. *et al* 2004 Frequency control of type-I ELMs by magnetic triggering in ASDEX Upgrade *Plasma Phys. Control. Fusion* **46** L31–L39
[440] Gerhardt S.P. *et al* 2010 First observation of ELM pacing with vertical jogs in a spherical torus *Nucl. Fusion* **50** 064015
[441] Kim J. *et al* 2012 ELM control experiments in the KSTAR device *Nucl. Fusion* **52** 114011
[442] de la Luna E. *et al* 2015 Understanding the physics of ELM pacing via vertical kicks in JET in view of ITER *Nucl. Fusion* **56** 026001
[443] Rapp J. *et al* 2004 Reduction of divertor heat load in JET ELMy H-modes using impurity seeding techniques *Nucl. Fusion* **44** 312
[444] Komm M., Faitsch M., Henderson S., Bernert M., Brida D., Février O., Järvinen A., Silvagni D. and Tskhakaya D. (The ASDEX Upgrade Team and The EUROfusion MST1 Team) 2023 Mitigation of divertor edge localised mode power loading by impurity seeding *Nucl. Fusion* **63** 126018
[445] Stober J., Maraschek M., Conway G.D., Gruber O., Herrmann A., Sips A.C.C., Treutterer W. and Zohm H. (ASDEX Upgrade Team) 2001 Type II ELMy H modes on ASDEX Upgrade with good confinement at high density *Nucl. Fusion* **41** 1123–34
[446] Saibene G. *et al* 2005 Characterization of small ELM experiments in highly shaped single null and quasi-double-null plasmas in JET *Nucl. Fusion* **45** 297
[447] Kamada Y., Oikawa T., Lao L., Takizuka T., Hatae T., Isayama A., Manickam J., Okabayashi M., Fukuda T. and Tsuchiya K. 2000 Disappearance of giant ELMs and appearance of minute grassy ELMs in JT-60U high-triangularity discharges *Plasma Phys. Control. Fusion* **42** A247–53
[448] Xu G.S. *et al* 2019 Promising high-confinement regime for steady-state fusion *Phys. Rev. Lett.* **122** 255001
[449] Burrell K.H. *et al* 2016 Discovery of stationary operation of quiescent H-mode plasmas with net-zero neutral beam injection torque and high energy confinement on DIII-D *Phys. Plasmas* **23** 056103
[450] Chen X. *et al* 2017 Bifurcation of quiescent H-mode to a wide pedestal regime in DIII-D and advances in the understanding of edge harmonic oscillations *Nucl. Fusion* **57** 086008
[451] Kirk A., Wilson H.R., Counsell G.F., Akers R., Arends E., Cowley S.C., Dowling J., Lloyd B., Price M. and Walsh M. 2004 Spatial and temporal structure of edge-localized modes *Phys. Rev. Lett.* **92** 245002
[452] Kirk A. *et al* 2006 Filament structures at the plasma edge on MAST *Plasma Phys. Control. Fusion* **48** B433–41
[453] Leonard A.W. 2014 Edge-localized-modes in tokamaks *Phys. Plasmas* **21** 090501
[454] Eich T. *et al* 2005 Type-I ELM substructure on the divertor target plates in ASDEX Upgrade *Plasma Phys. Control. Fusion* **47** 815–42
[455] Boedo J.A. *et al* 2005 Edge-localized mode dynamics and transport in the scrape-off layer of the DIII-D tokamak *Phys. Plasmas* **12** 072516
[456] Eich T., Herrmann A. and Neuhauser J. (ASDEX Upgrade Team) 2003 Nonaxisymmetric energy deposition pattern on ASDEX Upgrade divertor target plates during Type-I edge-localized modes *Phys. Rev. Lett.* **91** 195003
[457] Herrmann A. *et al* 2007 The filamentary structure of ELMs in the scrape-off layer in ASDEX Upgrade *J. Nucl. Mater.* **363–365** 528–33
[458] Silva C., Gonçalves B., Hidalgo C., Erents K., Loarte A., Matthews G. and Pedrosa M. 2005 Determination of the particle and energy fluxes in the JET far SOL during ELMs using the reciprocating probe diagnostic *J. Nucl. Mater.* **337–339** 722–6
[459] Bae M.-K., Pitts R.A., Bak J.G., Hong S.-H., Kim H.S., Lee H.H., Kang I.J. and Chung K.-S. 2017 Type I ELM filament heat fluxes on the KSTAR main chamber wall *Nucl. Mater. Energy* **12** 1259–64
[460] Kirk A. *et al* 2005 Structure of ELMs in MAST and the implications for energy deposition *Plasma Phys. Control. Fusion* **47** 315–33
[461] Pitts R.A., Fundamenski W., Erents S.K., Andrew Y., Loarte A. and Silva C. (JET-EFDA Contributors) 2005 Far SOL ELM ion energies in JET *Nucl. Fusion* **46** 82–98
[462] Herrmann A., Eich T., Rohde V., Fuchs C.J. and Neuhauser J. (ASDEX Upgrade Team) 2004 Power deposition outside the divertor in ASDEX Upgrade *Plasma Phys. Control. Fusion* **46** 971–9
[463] Pitts R.A. *et al* 2009 The impact of large ELMs on JET *J. Nucl. Mater.* **390–391** 755–9
[464] Rudakov D.L. *et al* 2009 Plasma interactions with the outboard chamber wall in DIII-D *J. Nucl. Mater.* **390–391** 785–8
[465] Herrmann A., Neuhauser J., Rohde V., Dux R., Eich T., Fuchs C.J. and Ye M.Y. 2005 Interaction of ELMs and fast particles with in-vessel components in ASDEX Upgrade *J. Nucl. Mater.* **337–339** 697–701
[466] Perillo R., Boedo J.A., Lasnier C.J., Rudakov D.L., Osborne T. and Watkins J.G. 2021 ELM and inter-ELM heat and particle flux to a secondary divertor in the DIII-D tokamak *Nucl. Fusion* **61** 086024
[467] Perillo R., Boedo J.A., Lasnier C.J., Bykov I., Marini C. and Watkins J.G. 2022 Quantifying heat and particle flux to primary and secondary divertors for various types of edge-localized-modes *Phys. Plasmas* **29** 052506
[468] Kirk A., Lisgo S., Nardon E., Eich T., Herrmann A., Kallenbach A. and Loarte A. 2009 Physics of ELM power fluxes to plasma facing components and implications for ITER *J. Nucl. Mater.* **390–391** 727–32
[469] Evans T.E. 2013 ELM mitigation techniques *J. Nucl. Mater.* **438** S11
[470] Suttrop W. *et al* 2018 Experimental conditions to suppress edge localised modes by magnetic perturbations in the ASDEX Upgrade tokamak *Nucl. Fusion* **58** 096031
[471] Evans T.E. *et al* 2004 Suppression of large edge-localized modes in high-confinement DIII-D plasmas with a stochastic magnetic boundary *Phys. Rev. Lett.* **92** 235003
[472] Evans T.E. *et al* 2005 Suppression of large edge localized modes with edge resonant magnetic fields in high confinement DIII-D plasmas *Nucl. Fusion* **45** 595–607
[473] Sun Y. *et al* 2016 Nonlinear transition from mitigation to suppression of the edge localized mode with resonant

magnetic perturbations in the EAST tokamak *Phys. Rev. Lett.* **117** 115001

[474] Sun Y. *et al* 2021 First demonstration of full ELM suppression in low input torque plasmas to support ITER research plan using n = 4 RMP in EAST *Nucl. Fusion* **61** 106037

[475] Liang Y. *et al* 2007 Active control of type-I edge-localized modes with n = 1 perturbation fields in the JET tokamak *Phys. Rev. Lett.* **98** 265004

[476] Liang Y. *et al* 2013 Mitigation of type-I ELMs with n = 2 fields on JET with ITER-like wall *Nucl. Fusion* **53** 073036

[477] Jeon Y.M. *et al* 2012 Suppression of edge localized modes in high-confinement KSTAR plasmas by nonaxisymmetric magnetic perturbations *Phys. Rev. Lett.* **109** 035004

[478] Kirk A., Liu Y., Nardon E., Tamain P., Cahyna P., Chapman I., Denner P., Meyer H., Mordijck S. and Temple D. 2011 Magnetic perturbation experiments on MAST L- and H-mode plasmas using internal coils *Plasma Phys. Control. Fusion* **53** 065011

[479] Polevoi A.R., Sugihara M., Takenaga H., Isayama A., Oyama N., Loarte A., Saibene G. and Pereverzev G.V. 2003 Pellet injection as a possible tool for plasma performance improvement *Nucl. Fusion* **43** 1072–6

[480] Futatani S., Huijsmans G., Loarte A., Baylor L.R., Commaux N., Jernigan T.C., Fenstermacher M.E., Lasnier C., Osborne T.H. and Pegourié B. 2014 Non-linear MHD modelling of ELM triggering by pellet injection in DIII-D and implications for ITER *Nucl. Fusion* **54** 073008

[481] Artola F.J., Huijsmans G.T.A., Hoelzl M., Beyer P., Loarte A. and Gribov Y. 2018 Non-linear magnetohydrodynamic simulations of edge localised mode triggering via vertical position oscillations in ITER *Nucl. Fusion* **58** 096018

[482] Viezzer E. 2018 Access and sustainment of naturally ELM-free and small-ELM regimes *Nucl. Fusion* **58** 115002

[483] Paz-Soldan C. 2021 Plasma performance and operational space without ELMs in DIII-D *Plasma Phys. Control. Fusion* **63** 083001

[484] Kirk A. *et al* 2013 Understanding the effect resonant magnetic perturbations have on ELMs *Plasma Phys. Control. Fusion* **55** 124003

[485] Bécoulet M. *et al* 2008 Numerical study of the resonant magnetic perturbations for Type I edge localized modes control in ITER *Nucl. Fusion* **48** 024003

[486] Schaffer M.J., Menard J.E., Aldan M.P., Bialek J.M., Evans T.E. and Moyer R.A. 2008 Study of in-vessel nonaxisymmetric ELM suppression coil concepts for ITER *Nucl. Fusion* **48** 024004

[487] Evans T.E., Orlov D.M., Wingen A., Wu W., Loarte A., Casper T.A., Schmitz O., Saibene G., Schaffer M.J. and Daly E. 2013 3D vacuum magnetic field modelling of the ITER ELM control coil during standard operating scenarios *Nucl. Fusion* **53** 093029

[488] Neumeyer C. *et al* 2011 Design of the ITER in-vessel coils *Fusion Sci. Technol.* **60** 95–99

[489] Daly E.F. *et al* 2013 Update on design of the ITER in-vessel coils *Fusion Sci. Technol.* **64** 168

[490] Kukushkin A.S., Pacher H.D., Kotov V., Pacher G.W. and Reiter D. 2011 Finalizing the ITER divertor design: the key role of SOLPS modeling *Fusion Eng. Des.* **86** 2865

[491] Evans T.E. *et al* 2008 RMP ELM suppression in DIII-D plasmas with ITER similar shapes and collisionalities *Nucl. Fusion* **48** 24002

[492] Huijsmans G.T.A., Chang C.S., Ferraro N., Sugiyama L., Waelbroeck F., Xu X.Q., Loarte A. and Futatani S. 2015 Modelling of edge localised modes and edge localised mode control *Phys. Plasmas* **22** 021805

[493] Feng Y., Sardei F. and Kisslinger J. 1999 3D fluid modelling of the edge plasma by means of a Monte Carlo technique *J. Nucl. Mater.* **266–269** 812–8

[494] Feng Y., Sardei F., Kisslinger J., Grigull P., McCormick K. and Reiter D. 2004 3D edge modeling and island divertor physics *Contrib. Plasma Phys.* **44** 57–69

[495] Feng Y. *et al* 2014 Recent improvements in the EMC3-Eirene code *Contrib. Plasma Phys.* **54** 426–31

[496] Frerichs H., Reiter D., Feng Y. and Harting D. 2010 Block-structured grids in Lagrangian 3D edge plasma transport simulations *Comput. Phys. Commun.* **181** 61–70

[497] Ghendrih P., Grosman A. and Capes H. 1996 Theoretical and experimental investigations of stochastic boundaries in tokamaks *Plasma Phys. Control. Fusion* **38** 1653

[498] Boozer A. 2015 Non-axisymmetric magnetic fields and toroidal plasma confinement *Nucl. Fusion* **55** 025001

[499] Evans T.E. 2015 Resonant magnetic perturbations of edge-plasmas in toroidal confinement devices *Plasma Phys. Control. Fusion* **57** 123001

[500] Roeder R.K.W., Rapopor B.I. and Evans T.E. 2003 Explicit calculations of homoclinic tangles in tokamaks *Phys. Plasmas* **10** 3796

[501] Evans T.E., Roeder R.K.W., Carter J.A. and Rapoport B.I. 2004 Homoclinic tangles, bifurcations and edge stochasticity in diverted tokamaks *Contrib. Plasma Phys.* **44** 235–40

[502] Evans T.E., Roeder R.K.W., Carter J.A., Rapoport B.I., Fenstermacher M.E. and Lasnier C.J. 2005 Experimental signatures of homoclinic tangles in poloidally diverted tokamaks *J. Phys.: Conf. Ser.* **7** 174

[503] Abdullaev S.S. 2014 Stable and unstable manifolds and the structure of magnetic footprints *Nucl. Fusion* **54** 064004

[504] Punjabi A. and Boozer A. 2014 Homoclinic tangle in tokamak divertors *Phys. Lett.* A **378** 2410

[505] Frerichs H., Schmitz O., Waters I., Canal G.P., Evans T.E., Feng Y. and Soukhanovskii V.A. 2016 Exploration of magnetic perturbation effects on advanced divertor configurations in NSTX-U *Phys. Plasmas* **23** 062517

[506] Kirk A., Harrison J., Liu Y., Nardon E., Chapman I.T. and Denner P. 2012 Observation of lobes near the X point in resonant magnetic perturbation experiments on MAST *Phys. Rev. Lett.* **108** 255003

[507] Kirk A. *et al* 2013 Understanding edge-localized mode mitigation by resonant magnetic perturbations on MAST *Nucl. Fusion* **53** 043007

[508] Abdullaev S.S., Finken K.H., Jakubowski M. and Lehnen M. 2006 Mappings of stochastic field lines in poloidal divertor tokamaks *Nucl. Fusion* **46** S113–26

[509] Wingen A., Evans T.E. and Spatschek K.H. 2009 Footprint structures due to resonant magnetic perturbations in DIII-D *Phys. Plasmas* **16** 042504

[510] Wingen A., Evans T.E. and Spatschek K.H. 2009 High resolution numerical studies of separatrix splitting due to non-axisymmetric perturbation in DIII-D *Nucl. Fusion* **49** 055027

[511] Buttery R.J., Hender T.C., Ashall J.D., Axon K.B., Blow G. and Fielding S.J. 1996 Effects of resonant magnetic perturbations on divertor target power loads in COMPASS-D *Nucl. Fusion* **36** 1369

[512] Jakubowski M.W., Abdullaev S.S., Finken K.H. and Team t.T. 2004 Modelling of the magnetic field structures and first measurements of heat fluxes for TEXTOR-DED operation *Nucl. Fusion* **44** S1–S11

[513] Schmitz O. *et al* 2008 Identification and analysis of transport domains in the stochastic boundary of

TEXTOR-DED for different mode spectra *Nucl. Fusion* **48** 024009

[514] Frerichs H., Clever M., Feng Y., Lehnen M., Reiter D. and Schmitz O. 2012 Numerical analysis of particle recycling in the TEXTOR helical divertor *Nucl. Fusion* **52** 023001

[515] Jakubowski M.W., Wingen A., Abdullaev S.S., Finken K.H., Lehnen M., Spatschek K.H. and Wolf R.C. 2007 Observation of the heteroclinic tangles in the heat flux pattern of the ergodic divertor at TEXTOR *J. Nucl. Mater.* **363–365** 371–6

[516] Evans T.E., Joseph I., Moyer R.A., Fenstermacher M.E., Lasnier C.J. and Yan L.W. 2007 Experimental and numerical studies of separatrix splitting and magnetic footprints in DIII-D *J. Nucl. Mater.* **363–365** 570

[517] Schmitz O. *et al* 2008 Aspects of three dimensional transport for ELM control experiments in ITER-similar shape plasmas at low collisionality in DIII-D *Plasma Phys. Control. Fusion* **50** 124029

[518] Nardon E. *et al* 2011 Strike-point splitting induced by external magnetic perturbations: observations on JET and MAST and associated modelling *J. Nucl. Mater.* **415** S914–7

[519] Harting D.M., Liang Y., Jachmich S., Koslowski R., Arnoux G., Devaux S., Eich T., Nardon E., Reiter D. and Thomsen H. 2012 Strike point splitting in the heat and particle flux profiles compared with the edge magnetic topology in a n = 2 resonant magnetic perturbation field at JET *Nucl. Fusion* **52** 054009

[520] Cahyna P., Peterka M., Kirk A., Thornton A., Harrison J., Muir D. and Panek R. 2013 Strike point splitting induced by the application of magnetic perturbations on MAST *J. Nucl. Mater.* **438** S326–9

[521] Thornton A., Kirk A., Cahyna P., Chapman I.T., Harrison J.R. and Liu Y. 2014 The effect of resonant magnetic perturbations on the divertor heat and particle fluxes in MAST *Nucl. Fusion* **54** 064011

[522] Lunt T. *et al* 2012 First EMC3-Eirene simulations of the edge magnetic perturbations at ASDEX Upgrade compared with the experiment *Nucl. Fusion* **52** 054013

[523] Faitsch M., Sieglin B., Eich T., Herrmann A. and Suttrop W. 2017 Divertor heat load in ASDEX Upgrade L-mode in presence of external magnetic perturbation *Plasma Phys. Control. Fusion* **59** 095006

[524] Brida D. *et al* 2017 Heat flux pattern in detached L-modes and ELM mitigated H-modes with rotating magnetic perturbations in ASDEX Upgrade *Nucl. Fusion* **57** 116006

[525] Jia M., Sun Y., Zhong F., Li H., Li G., Wang L., Gan K., Zhang B., Qian J. and Shen B. 2016 Vacuum modeling of three-dimensional magnetic field topology under resonant magnetic perturbations on EAST *Plasma Phys. Control. Fusion* **58** 055010

[526] Jia M. *et al* 2018 Control of three dimensional particle flux to divertor using rotating RMP in the EAST tokamak *Nucl. Fusion* **58** 046015

[527] Lee H.H. *et al* 2017 Thermographic studies of outer target heat fluxes on KSTAR *Nucl. Mater. Energy* **12** 541–7

[528] In Y. *et al* 2017 Enhanced understanding of non-axisymmetric intrinsic and controlled field impacts in tokamaks *Nucl. Fusion* **57** 116054

[529] In Y., Loarte A., Lee H.H., Kim K., Jeon Y.M., Park J.-K., Ahn J.-W., Park G.Y., Kim M. and Park H. 2019 Test of the ITER-like resonant magnetic perturbation configurations for edge-localized mode crash suppression on KSTAR *Nucl. Fusion* **59** 126045

[530] Cahyna P., Peterka M., Nardon E., Frerichs H. and Panek R. 2014 Method for comparison of tokamak divertor strike point data with magnetic perturbation models *Nucl. Fusion* **54** 064002

[531] Joseph I. *et al* 2008 Calculation of stochastic thermal transport due to resonant magnetic perturbations in DIII-D *Nucl. Fusion* **48** 045009

[532] Frerichs H., Schmitz O., Reiter D., Cahyna P., Feng Y. and Evans T.E. 2013 Numerical sensitivity analysis of divertor heat flux and edge temperature at DIII-D under the influence of resonant magnetic perturbations *J. Nucl. Mater.* **438** S360–3

[533] Brida D., Lunt T., Faitsch M., Wischmeier M., Feng Y., Suttrop W., Stroth U. and Eich T. 2019 Effect of magnetic perturbation fields on power decay length in EMC3-EIRENE simulations and comparison to experiment in ASDEX Upgrade *Nucl. Mater. Energy* **19** 205–10

[534] Abdullaev S.S., Jakubowski M., Lehnen M., Schmitz O. and Unterberg B. 2008 On description of magnetic stochasticity in poloidal divertor tokamaks *Phys. Plasmas* **15** 042508

[535] Izzo V.A. and Joseph I. 2008 RMP enhanced transport and rotational screening in simulations of DIII-D plasmas *Nucl. Fusion* **48** 115004

[536] Heyn M.F., Ivanov I.B., Kasilov S.V., Kernbichler W., Joseph I., Moyer R.A. and Runov A.M. 2008 Kinetic estimate of the shielding of resonant magnetic field perturbations by the plasma in DIII-D *Nucl. Fusion* **48** 024005

[537] Bécoulet A.M. *et al* 2012 Screening of resonant magnetic perturbations by flows in tokamaks *Nucl. Fusion* **52** 054003

[538] Hu Q.M., Nazikian R., Grierson B.A., Logan N.C., Paz-Soldan C. and Yu Q. 2020 The role of edge resonant magnetic perturbations in edge-localized-mode suppression and density pump-out in low-collisionality DIII-D plasmas *Nucl. Fusion* **60** 076001

[539] Hu Q.M., Nazikian R., Grierson B.,., Logan N.,., Orlov D.,., Paz-Soldan C. and Yu Q. 2020 Wide operational windows of edge-localized mode suppression by resonant magnetic perturbations in the DIII-D tokamak *Phys. Rev. Lett.* **125** 045001

[540] Nardon E., Tamain P., Bécoulet M., Huysmans G. and Waelbroeck F.L. 2010 Quasi-linear MHD modelling of H-mode plasma response to resonant magnetic perturbations *Nucl. Fusion* **50** 034002

[541] Cahyna P. and Nardon E. (JET EFDA Contributors) 2011 Model for screening of resonant magnetic perturbations by plasma in a realistic tokamak geometry and its impact on divertor strike points *J. Nucl. Mater.* **415** S927–31

[542] Brida D. *et al* 2017 Determination of the stochastic layer properties induced by magnetic perturbations via heat pulse experiments at ASDEX Upgrade *Nucl. Mater. Energy* **12** 831–7

[543] Frerichs H., Reiter D., Schmitz O., Cahyna P., Evans T.E., Feng Y. and Nardon E. 2012 Impact of screening of resonant magnetic perturbations in 3D edge plasma transport simulations for DIII-D *Phys. Plasmas* **19** 052507

[544] Lore J.D., Briesemeister A.R., Ferraro N.M., Frerichs H., Lyons B., McLean A., Park J.-K. and Shafer M.W. 2017 Pedestal-to-wall 3D fluid transport simulations on DIII-D *Nucl. Fusion* **57** 056025

[545] Lanctot M.J. *et al* 2011 Measurement and modeling of three-dimensional equilibria in DIII-D *Phys. Plasmas* **18** 056121

[546] Lanctot M.J. *et al* 2013 Sustained suppression of type-I edge-localized modes with dominantly n = 2 magnetic fields in DIII-D *Nucl. Fusion* **53** 083019

[547] Ryan D.A. *et al* 2015 Toroidal modelling of resonant magnetic perturbations response in ASDEX-Upgrade:

coupling between field pitch aligned response and kink amplification *Plasma Phys. Control. Fusion* **57** 095008

[548] Orain F. *et al* 2017 Non-linear modeling of the plasma response to RMPs in ASDEX Upgrade *Nucl. Fusion* **57** 022013

[549] Park J.-K., Schaffer M.J., Menard J.E. and Boozer A.H. 2007 Control of asymmetric magnetic perturbations in tokamaks *Phys. Rev. Lett.* **99** 195003

[550] Park J.-K., Menard J.E., Boozer A.H., Schaffer M.J. and Wolfe S.A. 2010 Ideal perturbed equilibria in tokamaks and control of external magnetic perturbations *Contrib. Plasma Phys.* **50** 669

[551] Park J.-K. and Logan N.C. 2017 Self-consistent perturbed equilibrium with neoclassical toroidal torque in tokamaks *Phys. Plasmas* **24** 032505

[552] Suzuki Y., Nakajima N., Watanabe K., Nakamura Y. and Hayashi T. 2006 Development and application of HINT2 to helical system plasmas *Nucl. Fusion* **46** L19

[553] Orain F. *et al* 2013 Non-linear magnetohydrodynamic modeling of plasma response to resonant magnetic perturbations *Phys. Plasmas* **20** 102510

[554] Jardin S.C., Ferraro N., Luo X., Chen J., Breslau J., Jansen K.E. and Shephard M.S. 2008 The M3D-C^1 approach to simulating 3D 2-fluid magnetohydrodynamics in magnetic fusion experiments *J. Phys.: Conf. Ser.* **125** 012044

[555] Ferraro N.M. 2012 Calculations of two-fluid linear response to non-axisymmetric fields in tokamaks *Phys. Plasmas* **19** 056105

[556] Liu Y.Q., Bondeson A., Fransson C.M., Lennartson B. and Breitholtz C. 2000 Feedback stabilization of nonaxisymmetric resistive wall modes in tokamaks. I. Electromagnetic model *Phys. Plasmas* **7** 3681

[557] Liu Y., Kirk A. and Nardon E. 2010 Full toroidal plasma response to externally applied nonaxisymmetric magnetic fields *Phys. Plasmas* **17** 122502

[558] Turnbull A.D. 2012 Plasma response models for non-axisymmetric perturbations *Nucl. Fusion* **52** 054016

[559] Reiman A. *et al* 2015 Tokamak plasma high field side response to an n = 3 magnetic perturbation: a comparison of 3D equilibrium solutions from seven different codes *Nucl. Fusion* **55** 063026

[560] Liu Y., Ham C.J., Kirk A., Li L.i., Loarte A., Ryan D.A., Sun Y., Suttrop W., Yang X. and Zhou L. 2016 ELM control with RMP: plasma response models and the role of edge peeling response *Plasma Phys. Control. Fusion* **58** 114005

[561] Munaretto S., Orlov D.M., Paz-Soldan C., Bykov I., Lasnier C.J., Lyons B.C. and Wang H. 2022 Controlling the size of non-axisymmetric magnetic footprints using resonant magnetic perturbations *Nucl. Fusion* **62** 026018

[562] Frerichs H. *et al* 2014 Impact of an M3D-C1 modeled plasma response on simulations of the DIII-D plasma edge with EMC3-EIRENE *Proc. 41st EPS Conf. on Controlled Fusion and Plasma Physics* (*Europhysics Conf. Abstracts* vol 38F) *(Berlin, Germany, 23–27 June 2014)* (European Physical Society) P2.025 (available at: https://info.fusion.ciemat.es/OCS/EPS2014PAP/pdf/P2.025.pdf)

[563] Jakubowski M. *et al* 2011 Toroidally resolved structure of divertor heat flux in RMP H-mode discharges on DIII-D *J. Nucl. Mater.* **415** S901–5

[564] Jakubowski M.W. *et al* 2010 Influence of the resonant magnetic perturbation on the plasma boundary in DIII-D *Contrib. Plasma Phys.* **50** 701

[565] Briesemeister A.R. *et al* 2017 Changes in divertor conditions in response to changing core density with RMPs *Nucl. Fusion* **57** 076038

[566] Frerichs H., Schmitz O., Reiter D., Evans T.E. and Feng Y. 2014 Striation pattern of target particle and heat fluxes in three dimensional simulations for DIII-D *Phys. Plasmas* **21** 020702

[567] Ahn J.-W., Canik J.M., Soukhanovskii V.A., Maingi R. and Battaglia D.J. 2010 Modification of divertor heat and particle flux profiles with applied 3D fields in NSTX H-mode plasmas *Nucl. Fusion* **50** 045010

[568] Lore J.D., Canik J.M., Feng Y., Ahn J.-W., Maingi R. and Soukhanovskii V. 2012 Implementation of the 3D edge plasma code EMC3-EIRENE on NSTX *Nucl. Fusion* **52** 054012

[569] Ahn J.-W., Maingi R., Canik J.M., McLean A.G., Lore J.D., Park J.-K., Soukhanovskii V.A., Gray T.K. and Roquemore A.L. 2011 Effect of nonaxisymmetric magnetic perturbations on divertor heat and particle flux profiles in National Spherical Torus Experiment *Phys. Plasmas* **18** 056108

[570] Faitsch M., Sieglin B., Eich T., Herrmann A. and Suttrop W. 2017 2D heat flux in ASDEX Upgrade L-mode with magnetic perturbation *Nucl. Mater. Energy* **12** 1020

[571] Faitsch M., Sieglin B., Brida D., Suttrop W., Lunt T., Eich T. and Wischmeier M. 2019 Effect of magnetic perturbations for ELM control on divertor power loads, detachment and consequences of field penetration in ASDEX Upgrade *Plasma Phys. Control. Fusion* **61** 014008

[572] Liang R., Gong X., Zhang B., Yang Z., Jia M., Sun Y., Ma Q., Zhang J., Hu Y. and Qian J. 2022 Study on divertor heat flux under n = 3 and n = 4 resonant magnetic perturbations using infrared thermography diagnostic in EAST *Plasma Sci. Technol.* **24** 105103

[573] Kim K., Ahn J.-W., Lee H.H., Park J.-K., Kang C.S., In Y., Kwak J.G., Yoon S.W., Oh O.K. and Choe W. 2017 Comparison of divertor heat flux splitting by 3D fields with field line tracing simulation in KSTAR *Phys. Plasmas* **24** 052506

[574] In Y. *et al* 2019 Tamed stability and transport using controlled non-axisymmetric fields in KSTAR *Nucl. Fusion* **59** 056009

[575] In Y. *et al* 2022 Toward holistic understanding of the ITER-like resonant magnetic perturbation (RMP) ELM control on KSTAR *Nucl. Fusion* **62** 066014

[576] Kim S.K. *et al* 2022 Nonlinear MHD modeling of n = 1 RMP-induced pedestal transport and mode coupling effects on ELM suppression in KSTAR *Nucl. Fusion* **62** 106021

[577] Victor B.S. *et al* 2020 Impurity transport in the pedestal of H-mode plasmas with resonant magnetic perturbations *Plasma Phys. Control. Fusion* **62** 095021

[578] Vogel G. *et al* 2021 Experimental and simulation study of impurity transport response to RMPs in RF-heated H-mode plasmas at EAST *J. Plasma Phys.* **87** 905870213

[579] Hinson E. *et al* 2020 Enhanced helium exhaust during edge-localized mode suppression by resonant magnetic perturbations at DIII-D *Nucl. Fusion* **60** 054004

[580] Schmitz O. *et al* 2016 Enhancement of helium exhaust by resonant magnetic perturbation fields at LHD and TEXTOR *Nucl. Fusion* **56** 106011

[581] Fenstermacher M.E. *et al* 2008 Effect of island overlap on edge localized mode suppression by resonant magnetic perturbations in DIII-D *Phys. Plasmas* **15** 056122

[582] Paz-Soldan C. *et al* 2015 Observation of a multimode plasma response and its relationship to density pumpout and edge-localized mode suppression *Phys. Rev. Lett.* **114** 105001

[583] Paz-Soldan C., Logan N.C., Haskey S.R., Nazikian R., Strait E.J., Chen X., Ferraro N.M., King J.D., Lyons B.C. and Park J.-K. 2016 Equilibrium drives of the low and

high field side n = 2 plasma response and impact on global confinement *Nucl. Fusion* **56** 056001

[584] Haskey S.R., Lanctot M.J., Liu Y.Q., Hanson J.M., Blackwell B.D. and Nazikian R. 2014 Linear ideal MHD predictions for n = 2 non-axisymmetric magnetic perturbations on DIII-D *Nucl. Fusion* **56** 035005

[585] Park J.-K. *et al* 2018 3D field phase-space control in tokamak plasmas *Nat. Phys.* **14** 1223–8

[586] Frerichs H., Van Blarcum J., Yang S.M., Park J.-K., Logan N.C., Feng Y. and Schmitz O. 2023 Plasma response impact on RMP divertor footprint modeling for KSTAR *Nucl. Mater. Energy* **34** 101380

[587] Ryan D.A., Liu Y.Q., Kirk A., Suttrop W., Dudson B., Dunne M. and Willensdorfer M. 2018 Experimental validation of coil phase parametrisation on ASDEX Upgrade and extension to ITER *Plasma Phys. Control. Fusion* **60** 065005

[588] Jia M. *et al* 2018 Dynamic divertor control using resonant mixed toroidal harmonic magnetic fields during ELM suppression in DIII-D *Phys. Plasmas* **25** 056102

[589] Gu S. *et al* 2919 Edge localized mode suppression and plasma response using mixed toroidal harmonic resonant magnetic perturbations in DIII-D *Nucl. Fusion* **59** 026012

[590] Bécoulet M. *et al* 2022 Non-linear MHD modelling of edge localized modes suppression by resonant magnetic perturbations in ITER *Nucl. Fusion* **62** 066022

[591] Li L., Liu Y.Q., Loarte A., Pinches S.D., Polevoi A., Liang Y. and Zhong F.C. 2019 Modeling 3D plasma boundary corrugation and tailoring toroidal torque profiles with resonant magnetic perturbation fields in ITER *Nucl. Fusion* **59** 096038

[592] Ahn J.-W. *et al* 2014 Characterization of divertor footprints and the pedestal plasmas in the presence of applied n = 3 fields for the attached and detached conditions in NSTX *Plasma Phys. Control. Fusion* **56** 015005

[593] Ahn J.-W. *et al* 2017 Effect of 3D magnetic perturbations on divertor conditions and detachment in tokamak and stellarator *Plasma Phys. Control. Fusion* **59** 084002

[594] Petrie T.W. *et al* 2011 Results from radiating divertor experiments with RMP ELM suppression and mitigation *Nucl. Fusion* **51** 073003

[595] Guo H.Y. *et al* 2016 Developing and validating advanced divertor solutions on DIII-D for next-step fusion devices *Nucl. Fusion* **56** 126010

[596] Jia M. *et al* 2021 Integrated ELM and divertor power flux control using RMPs with low input torque in EAST in support of the ITER research plan *Nucl. Fusion* **61** 106023

[597] Shin H., Hwang J., Han Y., Shin G., Lee H., Chai K.-B. and Choe W. 2023 Argon-seeded detachment during ELM control by RMPs in KSTAR *Nucl. Fusion* **63** 044003

[598] Frerichs H., Schmitz O., Bonnin X., Loarte A., Feng Y., Li L., Liu Y. and Reiter D. 2020 Detachment in fusion plasmas with symmetry breaking magnetic perturbation fields *Phys. Rev. Lett.* **125** 155001

[599] Frerichs H., Bonnin X., Feng Y., Li L., Liu Y.Q., Loarte A., Pitts R.A., Reiter D. and Schmitz O. 2021 Divertor detachment in the pre-fusion power operation phase in ITER during application of resonant magnetic perturbations *Nucl. Fusion* **61** 126027

[600] Frerichs H., Feng Y., Bonnin X., Pitts R.A., Reiter D. and Schmitz O. 2021 Volumetric recombination in EMC3-EIRENE: implementation and first application to the pre-fusion power operation phase in ITER *Phys. Plasmas* **28** 102503

[601] Frerichs H., van Blarcum J., Feng Y., Li L., Liu Y.Q., Loarte A., Park J.-K., Pitts R.A., Schmitz O. and Yang S.M. 2024 Heuristic predictions of RMP configurations for ELM suppression in ITER burning plasmas and their impact on divertor performance *Nucl. Fusion* **64** 076035

[602] Kobayashi M. *et al* 2013 Control of 3D edge radiation structure with resonant magnetic perturbation fields applied to the stochastic layer and stabilization of radiative divertor plasma in LHD *Nucl. Fusion* **53** 093032

[603] Kobayashi M. *et al* 2010 Detachment stabilization with n/m = 1/1 resonant magnetic perturbation field applied to the stochastic magnetic boundary of the Large Helical Device *Phys. Plasmas* **17** 056111

[604] Zhang H. *et al* 2017 Vertical profiles and two-dimensional distributions of carbon line emissions from C^{2+}–C^{5+} ions in attached and RMP-assisted detached plasmas of Large Helical Device *Phys. Plasmas* **24** 022510

[605] Pandya S.N. *et al* 2016 Dynamics of three-dimensional radiative structures during RMP assisted detached plasmas on the Large Helical Device and its comparison with EMC3-EIRENE modeling *Nucl. Fusion* **56** 046002

[606] Kobayashi M., Morita S. and Goto M. 2017 2D distribution of hydrogen/impurity radiation and flow formation in stochastic layer during detachment transition in LHD *Nucl. Mater. Energy* **12** 1043

[607] Tokar M. and Kobayashi M. 2020 Modeling of the resonant magnetic perturbation effect on detachment in the Large Helical Device *Plasma Phys. Control. Fusion* **62** 085011

[608] Kobayashi M. and Tokar M. 2020 Time-dependent plasma transport simulation for the study of edge impurity radiation dynamics with magnetic island in Large Helical Device *Contrib. Plasma Phys.* **60** e201900138

[609] Kobayashi M. *et al* 2019 Impact of a resonant magnetic perturbation field on impurity radiation, divertor footprint and core plasma transport in attached and detached plasmas in the Large Helical Device *Nucl. Fusion* **59** 096009

[610] Narushima Y., Kobayashi M., Akiyama T., Sakakibara S., Masuzaki S., Ashikawa N. and Ohno N. 2013 Behavior of plasma response field in detached plasma *Plasma Fusion Res.* **8** 1402058

[611] Oishi T. *et al* 2022 Spatial profiles of NeVI–NeX emission in ECR-heated discharges of the Large Helical Device with divertor detachment induced by RMP application and Ne impurity seeding *Plasma Fusion Res.* **17** 2402022

[612] Jakubowski M. *et al* 2021 Overview of the results from divertor experiments with attached and detached plasmas at Wendelstein 7-X and their implications for steady-state operation *Nucl. Fusion* **61** 106003

[613] Grigull P. *et al* 2001 First island divertor experiments on the W7-AS stellarator *Plasma Phys. Control. Fusion* **43** A175–93

[614] Bozhenkov S. *et al* 2017 Effect of error field correction coils on W7-X limiter loads *Nucl. Fusion* **57** 126030

[615] Schmitz O. *et al* (The W7-X Team) 2020 Stable heat and particle flux detachment with efficient particle exhaust in the island divertor of Wendelstein 7-X *Nucl. Fusion* **61** 016026

[616] Effenberg F. *et al* 2019 First demonstration of radiative power exhaust with impurity seeding in the island divertor at Wendelstein 7-X *Nucl. Fusion* **59** 106020

[617] Feng Y. *et al* 2021 Understanding detachment of the W7-X island divertor *Nucl. Fusion* **61** 086012

[618] Brezinsek S. 2015 Plasma-surface interaction in the Be/W environment: conclusions drawn from the JET-ILW for ITER *J. Nucl. Mater.* **463** 11–21

[619] Hakola A. *et al* 2021 Gross and net erosion balance of plasma-facing materials in full-W tokamaks *Nucl. Fusion* **61** 116006

[620] Lipschultz B. *et al* 2007 Plasma-surface interaction, scrape-off layer and divertor physics: implications for ITER *Nucl. Fusion* **47** 1189–205

[621] Pitts R.A. *et al* 2005 Material erosion and migration in tokamaks *Plasma Phys. Control. Fusion* **47** B303–22

[622] Matthews G.F. 2005 Material migration in divertor tokamaks *J. Nucl. Mater.* **337–339** 1–9

[623] Coad J.P., Rubel M., Likonen J., Bekris N., Brezinsek S., Matthews G.F., Mayer M. and Widdowson A.M. 2019 Material migration and fuel retention studies during the JET carbon divertor campaigns *Fusion Eng. Des.* **138** 78–108

[624] Roth J. *et al* 2008 Tritium inventory in ITER plasma-facing materials and tritium removal procedures *Plasma Phys. Control. Fusion* **50** 103001

[625] Roth J. *et al* 2009 Recent analysis of key plasma wall interactions issues for ITER *J. Nucl. Mater.* **390–391** 1–9

[626] Kirschner A., Borodin D., Droste S., Philipps V., Samm U., Federici G., Kukushkin A. and Loarte A. 2007 Modelling of tritium retention and target lifetime of the ITER divertor using the ERO code *J. Nucl. Mater.* **363–365** 91–95

[627] Neu R., Dux R., Geier A., Gruber O., Kallenbach A., Krieger K., Maier H., Pugno R., Rohde V. and Schweizer S. 2003 Tungsten as plasma-facing material in ASDEX Upgrade *Fusion Eng. Des.* **65** 367–74

[628] Philipps V. 2011 Tungsten as material for plasma-facing components in fusion devices *J. Nucl. Mater.* **415** 2–9

[629] Philipps V., Mertens P., Matthews G.F. and Maier H. 2010 Overview of the JET ITER-like wall project *Fusion Eng. Des.* **85** 1581–6

[630] Neu R. *et al* 2007 Plasma wall interaction and its implication in an all tungsten divertor tokamak *Plasma Phys. Control. Fusion* **49** B59–B70

[631] Neu R. *et al* 2013 Overview on plasma operation with a full tungsten wall in ASDEX Upgrade *J. Nucl. Mater.* **438** S34–S41

[632] Ding R. *et al* 2015 Material migration studies with an ITER first wall panel proxy on EAST *Nucl. Fusion* **55** 023013

[633] Gallo A. *et al* 2020 First efforts in numerical modeling of tungsten migration in WEST with SolEdge2D-EIRENE and ERO2.0 *Phys. Scr.* **T171** 014013

[634] Unterberg E.A., Donovan D.C., Duran J.D., Stangeby P.C., Zamperini S., Abrams T., Rudakov D.L., Wampler W.R. and Zach M.P. 2019 Use of isotopic tungsten tracers and a stable-isotope-mixing model to characterize divertor source location in the DIII-D metal rings campaign *Nucl. Mater. Energy* **19** 358–63

[635] Ding R. *et al* 2016 Simulation of gross and net erosion of high-Z materials in the DIII-D divertor *Nucl. Fusion* **56** 016021

[636] Krat S., Gasparyan Y., Pisarev A., Bykov I., Mayer M., de Saint Aubin G., Balden M., Lungu C.P. and Widdowson A. 2015 Erosion at the inner wall of JET during the discharge campaign 2011–2012 in comparison with previous campaigns *J. Nucl. Mater.* **456** 106–10

[637] Brezinsek S. *et al* 2015 Beryllium migration in JET ITER-like wall plasmas *Nucl. Fusion* **55** 063021

[638] Mayer M., Krat S., Baron-Wiechec A., Gasparyan Y., Heinola K., Koivuranta S., Likonen J., Ruset C., de Saint-Aubin G. and Widdowson A. 2017 Erosion and deposition in the JET divertor during the second ITER-like wall campaign *Phys. Scr.* **T170** 014058

[639] Heinola K. *et al* 2016 Long-term fuel retention in JET ITER-Like Wall *Phys. Scr.* **T167** 014075

[640] Rubel M. *et al* 2018 Dust generation in tokamaks: overview of beryllium and tungsten dust characterisation in JET with the ITER-like wall *Fusion Eng. Des.* **136** 579–86

[641] Schmid K., Reinelt M. and Krieger K. 2011 An integrated model of impurity migration and wall composition dynamics for tokamaks *J. Nucl. Mater.* **415** S284–8

[642] Kirschner A., Philipps V., Winter J. and Kögler U. 2000 Simulation of the plasma-wall interaction in a tokamak with the Monte Carlo code ERO-TEXTOR *Nucl. Fusion* **40** 989–1001

[643] Romazanov J. *et al* 2017 First ERO2.0 modeling of Be erosion and non-local transport in JET ITER-like wall *Phys. Scr.* **T170** 014018

[644] Fundamenski W., Stangeby P.C. and Elder J.D. 1999 A CFD onion-skin model for the interpretation of edge experiments *J. Nucl. Mater.* **266–269** 1045–50

[645] Guillemaut C. *et al* 2014 Influence of atomic physics on EDGE2D-EIRENE simulations of JET divertor detachment with carbon and beryllium/tungsten plasma-facing components *Nucl. Fusion* **54** 093012

[646] Bufferand H. *et al* 2013 Near wall plasma simulation using penalization technique with the transport code SolEdge2D-Eirene *J. Nucl. Mater.* **438** S445–8

[647] Reiter D., Baelmans M. and Börner P. 2005 The EIRENE and B2-EIRENE codes *Fusion Sci. Technol.* **47** 172–86

[648] Matthews G.F. *et al* 2011 JET ITER-like wall—overview and experimental programme *Phys. Scr.* **T145** 014001

[649] Bucalossi J. *et al* 2014 The WEST project: testing ITER divertor high heat flux component technology in a steady state tokamak environment *Fusion Eng. Des.* **89** 907–12

[650] Li J., Luo G., Ding R., Yao D., Chen J., Cao L., Hu J. and Li Q. 2014 Plasma facing components for the Experimental Advanced Superconducting Tokamak and CFETR *Phys. Scr.* **T159** 014001

[651] Holtrop K., Buchenauer D., Chrobak C., Murphy C., Nygren R., Unterberg E. and Zach M. 2017 The design and use of tungsten coated TZM molybdenum tile inserts in the DIII-D tokamak divertor *Fusion Sci. Technol.* **72** 634–9

[652] Pospieszczyk A. *et al* 2001 Operation of TEXTOR-94 with tungsten poloidal main limiters *J. Nucl. Mater.* **290–293** 947–52

[653] Dux R. *et al* 2009 Plasma-wall interaction and plasma behaviour in the non-boronised all tungsten ASDEX Upgrade *J. Nucl. Mater.* **390–391** 858–63

[654] Barnard H.S., Lipschultz B. and Whyte D.G. 2011 A study of tungsten migration in the Alcator C-Mod divertor *J. Nucl. Mater.* **415** S301–4

[655] Brezinsek S. *et al* 2013 Fuel retention studies with the ITER-Like Wall in JET *Nucl. Fusion* **53** 083023

[656] Widdowson A. *et al* 2017 Overview of fuel inventory in JET with the ITER-like wall *Nucl. Fusion* **57** 086045

[657] Brezinsek S. *et al* 2019 Erosion, screening and migration of tungsten in the JET divertor *Nucl. Fusion* **59** 096035

[658] Strachan J.D. *et al* 2008 Modelling of carbon migration during JET ^{13}C injection experiments *Nucl. Fusion* **48** 105002

[659] Catarino N., Widdowson A., Baron-Wiechec A., Coad J.P., Heinola K., Rubel M. and Alves E. 2017 Time-resolved deposition in the remote region of the JET-ILW divertor: measurements and modelling *Phys. Scr.* **T170** 014059

[660] Likonen J. *et al* 2011 Deposition of ^{13}C tracer in the JET MkII-HD divertor *Phys. Scr.* **T145** 014004

[661] Coenen J.W. *et al* 2013 Long-term evolution of the impurity composition and impurity events with the ITER-like wall at JET *Nucl. Fusion* **53** 073043

[662] Brezinsek S. *et al* 2016 Characterisation of the deuterium recycling at the W divertor target plates in JET during steady-state plasma conditions and ELMs *Phys. Scr.* **T167** 014076

[663] Borodkina I., Borodin D., Brezinsek S., Tsvetkov I.V., Kurnaev V.A., Guillemaut C., Maslov M. and

Frassinetti L. 2017 Intra-ELM tungsten sputtering in JET ITER-like wall: analytical studies of Be impurity and ELM type influence *Phys. Scr.* **T170** 014065

[664] van Rooij G.J. *et al* 2013 Tungsten divertor erosion in all metal devices: lessons from the ITER like wall of JET *J. Nucl. Mater.* **438** S42–S47

[665] Kirschner A., Tskhakaya D., Brezinsek S., Borodin D., Romazanov J., Ding R., Eksaeva A. and Linsmeier C. 2017 Modelling of plasma-wall interaction and impurity transport in fusion devices and prompt deposition of tungsten as application *Plasma Phys. Control. Fusion* **60** 014041

[666] Kumpulainen H.A. *et al* 2022 ELM and inter-ELM tungsten erosion sources in high-power, JET ITER-like wall H-mode plasmas *Nucl. Mater. Energy* **33** 101264

[667] Widdowson A. *et al* 2017 Overview of the JET ITER-like wall divertor *Nucl. Mater. Energy* **12** 499–505

[668] van Rooij G.J. *et al* 2020 Tungsten divertor sources in WEST related to impurity inventory and local plasma conditions *Phys. Scr.* **T171** 014060

[669] Dux R., Janzer A. and Pütterich T. 2011 Main chamber sources and edge transport of tungsten in H-mode plasmas at ASDEX Upgrade *Nucl. Fusion* **51** 053002

[670] Hakola A. *et al* 2013 Global migration of impurities in tokamaks *Plasma Phys. Control. Fusion* **55** 124029

[671] Genova S.D. *et al* 2023 First 3D modelling of tungsten erosion and migration in WEST discharges adopting a toroidally non-symmetric wall geometry *Nucl. Mater. Energy* **34** 101340

[672] Winter J. 1996 Wall conditioning in fusion devices and its influence on plasma performance *Plasma Phys. Control. Fusion* **38** 1503–42

[673] Bortolon A. *et al* 2019 Real-time wall conditioning by controlled injection of boron and boron nitride powder in full tungsten wall ASDEX Upgrade *Nucl. Mater. Energy* **19** 384–9

[674] Bodner G. *et al* 2022 Initial results from boron powder injection experiments in WEST lower single null L-mode plasmas *Nucl. Fusion* **62** 086020

[675] Krieger K., Balden M., Bortolon A., Dux R., Griener M., Hegele K., Laggner F., Rohde V. and Wampler W.R. 2023 Wall conditioning effects and boron migration during boron powder injection in ASDEX Upgrade *Nucl. Mater. Energy* **34** 101374

[676] Zuo G.Z., Hu J.S., Li J.G., Sun Z., Mansfield D.K. and Zakharov L.E. 2013 Lithium coating for H-mode and high performance plasmas on EAST in ASIPP *J. Nucl. Mater.* **438** S90–S95

[677] Baldwin M.J., Doerner R.P., Nishijima D., Patino M., Simmonds M.J., Tynan G., Yu J.H. and Založnik A. 2019 Plasma-material-interaction research using PISCES linear plasma devices *Fusion Sci. Technol.* **75** 664–73

[678] Zlobinski M. *et al* 2019 Fuel Retention Diagnostic Setup (FREDIS) for desorption of gases from beryllium and tritium containing samples *Fusion Eng. Des.* **146** 1176–80

[679] De Temmerman G. *et al* 2021 Data on erosion and hydrogen fuel retention in beryllium plasma-facing materials *Nucl. Mater. Energy* **27** 100994

[680] Roth J., Eckstein W. and Bohdansky J. 1989 Beryllium self-sputtering—an interpolation of data for D, He, Ne and Ar *J. Nucl. Mater.* **165** 199–204

[681] Doerner R.P., Baldwin M.J., Buchenauer D., De Temmerman G. and Nishijima D. 2009 The role of beryllium deuteride in plasma-beryllium interactions *J. Nucl. Mater.* **390–391** 681–4

[682] Nishijima D., Doerner R.P., Baldwin M.J., De Temmerman G. and Hollmann E.M. 2008 Properties of BeD molecules in edge plasma relevant conditions *Plasma Phys. Control. Fusion* **50** 125007

[683] Reinelt M., Allouche A., Oberkofler M. and Linsmeier C. 2009 Retention mechanisms and binding states of deuterium implanted into beryllium *New J. Phys.* **11** 043023

[684] Björkas C., Vörtler K., Nordlund K., Nishijima D. and Doerner R. 2009 Chemical sputtering of Be due to D bombardment *New J. Phys.* **11** 123017

[685] Safi E., Valles G., Lasa A. and Nordlund K. 2017 Multi-scale modelling to relate beryllium surface temperature, deuterium concentration and erosion in fusion reactor environment *J. Phys. D: Appl. Phys.* **50** 204003

[686] Doerner R.P., Björkas C., Nishijima D. and Schwarz-Selinger T. 2013 Erosion of beryllium under high-flux plasma impact *J. Nucl. Mater.* **438** S272–5

[687] Eckstein W., Dohmen R., Mutzke A. and Schneider R. 2007 SDTrimSP: a Monte-Carlo code for calculating collision phenomena in randomized targets *Technical Report* IPP 12/3 (Max-Planck-Institut für Plasmaphysik)

[688] Mutzke A., Schneider R., Eckstein W. and Dohmen R. 2011 SDTrimSP version 5.00 *Technical Report* IPP 12/8 (Max-Planck-Institut für Plasmaphysik)

[689] Roth J., Eckstein W. and Guseva M. 1997 Erosion of Be as plasma-facing material *Fusion Eng. Des.* **37** 465–80

[690] Roth J. 2006 Status of knowledge of chemical erosion of carbon and critical issues for extrapolation to ITER *Phys. Scr.* **T124** 37–43

[691] Brezinsek S., Stamp M.F., Nishijima D., Borodin D., Devaux S., Krieger K., Marsen S., O'Mullane M., Bjoerkas C. and Kirschner A. 2014 Study of physical and chemical assisted physical sputtering of beryllium in the JET ITER-like wall *Nucl. Fusion* **54** 103001

[692] Borodin D. *et al* 2016 Improved ERO modelling for spectroscopy of physically and chemically assisted eroded beryllium from the JET-ILW *Nucl. Mater. Energy* **9** 604–9

[693] Borodin D. *et al* 2019 Improved ERO modelling of beryllium erosion at ITER upper first wall panel using JET-ILW and PISCES-B experience *Nucl. Mater. Energy* **19** 510–5

[694] Romazanov J. *et al* 2019 Beryllium global erosion and deposition at JET-ILW simulated with ERO2.0 *Nucl. Mater. Energy* **18** 331–8

[695] Baron-Wiechec A. *et al* 2015 Global erosion and deposition patterns in JET with the ITER-like wall *J. Nucl. Mater.* **463** 157–61

[696] Widdowson A. *et al* 2020 Fuel inventory and material migration of JET main chamber plasma facing components compared over three operational periods *Phys. Scr.* **T171** 014051

[697] Klepper C.C. *et al* 2016 Estimates of RF-induced erosion at antenna-connected beryllium plasma-facing components in JET *Phys. Scr.* **T167** 014035

[698] Dux R., Herrmann A., Kallenbach A., Neu R., Neuhauser J., Maier H., Pugno R., Pütterich T. and Rohde V. 2005 Plasma surface interaction with tungsten in ASDEX Upgrade *J. Nucl. Mater.* **337–339** 852–6

[699] Brezinsek S., Borodin D., Coenen J.W., Kondratjew D., Laengner M., Pospieszczyk A. and Samm U. 2011 Quantification of tungsten sputtering at W/C twin limiters in TEXTOR with the aid of local WF6 injection *Phys. Scr.* **T145** 014016

[700] Cupak C. *et al* 2021 Sputter yields of rough surfaces: importance of the mean surface inclination angle from nano- to microscopic rough regimes *Appl. Surf. Sci.* **570** 151204

[701] Schmid K., Mayer M., Adelhelm C., Balden M. and Lindig S. 2010 Impact of gyro-motion and sheath acceleration on the flux distribution on rough surfaces *Nucl. Fusion* **50** 105004

[702] Morgan T.W., Li Y., Balden M., Brezinsek S. and De Temmerman G. 2021 Combined high fluence and high cycle number transient loading of ITER-like monoblocks in Magnum-PSI *Nucl. Fusion* **61** 116045

[703] Brezinsek S. *et al* 2017 Plasma-wall interaction studies within the EUROfusion consortium: progress on plasma-facing components development and qualification *Nucl. Fusion* **57** 116041

[704] Eksaeva A. *et al* 2019 Surface roughness effect on Mo physical sputtering and re-deposition in the linear plasma device PSI-2 predicted by ERO2.0 *Nucl. Mater. Energy* **19** 13–18

[705] von Toussaint U., Mutzke A. and Manhard A. 2017 Sputtering of rough surfaces: a 3D simulation study *Phys. Scr.* **T170** 014056

[706] Eksaeva A. *et al* 2021 The impact of surface morphology on the erosion of metallic surfaces—modelling with the 3D Monte-Carlo code ERO2.0 *Nucl. Mater. Energy* **27** 100987

[707] Harder N.D., Brezinsek S., Pütterich T., Fedorczak N., Matthews G.F., Meigs A., Stamp M.F., van de Sanden M.C.M. and Van Rooij G.J. 2016 ELM-resolved divertor erosion in the JET ITER-like wall *Nucl. Fusion* **56** 026014

[708] Abrams T. *et al* 2018 Experimental validation of a model for particle recycling and tungsten erosion during ELMs in the DIII-D divertor *Nucl. Mater. Energy* **17** 164–73

[709] Huber A. *et al* 2021 Understanding tungsten erosion during inter/intra-ELM periods in He-dominated JET-ILW plasmas *Phys. Scr.* **96** 124046

[710] Brezinsek S., Pospieszczyk A., Sergienko G., Dux R., Cavedon M., Faitsch M. and Krieger K. 2019 Chemically assisted physical sputtering of tungsten: identification via the $^6\Pi \rightarrow {}^6\Sigma^+$ transition of WD in TEXTOR and ASDEX Upgrade plasmas *Nucl. Mater. Energy* **18** 50–55

[711] Zhang Q. *et al* 2022 Spectroscopic investigation of the tungsten deuteride sputtering in the EAST divertor *Nucl. Mater. Energy* **33** 101265

[712] Ding R. *et al* 2017 Advances in understanding of high-Z material erosion and re-deposition in low-Z wall environment in DIII-D *Nucl. Fusion* **57** 056016

[713] Naujoks D., Roth J., Krieger K., Lieder G. and Laux M. 1994 Erosion and redeposition in the ASDEX Upgrade divertor *J. Nucl. Mater.* **210** 43–50

[714] Kirschner A. *et al* 2019 Modelling of tungsten erosion and deposition in the divertor of JET-ILW in comparison to experimental findings *Nucl. Mater. Energy* **18** 239–44

[715] Guterl J., Bykov I., Ding R. and Snyder P. 2021 On the prediction and monitoring of tungsten prompt redeposition in tokamak divertors *Nucl. Mater. Energy* **27** 100948

[716] Doerner R.P. 2007 The implications of mixed-material plasma-facing surfaces in ITER *J. Nucl. Mater.* **363–365** 32–40

[717] Schmid K. and Roth J. 2003 Erosion of high-Z metals with typical impurity ions *J. Nucl. Mater.* **313–316** 302–10

[718] Naujoks D. and Eckstein W. 1996 Non-linear erosion effects in plasma experiments *J. Nucl. Mater.* **230** 93–100

[719] Ebisu S., Ohya K. and Tanabe T. 2006 Dynamic erosion and deposition on carbon and tungsten due to simultaneous bombardment with deuterium and beryllium ions in plasmas *Fusion Eng. Des.* **81** 253–8

[720] Bizyukov I. and Krieger K. 2007 Transition from tungsten erosion to carbon layer deposition with simultaneous bombardment of tungsten by helium and carbon *J. Appl. Phys.* **101** 104906

[721] Bizyukov I., Krieger K., Lee H., Schmid K., Haasz A.A. and Davis J.W. 2012 An overview of sputtering-related processes occurring at mixed surfaces formed by simultaneous C^+ and D^+ irradiation of W *J. Nucl. Mater.* **427** 401–10

[722] Dux R., Bobkov V., Fedorczak N., Iraschko K., Kallenbach A., Neu R., Pütterich T. and Rohde V. 2007 Tungsten erosion at the ICRH limiters in ASDEX Upgrade *J. Nucl. Mater.* **363–365** 112–6

[723] Urbanczyk G., Fedorczak N., Gunn J., Colas L., Li J.G. and Wang K. 2021 Perspective of analogy between heat loads and impurity production in L-mode discharges with ICRH in WEST *Nucl. Mater. Energy* **26** 100925

[724] Rohde V., Balden M. and Neu R. 2021 Arc behaviour on different materials in ASDEX Upgrade *Nucl. Mater. Energy* **29** 101083

[725] Ueda Y. *et al* 2010 Exposure of tungsten nano-structure to TEXTOR edge plasma *J. Nucl. Mater.* **415** S92–S95

[726] Kajita S., Yoshida N. and Ohno N. 2020 Tungsten fuzz: deposition effects and influence to fusion devices *Nucl. Mater. Energy* **25** 100828

[727] Petty T.J., Baldwin M.J., Hasan M.I., Doerner R.P. and Bradley J.W. 2015 Tungsten 'fuzz' growth re-examined: the dependence on ion fluence in non-erosive and erosive helium plasma *Nucl. Fusion* **55** 093033

[728] Brezinsek S. *et al* 2017 Surface modification of He pre-exposed tungsten samples by He plasma impact in the divertor manipulator of ASDEX Upgrade *Nucl. Mater. Energy* **12** 575–81

[729] Tsitrone E. *et al* 2022 Investigation of plasma wall interactions between tungsten plasma facing components and helium plasmas in the WEST tokamak *Nucl. Fusion* **62** 076028

[730] De Temmerman G., Doerner R.P. and Pitts R.A. 2019 A growth/annealing equilibrium model for helium-induced nanostructure with application to ITER *Nucl. Mater. Energy* **19** 255–61

[731] Nordlund K., Ghaly M., Averback R.S., Caturla M., de la Rubia T.D. and Tarus J. 1998 Defect production in collision cascades in elemental semiconductors and fcc metals *Phys. Rev.* B **57** 7556–70

[732] Schmid K., Krieger K., Lisgo S.W., Meisl G. and Brezinsek S. 2015 Quantitative modeling of fuel retention in the JET-C and JET-ILW wall configurations by WallDYN and predictions for ITER *J. Nucl. Mater.* **463** 66–72

[733] Summers H.P. and O'Mullane M.G. 2005 The atomic data and analysis structure *Nuclear Fusion Research: Understanding Plasma-Surface Interactions* (*Springer Series in Chemical Physics* vol 78) ed R.E.H. Clark and D.H. Reiter pp 399–413 (Technical Meeting of the International-Atomic-Energy-Agency (Inst. Plasmaphys., Forschungszentrum, Julich, Germany, 28–31 October 2002))

[734] Stangeby P.C. and Elder J.D. 1995 Impurity retention by divertors. I. One dimensional models *Nucl. Fusion* **35** 1391–412

[735] Schneider R., Bonnin X., Borrass K., Coster D.P., Kastelewicz H., Reiter D., Rozhansky V.A. and Braams B.J. 2006 Plasma edge physics with B2-Eirene *Contrib. Plasma Phys.* **46** 3–191

[736] Rognlien T.D., Brown P.N., Campbell R.B., Kaiser T.B., Knoll D.A., McHugh P.R., Porter G.D., Rensink M.E. and Smith G.R. 1994 2-D fluid transport simulations of gaseous/radiative divertors *Contrib. Plasma Phys.* **34** 362–7

[737] Stangeby P., Watkins J.G., Porter G.D., Elder J.D., Lisgo S., Reiter D., West W.P. and Whyte D.G. 2001 Onion-skin method (OSM) analysis of DIII-D edge measurements *J. Nucl. Mater.* **290–293** 733–7

[738] Widdowson A. *et al* 2014 Material migration patterns and overview of first surface analysis of the JET ITER-like wall *Phys. Scr.* **T159** 014010

[739] Romazanov J. *et al* 2022 Beryllium erosion and redeposition in ITER H, He and D-T discharges *Nucl. Fusion* **62** 036011

[740] Kirschner A. *et al* 2015 Modelling of the material transport and layer formation in the divertor of JET: comparison of ITER-like wall with full carbon wall conditions *J. Nucl. Mater.* **463** 116–22

[741] Guillemaut C. *et al* 2016 Experimental estimation of tungsten impurity sputtering due to Type I ELMs in JET-ITER-like wall using pedestal electron cyclotron emission and target Langmuir probe measurements *Phys. Scr.* **T167** 014005

[742] Guillemaut C. *et al* 2017 Main chamber wall plasma loads in JET-ITER-like wall at high radiated fraction *Nucl. Mater. Energy* **12** 234–40

[743] Herrmann A., Jaksic N., Leitenstern P., Greuner H., Krieger K., de Marné P., Oberkofler M., Rohde V. and Schall G. 2015 A large divertor manipulator for ASDEX Upgrade *Fusion Eng. Des.* **98–99** 1496–9

[744] Hakola A. *et al* 2016 Gross and net erosion of tungsten in the outer strike-point region of ASDEX Upgrade *Phys. Scr.* **T167** 014026

[745] Lahtinen A. *et al* 2022 Influence of surface morphology on erosion of plasma-facing components in H-mode plasmas of ASDEX Upgrade *Nucl. Mater. Energy* **33** 101266

[746] Hakola A., Koivuranta S., Likonen J., Herrmann A., Maier H., Mayer M., Neu R. and Rohde V. 2015 Erosion of tungsten and steel in the main chamber of ASDEX Upgrade *J. Nucl. Mater.* **463** 162–5

[747] Hakola A. *et al* 2014 Long-term erosion of plasma-facing materials with different surface roughness in ASDEX Upgrade *Phys. Scr.* **T159** 014027

[748] Hakola A., Airila M.I., Mellet N., Groth M., Karhunen J., Kurki-Suonio T., Makkonen T., Sillanpää H., Meisl G. and Oberkofler M. 2017 ERO and PIC simulations of gross and net erosion of tungsten in the outer strike-point region of ASDEX Upgrade *Nucl. Mater. Energy* **12** 423–8

[749] Meisl G. *et al* 2017 Nitrogen transport in ASDEX Upgrade: role of surface roughness and transport to the main wall *Nucl. Mater. Energy* **12** 51–59

[750] Corre Y. *et al* 2021 First temperature database achieved with Fiber Bragg Grating sensors in uncooled plasma facing components of the WEST lower divertor *Fusion Eng. Des.* **170** 112528

[751] Klepper C.C. *et al* 2022 Characterizing W sources in the all-W wall, all-RF WEST tokamak environment *Plasma Phys. Control. Fusion* **64** 104008

[752] Ciraolo G. *et al* 2021 Interpretative modeling of impurity transport and tungsten sources in WEST boundary plasma *Nucl. Fusion* **61** 126015

[753] Genova S.D. *et al* 2021 Modelling of tungsten contamination and screening in WEST plasma discharges *Nucl. Fusion* **61** 106019

[754] Balden M. *et al* 2021 Erosion and redeposition patterns on entire erosion marker tiles after exposure in the first operation phase of WEST *Phys. Scr.* **96** 124020

[755] Diez M. *et al* 2023 Overview of plasma-tungsten surfaces interactions on the divertor test sector in WEST during the C3 and C4 campaigns *Nucl. Mater. Energy* **34** 101399

[756] Martin C., Diez M., Campos A., Cabié M., Giacometti G., Balden M., Gallo A., Pegourié B., Bernard E. and Tsitrone E. 2021 First post-mortem analysis of deposits collected on ITER-like components in WEST after the C3 and C4 campaigns *Phys. Scr.* **96** 124035

[757] Stangeby P.C. *et al* 2022 Developing solid-surface plasma facing components for pilot plants and reactors with replenishable wall claddings and continuous surface conditioning. Part A: concepts and questions *Plasma Phys. Control. Fusion* **64** 055018

[758] Stangeby P.C. *et al* 2022 Developing solid-surface plasma facing components for pilot plants and reactors with replenishable wall claddings and continuous surface conditioning. Part B: required research in present tokamaks *Plasma Phys. Control. Fusion* **64** 055003

[759] Gaspar J. *et al* 2024 Thermal and statistical analysis of the high-Z tungsten-based UFOs observed during the first deuterium high fluence campaign of the WEST tokamak *Nucl. Mater. Energy* **41** 101745

[760] Mao H. *et al* 2017 The impacts of lithium and silicon coating on the W source in EAST *Nucl. Mater. Energy* **12** 447–52

[761] Chen X.H. *et al* 2021 The impact of ELM mitigation on tungsten source in the EAST divertor *Nucl. Fusion* **61** 046046

[762] Xie H., Ding R., Kirschner A., Chen J.L., Ding F., Mao H.M., Feng W., Borodin D. and Wang L. 2017 ERO modelling of tungsten erosion and re-deposition in EAST L mode discharges *Phys. Plasmas* **24** 092512

[763] Rudakov D.L. *et al* 2014 Net versus gross erosion of high-Z materials in the divertor of DIII-D *Phys. Scr.* **T159** 014030

[764] Abrams T. *et al* 2017 The inter-ELM tungsten erosion profile in DIII-D H-mode discharges and benchmarking with ERO+OEDGE modeling *Nucl. Fusion* **57** 056034

[765] Ding R. *et al* 2017 High-Z material erosion and its control in DIII-D carbon divertor *Nucl. Mater. Energy* **12** 247–52

[766] Xu G.L., Guterl J., Abrams T., Wang H.Q., Elder J.D., Unterberg E.A., Thomas D.M., Stangeby P.C., Guo H.Y. and Ye M.Y. 2019 Modeling of inter- and intra-edge-localized mode tungsten erosion during DIII-D H-mode discharges *Nucl. Fusion* **59** 126018

[767] Unterberg E.A. *et al* 2019 Localized divertor leakage measurements using isotopic tungsten sources during edge-localized mode-y H-mode discharges on DIII-D *Nucl. Fusion* **60** 016028

[768] Zamperini S.A., Nichols J.H., Stangeby P.C., Donovan D.C., Duran J.D., Elder J.D., Unterberg E.A. and Rudakov D.L. 2022 The role of Bt-dependent flows on W accumulation at the edge of the confined plasma *Nucl. Fusion* **62** 026037

[769] Abrams T. *et al* 2019 Impact of ELM control techniques on tungsten sputtering in the DIII-D divertor and extrapolations to ITER *Phys. Plasmas* **26** 062504

[770] Romazanov J. *et al* 2019 First Monte-Carlo modelling of global beryllium migration in ITER using ERO2.0 *Contrib. Plasma Phys.* **60** e201900149

[771] Romazanov J. *et al* 2021 A sensitivity analysis of numerical predictions for beryllium erosion and migration in ITER *Nucl. Mater. Energy* **26** 100904

[772] Lisgo S.W., Kukushkin A., Pitts R.A. and Reiter D. 2013 Design assessment of tungsten as an upper panel plasma facing material in ITER *J. Nucl. Mater.* **438** S580–4

[773] Anand H., Snipes J.A., Pitts R.A., De Vries P.C., Zabeo L., Gribov Y., Galperti C. and Coda S. 2018 Model-based real-time power flux estimator for the ITER first wall *Fusion Eng. Des.* **137** 143–51

[774] Carpentier S., Pitts R.A., Stangeby P.C., Elder J.D., Kukushkin A.S., Lisgo S., Fundamenski W. and

Moulton D. 2011 Modelling of beryllium erosion–redeposition on ITER first wall panels *J. Nucl. Mater.* **415** S165–9
[775] Borodin D. *et al* 2011 ERO code benchmarking of ITER first wall beryllium erosion/re-deposition against LIM predictions *Phys. Scr.* **T145** 014008
[776] Szabo P.S., Cupak C., Biber H., Jäggi N., Galli A., Wurz P. and Aumayr F. 2022 Analytical model for the sputtering of rough surfaces *Surf. Interfaces* **30** 101924
[777] Khan A., De Temmerman G., Lisgo S.W., Bonnin X., Anand H., Miller M.A., Pitts R.A., Schmid K. and Kukushkin A.S. 2019 WallDYN simulations of material migration and fuel retention in ITER low power H plasmas and high power neon-seeded DT plasmas *Nucl. Mater. Energy* **20** 100674
[778] Schmid K., Krieger K., Lisgo S.W., Meisl G. and Brezinsek S. 2015 WALLDYN simulations of global impurity migration in JET and extrapolations to ITER *Nucl. Fusion* **55** 053015
[779] Schmid K. 2022 An update of tritium co-deposition in ITER using WallDYN3D *Nucl. Mater. Energy* **33** 101230
[780] Hinson E.T., Schmitz O., Frerichs H., Abrams T., Briesemeister A., Rudakov D.L., Unterberg E.A., Wampler W.R., Watkins J.G. and Wang H.Q. 2017 Study of the impact of resonant magnetic perturbation fields on gross tungsten erosion using DiMES samples in DIII-D *Phys. Scr.* **T170** 014048
[781] Schmitz O. *et al* 2016 Three-dimensional modeling of plasma edge transport and divertor fluxes during application of resonant magnetic perturbations on ITER *Nucl. Fusion* **56** 066008
[782] Eksaeva A., Kirschner A., Romazanov J., Brezinsek S., Linsmeier C., Maviglia F., Siccinio M. and Ciattaglia S. 2022 Predictive 3D modelling of erosion and deposition in ITER with ERO2.0: from beryllium main wall, tungsten divertor to full-tungsten device *Phys. Scr.* **97** 014001
[783] Federici G. *et al* 2001 Plasma-material interactions in current tokamaks and their implications for next step fusion reactors *Nucl. Fusion* **41** 1967–2137
[784] Taylor N., Ciattaglia S., Cortes P., Iseli M., Rosanvallon S. and Topilski L. 2012 ITER safety and licensing update *Fusion Eng. Des.* **87** 476–81
[785] De Temmerman G., Baldwin M.J., Anthoine D., Heinola K., Jan A., Jepu I., Likonen J., Lungu C.P., Porosnicu C. and Pitts R.A. 2017 Efficiency of thermal outgassing for tritium retention measurement and removal in ITER *Nucl. Mater. Energy* **12** 267–72
[786] Andrew P. *et al* 1999 Tritium retention and clean-up in JET *Fusion Eng. Des.* **47** 233–45
[787] Skinner C.H. and Federici G. 2006 Is carbon a realistic choice for ITER's divertor? *Phys. Scr.* **T124** 18–22
[788] Bekris N., Coad J.P., Penzhorn R.-D., Knipe S., Doerr L., Rolli R. and Nägele W. 2005 Characterisation of flakes generated in JET after DD and DT plasma operations *J. Nucl. Mater.* **337–339** 659–63
[789] Skinner C.H. *et al* 2001 Studies of tritiated co-deposited layers in TFTR *J. Nucl. Mater.* **290–293** 486–90
[790] Loarer T. *et al* 2007 Gas balance and fuel retention in fusion devices *Nucl. Fusion* **47** 1112–20
[791] Loarer T. 2009 Fuel retention in tokamaks *J. Nucl. Mater.* **390–391** 20–28
[792] Neu R. *et al* 2007 Final steps to an all tungsten divertor tokamak *J. Nucl. Mater.* **363–365** 52–59
[793] Matthews G.F. *et al* 2007 Overview of the ITER-like wall project *Phys. Scr.* **T128** 137–43
[794] Paméla J., Matthews G.F., Philipps V. and Kamendje R. 2007 An ITER-like wall for JET *J. Nucl. Mater.* **363–365** 1–11
[795] Xu G.S. *et al* 2021 Physics design of new lower tungsten divertor for long-pulse high-power operations in EAST *Nucl. Fusion* **61** 126070
[796] Rohde V., Mertens V. and Scarabosio A. 2009 Gas balance in ASDEX Upgrade with tungsten first wall *J. Nucl. Mater.* **390–391** 474–7
[797] Rohde V., Mayer M., Mertens V., Neu R. and Sugiyama K. 2009 Dynamic and static deuterium inventory in ASDEX Upgrade with tungsten first wall *Nucl. Fusion* **49** 085031
[798] Mertens V., Haas G. and Rohde V. (ASDEX Upgrade Team) 2003 Hydrogen gas balance in ASDEX Upgrade with DIV IIB *Proc. 30th EPS Conf. on Controlled Fusion and Plasma Physics* (*Europhysics Conf. Abstracts* vol 27A) *(St. Petersburg, Russian Federation, 7–11 July 2003)* (European Physical Society) P–1.128 (available at: https://info.fusion.ciemat.es/OCS/EPS2003/PDF/P1_128.PDF)
[799] Mayer M. *et al* 2009 Carbon balance and deuterium inventory from a carbon dominated to a full tungsten ASDEX Upgrade *J. Nucl. Mater.* **390–391** 538–43
[800] Loarer T. *et al* 2013 Comparison of long term fuel retention in JET between carbon and the ITER-Like Wall *J. Nucl. Mater.* **438** S108–13
[801] Mayer M. *et al* 2016 Erosion and deposition in the JET divertor during the first ILW campaign *Phys. Scr.* **T167** 014051
[802] Pégourié B. *et al* 2009 Overview of the deuterium inventory campaign in Tore Supra: operational conditions and particle balance *J. Nucl. Mater.* **390–391** 550–5
[803] Mayer M. *et al* 2019 Ion beam analysis of fusion plasma-facing materials and components: facilities and research challenges *Nucl. Fusion* **60** 025001
[804] Miyasaka K., Tanabe T., Mank G., Finken K.H., Philipps V., Walsh D.S., Nishizawa K. and Saze T. 2001 Tritium detection in plasma facing component by imaging plate technique *J. Nucl. Mater.* **290–293** 448–53
[805] Zayachuk Y. *et al* 2023 Fuel desorption from JET-ILW materials: assessment of analytical approach and identification of sources of uncertainty and discrepancy *Nucl. Fusion* **63** 096010
[806] Philipps V. *et al* 2013 Development of laser-based techniques forin situcharacterization of the first wall in ITER and future fusion devices *Nucl. Fusion* **53** 093002
[807] Zlobinski M. *et al* 2024 First results of laser-induced desorption—quadrupole mass spectrometry (LID-QMS) at JET *Nucl. Fusion* **64** 086031
[808] Heinola K. *et al* 2017 Experience on divertor fuel retention after two ITER-Like Wall campaigns *Phys. Scr.* **T170** 014063
[809] Krat S. *et al* 2020 Comparison of erosion and deposition in JET divertor during the first three ITER-like wall campaigns *Phys. Scr.* **T171** 014059
[810] Widdowson A. *et al* 2021 Evaluation of tritium retention in plasma facing components during JET tritium operations *Phys. Scr.* **96** 124075
[811] Schmid K., Bauer J., Schwarz-Selinger T., Markelj S., Toussaint U.V., Manhard A. and Jacob W. 2017 Recent progress in the understanding of H transport and trapping in W *Phys. Scr.* **T170** 014037
[812] De Temmerman G., Baldwin M.J., Doerner R.P., Nishijima D. and Schmid K. 2008 An empirical scaling for deuterium retention in co-deposited beryllium layers *Nucl. Fusion* **48** 075008
[813] Roth J. and Schmid K. 2011 Hydrogen in tungsten as plasma-facing material *Phys. Scr.* **T145** 014031
[814] Ogorodnikova O.V., Roth J. and Mayer M. 2008 Ion-driven deuterium retention in tungsten *J. Appl. Phys.* **103** 034902

[815] Alimov V.K.H., Shu W.M., Roth J., Sugiyama K., Lindig S., Balden M., Isobe K. and Yamanishi T. 2009 Surface morphology and deuterium retention in tungsten exposed to low-energy, high flux pure and helium-seeded deuterium plasmas *Phys. Scr.* **T138** 014048

[816] Hatano Y. *et al* 2013 Deuterium trapping at defects created with neutron and ion irradiations in tungsten *Nucl. Fusion* **53** 073006

[817] Oya Y., Sun F., Yamauchi Y., Nobuta Y., Shimada M., Taylor C.N., Wampler W.R., Nakata M., Garrison L.M. and Hatano Y. 2020 D retention and depth profile behavior for single crystal tungsten with high temperature neutron irradiation *J. Nucl. Mater.* **539** 152323

[818] Pečovnik M., Schwarz-Selinger T. and Markelj S. 2021 Experiments and modelling of multiple sequential MeV ion irradiations and deuterium exposures in tungsten *J. Nucl. Mater.* **550** 152947

[819] Villari R. *et al* 2013 Nuclear analysis of the ITER full-tungsten divertor *Fusion Eng. Des.* **88** 2006–10

[820] Toyama T., Ami K., Inoue K., Nagai Y., Sato K., Xu Q. and Hatano Y. 2018 Deuterium trapping at vacancy clusters in electron/neutron-irradiated tungsten studied by positron annihilation spectroscopy *J. Nucl. Mater.* **499** 464–70

[821] Ogorodnikova O.V. 2015 Fundamental aspects of deuterium retention in tungsten at high flux plasma exposure *J. Appl. Phys.* **118** 074902

[822] Sugiyama K., Mayer M., Herrmann A., Krieger K., Rohde V., Balden M., Lindig S., Neu R. and Müller H.W. 2014 Deuterium retention in tungsten used in ASDEX Upgrade: comparison of tokamak and laboratory studies *Phys. Scr.* **T159** 014043

[823] Yajima M., Hatano Y., Alimov V.K., Toyama T., Kuwabara T., Schwarz-Selinger T., Oya Y., Spitsyn A.V. and Ohno N. 2021 Penetration of deuterium into neutron-irradiated tungsten under plasma exposure *Phys. Scr.* **96** 124042

[824] Hatano Y. *et al* 2013 Trapping of hydrogen isotopes in radiation defects formed in tungsten by neutron and ion irradiations *J. Nucl. Mater.* **438** S114–9

[825] Harutyunyan Z., Gasparyan Y., Ryabtsev S., Efimov V., Ogorodnikova O., Pisarev A. and Kanashenko S. 2021 Deuterium trapping in the subsurface layer of tungsten pre-irradiated with helium ions *J. Nucl. Mater.* **548** 152848

[826] Ueda Y., Lee H.T., Peng H.Y. and Ohtsuka Y. 2012 Deuterium permeation in tungsten by mixed ion irradiation *Fusion Eng. Des.* **87** 1356–62

[827] Baldwin M.J. and Doerner R.P. 2017 Hydrogen isotope transport across tungsten surfaces exposed to a fusion relevant He ion fluence *Nucl. Fusion* **57** 076031

[828] Markelj S., Schwarz-Selinger T., Pečovnik M., Chrominski W., Šestan A. and Zavašnik J. 2020 Deuterium transport and retention in the bulk of tungsten containing helium: the effect of helium concentration and microstructure *Nucl. Fusion* **60** 106029

[829] Finlay T.J., Davis J.W., Schwarz-Selinger T., Siketić Z. and Haasz A.A. 2017 Deuterium retention in recrystallized tungsten irradiated with simultaneous deuterium-neon ion beams *Nucl. Mater. Energy* **12** 1288–93

[830] Ishida M., Lee H.T. and Ueda Y. 2015 The influence of neon or argon impurities on deuterium permeation in tungsten *J. Nucl. Mater.* **463** 1062–5

[831] Cheng L. *et al* 2017 Mitigated blistering and deuterium retention in tungsten exposed to high-flux deuterium-neon mixed plasmas *Nucl. Fusion* **57** 046028

[832] Ogorodnikova O.V., Sugiyama K., Markin A., Gasparyan Y., Efimov V., Manhard A. and Balden M. 2011 Effect of nitrogen seeding into deuterium plasma on deuterium retention in tungsten *Phys. Scr.* **T145** 014034

[833] Kreter A. *et al* 2019 Influence of plasma impurities on the fuel retention in tungsten *Nucl. Fusion* **59** 086029

[834] Lee H.T., Ishida M., Ohtsuka Y. and Ueda Y. 2014 The influence of nitrogen on deuterium permeation through tungsten *Phys. Scr.* **T159** 014021

[835] Arredondo R., Schmid K., Ricapito I., Lukenskas A. and Spagnuolo G. 2022 Preliminary assessment of tritium permeation and retention in the European Water Cooled Lithium Lead Test Blanket Module with TESSIM-X *Nucl. Mater. Energy* **32** 101228

[836] Zhou H.-S. *et al* 2018 A tritium permeation 'short cut' for plasma-facing components of fusion reactors *Nucl. Fusion* **59** 014003

[837] Anderl R.A., Causey R.A., Davis J.W., Doerner R.P., Federici G., Haasz A.A., Longhurst G.R., Wampler W.R. and Wilson K.L. 1999 Hydrogen isotope retention in beryllium for tokamak plasma-facing applications *J. Nucl. Mater.* **273** 1–26

[838] Baldwin M.J., Schwarz-Selinger T. and Doerner R.P. 2017 D retention in Be exposed to fusion relevant mixed species D_2—He plasma *Nucl. Mater. Energy* **12** 678–82

[839] Kukushkin A.S., Pacher H.D., Loarte A., Komarov V., Kotov V., Merola M., Pacher G.W. and Reiter D. 2009 Analysis of performance of the optimized divertor in ITER *Nucl. Fusion* **49** 075008

[840] You J.H. *et al* 2016 European DEMO divertor target: operational requirements and material-design interface *Nucl. Mater. Energy* **9** 171–6

[841] De Temmerman G. and Doerner R.P. 2009 Deuterium retention and release in tungsten co-deposited layers *J. Nucl. Mater.* **389** 479–83

[842] Alimov V., Roth J., Shu W.M., Komarov D.A., Isobe K. and Yamanishi T. 2010 Deuterium trapping in tungsten deposition layers formed by deuterium plasma sputtering *J. Nucl. Mater.* **399** 225–30

[843] Putrik A.B., Klimov N.S., Gasparyan Y.M., Barsuk V.A., Efimov V.S., Podkovyrov V.L., Zhitlukhin A.M., Yaroshevskaya A.D. and Kovalenko D.V. 2014 Plasma-facing material erosion products formed under ITER-like transient loads at QSPA-T plasma gun facility *Fusion Sci. Technol.* **66** 70–76

[844] Doerner R.P., Baldwin M.J., De Temmerman G., Hanna J., Nishijima D., Roth J., Schmid K., Tynan G.R. and Umstadter K. 2009 Codeposition of deuterium with ITER materials *Nucl. Fusion* **49** 035002

[845] Baldwin M.J., Simmonds M.J., De Temmerman G. and Doerner R.P. 2020 Deuterium retention in Be-D co-deposits formed over an ITER relevant parameter space *Phys. Scr.* **T171** 014014

[846] Baldwin M.J., Založnik A., Simmonds M.J., De Temmerman G. and Doerner R.P. 2021 The influence of D_2 pressure on D retention and release from Be co-deposits *Nucl. Mater. Energy* **28** 101023

[847] Založnik A., Baldwin M.J., Doerner R.P., De Temmerman G. and Pitts R.A. 2022 Improved scaling law for the prediction of deuterium retention in beryllium co-deposits *Nucl. Fusion* **62** 036006

[848] Zibrov M.S., Baldwin M.J., Mayer M., Nguyen H.Q., Brezinsek S. and Doerner R.P. 2020 Deuterium retention in mixed Be-W-D codeposited layers *Nucl. Fusion* **60** 126005

[849] Hodille E., Payet M., Marascu V., Peillon S., Mougenot J., Ferro Y., Delaporte-Mathurin R., Leblond F., Bernard E. and Grisolia C. 2021 Modelling tritium adsorption and desorption from tungsten dust particles with a surface kinetic model *Nucl. Fusion* **61** 086030

[850] Peillon S. *et al* 2020 Dust sampling in WEST and tritium retention in tokamak-relevant tungsten particles *Nucl. Mater. Energy* **24** 100781

[851] Ogorodnikova O.V., Klimov K.S., Poskakalov A.G., Kaziev A.V., Kharkov M.M., Efimov V.S., Gasparyan Y.M., Volkov N.V., Alimov V.K. and Tokitani M. 2019 Deuterium and helium retention in W with and without He-induced W fuzz exposed to pulsed high-temperature deuterium plasma *J. Nucl. Mater.* **515** 150–9

[852] Rubel M. *et al* 2017 Fuel inventory and deposition in castellated structures in JET-ILW *Nucl. Fusion* **57** 066027

[853] Lee S.E. *et al* 2021 Global distribution of tritium in JET with the ITER-like wall *Nucl. Mater. Energy* **26** 100930

[854] Heinola K. *et al* 2015 Fuel retention in JET ITER-Like Wall from post-mortem analysis *J. Nucl. Mater.* **463** 961–5

[855] Loarer T. *et al* 2015 Plasma isotopic changeover experiments in JET under carbon and ITER-like wall conditions *Nucl. Fusion* **55** 043021

[856] Tokitani M. *et al* 2020 Surface morphology of the bulk tungsten divertor tiles from JET ITER-like wall *Phys. Scr.* **T171** 014010

[857] Fazinić S., Božičević-Mihali I., Provatas G., Tadić T., Rubel M., Fortuna-Zaleśna E. and Widdowson A. 2020 Micro-analyses of dust particles generated in the JET tokamak with the ITER-like wall *Nucl. Fusion* **60** 126031

[858] Maier H., Schmid K. and Eckstein W. 2005 On the lifetime of wall conditioning layers *J. Nucl. Mater.* **337–339** 480–4

[859] Sugiyama K., Mayer M., Rohde V., Balden M., Dürbeck T., Herrmann A., Lindig S., Wiltner A., Müller H.W. and Neu R. 2010 Deuterium inventory in the full-tungsten divertor of ASDEX Upgrade *Nucl. Fusion* **50** 035001

[860] Sugiyama K., Krieger K., Mayer M., Lindig S., Balden M. and Dürbeck T. 2011 Deuterium retention in bulk tungsten exposed to the outer divertor plasma of ASDEX Upgrade *Phys. Scr.* **T145** 014033

[861] Wauters T. *et al* 2022 Isotope removal experiment in JET-ILW in view of T-removal after the 2nd DT campaign at JET *Phys. Scr.* **97** 044001

[862] Heinola K., Likonen J., Ahlgren T., Brezinsek S., De Temmerman G., Jepu I., Matthews G.F., Pitts R.A. and Widdowson A. 2017 Long-term fuel retention and release in JET ITER-Like Wall at ITER-relevant baking temperatures *Nucl. Fusion* **57** 086024

[863] Založnik A., Doerner R.P. and De Temmerman G. 2020 Deuterium removal from beryllium co-deposits by simulated strike-point sweeping *Nucl. Mater. Energy* **24** 100750

[864] Roth J., Schwarz-Selinger T., Alimov V.K. and Markina E. 2013 Hydrogen isotope exchange in tungsten: discussion as removal method for tritium *J. Nucl. Mater.* **432** 341–7

[865] Nobuta Y., Hatano Y., Torikai Y., Matsuyama M., Abe S. and Yamauchi Y. 2016 Tritium desorption and tritium removal from tungsten pre-irradiated with helium *Fusion Eng. Des.* **109–111** 1179–82

[866] Nobuta Y., Hatano Y., Torikai Y. and Nakayama M. 2018 Effects of baking in deuterium atmosphere on tritium removal from tungsten *Fusion Eng. Des.* **136** 674–7

[867] Douai D. *et al* 2015 Wall conditioning for ITER: current experimental and modeling activities *J. Nucl. Mater.* **463** 150–6

[868] Douai D. *et al* 2013 Wall conditioning of JET with the ITER-Like Wall *J. Nucl. Mater.* **438** 1172–6

[869] Begrambekov L.B., Dovganyuk S.S., Evsin A.E. and Kaplevskiy A.S. 2018 On the possibility of low-temperature removal of hydrogen isotopes from tungsten in conditions of thermonuclear and plasma facilities *J. Phys.: Conf. Ser.* **1058** 012012

[870] Yang Y. *et al* 2014 Re-design of ITER glow discharge cleaning system based on a fixed electrode concept *Fusion Eng. Des.* **89** 1944–8

[871] Hagelaar G.J.M., Kogut D., Douai D. and Pitts R.A. 2014 Modelling of tokamak glow discharge cleaning I: physical principles *Plasma Phys. Control. Fusion* **57** 025008

[872] Kogut D., Douai D., Hagelaar G. and Pitts R.A. 2014 Modelling of tokamak glow discharge cleaning II: comparison with experiment and application to ITER *Plasma Phys. Control. Fusion* **57** 025009

[873] Kogut D., Douai D., Hagelaar G. and Pitts R.A. 2015 Modelling the ITER glow discharge plasma *J. Nucl. Mater.* **463** 1113–6

[874] Miyamoto M., Tokitani M., Tokunaga K., Fujiwara T., Yoshida N., Masuzaki S. and Komori A. 2004 Microscopic damage of materials exposed to glow discharge cleanings in LHD *J. Nucl. Mater.* **329–333** 742–6

[875] Shimada M. and Pitts R.A. 2011 Wall conditioning on ITER *J. Nucl. Mater.* **415** S1013–6

[876] Brezinsek S. *et al* 2021 Plasma-surface interaction in the stellarator W7-X: conclusions drawn from operation with graphite plasma-facing components *Nucl. Fusion* **62** 016006

[877] Rohde V., Dux R., Kallenbach A., Krieger K. and Neu R. 2007 Wall conditioning in ASDEX Upgrade *J. Nucl. Mater.* **363–365** 1369–74

[878] Härtl T., Drenik A., Kircher M., Rohde V., Stelzer F. and Zeidner W. 2017 Optimization of the ASDEX Upgrade glow discharge *Fusion Eng. Des.* **124** 283–6

[879] Jadeja K.A. *et al* 2019 Novel approach of pulsed-glow discharge wall conditioning in the ADITYA Upgrade tokamak *Nucl. Fusion* **59** 086005

[880] Tabarés F.L. (ed) 2021 *Plasma Applications for Material Modification* (Jenny Stanford Publishing)

[881] Litnovsky A. *et al* 2011 Overview of material migration and mixing, fuel retention and cleaning of ITER-like castellated structures in TEXTOR *J. Nucl. Mater.* **415** S289–92

[882] Goriaev A., Wauters T., Brakel R., Brezinsek S., Dinklage A., Fellinger J., Grote H., Moseev D., Sereda S. and Volzke O. 2020 Wall conditioning at the Wendelstein 7-X stellarator operating with a graphite divertor *Phys. Scr.* **T171** 014063

[883] Sakamoto Y. *et al* 1980 Electron cyclotron resonance discharge cleaning of JFT-2 tokamak (Jaeri) *J. Nucl. Mater.* **93–94** 333–7

[884] Douai D. *et al* 2017 Development of helium electron cyclotron wall conditioning on TCV *Nucl. Fusion* **58** 026018

[885] Fukumoto M., Nakano T., Itami K., Isayama A., Suzuki T. and Kubo H. 2017 Efficiency improvement by application of horizontal magnetic fields for second- and fundamental harmonic EC wall conditioning in JT-60U *Nucl. Mater. Energy* **12** 725–32

[886] Itami K., Hong S.-H., Bae Y.-S., Matsukawa M. and Kim W.-C. 2013 Wall-conditioning plasmas by ECRF heating in KSTAR *J. Nucl. Mater.* **438** S930–5

[887] Wauters T. *et al* 2023 Characterisation of electron cyclotron wall conditioning plasma in ASDEX Upgrade *Nucl. Fusion* **63** 066018

[888] Wauters T. *et al* 2020 Wall conditioning in fusion devices with superconducting coils *Plasma Phys. Control. Fusion* **62** 034002

[889] Stober J. *et al* 2011 ECRH-assisted plasma start-up with toroidally inclined launch: multi-machine comparison and perspectives for ITER *Nucl. Fusion* **51** 083031

[890] Wauters T. *et al* 2020 RF plasma simulations using the TOMATOR 1D code: a case study for TCV helium ECRH plasmas *Plasma Phys. Control. Fusion* **62** 105010

[891] Lyssoivan A. *et al* 2012 Simulation of ITER full-field ICWC scenario in JET: RF physics aspects *Plasma Phys. Control. Fusion* **54** 074014

[892] Tripský M., Wauters T., Lyssoivan A., Bobkov V., Schneider P.A., Stepanov I., Douai D., Van Eester D., Noterdaeme J.-M. and Van Schoor M. 2017 A PIC-MCC code RFdinity1d for simulation of discharge initiation by ICRF antenna *Nucl. Fusion* **57** 126043

[893] Lyssoivan A. *et al* 2014 Wave aspect of neutral gas breakdown with ICRF antenna in ICWC operation mode *Proc. 41th EPS Conf. on Controlled Fusion and Plasma Physics* (*Europhysics Conf. Abstracts* vol 38F) *(Berlin, Germany, 23–27 June 2014)* (European Physical Society) P–2.030 (available at: https://info.fusion.ciemat.es/OCS/EPS2014PAP/pdf/P2.030.pdf)

[894] de la Cal E. and Gauthier E. 2005 Review of radio frequency conditioning discharges with magnetic fields in superconducting fusion reactors *Plasma Phys. Control. Fusion* **47** 197–218

[895] Douai D. *et al* 2011 Recent results on ion cyclotron wall conditioning in mid and large size tokamaks *J. Nucl. Mater.* **415** S1021–8

[896] Moon S. *et al* 2021 Characterization of neutral particle fluxes from ICWC and ECWC plasmas in the TOMAS facility *Phys. Scr.* **96** 124025

[897] Wauters T., Lyssoivan A., Douai D., Marchuk O., Wünderlich D., Koch R., Sergienko G., Van Oost G. and Van Schoor M. 2011 0D model of magnetized hydrogen-helium wall conditioning plasmas *Plasma Phys. Control. Fusion* **53** 125003

[898] Hakola A. *et al* 2017 Plasma-wall interaction studies in the full-W ASDEX Upgrade during helium plasma discharges *Nucl. Fusion* **57** 066015

[899] Douai D. *et al* 2013 Ion cyclotron wall conditioning in KSTAR and ASDEX-Upgrade *Proc. 40th EPS Conf. on Controlled Fusion and Plasma Physics* (*Europhysics Conf. Abstracts* vol 37D) *(Helsinki, Finland, 1–5 July 2013)* (European Physical Society) P–2.120 (available at: https://info.fusion.ciemat.es/OCS/EPS2013PAP/pdf/P2.120.pdf)

[900] Hu J.S., Li J.G. and Zhao Y.P. 2008 He-ICR cleanings on full metallic walls in EAST full superconducting tokamak *J. Nucl. Mater.* **376** 207–10

[901] Wauters T. *et al* 2013 Self-consistent application of ion cyclotron wall conditioning for co-deposited layer removal and recovery of tokamak operation on TEXTOR *Nucl. Fusion* **53** 123001

[902] Lee D.S., Hong S.-H., Kim S., Kim K.-P., Kim S.-H., Kim J.-S., Wang S.-J., Kim W.-C., Park K.-R. and Kwak J.-G. (KSTAR Team) 2011 Ion cyclotron wall conditioning (ICWC) on KSTAR *Fusion Sci. Technol.* **60** 94–97

[903] Borodkina I. *et al* 2018 Isotope wall content control strategy in the upcoming D, H and T experimental campaigns in JET-ILW *Proc. 45th EPS Conf. on Controlled Fusion and Plasma Physics* (*Europhysics Conf. Abstracts* vol 42A) *(Prague, Czech Republic, 2–6 July 2018)* (European Physical Society) O–2.106 (available at: https://info.fusion.ciemat.es/OCS/EPS2018PAP/pdf/O2.106.pdf)

[904] Kolesnikov R.A., Bulmer R.H., LoDestro L.L., Casper T.A. and Pitts R.A. 2013 Equilibrium and vertical-instability considerations for vertical strike-point shifts on the ITER divertor targets *Nucl. Fusion* **53** 083021

[905] Park J.-S., Bonnin X., Pitts R., Gribov Y., Wauters T., Kavin A.A., Lukash V.E. and Khayrutdinov R.R. 2023 Feasibility of raised inner strike point equilibria scenario in ITER for detritiation from beryllium co-deposits *Nucl. Fusion* **63** 076027

[906] Matveev D. *et al* 2023 Tritium removal from JET-ILW after T and D–T experimental campaigns *Nucl. Fusion* **63** 112014

[907] Stangeby P. and Elder J. 1992 Calculation of observable quantities using a divertor impurity interpretive code, DIVIMP *J. Nucl. Mater.* **196–198** 258–63

[908] Schmid K., Lunt T. and Zhang W. 2020 Code/Code comparison of impurity transport in EMC3 and DIVIMP *Phys. Scr.* **T171** 014006

[909] Airila M.I. *et al* 2015 Preliminary Monte Carlo simulation of beryllium migration during JET ITER-like wall divertor operation *J. Nucl. Mater.* **463** 800–4

[910] Longhurst G.R. and Ambrosek J. 2005 Verification and validation of the tritium transport code TMAP7 *Fusion Sci. Technol.* **48** 468–71

[911] Delaporte-Mathurin R., Hodille E.A., Mougenot J., Charles Y. and Grisolia C. 2019 Finite element analysis of hydrogen retention in ITER plasma facing components using FESTIM *Nucl. Mater. Energy* **21** 100709

[912] Ogorodnikova O.V., Tyburska B., Alimov V.K. and Ertl K. 2011 The influence of radiation damage on the plasma-induced deuterium retention in self-implanted tungsten *J. Nucl. Mater.* **415** S661–6

[913] Skinner C.H. *et al* 2008 Recent advances on hydrogen retention in ITER's plasma-facing materials: beryllium, carbon and tungsten *Fusion Sci. Technol.* **54** 891–945

[914] Ferry L., Virot F., Ferro Y., Matveev D., Linsmeier C. and Barrachin M. 2019 Diffusivity of hydrogen and properties of point defects in beryllium investigated by DFT *J. Nucl. Mater.* **524** 323–9

[915] Lu G.-H., Zhou H.-B. and Becquart C.S. 2014 A review of modelling and simulation of hydrogen behaviour in tungsten at different scales *Nucl. Fusion* **54** 086001

[916] Heinola K. and Ahlgren T. 2010 Diffusion of hydrogen in bcc tungsten studied with first principle calculations *J. Appl. Phys.* **107** 113531

[917] Pisarev A. and Giniyatullin B. 2019 Influence of true diffusion coefficient on hydrogen diffusion in tungsten in the field of defects *J. Phys.: Conf. Ser.* **1370** 012061

[918] Benannoune S., Charles Y., Mougenot J., Gaspérini M. and De Temmerman G. 2019 Numerical simulation by finite element modelling of diffusion and transient hydrogen trapping processes in plasma facing components *Nucl. Mater. Energy* **19** 42–46

[919] Schmid K. 2016 Diffusion-trapping modelling of hydrogen recycling in tungsten under ELM-like heat loads *Phys. Scr.* **T167** 014025

[920] Heinola K., Ahlgren T., Brezinsek S., Vuoriheimo T. and Wiesen S. 2019 Modelling of the effect of ELMs on fuel retention at the bulk W divertor of JET *Nucl. Mater. Energy* **19** 397–402

[921] Poskakalov A.G., Gasparyan Y.M., Efimov V.S., Kovalenko D.V., Barsuk V.A., Klimov N.S., Zibrov M.S. and Ogorodnikova O.V. 2020 Influence of plasma heat loads relevant to ITER transient events on deuterium retention in tungsten *Phys. Scr.* **T171** 014062

[922] Hodille E.A. *et al* 2021 Modelling of hydrogen isotopes trapping, diffusion and permeation in divertor monoblocks under ITER-like conditions *Nucl. Fusion* **61** 126003

[923] Delaporte-Mathurin R., Hodille E., Mougenot J., De Temmerman G., Charles Y. and Grisolia C. 2020

Parametric study of hydrogenic inventory in the ITER divertor based on machine learning *Sci. Rep.* **10** 17798

[924] Schmid K., von Toussaint U. and Schwarz-Selinger T. 2014 Transport of hydrogen in metals with occupancy dependent trap energies *J. Appl. Phys.* **116** 134901

[925] Hodille E.A., Ferro Y., Fernandez N., Becquart C.S., Angot T., Layet J.M., Bisson R. and Grisolia C. 2016 Study of hydrogen isotopes behavior in tungsten by a multi trapping macroscopic rate equation model *Phys. Scr.* **T167** 014011

[926] Knaster J. *et al* 2017 Overview of the IFMIF/EVEDA project *Nucl. Fusion* **57** 102016

[927] Bernardi D. *et al* 2022 The IFMIF-DONES project: design status and main achievements within the EUROfusion FP8 work programme *J. Fusion Energy* **41** 24

[928] Federici G. 2023 Testing needs for the development and qualification of a breeding blanket for DEMO *Nucl. Fusion* **63** 125002

[929] Linke J., Du J., Loewenhoff T., Pintsuk G., Spilker B., Steudel I. and Wirtz M. 2019 Challenges for plasma-facing components in nuclear fusion *Matter Radiat. Extremes* **4** 056201

[930] Litnovsky A. *et al* 2021 Fusion-reactor materials *Encyclopedia of Nuclear Energy* ed E. Greenspan (Elsevier) pp 594–619

[931] Neu R. (ASDEX Upgrade Team, EU PWI Taskforce and JET EFDA Contributors) 2011 Preparing the scientific basis for an all metal ITER *Plasma Phys. Control. Fusion* **53** 124040

[932] Neu R. *et al* 2014 Experiences with tungsten plasma facing components in ASDEX upgrade and JET *IEEE Trans. Plasma Sci.* **42** 552–62

[933] Rieth M. *et al* 2011 Review on the EFDA programme on tungsten materials technology and science *J. Nucl. Mater.* **417** 463–7

[934] Ueda Y., Coenen J.W., De Temmerman G., Doerner R.P., Linke J., Philipps V. and Tsitrone E. 2014 Research status and issues of tungsten plasma facing materials for ITER and beyond *Fusion Eng. Des.* **89** 901

[935] Ueda Y., Schmid K., Balden M., Coenen J.W., Loewenhoff T., Ito A., Hasegawa A., Hardie C., Porton M. and Gilbert M. 2017 Baseline high heat flux and plasma facing materials for fusion *Nucl. Fusion* **57** 092006

[936] Rieth M. *et al* 2013 A brief summary of the progress on the EFDA tungsten materials program *J. Nucl. Mater.* **442** 173–80

[937] Luo G.-N. *et al* 2017 Overview of decade-long development of plasma-facing components at ASIPP *Nucl. Fusion* **57** 065001

[938] Merola M. *et al* 2010 ITER plasma-facing components *Fusion Eng. Des.* **85** 2312–22

[939] Merola M., Escourbiac F., Raffray R., Chappuis P., Hirai T. and Martin A. 2014 Overview and status of ITER internal components *Fusion Eng. Des.* **89** 890–5

[940] Merola M., Escourbiac F., Raffray A.R., Chappuis P., Hirai T. and Gicquel S. 2015 Engineering challenges and development of the ITER blanket system and divertor *Fusion Eng. Des.* **96–97** 34–41

[941] Raffray A.R. *et al* 2014 The ITER blanket system design challenge *Nucl. Fusion* **54** 033004

[942] Thomser C., Schmidt A., Bellin B., Buerger A., Linke J., Roedig M. and Zacchia F. 2011 High heat flux testing of beryllium components with improved diagnostics *Fusion Eng. Des.* **86** 2409–12

[943] Hirai T. *et al* 2016 Use of tungsten material for the ITER divertor *Nucl. Mater. Energy* **9** 616–22

[944] De Temmerman G., Hirai T. and Pitts R.A. 2018 The influence of plasma-surface interaction on the performance of tungsten at the ITER divertor vertical targets *Plasma Phys. Control. Fusion* **60** 044018

[945] Kočan M., Pitts R.A., Lisgo S.W., Loarte A., Gunn J.P. and Fuchs V. 2015 Modelling ELM heat flux deposition on the ITER main chamber wall *J. Nucl. Mater.* **463** 709–13

[946] Pitts R. *et al* 2022 First wall power flux management during plasma current ramp-up on ITER *Nucl. Fusion* **62** 096022

[947] Doerner R., Baldwin M., Lynch T. and Yu J. 2016 Retention in tungsten resulting from extremely high fluence plasma exposure *Nucl. Mater. Energy* **9** 89–92

[948] Profijt H.B., Potts S.E., van de Sanden M.C.M. and Kessels W.M.M. 2011 Plasma-assisted atomic layer deposition: basics, opportunities and challenges *J. Vac. Sci. Technol.* A **29** 050801

[949] Takagi T. 1984 Ion-surface interactions during thin-film deposition *J. Vac. Sci. Technol.* A **2** 382–8

[950] Krolas W. *et al* 2021 The IFMIF-DONES fusion oriented neutron source: evolution of the design *Nucl. Fusion* **61** 125002

[951] Thompson M., Drummond D., Sullivan J., Elliman R., Kluth P., Kirby N., Riley D. and Corr C.S. 2018 Effect of W self-implantation and He plasma exposure on early-stage defect and bubble formation in tungsten *Nucl. Fusion* **58** 066010

[952] Rayaprolu R., Möller S., Linsmeier C. and Spellerberg S. 2016 Simulation of neutron irradiation damage in tungsten using higher energy protons *Nucl. Mater. Energy* **9** 29–35

[953] Rieth M., Doerner R., Hasegawa A., Ueda Y. and Wirtz M. 2019 Behavior of tungsten under irradiation and plasma interaction *J. Nucl. Mater.* **519** 334–68

[954] Hirai T. *et al* 2016 Progress on performance assessment of ITER enhanced heat flux first wall technology after neutron irradiation *Phys. Scr.* **T167** 014072

[955] Katoh Y. *et al* 2019 Response of unalloyed tungsten to mixed spectrum neutrons *J. Nucl. Mater.* **520** 193–207

[956] Bolt H., Barabash V., Federici G., Linke J., Loarte A., Roth J. and Sato K. 2002 Plasma facing and high heat flux materials—needs for ITER and beyond *J. Nucl. Mater.* **307, Part 1** 43–52

[957] Jochen L. 2008 High heat flux performance of plasma facing materials and components under service conditions in future fusion reactors *Fusion Sci. Technol.* **53** 278–87

[958] Cui S., Doerner R.P., Simmonds M.J., Xu C., Wang Y., Dechaumphai E., Fu E., Tynan G.R. and Chen R. 2018 Thermal conductivity degradation and recovery in ion beam damaged tungsten at different temperature *J. Nucl. Mater.* **511** 141–7

[959] Linsmeier C., Unterberg B., Coenen J.W., Doerner R.P., Greuner H., Kreter A., Linke J. and Maier H. 2017 Material testing facilities and programs for plasma-facing component testing *Nucl. Fusion* **57** 092012

[960] Doerner R.P., Grossman A., Luckhardt S., Seraydarian R., Sze F.C., Whyte D.G. and Conn R.W. 1998 Response of beryllium to deuterium plasma bombardment *J. Nucl. Mater.* **257** 51–58

[961] Doerner R.P., Baldwin M., Hanna J., Linsmeier C., Nishijima D., Pugno R., Roth J., Schmid K. and Wiltner A. 2007 Interaction of beryllium containing plasma with ITER materials *Phys. Scr.* **T128** 115–20

[962] Unterberg B. *et al* 2011 New linear plasma devices in the Trilateral Euregio Cluster for an integrated approach to plasma surface interactions in fusion reactors *Fusion Eng. Des.* **86** 1797–800

[963] Morgan T.W., Balden M., Schwarz-Selinger T., Li Y., Loewenhoff T.H., Wirtz M., Brezinsek S. and De Temmerman G. 2020 ITER monoblock performance

under lifetime loading conditions in Magnum-PSI *Phys. Scr.* **T171** 014065

[964] Steudel I., Huber A., Kreter A., Linke J., Sergienko G., Unterberg B. and Wirtz M. 2016 Sequential and simultaneous thermal and particle exposure of tungsten *Phys. Scr.* **T167** 014053

[965] Lemahieu N., Balden M., Elgeti S., Greuner H., Linke J., Maier H., Pintsuk G., Wirtz M., Van Oost G. and Noterdaeme J.-M. 2016 H/He irradiation on tungsten exposed to ELM-like thermal shocks *Fusion Eng. Des.* **109–111** 169–74

[966] Lemahieu N., Greuner H., Linke J., Maier H., Pintsuk G., Van Oost G. and Wirtz M. 2015 Synergistic effects of ELMs and steady state H and H/He irradiation on tungsten *Fusion Eng. Des.* **98–99** 2020–4

[967] Huber A. *et al* 2013 Investigation of the impact on tungsten of transient heat loads induced by laser irradiation, electron beams and plasma guns *Fusion Sci. Technol.* **63** 197–200

[968] Loewenhoff T., Antusch S., Pintsuk G., Rieth M. and Wirtz M. 2019 High pulse number thermal shock testing of tungsten alloys produced by powder injection molding *Nucl. Mater. Energy* **20** 100680

[969] Yu J., Doerner R.P., Dittmar T., Höschen T., Schwarz-Selinger T. and Baldwin M.J. 2014 ITER-relevant transient heat loads on tungsten exposed to plasma and beryllium *Phys. Scr.* **T159** 014036

[970] Yu J.H., Baldwin M.J., Doerner R.P., Dittmar T., Hakola A., Höschen T., Likonen J., Nishijima D. and Toudeshki H.H. 2015 Transient heating effects on tungsten: ablation of Be layers and enhanced fuzz growth *J. Nucl. Mater.* **463** 299–302

[971] Yu J., Baldwin M.J. and Doerner R.P. 2017 Cracking and surface roughening of beryllium-tungsten alloy due to transient heating *Phys. Scr.* **2017** 014009

[972] Spilker B., Linke J., Pintsuk G. and Wirtz M. 2016 Experimental study of ELM-like heat loading on beryllium under ITER operational conditions *Phys. Scr.* **2016** 014024

[973] Spilker B., Linke J., Loewenhoff T., Pintsuk G. and Wirtz M. 2017 High pulse number transient heat loads on beryllium *Nucl. Mater. Energy* **12** 1184–8

[974] Spilker B., Linke J., Pintsuk G. and Wirtz M. 2015 Impact of the surface quality on the thermal shock performance of beryllium armor tiles for first wall applications *Fusion Eng. Des.* **109–111** 1692–6

[975] Spilker B., Linke J., Pintsuk G. and Wirtz M. 2016 Investigation of damages induced by ITER-relevant heat loads during massive gas injections on beryllium *Nucl. Mater. Energy* **9** 145–52

[976] Spilker B., Linke J., Loewenhoff T., Pintsuk G. and Wirtz M. 2019 Performance estimation of beryllium under ITER relevant transient thermal loads *Nucl. Mater. Energy* **18** 291–6

[977] Spilker B., Linke J., Pintsuk G. and Wirtz M. 2017 Thermal shock induced oxidation of beryllium *Phys. Scr.* **T170** 014055

[978] Pintsuk G. 2012 Tungsten as a plasma-facing material *Comprehensive Nuclear Materials* (Elsevier) pp 551–81

[979] Linke J. *et al* 2011 Performance of different tungsten grades under transient thermal loads *Nucl. Fusion* **51** 073017

[980] Wirtz M., Linke J., Loewenhoff T., Pintsuk G. and Uytdenhouwen I. 2017 Transient heat load challenges for plasma-facing materials during long-term operation *Nucl. Mater. Energy* **12** 148–55

[981] Loewenhoff T., Bardin S., Greuner H., Linke J., Maier H., Morgan T.W., Pintsuk G., Pitts R.A., Riccardi B. and De Temmerman G. 2015 Impact of combined transient plasma/heat loads on tungsten performance below and above recrystallization temperature *Nucl. Fusion* **55** 123004

[982] Loewenhoff T., Bürger A., Linke J., Pintsuk G., Schmidt A., Singheiser L. and Thomser C. 2011 Evolution of tungsten degradation under combined high cycle edge-localized mode and steady-state heat loads *Phys. Scr.* **T145** 014057

[983] Loewenhoff T., Linke J., Pintsuk G. and Thomser C. 2012 Tungsten and CFC degradation under combined high cycle transient and steady state heat loads *Fusion Eng. Des.* **87** 1201–5

[984] Greuner H., Maier H., Balden M., Boeswirth B. and Linsmeier C. 2011 Investigation of W components exposed to high thermal and high H/He fluxes *J. Nucl. Mater.* **417** 495–8

[985] Rieth M. 2013 Recent progress in research on tungsten materials for nuclear fusion applications in Europe *J. Nucl. Mater.* **432** 482–500

[986] Panayotis S. *et al* 2017 Self-castellation of tungsten monoblock under high heat flux loading and impact of material properties *Nucl. Mater. Energy* **12** 200–4

[987] Pantleon W. 2021 Thermal stability of the microstructure in rolled tungsten for fusion reactors *Phys. Scr.* **96** 124036

[988] Wirtz M., Uytdenhouwen I., Barabash V., Escourbiac F., Hirai T., Linke J., Loewenhoff T., Panayotis S. and Pintsuk G. 2017 Material properties and their influence on the behaviour of tungsten as plasma facing material *Nucl. Fusion* **57** 066018

[989] Ciucani U.M., Thum A., Devos C. and Pantleon W. 2019 Recovery and recrystallization kinetics of differently rolled, thin tungsten plates in the temperature range from 1325 °C to 1400 °C *Nucl. Mater. Energy* **20** 100701

[990] Ciucani U.M. and Pantleon W. 2019 Stagnant recrystallization in warm-rolled tungsten in the temperature range from 1150 °C to 1300 °C *Fusion Eng. Des.* **146** 814–7

[991] Rasiński M., Kreter A., Torikai Y. and Linsmeier C. 2017 The microstructure of tungsten exposed to D plasma with different impurities *Nucl. Mater. Energy* **12** 302–6

[992] Li Y. *et al* 2021 Recrystallization-mediated crack initiation in tungsten under simultaneous high-flux hydrogen plasma loads and high-cycle transient heating *Nucl. Fusion* **61** 046018

[993] Guo W., Cheng L., De Temmerman G., Yuan Y. and Lu G.-H. 2018 Retarded recrystallization of helium-exposed tungsten *Nucl. Fusion* **58** 106011

[994] Lindig S., Balden M., Alimov V.K., Yamanishi T., Shu W.M. and Roth J. 2009 Subsurface morphology changes due to deuterium bombardment of tungsten *Phys. Scr.* **T138** 014040

[995] Luo G.-N., Shu W.M. and Nishi M. 2005 Incident energy dependence of blistering at tungsten irradiated by low energy high flux deuterium plasma beams *J. Nucl. Mater.* **347** 111–7

[996] Alimov V., Shu W.M., Roth J., Lindig S., Balden M., Isobe K. and Yamanishi T. 2011 Temperature dependence of surface topography and deuterium retention in tungsten exposed to low-energy, high-flux D plasma *J. Nucl. Mater.* **417** 572–5

[997] Manhard A. 2013 Deuterium inventory in tungsten after plasma exposure: a microstructural survey *PhD Thesis* Universität Augsburg

[998] Lindig S., Balden M., Alimov V.K., Manhard A., Höschen C., Höschen T., Tyburska-Püschel B. and Roth J. 2011 Sub-surface structures of ITER-grade W (Japan) and re-crystallized W after ITER-similar low-energy and high-flux D plasma loadings *Phys. Scr.* **T145** 014039

[999] Zibrov M., Balden M., Morgan T. and Mayer M. 2017 Deuterium trapping and surface modification of polycrystalline tungsten exposed to a high-flux plasma at high fluences *Nucl. Fusion* **57** 046004

[1000] Miyamoto M., Nishijima D., Ueda Y., Doerner R.P., Kurishita H., Baldwin M.J., Morito S., Ono K. and Hanna J. 2009 Observations of suppressed retention and blistering for tungsten exposed to deuterium-helium mixture plasmas *Nucl. Fusion* **49** 065035

[1001] Doerner R.P., Baldwin M.J., Nishijima D., Roth J. and Schmid K. 2011 Impact of beryllium surface layers on deuterium retention in tungsten *J. Nucl. Mater.* **415** S717–20

[1002] Yuan Y., Wang T., Kreter A., Reinhart M., Terra A., Möeller S., Cheng L., Linsmeier C. and Lu G.-H. 2021 Influence of neon seeding on the deuterium retention and surface modification of ITER-like forged tungsten *Nucl. Fusion* **61** 016007

[1003] Ueda Y., Shimada T. and Nishikawa M. 2004 Impacts of carbon impurities in hydrogen plasmas on tungsten blistering *Nucl. Fusion* **44** 62–67

[1004] Nishijima D., Iwakiri H., Amano K., Ye M.Y., Ohno N., Tokunaga K., Yoshida N. and Takamura S. 2005 Suppression of blister formation and deuterium retention on tungsten surface due to mechanical polishing and helium pre-exposure *Nucl. Fusion* **45** 669–74

[1005] Manhard A., Balden M. and Von T.U. 2017 Blister formation on rough and technical tungsten surfaces exposed to deuterium plasma *Nucl. Fusion* **57** 126012

[1006] Shu W., Kawasuso A., Miwa Y., Wakai E., Luo G.-N. and Yamanishi T. 2007 Microstructure dependence of deuterium retention and blistering in the near-surface region of tungsten exposed to high flux deuterium plasmas of 38 eV at 315 K *Phys. Scr.* **T128** 96–99

[1007] Jia Y.Z., Liu W., Xu B., Luo G.-N., Qu S.L., Morgan T.W. and De Temmerman G. 2016 Mechanism for orientation dependence of blisters on W surface exposed to D plasma at low temperature *J. Nucl. Mater.* **477** 165–71

[1008] Baldwin M.J. and Doerner R.P. 2008 Helium induced nanoscopic morphology on tungsten under fusion relevant plasma conditions *Nucl. Fusion* **48** 035001

[1009] Takamura S., Ohno N., Nishijima D. and Kajita S. 2006 Formation of nanostructured tungsten with arborescent shape due to helium plasma irradiation *Plasma Fusion Res.* **1** 051–051

[1010] Kajita S., Sakaguchi W., Ohno N., Yoshida N. and Saeki T. 2009 Formation process of tungsten nanostructure by the exposure to helium plasma under fusion relevant plasma conditions *Nucl. Fusion* **49** 095005

[1011] Nishijima D., Ye M.Y., Ohno N. and Takamura S. 2004 Formation mechanism of bubbles and holes on tungsten surface with low-energy and high-flux helium plasma irradiation in NAGDIS-II *J. Nucl. Mater.* **329–333** 1029–33

[1012] Tamura T., Kobayashi R., Ogata S. and Ito A.M. 2013 First-principles investigation of possible clustering of noble gas atoms implanted in bcc tungsten *Modelling Simul. Mater. Sci. Eng.* **22** 015002

[1013] Wirth B.D., Hammond K.D., Krasheninnikov S.I. and Maroudas D. 2015 Challenges and opportunities of modeling plasma-surface interactions in tungsten using high-performance computing *J. Nucl. Mater.* **463** 30–38

[1014] Kajita S., Yoshida N., Yoshihara R., Ohno N. and Yamagiwa M. 2011 TEM observation of the growth process of helium nanobubbles on tungsten: nanostructure formation mechanism *J. Nucl. Mater.* **418** 152–8

[1015] Wang K., Doerner R.P., Baldwin M.J., Meyer F.W., Bannister M.E., Darbal A., Stroud R. and Parish C.M. 2017 Morphologies of tungsten nanotendrils grown under helium exposure *Sci. Rep.* **7** 42315

[1016] Baldwin M.J., Doerner R.P., Nishijima D., Tokunaga K. and Ueda Y. 2009 The effects of high fluence mixed-species (deuterium, helium, beryllium) plasma interactions with tungsten *J. Nucl. Mater.* **390–391** 886–90

[1017] De Temmerman G., Bystrov K., Doerner R.P., Marot L., Wright G.M., Woller K.B., Whyte D.G. and Zielinski J.J. 2013 Helium effects on tungsten under fusion-relevant plasma loading conditions *J. Nucl. Mater.* **438** 78–83

[1018] De Temmerman G., Morgan T.W., van Eden G.G., de Kruif T., Wirtz M., Matejicek J., Chraska T., Pitts R.A. and Wright G.M. 2015 Effect of high-flux H/He plasma exposure on tungsten damage due to transient heat loads *J. Nucl. Mater.* **463** 198–201

[1019] Takamura S., Miyamoto T., Tomida Y., Minagawa T. and Ohno N. 2011 Investigation on the effect of temperature excursion on the helium defects of tungsten surface by using compact plasma device *J. Nucl. Mater.* **415** S100–3

[1020] Kajita S., De Temmerman G., Morgan T., van Eden S., de Kruif T. and Ohno N. 2014 Thermal response of nanostructured tungsten *Nucl. Fusion* **54** 033005

[1021] Yajima M., Yoshida N., Kajita S., Tokitani M., Baba T. and Ohno N. 2014 *In situ* observation of structural change of nanostructured tungsten during annealing *J. Nucl. Mater.* **449** 9–14

[1022] Nishijima D., Baldwin M.J., Doerner R.P. and Yu J.H. 2011 Sputtering properties of tungsten ‘fuzzy’ surfaces *J. Nucl. Mater.* **415** S96–S99

[1023] Takamura S., Miyamoto T. and Ohno N. 2012 Effects of fibre-form nanostructures on particle emissions from a tungsten surface in plasmas *Nucl. Fusion* **52** 123001

[1024] Kajita S., Yagi T., Kobayashi K., Tokitani M. and Ohno N. 2016 Measurement of thermophysical property of plasma forming tungsten nanofiber layer *Jpn. J. Appl. Phys.* **55** 056203

[1025] Doerner R.P., Nishijima D., Krasheninnikov S.I., Schwarz-Selinger T. and Zach M. 2018 Motion of W and He atoms during formation of W fuzz *Nucl. Fusion* **58** 066005

[1026] Takamura S. and Uesugi Y. 2015 Experimental identification for physical mechanism of fiber-form nanostructure growth on metal surfaces with helium plasma irradiation *Appl. Surf. Sci.* **356** 888–97

[1027] Hammond K.D. 2017 Helium, hydrogen and fuzz in plasma-facing materials *Mater. Res. Express* **4** 104002

[1028] Kajita S., Ito A.M. and Ibano K. 2022 Growth of fiberform nanostructures on metal surfaces by helium plasma irradiation *J. Appl. Phys.* **132** 181101

[1029] Patino M.I., Nishijima D., Tokitani M., Nagata D. and Doerner R.P. 2020 Material mixing during fuzz formation in W and Mo *Phys. Scr.* **T171** 014070

[1030] Patino M.I., Nishijima D., Tokitani M., Nagata D., Yu J.H. and Doerner R.P. 2021 Material migration in W and Mo during bubble growth and fuzz formation *Nucl. Fusion* **61** 076001

[1031] Woller K.B., Whyte D.G. and Wright G.M. 2017 Impact of helium ion energy modulation on tungsten surface morphology and nano-tendril growth *Nucl. Fusion* **57** 066005

[1032] Al-Ajlony A., Tripathi J.K. and Hassanein A. 2015 Role of carbon impurities on the surface morphology evolution of tungsten under high dose helium ion irradiation *J. Nucl. Mater.* **466** 569–75

[1033] Hwangbo D., Kajita S., Ohno N., McCarthy P., Bradley J.W. and Tanaka H. 2018 Growth of nano-tendril bundles on tungsten with impurity-rich He plasmas *Nucl. Fusion* **58** 096022

[1034] Kajita S., Kawaguchi S., Hwangbo D., Tanaka H. and Ohno N. 2018 Pulsation effects of incident ion energy on W fuzz growth *Plasma Fusion Res.* **13** 1205001

[1035] Kajita S., Kawaguchi S., Ohno N. and Yoshida N. 2018 Enhanced growth of large-scale nanostructures with metallic ion precipitation in helium plasmas *Sci. Rep.* **8** 56

[1036] Sakamoto R., Bernard E., Kreter A. and Yoshida N. 2016 Surface morphology of tungsten exposed to helium plasma at temperatures below fuzz formation threshold 1073 K *Nucl. Fusion* **57** 016040

[1037] Ohno N., Hirahata Y., Yamagiwa M., Kajita S., Takagi M., Yoshida N., Yoshihara R., Tokunaga T. and Tokitani M. 2013 Influence of crystal orientation on damages of tungsten exposed to helium plasma *J. Nucl. Mater.* **438** S879–82

[1038] Parish C.M., Hijazi H., Meyer H.M. and Meyer F.W. 2014 Effect of tungsten crystallographic orientation on He-ion-induced surface morphology changes *Acta Mater.* **62** 173–81

[1039] Nogami S., Hasegawa A., Fukuda M., Rieth M., Reiser J. and Pintsuk G. 2021 Mechanical properties of tungsten: recent research on modified tungsten materials in Japan *J. Nucl. Mater.* **543** 152506

[1040] Huber A. *et al* 2015 Combined impact of transient heat loads and steady-state plasma exposure on tungsten *Fusion Eng. Des.* **98–99** 1328–32

[1041] Cotterill P. 1961 The hydrogen embrittlement of metals *Prog. Mater. Sci.* **9** 205–301

[1042] Miyazawa T., Hwang T., Tsuchida K., Hattori T., Fukuda M., Nogami S. and Hasegawa A. 2018 Effects of helium on mechanical properties of tungsten for fusion applications *Nucl. Mater. Energy* **15** 154–7

[1043] Hasegawa A., Miyazawa T., Itou D., Hattori T., Yohida K. and Nogami S. 2020 Helium effects on recovery and recrystallization of powder metallurgically processed tungsten *Phys. Scr.* **T171** 014016

[1044] Guo W. *et al* 2020 Effect of helium ion irradiation on tungsten recrystallization *Phys. Scr.* **2020** 014004

[1045] Hasegawa A., Sato Y., Hattori T., Kanamaru R., Du L., Miyazawa T. and Nogami S. 2021 Helium effects on tensile properties of powder metallurgical-processed tungsten for fusion reactor applications *Nucl. Mater. Energy* **29** 101076

[1046] Song K., Thompson M., De Temmerman G. and Corr C.S. 2019 Temperature dependence of retarded recrystallisation in helium plasma-exposed tungsten *Nucl. Fusion* **59** 096031

[1047] Khan A. *et al* 2020 Helium irradiation effects on the surface modification and recrystallization of tungsten *Phys. Scr.* **2020** 014050

[1048] Shah V., Beune J.T.S., Li Y., Loewenhoff T., Wirtz M., Morgan T.W. and van Dommelen J.A.W. 2021 Recrystallization behaviour of high-flux hydrogen plasma exposed tungsten *J. Nucl. Mater.* **545** 152748

[1049] Mattox D.M. and Sharp D.J. 1979 Influence of surface morphology on the low energy hydrogen ion erosion yields of beryllium *J. Nucl. Mater.* **80** 115–9

[1050] Miyamoto M., Sugimoto Y., Nishijima D., Baldwin M.J., Doerner R.P., Zaloznik A., Kim J.H. and Nakamichi M. 2021 Comparative study of surface modification and D retention between beryllium and beryllides under high flux plasma exposure *Nucl. Mater. Energy* **27** 101014

[1051] Doerner R.P., Nishijima D. and Schwarz-Selinger T. 2014 Impact of surface morphology on sputtering during high-fluence plasma exposure *Phys. Scr.* **T159** 014040

[1052] Doerner R.P., Baldwin M.J. and Nishijima D. 2014 Plasma-induced morphology of beryllium targets exposed in PISCES-B *J. Nucl. Mater.* **455** 1–4

[1053] Ouaras K., Hassouni K., Delacqua L.C., Lombardi G., Vrel D. and Bonnin X. 2015 Tungsten dust nanoparticles generation from blistering bursts under hydrogen environment in microwave ECR discharge *J. Nucl. Mater.* **466** 65–68

[1054] Song J., Kim N.-K., Kim H.-S., Jin Y., Roh K.-B. and Kim G.-H. 2016 Deuterium ion irradiation induced blister formation and destruction *Fusion Eng. Des.* **109–111** 624–8

[1055] Herrmann A., Greuner H., Jaksic N., Balden M., Kallenbach A., Krieger K., de Marné P., Rohde V., Scarabosio A. and Schall G. 2015 Solid tungsten Divertor-III for ASDEX Upgrade and contributions to ITER *Nucl. Fusion* **55** 063015

[1056] Lipschultz B., Coenen J.W., Barnard H.S., Howard N.T., Reinke M.L., Whyte D.G. and Wright G.M. 2012 Divertor tungsten tile melting and its effect on core plasma performance *Nucl. Fusion* **52** 123002

[1057] Matthews G.F. 2013 Plasma operation with an all metal first-wall: comparison of an ITER-like wall with a carbon wall in JET *J. Nucl. Mater.* **438** S2–S10

[1058] Yao D.M. *et al* 2015 Design, R & D and commissioning of EAST tungsten divertor *Phys. Scr.* **T167** 014003

[1059] Bucalossi J. *et al* 2022 Operating a full tungsten actively cooled tokamak: overview of WEST first phase of operation *Nucl. Fusion* **62** 042007

[1060] Gunn J.P. *et al* 2021 Thermal loads in gaps between ITER divertor monoblocks: first lessons learnt from WEST *Nucl. Mater. Energy* **27** 100920

[1061] Durif A., Richou M., Corre Y., Delommez C. and Gunn J.-P. 2022 Leading edge cracking observed in WEST *Phys. Scr.* **97** 074004

[1062] Li J. and Wan Y. 2021 The Experimental Advanced Superconducting Tokamak *Engineering* **7** 1523–8

[1063] Zhu D. *et al* 2023 *In situ* melting phenomena on W plasma-facing components for lower divertor during long-pulse plasma operations in EAST *Nucl. Fusion* **63** 036022

[1064] Gao B., Ding R., Zhang L., Li C., Xie H., Zeng L., Yang J., Wang B., Zhu D. and Chen J. 2021 Impact of W monoblock damage on EAST operations in recent campaigns *Fusion Eng. Des.* **169** 112623

[1065] Xi Y., He G., Zan X., Wang K., Zhu D., Luo L., Ding R. and Wu Y. 2023 Characterization of the crack and recrystallization of W/Cu monoblocks of the upper divertor in EAST *Appl. Sci.* **13** 745

[1066] Zammuto I. *et al* 2018 Cracks avoidance with a modified solid tungsten divertor in ASDEX Upgrade *Fusion Eng. Des.* **136** 1052–7

[1067] Neu R. *et al* 2017 Investigations on tungsten heavy alloys for use as plasma facing material *Fusion Eng. Des.* **124** 450–4

[1068] Yao G., Shen X., Liu J.-Q., Zhu X.-Y., Luo L. and Wu Y. 2024 Study on damage behavior of the outer horizontal target in the EAST lower divertor after plasma operations *Nucl. Mater. Energy* **39** 101640

[1069] Krieger K. *et al* 2020 Impact of H-mode plasma operation on pre-damaged tungsten divertor tiles in ASDEX Upgrade *Phys. Scr.* **T171** 014037

[1070] Richou M. *et al* 2021 First plasma exposure of a pre-damaged ITER-like plasma facing unit in the WEST tokamak: procedure for the PFU preparation and lessons learnt *Nucl. Fusion* **62** 056010

[1071] Corre Y. *et al* 2023 Plasma exposure of a pre-damaged ITER-like plasma facing unit in the WEST tokamak:

in-situ and post-mortem measurements *Nucl. Mater. Energy* **34** 101366

[1072] Taylor N. and Cortes P. 2014 Lessons learnt from ITER safety and licensing for DEMO and future nuclear fusion facilities *Fusion Eng. Des.* **89** 1995–2000

[1073] Ratynskaia S., Bortolon A. and Krasheninnikov S.I. 2022 Dust and powder in fusion plasmas: recent developments in theory, modeling and experiments *Rev. Mod. Plasma Phys.* **6** 20

[1074] Balden M., Endstrasser N., Humrickhouse P.W., Rohde V., Rasinski M., von Toussaint U., Elgeti S. and Neu R. 2014 Collection strategy, inner morphology and size distribution of dust particles in ASDEX Upgrade *Nucl. Fusion* **54** 073010

[1075] Ratynskaia S. *et al* 2018 Interaction of metal dust adhered on castellated substrates with the ELMy H-mode plasmas of ASDEX-Upgrade *Nucl. Fusion* **58** 106023

[1076] Arnas C. *et al* 2023 Micron-sized dust and nanoparticles produced in the WEST tokamak *Nucl. Mater. Energy* **36** 101471

[1077] Arnas C. *et al* 2017 Characterization and origin of large size dust particles produced in the Alcator C-Mod tokamak *Nucl. Mater. Energy* **11** 12–19

[1078] Manhard A. and Gao L. 2018 Blisters formed by D plasma exposure in an electron-transparent tungsten sample *Nucl. Mater. Energy* **17** 248–52

[1079] Wright G.M., Brunner D., Baldwin M.J., Doerner R.P., Labombard B., Lipschultz B., Terry J.L. and Whyte D.G. 2012 Tungsten nano-tendril growth in the Alcator C-Mod divertor *Nucl. Fusion* **52** 042003

[1080] Wright G.M. *et al* 2013 Comparison of tungsten nano-tendrils grown in Alcator C-Mod and linear plasma devices *J. Nucl. Mater.* **438** 84–89

[1081] Rudakov D.L. *et al* 2016 Exposures of tungsten nanostructures to divertor plasmas in DIII-D *Phys. Scr.* **2016** 014055

[1082] Tokitani M., Masuzaki S., Kasahara H., Yoshimura Y., Sakamoto R., Yoshida N., Ueda Y., Mutoh T. and Nagata S. 2017 Initial growth phase of W-fuzz formation in ultra-long pulse helium discharge in LHD *Nucl. Mater. Energy* **12** 1358–62

[1083] Rasiński M. *et al* 2023 FIB line marking as a tool for local erosion/deposition/fuzz formation measurements in ASDEX Upgrade during the He campaign *Nucl. Mater. Energy* **37** 101539

[1084] Brooks J.N. 2013 Analysis of tungsten migration from the C-MOD divertor; prediction of high redeposition rate and code validation progress *Nucl. Fusion* **53** 042001

[1085] Neu R. *et al* 1996 The tungsten divertor experiment at ASDEX Upgrade *Plasma Phys. Control. Fusion* **38** A165–79

[1086] Guterl J., Abrams T., Johnson C.A., Jaervinen A., Wang H.Q., McLean A.G., Rudakov D., Wampler W.R., Guo H.Y. and Snyder P. 2019 ERO modeling and analysis of tungsten erosion and migration from a toroidally symmetric source in the DIII-D divertor *Nucl. Fusion* **60** 016018

[1087] Gunn J.P., Hirai T., Corre Y., Escourbiac F., Grosjean A. and Pitts R.A. 2019 A study of planar toroidal-poloidal beveling of monoblocks on the ITER divertor outer vertical target *Nucl. Fusion* **59** 126043

[1088] Gunn J.P., Carpentier-Chouchana S., Dejarnac R., Escourbiac F., Hirai T., Komm M., Kukushkin A., Panayotis S. and Pitts R.A. 2017 Ion orbit modelling of ELM heat loads on ITER divertor vertical targets *Nucl. Mater. Energy* **12** 75–83

[1089] Corre Y. *et al* 2023 Testing of ITER-grade plasma facing units in the WEST tokamak: progress in understanding heat loading and damage mechanisms *Nucl. Mater. Energy* **37** 101546

[1090] Durif A., Richou M., Bergheau J.-M., Gallais L., Kermouche G. and Pintsuk G. 2022 T-REX: numerical tool for tungsten damage assessment for DEMO *J. Nucl. Mater.* **569** 153906

[1091] Durif A., Richou M., Bergheau J.-M., Corre Y., Diez M., Reilhac P., Gunn J.P. and Tsitrone E. 2023 Edge cracking of WEST tungsten actively cooled plasma facing components after plasma operation *Fusion Eng. Des.* **188** 113441

[1092] Richou M., Durif A., Lenci M., Mondon M., Minissale M., Gallais L., Kermouche G. and De Temmerman G. 2020 Recrystallization at high temperature of two tungsten materials complying with the ITER specifications *J. Nucl. Mater.* **542** 152418

[1093] Dejarnac R., Gunn J.P., Vondracek P., Komm M., Panek R. and Pitts R.A. 2019 Physics of toroidal gap heat loading on castellated plasma-facing components *Nucl. Mater. Energy* **19** 19–27

[1094] Krieger K. *et al* 2023 Investigation of ELM-related Larmor ion flux into toroidal gaps of divertor target plates *Nucl. Fusion* **63** 066021

[1095] De Temmerman G., Daniels J., Bystrov K., van den Berg M.A. and Zielinski J.J. 2013 Melt-layer motion and droplet ejection under divertor-relevant plasma conditions *Nucl. Fusion* **53** 023008

[1096] Greuner H., Böswirth B., Hunger K., Khan A., Barrett T.R., Gallay F., Richou M., Visca E., Müller A.V. and You J.H. 2020 Assessment of the high heat flux performance of European DEMO divertor mock-ups *Phys. Scr.* **T171** 014003

[1097] Neu R. *et al* 2023 Material and component developments for the DEMO divertor using fibre reinforcement and additive manufacturing *Mater. Res. Express* **10** 116516

[1098] You J. *et al* 2022 Divertor of the European DEMO: engineering and technologies for power exhaust *Fusion Eng. Des.* **175** 113010

[1099] You J.-H., Greuner H., Böswirth B., Hunger K., Roccella S. and Roche H. 2022 High-heat-flux performance limit of tungsten monoblock targets: impact on the armor materials and implications for power exhaust capacity *Nucl. Mater. Energy* **33** 101307

[1100] You J. *et al* 2022 Limiters for DEMO wall protection: initial design concepts and technology options *Fusion Eng. Des.* **174** 112988

[1101] Mitteau R., Sugihara M., Raffray R., Carpentier-Chouchana S., Labidi H., Merola M., Pitts R.A. and Stangeby P. 2011 Lifetime analysis of the ITER first wall under steady-state and off-normal loads *Phys. Scr.* **T145** 014081

[1102] Lehnen M. *et al* 2015 Disruptions in ITER and strategies for their control and mitigation *Nucl. Mater. Energy* **463** 39

[1103] Lehnen M. *et al* 2016 Plasma disruption management *ITER 26th IAEAFusion Energy Conf.—Programme, Contributions and Conf. Material (Kyoto, Japan, 17–22 October 2016)* (International Atomic Energy Agency (IAEA)) EX P6–39 (available at: https://nucleus.iaea.org/sites/fusionportal/Shared%20Documents/FEC%202016/fec2016-preprints/preprint0314.pdf)

[1104] Komm M., Gunn J.P., Dejarnac R., Pánek R., Pitts R.A. and Podolník A. 2017 Particle-in-cell simulations of the plasma interaction with poloidal gaps in the ITER divertor outer vertical target *Nucl. Fusion* **57** 126047

[1105] Dejarnac R. *et al* 2018 Heat loads on poloidal and toroidal edges of castellated plasma-facing components in COMPASS *Nucl. Fusion* **58** 066003

[1106] Hong S.-H., Pitts R.A., Lee H.-H., Bang E., Kang C.-S., Kim K.-M. and Kim H.-T. 2017 Inter-ELM heat loads on tungsten leading edge in the KSTAR divertor *Nucl. Mater. Energy* **12** 1122–9

[1107] Herrmann A., Greuner H., Fuchs J.C., de Marné P. and Neu R. 2009 Experiences with tungsten coatings in high heat flux tests and under plasma load in ASDEX Upgrade *Phys. Scr.* **T138** 014059

[1108] Herrmann A., Zammuto I., Balden M., Greuner H., Jaksic N., Kallenbach A., Li M., Neu R. and Rohde V. 2017 Experiences with a solid tungsten divertor in ASDEX Upgrade *Nucl. Mater. Energy* **12** 205–9

[1109] Coenen J.W., Krieger K., Lipschultz B., Dux R., Kallenbach A., Lunt T., Mueller H.W., Potzel S., Neu R. and Terra A. 2013 Evolution of surface melt damage, its influence on plasma performance and prospects of recovery *J. Nucl. Mater.* **438** S27–S33

[1110] Gao B., Ding R., Xie H., Zeng L., Zhang L., Wang B., Li C., Zhu D., Yan R. and Chen J. 2020 Plasma-facing components damage and its effects on plasma performance in EAST tokamak *Fusion Eng. Des.* **156** 111616

[1111] Lei Y. *et al* 2021 Result and discussion on the evolution of *in-situ* leading edge-induced melting on W divertor targets in EAST *Nucl. Mater. Energy* **27** 100997

[1112] Zhu D., Li C., Ding R., Wang B., Chen J., Gao B., Gu Y. and Gong X. 2020 Characterization of the *in situ* leading-edge-induced melting on the ITER-like tungsten divertor in EAST *Nucl. Fusion* **60** 016036

[1113] Li C., Zhu D., Ding R., Wang B., Chen J., Gao B. and Lei Y. 2020 Characterization on the melting failure of CuCrZr cooling tube of W/Cu monoblocks during plasma operations in EAST *Nucl. Mater. Energy* **25** 100847

[1114] Sergienko G. *et al* 2007 Erosion of a tungsten limiter under high heat flux in TEXTOR *J. Nucl. Mater.* **363–365** 96–100

[1115] Sergienko G. *et al* 2007 Experience with bulk tungsten test-limiters under high heat loads: melting and melt layer propagation *Phys. Scr.* **T128** 81

[1116] Coenen J.W., Philipps V., Brezinsek S., Bazylev B., Kreter A., Hirai T., Laengner M., Tanabe T., Ueda Y. and Samm U. 2011 Analysis of tungsten melt-layer motion and splashing under tokamak conditions at TEXTOR *Nucl. Fusion* **51** 083008

[1117] Coenen J.W. *et al* 2011 Tungsten melt layer motion and splashing on castellated tungsten surfaces at the tokamak TEXTOR *J. Nucl. Mater.* **415** S78–S82

[1118] Coenen J.W. *et al* 2012 Material and power-handling properties of tungsten PFCs after steady-state melting and additional transient high-heat-flux exposure *Fusion Sci. Technol.* **61** 129–35

[1119] Komm M., Ratynskaia S., Tolias P. and Podolnik A. 2020 Space-charge limited thermionic sheaths in magnetized fusion plasmas *Nucl. Fusion* **60** 054002

[1120] Coenen J.W. *et al* 2015 ELM-induced transient tungsten melting in the JET divertor *Nucl. Fusion* **55** 023010

[1121] Matthews G.F. *et al* 2016 Melt damage to the JET ITER-Like Wall and divertor *Phys. Scr.* **T167** 014070

[1122] Ratynskaia S., Thorén E., Tolias P., Pitts R.A., Krieger K., Vignitchouk L. and Iglesias D. 2020 Resolidification-controlled melt dynamics under fast transient tokamak plasma loads *Nucl. Fusion* **60** 104001

[1123] Thorén E., Ratynskaia S., Tolias P. and Pitts R.A. 2021 The MEMOS-U code description of macroscopic melt dynamics in fusion devices *Plasma Phys. Control. Fusion* **63** 035021

[1124] Krieger K. *et al* 2018 Experiments on transient melting of tungsten by ELMs in ASDEX Upgrade *Nucl. Fusion* **58** 026024

[1125] Krieger K. *et al* 2017 Investigation of transient melting of tungsten by ELMs in ASDEX Upgrade *Phys. Scr.* **T170** 014030

[1126] Thorén E., Ratynskaia S., Tolias P., Pitts R.A., Krieger K., Komm M. and Balden M. 2018 MEMOS 3D modelling of ELM-induced transient melt damage on an inclined tungsten surface in the ASDEX Upgrade outer divertor *Nucl. Mater. Energy* **17** 194–9

[1127] Jepu I. *et al* 2019 Beryllium melting and erosion on the upper dump plates in JET during three ITER-like wall campaigns *Nucl. Fusion* **59** 086009

[1128] Ratynskaia S., Thorén E., Tolias P., Pitts R.A. and Krieger K. 2021 The MEMOS-U macroscopic melt dynamics code-benchmarking and applications *Phys. Scr.* **96** 124009

[1129] Corre Y. *et al* 2021 Sustained W-melting experiments on actively cooled ITER-like plasma facing unit in WEST *Phys. Scr.* **96** 124057

[1130] Ratynskaia S., Paschalidis K., Tolias P., Krieger K., Corre Y., Balden M., Faitsch M., Grosjean A., Tichit Q. and Pitts R.A. 2022 Experiments and modelling on ASDEX Upgrade and WEST in support of tool development for tokamak reactor armour melting assessments *Nucl. Mater. Energy* **33** 101303

[1131] Krieger K., Lunt T., Dux R., Janzer A., Kallenbach A., Müller H.W., Neu R., Pütterich T. and Rohde V. 2011 Induced tungsten melting events in the divertor of ASDEX Upgrade and their influence on plasma performance *J. Nucl. Mater.* **415** S297–300

[1132] Krieger K., Lunt T., Dux R., Janzer A., Müller H.W., Potzel S., Pütterich T. and Yang Z. 2011 Controlled tungsten melting and droplet ejection studies in ASDEX Upgrade *Phys. Scr.* **T145** 014067

[1133] Yang Z., Krieger K., Lunt T., Brochard F., Briancon J.-L., Neu R., Dux R., Janzer A., Potzel S. and Pütterich T. 2013 3D trajectories re-construction of droplets ejected in controlled tungsten melting studies in ASDEX Upgrade *J. Nucl. Mater.* **438** S846–51

[1134] Iglesias D. *et al* 2018 An improved model for the accurate calculation of parallel heat fluxes at the JET bulk tungsten outer divertor *Nucl. Fusion* **58** 106034

[1135] Coenen J.W. *et al* 2017 Transient induced tungsten melting at the Joint European Torus (JET) *Phys. Scr.* **T170** 014013

[1136] Vignitchouk L., Ratynskaia S., Pitts R.A. and Lehnen M. (JET Contributors) 2022 Simulations of liquid metal flows over plasma-facing component edges and application to beryllium melt events in JET *Nucl. Fusion* **62** 036016

[1137] Ratynskaia S., Paschalidis K., Krieger K., Vignitchouk L., Tolias P., Balden M., Faitsch M., Rohde V., Corre Y. and Pitts R.A. 2024 Metallic melt transport across castellated tiles *Nucl. Fusion* **64** 036012

[1138] Shoshin A.A. *et al* 2011 Plasma-surface interaction during ITER type I ELMs: comparison of simulation with QSPA Kh-50 and the GOL-3 facilities *Fusion Sci. Technol.* **59** 57–60

[1139] Klimov N. *et al* 2011 Experimental study of PFCs erosion and eroded material deposition under ITER-like transient loads at the plasma gun facility QSPA-T *J. Nucl. Mater.* **415** S59–S64

[1140] Kupriyanov I.B., Nikolaev G.N., Kurbatova L.A., Porezanov N.P., Podkovyrov V.L., Muzichenko A.D., Zhitlukhin A.M., Gervash A.A. and Safronov V.M. 2015 Erosion of beryllium under ITER-relevant transient plasma loads *J. Nucl. Mater.* **463** 781–6

[1141] Klimov N.S. *et al* 2017 Beryllium layer response to ITER-like ELM plasma pulses in QSPA-Be *Nucl. Mater. Energy* **12** 433–40

[1142] Arzhannikov A.V. *et al* 2013 Surface modification and droplet formation of tungsten under hot plasma irradiation at the GOL-3 *J. Nucl. Mater.* **438** S677–80

[1143] Morgan T.W., van Eden G.G., de Kruif T.M., van den Berg M.A., Matejicek J., Chraska T. and De Temmerman G. 2014 ELM-induced melting: assessment of shallow melt layer damage and the power handling capability of tungsten in a linear plasma device *Phys. Scr.* **T159** 014022

[1144] Garkusha I.E., Arkhipov N.I., Klimov N.S., Makhlaj V.A., Safronov V.M., Landman I. and Tereshin V.I. 2009 The latest results from ELM-simulation experiments in plasma accelerators *Phys. Scr.* **T138** 014054

[1145] Garkusha I.E., Makhlai V.A., Aksenov N.N., Bazylev B., Landman I., Sadowski M. and Skladnik-Sadowska E. 2014 Tungsten melt losses under QSPA Kh-50 plasma exposures simulating ITER ELMs and disruptions *Fusion Sci. Technol.* **65** 186–93

[1146] Makhlai V.A. *et al* 2019 Influence of surface tension on macroscopic erosion of castellated tungsten surfaces during repetitive transient plasma loads *Nucl. Mater. Energy* **19** 493

[1147] Makhlai V.A., Herashchenko S.S., Aksenov N.N., Byrka O.V., Garkusha I.E., Wirtz M. and Spilker B. 2020 Damaging of inclined/misaligned castellated tungsten surfces exposed to a large number of repetitive QSPA plasma loads *Phys. Scr.* **T171** 014047

[1148] Berger M., Coursey J., Zucker M. and Chang J. 2005 *Estar, Pstar and Astar: Computer Programs for Calculating Stopping-Power and Range tables for Electrons, Protons and Helium Ions (Version 1.2.3)* (National Institute of Standards and Technology)

[1149] Berger M. and Seltzer S. 1964 *tables of Energy Losses and Ranges of Electrons and Positrons* (National Aeronautics and Space Administration)

[1150] Sizyuk V. and Hassanein A. 2009 Self-consistent analysis of the effect of runaway electrons on plasma facing components in ITER *Nucl. Fusion* **49** 095003

[1151] De A.M. *et al* 2023 Evidence for high-velocity solid dust generation induced by runaway electron impact in FTU *Nucl. Fusion* **63** 014001

[1152] Ratynskaia S., Vignitchouk L. and Tolias P. 2022 Modelling of dust generation, transport and remobilization in full-metal fusion reactors *Plasma Phys. Control. Fusion* **64** 044004

[1153] Thorén E., Tolias P., Ratynskaia S., Pitts R.A. and Krieger K. 2018 Self-consistent description of the replacement current driving melt layer motion in fusion devices *Nucl. Fusion* **58** 106003

[1154] Pitts R.A. *et al* 2015 Final case for a stainless steel diagnostic first wall on ITER *J. Nucl. Mater.* **463** 748–52

[1155] Coburn J. *et al* 2022 Energy deposition and melt deformation on the ITER first wall due to disruptions and vertical displacement events *Nucl. Fusion* **62** 016001

[1156] Çengel Y.A. and Cimbala J.M. 2006 *Fluid Mechanics: Fundamentals and Applications* (McGraw-Hill)

[1157] de Gennes P.G. 1985 Wetting: statics and dynamics *Rev. Mod. Phys.* **57** 827–63

[1158] Eustathopoulos N., Nicholas M.G. and Drevet B. 1999 *Wettability at High Temperatures* vol 3 (Pergamon)

[1159] Herring C. and Nichols M.H. 1949 Thermionic emission *Rev. Mod. Phys.* **21** 185–270

[1160] Nottingham W.B. 1956 *Thermionic Emission* (Springer) pp 1–175

[1161] Bronshtein I.M. and Fraiman B.C. 1969 *Vtorichnaya Elektronnaya Emissiya (Secondary Electron Emission)* (Nauka)

[1162] Tolias P. 2014 On electron backscattering from dust grains in fusion plasmas *Plasma Phys. Control. Fusion* **56** 045003

[1163] Tolias P. 2014 On secondary electron emission and its semi-empirical description *Plasma Phys. Control. Fusion* **56** 123002

[1164] Abroyan I.A., Eremeev M.A. and Petrov N.N. 1967 Excitation of electrons in solids by relatively slow atomic particles *Sov. Phys. - Usp.* **10** 332–67

[1165] Hasselkamp D. *et al* 1992 *Particle Induced Electron Emission II* (Springer)

[1166] Vignitchouk L., Ratynskaia S., Tolias P., Pitts R.A., De Temmerman G., Lehnen M. and Kiramov D. 2018 Survival and in-vessel redistribution of beryllium droplets after ITER disruptions *Nucl. Fusion* **58** 076008

[1167] Tolias P., Komm M., Ratynskaia S. and Podolnik A. 2023 ITER relevant multi-emissive sheaths at normal magnetic field inclination *Nucl. Fusion* **63** 026007

[1168] Tolias P., Komm M., Ratynskaia S. and Podolnik A. 2020 Origin and nature of the emissive sheath surrounding hot tungsten tokamak surfaces *Nucl. Mater. Energy* **25** 100818

[1169] Hobbs G.D. and Wesson J.A. 1967 Heat flow through a Langmuir sheath in presence of electron emission *Plasma Phys.* **9** 85

[1170] Takamura S., Ohno N., Ye M.Y. and Kuwabara T. 2004 Space-charge limited current from plasma-facing material surface *Contrib. Plasma Phys.* **44** 126

[1171] Tskhakaya D. and Kuhn S. 2000 Influence of initial energy on the effective secondary-electron emission coefficient in the presence of an oblique magnetic field *Contrib. Plasma Phys.* **40** 484

[1172] Igitkhanov Y. and Janeschitz G. 2001 Attenuation of secondary electron emission from divertor plates due to magnetic field inclination *J. Nucl. Mater.* **290–293** 99

[1173] Komm M., Ratynskaia S., Tolias P., Cavalier J., Dejarnac R., Gunn J.P. and Podolnik A. 2017 On thermionic emission from plasma-facing components in tokamak-relevant conditions *Plasma Phys. Control. Fusion* **59** 094002

[1174] Komm M., Tolias P., Ratynskaia S., Dejarnac R., Gunn J.P., Krieger K., Podolnik A., Pitts R.A. and Panek R. 2017 Simulations of thermionic suppression during tungsten transient melting experiments *Phys. Scr.* **T170** 014069

[1175] Campanell M.D. 2013 Negative plasma potential relative to electron-emitting surfaces *Phys. Rev.* E **88** 033103

[1176] Campanell M.D. and Umansky M.V. 2016 Strongly emitting surfaces unable to float below plasma potential *Phys. Rev. Lett.* **116** 085003

[1177] Campanell M.D. and Umansky M.V. 2017 Are two plasma equilibrium states possible when the emission coefficient exceeds unity? *Phys. Plasmas* **24** 057101

[1178] Campanell M.D. 2020 Possible mitigation of tokamak plasma-surface interactions using thermionic divertor plates with inverse sheaths *Phys. Plasmas* **27** 042511

[1179] Campanell M.D. and Johnson G.R. 2019 Thermionic cooling of the target plasma to a sub-eV temperature *Phys. Rev. Lett.* **122** 015003

[1180] Knudsen M. 1950 *Kinetic Theory of Gases* 3rd edn (Wiley)

[1181] Antoine C. 1888 Tensions des vapeurs: nouvelle relation entre les tensions et les temperatures *C. R. Séances Acad. Sci.* **107** 681–4

[1182] Krasheninnikov S.I., Pigarov A.Y. and Lee W. 2015 Physics of the edge plasma and first wall in fusion devices: synergistic effects *Plasma Phys. Control. Fusion* **57** 044009

[1183] Skovorodin D.I., Pshenov A.A., Arakcheev A.S., Eksaeva E.A., Marenkov E.D. and Krasheninnikov S.I. 2016 Vapor shielding models and the energy absorbed by

divertor targets during transient events *Phys. Plasmas* **23** 022501
[1184] Bejan A. and Kraus A.D. 2003 *Heat Transfer Handbook* (Wiley)
[1185] Pestchanyi S., Pitts R.A. and Lehnen M. 2016 Simulation of divertor targets shielding during transients in ITER *Fusion Eng. Des.* **109–111** 141
[1186] Kapitza P.L. 1964 *Collected Papers of P. L. Kapitza* vol II (The Macmillan Company)
[1187] Vreugdenhil C.B. 1994 *Numerical Methods for Shallow Water Flow* (Springer)
[1188] Paschalidis K., Ratynskaia S., Lucco C.F. and Tolias P. 2023 Melt dynamics with MEMENTO—Code development and numerical benchmarks *Nucl. Mater. Energy* **37** 101545
[1189] Paschalidis K., Lucco C.F., Ratynskaia S., Tolias P. and Brandt L. 2024 The MEMENTO code for modeling of macroscopic melt motion in fusion devices *Fusion Eng. Des.* **206** 114603
[1190] Miloshevsky G.V. and Hassanein A. 2010 Modelling of Kelvin-Helmholtz instability and splashing of melt layers from plasma-facing components in tokamaks under plasma impact *Nucl. Fusion* **50** 115005
[1191] Miloshevsky G.V. and Hassanein A. 2011 Modeling of macroscopic melt layer splashing during plasma instabilities *J. Nucl. Mater.* **415** S74–S77
[1192] Miloshevsky G.V. and Hassanein A. 2014 Effects of plasma flow velocity on melt-layer splashing and erosion during plasma instabilities *Nucl. Fusion* **54** 033008
[1193] Vignitchouk L., Ratynskaia S., Pitts R.A. and Lehnen M. 2023 Beryllium melt instabilities and ejection during unmitigated current quenches in ITER *Nucl. Fusion* **63** 016004
[1194] Mesyats G.A. and Uimanov I.V. 2015 Hydrodynamics of the molten metal during the crater formation on the cathode surface in a vacuum arc *IEEE Trans. Plasma Sci.* **43** 2241
[1195] Kaufmann H.T.C., Cunha M.D., Benilov M.S., Hartmann W. and Wenzel N. 2017 Detailed numerical simulation of cathode spots in vacuum arcs: interplay of different mechanisms and ejection of droplets *J. Appl. Phys.* **122** 163303
[1196] Vignitchouk L., Khodak A., Ratynskaia S. and Kaganovich I.D. 2020 Numerical benchmark of transient pressure-driven metallic melt flows *Nucl. Mater. Energy* **25** 100826
[1197] Landman I.S. 2009 Tokamak code TOKES models and implementations *Technical Report* FZKA-7496 (Forschungszentrum Karlsruhe Karlruhe)
[1198] Hassanein A. and Konkashbaev I. 1999 Comprehensive physical models and simulation package for plasma/material interactions during plasma instabilities *J. Nucl. Mater.* **273** 326–33
[1199] Sizyuk V. and Hassanein A. 2010 Damage to nearby divertor components of ITER-like devices during giant ELMs and disruptions *Nucl. Fusion* **50** 115004
[1200] Sizyuk V. and Hassanein A. 2018 Comprehensive 3-D simulation and performance of ITER plasma facing and nearby components during transient events—Serious design issues *Phys. Plasmas* **25** 062508
[1201] Hassanein A. and Sizyuk V. 2021 Potential design problems for ITER fusion device *Sci. Rep.* **11** 2069
[1202] Ibano K., Kikuchi Y., Togo S., Ueda Y. and Takizuka T. 2019 Estimation of suppressed erosion by vapor shielding at Be and W walls under transient loads *Nucl. Fusion* **59** 076001
[1203] Paschalidis K., Ratynskaia S., Tolias P. and Pitts R. 2024 Impact of repetitive ELM transients on ITER divertor tungsten monoblock top surfaces *Nucl. Fusion* **64** 126022
[1204] Coburn J., Thoren E., Pitts R.A., Anand H., Lehnen M., Kos L., Brank M., Ratynskaia S. and Tolias P. 2020 First wall energy deposition during vertical displacement events on ITER *Phys. Scr.* **T171** 014076
[1205] Coburn J. *et al* 2021 Reassessing energy deposition for the ITER 5 MA vertical displacement event with an improved DINA model *Nucl. Mater. Energy* **28** 101016
[1206] Kos L., Pitts R.A., Simič G., Brank M., Anand H. and Arter W. 2019 SMITER: a field-line tracing environment for ITER *Fusion Eng. Des.* **146** 1796
[1207] Lukash V.E. and Khairutdinov R.R. 1996 Numerical simulation of halo currents in tokamaks *Plasma Phys. Rep.* **22** 91–96
[1208] Miyamoto S., Isayama A., Bandyopadhyay I., Jardin S.C., Khayrutdinov R.R., Lukash V.E., Kusama Y. and Sugihara M. 2014 Inter-code comparison benchmark between DINA and TSC for ITER disruption modelling *Nucl. Fusion* **54** 083002
[1209] Bartels H.-W. 1994 Impact of runaway electrons *Fusion Eng. Des.* **23** 323–8
[1210] Cardella A., Gorenflo H., Lodato A., Ioki K. and Raffray R. 2000 Effects of plasma disruption events on ITER first wall materials *J. Nucl. Mater.* **283–287** 1105
[1211] Maddaluno G., Maruccia G., Merola M. and Rollet S. 2003 Energy deposition and thermal effects of runaway electrons in ITER-FEAT plasma facing components *J. Nucl. Mater.* **313–316** 651–6
[1212] Bazylev B., Arnoux G., Brezinsek S., Igitkhanov Y., Lehnen M., Riccardo V. and Kiptily V. 2013 Modeling of the impact of runaway electrons on the ILW in JET *J. Nucl. Mater.* **438** S237–40
[1213] Allison J. *et al* 2016 Recent developments in GEANT4 *Nucl. Instrum. Methods Phys. Res.* A **835** 186–225
[1214] Miloshevsky G.V. and Hassanein A. 2014 Stability and erosion of melt layers developed on plasma facing components of tokamaks *Nucl. Fusion* **54** 043016
[1215] Zhang C. and Miloshevsky G. 2023 OpenFOAM modeling of beryllium melt motion and splashing from first wall in ITER *Phys. Scr.* **98** 095611